

The Telecommunications and Data Acquisition Progress Report 42-97

January-March 1989

E. C. Posner
Editor

(NASA-CR-185431) THE TELECOMMUNICATIONS AND
DATA ACQUISITION REPORT Progress Report,
Jan. - Mar. 1989 (Jet Propulsion Lab.)
394 p CSCL 17B

N89-27871
--THRU--
N89-27906
Unclas
0218055
G3/32

May 15, 1989



National Aeronautics and
Space Administration

Jet Propulsion Laboratory
California Institute of Technology
Pasadena, California

The Telecommunications and Data Acquisition Progress Report 42-97

January–March 1989

E. C. Posner
Editor

May 15, 1989



National Aeronautics and
Space Administration

Jet Propulsion Laboratory
California Institute of Technology
Pasadena, California

The research described in this publication was carried out by the Jet Propulsion Laboratory, California Institute of Technology, under a contract with the National Aeronautics and Space Administration.

Reference herein to any specific commercial product, process, or service by trade name, trademark, manufacturer, or otherwise, does not constitute or imply its endorsement by the United States Government or the Jet Propulsion Laboratory, California Institute of Technology.

Preface

This quarterly publication provides archival reports on developments in programs managed by JPL's Office of Telecommunications and Data Acquisition (TDA). In space communications, radio navigation, radio science, and ground-based radio and radar astronomy, it reports on activities of the Deep Space Network (DSN) and its associated Ground Communications Facility (GCF) in planning, in supporting research and technology, in implementation, and in operations. Also included is TDA-funded activity at JPL on data and information systems and reimbursable DSN work performed for other space agencies through NASA. The preceding work is all performed for NASA's Office of Space Operations (OSO). The TDA Office also performs work funded by two other NASA program offices through and with the cooperation of the Office of Space Operations. These are the Orbital Debris Radar Program (with the Office of Space Station) and 21st Century Communication Studies (with the Office of Exploration).

In the search for extraterrestrial intelligence (SETI), the *TDA Progress Report* reports on implementation and operations for searching the microwave spectrum. In solar system radar, it reports on the uses of the Goldstone Solar System Radar for scientific exploration of the planets, their rings and satellites, asteroids, and comets. In radio astronomy, the areas of support include spectroscopy, very long baseline interferometry, and astrometry. These three programs are performed for NASA's Office of Space Science and Applications (OSSA), with support by the Office of Space Operations for the station support time.

Finally, tasks funded under the JPL Director's Discretionary Fund and the Caltech President's Fund which involve the TDA Office are included.

This and each succeeding issue of the *TDA Progress Report* will present material in some, but not necessarily all, of the following categories:

OSO Tasks:

- DSN Advanced Systems
 - Tracking and Ground-Based Navigation
 - Communications, Spacecraft-Ground
 - Station Control and System Technology
 - Network Data Processing and Productivity
- DSN Systems Implementation
 - Capabilities for Existing Projects
 - Capabilities for New Projects
 - New Initiatives
 - Network Upgrade and Sustaining
- DSN Operations
 - Network Operations and Operations Support
 - Mission Interface and Support
 - TDA Program Management and Analysis
- Communications Implementation and Operations
- Data and Information Systems
- Flight-Ground Advanced Engineering

OSO Cooperative Tasks:

- Orbital Debris Radar Program
- 21st Century Communication Studies

OSSA Tasks:

Search for Extraterrestrial Intelligence
Goldstone Solar System Radar
Radio Astronomy

Discretionary Funded Tasks

Contents

OSO TASKS DSN Advanced Systems TRACKING AND GROUND-BASED NAVIGATION

Estimation and Filtering Techniques for High-Accuracy GPS Applications	1	51
S. M. Lichten NASA Code 310-10-61-84-04		
High-Precision Radiometric Tracking for Planetary Approach and Encounter in the Inner Solar System	21	52
C. S. Christensen, S. W. Thurman, J. M. Davidson, M. H. Finger, and W. M. Folkner NASA Code 310-10-63-88-01		
The Effect of Spatial and Temporal Wet-Troposphere Fluctuations on Connected Element Interferometry	47	53
C. D. Edwards NASA Code 310-10-60-87-02		
New Ion Trap for Atomic Frequency Standard Applications	58	54
J. D. Prestage, G. J. Dick, and L. Maleki NASA Code 310-10-62-16-00		
Operational Parameters for the Superconducting Cavity Maser	64	55
R. T. Wang, G. J. Dick, and D. M. Strayer NASA Code 310-10-62-34-00		
Operating and Environmental Characteristics of Sigma Tau Hydrogen Masers Used in the Very Long Baseline Array (VLBA)	72	56
T. K. Tucker NASA Code 310-10-62-85-00		
State-of-the-Art Fiber Optics for Short Distance Frequency Reference Distribution	81	57
G. Lutes and L. Primas NASA Code 310-10-62-16-00		
Stabilized Fiber-Optic Frequency Distribution System	88	58
L. E. Primas, G. F. Lutes, and R. L. Sydnor NASA Code 310-10-62-16-00		

COMMUNICATIONS, SPACECRAFT-GROUND

A New Method for Analysis of Limit Cycle Behavior of the NASA/JPL 70-Meter Antenna Axis Servos	98	59
R. E. Hill NASA Code 310-20-65-63-00		
Application of Optimal Control Theory to the Design of the NASA/JPL 70-Meter Antenna Axis Servos	112	60
L. S. Alvarez and J. Nickerson NASA Code 310-20-65-63-00		
Precision Pointing Compensation for DSN Antennas With Optical Distance Measuring Sensors	127	61
R. E. Scheid NASA Code 310-20-65-67-00		

The Effects of Atmospheric Turbulence on Precision Optical Measurements Used for Antenna-Pointing Compensation	141	52
N. Nerheim NASA Code 310-20-65-67-00		
A Multiflare Horn With 1-Megawatt Power Handling Capability	149	513
D. J. Hoppe NASA Code 310-20-64-86-02		
Thermal Measurements of Microwave Transmitter Feedhorn Window	156	514
R. M. Perez and D. J. Hoppe NASA Code 310-20-64-86-02		
A New Analysis of Beam-Waveguide Antennas Considering the Presence of the Enclosure	162	515
A. G. Cha NASA Code 310-20-65-86-02		
Multipurpose Exciter With Low Phase Noise	169	516
B. Conroy and D. Le NASA Code 310-20-64-22-00		
Software Package for Performing Experiments About the Convolutionally Encoded Voyager 1 Link	175	517
U. Cheng NASA Code 310-30-71-83-02		
The Use of Interleaving for Reducing Radio Loss in Trellis-Coded Modulation Systems	180	518
D. Divsalar and M. K. Simon NASA Code 310-30-41-83-04		
Performance of Concatenated Codes Using 8-Bit and 10-Bit Reed-Solomon Codes	194	519
F. Pollara and K.-M. Cheung NASA Code 310-30-71-83-02		
Decoding of 1/2-Rate (24, 12) Golay Codes	202	520
T.-K. Truong, I. S. Reed, and X. Yin NASA Code 310-30-70-87-02		
The Weight Distribution and Randomness of Linear Codes	208	521
K.-M. Cheung NASA Code 310-30-71-83-02		
Effective Amplifier Noise for an Optical Receiver Based on Linear Mode Avalanche Photodiodes	216	522
C.-C. Chen NASA Code 310-20-67-63-00		
A Visibility Characterization Program for Optical Communications Through the Atmosphere	221	523
K. Cowles NASA Code 310-20-67-88-03		
Options for Daytime Monitoring of Atmospheric Visibility in Optical Communications	226	524
D. Erickson and K. Cowles NASA Code 310-20-67-88-03		
Site Selection Criteria for the Optical Atmospheric Visibility Monitoring Telescopes	235	525
K. Cowles NASA Code 310-20-67-88-03		

A Novel Approach to a PPM-Modulated Frequency-Doubled Electro-Optic Cavity-Dumped Nd:YAG Laser	240	526
D. L. Robinson		
NASA Code 310-20-67-88-03		

DSN Systems Implementation CAPABILITIES FOR EXISTING PROJECTS

Microwave Time Delays for the X/S-Band Feed System at X-Band	248	527
J. Chen		
NASA Code 314-40-57-23-09		
DSN Radio Science System Design and Testing for Voyager-Neptune Encounter	252	528
N. C. Ham, T. A. Rebold, and J. F. Weese		
NASA Code 314-40-41-81-11		
Accuracy of Telemetry Signal Power Loss in a Filter as an Estimate for Telemetry Degradation	285	529
M. A. Koerner		
NASA Code 314-40-41-81-11		
The DSS-14 C-Band Exciter	292	530
D. R. Rowan		
NASA Code 314-30-64-70-05		

CAPABILITIES FOR NEW PROJECTS

Orthogonal Sets of Data Windows Constructed From Trigonometric Polynomials	300	531
C. A. Greenhall		
NASA Code 314-40-41-82-07		

NETWORK UPGRADE AND SUSTAINING

DSN 70-Meter Antenna Microwave Optics Design and Performance Improvements		
Part I: Design Optimization	306	532
D. A. Bathker and S. D. Slobin		
NASA Code 314-30-56-44-01		
DSN 70-Meter Antenna X- and S-Band Calibration Part I: Gain Measurements	314	533
P. H. Richter and S. D. Slobin		
NASA Code 314-40-41-81-27		
DSN 70-Meter Antenna X- and S-Band Calibration Part II: System Noise Temperature Measurements and Telecommunications Link Evaluation	352	534
S. D. Slobin and P. H. Richter		
NASA Code 314-40-41-81-27		

DSN Operations NETWORK OPERATIONS AND OPERATIONS SUPPORT

Reanalysis, Compatibility, and Correlation in Analysis of Modified Antenna Structures	367	535
R. Levy		
NASA Code 310-20-65-04-10		

Estimation and Filtering Techniques for High-Accuracy GPS Applications

S. M. Lichten

Tracking Systems and Applications Section

Techniques for determination of very precise orbits for satellites of the Global Positioning System (GPS) are currently being studied and demonstrated. These techniques can be used to make cm-accurate measurements of station locations relative to the geocenter, monitor earth orientation over timescales of hours, and provide tropospheric and clock delay calibrations during observations made with deep space radio antennas at sites where the GPS receivers have been collocated. For high-earth orbiters, meter-level knowledge of position will be available from GPS, while at low altitudes, sub-decimeter accuracy will be possible. Estimation of satellite orbits and other parameters such as ground station positions is carried out with a multi-satellite batch sequential pseudo-epoch state process noise filter. Both square-root information filtering (SRIF) and UD-factorized covariance filtering formulations are implemented in the software. A Bierman-modified Rauch-Tung-Striebel (BRTS) smoother runs in conjunction with the SRIF and UD filters to compute smoothed estimates and covariances. The filtering algorithms have been arranged to take advantage of sparse matrices and other characteristics of the GPS measurement scenarios. The filter includes unique error evaluation capabilities to assess effects from mismodeling. Process noise plays a key role in the orbit determination for stochastic behavior of transmitter/receiver clocks, atmosphere-induced delay fluctuations, and unmodeled satellite accelerations. The efficiency and accuracy of the SRIF and UD filter formulations are compared for GPS processing under a variety of conditions. With data from recent GPS experiments using the seven satellites currently in orbit, continental ground baselines have been measured with GPS and with VLBI which agree to within 2.5 cm over distances of 2000 km, corresponding to a relative baseline accuracy of better than 1.5 parts in 10^8 .

I. Introduction

The Global Positioning System (GPS) will consist of at least 21 satellites launched by the United States Department of Defense equally spaced in six orbit planes at about 20,000 km altitude. The satellite constellation, currently consisting of

seven operating satellites, is expected to be complete by the early 1990s. Many types of scientific applications are uniquely suited to the precise positioning capabilities provided by GPS. The relatively high precision, low cost, mobility, and convenience of GPS receivers make GPS-based positioning attractive. Dense GPS ground networks are already operating in North

America, South America, Europe, and Japan to monitor cm-level crustal motions in geologically active regions. Initial results from GPS experiments since 1985 are encouraging and suggest that accuracies may be obtained equaling those available from other generally more restrictive techniques, such as Very Long Baseline Interferometry (VLBI) or satellite laser ranging (SLR). When the GPS constellation is complete, a worldwide ground tracking network equipped with advanced GPS receivers will enable sub-decimeter low-earth orbiter position accuracies to be achieved for satellites such as TOPEX/Poseidon [1] and the Earth Observing System (Eos) platforms [2, 3]. This worldwide tracking network will also be used to monitor earth orientation over timescales of less than one day [4], improve relative station positions at the cm level, determine absolute station positions relative to the geocenter with accuracy of better than 5 cm [5], enable global time transfer at the nanosecond level, and provide precise calibrations of path delays from the ionosphere and troposphere. The improved knowledge of earth orientation, station positions, time transfer, and media calibration will be used at NASA's Deep Space Network (DSN) tracking stations in support of navigation for planetary exploration missions. The GPS-based tracking network will also provide a meter-level orbit determination capability at the DSN for certain high-earth orbiters [6].

In this article, an overview of GPS signal structure and positioning techniques will be presented. A section describing the filter/smoothing software developed and used at the Jet Propulsion Laboratory (JPL) for GPS orbit determination and parameter estimation will highlight some of the filtering techniques and algorithms which are especially useful in GPS-based least-squares parameter estimation. Recent high-accuracy GPS orbit and ground baseline results will also be presented to demonstrate the feasibility and potential of high-accuracy GPS-based navigation and positioning applications.

II. GPS Signal Structure and Positioning Techniques

The Global Positioning System is designed so that typically four to eight GPS satellites are visible simultaneously at any time from most locations in the world. The GPS satellites transmit down towards the Earth carrier signals at two L-band frequencies (1.227 and 1.575 GHz), which are modulated by a pseudorandom noise code, the P-code (Fig. 1). The two frequencies enable the user to remove most of the signal delay originating in the ionosphere. When four satellites are in view, the user equipped with a receiver which can receive the GPS P-code has enough information to solve for the user position and the user clock offset from GPS time. This is the simplest and most basic GPS positioning technique, often called *direct GPS tracking* (Fig. 2a). A second code, the coarse acquisition

(C/A) code meant for acquiring and locking onto the GPS signal, can also be used for user positioning, but with somewhat degraded accuracy compared to the P-code. Part of the navigation message broadcast down on the P-code includes the ephemeris for each satellite and the clock offset of each satellite from the reference GPS time. The accuracy of the broadcast ephemeris (about 10–20 m) and the clock information currently limit user positioning accuracy to about 10–15 m with real-time techniques using the P-code. The P-code observable is often called a *pseudorange* since it measures the range to the satellite but includes offsets between the transmitter and receiver clocks.

To improve positioning accuracy through cancellation of clock errors and partial cancellation of ephemeris errors, *differential GPS tracking* techniques are employed (Fig. 2b). Instantaneous P-code positioning accuracy of 1–3 m is possible with differential GPS tracking. For certain military applications as well as for some real-time applications such as an earth orbiter docking with the space station, accuracies obtainable with instantaneous direct or differential GPS tracking are sufficient.

There are several strategies for reducing the GPS error budget further for high-accuracy applications, which include cm-level station determination, meter-level high-earth orbit estimation, cm-level earth orientation monitoring, and sub-nanosecond time transfer. The high-precision strategies include use of precise GPS carrier phase tracking and averaging over several hours or more, use of dynamical information to reduce the number of degrees of freedom, and estimation of improved GPS orbits and clocks along with determination of other estimated parameters from the tracking data. The GPS carrier phase provides a very precise measure of *range change*, but is ambiguous in absolute range to an integer number of carrier wavelengths. Measurement noise with modern GPS receivers over five-minute intervals is typically several mm with the dual frequency combined carrier signal (to remove ionospheric effects). If the satellites are tracked for several hours, the signatures in the data enable estimation of the integer cycle ambiguities along with the other parameters. A more powerful approach is to process the P-code pseudorange, which can be one or two (or more) orders of magnitude noisier but provides a measure of absolute range, along with the carrier phase. This constrains the clocks and carrier phase range ambiguities so that the solutions are strengthened considerably.

Most commercial receivers provide pseudorange with measurement scatter of 60–200 cm over five-minute averaging intervals. Most of this scatter is due to multipath characteristics of the ground site and antenna. The Rogue receiver was designed at JPL with the goal of substantially reducing pseudorange measurement scatter. The Rogue, which features

digital baseband electronics, can track up to eight satellites simultaneously with dual-frequency carrier phase and pseudorange. A new antenna design shows considerable promise in reducing P-code multipath by an order of magnitude (Fig. 3). This design includes a drooped cross-dipole antenna with a non-absorbing backplane which has concentric choke rings machined from an aluminum disk spaced to maximally eliminate multipath signals. When GPS equipment such as the Rogue receiver and its new antenna design are routinely used in the field, a substantial improvement in tracking performance and system accuracy is expected.

III. Formulation of the Least-Squares Problem

As discussed above, to improve GPS-based tracking performance, GPS carrier phase and pseudorange can be received over a period of hours and parameters then estimated using dynamical model information. At JPL, the GPS orbit determination problem is reduced to a system of linear equations which can be solved with a batch-sequential process noise filter. This approach requires a moderately accurate nominal model for the GPS orbits and station locations so that only the linear terms in an expansion for deviations from this nominal model need be retained. It has been found that initial GPS epoch states should be accurate to about 1 km and receiver locations should be known to within a few hundred meters.¹ The initial GPS epoch states are numerically integrated with a multi-step Adams method² in the J2000 inertial reference frame [7]. Variational partial derivatives are computed relating the change in satellite position and velocity with respect to changes in the initial epoch states and with respect to force parameters. The Earth's gravity field is expressed in terms of a spherical harmonic expansion, and the gravitational effects of the sun, moon, and planets are represented as due to point masses. The JPL software includes the ROCK4 [8-10] GPS solar radiation pressure model, allows for estimation of arbitrary unmodeled accelerations on the satellite, and includes impulsive motor burns when needed to model GPS maneuvers. Typically the broadcast ephemeris or a more precise ephemeris produced by the Naval Surface Weapons Center (NSWC) is used for the nominal trajectory.

Precise earth models are used both to model the measurements and to compute the partials for measurements with

respect to model parameters [11] as a function of time. The algorithms used are based on ones developed for Very Long Baseline Interferometry (VLBI), an extremely accurate astrometric technique which uses radio astronomical measurements of fixed point sources (quasars) [12] for deep space navigation and determination of ground baselines and earth orientation. The models include UT1-UTC, polar motion, nutation, precession, solid earth tides, ocean tidal loading, general relativistic clock corrections, and the Lanyi tropospheric delay mapping function [13], which relates the tropospheric delay at various elevations to its value at the zenith. Through the chain rule, the partials are referred to the GPS epoch states. The GIPSY (GPS Inferred Positioning SYstem) software is used for GPS data processing. The OASIS (Orbit Analysis and SIMulation Software) software, developed at JPL^{3,4} for covariance analysis and simulations, shares most programs with GIPSY but has a streamlined, simplified models module.

The difference, z , between each observation and its computed predicted value from the nominal model is calculated. The measurement equation is

$$z = A_x x + A_p p + A_y y + \nu \quad (1)$$

where A is a row from the matrix of measurement partials, x is the satellite state vector (usually three position and three velocity components), p is the vector of process noise parameters, y is a vector of bias (constant) parameters, and ν is a zero mean white noise with $\langle \nu^2 \rangle$ equal to the measurement noise variance. The OASIS/GIPSY filter is a multi-satellite program, so each satellite in turn has its associated state vector $= (x^T, p^T, y^T)^T$, and these are ordered one after the other in the total state vector X , with common parameters (such as station locations) placed at the end. The measurements are combined and an optimal least-squares solution for the estimated parameters determined in the filter. The filter divides the measurements into finite time intervals known as *batches*. Within each batch, all process noise parameters—parameters which are modeled as stochastically time-varying—are assumed to be piecewise constant. After the filter processes the measurements in a given batch, to update the estimates and covariance for the parameters a *time update* is performed to fold in the effects of process noise. Measurements are then processed in the next batch, and so on. After filtering is completed, a smoother works recursively backwards in time to update op-

¹If the nominal model is not accurate enough, the output from the filter can be used as the new nominal model and the solution can be iterated.

²F. T. Krough, "Changing Stepsize in the Integration of Differential Equations Using Modified Differences," JPL Section 914 TM No. 312 (internal document), March 20, 1973.

³S. C. Wu, W. I. Bertiger, J. S. Border, S. M. Lichten, R. F. Sunseri, B. G. Williams, and J. T. Wu, *OASIS User's Guide, V. 1.0*, JPL D-3138 (internal document), April 1, 1986.

⁴S. C. Wu, W. I. Bertiger, J. S. Border, S. M. Lichten, R. F. Sunseri, B. G. Williams, P. J. Wolff, and J. T. Wu, *OASIS Mathematical Description, V. 1.0*, JPL D-3139 (internal document), April 1, 1986.

timally computed estimates and covariances when the presence of process noise requires it.

Both the OASIS and GIPSY software use the same filter for estimate/covariance computation. The filter offers the user the choice of two different mechanizations: the square-root information filter (SRIF), or the UD-factorized filter. Both mechanizations are based on the algorithms developed in [14] by Bierman. The smoother is formulated in terms of UD backwards pass recursions and works with output from either the SRIF or UD filter. Both the filter and the smoother make heavy use of the Bierman Estimation Subroutine Library (ESL) [15].

A. UD Filter Formulation for Measurement Processing

The conventional Kalman filter has a measurement update mechanization based on the *covariance matrix*, \mathbf{P} . Let the estimate vector and covariance matrix be \mathbf{X} and \mathbf{P} , with the convention that \sim denotes quantities before measurement updating and $\hat{}$ denotes quantities after the measurement update. Then

$$\begin{aligned}\hat{\mathbf{X}} &= \tilde{\mathbf{X}} + \hat{\mathbf{K}} (z - \mathbf{A}\tilde{\mathbf{X}}) \\ &= \tilde{\mathbf{X}} + (\hat{\mathbf{G}}/\alpha) (z - \mathbf{A}\tilde{\mathbf{X}}) \\ \hat{\mathbf{P}} &= \tilde{\mathbf{P}} - (1/\alpha) \hat{\mathbf{G}}\hat{\mathbf{G}}^T\end{aligned}\quad (2)$$

where \mathbf{A} is a row vector of measurement partials, \mathbf{G} is the *normalized* Kalman gain vector, which is related to the unnormalized Kalman filter gain, \mathbf{K} , by

$$\hat{\mathbf{G}} = \tilde{\mathbf{P}}\mathbf{A}^T = \alpha\hat{\mathbf{K}}\quad (3)$$

and $\alpha = \tilde{\mathbf{P}}\mathbf{A}^T\mathbf{A} + r$ is the innovations, or prediction residual variance. The measurement variance is r . It is assumed here that the vector of observation errors, ν_i , is described by $E(\nu_i) = 0$, $E(\nu\nu^T) = \mathbf{P}_\nu$, for $i = 1, \dots, m$, and $\mathbf{P}_\nu = \text{Diag}(r_1, \dots, r_m)$ for the measurement variances. In the case of correlated measurement noise, whitening procedures can be used to uncouple the measurements and yield diagonal \mathbf{P}_ν [14], so the formulas presented here are valid without loss of generality.

The conventional Kalman measurement update (Eq. 2) has been shown to be sensitive to computer roundoff with sometimes catastrophic loss of accuracy from imperfect cancellation when positive quantities are differenced. Conventional Kalman algorithms have also exhibited sensitivity to numerical ill-conditioning [14, 16]. A comprehensive comparison of conventional, stabilized, and factorized formulations of the Kalman filter for a spacecraft navigation problem [16] demonstrated convincingly the superior numerical characteristics of

the factorized Kalman filter approach. Ill-conditioning with unfactorized Kalman filters is sometimes attributed to large a priori state uncertainties and relatively small data covariances. These very attributes, however, typify many GPS earth orbiter problems relying on the GPS carrier phase data type: the carrier phase data variance is on the order of 10^{-5} m^2 while the a priori position covariance could be between 1 and 10^6 m^2 . Another filter characteristic associated with ill-conditioning is a very low level of process noise. However, low process noise levels are common in high-precision GPS applications when stochastic models are used to model slowly varying tropospheric delay variations, GPS force parameters, and stable hydrogen maser station clocks. Near-singular covariance matrices are sometimes encountered in GPS orbit filtering because of different receiver characteristics. At some sites, GPS receivers were operated side by side in experiments which took place in 1985 where one receiver was capable of producing GPS carrier phase and P-code pseudorange and the other could only produce carrier phase data (codeless). The clock offset for the code receiver could be determined much more precisely than for the phase-only receiver: the clock variances were typically $2.5 \times 10^{-7} \mu\text{sec}^2$ for the code receivers while codeless receiver clock variances are typically $10^4 \mu\text{sec}^2$. Furthermore, since these clock parameters are often modeled with process noise, their variances vary considerably in the course of a run as satellites move through different geometries with good and bad observability. With GPS scenarios, severe numerical difficulties were sometimes encountered when mapping orbits and baselines to various coordinate systems when using the unfactored covariance matrix; with factored or square-root form, however, these mappings were stabilized and no numerical problems have been noted. Experience at JPL with deep space tracking estimation software has also resulted in complete conversion to factorized (or square-root) Kalman filter mechanizations in the orbit determination program used for missions involving such spacecraft as the Voyager, Magellan, and Galileo interplanetary probes. With efficient algorithms [14–16], there is only an insignificant penalty in computation speed when using factorized instead of conventional Kalman filters.

An extremely stable factorized version of the Kalman measurement update equations exists for the \mathbf{U} and \mathbf{D} factors of the covariance matrix, where \mathbf{U} is an upper triangular matrix and \mathbf{D} is a diagonal matrix:

$$\mathbf{P} = \mathbf{U}\mathbf{D}\mathbf{U}^T\quad (4)$$

The method used is an upper triangular UD Cholesky square-root-free factorization with the geometric form reduction described in [14]. In order to save storage, \mathbf{U} is vector stored, and the factorization is chosen so that \mathbf{U} has unity on its diagonals and \mathbf{D} can be stored in those locations. It is con-

venient to store the estimates, \mathbf{X} , in the last column appended on the end of the UD matrix.

With the UD factorization, the measurement update can be expressed as

$$\hat{\mathbf{P}} = \hat{\mathbf{U}}\hat{\mathbf{D}}\hat{\mathbf{U}}^T = \tilde{\mathbf{U}}(\tilde{\mathbf{D}} - c\mathbf{V}\mathbf{V}^T)\tilde{\mathbf{U}}^T \quad (5)$$

where

$$\mathbf{V} = \tilde{\mathbf{D}}\mathbf{F}$$

$$\mathbf{F} = (\mathbf{A}\tilde{\mathbf{U}})^T$$

The scalar $c = 1/\alpha = 1/(r + \mathbf{V}^T\mathbf{F})$ is computed from the prior covariance and the current measurement noise. Thus, the normalized Kalman gain can be expressed in terms of the UD factors as

$$\hat{\mathbf{G}} = \tilde{\mathbf{U}}\tilde{\mathbf{D}}\tilde{\mathbf{U}}^T\mathbf{A}^T = \tilde{\mathbf{U}}\mathbf{V} \quad (6)$$

The measurement update algorithm used in the OASIS/GIPSY filter is the Bierman-Carlson-Gentleman update [14, 16, 17]. This algorithm avoids explicit differencing when computing updated diagonals because explicit differencing for these terms makes the update prone to loss of accuracy due to imperfect cancellation, leading to negative diagonals in extreme cases.

The UD filter processes measurements one at a time. Before updating, each measurement is tested for consistency with the prior estimates and covariance. If the measurement fails the test, it is considered to be an outlier and not processed. The prediction residual must satisfy the criterion

$$(z - \mathbf{A}\tilde{\mathbf{X}})^2 \leq TST\alpha \quad (7)$$

where TST is the level of acceptance and α is the innovations variance defined above. For example, $TST = 9$ is a $3\text{-}\sigma$ test. If Eq. 7 is satisfied, the estimates and covariance are updated.

B. SRIF Formulation for Measurement Processing

The SRIF data equations are

$$\tilde{\mathbf{z}} = \tilde{\mathbf{R}}\tilde{\mathbf{X}} + \tilde{\mathbf{v}} \quad (8)$$

where

$$\tilde{\mathbf{P}} = \tilde{\mathbf{R}}^{-1}\tilde{\mathbf{R}}^{-T}$$

and estimates are retrieved as

$$\mathbf{X} = \mathbf{R}^{-1}\mathbf{z}$$

The square-root information array $[\mathbf{R}:\mathbf{z}]$ is analogous to the UD-factored covariance with estimates in the last column of the UD matrix. The square-root information matrix, \mathbf{R} , like the \mathbf{U} matrix, is upper triangular and vector stored. Note that for the SRIF, the noise \mathbf{v} is zero mean as before but has unit covariance, so \mathbf{z} and \mathbf{v} have been normalized by the measurement noise.⁵ The SRIF data processing algorithm in the OASIS/GIPSY software follows [14] and [18] in applying orthogonal Householder transformations, \mathbf{T}_H , to an augmented information array

$$\mathbf{T}_H \begin{bmatrix} \tilde{\mathbf{R}} & \tilde{\mathbf{z}} \\ \mathbf{A} & \mathbf{z} \end{bmatrix} = \begin{bmatrix} \hat{\mathbf{R}} & \hat{\mathbf{z}} \\ \mathbf{0} & \mathbf{e} \end{bmatrix} \quad (9)$$

The measurement partials (normalized) are in \mathbf{A} , and \mathbf{e} contains information about the post-fit residuals. The matrix \mathbf{A} ordinarily holds a subset of the data, since on some computers, available memory or disk space limits how many measurements can be processed at once. When process noise is included, the measurements to be processed together in a buffer must lie in the same time batch. The i th row in \mathbf{A} contains the i th measurement in this measurement buffer, so when the i th elementary Householder transformation is applied, only the i th row of \mathbf{R} and all columns to the right of column i in \mathbf{A} are affected. The Householder transformation, as implemented in the filter, maintains the upper triangularity of the \mathbf{R} matrix [14, 18].

The effect of the size of the measurement buffer on the speed of the SRIF on a DEC Microvax II is shown in Fig. 4. Beyond a buffer of about 50 measurements, little increase in speed is seen. However, for very small buffer sizes, the Householder transformation becomes inefficient. The reason for this is that, based on the operation counts in [14], for additions and multiplications the ratio of (overhead)/(total processing time) in processing each measurement buffer with M_b measurements is $3/(3+2M_b)$ and $1/(1+2M_b)$, respectively.

There is also an additional amount of overhead from the N square roots, N divisions, $2N$ additions, and N multiplications needed for each buffer being processed, where N is the number of parameters estimated. The penalty from these extra operations depends somewhat on the relative CPU speed of these

⁵To distinguish these normalized quantities from the unnormalized ones from the discussion of the UD filter, we represent them without italics.

operations. The case shown in Fig. 4 corresponds to 3666 measurements with 192 estimated parameters for a SRIF running on a DEC Microvax, where square roots and divisions are about 8 and 1.5 times as expensive as additions or multiplications, respectively. The composite ratio of overhead to processing time was calculated and would be 60 percent for this run with $M_b = 1$, and less than 1 percent for $M_b = 100$, in rough agreement with the curve in Fig. 4.

C. Process Noise

Stochastic processes in the GPS orbit software are assumed to be piecewise constant over a specified batch interval. Currently, first-order Gauss-Markov random processes models are used. At the end of a batch, a process noise time update adds noise to the covariance matrix and thus causes the time-varying behavior of the stochastic parameters. The process noise time update for the j th batch maps the estimates and covariance for the stochastic parameters into the batch $j+1$:

$$\begin{aligned} \mathbf{x}_{j+1} &= \mathbf{x}_j + \Phi_p(j)\mathbf{p}_j \\ \mathbf{p}_{j+1} &= \mathbf{M}_j\mathbf{p}_j + \mathbf{w}_j \\ \mathbf{P}_{j+1} &= \Phi\mathbf{P}_j\Phi^T + \mathbf{Q} \end{aligned} \quad (10)$$

where

$$\Phi = \begin{bmatrix} \mathbf{I}_x & \Phi_p(j) & 0 \\ 0 & \mathbf{M}_j & 0 \\ 0 & 0 & \mathbf{I}_y \end{bmatrix}$$

and, as in Eq. (1), the estimated parameters are partitioned into satellite states, process noise parameters, and bias (constant) parameters

$$\mathbf{X} = \begin{bmatrix} \mathbf{x} \\ \mathbf{p} \\ \mathbf{y} \end{bmatrix} \quad (11)$$

\mathbf{M} is a diagonal process noise mapping matrix. The process noise \mathbf{w}_j is a random process with zero mean and for the i th process noise parameter,

$$E(w_{ij}w_{ik}) = q_{ij}\delta_{jk} \quad (12)$$

with the covariance matrix \mathbf{Q} zero except for diagonal elements q_i in the j th batch, and δ_{jk} is the Kronecker delta function. The diagonal entries of \mathbf{M} are given by

$$m_{ij} = \exp [-(t_{j+1} - t_j)/\tau_{ij}] \quad (13)$$

where t_j is the start time for the j th batch and τ_{ij} is the time constant for the i th stochastic parameter at the j th batch. The corresponding diagonal entry in the matrix \mathbf{Q} is

$$q_{ij} = (1 - m_{ij}^2)\sigma_{iss}^2 \quad (14)$$

where σ_{iss} , the steady-state sigma for the i th stochastic parameter, is the noise level which would be reached if the system were left undisturbed for a time much greater than τ .⁶ For white process noise, $\tau = 0$, $m = 0$, and as can be seen in Eq. (10), the filter resets the covariance for the process noise parameters at the end of each batch, including zeroing of off-diagonal terms and putting in q for the variance on the diagonal. The opposite limiting case is the random walk: here both σ_{ss} and τ are unbounded ($\tau = \infty$) and a steady-state is never reached. For the random walk, \mathbf{M} is equal to the identity matrix, and it is the rate of change of the process noise covariance, $\dot{\mathbf{q}} = d\mathbf{q}/dt = \Delta\mathbf{q}/\Delta t$, which characterizes the process, where Δt is the batch size and $\Delta\mathbf{q}$ is the amount of noise added per batch. The Allan variance [19], $\sigma_A^2(\Delta t)$, which is often used to characterize clock and atmospheric fluctuations [12], can be defined in terms of $\dot{\mathbf{q}}$:

$$\sigma_A^2(\Delta t) = \dot{\mathbf{q}}/\Delta t \text{ (random walk)} \quad (15)$$

Thus a random walk process has a slope of -1 for the log-log relation between the Allan variance and Δt .

The matrix $\Phi_p(j)$, represents the *deterministic* portion of the time update and is nonzero only when there is a dynamic coupling between process noise parameters and satellite states. \mathbf{M} contains the *stochastic* portion of the time update. \mathbf{x}_j represents the *pseudo-epoch state* of the spacecraft [14]. The *current state*, $\mathbf{x}(t)$, would be mapped according to

$$\begin{bmatrix} \mathbf{x}(t) \\ \mathbf{p}(t) \\ \mathbf{y} \end{bmatrix}_{j+1} = \begin{bmatrix} \Phi_x(t_{j+1}, t_j) & \Phi_p(t_{j+1}, t_j) & \Phi_y(t_{j+1}, t_j) \\ 0 & \mathbf{M}_j & 0 \\ 0 & 0 & \mathbf{I}_y \end{bmatrix} \begin{bmatrix} \mathbf{x}(t) \\ \mathbf{p}(t) \\ \mathbf{y} \end{bmatrix}_j + \begin{bmatrix} 0 \\ \mathbf{w} \\ 0 \end{bmatrix} \quad (16)$$

The *pseudo-epoch state*, \mathbf{x}_j , is defined relative to the current state, $\mathbf{x}(t)$, from

⁶Although σ_{ss} and τ can vary with time, the subscript j has been left off σ_{ss} for simplicity of notation.

$$\mathbf{x}(t_j) = \Phi_x(t_j, t_0)\mathbf{x}_j + \Phi_y(t_j, t_0)\mathbf{y} \quad (17)$$

$$\mathbf{x}_j = \Phi_x^{-1}(t_j, t_0) [\mathbf{x}(t_j) - \Phi_y(t_j, t_0)\mathbf{y}]$$

With this definition, if the pseudo-epoch state is used in the filter instead of the current state, the time update of Eq. (10) results:

$$\begin{bmatrix} \mathbf{x} \\ \mathbf{p} \\ \mathbf{y} \end{bmatrix}_{j+1} = \begin{bmatrix} \mathbf{I}_x & \Phi_p(j) & 0 \\ 0 & \mathbf{M}_j & 0 \\ 0 & 0 & \mathbf{I}_y \end{bmatrix} \begin{bmatrix} \mathbf{x} \\ \mathbf{p} \\ \mathbf{y} \end{bmatrix}_j + \begin{bmatrix} 0 \\ \mathbf{w} \\ 0 \end{bmatrix}_j \quad (18)$$

The mapping matrix $\Phi_p(j)$ used in the pseudo-epoch state filter is calculated from the variational partials:

$$\begin{aligned} \Phi_p(j) &= [\Phi_x(t_{j+1}, t_0)]^{-1} \Phi_p(t_{j+1}, t_0) \\ &\quad - [\Phi_x(t_j, t_0)]^{-1} \Phi_p(t_j, t_0) = \left. \frac{\partial \mathbf{x}_{j+1}}{\partial \mathbf{p}_j} \right|_{\mathbf{p}_j=0} \quad (19) \end{aligned}$$

The use of the pseudo-epoch state formulation saves considerable computation in the filter and smoother since the UD time update is accomplished with sparse matrix multiply routines. When no dynamic stochastic parameters are present, the pseudo-epoch state is the same as the true epoch state. Because of the pseudo-epoch state formulation, most of the mapping matrix is filled with zeros or ones (see Eq. 18). The state vector \mathbf{X} is arranged so that the satellite state for each satellite and the associated stochastic parameters are grouped at the top. A subroutine loop performs the sparse matrix multiply to update the \mathbf{U} matrix and estimates for each spacecraft in turn, making efficient use of knowledge of the implicit zeros and ones for the deterministic mapping. After the deterministic Φ_p mappings for all the satellite are finished, the stochastic \mathbf{M} mappings are performed to update the process noise states. The UD stochastic update is accomplished with the Bierman-Thornton one-at-a-time update [14, 17, 20]. The deterministic portion of the SRIF time update also takes advantage of the sparse mapping matrix structure. The stochastic SRIF time update uses Givens transformations which exploit the upper triangular structure of the \mathbf{R} matrix.

Both the UD and SRIF time updates use subroutines of the ESL for most of the matrix operations. The SRIF stochastic update includes calculation of the smooth gain arrays which must be saved if smoothing will be done later. For the UD filter, these smooth gains are calculated in a separate routine which can be skipped if smoothing will not be needed.

D. Smoothing

The OASIS/GIPSY smoother incorporates Bierman's modification of the Rauch-Tung-Streibel (RTS) smoother [21], known as the BRTS, including the new reformulation of Bierman's original UD smoother [22, 23]. The smoother algorithm makes use of a decomposition of the linear model dynamical equations so that rank-1 and rank-2 matrix modifications can be substituted for more complex (and costly) covariance updates. The smoothing algorithm uses the UD formulation, is based on numerically stable Givens reflections, and runs "backwards" in time using a recursive method for generating smoothed estimates and smoothed UD factors. The last (terminal) filter UD or SRIF matrix is used to initialize the smoother, so in the case of the SRIF, the terminal square-root information array is inverted to UD form. The smoother has considerable flexibility in the handling of singular and near-singular covariance matrices. As with the deterministic and stochastic filter time updates, the OASIS/GIPSY implementation of Bierman's smoothing algorithm takes advantage of the sparse matrix structure which typifies GPS scenarios and orders parameters to minimize CPU cycles, memory requirements, and disk storage.

E. Evaluation of Filter Mismodeling

The OASIS/GIPSY filter has a number of options for evaluating filter models used for parameter estimation and covariance analysis. These include *consider analysis* for both the UD and SRIF formulations, and a unique *evaluation mode* available only with the UD filter.

Consider parameters are usually bias parameters not included in the estimated parameter state vector. From the measurement partials, the sensitivity of estimated parameters to these considered (not estimated) parameters can be computed in the filter. There are several reasons for not estimating a parameter: (1) certain parameters, such as fiducial station locations, may be held fixed in order to define a reference frame and/or length scale; (2) it may be computationally impossible to adjust certain parameters, such as all the coefficients in a gravity field; (3) a physical effect cannot be modeled adequately to produce a reliable estimate, yet it is still desirable to calculate the penalty for leaving it out of the filter model (state vector). By including the effects of considered parameters, the ordinarily overly optimistic computed covariance for the estimated parameters is degraded somewhat depending on the sensitivities, and a more realistic covariance may result.

Let \mathbf{y}_c be the unestimated considered parameters with measurement partials \mathbf{A}_c . Then the sensitivity is [14]

$$\mathbf{S} = \frac{\partial(\mathbf{X} - \hat{\mathbf{X}})}{\partial \mathbf{y}_c} = -\hat{\mathbf{P}}\mathbf{A}^T\mathbf{P}_v^{-1}\mathbf{A}_c \quad (20)$$

where the \sim denotes the quantities computed from the filter measurement and time updates without including the effects of the y_c parameters, and P_v is the measurement noise covariance matrix. The *consider covariance*, which includes effects from both estimated and considered parameters, is defined as

$$P_{con} = \hat{P} + SP_c S^T \quad (21)$$

where P_c is the covariance matrix for the considered (unadjusted) parameters.

Both the SRIF and UD filter implementations in the GIPSY/OASIS software can handle any parameter as estimated or considered. However, only the UD filter has more general filter error evaluation capabilities, of which consider analysis is one type. The general error evaluation algorithm [24] permits evaluation of the effects of designing a filter without the correct data noise, a priori covariance, data weights, or process noise model. A *truth model* and filter model are specified, and the evaluation mode of the UD filter allows the user to assess the effects of mismodeling on filter accuracy. Under real conditions, the truth model is not actually known, so a filter analyst usually tries to look at a range of possible truth models to see if, over a range of reasonable truth models, the filter results are especially sensitive to any parts of the filtering strategy being used. The goal is to design a filter model which is reasonably accurate based on available information about the problem, but which is also stable so that the results will not be strongly degraded if slightly incorrect filtering parameters are used. In [25] is an example of a comprehensive filter evaluation which studied the use of stochastic solar radiation pressure models for GPS orbit determination. A number of process noise inputs were identified for which the filter showed little sensitivity to mismodeling. These process noise models were later used successfully for estimation of small GPS accelerations over arcs of several weeks (also see Section IV of this article).

In the evaluation mode, the filter uses suboptimal Kalman gains saved in an evaluation file from an earlier filter which is run purposely with what is believed to be an incorrect model in order to generate suboptimal gains. The measurement update is expressed as

$$\hat{P} = (I - \hat{K}A)\tilde{P} + \alpha(K - \hat{K})(K - \hat{K})^T \quad (22)$$

where the *optimal* Kalman gain is \hat{K} and the arbitrary gain from the evaluation file is K . Let $\tilde{P} = (I - \hat{K}A)\tilde{P}$ and $\tilde{U}\tilde{D}\tilde{U}^T = \tilde{P}$. Then \hat{K} and α are computed using the measurement update formulas in Eqs. (2-4), and the vector $\lambda = K - \hat{K}$ is formed. A rank-1 update computes the UD covariance factors:

$$\hat{U}\hat{D}\hat{U}^T = \tilde{U}\tilde{D}\tilde{U}^T + \alpha\lambda\lambda^T \quad (23)$$

The time update in the evaluation mode follows the same form as the original filter time update except that the original filter stochastic time constants and process noise sigmas are replaced with the evaluation mode time constants and process noise sigmas.

F. Performance Comparisons Between the UD Filter and the SRIF

The dual-filter option in the OASIS/GIPSY software facilitates comparisons between the UD and SRIF programs. Many tests have been conducted to examine the numerical stability and speed of these two filters. At this time, they appear to be equally stable and numerically sound. However, there can be a substantial difference in processing speed, depending on the type of problem being filtered. Our experience with timing the UD and SRIF algorithms matches very closely the predictions in [14]. The SRIF measurement processor is about 33 percent faster than the UD measurement processor. For time updates, however, the UD algorithm is substantially faster when smoothing gains are not needed. If smoothing gains are computed in the filter for later use in smoothing, then once again the SRIF runs faster. Smoothing itself takes essentially the same amount of time whether the UD or SRIF filter was run first. For any specific filter run, the comparison between SRIF and UD run times depends on the number of stochastic parameters, the number of batch intervals, and the number of measurements. For typical GPS orbit estimation scenarios involving the geodetic and low-earth orbiter applications described below, the SRIF is as much as 50 percent faster than the UD filter for complicated cases requiring smoothing. If the sensitivities in a consider analysis are needed for stochastically estimated parameters, the sensitivity matrix must also be smoothed. Sensitivity smoothing in the OASIS/GIPSY filter occurs in a natural and efficient way with the SRIF, while the UD sensitivity smoothing is usually substantially slower. The UD filter is about 25 percent faster than the SRIF in simple runs when no smoothing is needed.

With the UD formulation in OASIS/GIPSY, the analyst is permitted to have the variance of a parameter equal zero. In certain analyses, such as a case where it is desired to constrain a parameter to a specific value, this capability can be useful. On the other hand, the SRIF formulation permits zeros on the diagonals of the information array, corresponding to an infinitely large covariance. As discussed above, the SRIF tends to be faster in situations when many measurements are being processed or when smoothing is needed. Only the UD filter, however, has an *evaluation mode* for studying filter mismodeling. The decision to fully implement both filter mechanizations in the OASIS/GIPSY software allows the analyst full

flexibility in the selection of the most efficient and appropriate filter for each specific situation.

IV. GPS Positioning Applications

Even though only seven GPS satellites are currently operating, high-accuracy geodetic results have already been obtained. In addition to the geodetic studies carried out with the existing limited set of satellites, numerous covariance analyses and simulations have been conducted in preparation for the full 21-satellite constellation expected to be operational in the early 1990s. A number of new approaches to high-accuracy earth-orbiter and ground positioning applications show great promise for demanding projects of the future such as TOPEX and Eos. In this section, a sampling of these results and new tracking techniques will be presented, with emphasis on how the orbit determination and filtering strategy play a role in GPS-based positioning and navigation.

A. Ground Station Positioning Results

A number of GPS campaigns and experiments took place in 1984 and 1985 [26, 27], in which typically 5–10 GPS receivers were located at sites of geodetic or geophysical interest. Baseline results showing precision and accuracy of 2–4 parts in 10^7 relative to baseline length were initially reported [27–29], with quality of the baselines generally assessed by comparison to VLBI and SLR, and by daily repeatability of the solutions. To reach these accuracies, GPS orbits were improved through estimation, generally with single-batch least-squares fits with doubly differenced dual-frequency carrier phase. Double differencing is a technique for cancellation of GPS and station clock errors which requires simultaneous mutual visibility. In most, but not all of these cases, fiducial or reference ground sites were held fixed where GPS receivers were collocated with very precisely determined VLBI antennas in order to establish a reference frame and length scale. Without orbit improvement, GPS positioning results obtained using broadcast ephemerides only were, in most cases, about an order of magnitude worse.

In [30], results were presented from one of the 1985 GPS experiments showing accuracy and daily repeatability of 1–2 parts in 10^7 for baselines up to 313 km. This improvement was due to a number of factors, including combining more than one eight-hour daily pass for orbit estimation, bias fixing, and an improved fiducial network geometry. Bias fixing is a technique for applying the constraint that the carrier phase range ambiguity be an integer number of wavelengths. This ambiguity is determined for as many baseline-satellite combinations as possible, and the overall solutions are readjusted while the ambiguities are fixed at their integer values [31, 32]. One approach to bias fixing [33] uses the SRIF formulation

to optimally adjust all the biases and other estimated parameters and to update the covariance matrix with an algorithm which is fast and does not require iterating or expensive re-filtering. The major weakness with solutions from only carrier phase data is a relatively low accuracy in the eastern baseline components due to the predominantly north-south GPS satellite tracks. Bias fixing can largely remove this weakness in the eastern directions.

Kalman (factored covariance) filter-oriented approaches to the GPS estimation problem with emphasis on orbit determination further improved baseline results to the level of 2–4 parts in 10^8 [34] for baseline distances of more than 1000 km. The key strategies emphasized included multi-day (one-week) Kalman filtered orbit solutions, simultaneous parameter estimation, determination of three (instead of the usual two) GPS solar radiation pressure parameters, random-walk models for zenith troposphere delay fluctuations, and simultaneous processing of carrier phase and pseudorange data. The pseudorange data tightly constrain the clocks and carrier phase ambiguities, improving the results particularly in the east for baselines and down-track for orbits. The transmitter and receiver clocks are estimated as white noise parameters, leading to essentially the same results as double differencing but with considerably less complexity. Direct comparisons between independent GPS orbit solutions [34] indicated orbit precisions of 1–2 m had been achieved. Further refinements to the filtering strategies have produced improved GPS accuracies of better than 1 m for orbits and 1–2 parts in 10^8 for baselines up to 2000 km [35]. These additional refinements included modeling of a GPS maneuver which enabled the data arcs to be extended from one to two weeks and constrained stochastic GPS force parameter estimation. Figure 5 shows locations of ground receivers from North American GPS experiments in 1985 and 1986. Figure 6 shows the improvement in daily baseline repeatability using two-week orbit arcs when process noise models for force parameters were used. For arcs of one week or less, it was not necessary to use stochastic force models. In these experiments, all the measurements were confined to the same eight-hour interval each day and it was not possible to determine whether stochastic solar pressure or stochastic three-dimensional thrust parameters fit the data better. It is expected that in the future, with longer arcs and a more global tracking network, the physical nature of these stochastic forces will be better understood.

Orbit verification to better than 1 m is illustrated in Figs. 7 and 8. In each test, the data were partitioned into one-week arcs and independent orbit solutions were obtained and compared. The interleaved arc orbit comparison (Figs. 7a and 7b) shows sub-meter repeatability for two well-tracked satellites. A more strenuous test using orbit prediction is shown in Figs. 8(a) and 8(b), demonstrating sub-meter agreement for

GPS 8. Figure 8(b) also shows how the results improve when pseudorange is processed with carrier phase and stochastic models for tropospheric delay fluctuations are used.

A convincing test of GPS-based positioning accuracy comes from comparisons between 2000-km GPS-determined baselines with VLBI measurements of the same baselines. VLBI is a completely independent geodetic system referenced to the inertial quasar-defined frame, whereas the GPS-based techniques use fiducial points tied to the VLBI system through local surveys to determine accurate GPS orbits, thereby transferring fiducial control to other stations whose coordinates are estimated. Figure 9 shows that 2000-km baselines determined with GPS agree with VLBI to better than 1.5 parts in 10^8 accuracy, which is close to the advertised accuracy of the VLBI system itself.

Recent improvements in bias fixing techniques [33, 36, 37] have enabled successful ambiguity resolution over regions up to 2000 km in extent. In these cases, cm-level agreement between GPS and VLBI has been achieved in horizontal baseline components with single-day arcs, provided that the stations are spaced appropriately in these regions so that ambiguity resolution can proceed over all or nearly all station-satellite combinations. To reach high accuracy in the vertical baseline components as well, multi-day arcs seem to be needed at the present time, but with worldwide tracking networks and additional GPS satellites, shorter tracking arcs will be adequate. GPS solutions seem to show lower scatter than VLBI solutions in the vertical component, perhaps because the GPS measurements are robust enough to estimate the troposphere stochastically with sub-centimeter precision.

B. Earth Orbiter Positioning with GPS

The TOPEX/Poseidon satellite [38], scheduled for launch in late 1991, will lead to significant progress in the study of the interaction of the oceans and climate on a global scale. To understand global weather patterns, experiments like TOPEX are needed to study the world ocean's circulation. The oceans redistribute heat, with warm currents carrying one-half of the excess heat from the tropics to the poles. The seas hold much more heat than the atmosphere and moderate the seasonal temperature fluctuations. Global circulation is observable from space because ocean movement causes bulges and depressions. The sea surface height can be measured with satellite altimeters, as Seasat demonstrated in 1978. The detailed sea surface topography is a complicated function of ocean currents and the geopotential. A complete analysis of TOPEX data will separate the mean sea surface, or marine geoid, from time-varying currents, using repeat orbits and averaging techniques. The ability to map global ocean currents with TOPEX will have far-ranging benefits affecting weather and climate predic-

tion, fishing, commerce, and shipping. The El Niño effect, which is a huge atmospheric seesaw leading to weather reversals, floods, economic hardship, heavy rain, and droughts, may be predictable in advance and eventually better understood through monitoring of the ocean surface with satellites like TOPEX, since it is typically accompanied by a raised mean ocean level of about 20 cm and an increase in the ocean temperature of about 2 deg C off the western coast of South America.

TOPEX will fly in low-earth orbit at about a 1334-km altitude, carry an altimeter precise to about 2 cm to determine the range between the satellite and the sea surface, and will map the topography of the ocean surface. A key to the success of the mission is that the TOPEX orbit altitude error be kept below about 13 cm during the mission. Several different orbit determination techniques will be used on TOPEX, including ground-based laser ranging, but TOPEX will also carry a GPS flight receiver as part of an experiment to demonstrate precise low-earth satellite orbit determination. The TOPEX GPS demo is the first of the anticipated high-precision earth orbiter GPS applications for satellites at a wide range of altitudes, including geosynchronous as well as highly elliptical orbits.

The major error source for differential GPS dynamic tracking of TOPEX [1] is uncertainty in the model for the geopotential. This is also expected to be the limiting error for other tracking techniques [38]. Recent attention has focused on an orbit determination approach using differential GPS in which the orbit filter is designed to desensitize the results as much as possible from gravity errors [39]. A three-dimensional fictitious force is modeled as process noise and estimated in this approach, referred to as *reduced dynamic tracking*. The role these stochastic force parameters play in the orbit filter is controlled through the process noise τ and σ_{ss} (Eqs. 11–14), and depends on the accuracy of the dynamic models for the satellite. If the dynamic models are very poor, the proper strategy is to set $\tau \rightarrow 0$ and $\sigma_{ss} \rightarrow \infty$, and this is the limiting case of *non-dynamic tracking*. The other limiting case is *purely dynamic tracking* in which maximal weight is given to the dynamic models and the stochastic force parameters are essentially turned off ($\tau \rightarrow \infty$ and $\sigma_{ss} = 0$). In between is *reduced dynamic tracking*, where a finite τ and σ_{ss} determine how much reliance is placed on the dynamics and to what extent the unmodeled forces will be fitted out with the data. Although gravity is the major error source for TOPEX, the techniques used to minimize gravity-related orbit errors on TOPEX will also be useful for minimizing virtually any mis-modeled force for other satellites using differential GPS tracking.

Figure 10 compares predicted performance of non-dynamic, reduced-dynamic, and dynamic techniques for TOPEX orbit

determination with GPS. Six globally distributed GPS ground receivers and the one TOPEX flight receiver were assumed to produce 5-cm pseudorange and 0.5-cm carrier phase over five-minute data intervals in a single two-hour arc for this covariance study. This level of performance can be achieved only with advanced receiver and antenna design, but current results with the Rogue receiver/antenna are very encouraging and indicate that these accuracies can be met (Fig. 3). The predicted altitude error shown in Fig. 10 for the dynamic solution strategy is dominated by the gravity field error, assumed to be 50 percent of the difference between the GEM12 and GEM10 fields. A comparison with the covariance matrix for the GEM-T1 [40] gravity field shows that representing the gravity error with the 50-percent geopotential difference for this analysis produces about the same results as produced with the current (GEM-T1) gravity field covariance. The large (~ 25 -cm) excursions for the dynamic tracking approach occur over regions of the earth where the gravity field is poorly known, such as over the oceans. However, these oceanic regions are the key regions for an oceanographic experiment such as TOPEX. The non-dynamic approach also suffers from occasional sudden increases in the altitude error, primarily due to times of weaker viewing geometry. Since the non-dynamic tracking solutions are more data-intensive, they are more sensitive to times when viewing geometry is compromised. The reduced dynamic strategy performs best overall. The stochastic force parameter estimation (τ , σ_{ss}) was chosen to be optimal for a gravity field accurate to about the level of the current GEM-T1 field, but as pointed out in [39], even if the accuracy of the gravity field is only approximately known, the results are insensitive to the stochastic model as long as a relatively conservative approach is taken. This is one of the main advantages of the reduced dynamic tracking strategy.

The reduced and non-dynamic techniques compensate not only for gravity mismodeling, but also for *any* type of force or acceleration affecting spacecraft motion, such as drag, radiation pressure, gas leaks, maneuvers, etc. Estimation of fictitious thrust parameters for the GPS orbits themselves when tracking over relatively long (two-week) arcs (Fig. 6) is a simple example of the application of reduced dynamic concepts to satellites in high-earth orbits. It was found that the results in Fig. 6 showed very little sensitivity to τ and σ_{ss} over a wide range of values, as predicted in [39]. The GPS orbit strategy, however, still places very high weight on dynamic models since the constrained stochastic forces being estimated represent a tiny perturbation to the purely dynamic orbit determination.

C. Other Related GPS Applications

Certain GPS applications show great promise but require a global tracking network and a full GPS constellation, such as earth orientation monitoring [4]. Ultimately, the filtering and

estimation strategy may be a major factor in the utility of GPS for earth orientation because one of the advantages of GPS is the high time resolution it provides. Another example of the importance of Kalman filtering is the determination of tropospheric zenith delay parameters as part of the GPS orbit determination process. GPS-based techniques have the potential of tracking tropospheric fluctuations at sub-centimeter levels with resolution of a few minutes. A GPS-based network for earth orientation monitoring, troposphere calibration, and determination of geocentric station coordinates is being studied for use in the Deep Space Network since these are major limiting errors for deep space navigation and planetary exploration. GPS tracking will be able to determine the location of the geocenter relative to any set of ground stations with an accuracy of better than 5 cm [5], in addition to its cm-level *relative* station positioning capability. The NSW precise ephemeris, which is determined from a worldwide Air Force tracking network and is more accurate than the 10–20-m ephemeris broadcast down on the P-code, is currently determined along with values for earth orientation parameters [41] using a SRIF and RTS smoother [42] and process noise models for polynomial clock coefficients, troposphere parameters, and solar pressure coefficients. GPS also has the potential for global time transfer at the sub-nanosec level, which would hold great benefits for the Deep Space Network and other radio astronomy observatories.

If GPS antennas are placed at different points on an airplane, the attitude of the aircraft can in principle be determined from GPS measurements. An experiment was recently conducted [43] to demonstrate aircraft position, velocity, and attitude determination using GPS for a synthetic aperture radar experiment to study ocean currents, and the data are being analyzed at JPL. GPS receivers can also be placed on ships and buoys for research in seafloor geodesy [44], a relatively new field.

There are numerous real or near-real-time non-military GPS applications in which the cm-level accuracies required for geodesy or low-earth orbiter positioning are not essential but for which estimation speed is important. The NASA Symposium on GPS Space Applications, held in Pasadena, California, November 18–19, 1987, emphasized many of the near-real-time positioning and navigation GPS applications for spacecraft maneuvering near the Space Station and for other earth orbiters, including those at high earth altitude. Since many earth-orbiting satellites launched in the future will carry GPS equipment, including the Space Shuttle, it is likely that GPS will have an increasingly visible role in a variety of different missions. Although observing GPS from high earth altitude poses some special visibility problems, detailed analysis predicts that meter-level orbit accuracy can be achieved even for geosynchronous satellites [6].

In the future, it is expected that factorized filtering techniques will be applied to problems which would strain present computing resources to the limit. One example is recovery of gravity coefficients from GPS and low earth orbiter differential tracking data. Because there can be thousands of gravity coefficients and the data arcs required include many satellite orbit revolutions, the number of estimated parameters is expected to be in the tens of thousands [45]. Numerical stability in these situations demands extremely stable, factorized filtering algorithms. Large problems such as this one would be intractable, even on a supercomputer, were it not possible to take advantage of the local block structure in the factored covariance matrix and the fact that much of the matrix is filled with zeros [45].

V. Summary

The GPS multi-parameter estimation problem with orbit adjustment is well suited to a linearized batch sequential filter. Both the SRIF and UD-factorized filters have been used for high-accuracy GPS applications. Although neither is preferred over the other with regard to numerics, for different situations one or the other is sometimes more convenient or less expensive from a computational viewpoint. Determination of station locations to the cm level is currently feasible using GPS, with accuracy rivaling other state-of-the-art geodetic techniques. Accuracies of 1–2 parts in 10^8 relative to baseline lengths up to 2000 km have been demonstrated over base-

lines measured independently by radio astronomy interferometric methods, and GPS orbits determined simultaneously can now be estimated to better than 1-m accuracy. Key aspects of the estimation strategy include: collocation of three or four GPS receivers at fiducial sites with a priori, well-known coordinates; process noise modeling of fluctuating quantities such as clocks, tropospheric delays, and small but significant unmodeled satellite accelerations; multi-day orbit solutions; combined processing of pseudorange and carrier phase; and bias fixing techniques to apply integer constraints to carrier phase ambiguities. Future high-accuracy GPS applications also include sub-decimeter orbit determination for satellites such as TOPEX and Eos with non-dynamic and reduced dynamic tracking techniques, which use process noise to desensitize the filter to unmodeled or mismodeled forces.

Although considerable progress has been made in just a few years in the development of strategies for precise positioning with GPS, improvements in GPS technology promise even more gains in the near future as advanced receivers and antennas become available. Global tracking networks will greatly increase the scientific potential of GPS, and will also lead to a dramatic increase in the number of estimated state parameters. Precise pseudorange with noise of several cm will significantly advance virtually all the GPS positioning techniques developed so far. Such precise data and the anticipated filtering with very large, sparse matrices will probably require re-examination and further enhancement of the filtering approaches currently being used.

Acknowledgments

Gerald J. Bierman played a major role in developing the algorithms and filtering techniques which are discussed in this article, as can be seen from the numerous references to his work. His contributions, however, extend far beyond his analyses, algorithms, publications, and computer programs, which are recognized as the state of the art. He was a gifted yet unassuming man who shared with me his friendship as well as his extraordinary mathematical insight on the complex problems we worked on together. For me and my colleagues, his death was a great personal and professional loss.

I also thank S. C. Wu, R. P. Malla, A. P. Freedman, W. I. Bertiger, T. P. Yunck, T. Meehan, and J. T. Wu, whose work has contributed to the ideas and results presented here.

References

- [1] S. M. Lichten, S. C. Wu, J. T. Wu, T. P. Yunck, "Precise Positioning Capabilities for TOPEX Using Differential GPS Techniques," AAS/AIAA Astrodynamics Specialist Conference, Vail, Colorado, paper AAS 85-401, August 12-15, 1985, published in *Astrodynamics 1985*, (ed. Kaufman et al.), vol. 58 of *Advances in the Astronautical Sciences*, pp. 597-614, 1986.
- [2] "Earth Observing System: Science and Mission Requirements Working Group Report," NASA Technical Memorandum 86129, Goddard Space Flight Center, Greenbelt, Maryland, August 1984.
- [3] T. P. Yunck, G. F. Lindal, and C.-H. Liu, "The Role of GPS in Precise Earth Observation," *Proceedings of the IEEE Position, Location, and Navigation Symposium*, Orlando, Florida, pp. 251-258, November 1988.
- [4] A. P. Freedman and J. O. Dickey, "Usefulness of GPS for the Precise Determination of Earth Orientation Parameters," *EOS*, vol. 68, no. 44, p. 1245, November 3, 1987.
- [5] S. C. Wu and R. P. Malla, "Determination of a Geocentric Coordinate Frame for GPS Measurements," *Proceedings AIAA/AAS Astrodynamics Conference*, Minneapolis, Minnesota, paper 88-4210, pp. 1-7, August 15-17, 1988.
- [6] S. C. Wu, "Differential GPS Approaches to Orbit Determination of High-Altitude Earth Satellites," AAS/AIAA Astrodynamics Specialist Conference, Vail, Colorado, paper AAS 85-430, August 12-15, 1985, published in *Astrodynamics 1985*, (ed. Kaufman et al.), vol. 58 of *Advances in the Astronautical Sciences*, pp. 1203-1220, 1986.
- [7] W. Melbourne, R. Anderle, M. Feissel, R. King, D. McCarthy, D. Smith, B. Tapley, and B. Vincente, "Project MERIT Standards," *United States Naval Observatory Circular No. 167*, U. S. Naval Observatory, Washington, D. C., December 27, 1983.
- [8] General Dynamics, Electronics Division, *Interface Control Document 9000760*, El Segundo, California, 1976.
- [9] D. A. Kerr, "Technical Operating Report for Navstar Block II Satellite," *Volume IV: Solar Force Model*, SSD81-0164-4, Rockwell International, El Segundo, California, 1982.
- [10] W. Porter, *Torque Model for the GPS Space Vehicle System*, Rockwell International, El Segundo, California, 1976.
- [11] O. J. Sovers, and J. S. Border, *Observational Model and Parameter Partial for the JPL Geodetic GPS Modeling Software GPSOMC*, JPL 87-21, Rev. 1, Jet Propulsion Laboratory, Pasadena, California, December 15, 1988.
- [12] A. R. Thompson, J. M. Moran, and G. W. Swenson, *Interferometry and Synthesis in Radio Astronomy*, New York: John Wiley & Sons, 1986.
- [13] G. E. Lanyi, "Tropospheric Delay Effects in Radio Interferometry," *TDA Progress Report 42-78*, vol. April-June 1984, Jet Propulsion Laboratory, Pasadena, California, pp. 152-159, August 15, 1984.
- [14] G. J. Bierman, *Factorization Methods for Discrete Sequential Estimation*, Orlando, Florida: Academic Press, 1977.

- [15] G. J. Bierman and K. H. Bierman, *Estimation Subroutine Library: Preliminary User Guide (August 1984)*, FEA Report No. 81584, Factorized Estimation Applications, Inc., Canoga Park, California, 1984.
- [16] C. L. Thornton, "Triangular Covariance Factorizations for Kalman Filtering," JPL TM 33-798, Jet Propulsion Laboratory, Pasadena, California, October 1976.
- [17] C. L. Thornton and G. J. Bierman, "UDU^T Covariance Factorization for Kalman Filtering," in *Control and Dynamic Systems, Advances in Theory and Application*, vol. 16, ed. C. T. Leondes, New York: Academic Press, 1980.
- [18] C. L. Lawson and R. J. Hanson, *Solving Least Squares Problems*, Englewood Cliffs, New Jersey: Prentice-Hall, 1974.
- [19] D. W. Allan, "Statistics of Atomic Frequency Standards," *Proc. IEEE*, vol. 54, pp. 221-230, 1966.
- [20] C. L. Thornton and G. J. Bierman, "Gram-Schmidt Algorithms for Covariance Propagation," *Inst. J. Control*, vol. 25, pp. 243-260, 1977.
- [21] H. E. Rauch, F. Tung, and C. T. Streibel, "Maximum Likelihood Estimates of Linear Dynamic Systems," *AIJA J.*, vol. 3, pp. 1445-1450, 1965.
- [22] G. J. Bierman, "A New Computationally Efficient Fixed-Interval, Discrete-Time Smoother," *Automatica*, vol. 19, pp. 503-511, 1983.
- [23] G. J. Bierman, *A Reformulation of the Rauch-Tung-Streibel Discrete Time Fixed Interval Smoother*, Bierman and Associate Report No. 870717, Studio City, California, 1987.
- [24] C. L. Thornton and G. J. Bierman, "Filtering and Error Analysis Via the UDU^T Covariance Factorization," *IEEE Trans. on Automatic Control*, vol. AC-23, no. 5, pp. 901-907, 1978.
- [25] G. A. Shoults, *Filtering Strategies for Non-Gravitational Accelerations With Applications to the Global Positioning System*, Masters Thesis, Purdue University, West Lafayette, Indiana, December 1987.
- [26] J. M. Davidson, C. L. Thornton, S. A. Stephens, G. Blewitt, S. M. Lichten, O. J. Sovers, P. M. Kroger, L. L. Skrumeda, J. S. Border, R. E. Neilan, C. J. Vegas, B. G. Williams, J. T. Freymueller, T. H. Dixon, and W. G. Melbourne, *The Spring 1985 High Precision Baseline Test of the JPL GPS-Based Geodetic System*, JPL 87-35, Jet Propulsion Laboratory, Pasadena, California, November 15, 1987.
- [27] G. Beutler, I. Bauersima, W. Gurtner, M. Rothacher, and T. Schildknecht, "Evaluation of the 1984 Alaska Global Positioning System Campaign With the Bernese GPS Software," *J. Geophys. Res.*, vol. 92, pp. 1295-1303, February 1987.
- [28] R. I. Abbot, Y. Bock, C. C. Counselman III, R. W. King, S. A. Gourevitch, and B. J. Rosen, "Interferometric Determination of GPS Satellite Orbits," *Proceedings First International Symposium on Precise Positioning with GPS-1985*, ed. C. Goad, vol. I, pp. 63-72, National Geodetic Information Center, NOAA, Rockville, Maryland, 1985.
- [29] R. I. Abbot, Y. Bock, C. C. Counselman, and R. W. King, "GPS Orbit Determination," *Proceedings of the Fourth International Geodetic Symposium on Satellite Positioning*, vol. I, pp. 271-274, Applied Research Laboratories, University of Texas, Austin, Texas, 1986.

- [30] Y. Bock, R. I. Abbot, C. C. Counselman III, and R. W. King, "A Demonstration of 1-2 Parts in 10^7 Accuracy Using GPS," *Bull. Geod.*, vol. 60, pp. 241-254, 1986.
- [31] Y. Bock, C. C. Counselman III, S. A. Gourevitch, and R. W. King, "Establishment of Three-Dimensional Control by Interferometry with the Global Positioning System," *J. Geophys. Res.*, vol. 90, pp. 7689-7703, 1985.
- [32] P. L. Bender and D. R. Larden, "GPS Carrier Phase Ambiguity Resolution Over Long Baselines," *Proceedings First International Symposium on Precise Positioning with GPS-1985*, ed. C. Goad, vol. I, pp. 357-362, National Geodetic Information Center, NOAA, Rockville, Maryland, 1985.
- [33] G. Blewitt, "Carrier Phase Ambiguity Resolution for the Global Positioning System Applied to Geodetic Baselines Up to 2000 km," submitted to *J. Geophys. Res.*, 1988.
- [34] S. M. Lichten and J. S. Border, "Strategies For High Precision GPS Orbit Determination," *J. Geophys. Res.*, vol. 92, pp. 12751-12762, November 1987.
- [35] W. I. Bertiger, S. M. Lichten, and E. C. Katsigris, "A Demonstration of Sub-Meter GPS Orbit Determination and High Precision User Positioning," *Proceedings Position, Location, and Navigation Symposium, 1988 (PLANS)*, IEEE, Orlando, Florida, Nov. 29-Dec. 2, 1988.
- [36] D. Dong and Y. Bock, "GPS Network Analysis: Ambiguity Resolution," *EOS*, vol. 69, no. 16, p. 325, April 1988.
- [37] G. Blewitt, "Successful GPS Carrier Phase Ambiguity Resolution for Baselines up to 2000 km in Length," *EOS*, vol. 69, no. 16, p. 325, April 1988.
- [38] G. H. Born, C. Wunsch, and C. A. Yamarone, "TOPEX: Observing the Oceans from Space," *EOS*, vol. 65, no. 28, pp. 433-434, July 1984.
- [39] S. C. Wu, T. P. Yunck, and C. L. Thornton, "Reduced-Dynamic Technique for Precise Orbit Determination of Low Earth Satellites," paper AAS 87-410, presented at AAS/AIAA Astrodynamics Specialist Conference, Kalispell, Montana, August 10-13, 1987.
- [40] J. G. Marsh et al., "A New Gravitational Model for the Earth from Satellite Tracking Data: GEM-T1," *J. Geophys. Res.*, vol. 93, pp. 6169-6215, 1988.
- [41] E. R. Swift, "Comparison of GPS-Derived Earth Orientation Parameters with Final BIH/IERS Values," *EOS*, vol. 69, no. 44, p. 1154, November 1988.
- [42] E. R. Swift, "NSWC's GPS Orbit/Clock Determination System," *Proceedings First International Symposium on Precise Positioning with GPS-1985*, ed. C. Goad, vol. I, pp. 51-62, National Geodetic Information Center, NOAA, Rockville, Maryland, 1985.
- [43] J. M. Srinivasan et al., "Measurement of Aircraft Position, Velocity, and Orientation Using Rogue GPS Receivers: A Preliminary Report," presented at the Crustal Dynamics Project Principal Investigators' Working Group Meeting, Munich, Germany, Oct. 18-20, 1988.
- [44] M. C. McIntyre, "Results of a Seafloor Positioning System Sea-Trial," *EOS*, vol. 69, no. 44, p. 1150, November 1988.
- [45] S. C. Wu, J. T. Wu, and W. I. Bertiger, "An Efficient Technique for Gravity Recovery Using a Low Earth Satellite," to appear in *Proceedings of the Fifth International Symposium on Satellite Positioning*, Las Cruces, New Mexico, March 13-17, 1989.

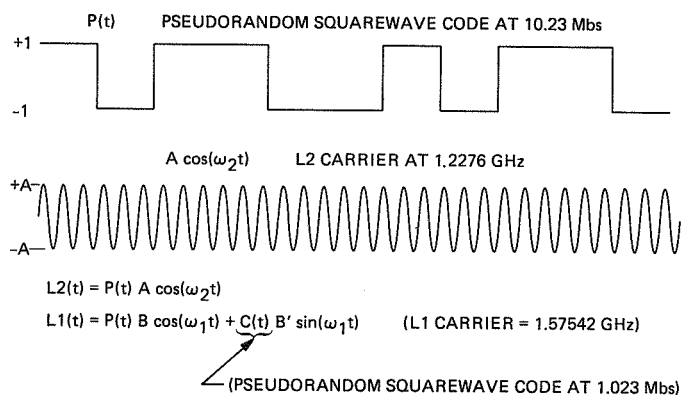


Fig. 1. GPS carrier phase is modulated by the P-code [P(t)] and the C/A code [C(t)]. The P-code contains nominal values for GPS orbits and clocks. Carrier phase and P-code pseudorange are used in high-accuracy applications.

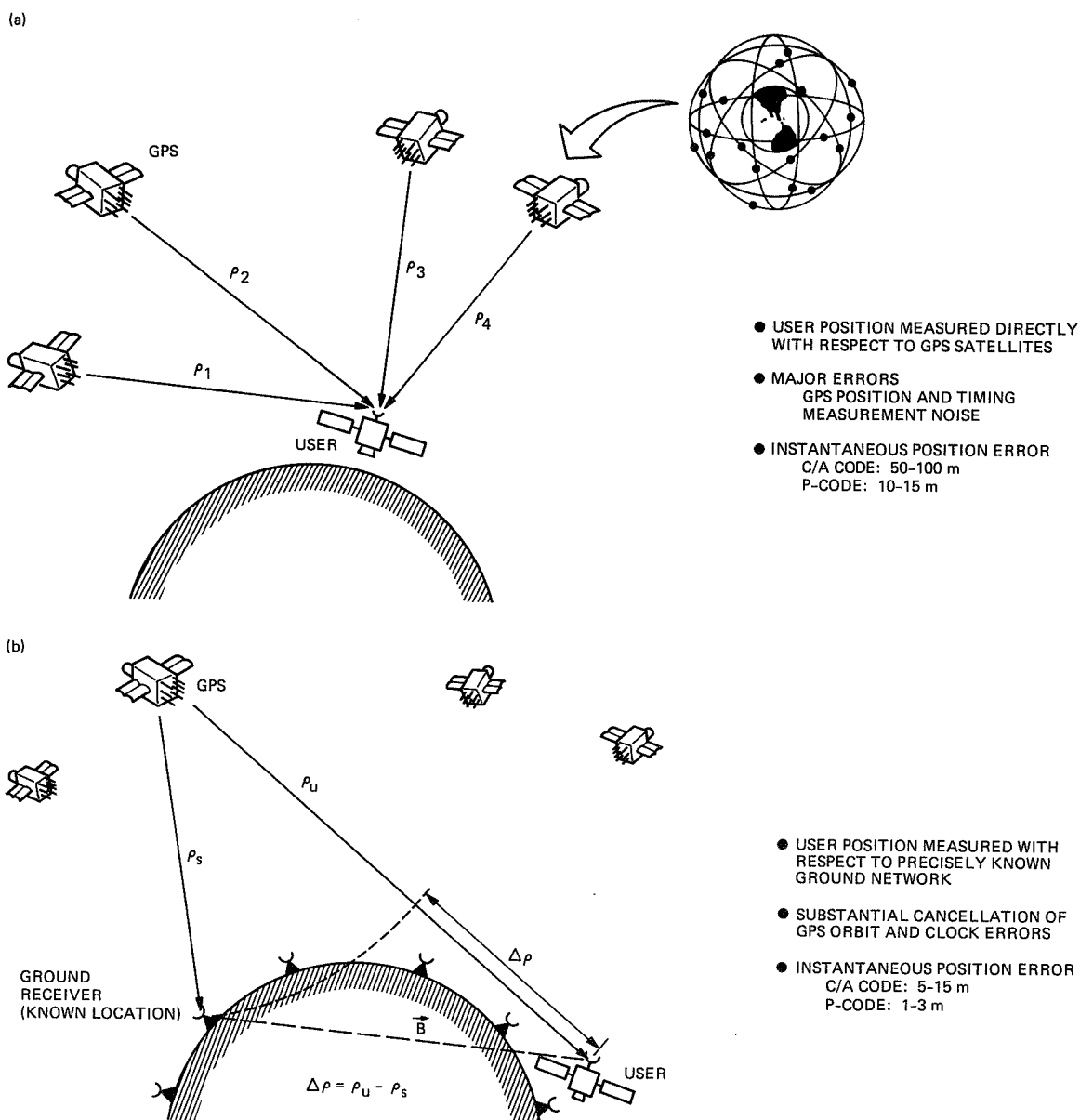


Fig. 2. (a) Direct GPS tracking, and (b) differential GPS tracking.

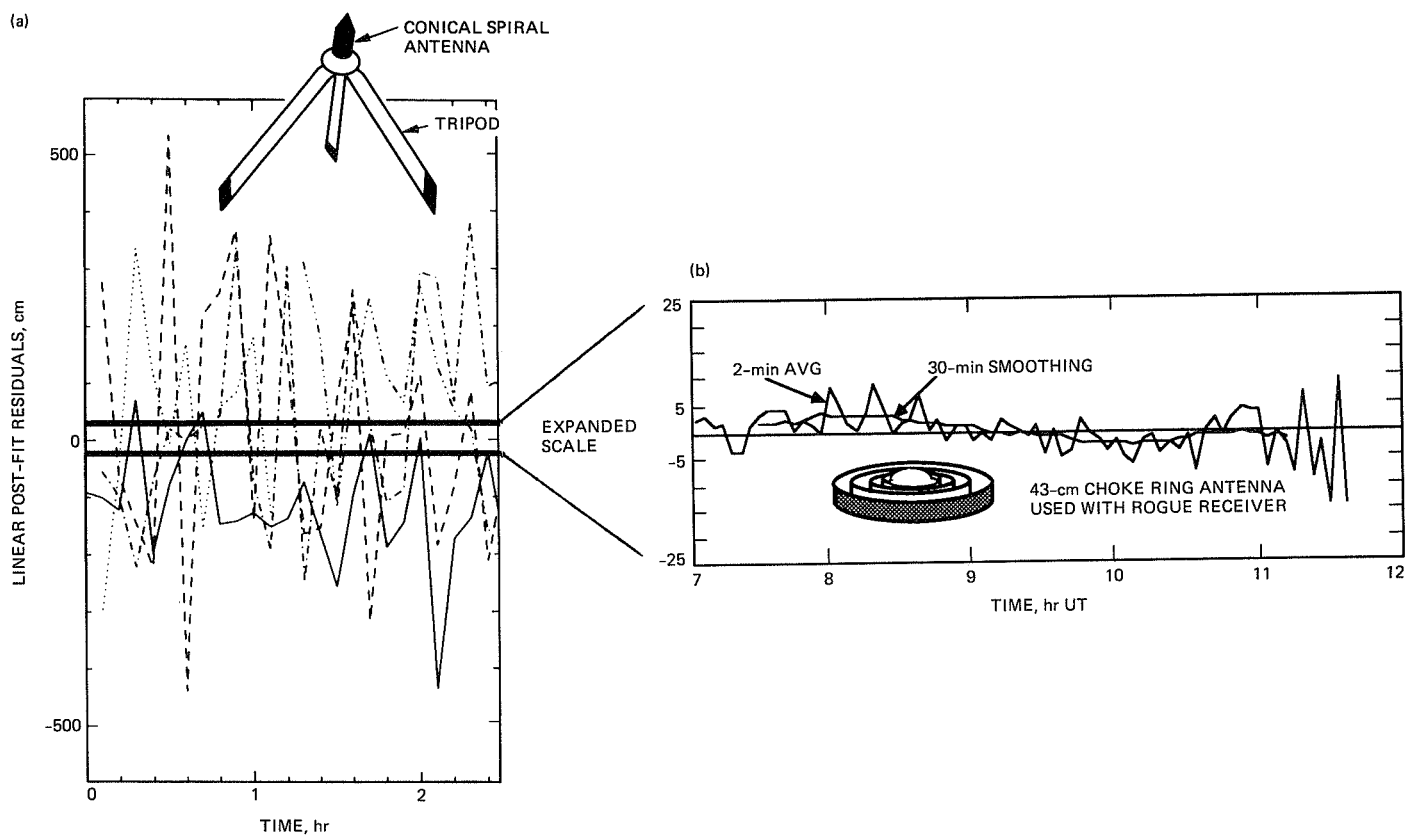


Fig. 3. Comparison between performance with different antenna and receiver designs: (a) post-fit residuals, mostly multipath, for dual-frequency pseudorange averaged over six minutes from a common TI antenna/receiver combination, and (b) pseudorange scatter obtained in January 1988 with the JPL Rogue receiver and a choke ring antenna designed to minimize multipath, for single-frequency data averaged over 2- and 30-minute intervals.

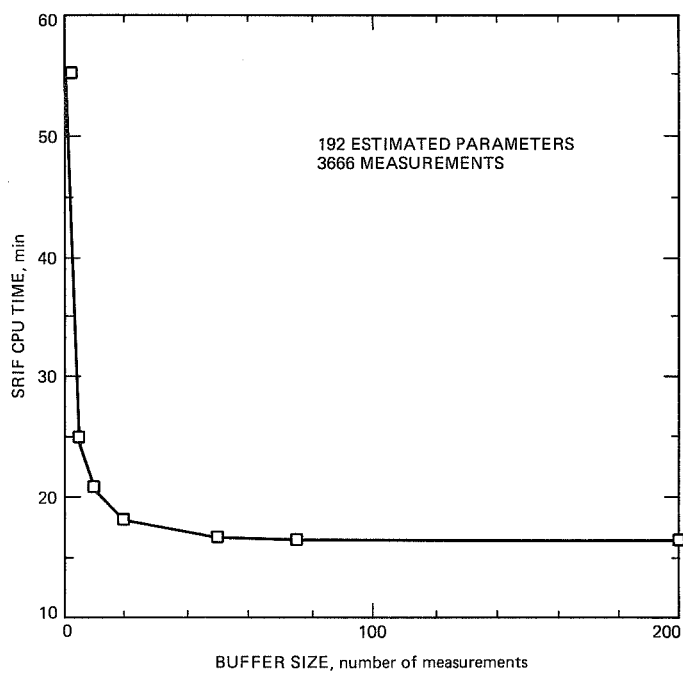


Fig. 4. Comparison of CPU time required for the SRIF for different measurement buffer sizes.

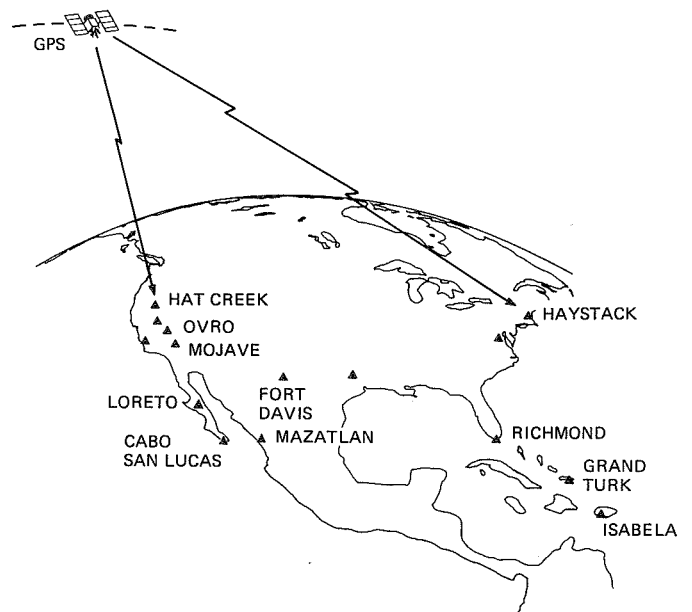


Fig. 5. Locations of ground receivers during 1985 and 1986 GPS experiments.

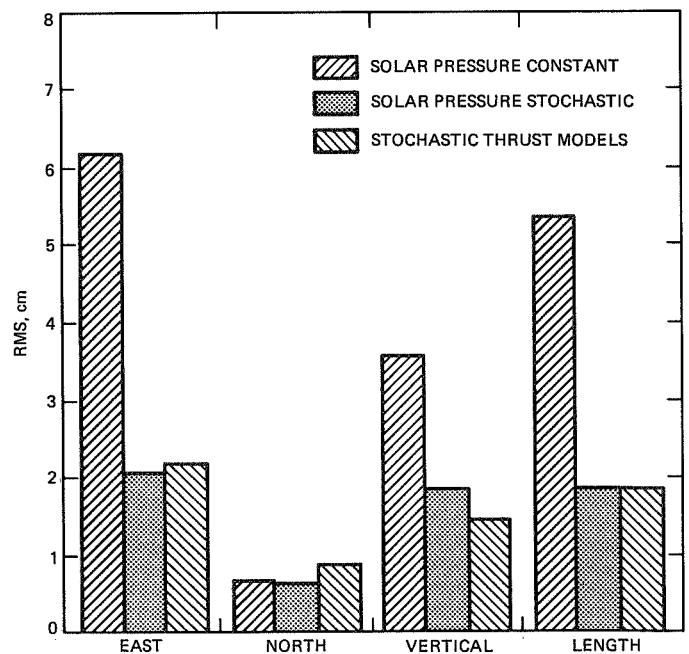


Fig. 6. Daily repeatability for the 1314-km Mojave, California – Fort Davis, Texas baseline, for a two-week data arc in November, 1985. Lowest scatter is obtained with process noise force models.

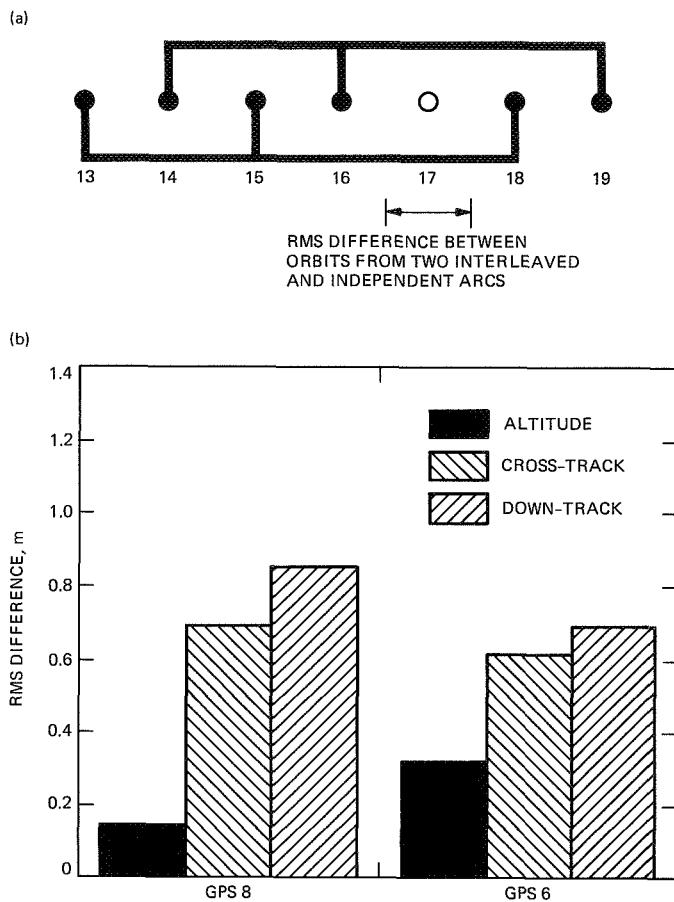


Fig. 7. (a) RMS orbit difference is computed from interleaved orbits determined independently from November 13–15–18 and November 14–16–19; (b) RMS for GPS 6 and GPS 8 is shown computed over a 24-hour period on November 17 when no measurements were used for either solution as shown in (a).

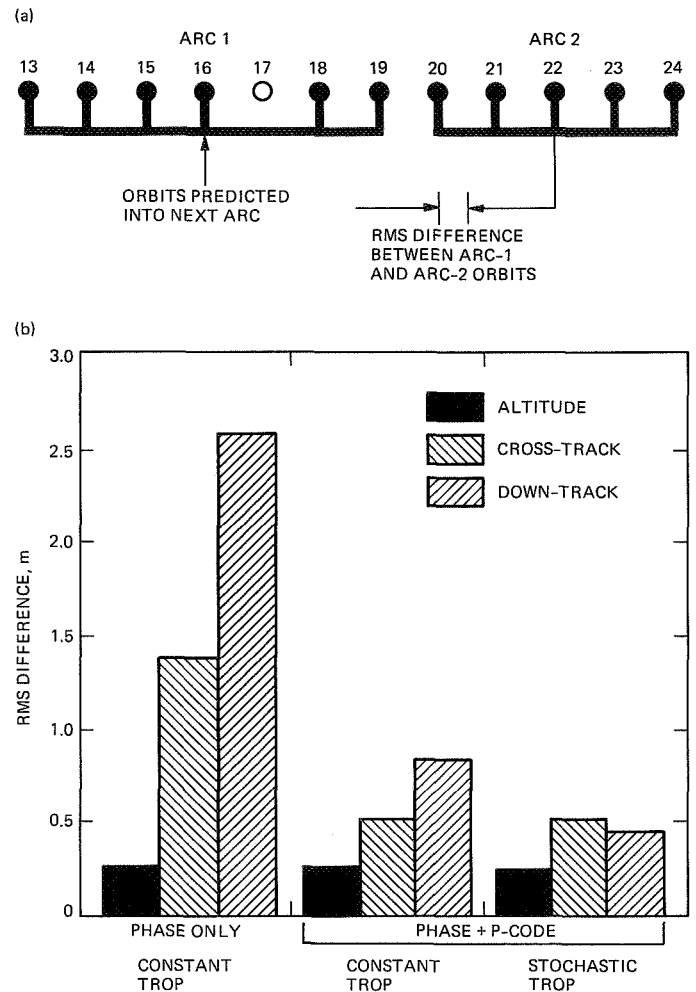


Fig. 8. (a) One week arcs in November 1985 used for orbit prediction and RMS computation. Orbits from the first week are mapped ahead and compared to orbits determined independently using data only from the second week; (b) prediction test (Fig. 8a) for GPS 8 shows RMS well below 1 meter in all three components, with best results obtained using stochastic troposphere models and combined carrier phase and P-code pseudorange. RMS is computed over a 6-hour interval.

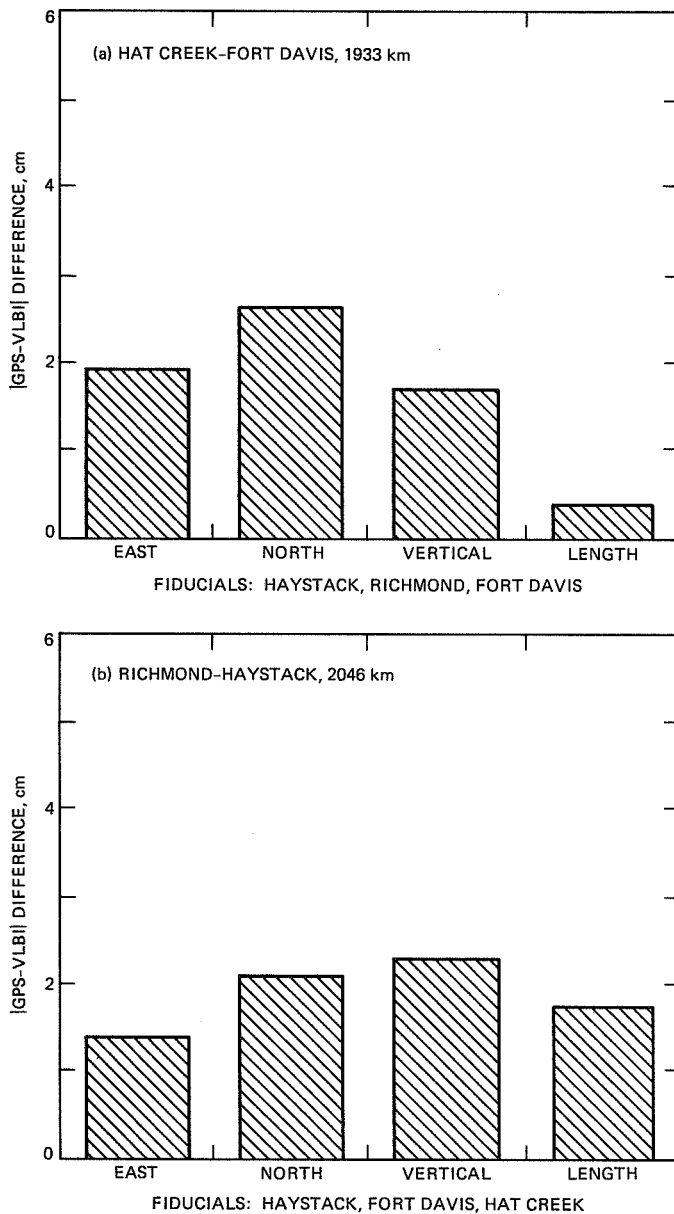


Fig. 9. Comparison between GPS and VLBI independent measurements of 2000-km baselines shows agreement of 1–2 parts in 10^8 in all vector components: (a) Hat Creek–Fort Davis, and (b) Richmond–Haystack.

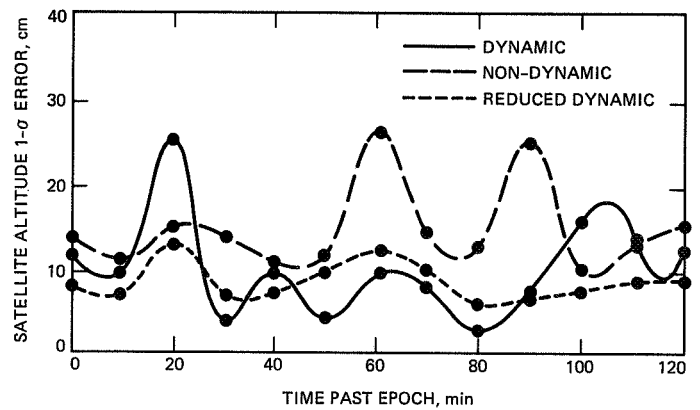


Fig. 10. Predicted altitude accuracy for TOPEX orbit determination using dynamic, reduced dynamic, and non-dynamic tracking techniques.

High-Precision Radiometric Tracking for Planetary Approach and Encounter in the Inner Solar System

C. S. Christensen and S. W. Thurman
Navigation Systems Section

J. M. Davidson, M. H. Finger, and W. M. Folkner
Tracking Systems and Applications Section

The benefits of improved radiometric tracking data have been studied for planetary approach within the inner Solar System using the Mars Rover Sample Return trajectory as a model. It was found that the benefit of improved data to approach and encounter navigation was highly dependent on the a priori uncertainties assumed for several non-estimated parameters, including those for frame-tie, Earth orientation, troposphere delay, and station locations. With these errors at their current levels, navigational performance was found to be insensitive to enhancements in data accuracy. However, when expected improvements in these errors are modeled, performance with current-accuracy data significantly improves, with substantial further improvements possible with enhancements in data accuracy.

I. Introduction

An investigation of the benefits of improved radiometric tracking data for interplanetary navigation has been initiated. The goals are to determine the limitations imposed on navigation performance by radiometric data accuracy and how to best utilize this high-accuracy data to optimize navigation performance. For this purpose, covariance analyses using the Orbit Determination Program (ODP) have been performed, including two-way Doppler, two-way range, and Delta Differenced One-way Range (Δ DOR) measurements with various assumed accuracies for each data type. Three sets of results are presented, with the Mars Rover Sample Return (MRSR) Mis-

sion cruise and encounter trajectory used as a model for each set.^{1,2}

Since only a single trajectory has been studied, some caution is needed in generalizing the results. In particular, the

¹ A. Konopliv, "Cruise Navigation Analysis for MRSR with Radiometric Data Only," JPL IOM 314.4-608 (internal document), Jet Propulsion Laboratory, Pasadena, California, December 2, 1987.

² A. Konopliv, "MRSR Approach Navigation—More Results for Radiometric and Optical Data," JPL IOM 314.4-621 (internal document), Jet Propulsion Laboratory, Pasadena, California, April 7, 1988.

ephemeris of Mars is the best known of all the planets (excluding Earth), so that this study may present the most favorable case. Also note that for this model trajectory, encounter takes place when Mars is near its most southerly declination. An encounter lying closer to the celestial equator might affect the impact of Doppler data on the total orbit determination accuracy, and a trajectory lying in the northern sky might give added strength to the Δ DOR measurements because of the increased visibility on the Goldstone/Spain baseline. However, it is expected that the effects of these variations on the studies presented in this work will be either minor, since the impact of Doppler data is generally limited, or possibly beneficial, since the impact of Δ DOR data is strongly positive.

For the first set of results (solution set number one), the ephemeris and station location a priori uncertainties used are appropriate for the present time and near future (i.e., 1988–1990). A simple equivalent station location error (ESLE) approach was adopted, in which a priori uncertainties in Earth orientation and troposphere are lumped together with the station location uncertainties to give one “equivalent” station location covariance which accounts for the errors in all three quantities. For these runs, the ESLE and ephemeris errors were considered as unestimated systematic errors. In the covariance analysis results, the considered ephemeris errors made the dominant contribution to the total orbit determination uncertainty for nearly all combinations of data. Also, it was found that for improved range and Doppler accuracy the ESLE contribution to the orbit determination uncertainty grew in size, causing the total uncertainty to increase as data became more accurate. These results were not unexpected, but they are presented here to serve as a benchmark for comparison with later runs.

For solution set number two, the a priori ephemeris covariance of set one was replaced by another in which it had been assumed that the right ascension offset between the dynamical reference frame of the planets and the Very Long Baseline Interferometry (VLBI) quasar frame had been established at the level of 5 nanoradians. This step resulted in an ephemeris with an a priori frame tie error of about 5 nanoradians in each of the three rotational directions. In addition, the ESLE approach was abandoned and replaced by a more physically realistic one in which station location and troposphere errors are considered independently and in which Earth orientation parameters are estimated stochastically. All a priori uncertainties used, except for that of the ephemeris, were the same as in solution set one. It was found that the contributions of ephemeris and station errors to the orbit determination uncertainty decreased significantly and that the total uncertainties (compared to those of solution set one) were smaller by factors of up to eight, depending on the combination of observables and accuracies assumed.

Solution set three differs from solution set two in that new a priori errors for station location, troposphere, and Earth orientation parameters are adopted, representing higher levels of accuracy for these calibrations, as should be available in the mid- to late 1990s. These results showed that orbit determination uncertainties could be decreased by an additional 10–60 percent (compared to those of set two), again depending on the combination of observables and accuracies assumed.

The results from the analyses described above suggest that orbit determination for missions to the inner planets will benefit most significantly from an improved determination of the tie between the dynamical frame of the planets and the inertial frame of the quasars. There is a reasonable hope of determining this tie for the inner planets at the level of 5–10 nanoradians within the next few years. Promising measurement techniques include improved ground surveys linking key Lunar Laser Ranging (LLR) and VLBI sites,³ VLBI observations of short-period pulsars [1], observations of planetary occultations of quasars,⁴ and VLBI measurements during the Phobos Lander Mission⁵ and the Mars Orbiter Mission.

With this frame tie established, further advances in orbit determination accuracy can result from improved radiometric data. Achieving the full benefit of more accurate data will require two additional efforts. First, improvements in modeling are required. Station location, troposphere, and Earth orientation errors need to be given a physically realistic representation, with separate parameters and partial derivatives provided for each. Second, improvements in calibration are required. Reductions in the present a priori errors for station locations, troposphere delays, and Earth orientation will significantly enhance orbit determination with high-accuracy radiometric data types. These calibration improvements are expected to be achieved through advances in VLBI and GPS technology.

Once these improvements are implemented, navigational performance for cruise and encounter to the inner planets will benefit significantly from improved radiometric data. For these mission scenarios, improvement in the accuracy of Δ DOR observables has the greatest effect on spacecraft posi-

³A. E. Niell, “Absolute Geocentric DSN Station Locations and Radio-Planetary Frame Tie,” JPL IOM 335.2-159 (internal document), Jet Propulsion Laboratory, Pasadena, California, March 21, 1984.

⁴R. Linfield, “The Need for DSS-43 on July 19, 1988 for a Venus Occultation,” JPL IOM 335.3-88-51 (internal document), Jet Propulsion Laboratory, Pasadena, California, April 25, 1988.

⁵C. E. Hildebrand, “First Cut at Phobos Lander VLBI Errors,” JPL IOM 335.1-87-29 (internal document), Jet Propulsion Laboratory, Pasadena, California, February 3, 1987.

tional covariances at encounter. Improving the Δ DOR accuracy from 50 nrad to 5 nrad was found to reduce orbit determination uncertainties by a factor of three when the Δ DOR data was used in conjunction with 10-m range and 1-mm/sec Doppler. Improvements in range and Doppler accuracy can be beneficial, but in general will have a more limited effect, except in the absence of Δ DOR data. In this regard, 10-cm accuracy range proves to be a powerful stand-alone data type, producing results superior to those achievable with the 10-m range, 1-mm/sec Doppler, and 50-nrad Δ DOR data type combination.

II. Trajectory and Observation Schedule

The three sets of results presented here are based on the Mars Rover Sample Return (MRSR) Mission approach trajectory discussed by A. Konopliv.⁶ With this trajectory the spacecraft encounters Mars on October 7, 1999. All the orbital solutions presented are based on a common observation schedule, which is summarized in Table 1. The first data point is taken 85 days before Mars aerocapture and the last point is taken 2 days before Mars encounter. Two-way Doppler and two-way range were scheduled from the three stations DSS-11, DSS-44, and DSS-61. Doppler and range data were scheduled from each station for one pass every sixth day, with stations alternating so that a pass was scheduled somewhere for every other day. A minimum spacecraft elevation of 10 deg was required for this data. A one-hour integration time was used for Doppler data, while range measurements were scheduled approximately every hour within a pass. The Δ DOR measurements on the DSS-11-DSS-44 and DSS-11-DSS-61 baselines were scheduled once every sixth day with quasars selected to be within 10 deg of the spacecraft. Δ DOR data below 5-deg elevation was eliminated. The total amount of data scheduled was 309 Doppler points, 296 range points, and 28 Δ DOR points.

III. Estimation Strategy and Error Modeling Common to All Solutions

The covariance analyses were performed with the ODP using batch sequential estimation. A batch time interval of one day was used in all cases. This was chosen to be small compared to the correlation time constants of all stochastically estimated variables. For all runs, estimated parameters include those for spacecraft initial state, solar pressure, and a random nongravitational acceleration. Considered parameters include those for a constant nongravitational acceleration, Mars GM and J2, and quasar directions. The error modeling common to all solutions will be discussed in this section and is summarized

in Table 2. Modeling specific to solutions sets one, two and three are summarized in Tables 3, 4, and 5 respectively, and will be discussed in later sections.

Since the interest is in the effects of data accuracy on orbit determination accuracy, the initial position and velocity of the spacecraft were estimated with large a priori uncertainties of 10,000 km for each position coordinate and 1 km/s for each velocity component. These large values were chosen so that the final state determination would not be dependent on the a priori values.

A solar pressure model was included. This model assumes that the spacecraft has a mass of 1000 kg and presents an area of 17 m² toward the Sun. The solar pressure force is calculated as the force on an opaque body with this projected area times a reflectivity vector \vec{G} . The components of \vec{G} are assumed to be constant in a coordinate system defined by the Sun-spacecraft and Sun-Canopus directions. The component of \vec{G} directed away from the Sun, G_r , was estimated with an a priori uncertainty of 0.13, while the components of \vec{G} perpendicular to the Sun-spacecraft direction, G_x and G_y , were each estimated with an a priori uncertainty of 0.01. This modeling is the same as used by Konopliv.

To account for other non-gravitational forces, both stochastic and constant accelerations were employed. Stochastic accelerations of 10⁻¹² km/sec² per component were estimated with a 5-day correlation time. Constant accelerations with a priori uncertainties of 10⁻¹² km/sec² per component were considered.

To account for uncertainties in the Martian gravity field, the GM and J2 of Mars were considered with uncertainties of 0.15 km³/sec² and 4.4 × 10⁻⁷, respectively. Although these uncertainties are 10 times the formal errors, their effects on the orbit determination accuracy are never very significant.

The philosophical viewpoint has been taken that the fundamental reference frame for navigation is that determined by the quasars. It is believed that this allows the simplest representation of errors in orientation between the radio frame, the terrestrial reference frame, and the dynamical reference frame of the ephemerides. Presently the quasar catalog is internally consistent at the 5- to 10-nrad level [2]. Therefore, independent 5-nrad per component errors for each quasar direction have been considered.

Each solution set consists of ODP runs performed with different combinations of data types and accuracies. Data accuracies used were 30 cm or 3 cm for the Δ DOR, corresponding to about 50- or 5-nrad angular uncertainty, 1000 m, 10 m, or or 0.1 m for the range, and 1.0 mm/sec or 0.01 mm/sec for

⁶See Footnotes 1 and 2.

the Doppler. Runs were made with all possible combinations of these data accuracies. Runs were also made with Δ DOR and range only, Δ DOR and Doppler only, range and Doppler only, Δ DOR only, Doppler only, and range only. This led to a total of 35 runs for each solution set.

IV. Solution Set One

A. Error Modeling

Solution set one represents a first cut at investigating the dependence of orbit determination accuracy on radiometric data accuracy. For this set, relatively simple extrapolations of present day estimates of the errors for the ephemeris, the station locations, and other error sources were adopted. The results of this first solution set provided the information necessary to focus on the important error terms and neglect largely irrelevant terms. The error models particular to solution set one are summarized in Table 3.

The ephemeris errors used were supplied by M. E. Standish of the Navigation Systems Section in the form of a joint Earth-Mars set-III parameter covariance matrix. This ephemeris covariance represents the formal calculated errors appropriate for a modern ephemeris. These formal errors are often multiplied by a scale factor of two to five to make a crude allowance for systematic error. However, examination of the covariance matrix shows that the dominant component of error consists of a 100-nrad uncertainty in the zero point of right ascension for the ephemeris. All other orientation components of the ephemeris covariance are on the order of 5 nrad. Since the radio frame has been adopted as the fundamental frame for navigation, this right ascension uncertainty should correspond to the major component of the frame tie error between the planetary frame and the radio frame. The 100-nrad value for this uncertainty is consistent with the current estimate of the planetary-radio frame tie error for the inner planets [3, 4]. Therefore, the ephemeris errors are considered with no scaling. By doing so, the present frame-tie error is correctly modeled, but errors for the internal consistency of the ephemeris that are at present too small may be incorporated.

For solution set one the common "equivalent station location error" (ESLE) approach was adopted in which geocentric station coordinate, Earth orientation, and media calibration errors are lumped together into a single set of effective station errors. Present VLBI measurements establish Deep Space Network (DSN) baselines to 10 cm in the radio frame [5]. Geocentric station locations can potentially be derived from these baselines and Global Positioning System (GPS) satellite tracking data [6] with errors on the level of 10 cm. Therefore, 10-cm per component errors for the geocentric station coordinate contribution to the ESLEs have been used.

Due to unmodelable changes in the Earth's rotation rate and pole location, accurate information about the orientation of the Earth can be obtained only through a constant monitoring program. The largest component of error is in UT1-UTC, an offset in right ascension. The JPL Time and Earth Motion Precision Observations (TEMPO) deliveries for Magellan are expected to have a worst case (10-day extrapolation) UT1-UTC error of 50 nrad.⁷ This error has been accounted for by adding to the station location a priori covariance matrix a 50-nrad longitude error, fully correlated between stations.

For the media errors it was assumed that dual-frequency tracking could be used to calibrate out the ionosphere error and that the 4-cm wet troposphere error [7] derived from using monthly averages would not contribute significantly to the equivalent station location error. Hence, for solution set one ionosphere and troposphere errors were not explicitly included.

B. Results

To compare the results for the large number of combinations of data accuracies employed here, most results are presented in the form of root-sum-squared (RSS) position uncertainties at the nominal time of closest approach to Mars. In contrast, the critical navigational requirement of MRSR delivery is control of the angle of atmospheric entry. The RSS position error was chosen as a figure of merit over the more mission-specific angle of entry because it was felt to be more generally reflective of the overall accuracy of the orbit determination. In practice it has been found that the dominant error sources affect most of the orbit parameter uncertainties, and that the general trends in changes in orbit determination uncertainty with changes in data accuracy are visible in any figure of merit.

Table 6 gives the RSS position uncertainty at closest approach for all combinations of data types and accuracies with a breakdown of the total RSS uncertainties into calculated uncertainty and the contributions from considered errors. The 35 cases are listed by the Δ DOR accuracy, Doppler accuracy, and range accuracy. The main conclusions from solution set one are demonstrated by the three cases depicted in Fig. 1. In Fig. 1 the RSS uncertainty is broken down into components for the cases which include 30-cm Δ DOR, 1-mm/sec Doppler, and 1000-m, 10-m, or 0.1-m range. The dominant contribution is due to the considered ephemeris errors and is virtually constant regardless of data accuracies.

⁷T. F. Runge, "UTPM Calibration Accuracy for Magellan," JPL IOM 335.5-87.81 (internal document), Jet Propulsion Laboratory, Pasadena, California, April 30, 1987.

The calculated uncertainty decreases with improving range accuracy, with a significant improvement between the 10-m and 0.1-m case. This is because the 0.1-m range taken over an entire pass contains angular information with an accuracy of about 0.1 m divided by the diameter of the Earth, which is competitive with the 30-cm Δ DOR accuracy and reduces the dominant plane of the sky error.

However, the consider contribution due to the equivalent station location errors increases with improved range accuracy. For the 0.1-m range case the station location contribution is larger than the calculated uncertainty and the total uncertainty is larger than for the cases with less accurate range. This behavior is due to the estimation strategy employed. The station location errors have been considered rather than estimated. The spacecraft state estimate is therefore made without accounting for these errors. The effects of the station location errors upon this suboptimal estimate are then accounted for in the consider analysis. As the range accuracy approaches the level of the equivalent station location errors, the suboptimal nature of the estimate becomes more important than the accuracy of the data. A common approach that avoids this behavior, and gains some benefit from improved data accuracy, is to deweight the more accurate range data. For example, if the 0.1-m range were treated as if it were 10-m range, then the station location uncertainty consider contribution to the total error would be the same as for the 10-m range case, but the improved data accuracy would reduce the actual error somewhat below that for the 10-m case. However, ODP has no capability to evaluate the actual error that results from this procedure. To gain the full benefit of the more accurate range will require improvements in the modeling of the error sources that have been lumped into the equivalent station location errors.

Figures 2, 3, and 4 examine the B-plane (impact parameter plane) components for the same cases used in Fig. 1. Figure 2 shows the uncertainty breakdown in $B \cdot R$ (perpendicular to the Mars orbital plane). Figure 3 shows the uncertainties in $B \cdot T$ (in the Mars orbital plane). Figure 3 shows the uncertainty breakdown for the linearized time of flight (LTOF). These figures show that the trends seen in the RSS position uncertainty figure are preserved in each component in the B-plane, with the ephemeris contribution being dominant and independent of data accuracy, and the station location contribution and the total uncertainty increasing with improved range.

V. Solution Set Two

A. Error Modeling

The orbit determination uncertainties predicted with solution set one were dominated by the considered ephemeris

errors, and also, for the most accurate range or Doppler, by the equivalent station location errors. Experiments in the near future promise dramatic reductions in the planetary-radio frame-tie error. This reduction has been incorporated in the error modeling for solution set two. In addition, the equivalent station location error approach has been abandoned in favor of explicitly modeled station coordinates, Earth orientation, and troposphere errors, allowing the effects of each of these error sources to be individually examined. These changes in error modeling are summarized in Table 4.

Determination of the orientation of the dynamical reference frame of the planets relative to the VLBI quasar frame can be accomplished by several methods. One approach suggested by A. E. Niell⁸ involves linking Lunar Laser Ranging (LLR) sites, which have accurate positions in the planetary frame, to the DSN network. The LLR data establish the geocentric locations of these sites to better than 10-cm accuracy.⁹ These locations could be combined with VLBI-determined DSN baseline measurements (also accurate to 10 cm) to provide the frame-tie information. Previous efforts to do this have suffered from insufficient measurements relating the LLR sites to the DSN sites.^{10,11} The McDonald LLR site has been accurately measured with respect to the Fort Davis VLBI site to provide one link between the frames. Fixing the LLR network to the VLBI network at one point does not determine rotations about that point however. At least one other link between the networks is needed to establish the right ascension frame tie. Recent GPS measurements of the baseline between the Haleakala LLR site and the nearby Kokee Park VLBI site may be used to provide a second link between the networks [8, 9]. This may resolve the right ascension frame tie to 5–10 nrad since the relative declination is already known to the 5-nrad level. Further measurements connecting the VLBI network to the LLR network are desirable to provide a more complete solution.

The more direct approaches to establishing the frame tie involve astronomical observations. Comparison of the directions measured to short-period pulsars by radio interferometry and the directions determined by analysis of pulse arrival times can be used to establish the orientation of the planetary

⁸See Footnote 3.

⁹X. X. Newhall, personal communication.

¹⁰See Footnote 3.

¹¹D. Jones, "A. E. Niell's Method for Comparing DSN Station Locations to Determine Extragalactic-Planetary Frame Tie," JPL IOM (internal document), Jet Propulsion Laboratory, Pasadena, California, November 30, 1986.

frame relative to the radio frame [1]. The direction to the millisecond pulsar 1937+21 is known from timing analysis to 5 nrad relative to the Earth's orbit. At present the direction in the radio frame has only been established to 250 nrad by a VLA observation. Future VLBI observations promise greatly improved accuracy. Radio observations of the occultation of quasars by planets yield information on the frame tie. An occultation of P 0507+17 by Venus¹² has been observed, and is currently being analyzed. VLBI observations of spacecraft during encounters have established the present 100-nrad knowledge of the frame tie [3, 4]. The upcoming Phobos Lander frame-tie experiment is expected to provide a planetary-radio frame of much improved accuracy.¹³ A similar experiment could be included with the Mars Observer mission to confirm the Phobos results in time for the MRSR mission.

For solution set two it has been assumed that the right ascension offset between the dynamical reference system of the planets and the VLBI quasar system has been established at the 5-nrad level. A new Earth-Mars ephemeris covariance matrix was produced by inverting the original covariance used in solution set one to obtain the information matrix, adding a 5-nrad measurement of the offset in right ascension of Earth's orbit from its nominal orbit, and reinverting. It is stressed that only an improvement in the knowledge of the orientation in right ascension of the figure of the Earth's orbit has been assumed. No new information has been added about the Earth's phase in its orbit, or about the level of errors that change the shape or period of the orbit, or that rotate the orbit about axes that lie in the plane of Earth's equator. Any improvement in the Martian ephemeris is due entirely to its existing accuracy relative to Earth's ephemeris.

The behavior of the equivalent station location errors contribution to the orbit determination uncertainty prompted us to separate the Earth orientation error from the geocentric station location errors. The Earth orientation error is random and should have signature and temporal behavior significantly different from the geocentric station coordinate offsets and deserves to be modeled explicitly. The ODP link REGRES does not generate Earth orientation partials. Code has therefore been written to include the partial derivatives for Earth orientation in the ODP REGRES file via the ODMODIFY program. The desired partials may be calculated by the chain rule:

$$\frac{\partial X}{\partial \theta_i} = \sum_{j=1}^3 \left[\frac{\partial X}{\partial u_j} \frac{\partial u_j}{\partial \theta_i} + \frac{\partial X}{\partial v_j} \frac{\partial v_j}{\partial \theta_i} + \frac{\partial X}{\partial \lambda_j} \frac{\partial \lambda_j}{\partial \theta_i} \right] \quad (1)$$

¹² See Footnote 4.

¹³ See Footnote 5.

where X is the measured quantity, θ_1 and θ_2 represent rotations about the equatorial x and y axes (i.e., polar motion), θ_3 is an angle corresponding to UT1-UTC, and u_j , v_j , and λ_j are the cylindrical coordinates of station j . The partial derivatives of the measurements with respect to the station coordinates are available on the REGRES file. The partial derivatives of the station coordinates with respect to the Earth orientation angles are given by [10]

$$\begin{aligned} \frac{\partial u_j}{\partial \theta_1} &= -v_j \cos \lambda_j & \frac{\partial v_j}{\partial \theta_1} &= u_j \cos \lambda_j & \frac{\partial \lambda_j}{\partial \theta_1} &= \frac{v_j}{u_j} \sin \lambda_j \\ \frac{\partial u_j}{\partial \theta_2} &= v_j \sin \lambda_j & \frac{\partial v_j}{\partial \theta_2} &= -u_j \sin \lambda_j & \frac{\partial \lambda_j}{\partial \theta_2} &= \frac{v_j}{u_j} \cos \lambda_j \\ \frac{\partial u_j}{\partial \theta_3} &= 0 & \frac{\partial v_j}{\partial \theta_3} &= 0 & \frac{\partial \lambda_j}{\partial \theta_3} &= 1 \end{aligned} \quad (2)$$

Since the Earth orientation is a random error, for solution set two the Earth orientation angle errors are estimated as stochastic variables. A better treatment might be to consider unadjusted Earth orientation errors as stochastic variables, but this capability does not presently exist in the ODP. A priori errors of 8 nrad in the pole location and 50 nrad in UT1-UTC were assumed, corresponding to the level of error expected after 10 days of extrapolation from the last TEMPO measurement. Some correlation is expected in the errors from day to day, but little correlation between errors at separate times of measurement. Therefore, a 3.5-day correlation time was chosen as midway between two measurements taken one week apart.

For the geocentric station locations, 10-cm per coordinate errors were assumed. Thus the combination of station location error and Earth orientation error for solution set two corresponds to the equivalent station location errors used for solution set one.

Since we have broken apart the ESLE model, for this solution set the wet and dry troposphere delay errors were included using the existing partials in link REGRES. While the troposphere might be better estimated stochastically, it was desired to examine the effect of these errors separately from the Earth orientation errors and therefore only a constant 4-cm wet troposphere zenith delay error and a constant 1-cm dry troposphere zenith delay error for each station were considered.

B. Results

The RSS uncertainty results for solution set two are listed in Table 7. For these results the uncertainty contribution due to the considered ephemeris error is about 2.5 km. The considered station location error contribution is always less than the calculated uncertainty. The total uncertainty generally decreases with improved data. An exception occurs when the accuracy of the Doppler is improved from 1 mm/sec to 0.01 mm/sec with both Δ DOR and range included. In that case the increase of the considered station location error contribution still nets a small increase in the total uncertainty.

Figure 5 shows the results for the cases with 30-cm Δ DOR accuracy, 1-mm/sec Doppler accuracy, and the three different range accuracies. For these cases the calculated uncertainty is the dominant term and improves slightly with improved range accuracy. Comparison between Fig. 5 and Fig. 1 shows that the considered station location errors contribution has been reduced from 3.6 km to 0.25 km for the 10-m range case and from 18.0 km to 1.3 km for the 0.1-m range case. This shows that the largest portion of the original station location error contribution to the RSS uncertainty was due to the Earth orientation errors, which for solution set two are incorporated in the calculated uncertainty. The calculated uncertainty increased as a result, although by less than 5 percent for the cases in Fig. 5.

Figure 6 shows a comparison of the root-sum-square of the calculated uncertainty and uncertainty contribution due to station location errors for the cases from solution sets one and two that use 30-cm Δ DOR, 1-mm/sec Doppler, and 1000-m, 10-m, or 0.1-m range. This combination differs between the two sets only in the treatment of the Earth orientation errors. The more realistic treatment with estimated stochastic Earth orientation parameters produces an improved result for the more accurate data.

Figure 7 shows the RSS position uncertainty breakdown for the solution set two cases with 3-cm Δ DOR accuracy, 1-mm/sec Doppler accuracy, and the three different range accuracies. For these cases the change in range accuracy from 1000 m to 10 m or 0.1 m produces less than 3-percent change in all components. With 30-cm Δ DOR, the 0.1-m range information provides useful plane of the sky information, but that information is not competitive with 3-cm Δ DOR data. Thus, the error ellipsoid is dominated by the Δ DOR data accuracy. Figure 8 shows the B-plane uncertainty breakdowns for the case with 3-cm Δ DOR, 1-mm/sec Doppler, and 10-m range. The total uncertainties are comparable with those predicted for the MRSR mission by Konopoliv¹⁴ assuming both radio-

metric and onboard optical and more conservative error modeling. This suggests that the mission requirements could be met without onboard optical data, if more accurate Δ DOR data is available, and the radio-planetary frame-tie is improved.

In the absence of Δ DOR data the orbit determination uncertainty becomes strongly dependent on the range accuracy. Improved Doppler accuracy also improves the solution, although the Doppler-only solutions are much worse than the Doppler-plus-range solutions. Figure 9 shows the RSS uncertainties for six cases: 10-m range only, 0.1-m range only, 1-mm/sec Doppler only, and 1-mm/sec Doppler with 1000-m, 10-m, and 0.1-m range. The 10-m range only solution is better than the 1-mm/sec Doppler only solution by about 40 percent. Increased range accuracy results in significantly better results. The 0.1-m range only solution, which is almost the same as the 1-mm/sec Doppler with 0.1-m range solution, is nearly as good as the solution with 30-cm Δ DOR, 1-mm/sec Doppler, and 0.1-m range shown in Fig. 5. The results without Δ DOR that have 0.01-mm/sec Doppler and either 1000-m, 10-m, or 0.1-m range (not shown in Fig. 9) have little dependence on range accuracy and are about the same as the 0.1-m range only solution.

VI. Solution Set Three

A. Error Modeling

The results presented so far are based on existing capabilities (with the exception of the data accuracies). By the mid-1990s it will be possible to have improved Earth orientation measurements, improved station locations, and troposphere corrections. In solution set three the benefits of such improvements are examined. The error modeling used in solution set three is summarized in Table 5. It has been assumed that 3-cm accuracy station coordinates will be available [11, 12]. Using a combination of weekly IRIS VLBI Earth orientation measurements and daily GPS Earth orientation rate measurements, 7-nrad UT1-UTC calibrations and 5-nrad pole location determinations should be possible [13]. It has been assumed that the use of water vapor radiometers will reduce the error in wet troposphere zenith delays to 0.5 cm [14].¹⁵ Study of the dry troposphere delay is difficult given the current level of errors in the wet delay. Little improvement in the dry troposphere delay is envisioned, and this error has been left at 1.0 cm. Although improvements in the internal accuracy of the ephemeris are likely, they are difficult to model. Therefore the ephemeris errors used in solution set two have been maintained.

¹⁴See Footnote 2.

¹⁵S. E. Robinson, "Approximate Error Budget for Wet Delay Estimation," JPL IOM 335.4-571 (internal document), Jet Propulsion Laboratory, Pasadena, California, March 1986.

B. Results

The results for the ODP runs for solution set three are listed in Table 8. This table shows that, given the improved modeling of solution set three, the use of any one of the high-accuracy data types (0.1-m range, 0.01-mm/sec Doppler, or 3-cm Δ DOR) results in a significant decrease in the total error. This is illustrated in Figs. 10 and 11, which compare the results of solution sets two and three. In these figures, the ODP runs with 10-m range, 1-mm/sec Doppler, and 30-cm Δ DOR are designated as the "nominal" cases. For solution set one, this case had a total RSS error of 40.7 km. This result was improved to 12.3 km in solution set two due solely to the reduction in the ephemeris error contribution; the change in the Earth orientation modeling had little effect. In solution set three the total error for the nominal case is found to be essentially unchanged at 12.0 km. For the remainder of this article, this total error value of 12.0 km will be used as the benchmark by which the quality of all solutions will be judged.

Some combinations of data accuracies in set three do indeed produce a total error less than the 12.0 km of the nominal solution. Figures 10 and 11 show the error breakdown for selected combinations of data weights with the solution set two and solution set three error models. The first case shown in each figure is the nominal one with 30-cm Δ DOR, 10-m range, and 1-mm/sec Doppler. The total position uncertainty is dominated by the calculated uncertainty, with the bias acceleration error being the next largest contribution. The station and troposphere contributions for this case are reduced in solution set three but do not appreciably affect the total.

The second case in Figs. 10 and 11 differs from the nominal by using 0.1-m range along with 30-cm Δ DOR and 1-mm/sec Doppler. In solution set two the total uncertainty of 10.9 km for this case is slightly better than the nominal. The total uncertainty improves to 6.7 km in solution set three. This improvement is primarily due to the reduction in the calculated uncertainty, resulting from improved Earth orientation. The station and troposphere error contributions would be significant in solution set three if the a priori errors of these had been left at the more pessimistic solution set two level.

The third case in Figs. 10 and 11 includes 0.01-mm/sec Doppler with the nominal 30-cm Δ DOR and 10-m range. In solution set two this case has a larger total uncertainty than the nominal due to the troposphere and station error contributions. In solution set three the total of 5.1 km for this case is less than half of the nominal. The reduction in the station and troposphere components is the main reason for this improvement, but the improved Earth orientation has also made a large effect by reducing the calculated uncertainty by 50 percent.

The fourth case in Figs. 10 and 11 uses Δ DOR improved to 3 cm along with 10-m range and 1-mm/sec Doppler. The total uncertainty for this case is less than half the nominal in both solution set two and solution set three. The improvement in the troposphere contribution is responsible for the reduction in total uncertainty from 5.2 km in solution set two to 4.0 km in solution set three. The improved Earth orientation and station location accuracy have negligible effect.

The final case included in Figs. 10 and 11 uses only 0.1-m range. These results show that range is the strongest stand-alone data type of the three examined. The total uncertainty for this case is 15.3 km in solution set two, which is only 22 percent worse than the nominal case. In solution set three the total uncertainty is 7.5 km, which is 60 percent of the nominal value. The improvement from solution set two to solution set three results from both the improved Earth orientation and the reduced station location errors. The strength of this data type as a stand-alone observable may have important implications for another area of advanced study, Earth-based navigation based on optical telemetry.¹⁶

VII. Summary and Conclusion

It has been found that approach navigation for missions to the inner planets in the mid-1990s may benefit significantly from improved tracking data, provided that the right ascension uncertainty for the planetary ephemerides is reduced. This improved frame tie can result from improved ground surveys linking key VLBI and LLR stations, short-period pulsar observations, observations of occultations of quasars by planets, and VLBI observations during the Phobos Lander Mission and the Mars Observer Mission. Without this improved frame tie, the orbit determination accuracy is insensitive to improvements in the data accuracy. If the frame tie can be established at the 5-nrad level, an immediate improvement of a factor of three in orbit determination accuracy results (for the nominal case with 30-cm Δ DOR, 1000-m range, and 1-mm/sec Doppler). An additional factor of two improvement can then be attained by improving the Δ DOR accuracy to 3 cm.

Error model improvements studied here include improved representation of the station locations and Earth orientation errors. Orbit determination accuracy actually degrades with improved range and Doppler data when station location errors

¹⁶W. M. Folkner, M. H. Finger, and J. M. Davidson, "Implications of Daytime Sky Brightness for Ground-Based Optical Navigation," JPL IOM 335.3-88-114 (internal document), Jet Propulsion Laboratory, Pasadena, California, October 28, 1988.

are forced to account for Earth orientation errors. Separating the Earth orientation and the geocentric station location errors, as was done in Section IV, provides a more physically meaningful model, such that improvements in range or Doppler accuracies result in improved orbit solutions. This model also allows an examination of how improved station locations and Earth orientation, as can be provided by GPS techniques, can best be applied. Another improvement studied was the reduced troposphere error, which might be attained by GPS or water vapor radiometer techniques.

Improved Δ DOR data reduced orbit determination errors without any improvements in station location and Earth orientation calibration, although improved troposphere calibrations provided an additional 30-percent reduction in orbit determination error for cases involving 3-cm Δ DOR data. After the initial model change in which Earth orientation errors were separated from station location errors, it was found that improved range produced an improved orbit solution. In fact range was found to be by far the most useful stand-alone data

type. After incorporating the improvements to the Earth orientation and station location calibrations expected in the mid-1990s, 0.1-m range was found to provide nearly a factor of two better orbit determination accuracy than 10-m range. To benefit from high-accuracy Doppler it was found that sub-centimeter accuracy troposphere calibrations are required as well as the expected improvements in Earth orientation calibration and station location errors. Given these improvements, the utilization of 0.01-mm/sec Doppler can provide a factor of two improvement in orbit determination accuracy over 1-mm/sec Doppler.

These studies have been done in the absence of onboard optical data and hence do not show how improved radiometric data may complement onboard optical data. However, it has been shown that radiometric data alone can perform competitively with existing onboard optical orbit determination. This may be useful in the context of repeat missions to Mars or other inner planets when not every mission requires a camera for scientific purposes.

Acknowledgments

The authors would like to thank Jim Border, Alex Konopliv, Jim McDanell, Myles Standish, Cathy Thornton, Robert Treuhaft, and Jim Williams for helpful suggestions and discussions.

References

- [1] D. C. Backer, E. B. Fomalont, W. M. Goss, J. H. Taylor, and J. M. Weisberg, "Accurate Timing and Interferometer Positions for the Millisecond Pulsar 1937+21 and the Binary Pulsar 1913+16," *Astr. J.*, vol. 90, pp. 2275-2280, 1985.
- [2] O. J. Sovers, C. D. Edwards, C. S. Jacobs, G. E. Lanyi, K. M. Liewer, and R. N. Treuhaft, "Astrometric Results of 1978-85 Deep Space Network Radio Interferometry: The JPL 1987-1 Extragalactic Source Catalog," *Astr. J.* vol. 95, pp. 1647-1658, June 1988.
- [3] X. X. Newhall, R. A. Preston, and P. B. Esposito, "Relating the JPL VLBI Reference Frame and the Planetary Ephemerides," in *Astrometric Techniques, Proceedings of the 109th Symposium of the IAU*, pp. 789-794, January 1984.
- [4] T. P. McElrath and R. S. Bhat, "Determination of the Inner Planet Frame Tie Using VLBI Data," *Proceedings of the AIAA Astrodynamics Conference*, paper 88-4234, August 15, 1988.
- [5] O. J. Sovers et al., "Radio Interferometric Determination of Intercontinental Baselines and Earth Orientation Utilizing Deep Space Network Antennas: 1971-1980," *J. Geophys. Res.*, vol. 89, pp. 7597-7607, 1984.
- [6] R. Malla, "Deriving a Unique Reference Frame for GPS Measurements," *IEEE Position Location and Navigation Symposium*, pp. 177-184, 1988.
- [7] C. A. Chao, "The Tropospheric Calibration Model for Mariner Mars 1971," *JPL Technical Report 32-1587*, Jet Propulsion Laboratory, Pasadena, California, pp. 61-76, 1974.
- [8] X. Wu and P. L. Bender, "Carrier Phase Ambiguity Resolution and Recovery of Kauai-Maui Baseline," *EOS Trans. AGU*, vol. 69, p. 1151, 1988.
- [9] W. E. Carter et al., "Difference Between the VLBI and SLR Terrestrial Reference Frames," *EOS Trans. AGU*, vol. 69, p. 1153, 1988.
- [10] T. D. Moyer, "Mathematical Formulation of the Double-Precision Orbit Determination Program (DPODP)," *JPL Technical Report 32-1527*, Jet Propulsion Laboratory, Pasadena, California, May 15, 1971.
- [11] S. M. Lichten, W. I. Bertiger, and E. C. Katsigris, "Sub-Meter GPS Orbit Determination and High-Precision User Positioning: A Demonstration," *Proceeding of the AIAA Astrodynamics Conference*, paper 88-4211, August 15, 1988.
- [12] S. M. Lichten and J. S. Border, "Strategies for High Precision GPS Orbit Determination," *J. Geophys. Res.*, vol. 92, pp. 12751-12762, 1987.
- [13] A. Freedman and J. Dickey, "Usefulness of GPS for Precise Determination of Earth Orientation Parameters," *EOS Trans. AGU*, vol. 68, p. 1245, 1987.
- [14] S. E. Robinson, "The Profile Algorithm for Microwave Delay Estimation From Water Vapor Radiometer Data," *Radio Science*, vol. 23, pp. 401-408, 1988.

Table 1. Observation schedule for MRSR study

Doppler and range data	DSS-11	DSS-44	DSS-61
First pass	July 16	July 18	July 20
Last pass	Oct. 2	Oct. 4	Sept. 30
Number of passes	14	14	13
Number of Doppler points	92	141	76
Number of range points	84	134	78
Δ DOR data	DSS-11–DSS-44	DSS-11–DSS-61	
First measurement	July 19	July 18	
Last measurement	Oct. 5	Oct. 4	
Number of measurements	14	14	

Table 2. Error modeling common to all solutions

Error source	Treatment	A priori uncertainty
Initial state		
Position	Estimated	1.0×10^4 km per component
Velocity	Estimated	1.0 km/sec per component
Solar pressure		
G_r	Estimated	1.3×10^{-1}
G_x	Estimated	1.0×10^{-2}
G_y	Estimated	1.0×10^{-2}
Other accelerations		
Constant	Considered	1.0×10^{-12} km/sec ² per component
Random	Estimated stochastically	1.0×10^{-12} km/sec ² per component $\tau = 5$ days
Mars GM	Considered	1.5×10^{-1} km ³ /sec ²
Mars J2	Considered	4.4×10^{-7}
Quasar directions	Considered	5.0×10^{-9} radians per component

Table 3. Error modeling for set one solutions

Error source	Treatment	A priori uncertainty
Station coordinates	Lumped in	10.0 cm per component
UT1-UTC	considered ESLE	5.0×10^{-8} radians
Earth-Mars ephemeris	Considered	$1.0 \times$ Standish covariance

Table 4. Error modeling for set two solutions

Error source	Treatment	A priori uncertainty
Station coordinates	Considered	10.0 cm per component
Earth orientation		
UT1-UTC	Estimated	5.0×10^{-8} radians
Pole direction	stochastically	8.0×10^{-9} radians per component $\tau = 3.5$ days
Troposphere		
Wet	Considered	4.0 cm
Dry	Considered	1.0 cm
Earth-Mars ephemeris	Considered	Standish covariance with RA offset error reduced to 5.0×10^{-9} radians

Table 5. Error modeling for set three solutions

Error source	Treatment	A priori uncertainty
Station coordinates	Considered	3.0 cm per component
Earth orientation		
UT1-UTC	Estimated	6.3×10^{-9} radians
Pole direction	stochastically	4.7×10^{-9} radians per component $\tau = 3.5$ days
Troposphere		
Wet	Considered	0.5 cm
Dry	Considered	1.0 cm
Earth-Mars ephemeris	Considered	Standish covariance with RA offset error reduced to 5.0×10^{-9} radians

Table 6. Data from solution set one

Δ DOR accuracy, cm	Doppler accuracy, mm/sec	Range accuracy, m	Calculated error, km	Station consider, km	Ephemeris consider, km	GM, J2 consider, km	Quasar consider, km	Bias acceleration consider, km	Total RSS error, km
-	-	1000	1308.	0.772	3.164	3.601	0.000	99.75	1312.
-	-	10	75.42	8.965	17.41	0.906	0.000	49.79	92.48
-	-	0.1	5.236	20.12	39.72	0.138	0.000	3.622	44.98
-	1	-	134.2	12.92	24.66	0.681	0.000	80.33	158.9
-	1	1000	43.53	13.32	25.68	0.474	0.000	31.68	61.12
-	1	10	22.88	18.10	35.93	0.044	0.000	13.96	48.34
-	1	0.1	5.202	20.12	39.73	0.138	0.000	3.599	44.98
-	0.01	-	55.27	60.86	106.4	4.470	0.000	40.32	140.5
-	0.01	1000	2.003	21.32	40.88	0.159	0.000	0.950	46.15
-	0.01	10	1.994	21.22	40.89	0.160	0.000	0.942	46.12
-	0.01	0.1	1.351	21.12	41.04	0.170	0.000	0.523	46.18
30	-	-	351.2	3.753	38.80	0.492	68.10	63.33	365.4
30	-	1000	10.22	0.164	38.57	0.138	1.331	7.895	40.70
30	-	10	10.02	0.199	38.84	0.161	1.310	7.219	40.77
30	-	0.1	4.642	18.03	39.72	0.137	0.372	3.260	43.99
30	1	-	93.03	10.79	41.27	0.281	9.172	49.97	114.3
30	1	1000	9.886	0.853	38.88	0.163	1.286	7.144	40.77
30	1	10	9.354	3.637	38.78	0.151	1.141	6.884	40.67
30	1	0.1	4.624	18.04	39.73	0.137	0.369	3.243	44.00
30	0.01	-	24.94	134.9	44.34	0.851	6.871	8.722	144.6
30	0.01	1000	1.975	20.67	40.79	0.154	0.0079	0.925	45.78
30	0.01	10	1.967	20.58	40.81	0.155	0.078	0.919	45.75
30	0.01	0.1	1.346	20.92	41.02	0.168	0.026	0.519	46.06
3	-	-	127.0	16.22	39.68	0.681	56.23	89.71	170.8
3	-	1000	1.856	0.287	40.16	0.103	2.305	0.770	40.28
3	-	10	1.812	0.282	40.20	0.110	2.261	0.793	40.31
3	-	0.1	1.764	1.545	40.21	0.111	2.132	0.765	40.34
3	1	-	73.53	9.266	42.43	0.612	13.33	66.07	108.8
3	1	1000	1.811	0.285	40.23	0.112	2.259	0.793	40.34
3	1	10	1.810	0.281	40.23	0.112	2.258	0.793	40.34
3	1	0.1	1.763	1.564	40.21	0.111	2.130	0.765	40.34
3	0.01	-	5.772	156.4	39.35	0.076	7.213	0.683	161.5
3	0.01	1000	1.255	8.191	39.42	0.071	1.664	0.468	40.32
3	0.01	10	1.250	8.183	39.43	0.072	1.661	0.466	40.33
3	0.01	0.1	1.095	12.30	40.05	0.107	1.139	0.389	41.93

Note: Earth orientation error is included as a 50-nrad rotation uncertainty in the 10-cm ESLE station location errors. The ephemeris covariance is from M. Standish.

Table 7. Data from solution set two

Δ DOR accuracy, cm	Doppler accuracy, mm/sec	Range accuracy, m	Calculated error, km	Station consider, km	Troposphere consider, km	Ephemeris consider, km	GM, J2 consider, km	Quasar consider, km	Bias acceleration consider, km	Total RSS error, km
-	-	1000	1307.	0.423	0.327	1.010	3.601	0.000	99.75	1312.
-	-	10	75.47	2.842	1.214	1.323	0.907	0.000	49.82	90.50
-	-	0.1	11.02	5.386	2.311	2.397	0.103	0.000	8.461	15.27
-	1	-	134.4	4.739	4.710	1.651	0.688	0.000	80.65	156.9
-	1	1000	43.89	4.584	4.261	1.723	0.483	0.000	32.02	54.72
-	1	10	24.21	4.761	3.528	2.252	0.036	0.000	14.74	29.05
-	1	0.1	10.99	5.384	2.372	2.397	0.103	0.000	8.453	15.25
-	0.01	-	91.03	36.83	91.80	5.046	3.359	0.000	51.12	143.9
-	0.01	1000	9.999	5.301	7.354	2.354	0.072	0.000	7.712	15.72
-	0.01	10	9.960	5.221	9.663	2.354	0.072	0.000	7.675	16.86
-	0.01	0.1	9.857	6.200	8.932	2.347	0.069	0.000	7.529	16.66
30	-	-	351.3	2.445	27.70	2.644	0.492	68.09	63.35	364.4
30	-	1000	10.22	0.137	2.612	2.464	0.137	1.330	7.896	13.48
30	-	10	10.02	0.141	2.562	2.477	0.161	1.310	7.219	12.92
30	-	0.1	7.707	3.262	2.568	2.472	0.136	0.912	5.841	10.85
30	1	-	93.13	3.450	6.426	2.786	0.276	9.192	50.07	106.4
30	1	1000	9.890	0.414	2.659	2.479	0.163	1.287	7.147	12.80
30	1	10	9.466	0.730	2.289	2.473	0.151	1.169	6.935	12.29
30	1	0.1	7.692	3.308	2.665	2.472	0.136	0.914	5.834	10.872
30	0.01	-	44.47	35.16	37.27	2.749	1.098	5.483	15.93	69.97
30	0.01	1000	6.500	5.301	10.59	2.457	0.115	1.082	5.022	14.66
30	0.01	10	6.497	5.293	10.52	2.456	0.115	1.080	5.017	14.61
30	0.01	0.1	6.478	5.213	9.858	2.452	0.112	1.075	4.991	14.09
3	-	-	127.3	11.45	112.8	2.707	0.676	56.73	89.91	200.9
3	-	1000	1.858	0.279	3.373	2.561	0.103	2.294	0.770	5.229
3	-	10	1.814	0.275	3.385	2.563	0.110	2.250	0.794	5.206
3	-	0.1	1.805	0.263	3.340	2.565	0.112	2.235	0.789	5.166
3	1	-	73.64	3.330	6.260	2.817	0.611	13.43	66.18	100.2
3	1	1000	1.813	0.275	3.385	2.565	0.112	2.248	0.794	5.205
3	1	10	1.812	0.274	3.380	2.565	0.112	2.247	0.794	5.201
3	1	0.1	1.804	0.264	3.341	2.565	0.112	2.235	0.789	5.166
3	0.01	-	32.78	82.93	126.1	2.690	0.892	8.305	12.75	155.2
3	0.01	1000	1.727	1.411	4.940	2.547	0.095	2.220	0.732	6.430
3	0.01	10	1.726	1.425	4.995	2.547	0.095	2.220	0.732	6.475
3	0.01	0.1	1.716	1.581	4.652	2.544	0.092	2.225	0.724	6.248

Note: Earth orientation is estimated stochastically with 8-nrad polar and 50-nrad UT1-UTC uncertainties. Station location errors are 10 cm. The zenith wet troposphere error is 4 cm. The modified ephemeris covariance includes a 5-nrad measurement of right ascension offset from the quasar frame.

Table 8. Data from solution set three

Δ DOR accuracy, cm	Doppler accuracy, mm/sec	Range accuracy, m	Calculated error, km	Station consider, km	Troposphere consider, km	Ephemeris consider, km	GM, J2 consider, km	Quasar consider, km	Bias acceleration consider, km	Total RSS error, km
-	-	1000	1308.	0.127	0.090	1.010	3.601	0.000	99.75	1312.
-	-	10	75.42	0.853	0.336	1.324	0.906	0.000	49.79	90.40
-	-	0.1	5.532	1.715	0.649	2.524	0.140	0.000	3.933	7.472
-	1	-	134.2	1.428	1.287	1.659	0.681	0.000	80.34	156.4
-	1	1000	43.54	1.378	1.167	1.732	0.474	0.000	31.68	53.91
-	1	10	22.91	1.443	0.964	2.289	0.044	0.000	13.97	26.98
-	1	0.1	5.501	1.715	0.660	2.524	0.141	0.000	3.912	7.438
-	0.01	-	66.77	10.01	13.81	5.359	2.867	0.000	50.53	85.67
-	0.01	1000	3.105	2.211	1.911	2.593	0.165	0.000	1.764	5.295
-	0.01	10	3.091	2.091	2.027	2.593	0.165	0.000	1.751	5.277
-	0.01	0.1	2.658	2.173	3.097	2.593	0.164	0.000	1.322	5.466
30	-	-	351.2	0.734	6.856	2.644	0.492	68.10	63.33	363.4
30	-	1000	10.22	0.041	0.654	2.464	0.138	1.331	7.895	13.24
30	-	10	10.22	0.042	0.641	2.477	0.161	1.310	7.219	12.68
30	-	0.1	4.892	1.318	0.363	2.528	0.138	0.399	3.484	6.671
30	1	-	93.03	1.044	1.668	2.787	0.280	9.173	49.97	106.1
30	1	1000	9.886	0.125	0.670	2.479	0.163	1.286	7.144	12.53
30	1	10	9.357	0.259	0.554	2.474	0.151	1.142	6.885	11.95
30	1	0.1	4.875	1.321	0.371	2.528	0.138	0.396	3.470	6.652
30	0.01	-	26.89	17.75	9.810	2.631	0.424	7.132	8.867	35.65
30	0.01	1000	2.981	1.990	1.940	2.583	0.153	0.201	1.635	5.101
30	0.01	10	2.969	1.885	2.024	2.583	0.154	0.199	1.628	5.084
30	0.01	0.1	2.603	2.032	2.979	2.587	0.157	0.124	1.276	5.305
3	-	-	127.0	3.608	28.78	2.706	0.680	56.27	89.71	167.9
3	-	1000	1.856	0.084	0.851	2.561	0.103	2.305	0.770	4.081
3	-	10	1.812	0.083	0.854	2.563	0.110	2.260	0.793	4.042
3	-	0.1	1.771	0.103	0.798	2.564	0.111	2.151	0.770	3.948
3	1	-	73.53	1.133	1.814	2.815	0.611	13.34	66.07	99.81
3	1	1000	1.811	0.083	0.854	2.565	0.112	2.258	0.793	4.042
3	1	10	1.810	0.083	0.853	2.565	0.112	2.257	0.793	4.040
3	1	0.1	1.771	0.104	0.798	2.564	0.111	2.150	0.769	3.947
3	0.01	-	8.585	12.35	14.60	2.522	0.110	7.063	1.117	22.29
3	0.01	1000	1.517	0.754	1.571	2.536	0.084	1.915	0.602	3.976
3	0.01	10	1.516	0.749	1.562	2.536	0.0842	1.912	0.602	3.969
3	0.01	0.1	1.505	0.713	1.567	2.540	0.089	1.845	0.594	3.930

Note: Earth orientation is estimated stochastically with 4.7-nrad polar and 6.3-nrad UT1-UTC uncertainties. Station location errors are 3 cm. The zenith wet troposphere error is 5 mm. The zenith dry troposphere error is 10 mm. The modified ephemeris covariance is the same as that used in solution set two.

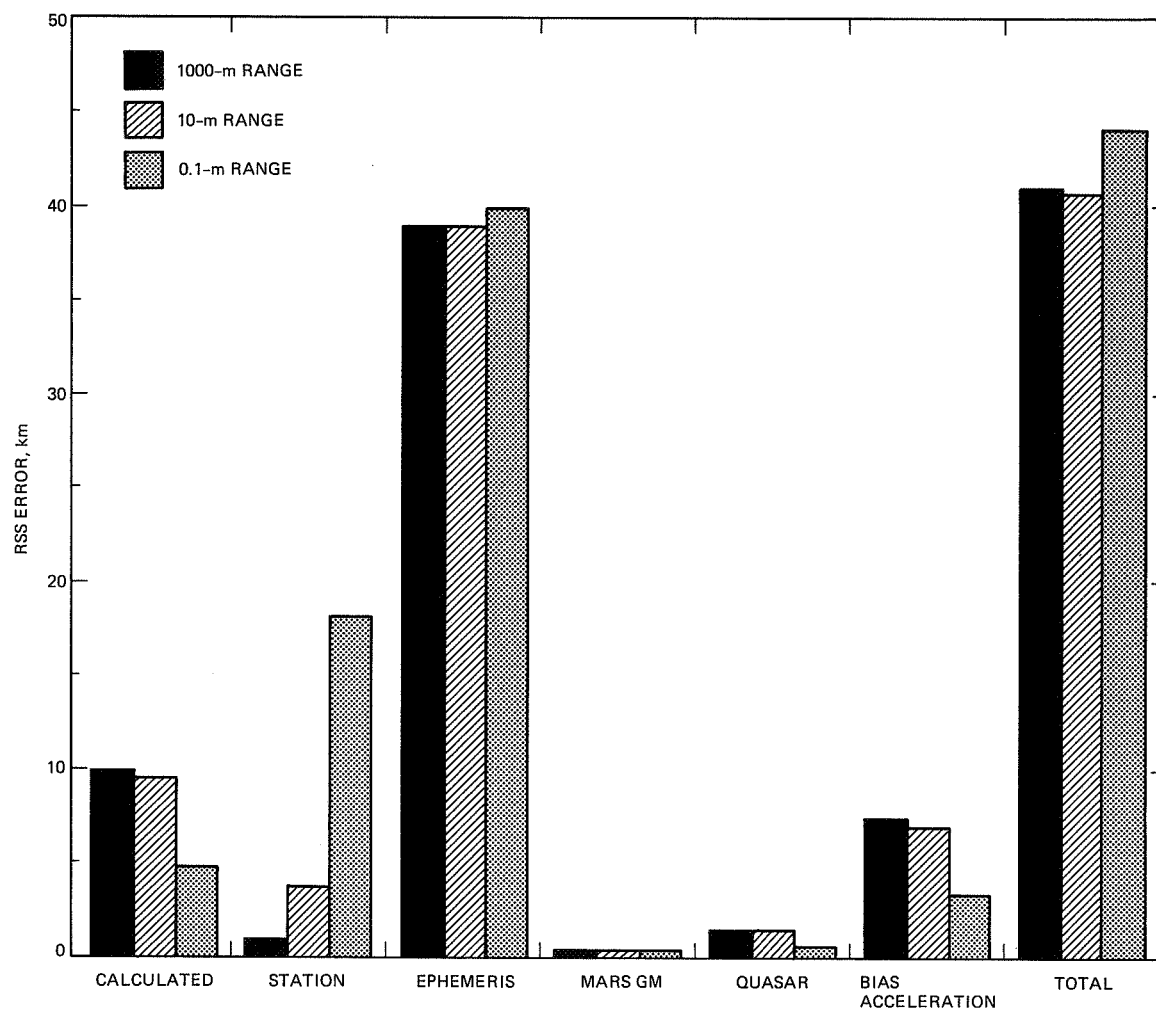


Fig. 1. RSS error breakdown for cases from solution set one with 30-cm Δ DOR, 1-mm/sec Doppler, and 1000-m, 10-m, or 0.1-m range.

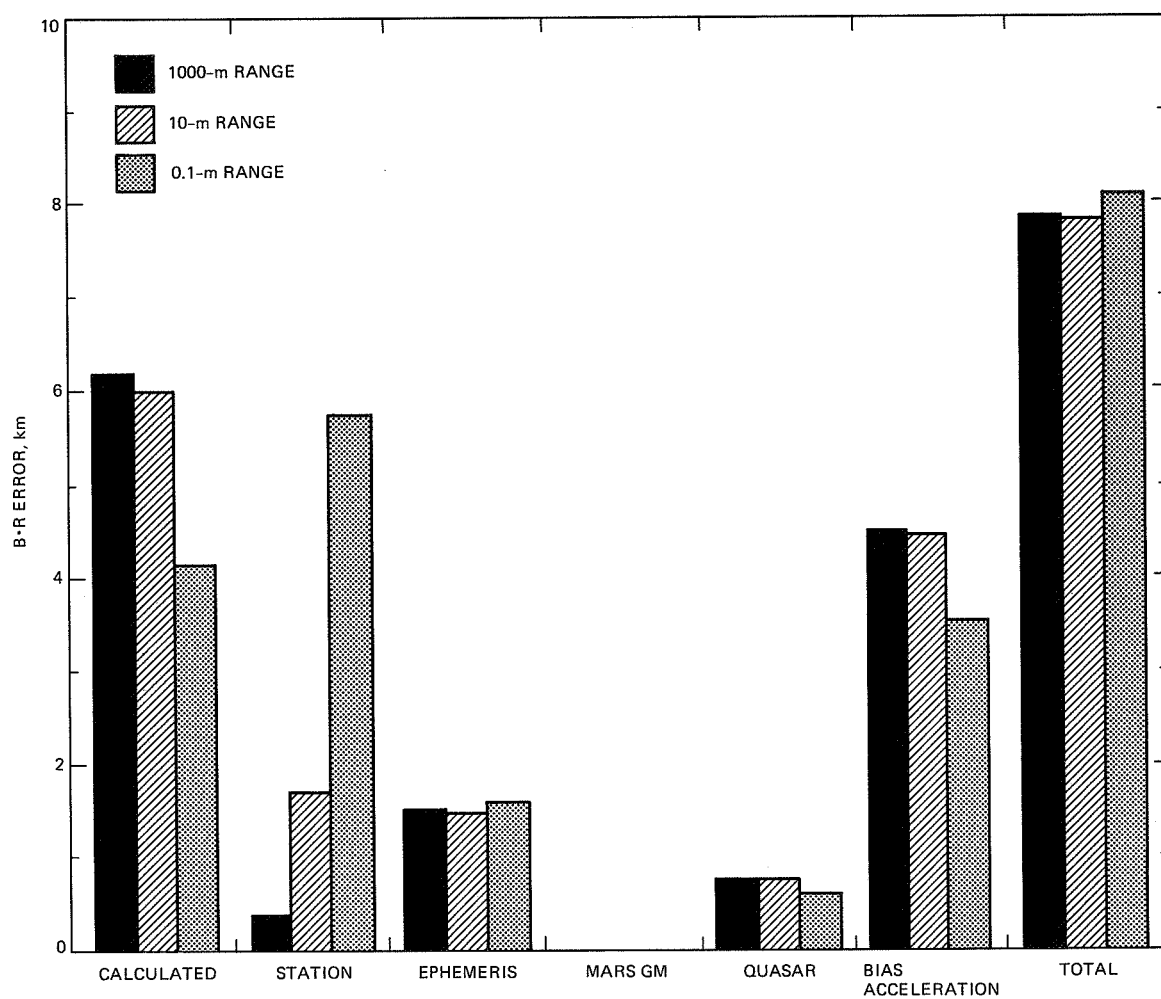


Fig. 2. $B \cdot R$ error breakdown for cases from solution set one with 30-cm ΔDOR , 1-mm/sec Doppler, and 1000-m, 10-m, or 0.1-m range.

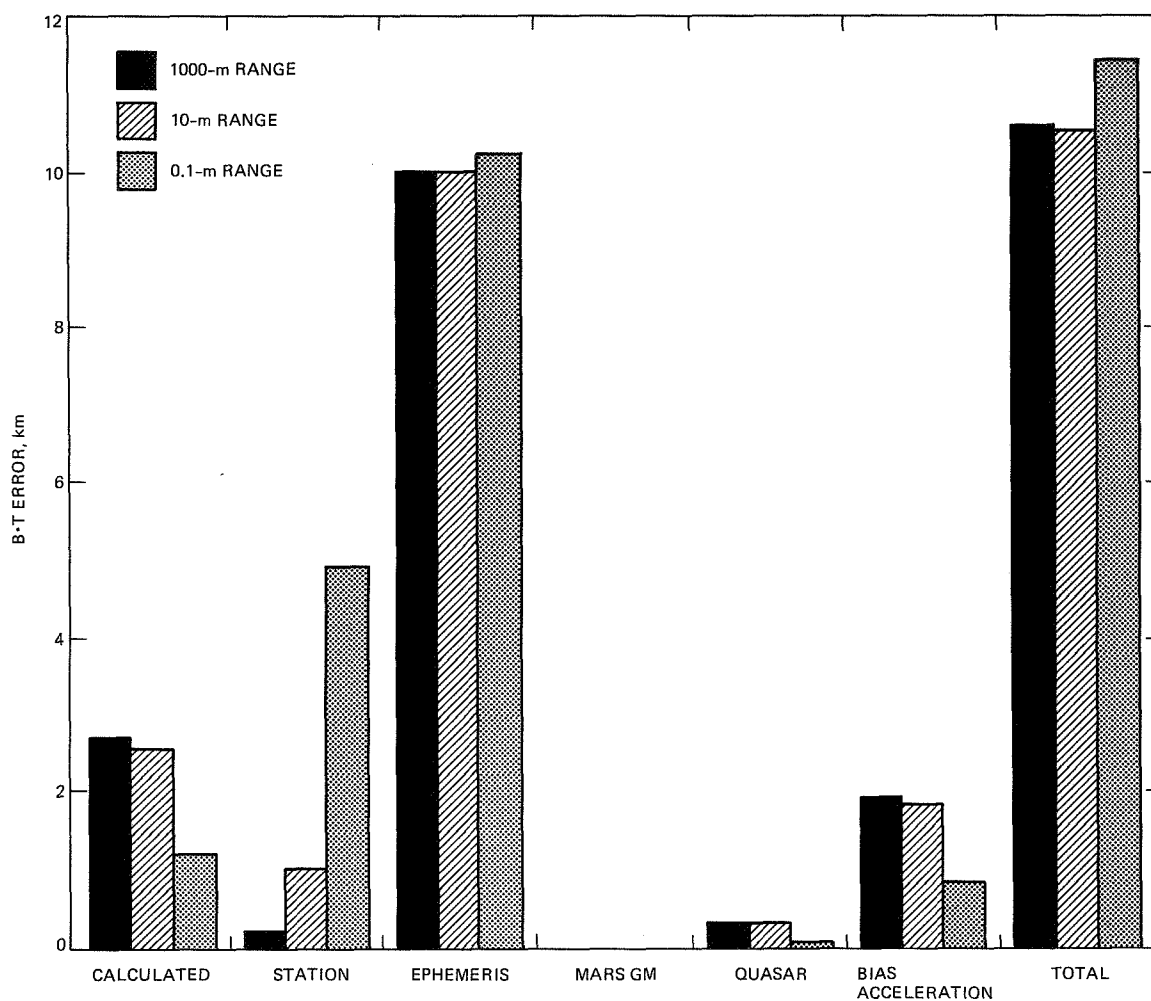


Fig. 3. $B \cdot T$ error breakdown for cases from solution set one with 30-cm ΔDOR , 1-mm/sec Doppler, and 1000-m, 10-m, or 0.1-m range.

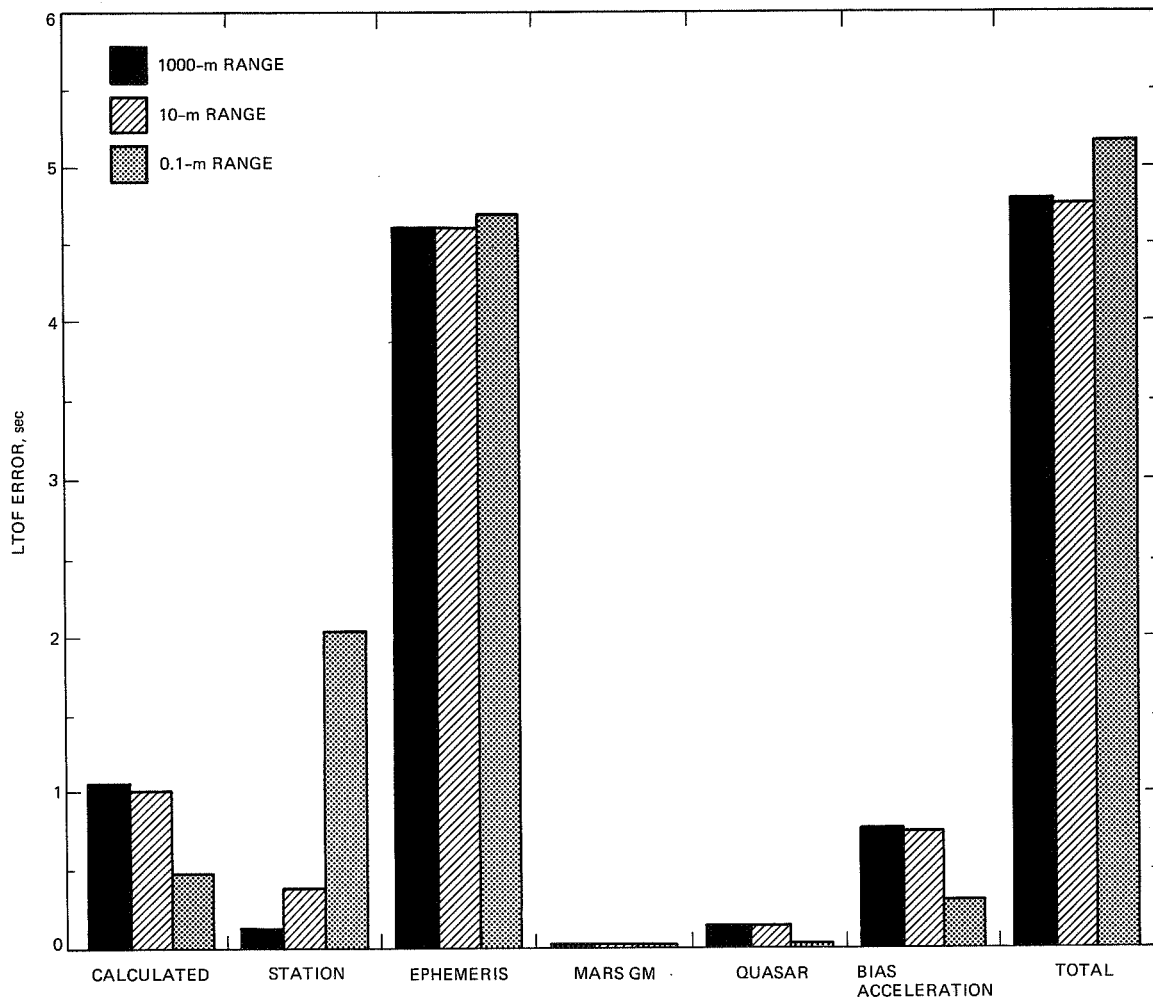


Fig. 4. LTOF error breakdown for cases from solution set one with 30-cm Δ DOR, 1-mm/sec Doppler, and 1000-m, 10-m, or 0.1-m range.

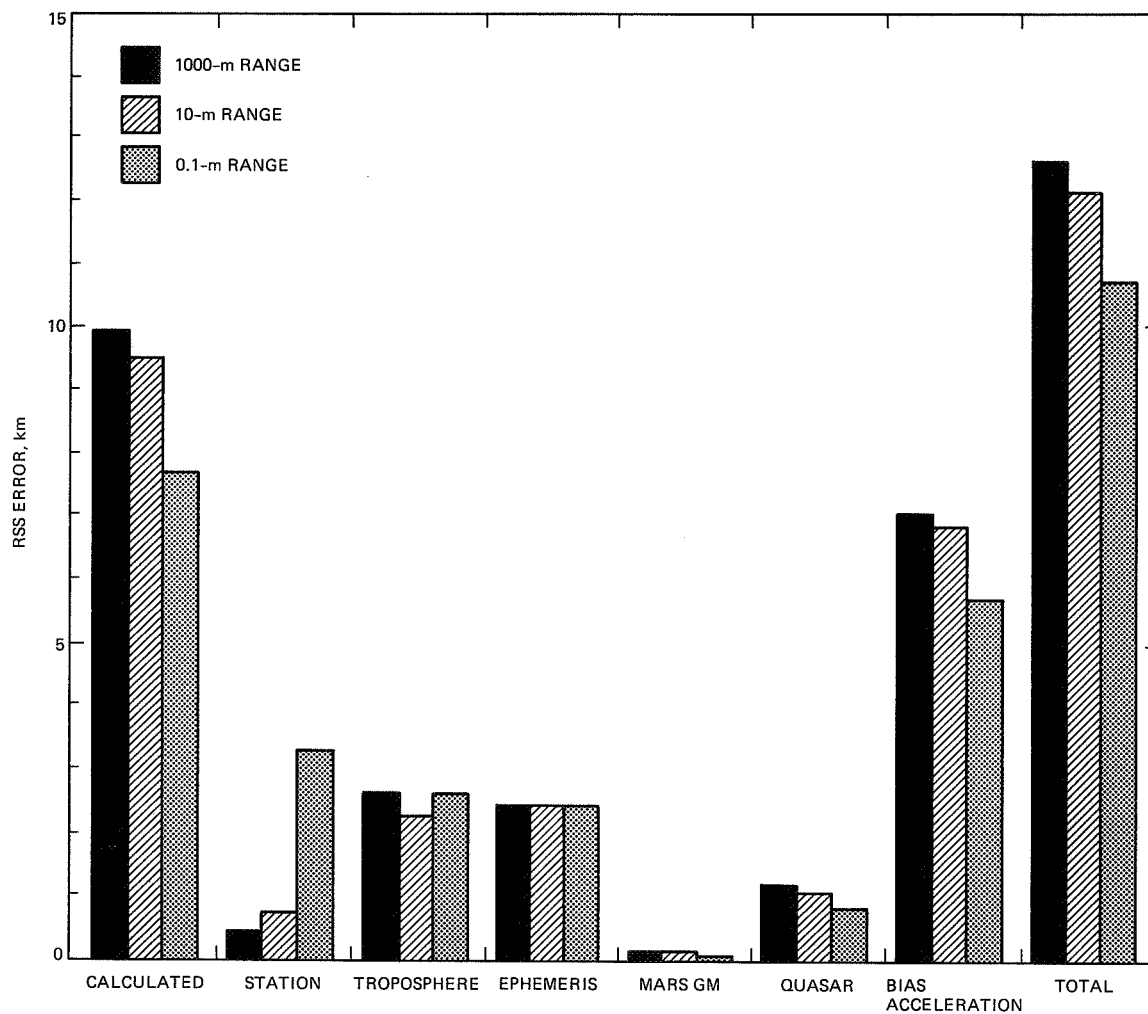


Fig. 5. RSS error breakdown for cases from solution set two with 30-cm Δ DOR, 1-mm/sec Doppler, and 1000-m, 10-m, or 0.1-m range.

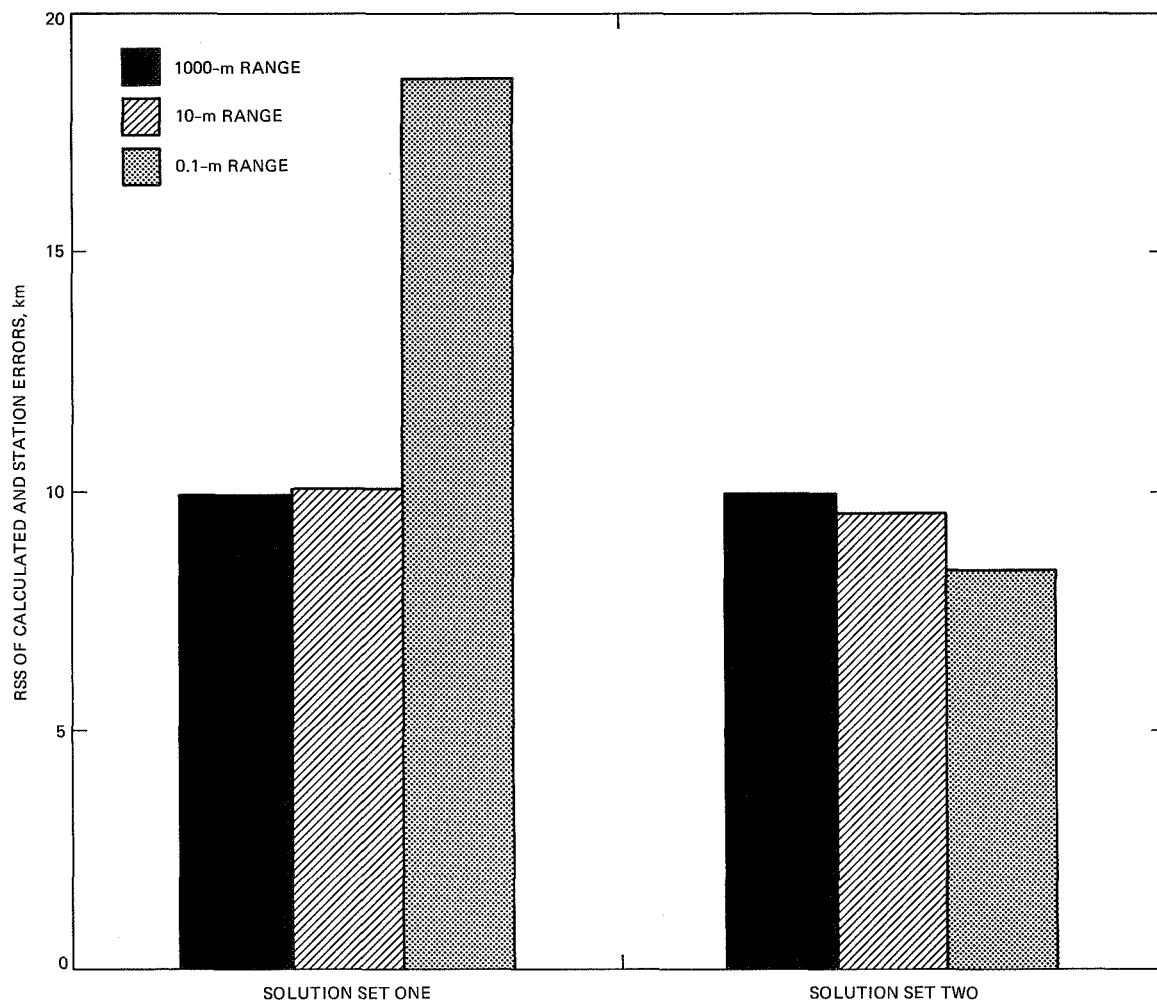


Fig. 6. Comparison of the RSS sum of calculated and station location errors for the cases in solution sets one and two with 30-cm Δ DOR, 1-mm/sec Doppler, and 1000-m, 10-m, or 0.1-m range.

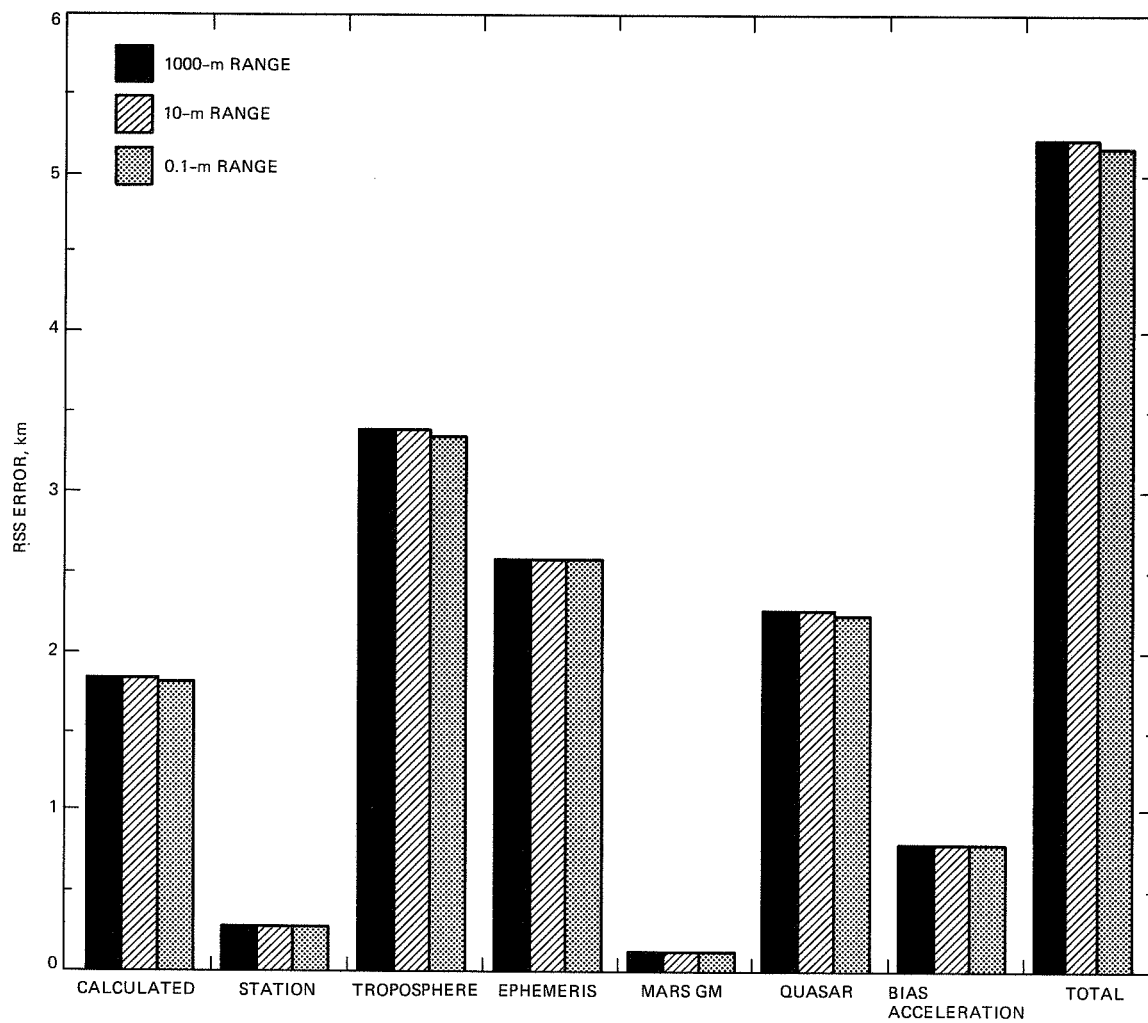


Fig. 7. RSS error breakdown for cases from solution set two with 3-cm Δ DOR, 1-mm/sec Doppler, and 1000-m, 10-m, or 0.1-m range.

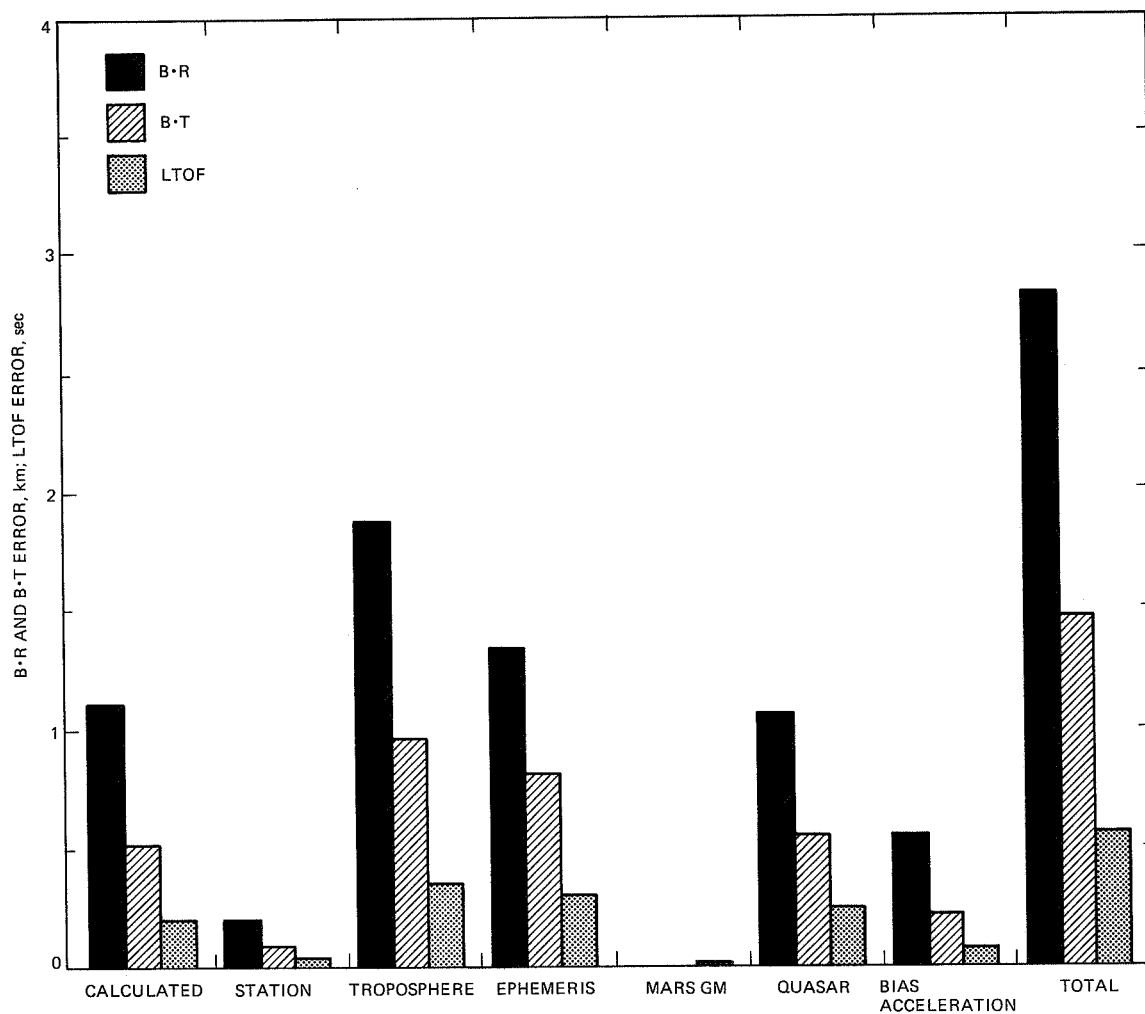


Fig. 8. B-plane error breakdown for the case from solution set two with 3-cm Δ DOR, 1-mm/sec Doppler, and 10-m range.

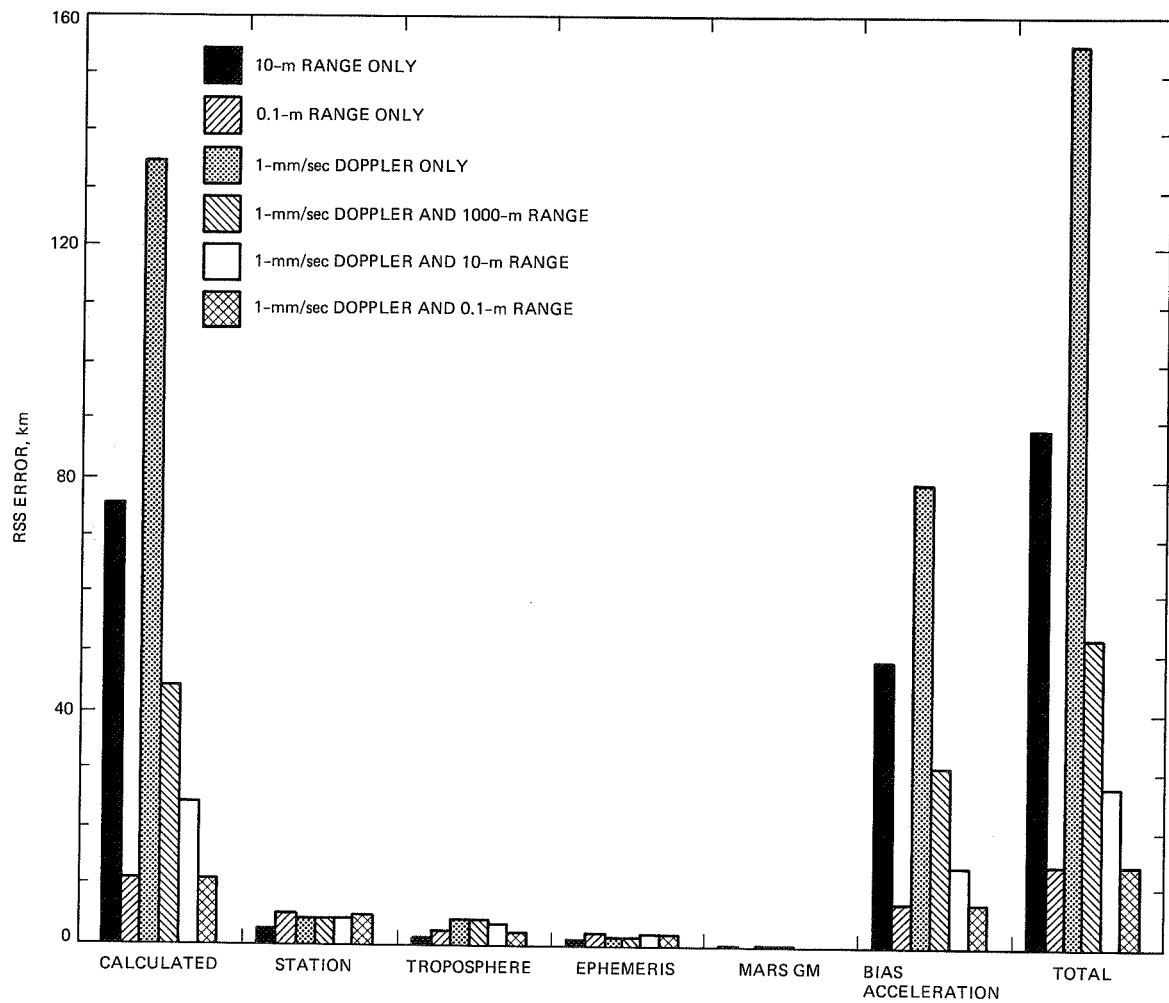


Fig. 9. RSS error breakdown for selected cases from solution set two with no Δ DOR data.

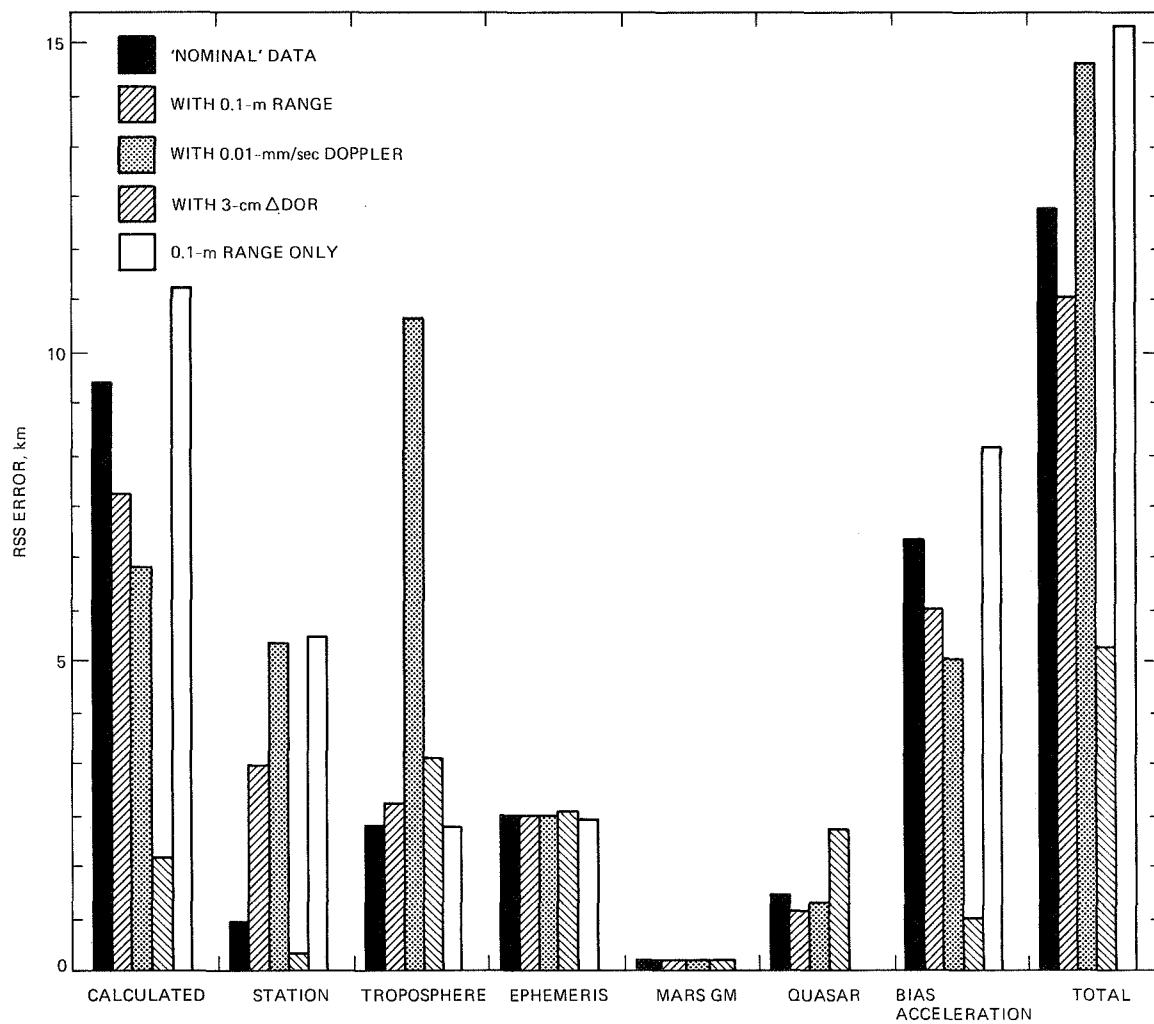


Fig. 10. RSS error breakdown for selected cases from solution set two. The nominal case uses 30-cm Δ DOR, 1-mm/sec Doppler, and 10-m range. Three of the remaining cases depart from the nominal case by the improvement of, as indicated, one of the data accuracies. The final case uses 0.1-m range only.

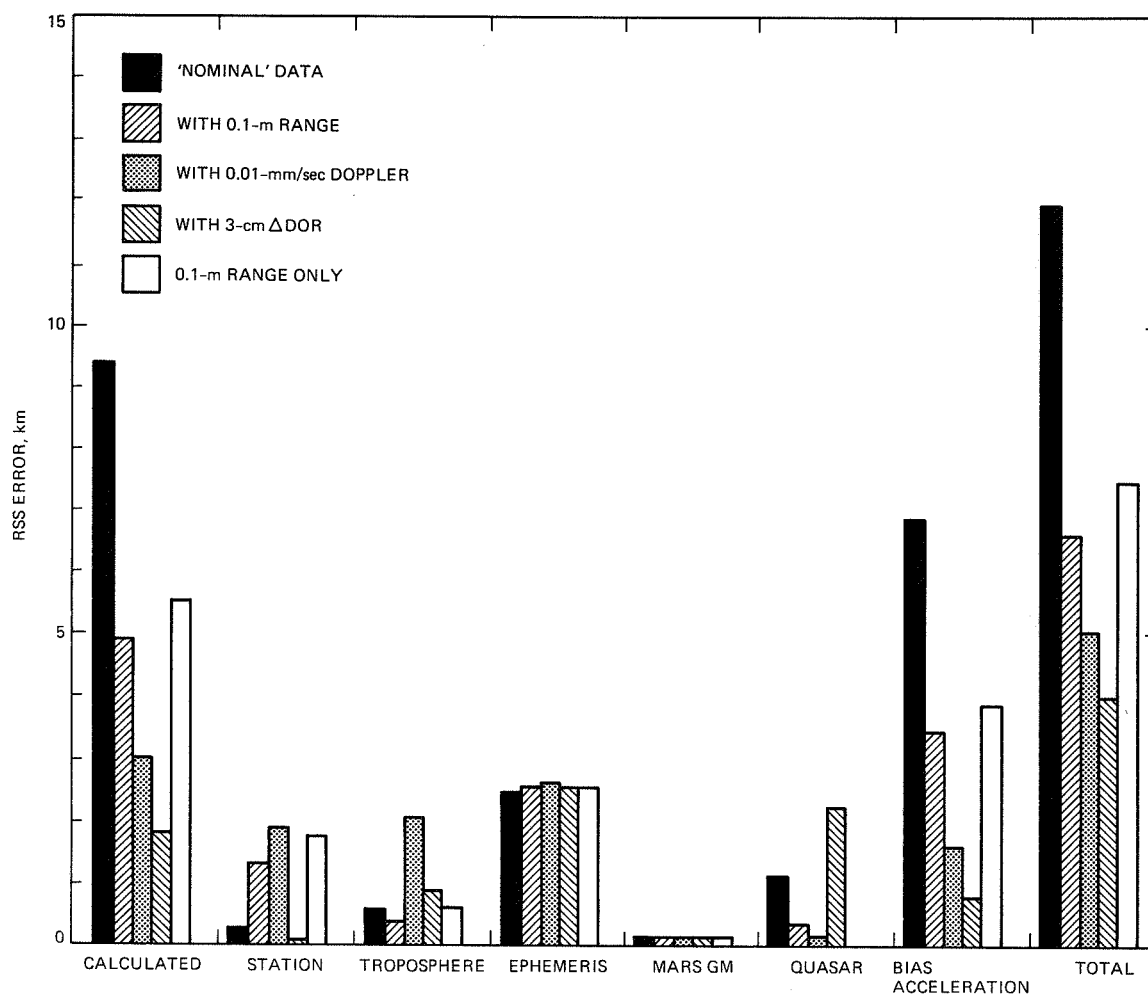


Fig. 11. RSS error breakdown for selected cases from solution set three. The data accuracy combinations are the same as in Fig. 10. The nominal case uses 30-cm Δ DOR, 1-mm/sec Doppler, and 10-m range. Three of the remaining cases depart from the nominal case by the improvement of, as indicated, one of the data accuracies. The final case uses 0.1-m range only.

The Effect of Spatial and Temporal Wet-Troposphere Fluctuations on Connected Element Interferometry

C. D. Edwards

Tracking Systems and Applications Section

Numerical integrations of the structure function of tropospheric inhomogeneities have been performed to assess the impact of water vapor fluctuations on connected element interferometry (CEI). The expectation value of the RMS troposphere error for a differential spacecraft-quasar observation is derived by integrating the spatial refractivity structure function along raypaths to both the spacecraft and quasar from two spatially separated sites. Correlations between the tropospheric conditions at the two sites, which can become significant for short baseline observations, are fully accounted for in this calculation. Temporal effects are treated by assuming a frozen-flow model in which a fixed spatial distribution blows over both sites. Two "nominal" observation scenarios are considered, along with variations to study the dependence of the resultant differential troposphere errors on baseline length, observation time, source separation angle, and elevation. Consecutive differential observations are found to be almost completely uncorrelated, implying that averaging many repeated differential observations can quickly reduce the troposphere error.

I. Introduction

Uncalibrated signal delays due to propagation through the earth's atmosphere constitute one of the dominant error sources for Very Long Baseline Interferometry (VLBI). In particular, the delay component due to the wet troposphere is difficult to calibrate and can vary significantly both temporally and from site to site. For intercontinental measurements, the troposphere is typically modeled as a horizontally stratified distribution of water vapor, and a single parameter, the zenith wet troposphere delay, characterizes the troposphere at a given epoch and site. A mapping function (e.g., the Lanyi

mapping function [1]) is used to determine the troposphere delay at other elevation angles. Surface meteorology can provide zenith wet troposphere calibrations with an accuracy of about 3 cm^1 [2], while water vapor radiometry offers the potential for 1-cm zenith calibrations [3].

¹S. E. Robinson, "Errors in Surface Model Estimates of Zenith Wet Path Delays Near DSN Stations," JPL Interoffice Memorandum 335.4-594 (internal document), Jet Propulsion Laboratory, Pasadena, California, September 3, 1986.

In reality, the troposphere deviates significantly from this stratified model, because of spatial and temporal variations in the water vapor distribution. Tatarski [4] and Ishimaru [5] characterize spatial variations in the density of water vapor according to a power law structure function derived from Kolmogorov turbulence theory. Treuhaft and Lanyi [6, 7] have performed numerical integrations of this power law to derive a spatial structure function

$$D_{\tau, \theta, \phi}(\rho) = \langle (\tau_{\theta, \phi}(\mathbf{x} + \rho) - \tau_{\theta, \phi}(\mathbf{x}))^2 \rangle \quad (1)$$

where $\tau_{\theta, \phi}(\mathbf{x})$ is the wet tropospheric delay, observed from position \mathbf{x} at elevation θ and azimuth ϕ relative to the baseline vector ρ . To the extent that the wet troposphere can be modeled as a fixed spatial distribution of water vapor blowing over a site, this spatial structure function can also be used to describe temporal variations at a single site by replacing the baseline vector ρ with the product of windspeed \mathbf{v} and time t [5–7].

Using the DSN Block 0 VLBI dataset, Treuhaft and Lanyi [6, 7] have shown that these temporal variations are a dominant error source for the VLBI phase-rate observable. On the other hand, given Block 0 system noise contributions, the delay-observable error for intercontinental VLBI is dominated more by overall zenith delay uncertainty than by the small-scale spatial and temporal fluctuations at each site. Certain observation scenarios, however, can lead to a significant reduction in the error component due to the zenith uncertainty and thereby increase the relative importance of the stochastic troposphere errors. For Delta-Differenced One-way Range (ΔDOR) observations, in which delay measurements are made for a pair of angularly close radio sources (typically a spacecraft and a quasar), significant cancellation is obtained in the tropospheric delay error due to the proximity of the raypaths at each site. In addition, for short baseline observations, the troposphere delays over the two stations become highly correlated. In both these scenarios, the troposphere delay error due to zenith delay uncertainty in the context of a stratified troposphere model is greatly reduced. A proper understanding of the delay error budget requires a careful treatment of the spatial and temporal troposphere inhomogeneities.

In this article, both these sources of correlation are considered. Numerical integrations are performed to calculate the size of delay errors for differential delay observations of a pair of radio sources on short baselines. The motivation for this analysis is a desire to quantify the impact of the wet troposphere on differential spacecraft-quasar CEI navigation measurements and to explore the dependence of the troposphere error on observation parameters such as baseline length, time difference between observations, source-pair separation angle,

and elevation angle. These results should also be of interest for GPS applications; in particular, the calculations reported here are relevant to the proper weighting of spacecraft-differenced range data on small-scale regional networks.

For CEI, it is crucial to understand the delay error budget at the millimeter level, since a 1-mm delay error on a 20-km baseline represents a 50-nrad angular error. (To put this in perspective, Block I VLBI on intercontinental baselines will deliver roughly 50-nrad angular accuracy for the upcoming Galileo mission.²) This article refers to the CEI differential delay measurement as $\Delta\text{DO}\Phi$ to emphasize that the observable is based on the highly precise phase-delay datatype. Existing Block 0 VLBI observations on the DSS-12–DSS-13 and DSS-13–OVRO baselines have already demonstrated phase-delay precision (based on quasar SNR) of under 1 psec, with residual scatter for angularly close sources on the order of 10 psec [8, 9].

The analysis reported here constitutes a straightforward extension of the work of Treuhaft and Lanyi [6, 7]. Whereas their structure function $D_{\tau, \theta, \phi}(\rho)$ represents the expected variance of the troposphere delay along two lines of sight, separated by a distance ρ , the calculations here will involve four lines of sight, one at each station for each of the two radio sources. All correlations among the fluctuations on these four raypaths are accounted for in this analysis.

II. Derivation of the $\Delta\text{DO}\Phi$ Troposphere Error

Let $\tau_{\Delta\text{DO}\Phi}$ be the troposphere-induced differential phase-delay error:

$$\begin{aligned} \tau_{\Delta\text{DO}\Phi} = & [\tau_{\theta_A, \phi_A}(\rho) - \tau_{\theta_A, \phi_A}(0)] \\ & - [\tau_{\theta_B, \phi_B}(\rho - \mathbf{v} \delta t) - \tau_{\theta_B, \phi_B}(-\mathbf{v} \delta t)] \end{aligned} \quad (2)$$

Each τ represents the troposphere delay along a certain line-of-sight. The indices A and B refer to the two radio sources, ρ is the vector between the two sites, \mathbf{v} is the wind velocity, and δt is the time between observations of A and B . The first two

²J. B. Thomas, "An Error Analysis for Galileo Angular Position Measurements with the Block I ΔDOR System," JPL Engineering Memorandum 335-26 (internal document), Jet Propulsion Laboratory, Pasadena, California, November 11, 1981.

terms represent the differential troposphere between the two stations (at positions $\mathbf{0}$ and $\boldsymbol{\rho}$) for the observation of source A , while the second two terms represent the differential troposphere observed at time δt later for the observation of source B .

Following the approach of Treuhaft and Lanyi [6, 7], each of the four path delays in this formula can be expressed as an integration of the refractivity $\chi(\mathbf{r})$ along the given raypath:

$$\tau_{\theta_A, \phi_A}(\mathbf{x}) = \frac{1}{\sin \theta_A} \int_0^h dz \chi(\mathbf{x} + \mathbf{r}(\theta_A, \phi_A, z)) \quad (3)$$

where \mathbf{r} ranges along the θ_A, ϕ_A line-of-sight, and where the ray-path integration has been truncated at height h . One assumes that $\langle \chi(\mathbf{r}) \rangle$ and $\langle \chi^2(\mathbf{r}) \rangle$ are independent of \mathbf{r} . Also, throughout this analysis, one assumes a flat earth, and hence the azimuths and elevations at the two stations will be the same for any given source. For baseline lengths of tens or even a few hundreds of km, this is a reasonable approximation.

Substituting the delay path integrals of Eq. (3) into Eq. (2), one obtains

$$\begin{aligned} \langle \tau_{\Delta \text{DO}\Phi}^2 \rangle = & \left\langle \left\{ \frac{1}{\sin \theta_A} \int_0^h dz \chi(\boldsymbol{\rho} + \mathbf{r}(\theta_A, \phi_A, z)) \right. \right. \\ & - \frac{1}{\sin \theta_A} \int_0^h dz \chi(\mathbf{r}(\theta_A, \phi_A, z)) \\ & - \frac{1}{\sin \theta_B} \int_0^h dz \chi(\boldsymbol{\rho} - \mathbf{v} \delta t + \mathbf{r}(\theta_B, \phi_B, z')) \\ & \left. \left. + \frac{1}{\sin \theta_B} \int_0^h dz \chi(-\mathbf{v} \delta t + \mathbf{r}(\theta_B, \phi_B, z')) \right\}^2 \right\rangle \quad (4) \end{aligned}$$

By expanding this expression, interchanging the order of averaging and integration, and making use of the relation

$$D_\chi(|\mathbf{x}_1 - \mathbf{x}_2|) = 2\langle \chi^2 \rangle - 2\langle \chi(\mathbf{x}_1)\chi(\mathbf{x}_2) \rangle \quad (5)$$

the delay error is obtained as a double integral of a sum of refractivity structure functions:

$$\begin{aligned} \langle \tau_{\Delta \text{DO}\Phi}^2 \rangle = & \int_0^h \int_0^h dz dz' \left\{ - \frac{1}{\sin^2 \theta_A} D_\chi(|\mathbf{r}(\theta_A, \phi_A, z) - \mathbf{r}(\theta_A, \phi_A, z')|) \right. \\ & - \frac{1}{\sin^2 \theta_B} D_\chi(|\mathbf{r}(\theta_B, \phi_B, z) - \mathbf{r}(\theta_B, \phi_B, z')|) \\ & + \frac{1}{\sin^2 \theta_A} D_\chi(|\boldsymbol{\rho} + \mathbf{r}(\theta_A, \phi_A, z) - \mathbf{r}(\theta_A, \phi_A, z')|) \\ & + \frac{1}{\sin^2 \theta_B} D_\chi(|\boldsymbol{\rho} + \mathbf{r}(\theta_A, \phi_A, z) - \mathbf{r}(\theta_B, \phi_B, z')|) \\ & + \frac{2}{\sin \theta_A \sin \theta_B} D_\chi(|\mathbf{r}(\theta_A, \phi_A, z) + \mathbf{v} \delta t - \mathbf{r}(\theta_B, \phi_B, z')|) \\ & - \frac{1}{\sin \theta_A \sin \theta_B} D_\chi(|\boldsymbol{\rho} + \mathbf{r}(\theta_A, \phi_A, z) + \mathbf{v} \delta t - \mathbf{r}(\theta_B, \phi_B, z')|) \\ & \left. - \frac{1}{\sin \theta_A \sin \theta_B} D_\chi(|\mathbf{r}(\theta_A, \phi_A, z) - \boldsymbol{\rho} + \mathbf{v} \delta t - \mathbf{r}(\theta_B, \phi_B, z')|) \right\} \quad (6) \end{aligned}$$

Using the Kolmogorov expression for $D_\chi(r)$

$$D_\chi(r) = \langle (\chi(\mathbf{r}) - \chi(\mathbf{0}))^2 \rangle = C^2 r^{2/3} \quad (7)$$

Eq. (6) can be numerically integrated to estimate $\tau_{\Delta\text{DO}\Phi}^2$ as a function of ρ , δt , θ_A , ϕ_A , θ_B , and ϕ_B . C is a scale factor that characterizes the amplitude of refractivity fluctuations.

III. Numerical Integration Results

The double integration in Eq. (6) was evaluated numerically, using the same values for the three free parameters h , ν , and C as were used by Treuhaft and Lanyi [6, 7]: the effective troposphere height h was taken as 1 km, the wind speed ν_{wind} was set at 8 m/sec, and a fluctuation amplitude C of $2.4 \times 10^{-7} \text{ m}^{-1/3}$ was adopted. These results yield a normalization consistent with observed VLBI, WVR, and radiosonde data from the three DSN complexes.

Each $\Delta\text{DO}\Phi$ observation was specified by the following parameters:

- θ_0, ϕ_0 = the arithmetic mean of the elevation and azimuth angles of the two sources A and B
- δs = the separation angle (arclength) between the two radio sources; the separation can be solely in azimuth (equal elevation angles) or in elevation (equal azimuths)
- L = the baseline length between the two CEI stations (the baseline azimuth is fixed at 0)
- δt = the time separation between the two observations
- ϕ_{wind} = the wind azimuth

For this analysis, a “nominal” configuration was considered, with $\theta_0 = 45$ deg and $\phi_0 = 60$ deg. The baseline length L was set to 21 km, corresponding to the length of the DSS-13–DSS-14 and DSS-13–DSS-15 baselines at Goldstone, while the 8-m/sec wind was directed at an azimuth $\phi_{\text{wind}} = -60$ deg. A separation angle of 10 deg was adopted for δs , with a time separation δt of 200 sec. Two cases were considered: the AZ case, for which the angular source separation was solely azimuthal, and the EL case, for which the sources were separated solely in elevation. The configurations are summarized in Table 1.

The nominal configuration yielded an RMS $\Delta\text{DO}\Phi$ troposphere error of 4.52 mm for the AZ case and 4.56 mm for the EL case. To study the dependence of these errors on the observation scenario, the configuration parameters were varied one at a time over a range of values, and the $\Delta\text{DO}\Phi$ troposphere

error calculated as a function of that parameter. Four parameters were allowed to vary: the baseline length L , the time δt between observations, the mean elevation angle θ_0 , and the separation angle δs . Figures 1–4 show the results of varying each of these parameters about the nominal configurations.

A. Baseline Length Dependence

Figure 1 shows the calculated RMS $\Delta\text{DO}\Phi$ troposphere error

$$\sigma_{\Delta\text{DO}\Phi} \equiv \sqrt{\langle \tau_{\Delta\text{DO}\Phi}^2 \rangle} \quad (8)$$

as the baseline length L is allowed to vary from 1 km up to 1000 km, and all other parameters are held at their nominal values. The solid and dashed lines indicate the results for varying the AZ and EL configurations, respectively. For azimuthal source separation, very little dependence on baseline length is observed: $\sigma_{\Delta\text{DO}\Phi}$ is nearly saturated even at the nominal 21-km baseline length, and drops only to 3.1 mm when the baseline length is reduced to 1 km. For source separation in the elevation direction, $\sigma_{\Delta\text{DO}\Phi}$ again varies quite slowly for baseline lengths of under 100 km, but it does not saturate as in the AZ case; rather, $\sigma_{\Delta\text{DO}\Phi}$ continues to grow as L increases to 1000 km. This can be understood intuitively by returning to the stratified troposphere model in which the troposphere is fully characterized by a zenith value. For the EL configuration, the A and B sources are at different elevation angles and hence have different zenith mapping functions. Thus the EL case is sensitive to the zenith path-delay difference between the two sites, which tends to grow with baseline length. For the AZ case, the elevation angles of A and B are identical, and so any zenith delay difference is canceled.

Based on the slow L dependence observed in these plots, one is driven towards longer baselines, subject to the constraint, of course, that phase ambiguities can be reliably resolved. Since the troposphere delay error grows much slower than baseline length, the angular error $\sigma_{\Delta\text{DO}\Phi}/L$ will decrease rapidly with increasing baseline. For instance, increasing the baseline length from the nominal value of 21 km up to 200 km leads to less than a 20 percent increase in the troposphere error for the EL case (and nearly no increase at all for the AZ case), translating into better than an eight-fold improvement in angular accuracy.

B. Observation Time Dependence

In Fig. 2, one sees the effect of varying δt over the range from 10 sec to 10,000 sec. The observed dependence on δt is much stronger than for the baseline length. In the neighborhood of the nominal value of $\delta t = 200$ sec, the dependence is

fairly strong. For instance, for the EL case, reducing δt to 60 sec would lower $\sigma_{\Delta\text{DO}\Phi}$ to 2.6 mm, a reduction of over 40 percent. The AZ and EL cases look quite similar, with the most significant difference being a slightly lower $\sigma_{\Delta\text{DO}\Phi}$ for the AZ case at very short differential observation times.

This result suggests that minimizing the time separation of differential observations should be an important design goal for a CEI navigation system. In particular, maximum safe slew rates should be used, and observation times should be kept as short as possible while still providing sufficient SNR to keep the inherent data noise at or below the level of the troposphere. The wide bandwidth offered by fiber optics provides one means of reducing observation times. The current Block 0 system, with which existing phase-delay data have been obtained [8, 9], offers a 2-MHz observation bandwidth. Low-noise HEMT amplifiers and single-mode fibers can support bandwidths of several hundred MHz, leading to over an order of magnitude decrease in observation time for comparable SNR.

It should be pointed out that the calculations here are for a pair of instantaneous observations, separated by a time δt . For observations of finite length, δt would represent the time difference between the midpoints of each scan, i.e., half the scan time for source *A* plus half the scan time for source *B* plus the slew time in-between scans. A more accurate treatment would account for the averaging of the troposphere over a scan. In other words, for a scan length of T_s , the tropospheric path delay $\tau_{\theta_A, \phi_A}(\mathbf{x})$ should be replaced by a mean path delay over the length of the scan as follows:

$$\bar{\tau}_{\theta_A, \phi_A}(\mathbf{x}, T_s) = \frac{1}{T_s} \int_{-T_s/2}^{T_s/2} dt \tau_{\theta_A, \phi_A}(\mathbf{x} - \mathbf{v}t) \quad (9)$$

This averaging, by effectively acting as a low-pass filter on the troposphere with a cutoff frequency $\nu_c \approx 1/T_s$, will tend to reduce $\sigma_{\Delta\text{DO}\Phi}$ somewhat, particularly when the scan length T_s is a large fraction of the time difference δt between scan midpoints.

To quantify the size of this effect, such a calculation is carried out for the two nominal configurations, with a scan length T_s of 60 sec, and approximating the integral in Eq. (9) by dividing the scan into five sections:

$$\bar{\tau}_{\theta_A, \phi_A}(\mathbf{x}, T_s) = \frac{1}{5} \sum_{i=1}^5 \tau_{\theta_A, \phi_A}(\mathbf{x} - \mathbf{v}t_i) \quad (10)$$

where $t_i = \{-24, -12, 0, +12, +24\}$ sec for $i = \{1, \dots, 5\}$. Substituting these mean path delays into Eq. (2) yields an expression for $\tau_{\Delta\text{DO}\Phi}$ involving twenty separate raypaths. And when this is squared to evaluate $\langle \tau_{\Delta\text{DO}\Phi}^2 \rangle$, there are four-hundred cross-terms, posing a significantly larger computational task. A modification of the original program was made to evaluate this finite-length scan version of the $\Delta\text{DO}\Phi$ error. For the nominal EL configuration, the value of $\sigma_{\Delta\text{DO}\Phi}$ decreased only slightly to 4.42 mm, a change of only 3 percent. A similar reduction of about 3 percent was also obtained for the AZ case. Given the small size of these corrections, the assumption of instantaneous scans should not seriously affect the conclusions of this analysis. (Further subdividing the scans into more than five sections did not lead to any additional significant reductions, verifying that the summation in Eq. (10) is an adequate approximation of the integral in Eq. (9).)

C. Elevation Angle Dependence

Figure 3 shows the effect of varying the mean elevation angle of the two sources, while holding their angular arclength separation constant. For source separations in either the azimuth or elevation direction, the $\Delta\text{DO}\Phi$ troposphere error rises sharply for elevation angles below 30 deg. At these low elevations, the atmospheric pathlength of roughly $1/\sin(\theta)$ increases rapidly with decreasing elevation, with a consequent increase in the size of path delay variations. One distinct advantage of the shorter baselines used in CEI is that sources can be observed at much higher elevation angles. For a Goldstone CEI system, with latitude +35 deg, a source at zero declination has an elevation of 55 deg at transit. The ecliptic plane, in which most DSN missions take place, is inclined 23 deg with respect to the earth's polar axis, and so the ecliptic ranges from +23 deg to -23 deg declination. A source at +23 deg declination would transit at 78 deg elevation, while a source at -23 deg declination would transit at 32 deg elevation. Thus even an ecliptic plane source at extreme southern declinations could be observed from Goldstone at reasonable elevations. Nonetheless, southern declination observations from Goldstone can be expected to be of poorer resolution, given these lower elevation angles. As a result, optimal CEI tracking throughout the ecliptic may warrant a second CEI site in the southern hemisphere.

D. Angular Source Separation Dependence

Finally, in Fig. 4, the separation angle δs is varied, while the mean values of the azimuth and elevation angles for the two sources are kept fixed. For the AZ case, with both sources at the same elevation angle, $\sigma_{\Delta\text{DO}\Phi}$ is nearly independent of δs . For the EL case, $\sigma_{\Delta\text{DO}\Phi}$ varies slowly for separation angles δs less than 20 deg, but begins to rise sharply for δs above 40 deg.

To understand this, it is necessary to consider the various distance scales in the CEI observing geometry. The observation time scale of $\delta t = 200$ sec corresponds to a distance scale of $v_{wind} \times \delta t = 1.6$ km. At each site, there is another distance scale corresponding to the spatial separation of the two raypaths, which can be characterized by the distance r between the two raypaths at the effective troposphere height h . This distance r can be expressed

$$r = h \sqrt{\cot^2 \theta_A + \cot^2 \theta_B - 2 \cot \theta_A \cot \theta_B \cos(\phi_A - \phi_B)} \quad (11)$$

For the AZ case of $\theta_A = \theta_B = 45$ deg, $r = 2\sqrt{1 - \cos(\delta s)}$ which even for $\delta s = 60$ deg is 1.4 km. Thus, for the AZ case, the temporal errors associated with the difference between observations dominate the spatial errors due to source separation, at least for $\delta s < 60$ deg.

For the EL case, $\phi_A = \phi_B$, and so the effective raypath spatial separation is

$$r = |\cot \theta_A - \cot \theta_B| \quad (12)$$

which is 1.7 km for a δs of 40 deg, comparable to the 200 sec scale, and which rises to $r = 3.5$ km at $\delta s = 60$ deg. Thus for large elevation separations, the spatial scale begins to dominate over the temporal scale above $\delta s = 40$ deg. Here again is visible the complex interplay of the various distance scales involved in the CEI observing geometry.

The slow variation of $\sigma_{\Delta DO\Phi}$ with δs over the range of 0–20 deg means that for CEI observations it may be more profitable to use a strong quasar 20 deg from the spacecraft, rather than a weaker quasar within 5 deg. The stronger quasar would require a shorter scan length, thereby reducing the more dominant temporal troposphere variation. Of course, other error sources, such as gravity-induced antenna deformations, may argue for keeping source separation as small as possible.

IV. Discussion

These calculations should help in the system design of a dedicated CEI facility at Goldstone and should also serve as a tool for optimizing observations using such a system. It is important to remember, however, that the results obtained are dependent on the input parameters C , h , and v_{wind} .

Changing C will only change the overall normalization of the $\Delta DO\Phi$ error, but h and v_{wind} are two of the fundamental scales in the CEI $\Delta DO\Phi$ geometry; changing them will affect the shape of the functional dependence of $\sigma_{\Delta DO\Phi}$ on L , δt , θ_0 , and δs . It is likely that C , h , and v_{wind} change on a daily basis, and one important task would be to collect statistics on these parameters by fitting single-site temporal structure functions, perhaps using water vapor radiometers or spectral hygrometers as a source of data.

The results presented here represent the expected wet troposphere error for a single $\Delta DO\Phi$ error, with no external troposphere calibrations. A number of different techniques could provide further means for achieving significant reductions in the $\Delta DO\Phi$ troposphere error. For instance, water vapor radiometers may have the potential to supply differential line-of-sight path-delay calibrations at the millimeter level. Whereas overall zenith troposphere calibration requires highly accurate WVR gain calibrations, differential line-of-sight WVR calibrations place more stringent demands on the temporal stability of the WVR, and on accurate modeling of the WVR beam. Studies are under way to determine the short-term noise floor of current WVRs, and to quantify their utility for differential delay and delay rate calibrations. A 1-mm calibration capability could significantly reduce $\Delta DO\Phi$ troposphere errors, based on the expected level of fluctuations calculated here.

A second approach to reducing troposphere errors is to simply average many repeated $\Delta DO\Phi$ observations. Since the wet troposphere fluctuations are stochastic in nature, the troposphere error on the mean of many observations will be less than the error on each individual observation. Of course, additional observations will help only to the extent that they are uncorrelated from previous observations. The correlation between successive $\Delta DO\Phi$ observations is expressed analytically as

$$\rho(T_{sep}) = \frac{\langle \tau_{\Delta DO\Phi}(t=0) \tau_{\Delta DO\Phi}(t=T_{sep}) \rangle}{\sigma_{\Delta DO\Phi}^2} \quad (13)$$

where T_{sep} is the time separation between the two $\Delta DO\Phi$ observations (expressed as the difference between the epochs of the midpoints of the individual $\Delta DO\Phi$ observations). The denominator is the tropospheric delay variance for the individual $\Delta DO\Phi$ observations, while the numerator can be expanded as

$$\left\langle ([\tau_A(\rho) - \tau_A(0)] - [\tau_B(\rho - \mathbf{v}\delta t) - \tau_B(-\mathbf{v}\delta t)]) \right. \\ \left. \times ([\tau_A(\rho - \mathbf{v}T_{sep}) - \tau_A(-\mathbf{v}T_{sep})] - [\tau_B(\rho - \mathbf{v}\delta t - \mathbf{v}T_{sep}) - \tau_B(-\mathbf{v}\delta t - \mathbf{v}T_{sep})]) \right\rangle \quad (14)$$

where δt is, as in Eq. (2), the separation between the A and B sources within a single $\Delta\text{DO}\Phi$ observation. (The subscripts A and B implicitly refer to the source directions (θ_A, ϕ_A) and (θ_B, ϕ_B) .)

Figure 5 shows the results of evaluating $\rho(T_{sep})$ numerically for both the AZ and EL configurations. The calculation is similar to the calculation of $\sigma_{\Delta\text{DO}\Phi}$ in Section II, but with eight rather than four separate raypaths to consider. The time separation δt for the individual $\Delta\text{DO}\Phi$ observations was held fixed at 200 sec, and T_{sep} was allowed to vary from 10 sec up to 10^4 sec. (Note that for $T_{sep} < \delta t$, the two $\Delta\text{DO}\Phi$ observations actually overlap.) For both the AZ and EL configurations, $\rho(T_{sep})$ drops very quickly as T_{sep} increases. By the time T_{sep} has reached 200 sec, corresponding to back-to-back $\Delta\text{DO}\Phi$ observations with no idle time, $\rho(T_{sep})$ has dropped to well below 10 percent. In other words, at least for the geometry considered here, $\Delta\text{DO}\Phi$ observations could be conducted continuously, and the troposphere errors $\sigma_{\Delta\text{DO}\Phi}$ for adjacent observations would be almost entirely uncorrelated. This important conclusion means that the $\Delta\text{DO}\Phi$ troposphere error can be rapidly reduced to the millimeter level through statistical averaging of many consecutive observations.

Another technique which could further reduce CEI troposphere errors would be to apply the Local Reference Frame concept in which several quasar sources are observed along with the spacecraft. For intercontinental VLBI, a covariance study has shown [10] that referencing the spacecraft position to several spatially distributed quasars (instead of a single quasar as in traditional ΔDOR), enables dominant systematic error sources to be removed through parameter estimation. Although the $\Delta\text{DO}\Phi$ error budget is quite different, a similar technique might enable improved accuracy for short baselines. With quasars distributed spatially around the spacecraft, particularly over a range of elevation angles, it should be possible to filter out some of the large scale troposphere inhomogeneities which limit the $\Delta\text{DO}\Phi$ observable. This is another interesting area for future work.

One point which should be clear is that it is difficult to intuitively estimate the troposphere error for a specific geom-

etry, given the complex interplay of the various spatial and temporal dimensions. To obtain meaningful error estimates for differential observations on short baselines, it is essential to account for the statistics of wet troposphere fluctuations. It is hoped that future CEI covariance analyses and data reduction algorithms will incorporate these results.

V. Conclusions

CEI $\Delta\text{DO}\Phi$ observations achieve a high degree of double-differential troposphere cancellation due to the proximity of the stations and the small angular separation of the sources. Fluctuations along the four $\Delta\text{DO}\Phi$ raypaths are likely to be a dominant error source for CEI $\Delta\text{DO}\Phi$ navigation. The CEI $\Delta\text{DO}\Phi$ geometry contains many different distance scales, complicating any simple intuitive models. To quantify the effects of these fluctuations for an arbitrary observing geometry, an expression has been derived for the troposphere error $\sigma_{\Delta\text{DO}\Phi}$ expressed as a double integral of the refractivity structure function, similar to the single station or single source expressions derived by Treuhaft and Lanyi [6, 7], but accounting for all correlations among the four $\Delta\text{DO}\Phi$ raypaths.

For a nominal observation scenario, this double integral has been evaluated numerically, yielding troposphere-induced $\Delta\text{DO}\Phi$ errors of about 4.5 mm for 10-deg source separations, with a very slow dependence on baseline length. A much stronger dependence is observed for variations of the time difference between the A and B observations. For this nominal observation, $\sigma_{\Delta\text{DO}\Phi}$ can be reduced over 40 percent by lowering δt from 200 sec to 60 sec. Observations below 20 deg appear to be significantly degraded due to the rapidly increasing pathlength and resultant increased amplitude of fluctuations. For the nominal configuration, varying the angular source separation from 0 to 20 deg produced a very slow increase in $\sigma_{\Delta\text{DO}\Phi}$. However, as the source separation was increased beyond 40 deg in elevation, $\sigma_{\Delta\text{DO}\Phi}$ increased rapidly. Finally, the correlation between repeated $\Delta\text{DO}\Phi$ observations was calculated and found to be quite small, indicating that the troposphere fluctuation errors can be quickly reduced through averaging many repeated observations.

Acknowledgments

I would like to thank Gabor Lanyi and Bob Treuhaft for helpful discussions regarding the troposphere structure function, and Mark Finger for suggesting a technique for converting the two-dimensional troposphere integrals into more efficient one-dimensional integrals using Gauss's Law.

References

- [1] G. E. Lanyi, "Tropospheric Delay Effects in Radio Interferometry," *TDA Progress Report 42-78*, vol. April-June 1984, Jet Propulsion Laboratory, Pasadena, California, pp. 152-159, August 15, 1984.
- [2] C. C. Chao, "The Tropospheric Calibration Model for Mariner Mars 1971," NASA-JPL Technical Report TR-32-1587, Jet Propulsion Laboratory, Pasadena, California, pp. 61-76, 1974.
- [3] S. E. Robinson, "The Profile Algorithm for Microwave Delay Estimation from Water Vapor Radiometer Data," *Radio Sci.*, vol. 23, pp. 401-408, 1988.
- [4] V. I. Tatarski, *Wave Propagation in a Turbulent Medium*, New York: Dover, 1961.
- [5] A. Ishimaru, *Wave Propagation and Scattering in Random Media*, New York: Academic Press, 1978.
- [6] R. N. Treuhaft and G. E. Lanyi, "The Effect of the Dynamic Wet Troposphere on Radio Interferometric Measurements," *Radio Sci.*, vol. 22, pp. 251-265, 1987.
- [7] R. N. Treuhaft and G. E. Lanyi, "The Effect of the Dynamic Wet Troposphere on VLBI Measurements," *TDA Progress Report 42-84*, vol. October-December 1985, Jet Propulsion Laboratory, Pasadena, California, pp. 1-17, February 15, 1986.
- [8] C. Edwards, "Short Baseline Phase Delay Interferometry," *TDA Progress Report 42-91*, vol. July-September 1987, Jet Propulsion Laboratory, Pasadena, California, pp. 46-56, November 15, 1987.
- [9] C. Edwards, "Angular Navigation Capabilities of Short Baseline Phase Delay Interferometry," Paper 88-4287, AIAA/AAS Astrodynamics Conference, Minneapolis, Minnesota, August 15-17, 1988.
- [10] R. Treuhaft, "Few-Nanoradian Deep Space Navigation in Local Reference Frames," Paper 88-4288, AIAA/AAS Astrodynamics Conference, Minneapolis, Minnesota, August 15-17, 1988.

Table 1. Nominal observation configurations

Parameter	Measurement
θ_0	45 deg
ϕ_0	60 deg
δs	10 deg (either AZ or EL)
L	21 km
δt	200 sec
v_{wind}	8 m/sec
ϕ_{wind}	-60 deg
h	1 km
C	$2.4 \times 10^{-7} \text{ m}^{-1/3}$

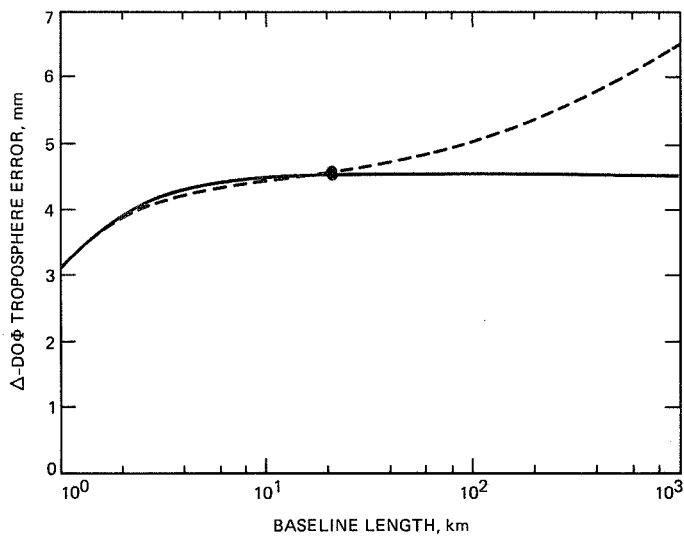


Fig. 1. Dependence of the $\Delta\text{DO}\Phi$ troposphere error on baseline length. For all plots, the solid line represents the AZ configuration (sources separated in azimuth) while the dashed line represents the EL configuration (sources separated in elevation.) For Figs. 1–4, the dot on each curve indicates the nominal AZ or EL configuration.

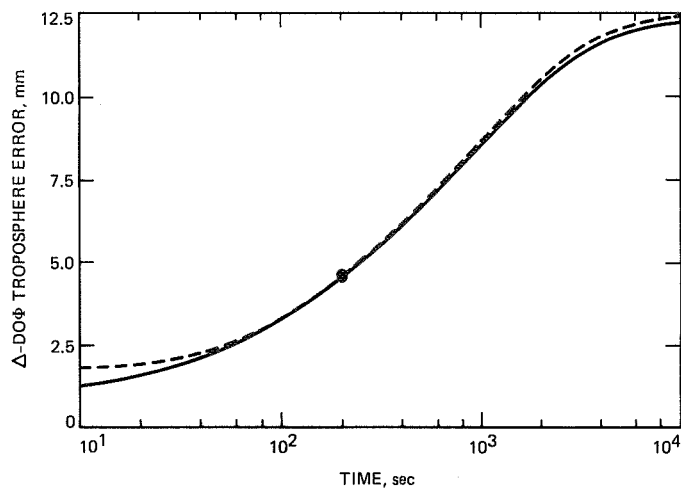


Fig. 2. Dependence of the $\Delta\text{DO}\Phi$ troposphere error on the time separation between observations.

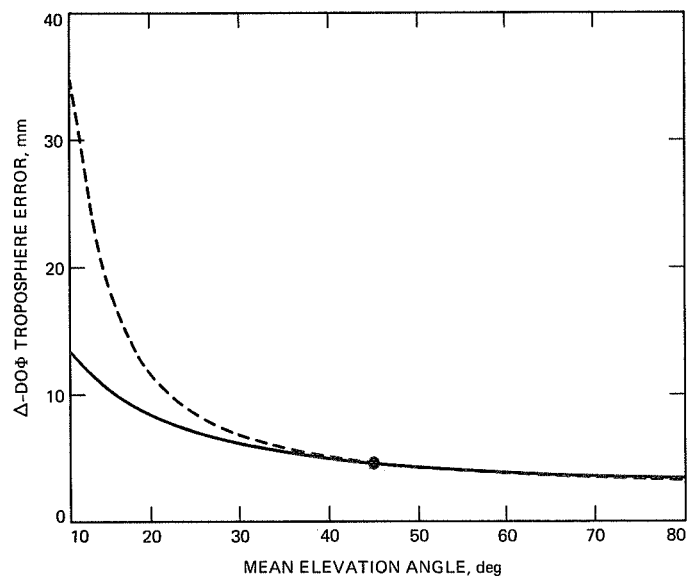


Fig. 3. Dependence of the $\Delta\text{DO}\Phi$ troposphere error on the mean elevation angle of the source pair. The separation arclength is held fixed as the mean elevation is varied.

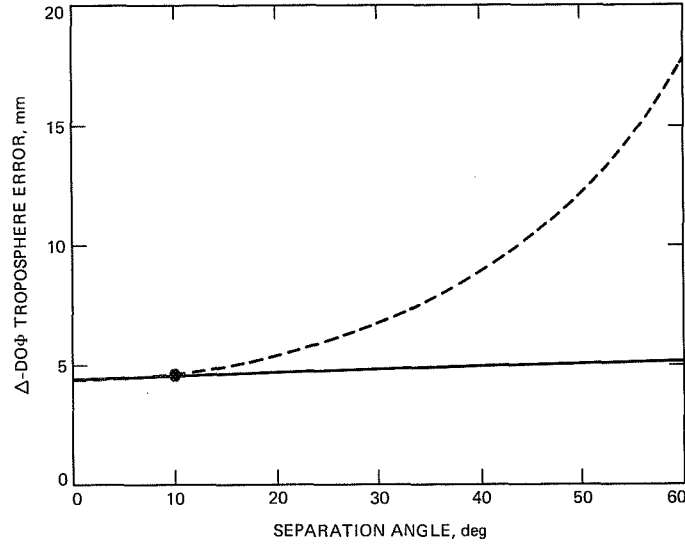


Fig. 4. Dependence of the $\Delta\text{DO}\Phi$ troposphere error on the separation angle of the source pair. The mean elevation angle is held fixed as the separation angle is varied.

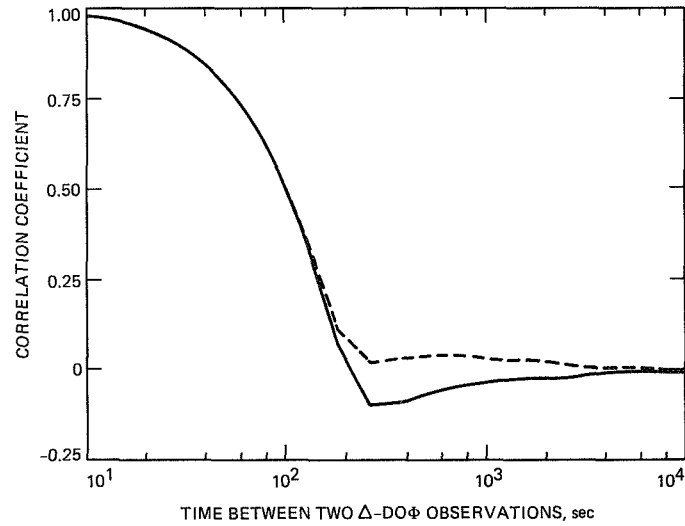


Fig. 5. Correlation between two successive $\Delta\text{DO}\Phi$ observations. The X-axis represents the time separation T_{sep} between the mid-points of the two $\Delta\text{DO}\Phi$ measurements. For each $\Delta\text{DO}\Phi$ observation, the observations of the *A* and *B* sources are separated by a time $\delta t = 200$ sec. So, for $T_{sep} < 200$ sec, the two $\Delta\text{DO}\Phi$ measurements actually overlap. Note that the correlation drops very quickly: consecutive non-overlapping $\Delta\text{DO}\Phi$ measurements are almost completely uncorrelated, indicating that statistical averaging can be used to reduce the size of the troposphere errors through repeated measurements.

54-72
218059
60.

N89-27875

New Ion Trap for Atomic Frequency Standard Applications

J. D. Prestage, G. J. Dick, and L. Maleki
Communications Systems Research Section

A novel linear ion trap that permits storage of a large number of ions with reduced susceptibility to the second-order Doppler effect caused by the radio frequency (RF) confining fields has been designed and built. This new trap should store about 20 times the number of ions a conventional RF trap stores with no corresponding increase in second-order Doppler shift from the confining field. In addition, the sensitivity of this shift to trapping parameters, i.e., RF voltage, RF frequency, and trap size, is greatly reduced.

I. Introduction

There has been much recent activity directed toward the development of trapped ion frequency standards, in part because ions confined in an electromagnetic trap are subjected to very small perturbations of their atomic energy levels. The inherent immunity to environmental changes that is afforded by suitably chosen ions suspended in DC or radio frequency (RF) quadrupole traps has led to the development of frequency standards with very good stability [1], [2]. Indeed, the trapped $^{199}\text{Hg}^+$ ion clock of [1] is the most stable clock yet developed for averaging times $\geq 10^6$ seconds [3]. However, certain applications, such as millisecond pulsar timing [4] and low frequency gravity wave detection across the solar system [5], require stabilities beyond that of present day standards.

Although the basic performance of the ion frequency source depends fundamentally on the number of ions in the trap, the largest source of frequency offset stems from the motion of the atoms caused by the trapping fields via the

second-order Doppler or relativistic time dilation effect [6].¹ Moreover, instability in certain trapping parameters (e.g., trap field strength, temperature, and the actual number of trapped particles) influences the frequency shift and leads to frequency instabilities. Since this offset also depends strongly on the number of ions, a trade-off situation results, where fewer ions are trapped in order to reduce the (relatively) large frequency offset that would otherwise result.

A hybrid RF/DC linear ion trap that should allow an increase in the stored ion number with no corresponding

¹ RF and Penning traps are both subject to second-order Doppler problems related to the trapping fields. In this article, attention is confined specifically to the case of RF traps. It is simply noted that, for the same number of stored ions, magnetron rotation of the ion cloud in a Penning trap leads to a second-order Doppler shift of magnitude comparable to that for an RF trap. A Penning trap-based clock is described in [6].

increase in second-order Doppler instabilities has been designed and constructed. The 20 times larger ion storage capacity should improve clock performance substantially. Alternatively, the Doppler shift from the trapping fields may be reduced by a factor of 10 below comparably loaded hyperbolic traps.

II. Second-Order Doppler Shift for Ions in an RF Trap

Figure 1 shows a conventional RF ion trap along with the applied voltages. The trapping forces are generated by the driven motion of the ions (at frequency Ω) in the inhomogeneous electric field created by the trap electrodes [7]. Ions are trapped around the node point of the oscillating electric field at the center of the trap for certain trap voltages, ionic masses, etc. The motion in each of three directions for a single ion in an RF trap is characterized by two frequencies, the fast driving frequency Ω and a slower secular frequency ω . An exact solution to the equations of motion shows that frequencies $k\Omega \pm \omega$, $k = 2, 3, \dots$ are also present. However, in the limit $\omega/\Omega \ll 1$, the ω and $\Omega \pm \omega$ frequencies dominate, and the kinetic energy (K.E.) of a particle, averaged over one cycle of Ω , separates into the kinetic energy of the secular motion and the kinetic energy of the driven motion. The average kinetic energy is transferred from the secular to the driven motion and back while the sum remains constant, just as a harmonic oscillator transfers energy from kinetic to potential and back. The second-order Doppler shift for a small and/or hot ion cloud, where interactions between ions are negligible, is

$$\begin{aligned} \left(\frac{\Delta f}{f}\right)_{\text{hot}} &= -\frac{1}{2} \frac{\langle v^2 \rangle}{c^2} = -\frac{\langle \text{total K.E.} \rangle}{mc^2} \\ &= -\frac{\langle \text{secular K.E.} + \text{driven K.E.} \rangle}{mc^2} \\ &= -2 \frac{\langle \text{secular K.E.} \rangle}{mc^2} \\ &= -\frac{3k_B T}{mc^2} \end{aligned} \quad (1)$$

where $\langle \rangle$ indicates a time average over one cycle of Ω . An average over one cycle of ω was obtained to equate the secular and driven K.E. This is the same as a simple harmonic oscillator where the average K.E. is equal to the average potential.

Now consider the case in which many ions are contained in a trap and interactions between ions dominate. In this cold cloud model [8], [9] of the trapped ions, displacements of

individual ions from the trap center are primarily due to electrostatic repulsion between the ions, and random thermal motion associated with temperature can be assumed to be small compared to driven motion due to the trap fields. Such clouds have a constant ion density out to the edge of the plasma where the density falls off in a distance characterized by the Debye length [9]

$$\lambda_D = \sqrt{\frac{k_B T \epsilon_o}{n_o q^2}} \quad (2)$$

This cold cloud model should be useful provided the ion cloud size is large compared to the Debye length. For room temperature Hg ions held in a trap with 50 kHz secular frequency, the Debye length is about 0.2 mm.

The trap shown in Fig. 1 is described by a pseudo-potential energy [7]

$$\phi = \frac{1}{2} (m\omega_\rho^2 \rho^2 + m\omega_z^2 z^2) \quad (3)$$

where

$$\omega_\rho^2 = \frac{2q^2 V_o^2}{m^2 \Omega^2 \epsilon^4} + \frac{2qU_o}{m\epsilon^2} \quad (4)$$

and

$$\omega_z^2 = \frac{8q^2 V_o^2}{m^2 \Omega^2 \epsilon^4} - \frac{4qU_o}{m\epsilon^2} \quad (5)$$

and ϵ describes the trap size. It is assumed that the DC and RF voltages are adjusted to make the trapping forces spherical so that the ion cloud is a sphere containing N ions out to radius R_{sph} . The pseudo-potential depicts trap forces as arising from a uniform “background” charge density computed from Poisson’s equation with the above pseudo-potential:

$$n_o = \frac{3\epsilon_o m \omega^2}{q^2} \quad (6)$$

Trapped positive ions neutralize the negative background of charge, matching its density out to a radius where the supply of ions is used up.

The oscillating electric field that generates the trapping force grows linearly with distance from the trap center. The corresponding amplitude of any ion’s driven oscillation is proportional to the strength of the driving field (i.e., also increas-

ing linearly with the distance from the trap center). The average square velocity of the driven motion for an ion at position (ρ, z) is

$$\langle v^2 \rangle = \frac{1}{2} \omega^2 (\rho^2 + 4z^2) \quad (7)$$

For a given trapping strength, reflected in force constant ω^2 , the density is fixed by Eq. (6), and the radius of the spherical cloud is determined once the ion number N has been specified. The second-order Doppler shift due to the micromotion is the spatial average of $-(1/2)(\langle v^2 \rangle/c^2)$ over the spherical ion cloud. Using Eq. (7) for the spatial variation of the micromotion

$$\left(\frac{\Delta f}{f} \right)_{sph} = -\frac{1}{2} \frac{\overline{\langle v^2 \rangle}}{c^2} \quad (8)$$

$$= -\frac{3}{10} \frac{\omega^2 R_{sph}^2}{c^2} \quad (9)$$

$$= -\frac{3}{10} \frac{1}{c^2} \left(\frac{N \omega q^2}{4\pi \epsilon_o m} \right)^{2/3} \quad (10)$$

For typical operating conditions [8], $N = 2 \cdot 10^6$ and $\omega = (2\pi) 50$ kHz, $\Delta f/f = 2 \cdot 10^{-12}$. This corresponds to a second-order Doppler shift that is about 10 times higher than the shift for free ^{199}Hg ions at room temperature, $\Delta f/f = 3k_B T/2mc^2 = 2 \cdot 10^{-13}$.

For increased signal-to-noise in the measured atomic resonance used in frequency standard applications, it is desirable to have as many trapped ions as possible. However, as has just been seen, larger ion clouds have larger second-order Doppler shifts. This frequency offset must be stabilized to a high degree in order to prevent degradation of long-term performance. To reduce this susceptibility to second-order Doppler shift, a hybrid RF/DC ion trap has been designed and constructed that replaces the single-field node of the hyperbolic trap with a line of nodes. The RF electrode structure producing this line of nodes of the RF field is shown in Fig. 2. The ions are trapped in the radial direction by the same RF trapping forces used in a conventional RF trap, and a secular motion in that direction of frequency ω is assumed. To prevent ions from escaping along the axis of the trap, DC biased “endcap” needle electrodes are mounted on each end. Unlike conventional RF or Paul traps, this linear trap holds positive or negative ions but not both simultaneously.

Near the central axis of the trap, one assumes a quadrupolar RF electric field

$$\phi = \frac{V_o(x^2 - y^2) \cos(\Omega t)}{2R^2} \quad (11)$$

which gives the corresponding pseudo-potential energy

$$\Phi = \frac{q^2 V_o^2}{4R^4 m \Omega^2} (x^2 + y^2) \quad (12)$$

$$\equiv m \frac{\omega^2}{2} \rho^2 \quad (13)$$

Poisson’s equation leads to a limiting charge density

$$n_o = \frac{2\epsilon_o m \omega^2}{q^2} \quad (14)$$

for ions held in this linear trap, where

$$\omega^2 = \frac{q^2 V_o^2}{2m^2 \Omega^2 R^4} \quad (15)$$

The motion induced by the RF trapping field is purely transverse and is given by

$$\langle v^2 \rangle = \omega^2 \rho^2 \quad (16)$$

As before, this quantity is averaged over the ion cloud to find the second-order Doppler shift

$$\left(\frac{\Delta f}{f} \right)_{lin} = -\frac{1}{2} \frac{\overline{\langle v^2 \rangle}}{c^2} = -\frac{\omega^2 R_c^2}{4c^2} \quad (17)$$

A cylindrical ion cloud of radius R_c and length L is assumed for simplicity. Equation (17) can be written in terms of total ion number, N , and trap length, L ,

$$\left(\frac{\Delta f}{f} \right)_{lin} = \left(\frac{q^2}{8\pi \epsilon_o m c^2} \right) \frac{N}{L} \quad (18)$$

In contrast to the spherical case, this expression contains no dependence on trap parameters except for the linear ion density N/L . This is also true for the relative Debye length:

$$\left(\frac{\lambda_D}{R_c}\right)^2 = \frac{1}{24} \frac{\left(\frac{\Delta f}{f}\right)_{hot}}{\left(\frac{\Delta f}{f}\right)_{lin}} \quad (19)$$

which must be small to ensure the validity of the “cold cloud” model. From this it is seen that the transverse dimension R of the trap may be reduced without penalty of performance, providing that operational parameters are appropriately scaled. This requires ω and Ω to vary as R^{-1} , and the applied voltage V_o to be held constant.

Assuming the traps hold the same number of ions, the second-order Doppler shift for the two traps can be compared

$$\left(\frac{\Delta f}{f}\right)_{lin} = \frac{5}{3} \frac{R_{sph}}{L} \left(\frac{\Delta f}{f}\right)_{sph} \quad (20)$$

As more ions are added to the linear trap, their average second-order Doppler shift increases. It equals that of the spherical ion cloud in the hyperbolic trap when

$$N_{lin} = \frac{3}{5} \frac{L}{R_{sph}} N_{sph} \quad (21)$$

A linear trap can thus store $(3/5)(L/R_{sph})$ times the ion number a conventional RF trap stores with no increase in average second-order Doppler shift. For the JPL-built trap, $L = 75$ mm. Taking $R_{sph} = 2.5$ mm for $2 \cdot 10^6$ $^{199}\text{Hg}^+$ ions [8], one sees that this linear trap should hold about 18 times the number of ions as that of [8].

III. Construction of a Linear Ion Trap

The linear trap built consists of four molybdenum rods equally spaced on an approximately 1-cm radius. Oxygen-free high-conductivity copper pins with DC bias are located at each end to confine ions in the axial direction and are about 75 mm apart.

The input optical system that performs state selection and also determines which hyperfine state the ions are in has been modified from the previous system [2]. The present system illuminates about 1/3 of the 75-mm long cylindrical ion cloud. An ion’s room temperature thermal motion along the axis of the trap gives an average round-trip time of 1.4 msec, a value

that is much smaller than any optical pumping, interrogation, or microwave resonance time. Thus, all the ions are illuminated, but with a lower average intensity.

In order to operate within the Lambe–Dicke regime [10], the 40.5-GHz microwave resonance radiation is propagated perpendicularly to the line of ions. The ions should then all feel phase variations of this radiation that is less than π , so that the first-order Doppler absorption in sidebands induced by an ion’s motion does not degrade the 40.5-GHz fundamental.

IV. Conclusions

Trapped ion frequency standards eliminate containing walls and their associated perturbations of the atomic transition frequencies by using electromagnetic fields alone to confine the particles. For any given trap, however, there exists a trade-off between the number of ions in the trap and a frequency shift due to second-order Doppler effects. This trade-off directly affects performance of the standard since the frequency shift is typically very much larger than the ultimate stability required and since the statistical limit to performance is directly related to ion number.

This performance trade-off was calculated for an RF trap with cylindrical geometry, a case not previously considered for a trapped ion frequency source. By replacing the single node in the RF trapping field for a spherical trap with a line of nodes, a cylindrical trap increases effective volume without increasing overall size. Furthermore, this performance is found to be independent of its transverse dimensions, as long as the driving frequency is scaled appropriately, with the driving voltage unchanged. More specifically, for the same frequency shift, a linear trap with length L can hold as many ions as a spherical trap with ion cloud diameter $6L/5$. In addition to the practical advantage of greatly reduced overall volume, a fundamental advantage is also allowed since operation within the Lambe–Dicke regime places a limit on the size of the ion cloud, a requirement that may be met for a cylindrical trap by irradiating the microwave atomic transition in a direction perpendicular to the trap’s longitudinal axis.

A trapped ion frequency source has been designed in which a cylindrical trap is implemented with a combination of RF and DC electric fields. With similar overall size and improved optical performance, this trap has 15 to 20 times the ion storage volume as conventional RF traps with no increase in second-order Doppler shift.

Acknowledgments

We wish to thank Dave Seidel for assisting in the design of the linear trap described here and G. R. Janik for helpful comments.

References

- [1] L. S. Cutler, R. P. Giffard, P. J. Wheeler, and G. M. R. Winkler, "Initial Operational Experience with a Mercury Ion Storage Frequency Standard," *Proc. 41st Ann. Symp. Freq. Control*, pp. 12-19, 1987.
- [2] J. D. Prestage, G. J. Dick, and L. Maleki, "The JPL Trapped Mercury Ion Frequency Standard," *TDA Progress Report 42-92*, vol. October-December 1987, Jet Propulsion Laboratory, Pasadena, California, pp. 13-19, February 1988.
- [3] D. W. Allan, "A Study of Long-Term Stability of Atomic Clocks," *Proc. 19th Ann. PTTI App. Plan. Meeting*, pp. 375-412, 1987.
- [4] L. A. Rawley, J. H. Taylor, M. M. Davis, and D. W. Allan, "Millisecond Pulsar PSR 1937+21: A Highly Stable Clock," *Science*, vol. 238, pp. 761-765, 1987.
- [5] J. W. Armstrong, F. B. Estabrook, and H. D. Wahlquist, "A Search for Sinusoidal Gravitational Radiation in the Period Range 30-2000 Seconds," *Astrophys. J.*, vol. 318, pp. 536-541, 1987.
- [6] J. J. Bollinger, J. D. Prestage, W. M. Itano, and D. J. Wineland, "Laser-Cooled-Atomic Frequency Standard," *Phys. Rev. Lett.*, vol. 54, pp. 1000-1003, 1985.
- [7] H. G. Dehmelt, "Radio-Frequency Spectroscopy of Stored Ions I: Storage," *Adv. At. Mol. Phys.*, vol. 3, pp. 53-72, 1967.
- [8] L. S. Cutler, R. P. Giffard, and M. D. McGuire, "Thermalization of ^{199}Hg Ion Macromotion by a Light Background Gas in an RF Quadrupole Trap," *Appl. Phys. B*, vol. 36, pp. 137-142, 1985.
- [9] S. A. Prasad and T. M. O'Neil, "Finite Length Thermal Equilibria of a Pure Electron Plasma Column," *Phys. Fluids*, vol. 22(2), pp. 278-281, 1979.
- [10] R. H. Dicke, "The Effect of Collisions upon the Doppler Width of Spectral Lines," *Phys. Rev.*, vol. 89, pp. 472-473, 1953.

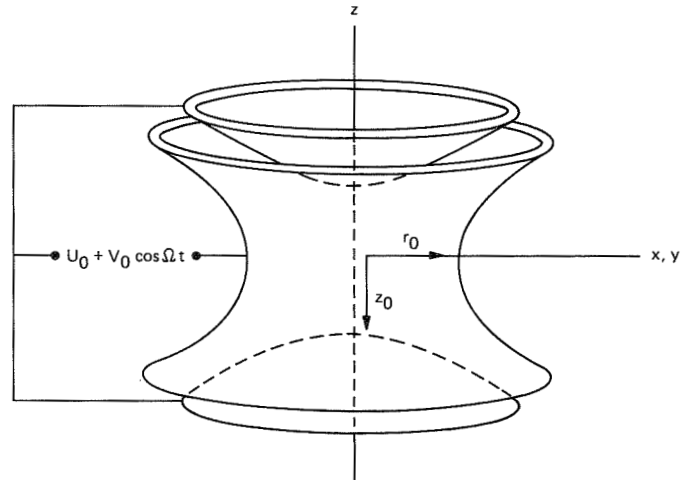


Fig. 1. A conventional hyperbolic RF ion trap. A node of the RF and DC fields is produced at the origin of the coordinate system shown.

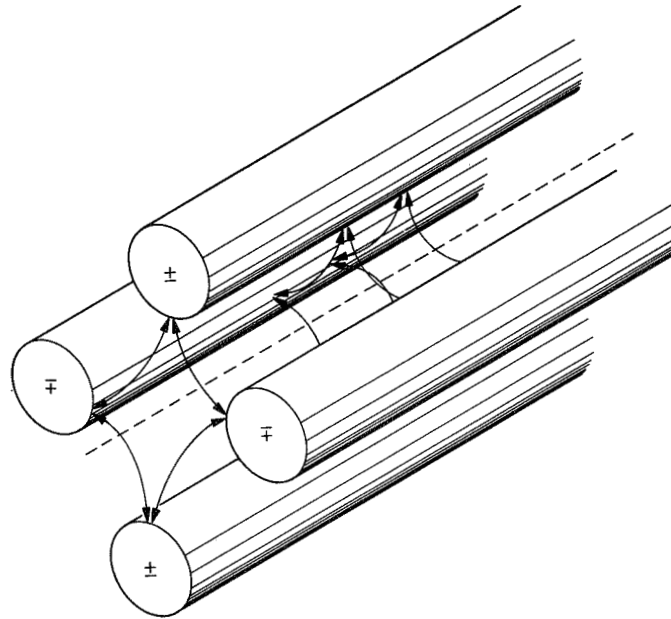


Fig. 2. The RF electrodes for a linear ion trap. Not shown are the DC endcap needle electrodes used to prevent the ions from escaping along the longitudinal axis. Ions are trapped around the line of nodes of the RF field with reduced susceptibility to second-order Doppler frequency shift.

Operational Parameters for the Superconducting Cavity Maser

R. T. Wang¹ and G. J. Dick

Communications Systems Research Section

D. M. Strayer

Applied Technologies Section

Tests of the superconducting cavity maser (SCM) ultra-stable frequency source have been made for the first time using a hydrogen maser for a frequency reference. In addition to characterizing the frequency stability, the sensitivity of the output frequency to several crucial parameters was determined for various operating conditions. Based on this determination, the refrigeration and thermal control systems of the SCM were modified. Subsequent tests showed substantially improved performance, especially at the longest averaging times.

I. Introduction

The superconducting cavity maser (SCM) [1], [2], [3] is an all-cryogenic oscillator which, like other cryogenic cavity oscillators, gives stability at short measuring times that is superior to that achievable by any other means. It differs from other superconducting cavity stabilized oscillator designs [4] in its use of a very rigid ($Q \approx 10^9$) sapphire-filled stabilizing cavity and in its all-cryogenic design, excitation being provided by an ultra-low noise cryogenic ruby maser.

Performance of the SCM at short times is superior to all conventional or atomic sources, even surpassing that of the active hydrogen maser. With similar Q s, the advantage of the

SCM is its larger output power, $\approx 10^{-9}$ watt versus $\approx 10^{-12}$ watt for the hydrogen maser. Long-term performance is limited by variations in the various operating parameters, such as temperature, drive power, output voltage standing wave ratio, etc., depending on the sensitivity of the SCM to these various parameters.

Figure 1 shows a diagram of the oscillator. The three-cavity design has been previously discussed [2]. Oscillation at the signal frequency (2.69 GHz) results from application of pump power (13.15 GHz) to the ruby, which creates an inversion of the energy level populations in the ruby crystal. The frequencies of the three modes of the coupled cavity system are spaced relatively close to each other (5 percent spacing) in order to couple effectively, but are spaced far enough from each other to allow mode selection. Only one of the modes is suitable for ultra-stable operation. Tuning the regenerative frequency of

¹During the time this work was done, this author held a National Research Council—NASA/JPL Research Associateship.

the ruby (2 percent bandwidth) to that of this high-Q stabilized mode is accomplished by adjusting the current through the superconducting solenoid. The purpose of the coupling resonator is to provide physical separation of the lead-coated sapphire resonator from the magnetic field of the solenoid.

Cooling of the oscillator itself is provided by the liquid helium pot attached to the bottom cavity, and thermal regulation is achieved by varying the power dissipation in the heater as shown. Both the heat leak into the system from the waveguide at the top and the cooling power of the helium pot are subject to variation, and it is seen that, even if the changes in these heat flows are exactly cancelled by the effect of the heater, varying temperature gradients in the oscillator still result.

Figure 2 shows the stability of this oscillator when measured with a hydrogen maser as reference. Also shown are the measured stability of the H-maser and calculated short-term stability for the SCM due to additive and in-oscillator noise for the present configuration. The major features shown in Fig. 2 are:

- (1) The need for a better reference at short times in order to properly characterize the SCM
- (2) The presence of in-oscillator noise due to back-coupling from the room-temperature amplifier
- (3) The presence of substantial long-term variations in the SCM

The first of these considerations can be dealt with only by the provision of a second cryogenic oscillator, something outside the scope of this article. The second can be solved by the addition of a cryogenic isolator to prevent room-temperature radiation from coupling from the output port back into the oscillator itself. This issue is addressed by a redesign of the oscillator to allow primary coupling of the signal from an additional port in the high-Q resonator.

The long-term variations, on the other hand, could arise from any of the various parameters on which the frequency of the SCM depends. This article primarily considers the sensitivity to and variation of the operational parameters for the SCM.

II. Operational Parameters

The significant operational parameters (parameters subject to variation during operation) of the SCM are presented in Table 1. Each of these parameters is described in terms of its significance as a tuning parameter and as a likely source of variability in the output frequency. Several of the parameters are discussed in more detail in the following section.

III. Technical

In this section, the dependence of frequency on temperature and on pump power and frequency are discussed in more detail. Additionally, the discovery of sensitivity of the output frequency to a thermal gradient across the three-cavity system has given rise to a new thermal regulation system. A diagram of this system, Fig. 1(b), and improved frequency stability results, Fig. 3, are presented.

A. Temperature Dependence

Figure 4 shows a plot of the temperature dependence of the output frequency for the SCM over the temperature range between 1 and 2 kelvins. From a functional point of view, the presence of a frequency maximum at about 1.57 kelvin is an extremely desirable feature since it allows operation of the oscillator in a region of nominally zero temperature coefficient. The quadratic coefficient in $\delta f/f$ at the maximum is $3.3 \cdot 10^{-9}/\text{kelvin}^2$. This means that a temperature accuracy of one millikelvin together with a stability of 30 microkelvins allows a frequency stability of

$$\frac{\delta f}{f} = 2 \cdot 10^{-16}$$

An additional advantage of this mode of operation is the ease of refrigeration at a temperature of 1.57 K in comparison to the initial design temperature of 0.9 K. New options for refrigeration are also available. For example, operation at 1.57 K allows the use of a continuous-flow helium cryostat rather than the batch-mode system required at the lower temperature.

The negative temperature coefficient exhibited by the data in Fig. 4 is easy to understand at the higher temperatures, and was anticipated in the design of the SCM. It is due to a combination of thermal expansion and superconducting penetration depth effects, both of which show a negative slope. However, both of these effects were expected to "freeze out" at the lowest temperatures—hence the (previous) 0.9 kelvin operating temperature. The contribution with positive slope at the lower temperatures had been observed previously, but its nature and cause had not been identified. Also, its consequence, the maximum with temperature, had not been discovered.

Measurements of the effect on the operating frequency of a temperature gradient across the oscillator now point to the ruby resonator as a likely candidate for the positive slope. The sign of the thermal gradient effect is consistent with this identification. In addition, the magnitude agrees with the measured slopes of low- and high-temperature parts combined with a rough estimate of the thermal conductivity of the coupling resonator. A positive temperature coefficient would result

from the demagnetization field due to the changing alignment of chromium spins in the ruby. Although the ruby resonator seems a likely candidate, the effect has not been positively identified.

B. Pump Power and Frequency

Figure 5 shows a plot based on measurements of the SCM output frequency dependence on pump power and frequency. Pump amplitude is shown in terms of the attenuation inserted in the pump waveguide. Due to vagaries of the plotting routine, attenuation was divided by a factor of 1000 before plotting. The discrete nature of the data is discernible in the ripples at the bottom of the valley in the center of the figure, for example.

Since the pump power is very much more difficult to stabilize than its frequency, the major feature of the plot shown is the valley down the middle where the sensitivity to pump power is greatly reduced. In this region the slope is typically $\leq 2 \cdot 10^{-13}/\text{dB}$, a value 100 times smaller than on the outside slopes. A second feature is the saturation at higher power, where the frequency changes less rapidly. These features are somewhat variable, with an extremum at low power also sometimes observed. A pronounced limiting effect, in which the oscillation amplitude shows a somewhat soft "clipping" effect, is also associated with pump frequencies showing the rapid variation of frequency with amplitude. Because of the variability between subsequent reworks of the oscillator assembly, it seems likely that this interaction is not fundamental to either the ruby maser or to the high-Q resonator but may be due to an interaction between pump and oscillation frequencies at a demountable joint in the coupling resonator.

C. Modification and Test

Figure 1(b) is a diagram showing the modified refrigeration and thermal regulation system. Where the old helium tank was located below the oscillator and attached at its lower extremity, the continuous flow cooler is now mounted above the oscillator in order to intercept the varying heat flow from above.

Compensation for these variations is now accomplished by means of a heater placed *above* the refrigerator, so that no thermal gradients are generated below the heater itself. Variations in cooling power in the refrigerator are also compensated for by this heater with no resultant gradients below the refrigerator. Except for incidental electrical leads associated with the thermometry, the only thermal contact to the oscillator takes place at one point, the top, and so thermal gradients are effectively eliminated.

Stability results obtained with the modified oscillator are shown in Fig. 5. Again, little information can be discerned regarding the short-term stability, except that it is better than that of the best available reference, the hydrogen maser. Long-term stability, however, has been significantly improved by the modifications, with results in the 10^{-15} range obtained for times longer than 30 seconds.

IV. Conclusions

A detailed study of the operating parameters of the superconducting cavity maser disclosed regions of operation for the various parameters that are substantially more advantageous than those previously found. On the basis of this study, the cryogenics of the oscillator were modified to optimize operation at a new operating temperature and to eliminate thermal gradients. Stability results for the modified SCM show substantially improved long-term stability compared to previous results. Results for shorter measuring times continue to be better than can be measured using the best reference presently available.

With the addition of the continuous flow refrigerator, it may now be possible to incorporate a closed-cycle refrigerator and so eliminate all need of disposable cryogens. Commercial coolers are available that could provide the needed 20-milliwatt helium flow presently used. Such a cooler would reduce the overall size by eliminating the need for a large helium reservoir. Possible performance degradation due to mechanical motion in the cooler would need to be examined experimentally.

Acknowledgments

Special thanks to Bill Diener for his assistance in ultrastable measurements, Roland Taylor for easy access to the capabilities of the Test Facility, Chuck Greenhall for software enhancements meeting our special requirements, and Tom Tucker for assistance and support with hydrogen maser measurements.

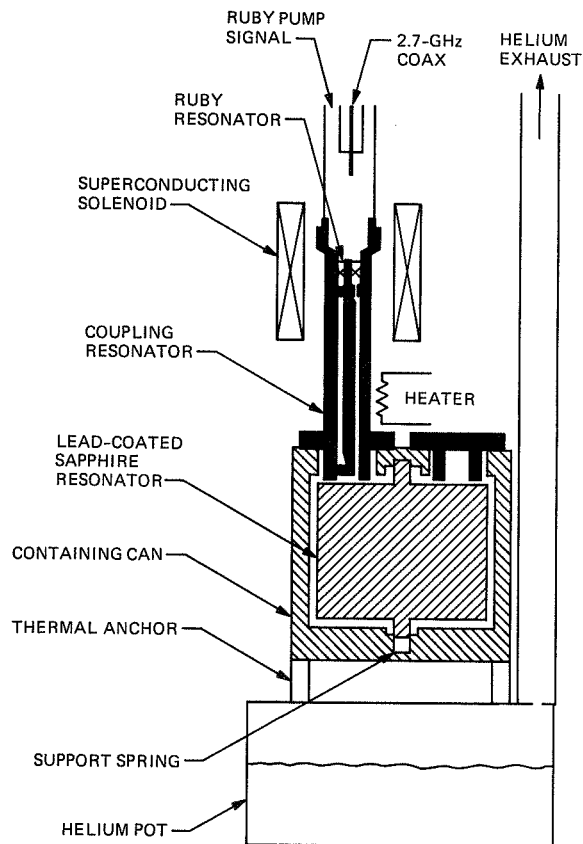
References

- [1] S. Thakoor, D. M. Strayer, G. J. Dick, and J. E. Mercereau, "A Lead-on-Sapphire Superconducting Cavity of Superior Quality," *J. Appl. Phys.*, vol. 59, pp. 854–858, 1986.
- [2] G. J. Dick and D. M. Strayer, "Development of the Superconducting Cavity Maser as a Stable Frequency Source," *Proceedings of the 38th Annual Frequency Control Symposium*, pp. 435–446, 1984.
- [3] D. M. Strayer and G. J. Dick, "The Superconducting Cavity Maser Oscillator—Toward Higher Stability," *Proceedings of the 18th Annual Precise Time and Time Interval (PTTI) Planning and Applications Meeting*, pp. 601–609, 1986.
- [4] S. R. Stein and J. P. Turneaure, "The Development of the Superconducting Cavity Stabilized Oscillator," *Proceedings of the 27th Annual Frequency Control Symposium*, pp. 414–420, 1975.

Table 1. Description of the significant operational parameters of the SCM

Parameter	Tuning Functionality	Significant Variability
Temperature	Operating range from below 0.8 K to above 2.0 K for normal SCM operation. Variation can change the sign of sensitivity of operational frequency to temperature. Proper choice allows operation with near-zero temperature coefficient.	Substantial instability. Medium- and long-term variability of 10^{-4} to 10^{-5} K. Sensitivity coefficient 0 to $\pm 10^{-9}/\text{K}$.
Thermal Gradient	No functional significance.	Marked problems due to variation in regulating heater power. Best expressed in terms of sensitivity to heat flow. Value is $\approx 10^{-9}/\text{watt}$. Value of heater power is typically 10^{-3} to 10^{-2} watt. Variability of heater power is 10 percent to 50 percent.
Magnetic Bias	Variable by 2 percent about optimum value of ≈ 500 gauss. No important effect on frequency sensitivity coefficients.	No problems observed. Sensitivity is $\approx 10^{-9}/\text{gauss}$. Use of a persistent-mode superconducting magnet at this relatively low field allows very high stability.
Pump Power	Oscillation requires 10^{-4} watts or more to be coupled to low temperature region. Depending on pump VSWR matching, may have 5 to 20 dB of range available for oscillation using 100 mW klystron source. Significant influence on sensitivity to pump power and frequency.	Substantial instability. Variability of amplitude of typical microwave sources is 10^{-2} to 10^{-4} dB. Essentially impossible to regulate power actually applied to ruby due to variations in thermal profile of feed waveguide. Sensitivity is 0 to $10^{-11}/\text{dB}$.
Pump Frequency	≈ 20 MHz variation allowed about optimum frequency of 13.15 GHz. Important influence on sensitivity of operational frequency to pump power.	No problems in principle due to ability to "bootstrap" pump stability from SCM stability. No significant problems in practice with quartz crystal-stabilized klystron source.
Signal Coupling	Influences fractional output power and signal VSWR sensitivity. Also (incidentally) an important tool for adjustment of pump VSWR.	Possible source of drift due to varying temperature profile with helium level. Magnitude not known.
Signal VSWR	No significant function.	Substantial burden placed on stability of room temperature signal connections. Maximum variability is $\approx 10^{-10}$. The fix for this is addition of a low-temperature isolator.

(a) ORIGINAL SCM OSCILLATOR



NOT SHOWN:
2-STAGE ELECTRONIC TEMPERATURE REGULATION
ELEMENTS AND FILL LINE TO HELIUM POT

(b) MODIFIED SCM OSCILLATOR

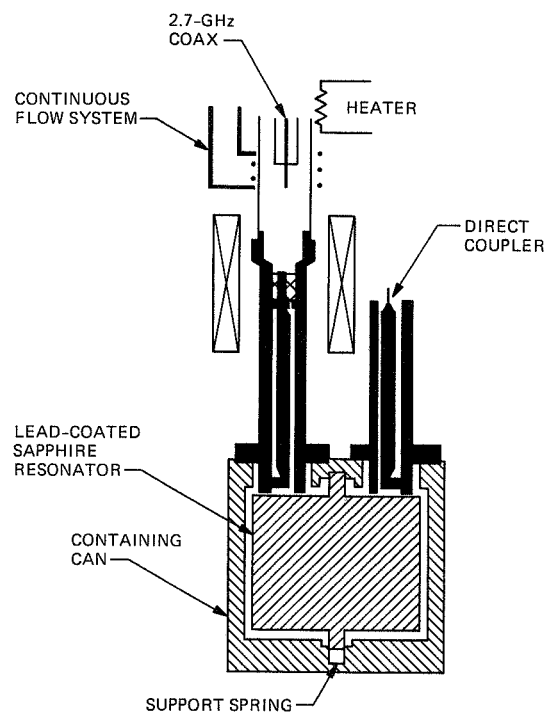


Fig. 1. Schematic diagrams of the SCM oscillator: (a) original configuration and (b) modified oscillator. Modifications prevent regulating heat flow from flowing through the oscillator itself. Direct coupler was not implemented for any data presented in this article.

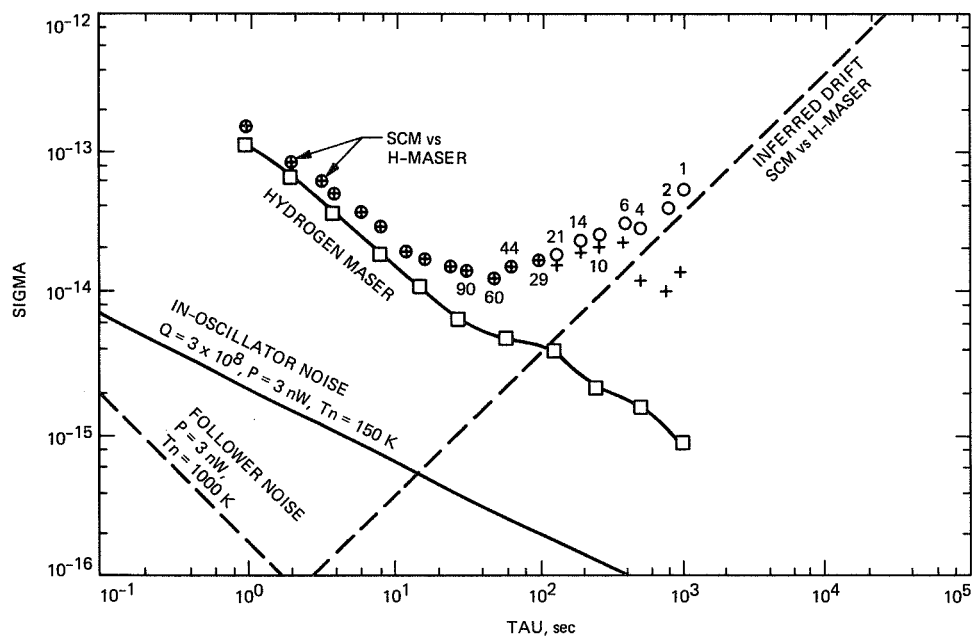


Fig. 2. Allan variance of stability of superconducting cavity maser in first tests with hydrogen maser reference oscillator. Points marked + show data with drift removed; data (circles) are accompanied by number of samples. Also shown are measured hydrogen maser stability and the calculated effect of in-oscillator and added noise based on measured operating conditions and an assumed in-oscillator noise temperature of 150 kelvins.

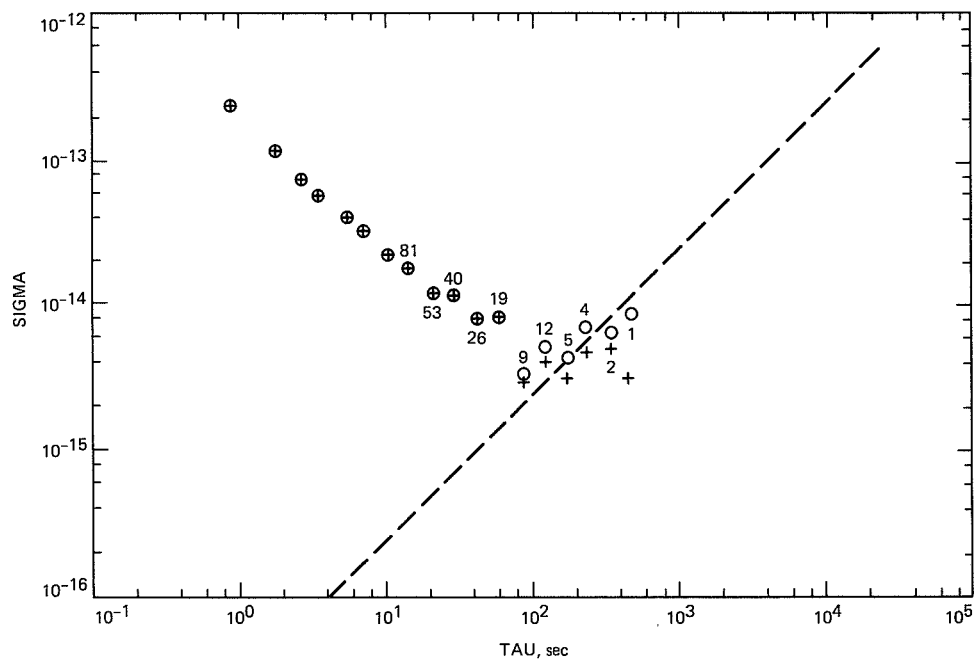


Fig. 3. Plot of Allan variance of SCM stability after modifications, H-maser reference.

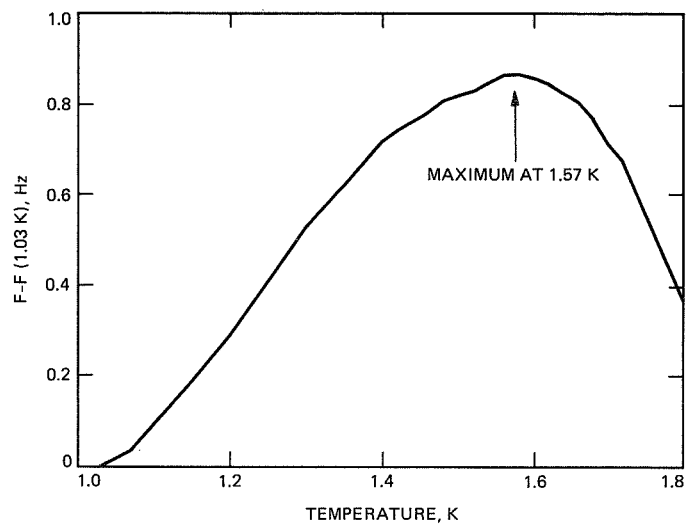


Fig. 4. Measured frequency versus temperature plot for range 1–1.8 kelvin. The 0.9-Hz frequency variation is referred to ≈ 2.69 GHz reference.

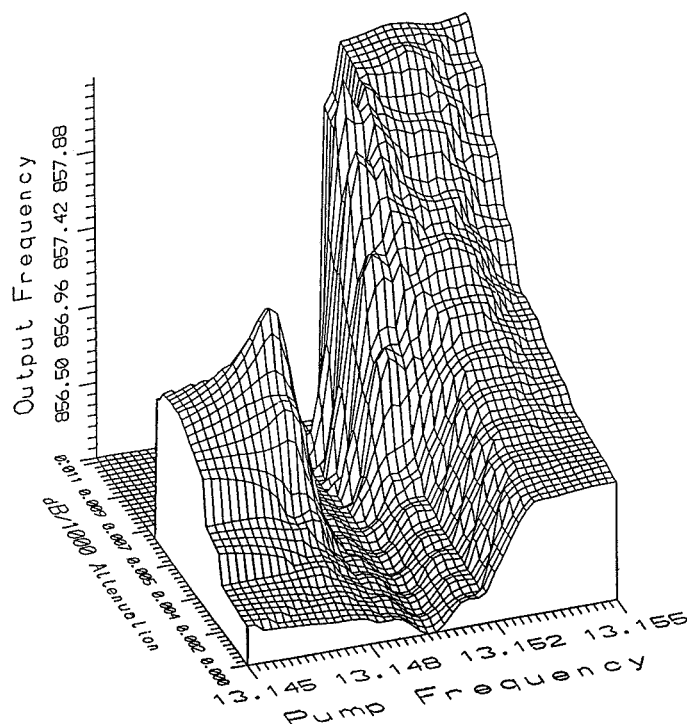


Fig. 5. Three-dimensional plot showing dependence of output frequency on pump signal frequency and power. Output frequency is referred to ≈ 2.69 GHz reference. Pump power is indicated by attenuation value. Due to vagaries of the plotting routine, the 0–11-dB attenuation range is plotted as dB/1000. Pump frequency is measured in GHz.

N 8 9 - 2 7 8 7 7

Operating and Environmental Characteristics of Sigma Tau Hydrogen Masers Used in the Very Long Baseline Array (VLBA)

T. K. Tucker

Communications Systems Research Section

This article presents the results obtained from performance evaluation of a pair of Sigma Tau Standards Corporation Model VLBA-112 active hydrogen maser frequency standards. These masers were manufactured for the National Radio Astronomy Observatory (NRAO) for use on the Very Long Baseline Array (VLBA) project and were furnished to the Jet Propulsion Laboratory (JPL) for the purpose of these tests.

Tests on the two masers were performed in the JPL Frequency Standards Laboratory (FSL) as a cooperative effort with NRAO and included the characterization of output frequency stability versus environmental factors such as temperature, humidity, magnetic field, and barometric pressure. The performance tests also included the determination of phase noise and Allan variance using both FSL and Sigma Tau masers as references. All tests were conducted under controlled laboratory conditions, with only the desired environmental and operational parameters varied to determine sensitivity to external environment.

I. Introduction

A. Purpose

The tests described herein were performed by the Jet Propulsion Laboratory (JPL) as a cooperative effort with the National Radio Astronomy Observatory (NRAO). JPL was chosen for this evaluation because of its unique testing capability and facilities, and in order to provide an independent evaluation of Sigma Tau hydrogen maser performance.

All tests were conducted at JPL in the Frequency Standards Research Laboratory Test Facility in Pasadena, California, between March and September 1988.

B. Sigma Tau Hydrogen Masers

The Model VLBA-112 is a compact and ruggedized active hydrogen maser manufactured by the Sigma Tau Corporation for NRAO for use on the Very Large Baseline Array (VLBA)

Project. The essential physical and electrical characteristics, as given by the manufacturer, are outlined in Table 1.

Prior to performance and environmental testing, the critical operating parameters of each of the masers, identified as Serial Numbers 2 and 3, were determined and recorded as shown in Table 2.

C. Test Facilities

The JPL Frequency Standards Laboratory is responsible for the research, development, and implementation of a wide variety of state-of-the-art frequency generation and distribution equipment used within the Deep Space Network (DSN). In order to achieve the demanding performance and reliability requirements, a substantial amount of assembly and subassembly testing is required. Toward this end, an extensive testing capability has been developed which includes special equipment, facilities, procedures, and personnel skilled in the testing and characterization of precision oscillators and other signal sources.

The stability and environmental tests which are routinely performed in this facility are as follows:

- (1) Allan variance
- (2) Spectral density of phase
- (3) Temperature sensitivity
- (4) Humidity sensitivity
- (5) Barometric pressure sensitivity
- (6) Magnetic field sensitivity

The instrumentation and test area has approximately 250 square meters of floor space and houses the necessary instrumentation and test equipment. Additionally, two active hydrogen maser frequency references are conveniently located in this area. All critical equipment, including the units under test, are powered by an uninterruptible power source. The entire test area, as well as the environmental control system, is backed up by an automatically switched motor generator. Temperature control is maintained to within ± 0.05 degrees Centigrade through the use of a doubly redundant air conditioning system. Magnetic field variations are minimized by the use of nonmagnetic construction materials throughout the facility. As an additional precaution, one of the reference hydrogen masers is housed in a magnetically shielded enclosure.

Environmental testing capability is provided by three Tenny Corporation environmental test chambers. Each chamber includes 6 square meters of floor space and is approximately 3 meters high, providing adequate space for equipment under test as well as required cables and peripherals.

The environmental testing capabilities are as shown in Table 3.

D. Test Plan

All tests were performed by FSTL personnel, in accordance with a test plan. This plan was prepared to establish the procedures and environmental conditions to be followed during the course of testing. The test plan is not intended to be a detailed test procedure, but is rather a description of the specified tests (i.e., spectral density of phase, Allan deviation, frequency stability, etc.), test conditions (i.e., temperature, humidity, barometric pressure) and documentation requirements. The plan also serves as a guide in the planning and scheduling of the overall test program. A copy of the test plan is included in the Appendix.

E. Measurement Systems

Figure 1 is a block diagram of the measurement system used to determine frequency stability and the Allan variance (deviation) between the Sigma Tau masers and the laboratory reference masers. Figure 2 is a block diagram of the measurement system used to determine the spectral density of phase of the two Sigma Tau masers at the 5, 10, and 100 MHz outputs.

II. Test Results

A. Sequence of Tests

The tests and test limits are shown in Table 4.

B. Allan Variance and Spectral Density of Phase Tests

Figures 3, 4, and 5 are plots of the Allan variance between the two Sigma Tau masers and also between each of the Sigma Tau masers and one of the laboratory reference masers which serve to verify near equal performance of the two Sigma Tau masers. Included in Fig. 2 is the measurement system noise floor. Figures 6, 7, and 8 are plots of the spectral density of phase between the two Sigma Tau masers at the 5, 10, and 100 MHz outputs. The spurious signals seen in each of the plots are predominantly the result of the autotuner modulation signal with some additional contribution from power supply noise.

C. Environmental Tests

The purpose of these tests was to characterize each maser in terms of frequency shift for a given change in environmental condition. In each test, the output frequency was carefully monitored while one of the environmental conditions was

varied as specified in Table 4. The results of each of these environmental tests are itemized below:

- (1) Output Frequency versus Temperature Tests. The masers were individually placed in the test chamber and the chamber temperature was cycled between 17 and 27 deg C; the resultant variation in output frequency was plotted. The frequency sensitivity as a function of ambient temperature is shown in Fig. 9.
- (2) Output Frequency versus Relative Humidity Tests. With the chamber temperature held constant, the chamber relative humidity was cycled between 20 and 80 percent, with a 48-hour stabilization period at each limit. The observed variations in output frequency versus the relative humidity were well below 1×10^{-14} .
- (3) Barometric Pressure Tests. No output frequency variations were observed as the masers were individually subjected to barometric pressures of 6 kPa above and below ambient pressure with a two-hour dwell at each extreme.
- (4) Magnetic Field Sensitivity Tests. In order to determine the maser magnetic field sensitivity, a 230-cm (≈ 90 -inch) Helmholtz coil was placed around the maser. The coil was positioned to provide a vertical

magnetic field and was centered around the maser physics unit. Since the magnetic shielding effectiveness is dependent upon the magnitude of the magnetic field, the sensitivity was measured at three different field values. The magnetic field sensitivity of each maser is shown in Table 5.

- (5) Output Frequency versus Power Supply Variations. With the internal battery supply disconnected, the input DC voltage was varied between 24 and 28 VDC. No output frequency shift was observed as a result of these supply variations.

III. Summary

A summary of the environmental sensitivities of the two Sigma Tau masers is presented in Table 6.

Throughout the test series the Sigma Tau masers performed reliably, and were well-behaved. Of particular interest is the fact that both masers were transported from Socorro, New Mexico to Pasadena, California, a distance of some 800 miles, in the back of a carry-all van. Only a minimum of protection from shock and vibration was provided during transit, and upon arrival both masers were within normal operating parameters.

Acknowledgments

The author wishes to acknowledge the generous contributions of several individuals to this effort; in particular, that of Albert Kirk and Bill Deiner of JPL for their assistance in the performance of the many tests. Additionally, the generous technical assistance of Harry Peters of the Sigma Tau Corp. during the initial setup and preparation for testing is gratefully acknowledged.

References

- [1] H. Peters, B. Owings, T. Oakley, and L. Beno, "Hydrogen Masers for Radio Astronomy," *Proc. 41st Ann. Freq. Control Symposium*, pp. 75-81, 1987.
- [2] H. Peters, "Design and Performance of New Hydrogen Masers Using Cavity Frequency Switching Servos," *Proc. 38th Ann. Freq. Control Symposium*, pp. 420-427, 1984.
- [3] *Operation and Instruction Manual, Atomic Hydrogen Maser Frequency Standard, Model VLBA-112*, Sigma Tau Standards Corporation, 1985.

Table 1. Physical and electrical characteristics

Size	cm	in.
Height	107	42
Width	46	18
Depth	76	30
Weight	kg	lbs
	238	525
Input power*	AC	DC
	115 V \pm 10% rms	24–28 V
	50–60 Hz	4 A (typ.)
	140 watts	
Outputs	MHz	V, rms
	100 (2 ea.)	1 \pm 0.3
	10 (1 ea.)	\approx 0.5
	5 (1 ea.)	1 \pm 0.3

*Build-in standby battery supply provides up to 10 hours of operation without input power.

Table 2. Operating characteristics

Parameter	S/N 2	S/N 3
Output power, dBm	–100	–100
Line Q	1.82×10^9	1.64×10^9
Cavity-loaded Q	33,000	37,800
Coupling factor	0.35	0.30
Rx noise figure, dB	<1	<1
Zeeman frequency, Hz	827.7	808.9

Note: All tests were performed in the AUTOTUNE mode.

Table 3. Environmental test capability

Parameter	Range
Temperature	15–35 deg C \pm 0.05 deg
Pressure	± 6 kPa \pm 120 Pa
Relative humidity	11–90% RH \pm 5%
Magnetic field	± 0.5 Gauss

Table 4. Test sequence and limits

Parameter	Range
Allan variance	–
Spectral density of phase	–
Temperature	17–27 deg C
Humidity	20–80% RH
Barometric pressure	± 6 kPa
Magnetic field	± 0.5 Gauss
Power supply variations	24–28 VDC

Table 5. Magnetic field sensitivity

Field Magnitude	Sensitivity/Gauss	
	S/N 2	S/N 3
Small (± 0.1 G)	-1.42×10^{-13}	-4.74×10^{-13}
Medium (± 0.25 G)	-1.05×10^{-13}	-3.98×10^{-13}
Large (± 0.5 G)	-8.04×10^{-14}	-3.17×10^{-13}

Table 6. Environmental sensitivity summary

Condition	S/N 2	S/N 3
Temperature (17–27°C)	$1.37 \times 10^{-14}/\text{deg C}$	$4.2 \times 10^{-14}/\text{deg C}$
Humidity (20–80% RH)	$<1 \times 10^{-14}$	$<1 \times 10^{-14}$
Barometric pressure (± 6 kPa)	$<1 \times 10^{-14}$	$<1 \times 10^{-14}$
Magnetic field (± 0.1 Gauss)	$-1.42 \times 10^{-13}/\text{Gauss}$	$-4.74 \times 10^{-13}/\text{Gauss}$
Power supply variations (24–28 VDC)	$<1 \times 10^{-14}$	$<1 \times 10^{-14}$

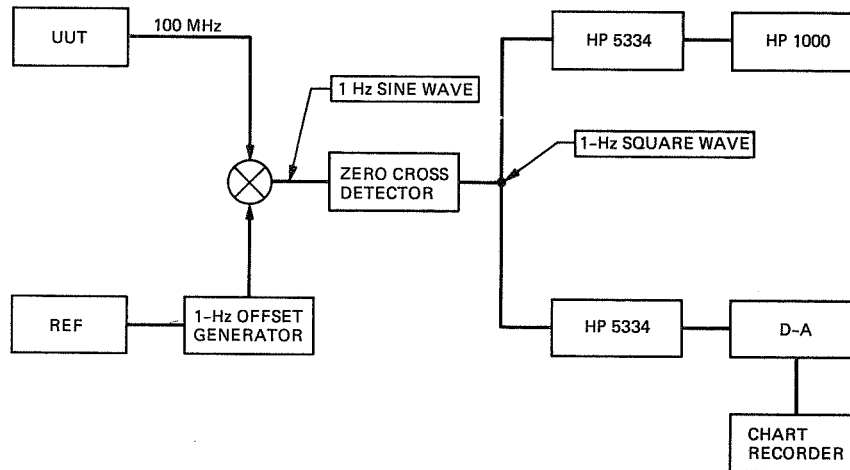


Fig. 1. Measurement system for frequency shift and Allan variance.

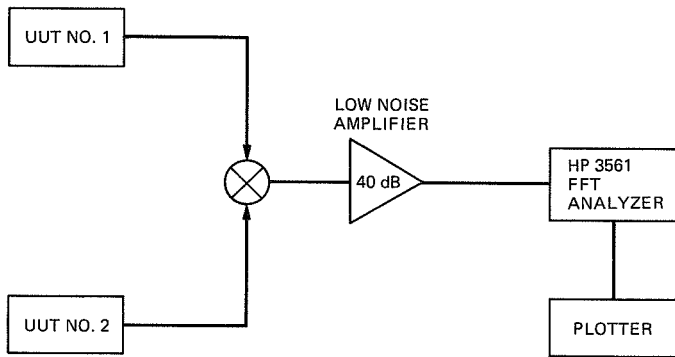


Fig. 2. Phase noise measurement system.

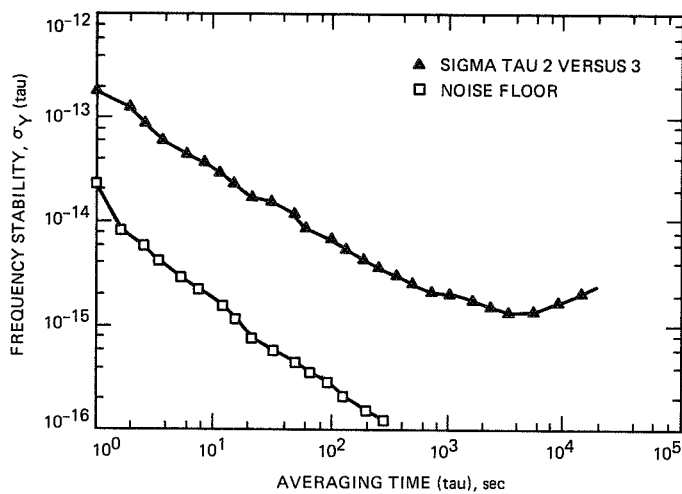


Fig. 3. Allan variance—Sigma Tau 2 versus 3.

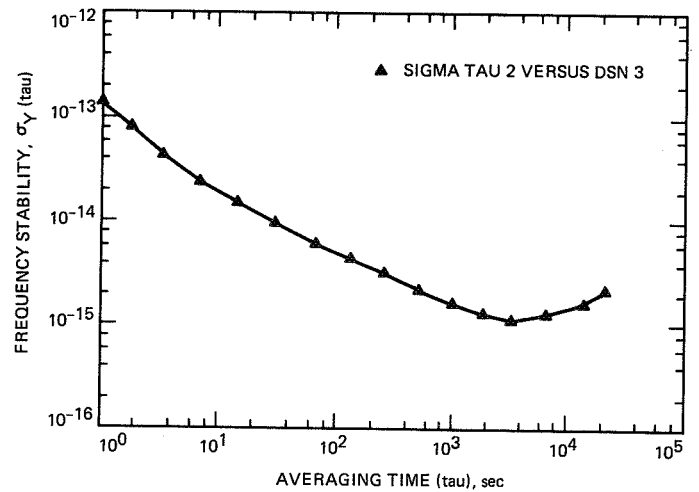


Fig. 4. Allan variance—Sigma Tau 2 versus reference maser.

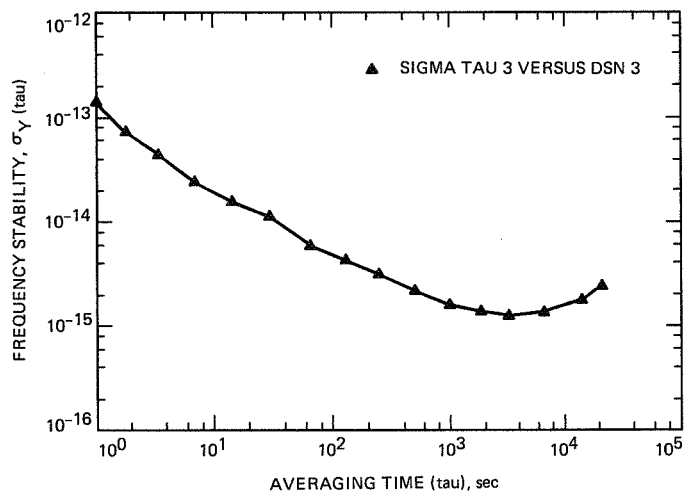


Fig. 5. Allan variance—Sigma Tau 3 versus reference maser.

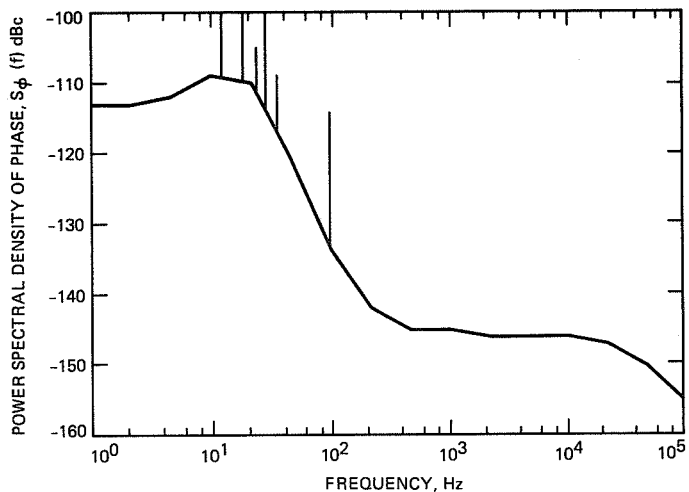


Fig. 7. Phase noise at 10-MHz outputs.

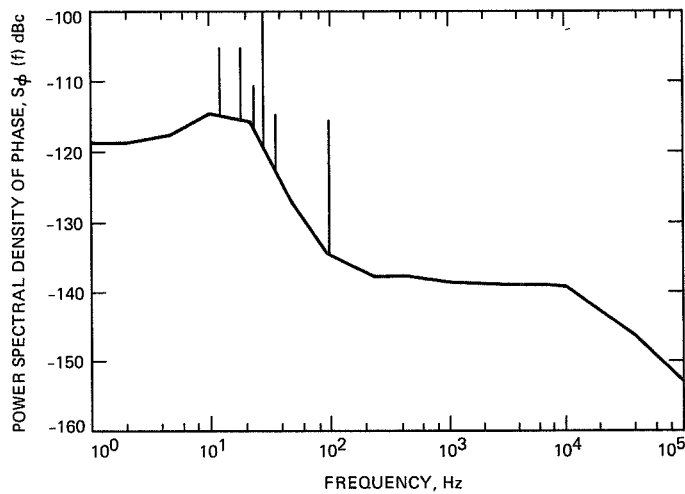


Fig. 6. Phase noise at 5-MHz outputs.

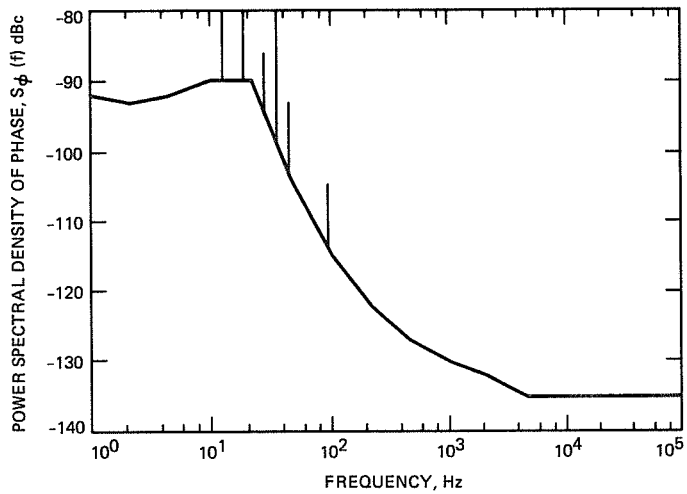


Fig. 8. Phase noise at 100-MHz outputs.

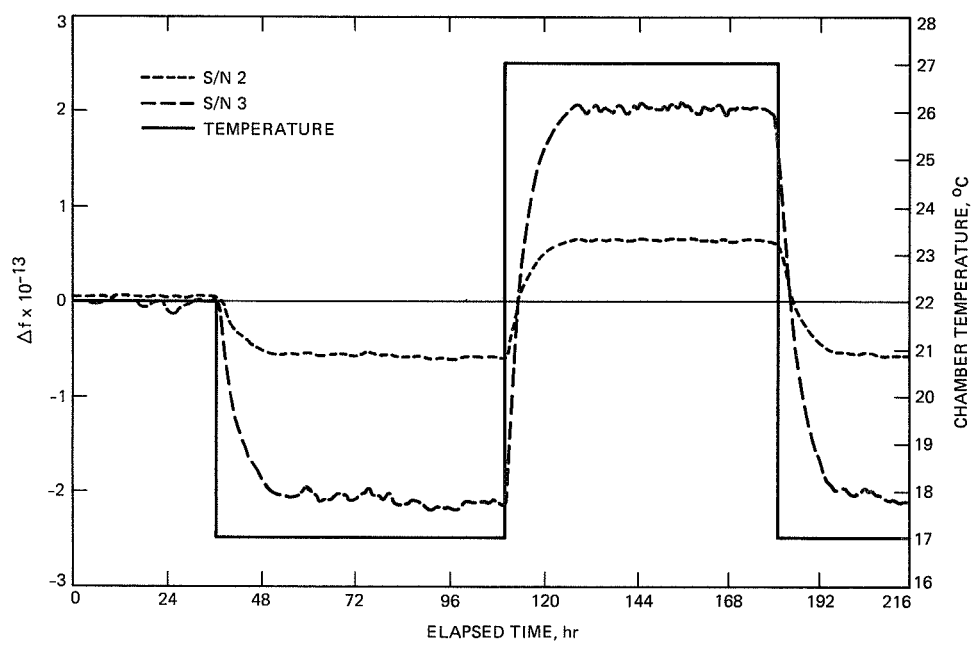


Fig. 9. Output frequency versus temperature.

Appendix

Outline of a Test Plan for Sigma Tau Hydrogen Masers

A. Introduction

1. **General Description.** This test plan outlines the tests and test sequences required to characterize a pair of hydrogen masers and is intended to outline the minimum test requirements, but not necessarily limit the scope of testing.

2. **Objective.** This document establishes the procedures for testing a pair of hydrogen masers manufactured by the Sigma Tau Corporation for the National Radio Astronomy Observatory (NRAO), for use on the Very Large Array (VLA) Project. The maser performance will be tested under laboratory conditions with the environmental and operational parameters varied as specified herein to determine sensitivity to external influences.

3. **Effectivity.** This procedure is effective for the JPL Frequency Standards Laboratory (FSL).

B. Applicable Documents

The following documents, of the issue in effect on the date of release of this document, form a part of this document to the extent specified herein:

Specifications

National Radio Astronomy Observatory

A53308001 Hydrogen Maser Frequency Standard,
Electrical Requirements

Sigma Tau Corporation

Model VLBA-112 Atomic Hydrogen Maser Frequency
Standard, Operation and Instruction
Manual

C. Test Equipment and Facilities

1. **Test Equipment.** Required test equipment is available in the Frequency Standards Test Laboratory (FSTL) and shall be selected by FSTL personnel as required to perform the tests delineated herein.

2. **Facilities.** All tests described herein are to be performed in the FSTL.

D. Test Procedures

1. **Introduction.** Tests in this section are to be performed generally as described. Additional tests may be performed as determined by FSTL personnel.

2. **Test Data.** All test data along with other pertinent information shall be recorded in the appropriate FSTL log book and the "Maser Operating Point and Test Conditions" form as a permanent record of the test results and conditions for each test series. If there is any question, record it in the log!

3. **Initial Tests.** Verify proper operation of each maser under room ambient conditions. Measure and record all operating points and test conditions as baseline data for subsequent tests. As a minimum, the initial tests to be performed are as follows:

- (1) RF output level at each output
- (2) Harmonic distortion at each output
- (3) Phase noise at each output
- (4) Allan variance (24-hour)
- (5) Output frequency versus reference
- (6) Verify proper operation of all operator controls
- (7) Zeeman frequency
- (8) Spin exchange frequency shift
- (9) Offset between autotuner and spin exchange tuning

4. **Power Supply Versus Output Frequency.** Measure the output frequency change versus input supply voltages as follows:

- (1) With PS2 and the external DC supply disconnected, measure the output frequency change as the input AC voltage on PS1 is varied through the range of 105 to 120 VAC.
- (2) With PS1 and the external DC supply disconnected, measure the output frequency change as the input AC voltage on PS2 is varied through the range of 105 to 120 VAC.
- (3) With PS1 and PS2 both disconnected, measure the output frequency change as the external DC supply voltage is varied through the range of 22 to 30 VDC.
- (4) Verify that both AC supplies are reconnected.

5. **Temperature Coefficient of Frequency.** Measure the output frequency change versus temperature over the range of +17 to +27 deg Celsius as follows:

- (1) With the maser stabilized at +22 deg, increase the chamber temperature to +27 deg and allow the maser

to stabilize until the output frequency is stable (48 hours minimum).

- (2) Reduce the chamber temperature to +17 deg and again permit the maser to stabilize.
- (3) Return the chamber temperature to +22 deg and permit the maser to stabilize.

6. Barometric Pressure Coefficient. Measure the output frequency versus barometric pressure over the range of ambient ± 6 kPa (± 24 inches of water) as follows:

- (1) With the chamber temperature stabilized at +22 deg Celsius, increase the chamber pressure to 6 kPa above ambient pressure. Permit the maser to stabilize at this pressure (two hours minimum).
- (2) Reduce the chamber pressure to ambient minus 6 kPa and again permit the maser to stabilize at this pressure or soak for two hours minimum.
- (3) Restore the chamber pressure to ambient barometric pressure.
- (4) Repeat the above cycle.

7. Humidity Test. Measure the output frequency versus ambient humidity over the range of 20 to 80 percent relative humidity as follows:

- (1) With the chamber stabilized at +22 deg Celsius, elevate the chamber humidity to 80 percent and permit the maser to stabilize at this setting (two days minimum).
- (2) Reduce the chamber humidity to 20 percent and again permit the maser to stabilize at this humidity or soak for two days minimum.

- (3) Open the chamber to ambient humidity conditions, and permit the maser to stabilize for a minimum of two days prior to conducting further tests.

8. Magnetic Field Coefficient. With the maser at standard ambient operating conditions of temperature and humidity, install the Helmholtz coil over the maser in a horizontal plane, centered about the cavity. This position yields a vertical magnetic field about the maser cavity shields. Vary the applied magnetic field as follows:

- (1) Increment the applied magnetic field ± 100 mGauss, and measure the Zeeman frequency, IF level, and frequency shift at each step.
- (2) Repeat step (1) using ± 250 mGauss increments.
- (3) Repeat step (1) using ± 500 mGauss increments.

9. Reverification Tests. Repeat all of the tests previously listed in Section D.3 above to verify that the maser is operating within normal operating parameters prior to performance of the final Allan variance, drift, and synthesizer calibrations.

10. Allan Variance. Perform an Allan variance test for a minimum of 4 days (longer if possible) to obtain data out to 1×10^5 seconds.

11. Synthesizer Calibration. Adjust the maser synthesizer frequency so that the maser output frequency is equal to the FSTL reference masers.

E. Concluding Procedures

After completion of the above tests, verify that all test equipment has been disconnected, and that all controls, covers, and connector dust caps are locked in place in preparation for shipment.

State-of-the-Art Fiber Optics for Short Distance Frequency Reference Distribution

G. Lutes and L. Primas
Communications Systems Research Section

A number of recently developed fiber-optic components that hold the promise of unprecedented stability for passively stabilized frequency distribution links are characterized. These components include a fiber-optic transmitter, an optical isolator, and a new type of fiber-optic cable. A novel laser transmitter exhibits extremely low sensitivity to intensity and polarization changes of reflected light due to cable flexure. This virtually eliminates one of the shortcomings in previous laser transmitters. A high-isolation, low-loss optical isolator has been developed which also virtually eliminates laser sensitivity to changes in intensity and polarization of reflected light. A newly developed fiber has been tested. This fiber has a thermal coefficient of delay of less than 0.5 parts per million per °C, nearly 20 times lower than the best coaxial hardline cable and 10 times lower than any previous fiber-optic cable. These components are highly suitable for distribution systems with short extent, such as within a Deep Space Communications Complex. In this article these new components are described and the test results presented.

I. Introduction

The transmitter exciter, local oscillator, and receiver delay calibration system in a Deep Space Station (DSS) require stable frequency references. Hydrogen maser frequency standards generate these frequency references, which then must be distributed to the systems that use them. The distribution system must not add appreciable phase noise or frequency instability to the signal being distributed.

All distribution systems degrade the phase and frequency stability of transmitted frequency reference signals [1]. A reduction in the signal-to-noise ratio (SNR) of a transmitted signal and delay changes in the transmission path are the pri-

mary causes of degradation. These effects are caused by distribution system noise, which reduces the SNR, and variations in the environmental temperature, which cause delay changes. The degree of delay change is dependent on the Thermal Coefficient of Delay (TCD) of the distribution system components.

Fiber-optic systems have several major advantages over conventional distribution systems, which usually employ coaxial cables. Since fiber-optic systems use all dielectric cable, they are not subject to ground loops and are generally immune to pick-up of electromagnetic interference (EMI) and radio frequency interference (RFI). The very low loss at high frequencies in a fiber-optic system helps preserve the SNR of a transmitted signal. Also, new fiber-optic cables with very low TCD,

recently developed and available commercially, can greatly reduce temperature induced delay changes.

A major disadvantage of fiber-optic systems in frequency distribution applications has been the laser's sensitivity to reflections from the cable. Light reflected back into the laser from the cable affects the phase of the optical carrier's modulation as measured across the laser. Cable flexure and vibration cause changes in the polarization and amplitude of this reflected light. These changes in the reflected light result in phase changes across the laser and therefore across the fiber-optic link [2]. Recent developments, which will be described in this article, have virtually eliminated this problem.

Because of the potential improvements in performance, the Time and Frequency Systems Research Group is developing stable, short distance fiber-optic links to distribute local frequency references within the Deep Space Stations (DSSs) of the Deep Space Network (DSN). These links will distribute the frequency reference signals from the frequency and timing interface in each station to the users within the station.

The requirements for the short links are quite different from the requirements for the long links used for frequency reference distribution between stations at the Goldstone Deep Space Communications Complex (DSCC). Because of cost-performance tradeoffs between short fiber-optic links and coaxial cable links, the short fiber-optic links must be relatively inexpensive, simple, and reliable.

The long distance fiber-optic links are more expensive and more complex, requiring optical and electronic feedback to stabilize the delay of a transmitted signal. The long links enable the use of a centralized frequency and timing facility, thus reducing the number of expensive frequency standards needed in a DSCC. Therefore, a higher cost for these links can be justified.

The performance of a short fiber-optic link is expected to be considerably better than the performance of an equivalent coaxial cable link. The fiber-optic link will eliminate ground loops and provide considerable improvement in the thermal stability of the cable. The optical fiber's superior thermal stability will reduce the need to add mass and insulation to the cable to increase its time constant. It will also reduce the temperature stability requirement for the air conditioning systems in certain areas of the stations.

The cables used in short fiber-optic links within a station may be exposed to temperature variations that can exceed 6°C in 20 minutes and 30°C in 12 hours over some portion of their length. They cannot be buried like long links at Goldstone to benefit from temperature isolation provided by

burial. These links may also be subjected to vibration from equipment such as air conditioners. For some applications the cables will be routed through the antenna wrap-up where they will be flexed when the antenna is moved. This relatively dynamic environment requires that the links be insensitive to cable vibration and flexure and that cables with low TCD be utilized.

In the remainder of this article, new technology that can be used to meet the special requirements of the short distance fiber-optic frequency reference distribution links will be discussed. Test results from an experiment that demonstrates an optically isolated laser's insensitivity to cable flexure and vibration will also be presented. Finally, a state-of-the-art fiber-optic frequency distribution link for short distance applications will be described.

II. Reducing Instabilities Caused by Reflections

Cable flexure can cause group delay changes as large as 200 psec across a fiber-optic link if no means is used to desensitize the laser diode to reflections. Optical isolation of the semiconductor laser diode can reduce such changes to less than 0.03 psec. The optical isolation can be obtained by the use of bulk optical isolators using the Faraday principle.

Optical isolators of this type consist of a polarizer to fix the polarization of the laser light, followed by a Faraday rotator which rotates the polarization vector by 45 degrees. The light at the output of the rotator enters an output polarizer with its axis rotated 45 degrees with respect to the polarization axis of the first polarizer. Therefore, the light passes through the output polarizer unimpeded. Because the Faraday principle is nonreciprocal in the forward and reverse directions, light reflected back into the isolator assembly experiences a rotation angle which is crossed with the axis of the input polarizer. The reflected light is therefore blocked, providing the reverse isolation.

The degree of isolation achieved by this type of isolator strongly depends on the amount of light scattered within the isolator. Once polarized reflected light scatters within the isolator, the polarization is lost, and components that do not have their axis crossed with the exit polarizer pass through and degrade the isolation.

Optical isolators of this type are manufactured by several companies. The isolation afforded is typically 35 to 40 dB and the forward loss is typically less than 2 dB. Although this level of isolation is very good, it is not adequate for precise fiber-optic frequency distribution. In order to improve laser isolation, one company in Japan has developed a laser diode with

an integral dual (two isolators in series) optical isolator.¹ This approach provides high isolation at the expense of an additional isolator and additional forward loss.

An optical isolator system developed at JPL to be used in frequency distribution links provides up to 70 dB isolation and 1.3 dB forward loss [3]. The JPL isolator system was assembled from a commercial bulk isolator, as described above, and expanded beam single-mode fiber connectors (Fig. 1). The first expanded beam connector expands and collimates the optical beam emitted by the fiber. The highly collimated beam passes through the isolator elements and is collected by the second connector. The total loss is only 1.3 dB in the forward direction.

The improvement in isolation of the JPL system is due to the narrow acceptance angle of the expanded beam connectors. The collimated reflected light with the appropriate polarization is rejected by the exit polarizer. The narrow acceptance angle of the input connector rejects the scattered reflected light exiting the isolator because it is not parallel to the axis of the isolator.

III. Low Thermal Coefficient of Delay Optical Fiber

Sumitomo Electric Industries, Ltd. of Japan has developed a low Thermal Coefficient of Delay (TCD) single-mode optical fiber [4]. This is an elegant means for reducing frequency instabilities in a reference frequency distribution system. It affords considerable improvement in transmission stability without adding to the complexity or reducing the reliability of the transmission system.

The TCD of this fiber has been measured at JPL and found to be less than 0.5 parts per million per °C (ppm/°C) from 0°C to 30°C. At around 0°C the TCD is zero. It rises slowly as the temperature rises and is 0.5 ppm at about 30°C. The curve in Fig. 2 shows the TCD for this fiber in ppm/°C versus temperature. Figure 3 compares the TCD of this fiber with the TCD of standard single-mode fiber and 7/8-inch diameter coaxial hardline (64-875 RG254/U). This coaxial hardline has the lowest average TCD for any coaxial cable measured by the Time and Frequency Systems Research Group at JPL. It can be seen that the TCD of the fiber at 25°C is 20 times lower than that of the coaxial cable. Use of the low TCD optical fiber would result in an Allan deviation 20 times lower than a system using the RSG254/U coaxial cable.

The TCD of a standard optical fiber results from two effects: the temperature dependence of the index of refraction of the fiber material, and the thermal coefficient of expansion of the fiber. An increase in temperature causes the index of refraction to decrease, which in turn decreases the group delay through the fiber. An increase in temperature also causes expansion of the fiber, which results in an increase in the group delay through the fiber. These two effects partially cancel resulting in a TCD for standard single-mode fiber of about +7 ppm/°C [5].

Sumitomo achieves a low TCD fiber by coating a standard fiber with an inner layer of elastic material and an outer layer of liquid crystal material having a negative thermal coefficient of expansion. This liquid crystal material compresses the fiber longitudinally with rising temperature. The compression of the fiber increases the index of refraction of the fiber material, which increases the group delay through the fiber. Compression of the fiber also decreases the change in length of the fiber, which decreases the group delay through the fiber. The result of these two effects is to impart a negative TCD to the fiber.

The thermal coefficient of expansion of the liquid crystal material is too high and would result in a net negative TCD for the fiber if it were applied directly to it. The layer of elastic material between the fiber and the liquid crystal coating couples the right amount of force from the liquid crystal material to the fiber to result in a near zero TCD for the fiber.

IV. Test Results

A single-mode fiber system using an isolated laser was tested in situ to demonstrate the capability to transmit precise reference frequencies through an antenna wrap-up. For this test a single-mode six-fiber cable was installed, as shown in Fig. 4, from the control room through the wrap-up of an antenna at the Goldstone DSCC. The cable, which is 850 meters long, is flexed when the antenna is moved.

A 100-MHz reference signal was transmitted through one fiber in the cable to the antenna and returned through another fiber back to the control room. At the control room the phase of the return signal was compared to the phase of the transmitted signal. Without the optical isolator between the cable and the laser transmitter, phase jumps were observed in the return signal when the antenna was moved. Figure 5(a) shows these phase jumps. However, when the optical isolator was used no phase jumps were observed as shown in Fig. 5(b).

The resultant Allan deviation for these measurements is shown in Fig. 6. The phase jumps observed when the optical isolator is not used cause the Allan deviation to be higher. The

¹Matsushita Electric Corporation of America, Secaucus, New Jersey, Model IMS09111-33.

C - 2

optical isolator eliminates the phase jumps and therefore reduces the Allan deviation.

V. A Stable Distribution Link

Figure 7 is a block diagram of a stable fiber-optic distribution link which uses the developments described in this article. The reference signal to be transmitted is applied to the modulation input of the laser transmitter. The laser transmitter is either desensitized to reflections by dithering the bias or is followed by an optical isolator. A low TCD optical fiber carries the transmitted signal from the laser transmitter to the optical detector. The optical detector is followed by a high gain wideband amplifier with low TCD. A phase locked filter at the output of the link reduces the noise bandwidth of the receiver, which reduces the short term noise of the signal. The bandwidth of this PLL is adjusted for best overall frequency

stability, which depends on the quality of the oscillator in the PLL and the quality of the signal being transmitted.

VI. Conclusion

Stable short distance fiber-optic links for frequency reference distribution have been demonstrated. They have been found to be as good as coaxial systems for short term noise and much better than coaxial systems for long term stability. This improved long term stability results in a lower Allan deviation than can be achieved with coaxial cable under identical environmental conditions. In some critical applications, active electronic feedback is used to reduce thermally generated delay change. The use of low TCD optical fiber may in some cases eliminate the need for active electronic reduction of delay variations. This could result in less complex distribution systems for some applications.

Acknowledgments

The authors thank P. Tu, N. Mroczka, and W. Diener for making measurements presented in this paper. The authors also thank S. Kato, S. Tanaka, T. Kakuta, and M. Shindo of Sumitomo Electric USA, Inc. and Sumitomo Electric Industries, Ltd. for providing low TCD fiber for testing as well as information and data. Finally, the authors thank L. Maleki, J. Dick, R. Sydnor, and R. Logan for their help and support throughout the course of this work.

References

- [1] G. Lutes, "Reference Frequency Distribution Over Optical Fibers: A Progress Report," *Proceedings of the 41st Annual Symposium on Frequency Control*, IEEE Catalog No. 87CH2427-3, Philadelphia, Pennsylvania, pp. 161-166, May 1987.
- [2] K. Y. Lau, "Microwave Phase Stability of Directly Modulated Semiconductor Injection Lasers," *Applied Physics Letters*, vol. 52, no. 17, pp. 1377-1378, April 1988.
- [3] G. Lutes, "Optical Isolator System for Fiber-optic Uses," *Applied Optics*, vol. 27, no. 7, pp. 1326-1328, April 1988.
- [4] T. Kakuta and S. Tanaka, *LCP Coated Optical Fiber with Zero Thermal Coefficient of Transmission Delay Time*, Sumitomo Electric Industries, Ltd., 1, Taya-cho, Sakae-ku, Yokohama, 244, Japan.
- [5] A. Bergman, S. T. Eng, A. R. Johnston, and G. F. Lutes, "Temperature Dependence of Phase for a Single-mode Fiber Cable," *Proc. Third International Conference on Integrated Optics and Optical Fiber Communications*, OSA-IEEE, San Francisco, California, p. 60, April 27-29, 1981.

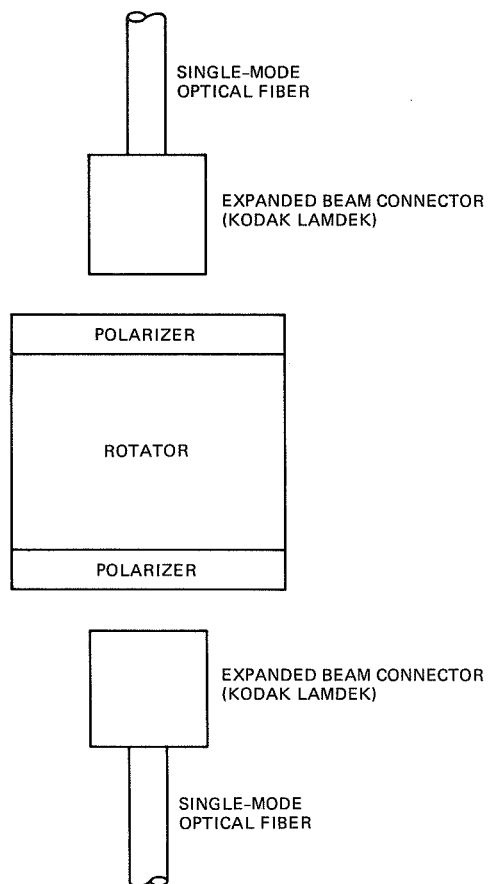


Fig. 1. A block diagram of the optical isolator assembly used to isolate the semiconductor laser from external reflections.

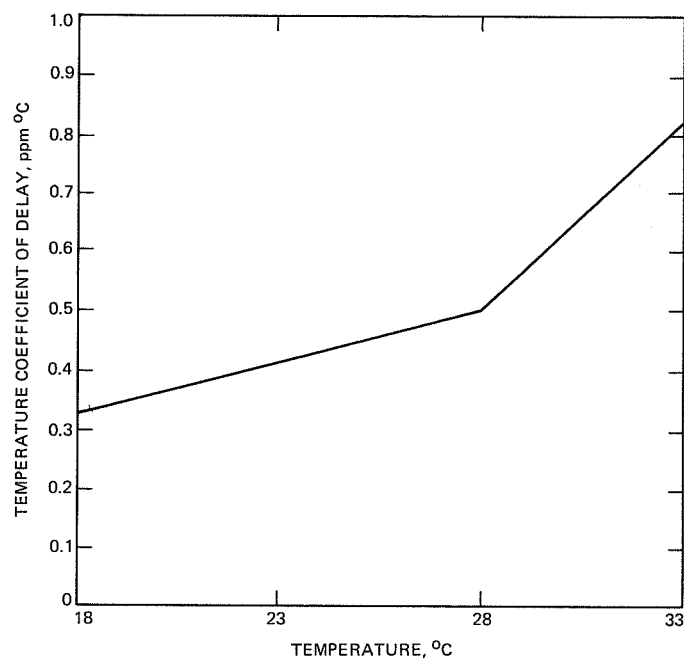


Fig. 2. The rate of change of group delay with respect to temperature for the Sumitomo low-TCD fiber.

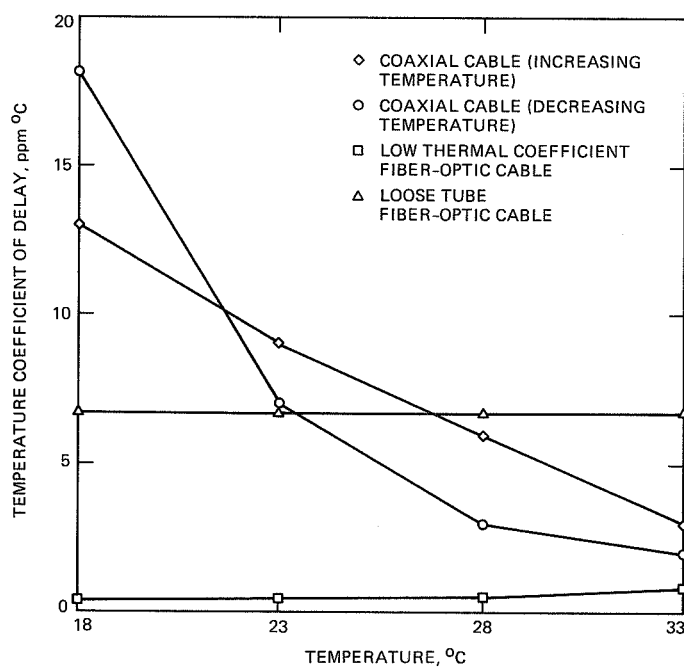


Fig. 3. A comparison of TCDs for the Sumitomo fiber, standard single-mode fiber, and 64-875 RG254/U, 7/8-inch diameter coaxial cable.

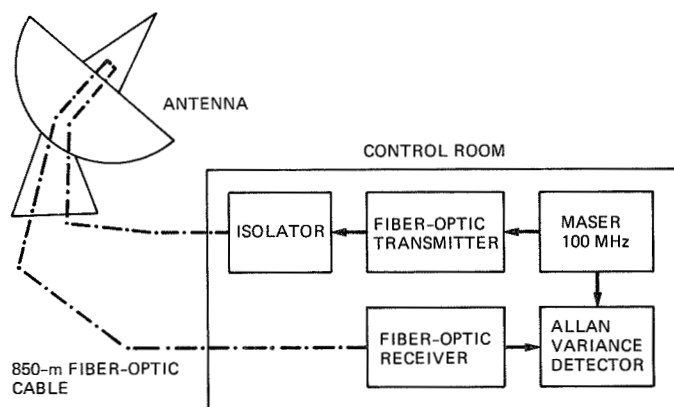


Fig. 4. A block diagram of the in-situ phase stability test.

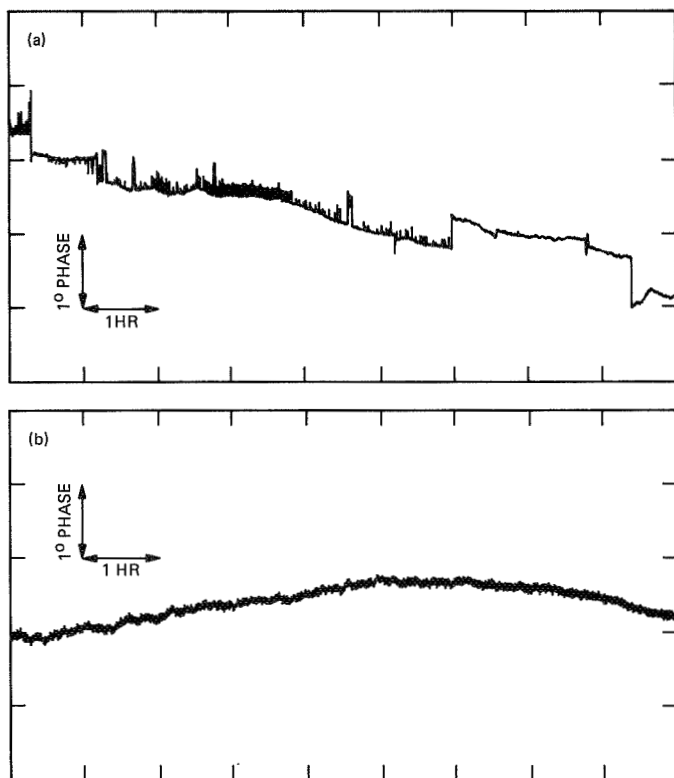


Fig. 5. Phase measured across a fiber-optic link which was installed through an antenna wrap-up such that the cable was flexed when the antenna moved: (a) without an optical isolator after the laser transmitter, (b) with an optical isolator after the laser transmitter.

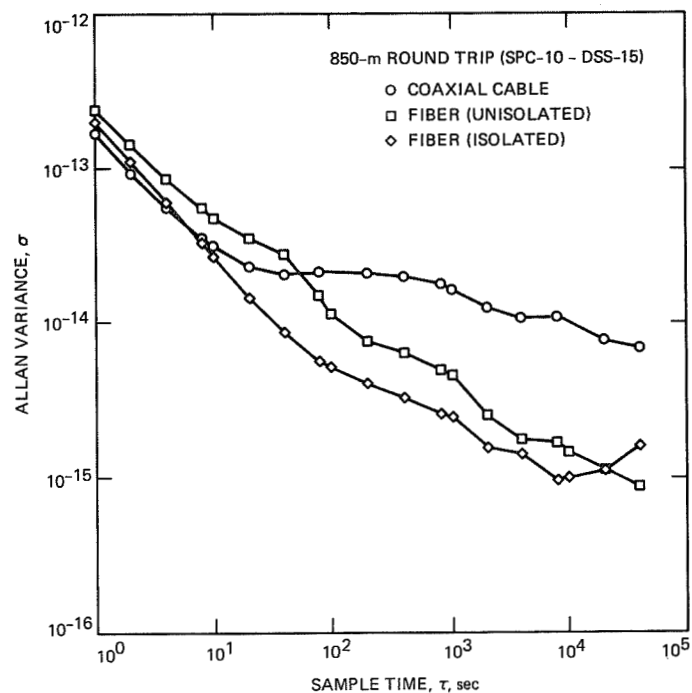


Fig. 6. The Allan variance of the phase noise shown in Fig. 3 (with and without an optical isolator) and for a coaxial cable installed in a similar route.

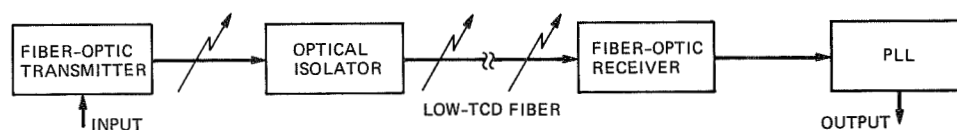


Fig. 7. A block diagram of a stable fiber-optic frequency reference distribution link.

52.11
218063

N 8 9 - 2 7 8 7 9

Stabilized Fiber-Optic Frequency Distribution System

L. E. Primas, G. F. Lutes, and R. L. Sydnor
Communications Systems Research Section

A technique for stabilizing reference frequencies transmitted over fiber-optic cable in a frequency distribution system is discussed. The distribution system utilizes fiber-optic cable as the transmission medium to distribute precise reference signals from a frequency standard to remote users. The stability goal of the distribution system is to transmit a 100-MHz signal over a 22-km fiber-optic cable and maintain a stability of 1 part in 10^{17} for 1000-second averaging times. Active stabilization of the link is required to reduce phase variations produced by environmental effects, and is achieved by transmitting the reference signal from the frequency standard to the remote unit and then reflecting back to the reference unit over the same optical fiber. By comparing the phase of the transmitted and reflected signals at the reference unit, phase variations of the remote signal can be measured. An error voltage derived from the phase difference between the two signals is used to add correction phase.

I. Introduction

With the current advances in the development of precise frequency standards, greater emphasis is being placed on frequency distribution systems that can distribute the reference signal derived from a standard without appreciably degrading it. Often the reference signal must be distributed tens of kilometers. The high cost of developing and maintaining a state-of-the-art frequency standard makes it beneficial to have one precise standard at a complex and to distribute the reference signal from this standard to various users within the complex. Furthermore, future scientific experiments may also gain from having coherent signals at several remote locations.

The Deep Space Network, supported by NASA/JPL [1], is a prime contender for such a distribution system. Projects supported by the DSN that require this type of distribution system include unmanned space flight projects, flight radio

science, radio and radar astronomy, very-long-baseline interferometry, geodynamic measurements, and the search for gravitational waves.

The frequency distribution system at Goldstone, California must distribute reference frequencies generated by a hydrogen maser over distances as great as 30 km. The 100-MHz signal generated by the maser typically has an Allan deviation of 1 part in 10^{15} for 1000-second averaging times. To ensure minimal degradation of the reference signal, the distribution system should be at least 10 times more stable than the frequency standard. With expected future improvements in frequency standards, even greater stability of the distribution system will be necessary.

There are two basic limitations in frequency distribution systems. The first is a distance limitation set by the signal-

to-noise-ratio (SNR) of the received signal. The SNR is limited by the amount of available input power from the frequency source and the loss in the distribution system. The second limitation is the degradation of the frequency stability due to variations in the group delay of the signal as it is transmitted through the medium. Variations in group delay are caused by physical changes in the transmission medium. A constant rate of change in group delay does not affect the frequency stability, but a change in the rate of group delay does degrade the frequency stability. This is shown in the following equation

$$\frac{d(\Delta f)}{dt} = f \frac{d^2 D}{dt^2}$$

where D is the group delay, Δf is the frequency offset, and f is the transmitted frequency. Variations in group delay are due primarily to temperature changes in the transmission medium. Thus they can be reduced by decreasing the temperature change, increasing the time constant of the medium, choosing a medium with a small thermal coefficient of delay (TCD), or using optical and electronic feedback.

II. Previous versus Current Frequency Distribution Systems

As previously stated, frequency distribution systems have been primarily limited by the distance allowable for distribution and the effects of changing group delay. Coaxial distribution systems are especially subject to these limitations. The loss in 2.22-cm (7/8-inch) diameter coaxial cable at 100 MHz is 6.4 dB/km (0.5 dB/100 ft) and the TCD is greater than 15 ppm/°C at 25 °C. The transmission length required to transmit a certain input power through a transmission medium and maintain a certain SNR is given by

$$L = \frac{P_{in} - \text{SNR} + 204}{32.81\alpha}$$

where

L = length of kilometers

P_{in} = input power in dBW

SNR = signal-to-noise ratio in dB

α = cable attenuation in dB/100 ft

Thus, with 1 kilowatt of input signal power, a 100-MHz reference signal can only be distributed 7 km and maintain a SNR of 120 dB, the level required by the fiber-optic link. This assumes a thermal noise power in a matched load resistance at 300 K of -204 dBW/Hz.

Microwave distribution systems have also been used in the Goldstone complex. Microwave distribution systems have shortcomings in that they are highly susceptible to interference and require large input powers and repeaters to go several kilometers. Because of the limited bandwidth of microwave systems, the 100-MHz signal cannot be transmitted directly over microwave links.

Fiber-optic cable is the best distribution medium for transmitting precise reference frequencies. The loss in typical fiber-optic cable is less than 0.5 dB/km at optical wavelength 1300 nm. A typical laser transmitter puts out 0 dBm and is attenuated less than 11 dB over 22 km. Standard single-mode fiber-optic cable has a TCD of 7 ppm/°C [2] making it less susceptible to temperature changes than coaxial cable. The fiber-optic cable used at the Goldstone complex is buried 1.5 m underground, making the fiber quite insensitive to diurnal temperature changes. Fiber-optic cable has additional advantages in that the fiber is insensitive to electromagnetic interference (EMI) and radio frequency interference (RFI) and can be made less sensitive to microphonics using an optical isolator between the laser transmitter and the fiber-optic cable [3]. Another advantage of using fiber-optic cable as the transmission medium is that the superior performance of the optical components make it quite practical to transmit the signal simultaneously in both directions in the same fiber. This proves to be a key factor in actively stabilizing the distribution system.

III. Active Stabilization of a Fiber-Optic Frequency Distribution System

Passive stabilization of fiber-optic transmission links, such as burial of the cable, limits achievable stabilities to one part in 10^{15} [4].

The frequency distribution system consists of a reference unit containing the frequency standard, and a remote unit, where the reference frequency is to be transmitted. The method for actively controlling the phase variations in the fiber is based on maintaining a constant phase relation between the input phase and the phase of the received signal.

A signal passing through the fiber-optic cable in both directions experiences identical delay in each of the two directions. The midpoint of the signal is at the far end of the cable and experiences exactly half of the round-trip delay. If the phases of the transmitted and received signals at the reference end of the cable are conjugate, the phase at the remote end is independent of phase delays in the medium (Fig. 1). An electronic device that detects the phases of the transmitted and received signals at the input to the fiber and adds enough phase to

maintain conjugation is called a phase conjugator (Fig. 2). The phase conjugator is the key element of the actively controlled fiber-optic distribution system.

The reference unit consists of the frequency standard, the phase conjugator, a fiber-optic transmitter, a fiber-optic receiver, an optical coupler, and a phase-lock loop (PLL) (Fig. 3). The remote unit consists of a 50/50 mirror, a fiber-optic receiver, and a PLL.

The phase conjugator compares the phase of the transmitted and received signals in the reference unit and an error voltage derived from the phased difference is used to control a voltage-controlled oscillator (VCO) (Fig. 4). The design of this phase conjugator requires a 100-MHz reference signal and a 20-MHz auxiliary signal. A previous design used a single 100-MHz reference signal, but required two precisely matched phase detectors and tightly controlled signal levels. By using the 20-MHz auxiliary signal, a single phase detector can be used to measure phase error.

The 100-MHz signal and the 20-MHz signals are multiplied together in mixer M1 to produce 80-MHz and 120-MHz signals [5]. A power splitter S1 separates the signal out of mixer M1 into two signal paths. Band-pass filters (BPFs) in each signal path separate the 80-MHz and 120-MHz signals. The 80-MHz signal and the 100-MHz signal from the VCO are multiplied in mixer M2 to produce a 20-MHz intermediate frequency (IF) signal. The 20-MHz IF signal contains the instantaneous phase difference between the VCO signal and the 80-MHz signal.

The 120-MHz signal and the 100-MHz signal reflected from the remote unit are multiplied together in mixer M3 to produce another IF signal. This 20-MHz IF signal contains the instantaneous phase difference between the reflected signal (100 MHz) and the 120-MHz signal.

The phase detector (PD) receives the two 20-MHz IF signals and produces an error voltage that is proportional to the phase difference between them. The error voltage is applied to the VCO control input through the inner loop filter (ILF). Delay changes in the fiber-optic cable result in changes in the control voltage; this voltage controls the phase of the VCO relative to the 100-MHz reference signal.

The output of the VCO is divided into two signals in the RF power splitter S2. One of the signals is received by mixer M2 and the other modulates the optical carrier emitted from the laser transmitter.

The modulated optical signal is transmitted to the remote unit through the optical coupler. The 50/50 mirror at the

remote unit reflects half of the optical signal back toward the reference unit while the other half passes through the mirror to the optical receiver. The receiver demodulates the optical signal and amplifies the resulting 100-MHz RF signal. A PLL filters the signal to be used at the remote unit [6]. The reflected optical signal returns to the reference unit where it passes through the optical coupler and is detected by another optical receiver. This signal is also filtered by another PLL and provides a constant amplitude signal into mixer M3. With the signal back at the reference unit, the system loop is closed.

IV. Stabilizer Test Setup

The latest [7] version of the stabilizer has each element packaged in an aluminum RFI-shielded box with 60 dB of power supply filtering. A new laser is used that is less sensitive to reflections back into the laser. The 80-MHz and 120-MHz band-pass filters were also improved.

The stabilizer does require initialization using a manual phase shifter (Fig. 4). The phase shifter is used to compensate for the delays in the fiber-optic transmitter and fiber-optic receiver, to ensure that the phases of the transmitted and received signals are conjugate at the input to the fiber.

The stabilizer was tested with a 4-km link of fiber which was placed on a fiber-optic test rack (Fig. 5). The test rack allows better air circulation and thus a shorter time constant for the tests. The entire rack was placed in a test chamber where the humidity, temperature, and pressure could be varied. The temperature in the chamber was varied in temperature steps of various sizes and over various time intervals. The phase at the reference unit (near-end) receiver and transmitter and the phase at the remote unit (far-end) receiver were compared to the 100-MHz reference signal (Fig. 6).

V. Results

Several tests were performed with the stabilizer. By measuring the response of the stabilizer to a step change and a linear variation in temperature, the correction factor of the stabilizer was determined. For a step change in temperature from 15 °C to 35 °C, the phase at the reference unit transmitter and receiver changed by 90 degrees and the phase at the remote unit changed by about 2 degrees; thus the stabilizer provided a 45 times improvement (Figs. 7(a)-7(d)). The glitch in the curve is probably due to optical leakage of the 100-MHz reference signal through the coupler directly into the reference unit receiver, causing a cross modulation of the leakage signal and the reflected signal. If the results of this experiment are considered over the first hour, the reference phases changed by 25 degrees while the remote phase changed by 0.5 degree,

for a 50 times improvement (Figs. 8(a)–8(d)). Results from the test with a linear change in temperature show 20 degrees of phase change at the reference unit and 0.1 degree of phase change at the remote unit, resulting in a 200 times improvement (Figs. 9(a)–9(d)). The ripple effect in the remote unit's phase is probably due to reflections from the end of the fiber into the fiber-optic transmitter. With more optical isolation this effect should be reduced.

VI. Future Improvements

The results of initial tests on the stabilizer are encouraging. The factor of 10 times reduction in phase variations with the stabilizer seems to be readily attainable, with potential for even greater improvements. New tests with a sinusoidal variation in temperature over diurnal time periods need to be performed to simulate more realistic time and temperature variations. Current tests have put the stabilizer through conditions too severe to realistically simulate field conditions, but the tests provide a basis from which realistic measurements will result.

The first step in improving the stabilizer is to reduce the losses in the system. Once losses are reduced, the return signal will be much larger than the leakage signal through the coupler. The phase variation caused by the difference between the return signal and the leakage signal is

$$\Phi = \arctan [10^{-R/20}]$$

where Φ is the phase variation in degrees and R is the difference between the return signal and the leakage signal in dB. Specifically, if the return signal is 40 dB greater than the leakage signal, the resulting phase variations will be 0.57 degree. By reducing the losses and making the return signal 60 dB greater than the leakage signal, the resulting phase variation will be 0.057 degree.

After the losses have been reduced, any further problems with leakage may be eliminated by using techniques such as transmitter/receiver switching. Switching the transmitter and receiver eliminates the interference problem of the leakage signal.

VII. Conclusion

A method of active stabilization of frequencies distributed over fiber-optic cable has been demonstrated and proves to be more than adequate for current frequency standards and distribution lengths. Current frequency standards require a 10 times reduction in phase variations, and the described stabilizer provides at least a 40 times reduction over a 4-km link. Theoretical calculations predict phase reduction factors of 500 will be attainable by reducing optical losses and leakage.

Acknowledgments

The authors wish to thank Phuong Tu, Bill Diener, and Al Kirk for their help in making the measurements.

References

- [1] *The Deep Space Network*, JPL 400-333, Jet Propulsion Laboratory, Pasadena, California, January 1988.
- [2] G. Lutes, "Experimental Optical Fiber Communications Link," *TDA Progress Report 42-59*, vol. July-August 1980, Jet Propulsion Laboratory, Pasadena, California, pp. 77-85, October 15, 1980.
- [3] G. Lutes, "Optical Fibers for the Distribution of Frequency and Timing References," *Proceedings of the 12th Annual Precise Time and Time Interval (PTTI) Applications and Planning Meeting*, NASA Conference Publication 2175, Goddard Space Flight Center, Greenbelt, Maryland, pp. 663-680, December 1980.
- [4] G. Lutes, "Reference Frequency Distribution Over Optical Fibers: A Progress Report," *Proceedings of the 41st Annual Frequency Control Symposium*, pp. 161-166, May 27-29, 1987.
- [5] A. P. Sage, *Linear Systems Control*, Chesterland, Ohio: Matrix Publishers, Inc., 1987.
- [6] F. M. Gardner, *Phaselock Techniques*, New York: John Wiley and Sons, Inc., 1966.
- [7] L. Primas, G. Lutes, and R. Sydnor, "Fiber Optic Frequency Transfer Link," *Proceedings of the 42nd Annual Symposium On Frequency Control*, pp. 478-484, June 1-3, 1988.

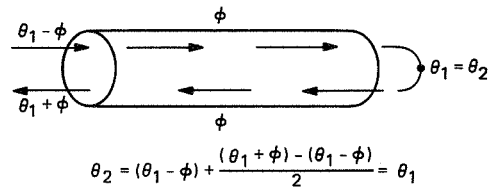


Fig. 1. Phase conjugation at input to optical fiber.

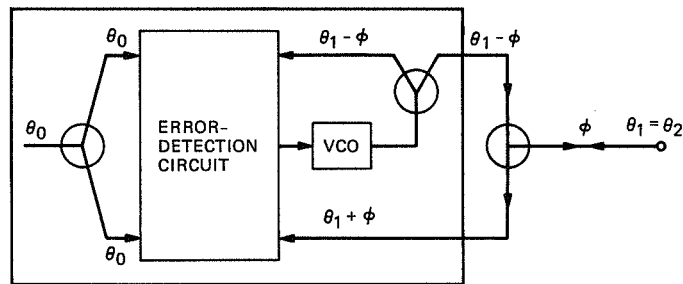


Fig. 2. Phase conjugator.

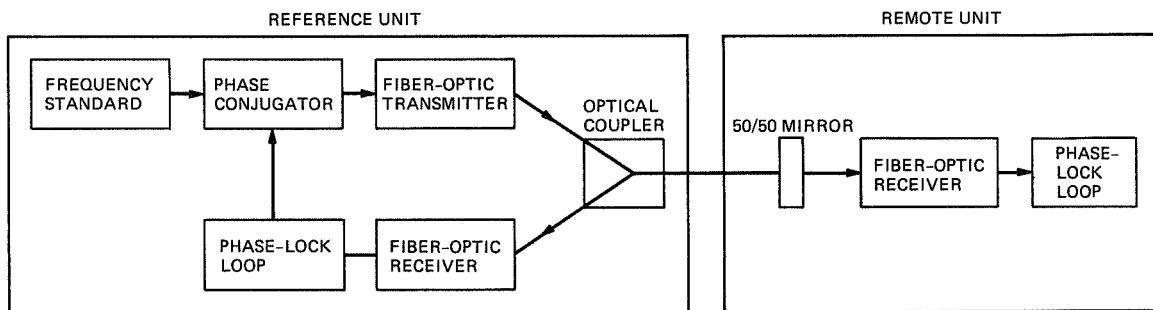


Fig. 3. Fiber-optic frequency distribution system.

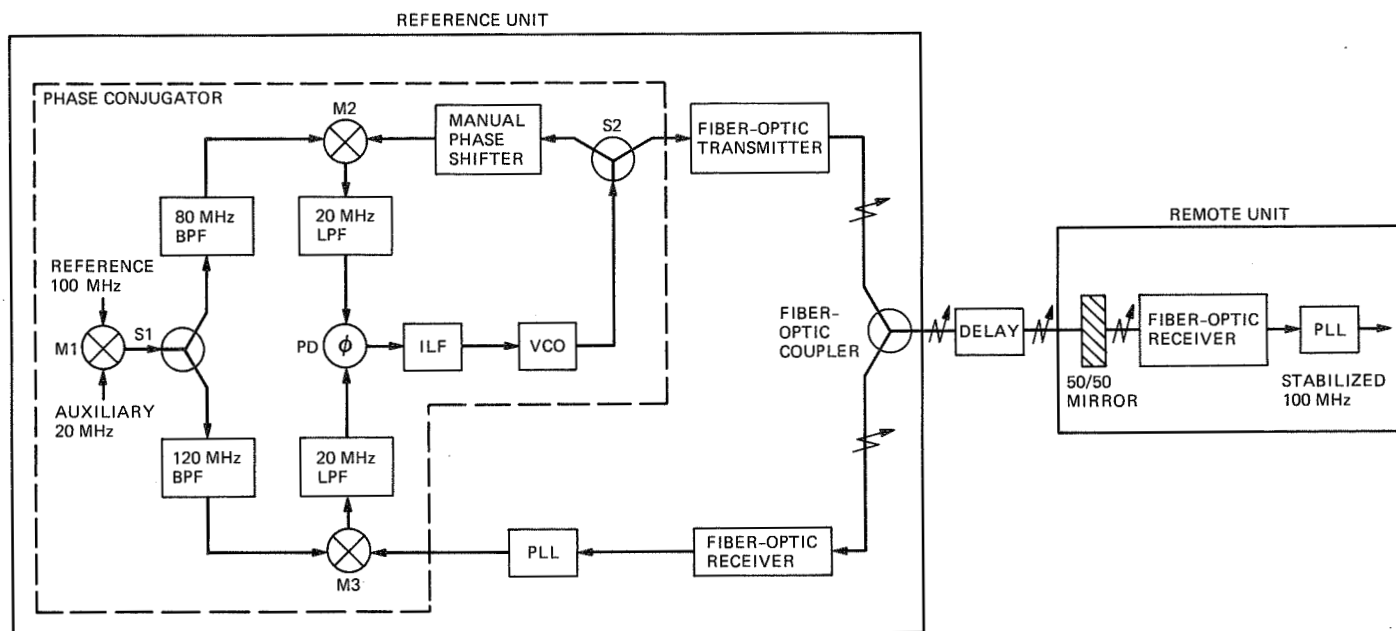


Fig. 4. Block diagram of fiber-optic stabilizer.

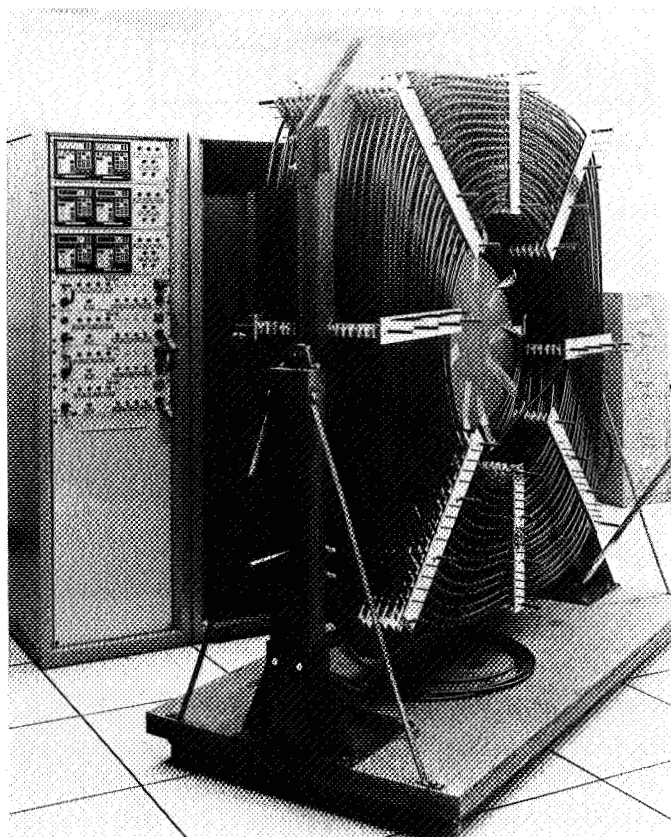


Fig. 5. Test rack for fiber-optic cable.

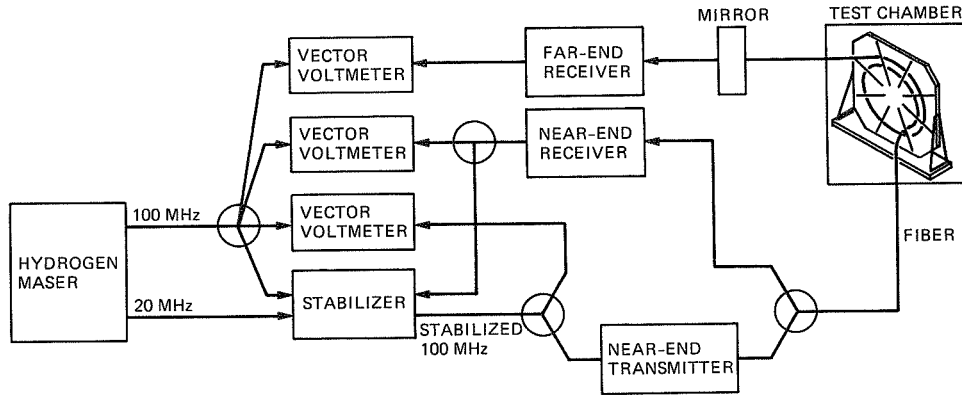


Fig. 6. Fiber-optic stabilizer measurement setup.

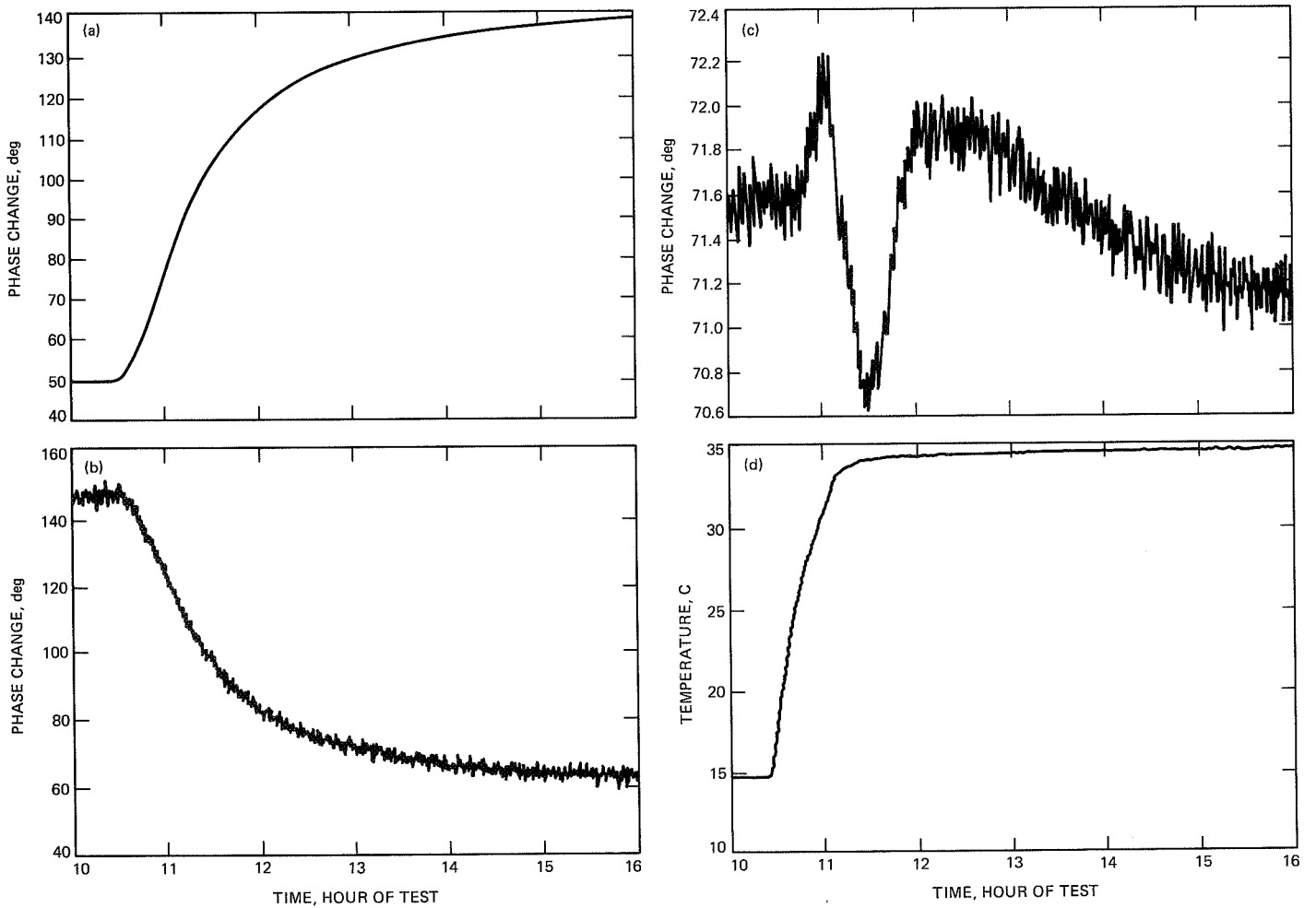


Fig. 7. Fiber-optic test results, phase step change in temperature 15 to 35°C: (a) reference unit (near-end) transmitter; (b) reference unit (near-end) receiver; (c) remote unit (far-end) receiver; (d) test chamber temperature.

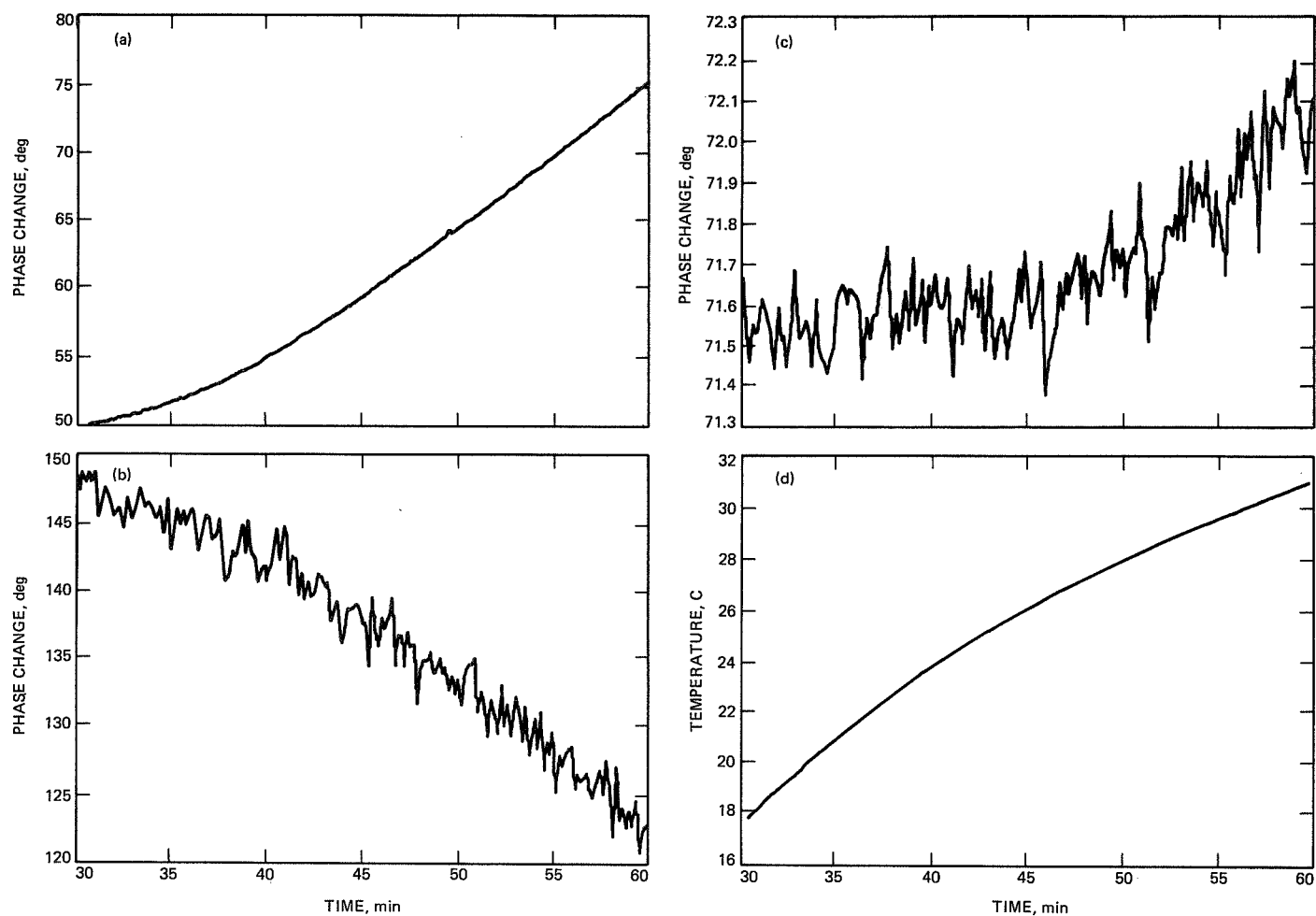


Fig. 8. Fiber-optic test results during the first hour, phase step change in temperature 15 to 35 °C: (a) reference unit (near-end) transmitter; (b) reference unit (near-end) receiver; (c) remote unit (far-end) receiver; (d) test chamber temperature.

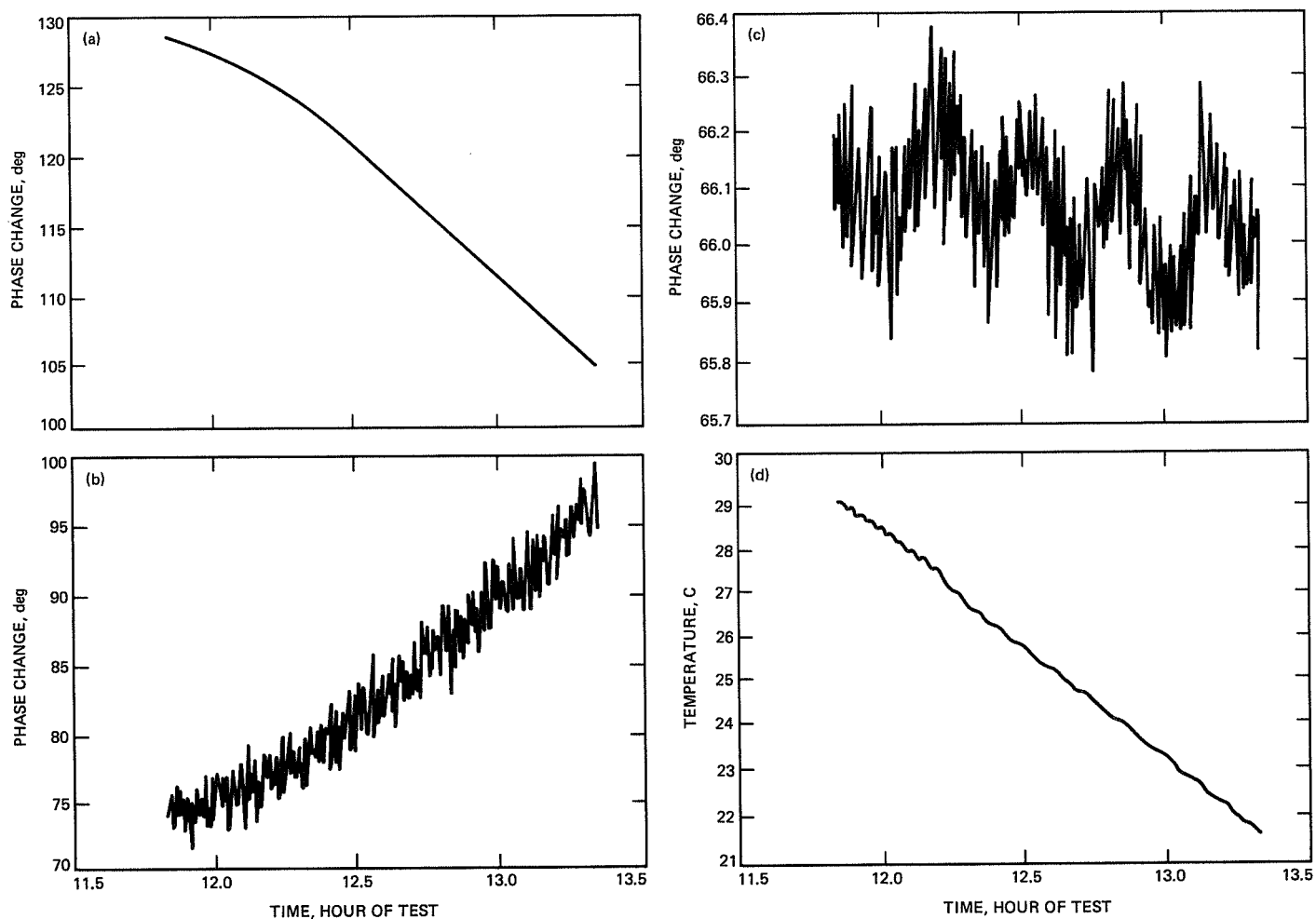


Fig. 9. Fiber-optic test results, linear change in temperature 29 to 22 °C: (a) reference unit (near-end) transmitter; (b) reference unit (near-end) receiver; (c) remote unit (far-end) receiver; (d) test chamber temperature.

A New Method for Analysis of Limit Cycle Behavior of the NASA/JPL 70-Meter Antenna Axis Servos

R. E. Hill

Ground Antennas and Facilities Engineering Section

A piecewise linear method of analyzing the effects of discontinuous nonlinearities on control system performance is described. The limit cycle oscillatory behavior of the system resulting from the nonlinearities is described in terms of a sequence of linear system transient responses. The equations are derived which relate the initial and the terminal conditions of successive transients and the boundary conditions imposed by the nonlinearities. The method leads to a convenient computation algorithm for prediction of limit cycle characteristics resulting from discontinuous nonlinearities such as friction, deadzones, and hysteresis.

I. Introduction

Recent occurrences where degradation of hydromechanical components has led to excessive limit cycle oscillations of the 70-m antenna axis servos have prompted investigations of the cause and possible methods of minimization of those oscillations. Excessive limit cycling is objectionable because it degrades antenna pointing accuracy, and is presumed to accelerate the mechanical wear degradation of actuator gears, bearings, and hydraulic motors. It is therefore important to devise methods to minimize limit cycling by alteration of the controller design, and to a limited extent, by installation of improved servovalves and hydraulic motors. Also, since it is presumed that limit cycling is aggravated by otherwise acceptable wear of mechanical devices, a more robust controller design with respect to limit cycling is desirable insofar as it

would necessitate less frequent component replacements due to wear.

This article describes the initial progress in the analytic assessment of the limit cycles resulting from various nonlinearities in the system. The ultimate product of this effort will be a set of quantitative relationships between limit cycle behavior and the control system parameters. Such relationships will facilitate the selection of control parameters to provide the best overall combination of linear servo and limit cycle performance.

The major nonlinearities in the axis servos result from friction associated with the hydraulic motors and gear reducers comprising the control actuators, as well as deadzone and

hysteresis effects in the associated hydraulic servovalves. Four such actuators are employed in each axis to apply control torque directly to antenna-mounted bull gears [1]. Because the gear reducers are heavily preloaded to prevent backlash, the gear tooth and bearing friction contribute a significant part of the total friction in the system.

Simulation studies of limit cycle behavior are of limited usefulness as a design tool because they provide little insight associating parameter adjustments with performance, and because they require long simulation runs to identify stable limit cycle conditions. The large magnitude of the friction, which is roughly 25 percent of the maximum available control moment, makes the simple simulation models frequently used for friction inadequate for application to the 70-m axis servos [2]. More precise computer simulation models for friction involve considerable complexity and also necessitate smaller integration times, thus increasing computation time and making broadbased parameter studies impractical.

Conventional analytic methods such as the second method of Liapunov [3], which require continuity of the system function and of its partial derivatives, are not directly applicable because friction represents a discontinuity. Describing function analysis can be applied to simple cases such as the hydraulic valve, where the nonlinearity can be represented by a cascade function block. However, the friction associated with the antenna axes introduces a degree of complexity to the computation of the describing functions which make that method unattractive. Because friction effects appear to be the least tractable by conventional methods, the new method was developed for systems involving friction with provisions for incorporation of other nonlinearities at a later stage in the development.

The accuracy of this approach is limited by two factors. First, the form of combination of effects from various nonlinearities is not considered and linear superposition is not expected to apply. Second, an ideal continuous time-state variable controller is assumed and consideration of friction-induced estimator error and correction effects is deferred until later in the study. Despite these limitations the method should still be effective in identifying the course of design to minimize limit cycle behavior.

II. Theoretical Background

The phenomenon of friction is discussed in most elementary textbooks on mechanics. In the case of the axis servos, friction results in a torque in a direction opposite to the direction of motion, or in the absence of motion, a direction opposite to the net applied torque. In the finite-motion case, the

friction torque is a constant amplitude known as the Coulomb friction. In the zero-motion case, the friction torque is equal and opposite to the applied torque until a critical level known as the static friction is exceeded. Thus, for any applied torque less than the static friction, the acceleration is zero and the system remains at rest. Because the friction torque instantaneously changes direction and amplitude at zero velocity, it is described by a discontinuous function.

In the presence of friction, a closed-loop linear system in motion behaves according to its linear equations of motion with a constant external torque corresponding to the Coulomb friction torque. When the system velocity reaches zero, the friction torque instantaneously changes direction and amplitude, according to the friction law described above. In most cases of interest here, the control torques are insufficient to instantaneously overcome the static friction so the system remains at rest for a finite period of time. At zero velocity, the static friction prevents any motion and effectively opens the rate and acceleration feedback loops. The system therefore behaves according to a set of open-loop linear equations which are formed from the closed-loop equations by deleting terms involving rate and acceleration. This open-loop transient response ends at the time the actuator torque becomes sufficient to overcome the static friction and motion commences.

The undisturbed system behavior can thus be described by a succession of linear transient responses with specific initial conditions and with an external torque disturbance corresponding to the Coulomb friction. The transients alternate between the open-loop and closed-loop responses with the initial conditions of each transient equal to the terminal conditions of the previous transient and the external torque alternating according to the direction of the velocity. Depending upon the initial conditions at the start of this sequence, the system either converges or diverges to a stable limit cycle. Alternatively, if a stable equilibrium exists, the system converges to the equilibrium point.

III. Applications

A. Limit Cycles in an Elementary PID Controller

A few basic insights can be obtained from analysis of the elementary proportional, integral, and derivative (PID) feedback controller of Fig. 1. The block diagram represents a system consisting of a pure inertia with rate, position, and integral error feedback and a linear, frequency-independent control amplifier and torque motor actuation device. For generality and convenience of analysis the torque gain and load inertia are lumped together in the rate loop gain K_3 . The single external input U represents the external torque, and the three-

element output vector Y corresponds to integral error, position, and rate.

The state-space matrices for the linear closed-loop system of Fig. 1 are

$$\mathbf{A} = \begin{bmatrix} 0 & 1 & 0 \\ 0 & 0 & 1 \\ -K_1 & -K_2 & -K_3 \end{bmatrix} \quad \mathbf{B} = \begin{bmatrix} 0 \\ 0 \\ J^{-1} \end{bmatrix}$$

$$\mathbf{C} = \begin{bmatrix} 1 & & \\ & 1 & \\ & & 1 \end{bmatrix} \quad \mathbf{D} = \begin{bmatrix} 0 \\ 0 \\ 0 \end{bmatrix}$$

where

$$\dot{\mathbf{x}} = \mathbf{A}\mathbf{x} + \mathbf{B}U$$

and

$$Y = \mathbf{C}\mathbf{x} + \mathbf{D}U$$

with U equal to the effective Coulomb friction torque in addition to any other external disturbance.

The open-loop system matrices \mathbf{A}_0 , \mathbf{B}_0 , \mathbf{C}_0 , and \mathbf{D}_0 are formed from the closed-loop matrices above by substituting zeros for the columns of \mathbf{A} and \mathbf{C} that correspond to rate. The \mathbf{B} and \mathbf{D} matrices are unchanged from their closed-loop values. Thus

$$\mathbf{A}_0 = \begin{bmatrix} 0 & 1 & 0 \\ 0 & 0 & 0 \\ -K_1 & -K_2 & 0 \end{bmatrix} \quad \mathbf{B}_0 = \begin{bmatrix} 0 \\ 0 \\ J^{-1} \end{bmatrix}$$

$$\mathbf{C}_0 = \begin{bmatrix} 1 & & \\ & 1 & \\ & & 0 \end{bmatrix} \quad \mathbf{D}_0 = \begin{bmatrix} 0 \\ 0 \\ 0 \end{bmatrix}$$

The behavior of the elementary PID system can be inferred from the block diagram of Fig. 1 and the corresponding equations with the torque input adjusted according to the known characteristics of the friction. When the system is initially at rest, any finite position error produces an increasing control

torque which eventually overcomes the friction, and the system begins to respond according to the closed-loop equations. The rate increases in a direction opposite to the initial position error until the control torque decreases to a level where the Coulomb friction decelerates the system toward zero rate. The closed-loop transient ends abruptly at the zero-rate point and subsequent behavior will again be governed by the open-loop equations.

The properties of the limit cycle oscillation are conveniently described by phase-plane projections of the three-dimensional state-space trajectories. For convenience of terminology, the plane corresponding to zero rate is referred to as the integral plane and the plane corresponding to zero integral is the rate plane. In the open-loop condition, the zero-rate condition defines a straight-line trajectory confined to the integral plane. The point of transition to closed-loop behavior is obtained from the equation describing the net torque acting on the inertia:

$$-K_1 x_1 - K_2 x_2 - K_3 x_3 + \frac{T_f}{J} = 0 \quad (1)$$

where T_f assumes the algebraic sign of $(K_1 x_1 + K_2 x_2)$.

In the integral plane, Eq. (1) defines two parallel lines which bound the open-loop condition. Outside the plane, Eq. (1) defines two parallel flat surfaces which correspond to the zero-acceleration conditions. All closed-loop trajectories cross these surfaces when the control torque decreases to the friction level and deceleration begins. These crossings thus indicate the peak-rate points and should not be confused with a return to open-loop conditions.

The form of the closed-loop transient is recognized from the block diagram of Fig. 1 as a combination of a damped sinusoid and a decreasing exponential. The relative phase of the sinusoid and amplitude of the exponential are linear functions of the initial conditions and of the friction level. Because the determination of conditions at the zero-rate crossings requires solution of transcendental equations, a numerical evaluation method of analysis was pursued in preference to a generalized closed-form analytic method. The numerical processing was facilitated by the use of PC Matlab, an interactive scientific calculation program with extensive linear algebra capabilities.

Figure 2 shows the integral plane phase portraits of a family of typical transients similar in form to the closed-loop transients and satisfying the initial conditions of Eq. (1), for a case where the static and Coulomb friction levels correspond to 1.5 and 1 rad/sec² respectively. The actual closed-loop transients differ from those shown in that they end at the points

of zero rate which are recognized as the regions of zero slope in the integral plane. Figure 3 traces the sequencing between closed-loop and open-loop transients and shows convergence toward a stable limit cycle. Figure 4 shows the corresponding rate-plane projection. The open-loop portions of the trajectory are recognizable as constant position lines in the integral plane of Fig. 3 extending from the closed-loop terminal conditions (zero rate) to the open-loop initial condition line of Eq. (1). The general properties of this open-loop transient can be inferred from the eigenvalues of the open-loop A_0 matrix, which in this case indicate a simple integration.

A few fundamental properties of the system behavior can be identified from Fig. 2 where the convergence of the un-terminated transient toward the respective nodal points is evident. From the block diagram of Fig. 1 it is seen that the two nodal points correspond to the equilibrium condition where the control and friction torques combine to produce zero acceleration, rate, and position. The points of convergence thus satisfy the condition

$$|K_1 x_1| \leq \frac{T_{cf}}{J}$$

where T_{cf} is a positive constant corresponding to the Coulomb friction. It follows that any point on the straight line between the two nodal points corresponds to a stable equilibrium. Any point outside the nodal points or off their connecting line will result in finite acceleration and motion will continue until a stable equilibrium is reached.

Thus, the closed-loop initial conditions are dependent on the static friction and the nodal points are dependent on the Coulomb friction. Therefore, the initial condition lines will never intersect the stable equilibrium region unless the static and Coulomb levels are equal. Further, since Fig. 2 indicates that none of the possible trajectories cross zero rate at a zero-position condition, it follows that a finite limit cycle will always result unless the nodal points lie on the initial condition lines.

This leads to the conclusion that for any elementary PID controller with equal levels of static and Coulomb friction and in the absence of other nonlinearities, the system response will always converge to a stable equilibrium and no limit cycle will result. When the static friction exceeds the Coulomb friction level, the response from any initial condition off the line segment of stable equilibrium conditions will either converge or diverge to a stable limit cycle. A finite limit cycle condition will exist whether or not the closed-loop system response (the eigenvalues of A) is overdamped. Further, since the Coulomb friction increases the distance between the nodal points, its

increase with a constant static-Coulomb friction differential is expected to increase the time required to transit the open-loop trajectory, thus increasing the limit cycle period.

To investigate the relationships between the control gain and limit cycle behavior, a set of 60 different combinations of gains was prepared and the properties of the resulting stable limit cycles were evaluated. To ensure that all results correspond to reasonable closed-loop stability, the gains were calculated to produce a family of left-hand plane (LHP) pole locations. The 60 combinations of pole locations included damping ratios of 50, 70.7, and 86.6 percent of critical and five magnitudes between 0.3535 and 1.414 sec^{-1} for the complex pair, along with four real pole locations between -2.83 and -8.0 sec^{-1} . The static and Coulomb friction levels were arbitrarily set at 10 and 0 rad/sec^2 respectively for all combinations of gain.

The limit cycle properties of interest here are the position amplitude, the peak rate, and limit cycle period. These properties are readily determined once the initial conditions for a stable limit cycle have been identified. For the elementary PID controller, the initial conditions for a stable cycle are readily determined by Eq. (1), so all that is required is to start with an arbitrary initial condition and observe the terminal conditions of the resulting closed-loop transient. When the initial and terminal positions are equal and opposite, a stable limit cycle has been described. A simple recursive routine was used to implement this process, where the initial condition for each trial was equated to the geometric mean magnitude of the initial and terminal positions of the previous trial. Instability associated with small values was avoided by substituting the arithmetic mean in place of the geometric mean when either value was less than one-tenth of the other. This method was found to have superior convergence properties over methods using the arithmetic mean exclusively.

The position amplitude, peak rate, and period of the corresponding stable limit cycles are plotted against their corresponding gain parameters in Figs. 5, 6, and 7. The position amplitude of Fig. 5 approximates a $1.445 \pi/K_2$ relationship. The dispersion in the data appears to be the result of errors in determining the precise zero crossings of the discrete time solution of the transient response. The peak limit cycle rate approximates $8.354/K_3$. In this case the apparent dispersion is presumed to be valid data since a correlation to the reciprocal of the position gain K_2 was also identified. The influence of the position and rate gains on the limit cycle period is readily apparent in the limit cycle period of Fig. 7. Taken together, Figs. 5, 6, and 7 indicate that simultaneous minimization of position amplitude and peak rate along with maximum period represent mutually exclusive constraints on the integral, position, and rate gains. However, this conflict may

be resolved by minimizing a mean square rate which can be approximated by the rate squared, divided by the period.

B. Application to the 70-m Axis Servos

The dynamics of the 70-m antenna axis servos are far more complicated than those of the elementary PID controller described above, but the same principles of analysis apply. A simplified dynamic block diagram of the typical axis rate servo is shown in Fig. 8 where a rigid body approximation of the actual antenna structure is assumed. To condense the state-space model to the minimum number of states, the lead network in the tachometer feedback path is replaced with the equivalent acceleration-state feedback in Fig. 9 and the network pole at $-P_1$ is ignored. To accommodate representation

by open-loop and closed-loop state-space matrices, the position loop controller of Fig. 8 is replaced in Fig. 9 by the equivalent feedback gains which operate on the multivariable output Y . This distinction between the output and the states will become apparent when the nonlinearities are introduced.

With the conventional state-space representation of the system,

$$\dot{x} = Ax + BU$$

$$Y = Cx + DU$$

The multivariable A B C D matrices, before incorporating the position loop control gain K , are

$$A = \begin{bmatrix} 0 & 1 & 0 & 0 & 0 \\ 0 & 0 & 1 & 0 & 0 \\ 0 & 0 & 0 & 1/J_m & 0 \\ 0 & 0 & -(V^2 + K_R)/C_h & -(D_h + K_R/J_m Z_1)/C_h & (Z_2 - P_2)/C_h \\ 0 & 0 & -K_R & -K_R/J_m Z_1 & -P_2 \end{bmatrix}$$

$$B = \begin{bmatrix} 0 & 0 & 0 & 0 & 0 \\ 1 & 0 & 0 & 0 & 0 \\ 0 & 1/J_m & 0 & 0 & 0 \\ K_R/C_h & -K_R/J_m Z_1 C_h & V/C_h & 0 & 0 \\ K_R & -K_R/J_m Z_1 & 0 & 0 & 0 \end{bmatrix}$$

$$C = \begin{bmatrix} 1 & 0 & 0 & 0 & 0 \\ 0 & 1 & 0 & 0 & 0 \\ 0 & 0 & 1 & 0 & 0 \\ 0 & 0 & 0 & 1/J_m & 0 \\ 0 & 0 & 0 & 0 & 0 \end{bmatrix}$$

$$D = \begin{bmatrix} 0 & 0 & 0 & 0 & 0 \\ 0 & 0 & 0 & 0 & 0 \\ 0 & 0 & 0 & 0 & 0 \\ 0 & 1/J_m & 0 & 0 & 0 \end{bmatrix}$$

where the multivariable input U and output Y correspond to

$$U = \begin{bmatrix} -KY \\ \text{external torque} \\ \text{excess flow} \end{bmatrix} \quad Y = \begin{bmatrix} \text{integral position} \\ \text{position} \\ \text{rate} \\ \text{acceleration} \end{bmatrix}$$

The excess flow element in the input vector U is included to accommodate the future addition of a nonlinear representation of the hydraulic valve.

Incorporating the controller gain K into the state equations involves some unusual complexity since U includes Y and Y is also dependent on U when the input matrix D is nonzero. The

fundamental state equations for \dot{x} and Y can be expressed in a form to separate the $-KY$ from the other elements of U . Thus substituting $-B_1 KY + BU_{\text{Ext}}$ for BU and $-D_1 KY + DU_{\text{Ext}}$ for DU where B_1 and D_1 denote the first columns of B and D and U_{Ext} is U with the first element replaced by zero,

$$\dot{x} = Ax - B_1 KY + BU_{\text{Ext}}$$

$$Y = Cx - DU = Cx - D_1 KY + DU_{\text{Ext}}$$

which leads to

$$Y = [I + D_1 K]^{-1}(Cx + DU_{\text{Ext}})$$

and

$$\dot{x} = Ax - B_1 K [I + D_1 K]^{-1}(Cx + DU_{\text{Ext}}) + BU_{\text{Ext}}$$

These expressions for Y and \dot{x} define new A and C matrices for the general case involving position controller gain K .

In the specific case described here, the input U does not couple directly into Y since D_1 is a column of zeros. Thus C is unaffected by introduction of the controller gain K and the expressions for the closed-loop A_1 and B_1 simplify to

$$A_1 = A - B_1 KC$$

$$B_1 = B - B_1 KD$$

The open-loop system matrices A_0 and B_0 are formed by altering the closed-loop A_1 and B_1 to satisfy the constraint that the rate state \dot{x}_3 and the acceleration output y_4 must remain zero. This is accomplished by assigning zeros to the third rows of A_0 and B_0 , to the second column of B , and to elements $a_{0,3}$, $a_{0,5,3}$, and $a_{0,5,4}$ of A_0 and changing $a_{0,4,4}$ to $-D_h/C_h$. This process is the equivalent of breaking the forward paths through $1/J_m$ and the (-1) and $(-V)$ rate feedback paths. In actual practice, modifying the third columns of A and C is unnecessary because x_3 is already constrained to zero. For convenience in determining the breakaway condition, C and D are used unmodified in the open-loop case. This results in a finite value of the acceleration output y_4 , which is tested for a zero crossing to determine the end of the open-loop condition.

As in the case of the elementary PID controller discussed earlier, the end points of the open-loop and closed-loop transients are determined by the zero crossings of the rate and of the control-friction torque difference. The determination of initial conditions is more complicated, however, because the governing physical friction law fails to uniquely define more

than two of the five state variables. In the case of the closed-loop initial condition, the requirements of zero rate and acceleration define the third and fourth variables, whereas in the open-loop case the sole requirement of zero rate defines only the third variable. This difficulty was partially overcome by arbitrarily assigning a small value to the position variable and small time derivatives to the fourth and fifth state variables. Thus with x_2 and x_4 defined and $x_3 = 0$, x_1 and x_5 can be determined from solution of the matrix equation

$$\begin{bmatrix} a_{4,1}^{1} & a_{4,5}^{1} \\ a_{5,1}^{1} & a_{5,5}^{1} \end{bmatrix} \begin{bmatrix} x_1 \\ x_5 \end{bmatrix} + \begin{bmatrix} a_{4,2}^{1} & a_{4,4}^{1} \\ a_{5,2}^{1} & a_{5,4}^{1} \end{bmatrix} \begin{bmatrix} x_2 \\ x_4 \end{bmatrix} + \begin{bmatrix} b_{4,1}^{1} & b_{4,2}^{1} & b_{4,3}^{1} \\ b_{5,1}^{1} & b_{5,2}^{1} & b_{5,3}^{1} \end{bmatrix} \begin{bmatrix} 0 \\ T_{sf} \\ 0 \end{bmatrix} = \begin{bmatrix} v_4 \\ v_5 \end{bmatrix} \quad (2)$$

where T_{sf} represents the static friction and v_4 and v_5 represent the assigned values for \dot{x}_4 and \dot{x}_5 at time $t = 0+$. The use of the closed loop A_1 and B_1 in this expression ensures that the condition will be satisfied after the transient begins.

Figures 10, 11, and 12 illustrate the convergence resulting from the use of Eq. (2) for initial conditions with three different combinations of static and Coulomb friction. All three cases used initial conditions $x_2 = 0.02$ rad, $v_4 = -0.12$ rad/sec, and $v_5 = -0.01$ rad/sec. The plant variables are typical of the 70-m azimuth axis, and position control gain K is the phase-variable-form equivalent of the present values in the 70-m servo firmware [4]. Figures 10, 11, and 12 indicate that while the solutions always converge or diverge properly depending on the static-Coulomb friction difference, the initial conditions selected using Eq. (2) are far from those of the stable limit cycle.

Figure 11 indicates that unlike the elementary PID controller, the 70-m axis servos develops a finite limit cycle even when the levels of the static and Coulomb frictions are equal. A comparison of Figs. 10, 11, and 12 also seems to indicate a proportionality between the integral position amplitude and the static friction, as is the case for the elementary PID con-

troller. The magnitude of the proportionality constant is not obvious from the system equations.

IV. Conclusions

The piecewise linear method described here has been shown to be highly effective in evaluating friction-induced limit cycle behavior in the 70-m axis servos. The method is sufficiently

general such that it should be readily applicable to treatment of hysteresis and deadzone effects in the hydraulic valve and other nonlinearities characterized by a discontinuity between linear properties. In the next stage of development it should be possible to identify the basic parametric relationships between the system parameters and limit cycle properties. A knowledge of these relationships will enable system designers to develop improved servo designs with less objectionable limit cycle properties.

References

- [1] R. E. Hill, "A New State Space Model for the NASA/JPL 70-Meter Antenna Servo Controls," *TDA Progress Report 42-91*, vol. July-September 1987, Jet Propulsion Laboratory, Pasadena, California, pp. 285-294, November 15, 1987.
- [2] R. E. Hill, "A New Algorithm Modeling Friction in Dynamic Mechanical Systems," *TDA Progress Report 42-95*, vol. July-September 1988, Jet Propulsion Laboratory, Pasadena, California, pp. 51-57, November 15, 1988.
- [3] N. Minorsky, *Theory of Nonlinear Systems*, New York: McGraw-Hill, 1969.
- [4] L. S. Alvarez and J. Nickerson, "Application of Optimal Control Theory to the Design of the NASA/JPL 70-M Antenna Axis Servos," *TDA Progress Report 42-97*, Jet Propulsion Laboratory, Pasadena, California, this issue.

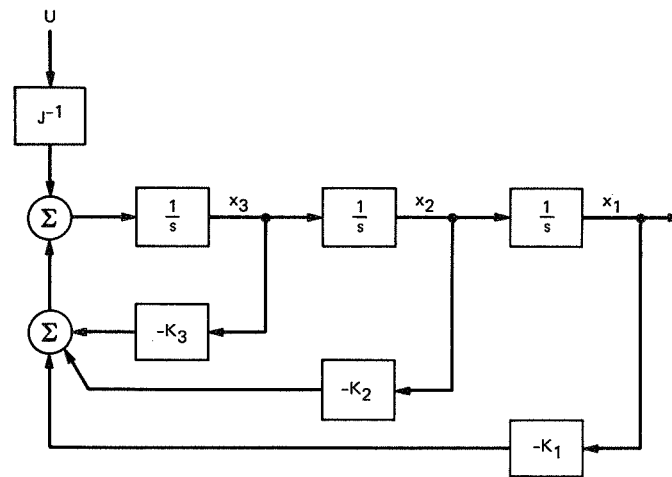


Fig. 1. Block diagram of an elementary PID controller.

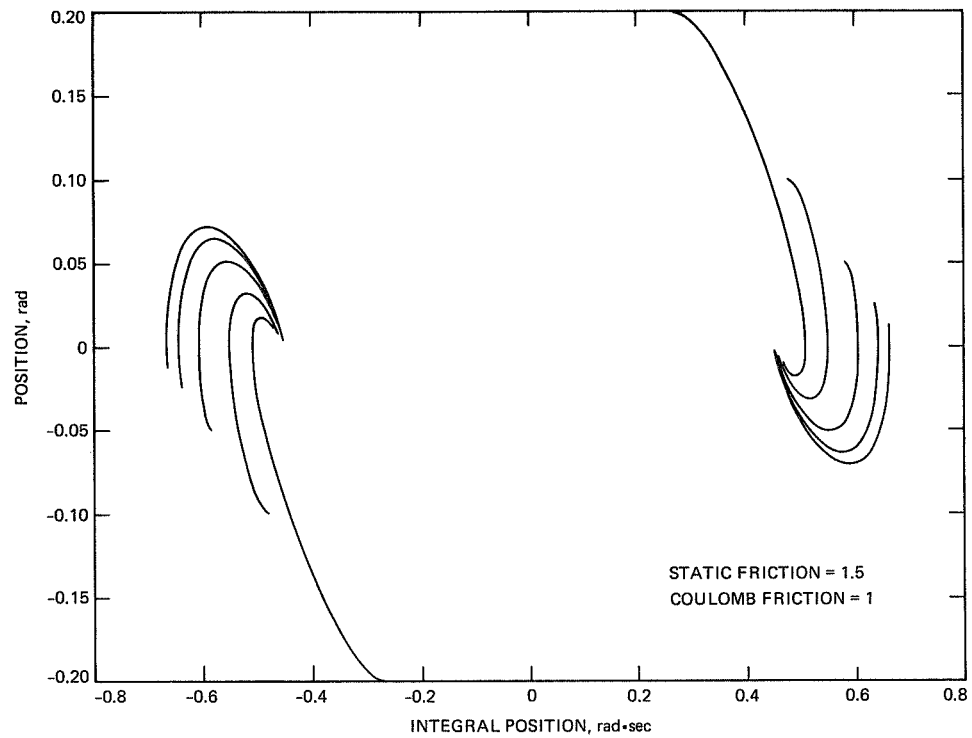


Fig. 2. Phase portrait of typical linear responses of the system in Fig. 1.

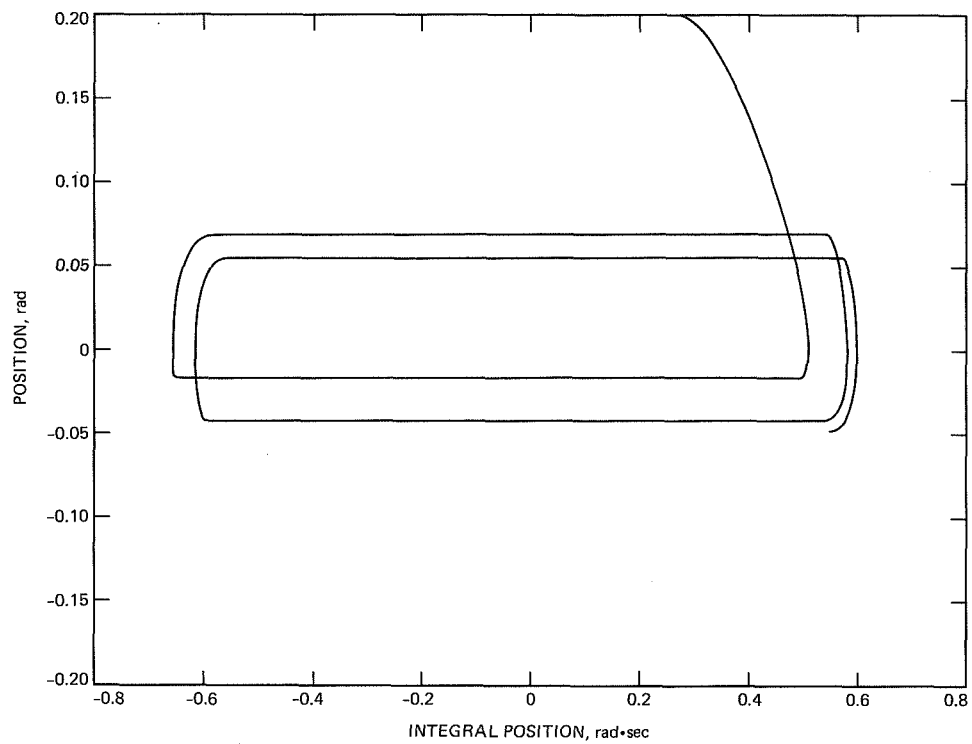


Fig. 3. Typical limit cycle portrait of the system in Fig. 1.

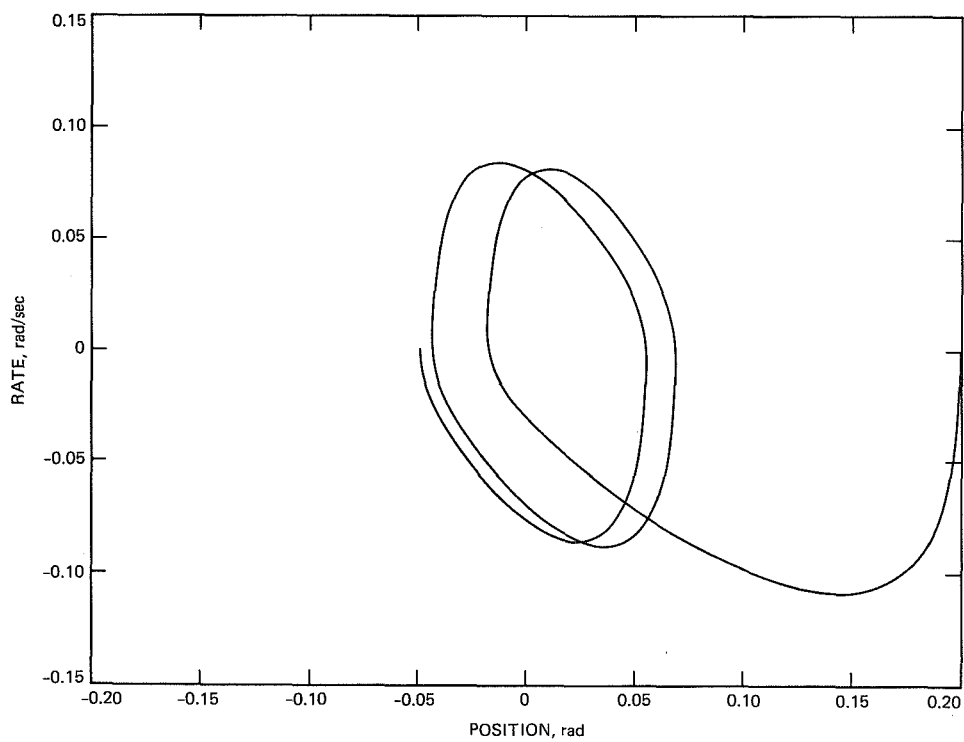


Fig. 4. Rate-plane projection corresponding to Fig. 3.

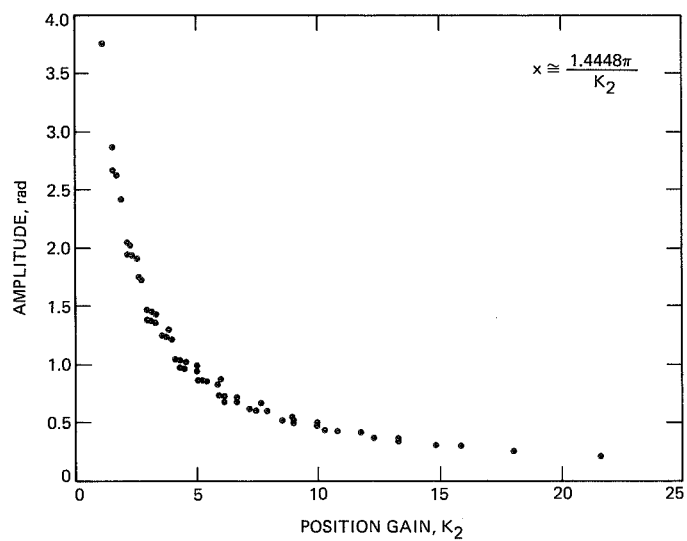


Fig. 5. Limit cycle position amplitude versus position gain for the system in Fig. 1.

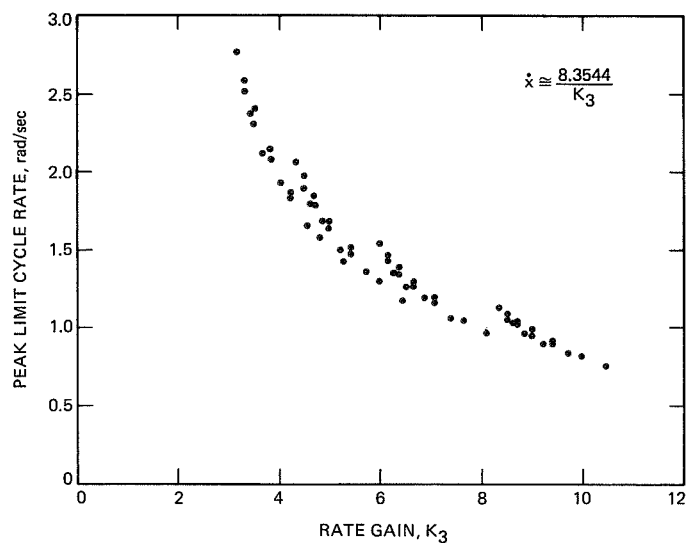


Fig. 6. Limit cycle peak-rate amplitude versus rate gain for the system in Fig. 1.

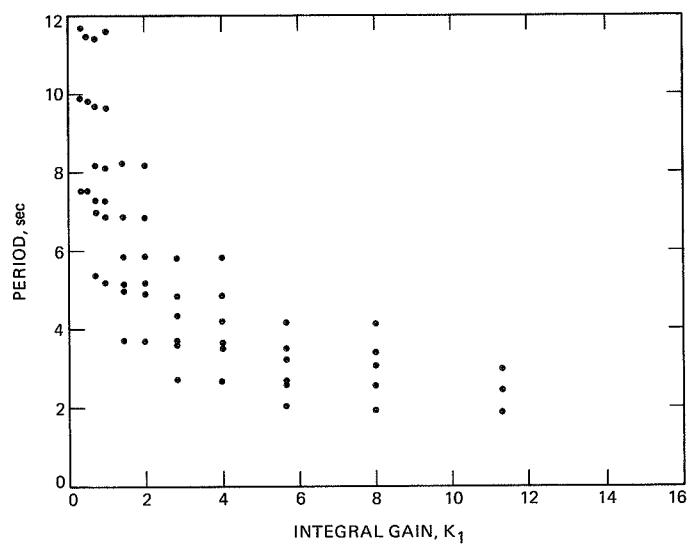


Fig. 7. Limit cycle period versus integral gain for the system in Fig. 1.

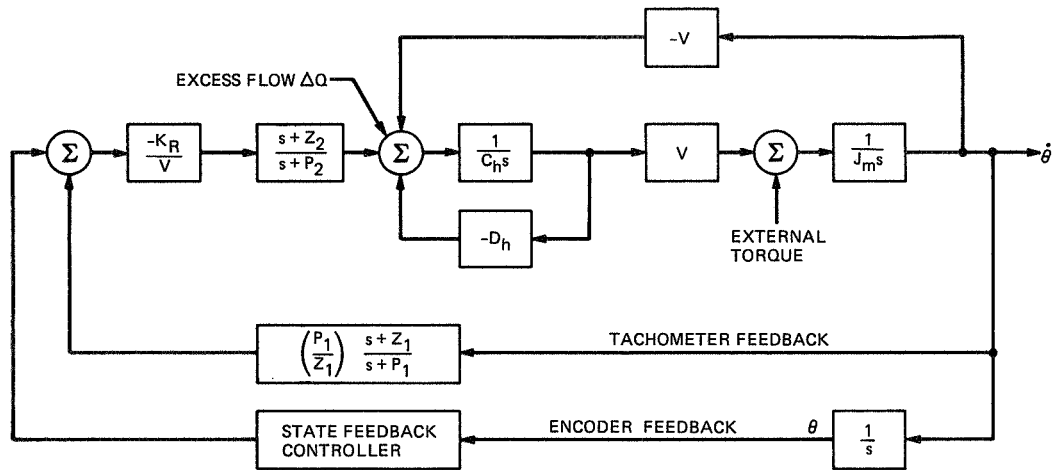


Fig. 8. Dynamic block diagram of the 70-m antenna axis servos.

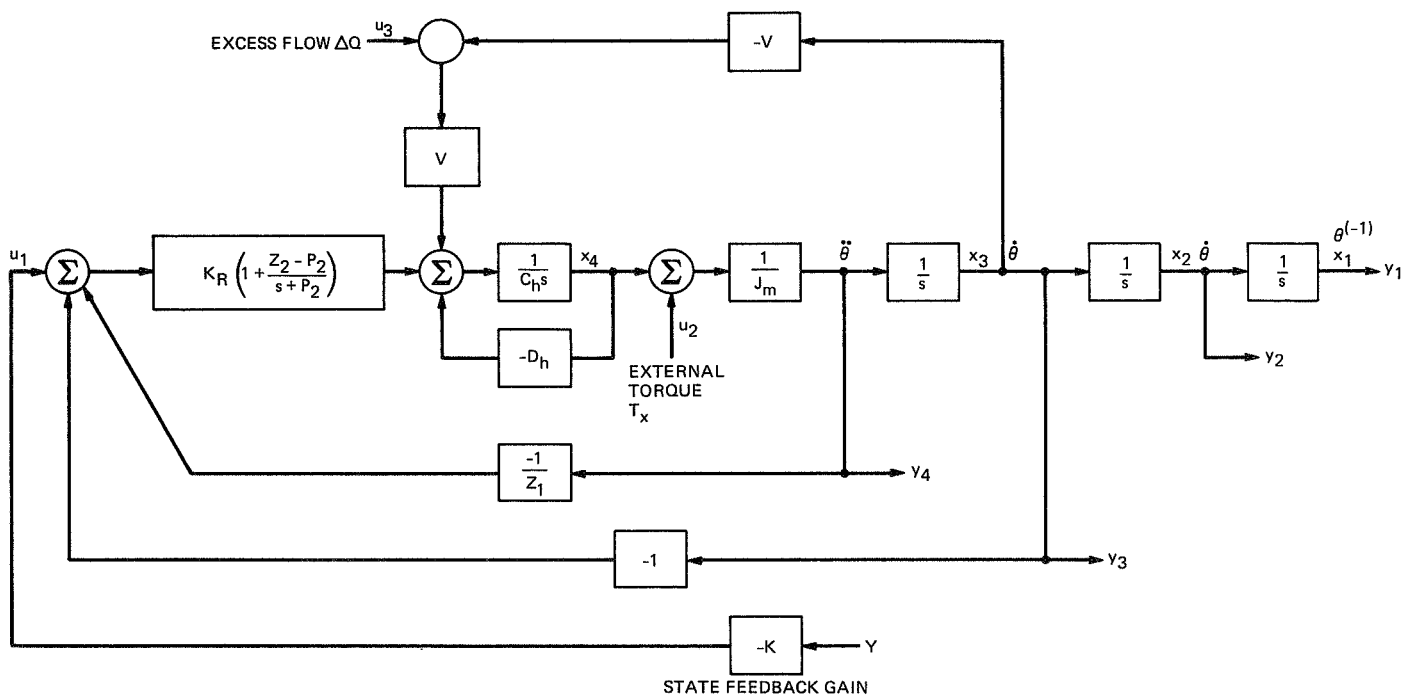


Fig. 9. Simplified multivariable system block diagram of the 70-m antenna axis servos.

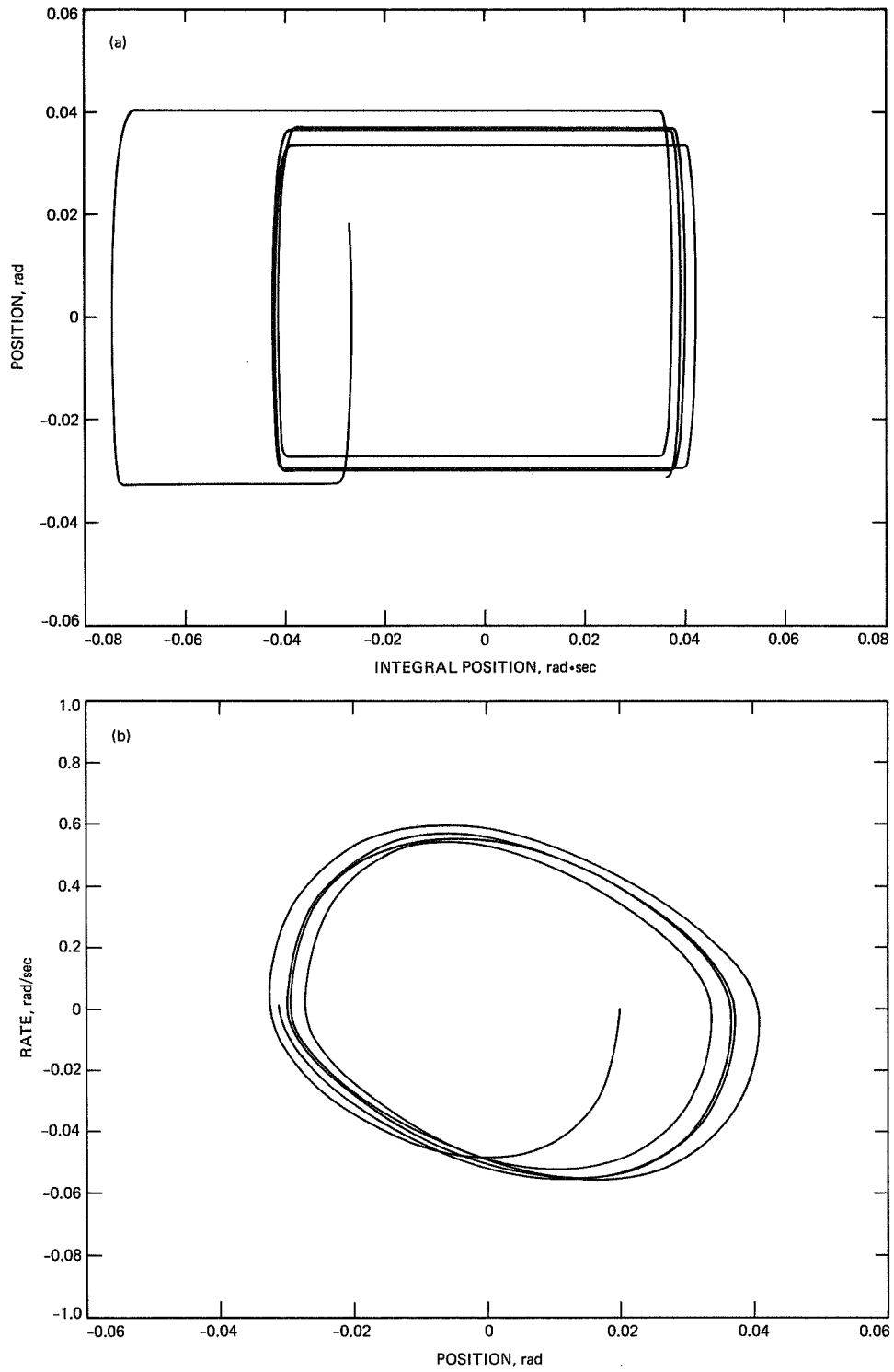


Fig. 10. 70-m axis servo limit cycle ($T_{fs} = 500$, $T_{fc} = 250$): (a) integral plane; (b) rate plane.

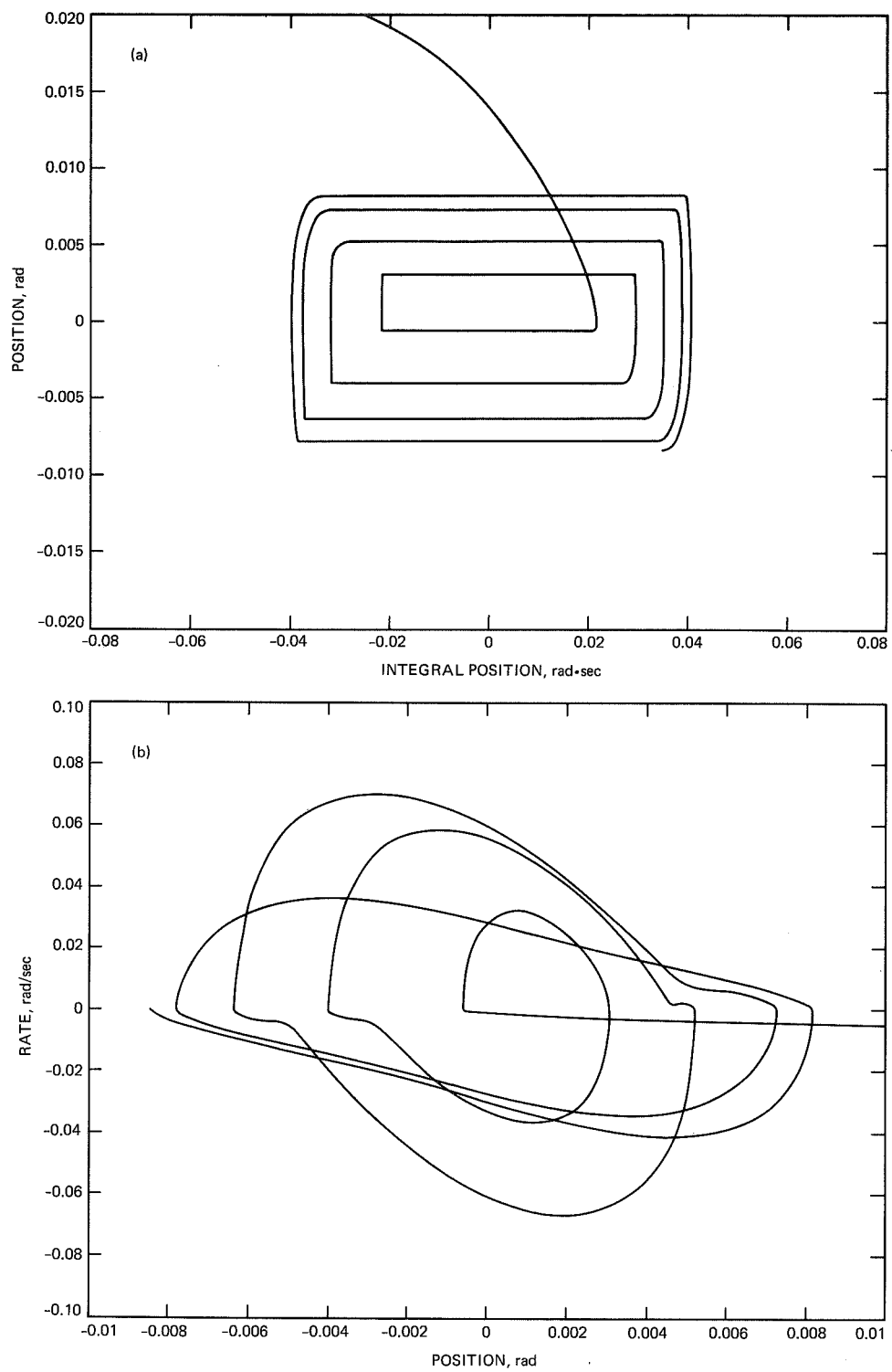


Fig. 11. 70-m axis servo limit cycle ($T_{fs} = 500$, $T_{fc} = 500$): (a) integral plane; (b) rate plane.

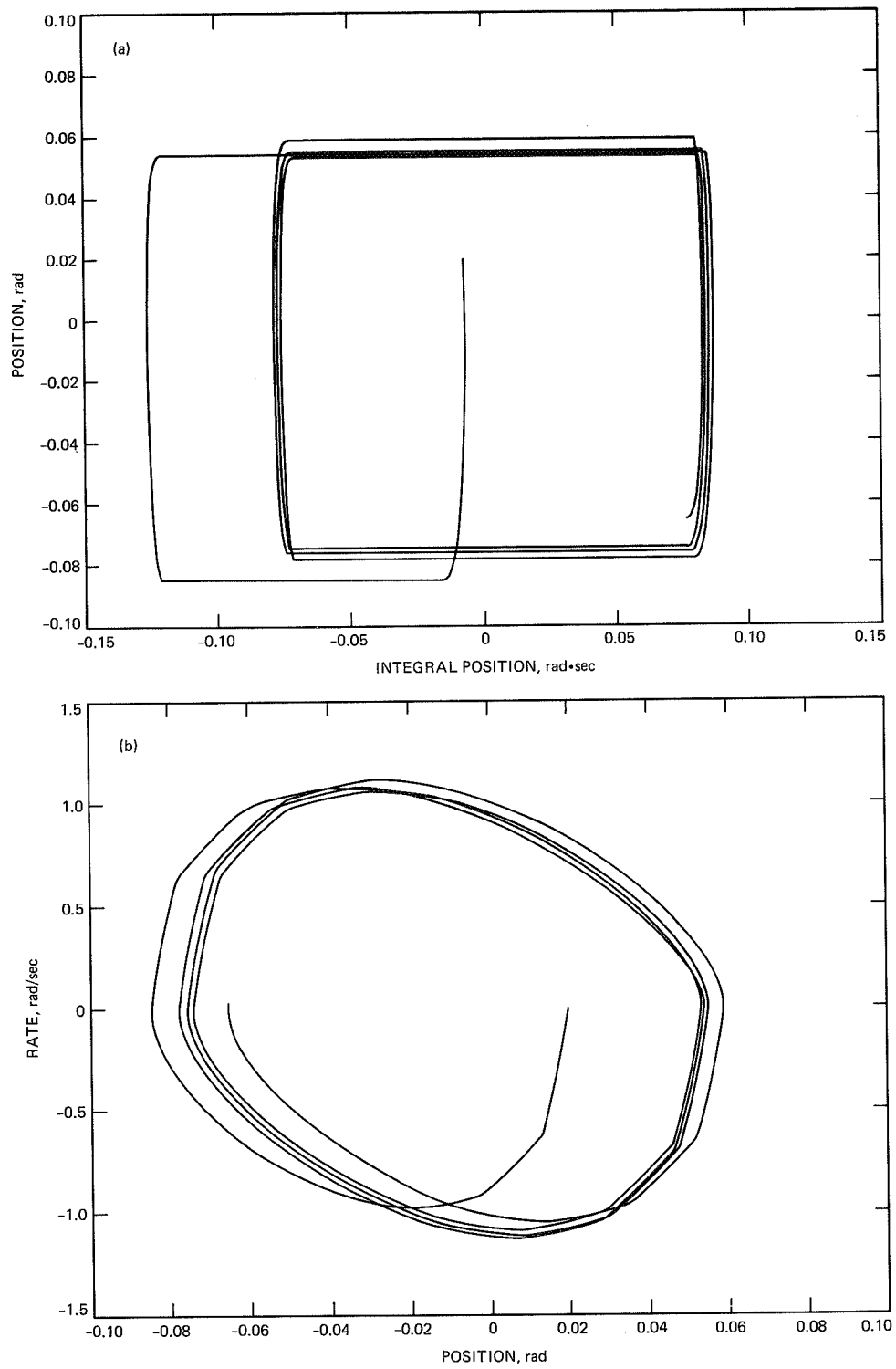


Fig. 12. 70-m axis servo limit cycle ($T_{fs} = 1000$, $T_{fc} = 500$): (a) integral plane; (b) rate plane.

310-233
218065

N 8 9 - 2 7 8 8 1

TDA Progress Report 42-97

January-March 1989

Application of Optimal Control Theory to the Design of the NASA/JPL 70-Meter Antenna Axis Servos

L. S. Alvarez and J. Nickerson

Ground Antenna and Facilities Engineering Section

The application of Linear Quadratic Gaussian (LQG) techniques to the design of the 70-m axis servos is described. Linear quadratic optimal control and Kalman filter theory are reviewed, and model development and verification are discussed. Families of optimal controller and Kalman filter gain vectors were generated by varying weight parameters. Performance specifications were used to select final gain vectors.

I. Introduction

This article presents the design of the position control algorithm for NASA's Deep Space Network antennas. The antennas are of an elevation over azimuth design and have two sets of transducers for measuring axis position. A 20-bit encoder is geared to the bull gear of each axis and measures angular displacements to approximately a third of a millidegree. Another position-sensing device is an autocollimator. The autocollimator measures the misalignment between an intermediate reference structure beneath the main paraboloid and a small reference antenna that is structurally isolated from the 70-m antenna. A control algorithm must be designed for both encoder feedback (known as the computer-mode control algorithm) and autocollimator feedback (known as the precision-mode control algorithm).

A state feedback controller with a constant gain estimator is used to close both the computer- and precision-mode control loops. The controller is based on a fifth-order state model with an added sixth state which integrates position error. A Kalman filter estimates state variables by using encoder feedback during both the computer and precision modes of opera-

tion. In the computer-mode algorithm, gains are applied to the integral error and position error (both formed from the position estimate and commanded position) and also applied to the remaining estimated states. In the precision-mode algorithm, control gains are similarly applied with the exception that now the estimated position error is replaced by the hardware-filtered autocollimator error and the integral error is numerically calculated based on this same error signal. The present implementation of the algorithm allows for different gains to be used for the computer and precision modes.

The objective is to design control and filter gains that minimize control effort while meeting performance characteristics, thereby reducing control system excitation of the lightly damped structure. This provides motivation to apply optimal control design techniques to determine controller gains.

Presented in this article are a brief review of optimal control theory and the step-by-step design process. The design process includes system model generation and the calculation of optimal controller and Kalman filter gains. The design methodology utilizes the Loop Transfer Recovery (LTR) method to calcu-

late the filter gains, and then both these and the state feedback gains are combined to form a Linear Quadratic Gaussian (LQG) controller. Most of the design procedure follows that reported in [1], but the estimator design is novel. Test results based on linear and nonlinear simulations are presented.

II. Theory

The LQG design method is applied to arrive at optimal linear output feedback control systems for the 70-m axis servos. The solution of the LQG problem is a combination of the Linear Quadratic Regulator (LQR) and Kalman filter problems. Both the optimal properties of LQG designs and the systematic nature of the design process served as motivation for its application. The design is separated into two problems: (1) designing a target closed-loop feedback control system using optimal control theory (specifically, an LQR control design is developed and then adapted for tracking), and (2) designing a Kalman filter to estimate inaccessible states.

A. The LQR Optimal Control Technique

The plant can be linearly modeled by a set of first-order differential equations of the form

$$\begin{aligned}\dot{\mathbf{x}}(t) &= \mathbf{A}\mathbf{x}(t) + \mathbf{B}\mathbf{u}(t) \quad ; \quad \mathbf{x}(0) = \mathbf{x}_0 \\ \mathbf{y}(t) &= \mathbf{C}\mathbf{x}(t)\end{aligned}\quad (1)$$

where \mathbf{x} is an $n \times 1$ state column vector; \mathbf{u} is an $m \times 1$ input column vector; \mathbf{y} is an $m \times 1$ output column vector; and \mathbf{A} , \mathbf{B} , and \mathbf{C} are coefficient matrices of appropriate dimensions. The control for a state variable feedback controller takes the form

$$\mathbf{u}(t) = -\mathbf{K}\mathbf{x}(t) \quad (2)$$

where \mathbf{K} is a feedback gain vector, not necessarily producing an optimum controller. Substituting Eq. (2) into Eq. (1) yields

$$\dot{\mathbf{x}}(t) = \mathbf{A}\mathbf{x}(t) - \mathbf{B}\mathbf{K}\mathbf{x}(t) = (\mathbf{A} - \mathbf{B}\mathbf{K})\mathbf{x}(t) \quad (3)$$

The plant dynamics are thus modified by the feedback gain vector \mathbf{K} .

State feedback is attractive because the closed-loop eigenvalues of the system are arbitrarily specified by the proper selection of the feedback vector \mathbf{K} . Numerical procedures exist that calculate \mathbf{K} for a desired set of eigenvalues [2]. Although a designer can iterate a pole selection until the closed-loop system meets performance criteria, there are no guarantees that the design is optimal.

The LQR optimal control problem to be presented is a specific example of a deterministic dynamic optimization problem. For a linear system, a quadratic performance index is used as a performance criterion. Given the system description in Eq. (1), the quadratic performance index J is of the form:

$$J = \int_0^{\infty} [\mathbf{x}^T(t) \mathbf{Q}\mathbf{x}(t) + \rho \mathbf{u}^T(t) \mathbf{R}\mathbf{u}(t)] dt \quad (4)$$

where \mathbf{Q} is a positive semi-definite matrix, \mathbf{R} is a positive definite matrix, and ρ is a positive non-zero scalar. The first term penalizes transient deviation of the state from the origin. The second term penalizes the amount of control effort used to control the states. Parameters \mathbf{Q} , \mathbf{R} , and ρ are weighting terms that adjust the penalties for transient deviation and control effort. The optimization problem is then to find the control $\mathbf{u}(t)$, $0 \leq t \leq \infty$, that minimizes the performance index J subject to the following dynamic constraints:

- (1) the plant is controllable or can be stabilized
- (2) the final time is $t = \infty$
- (3) $(\mathbf{A}, \mathbf{Q}^{1/2})$ is observable

The solution for the standard LQR problem is given in [2-4]; therefore, only the results are summarized below. The optimal steady-state solution yields the control law

$$\mathbf{u}(t) = -\mathbf{K}\mathbf{x}(t) \quad (5)$$

with the feedback gain matrix \mathbf{K} defined as

$$\mathbf{K} = \mathbf{R}^{-1} \mathbf{B}^T \mathbf{P} \quad (6)$$

where \mathbf{P} is a symmetric positive semi-definite solution to the Riccati equation in matrix form

$$\mathbf{A}^T \mathbf{P} + \mathbf{P}\mathbf{A} + \mathbf{Q} - \mathbf{P}\mathbf{B}\mathbf{R}^{-1} \mathbf{B}^T \mathbf{P} = 0 \quad (7)$$

Numerical procedures are used to solve the algebraic Riccati equation and calculate \mathbf{K} knowing the system and weighting matrices [2]. The LQR optimal design for state feedback control guarantees that the closed-loop system described by Eq. (3) is stable and that the LQR control law (Eq. 5) generates the minimum possible value of the quadratic cost objective J given by Eq. (4). In addition to the nominal closed-loop stability guarantee of analog LQR designs are its properties of robustness. An LQR-based system guarantees an infinite upward gain margin and a gain reduction of at least 1/2, or -6 dB, and a phase margin of at least ± 60 degrees. If the final implementation of this controller is in time-discretized (digital) form, then stability is degraded slightly from the continu-

ous case because of finite sampling time. This degradation should be investigated and quantified. A complete discussion of the discrete LQR problem may be found in [2] or [5]. It is stressed that all robustness and performance guarantees for continuous and discrete time LQR designs do not necessarily hold in observer/Kalman-filter-based feedback controllers. This fact may constitute a good argument to use state feedback when the physical states are accessible and do not cost an inordinate amount to sense.

B. The Kalman Filter

Implementation of state feedback requires knowledge of the entire state vector. When states are unmeasured they must be estimated. A closed-loop estimator is based on a plant model and the weighted difference between the estimated and actual output. Figure 1 describes state feedback implementation using an estimator. Typical errors in the estimated state vector may arise from modeling errors and from uncompensated deterministic and stochastic disturbances. These errors are corrected by feedback of the output estimation error with a feedback gain factor. In order to arrive at optimal estimation (or state reconstruction), the choice of this feedback gain can be based on the solution of the classical Kalman filter problem. Such an estimator, or filter, generates unbiased and minimum variance estimates of the plant state variables based upon past sensor measurements and applied controls.

Two of the many good references for optimal estimation theory (both in discrete and continuous time) and its application in optimal control problems are [4] and [5]. The following summarizes the solution to a simplified classical Kalman filter problem. The problem is based on the following stochastic plant dynamics:

$$\begin{aligned}\dot{\mathbf{x}}(t) &= \mathbf{A}\mathbf{x}(t) + \mathbf{B}\mathbf{u}(t) + \mathbf{N}\xi(t) \\ \mathbf{y}(t) &= \mathbf{C}\mathbf{x}(t) + \theta(t)\end{aligned}\quad (8)$$

where $\xi(t)$ and $\theta(t)$ are assumed to be Gaussian, zero mean, additive white process and sensor noise, with constant intensity matrices Ξ and Θ characterized as follows:

$$\begin{aligned}\text{covariance } [\xi(t); \xi(\tau)] &= E\{\xi(t)\xi^T(\tau)\} = \Xi\delta(t-\tau) \\ \Xi &= \Xi^T > 0\end{aligned}\quad (9)$$

$$\text{covariance } [\theta(t); \theta(\tau)] = E\{\theta(t)\theta^T(\tau)\} = \Theta\delta(t-\tau)$$

$$\Theta = \Theta^T > 0$$

where $E\{\cdot\}$ is the expectation operator. It is also assumed that $\theta(t)$ is independent of $\xi(t)$. The filter is driven by the control, $\mathbf{u}(t)$, and by the noisy measurement vector, $\mathbf{y}(t)$, and generates a real-time state estimate and output estimate based on the following filter equations:

$$\begin{aligned}\dot{\hat{\mathbf{x}}}(t) &= \mathbf{A}\hat{\mathbf{x}}(t) + \mathbf{B}\mathbf{u}(t) + \mathbf{L}[\mathbf{y}(t) - \mathbf{C}\hat{\mathbf{x}}(t)]; \hat{\mathbf{x}}(0) = E\{\mathbf{x}(0)\} \\ \hat{\mathbf{y}}(t) &= \mathbf{C}\hat{\mathbf{x}}(t)\end{aligned}\quad (10)$$

where \mathbf{L} is the optimal feedback gain vector. The choice of \mathbf{L} that yields the optimal solution to the formulated estimation problem is

$$\mathbf{L} = \Sigma \mathbf{C}^T \Theta^{-1} \quad (11)$$

where the so-called error covariance matrix Σ is calculated from the following filter algebraic Riccati equation (FARE) in matrix form:

$$\mathbf{O} = \mathbf{A}\Sigma + \Sigma\mathbf{A}^T + \mathbf{L}\Xi\mathbf{L}^T - \Sigma\mathbf{C}^T\Theta^{-1}\mathbf{C}\Sigma \quad (12)$$

A unique, steady-state, positive semi-definite solution matrix Σ to Eq. (12) exists if the following conditions are met:

- (1) $[\mathbf{A}, \mathbf{N}]$ is stabilizable
- (2) $[\mathbf{A}, \mathbf{C}]$ is detectable

Numerical solution methods to the FARE are given in [4]. The estimation error dynamics are obtained by subtracting Eq. (10) from Eq. (8) to yield

$$\dot{\tilde{\mathbf{x}}}(t) = (\mathbf{A} - \mathbf{L}\mathbf{C})\tilde{\mathbf{x}}(t) + \mathbf{L}\xi(t) \quad (13)$$

Thus, the error dynamics can be shown to be dependent on the selection of \mathbf{L} . The optimality of the Kalman filter can be interpreted as follows: if the measurements started at $t = -\infty$, then the state estimation vector has zero mean, i.e.,

$$E\{\tilde{\mathbf{x}}(t)\} = E\{\mathbf{x}(t) - \hat{\mathbf{x}}(t)\} = 0 \quad (14)$$

and the optimal error covariance matrix is Σ , i.e.,

$$\Sigma = E\{\tilde{\mathbf{x}}(t)\tilde{\mathbf{x}}^T(t)\} \quad (15)$$

such that any other gain \mathbf{L} will yield state estimation errors with *larger* variances. Given the stabilizability and detectability assumptions of the stochastic plant dynamics, the Kalman filter, viewed as a dynamic feedback system described by the state equations of Eq. (10), is guaranteed to be stable. Thus the eigenvalues of $(\mathbf{A} - \mathbf{LC})$ are strictly in the left-half s -plane.

III. Modeling

The LQG tracking controller designs for the 70-m axis servos are based on simplified fourth-order rate loop models. Figure 2 presents the linear model for the rate loops of the 70-m Az-El antenna. Shown is the computer mode of operation. Since the physical hardware designs for the Az and El axis rate loops differ very slightly, only the Az rate loop model and controller design are presented. A high-order theoretical model was simplified by eliminating fast dynamics and normalizing to yield the transfer function:

$$G(s) = \frac{Y(s)}{U(s)} = \frac{83.5(s+80)(s+4.4)}{(s+61.25)(s+2.39)[(s+8.75)^2 + (11.36)^2]} \quad (16)$$

where $U(s)$ is the input rate in degrees per second and $Y(s)$ is output rate in degrees per second. The simplified model in Eq. (16) represents a rigid antenna model.

Verification of the simple rate loop model of Eq. (16) was accomplished by using an HP 3562A dynamic signal analyzer

to measure the swept sinusoidal frequency response of the azimuth rate loop at DSS-14. Figures 3 and 4 present the measured gain and phase responses, respectively. These responses were compared with the simplified theoretical model. The accuracy of the approximation is illustrated by superimposing measured data upon the frequency response of the theoretical transfer function (Eq. 16), shown in Figs. 5 and 6.

The design of the LQR and Kalman filter require a state-space representation of the plant model. The plant transfer function, Eq. (16), was transferred into a diagonal canonical set of state-space equations of the form of Eq. (1) to yield

$$\begin{aligned} \dot{\mathbf{x}}(t) &= \begin{bmatrix} -61.25 & 0 & 0 & 0 \\ 0 & -8.747 & 11.360 & 0 \\ 0 & -11.360 & -8.747 & 0 \\ 0 & 0 & 0 & -2.393 \end{bmatrix} \mathbf{x}(t) + \begin{bmatrix} 0.7239 \\ -0.1982 \\ 0.9802 \\ 1.1421 \end{bmatrix} u(t) \\ y(t) &= [0.7239 \quad 9.226 \quad 0 \quad 1.1421] \mathbf{x}(t) \end{aligned} \quad (17)$$

where u is input rate and y is output rate. The state equations were then augmented to include states for position and integral of position. The augmented matrices are formed by using the output vector \mathbf{C} to form the integration of rate or position state and then adding the integration of position to form an integral of position state. The result for azimuth is

$$\begin{aligned} \dot{\mathbf{x}}(t) &= \begin{bmatrix} 0 & 1 & 0 & 0 & 0 & 0 \\ 0 & 0 & 0.7239 & 9.226 & 0 & 0 \\ 0 & 0 & -61.25 & 0 & 0 & 0 \\ 0 & 0 & 0 & -8.747 & 11.360 & 0 \\ 0 & 0 & 0 & -11.360 & -8.747 & 0 \\ 0 & 0 & 0 & 0 & 0 & -2.393 \end{bmatrix} \mathbf{x}(t) + \begin{bmatrix} 0 \\ 0 \\ 0.7239 \\ -0.1982 \\ 0.9802 \\ 1.1421 \end{bmatrix} u(t) \\ y(t) &= [0 \quad 1 \quad 0 \quad 0 \quad 0 \quad 0] \mathbf{x}(t) \end{aligned} \quad (18)$$

Augmenting increased the dimension of A from 4×4 to 6×6 , the dimension of B from 4×1 to 6×1 , and the dimension of C from 1×4 to 1×6 . The diagonal canonical form of the state equations was used to reduce computation and to ensure reasonable matrix numerical conditioning. Equation (18) describes a regulator, and will be used in the LQR design process.

IV. Linear Quadratic Regulator Design

The ultimate goal is to design an optimal tracking controller for the 70-m Az axis servo. However, the solution to a linear quadratic deterministic reference input tracking problem requires knowledge of the future values of the command input. For tracking systems in which the reference input is generated by an exogenous source, this uncertainty must be suitably translated to a stochastic optimization problem [4]. A different approach, taken in this article, was to proceed with an LQR design for the dynamic system of Eq. (18) and then adapt it to track command inputs. A visualization of this so-called LQ servo is presented in Fig. 7, in which the position state becomes the position error and the integral of position becomes the integral of position error. It is noted that the properties of the resultant LQR do not directly reflect the command-following properties of the LQ servo, which will ultimately dictate the choice of the final controller.

The LQR design depends on the selection of weighting matrices, which requires intuition and iteration. For the 70-m servo controller, the Q matrix is 6×6 , ρ is scalar, and R is taken to be the identity matrix. A general approach was used for the choice of the weighting matrix coefficients. The Q matrix is a unit diagonal with two modifications. First, eigenvalues of the A matrix which have a value greater than the foldover frequency are given minimal weighting. The final implementation of the controller is time-discretized with a sampling frequency of $f = 20$ Hz, so the foldover frequency computed by the formula $(f/2)^{2PI}$ is 62.8 radians/second. The eigenvalue at -60.80 is close to the foldover frequency and is therefore weighted lightly to minimize control effort applied to the eigenvalue frequency. The weighting matrix Q takes the form

$$Q = \begin{bmatrix} 1 & 0 & 0 & 0 & 0 & 0 \\ 0 & 1 & 0 & 0 & 0 & 0 \\ 0 & 0 & 0.0001 & 0 & 0 & 0 \\ 0 & 0 & 0 & 1 & 0 & 0 \\ 0 & 0 & 0 & 0 & 1 & 0 \\ 0 & 0 & 0 & 0 & 0 & 1 \end{bmatrix} \quad (19)$$

The second modification to the unit diagonal structure of Q allows the designer flexibility in selecting the optimal dynamics. The element Q_{11} is varied to provide greater weight on the integral error state and thus minimize tracking error. In addition to iterating Q_{11} to achieve desirable closed-loop performance and robustness, the scalar ρ is varied. In general, increasing the value of ρ increases penalty on the control and results in lower bandwidth designs, while conversely, a lower value of ρ produces higher bandwidths because penalty on control effort is decreased. Figure 8 presents various closed-position loop step responses corresponding to various LQ-based designs obtained by setting Q_{11} equal to 4 and iterating ρ . As the simulations indicate, the higher values of ρ result in closed-loop responses exhibiting slightly larger overshoots and longer settling times.

The final LQ-servo controller design chosen must achieve a desired bandwidth, step response overshoot, and settling time, and ensure satisfactory robustness properties. Robustness evaluation must take into account parameter changes in the rate loop model that do not directly correspond to changes in the forward gain of the position loop, which defines the classical characteristics of gain and phase margin. The final iteration results (based on the continuous time model) are presented below:

Q_{11}	ρ	k_1	k_2	k_3	k_4	k_5	k_6
4	10	0.6325	1.3417	0.0157	0.5338	0.6613	0.5270
Closed-loop poles, rad/sec: $-0.564 \pm 0.541j$, -2.4159 , $-8.7496 \pm 11.3605j$, -61.25							
Settling time: 5.7 sec							
Percent overshoot: 25.2 percent							

Figures 9, 10, and 11 show the open-loop and closed-loop frequency responses and the step response using the gain vector chosen above. The gain margin for this continuous time design is infinite and the phase margin is 65 deg. The tracking bandwidth is approximately 0.259 Hz. These values of the resultant LQ-servo design indicate that this optimal feedback vector yields a robust controller design.

V. The Kalman Filter Design

The Kalman filter design procedure consisted of selecting estimator dynamics and computing the filter gain vector. The integral-of-position error is easily obtained in real time by numerical integration, therefore a fifth-order Kalman filter was designed using the continuous plant model of Eq. (1) (excluding the first equation). Presently, the encoder feedback to the

estimator is assumed to be a smooth DC signal and no convenient mathematical model is available to characterize any associated noise. Thus the measurement noise intensity Θ can be utilized as a parameter in the filter design. Obviously, the different optimal gain vectors L will result for each choice of the filter parameters Θ and the process noise intensity matrix Ξ , which are both defined by Eq. (9). In this design the Loop Transfer Recovery (LTR) method is used to conveniently characterize these noise statistics of the stochastic plant model (Eq. 8).

A formal discussion of the LTR method is given in [6, 7], where it is applied to multivariable-error-only control systems in conjunction with LQR designs to form so-called LQG/LTR feedforward compensators. Here, in the iteration process of calculating and evaluating the optimal filter gains, the results of the LTR method are used to effectively reduce the parameterization to one scalar variable μ . The method defines the noise intensities to be

$$\begin{aligned}\Xi &\triangleq BB^T \\ \Theta &\triangleq \mu I\end{aligned}\quad (20)$$

The design parameter is varied and the PC-based control system package PROGRAM CC is used to solve the resulting filter algebraic Riccati equation and compute L . The Kalman filter performance is based on position response, estimator error dynamics, and noise rejection ability. The LQR and filter design are combined to form the LQG controller, and its position response should display the same performance as discussed for the LQ servo. The error dynamics should have adequate speed of response and minimal overshoot. The noise rejection of the LQG controllers is evaluated through simulations which include nonlinear plant dynamics, antenna structural dynamics, and encoder and D/A quantization effects. Several iterations of μ were made and the final Kalman filter design was chosen to be the following

μ	L_1	L_2	L_3	L_4	L_5	L_6
5	0.00	0.4118	0.00005	0.00311	-0.00048	0.04912
Closed-loop filter poles, rad/sec:				-0.4045, -2.5146, -8.9027 \pm 11.4776j, -61.2521		

VI. Simulation Results

The final implementation of the LQG controller is a time-discretized form. The linear system matrices A and B of Eq. (18) are transformed from the continuous time domain to the discrete (sampled data) time domain via sampling described by

a zero-order hold to produce the necessary discrete time system matrices. The computations of the discrete system matrices are based on a specific (50-msec) sample interval and negligible time delay between each encoder input and the corresponding rate command output. Both LQ and Kalman filter gains designed for the continuous plant model (Eq. 18) are used with the discrete system matrices in the controller algorithm. Through simulations, the difference between the system response of the LQG controller with both the continuous and discrete state-space matrices has been shown to be negligible. Readers are referred to [8] for a more in-depth review of the implementation of the digital computer-based controller.

Simulations for the continuous linear antenna model with the final discretized LQG controller are presented in Figs. 12–15. Shown are the position, position estimation error, and rate input command responses for a 10-mdeg-step input with zero initial conditions. The position response exhibits the same performance as that of the LQ-servo response of Fig. 11 except for a slight lag due to the digitized controller. The estimation error response of Fig. 13 is due to the discretization of the controller and exhibits a desired speed of response and minimal error overshoot. The commanded rate of Fig. 14 is an ideal smooth, decreasing function.

A more accurate performance evaluation is based on the nonlinear simulation models developed in [9]. The results for a 10-mdeg-step input are shown in Figs. 15–17, where now the position is the output of a 20-bit encoder, the estimation error is the difference between encoder output and estimated position, and the commanded rate is equivalent to the output of the D/A converter. The position response of Fig. 15 illustrates the encoder quantizing effects and additional small time lags (at time zero and at 2.8 sec) due to the friction associated with the hydraulic motor and gear reducer. However, performance characteristics are not severely degraded from those shown for the linear system of Fig. 12. The position estimation error response of Fig. 16 shows roughly the same dynamics of the initial error transient as the linear case of Fig. 13. The peak estimation error is 0.6 mdeg, which corresponds to approximately two least-significant encoder bits (0.0003433 deg/bit) for the 20-bit encoders. Each new position quantization level causes a step in estimation error with peak magnitude of one encoder bit as shown. The rate command of Fig. 17 is seen to be a decreasing function that oscillates between D/A quantization levels. The overall performance of this selected LQG controller is deemed satisfactory.

VII. Summary

The Linear Quadratic Gaussian (LQG) optimal control method has been presented and applied to develop a new type-II, state-feedback antenna position controller. Theory on

the controller and state estimation techniques (specifically the Linear Quadratic Regulator and Kalman filter), which when combined make up the LQG design, was presented. A simplified experimental transfer function model was developed and mapped into a diagonal canonical set of state equations. The model was then augmented to include position and integral-of-position to form the final design plant model. Next an LQR was designed for this system and adapted for command following; the result is the so-called LQ servo. Finally, a new method for choosing the Kalman filter gains using the Loop Transfer Recovery method was presented. Performance specifications dictated the selection of the final gain vectors. Linear and nonlinear simulation results were presented.

VIII. Potential Improvements

The final LQG controller gain selections were based on performance specifications. However, design methods for the

dynamic plant estimator can be improved further. Investigations are needed which will determine the estimator design criteria which take into account encoder quantization effects. Given this, the systematic LQG design process can be reapplied. Also, LQG/LTR error-only controllers as discussed in [6] should be developed for the precision mode of operation and be simulated against the current LQG controllers to evaluate any performance gains. The motivation for such an effort is that the Kalman filter (which estimates antenna rate and higher derivatives in precision mode) will now be driven by autocollimator measurements instead of encoder readings. Thus, quantization errors associated with the axis encoders can be avoided and high-resolution estimates based on the autocollimator signals will result. Both future position controller and estimator design work would utilize currently known values of the system nonlinearities, structure dynamics test data, estimates of modeling errors, and system component/disturbance stochastic models.

Acknowledgments

The authors would like to thank Jeff Mellstrom and Robert Hill for their help with the system simulations and extensive theoretical discussions.

References

- [1] J. A. Nickerson, "A New Linear Quadratic Optimal Controller for the 34-Meter High Efficiency Antenna Position Loop," *TDA Progress Report 42-90*, vol. April-June 1987, Jet Propulsion Laboratory, Pasadena, California, pp. 136-147, August 15, 1987.
- [2] G. F. Franklin and J. D. Powell, *Digital Control of Dynamic Systems*, Reading, Massachusetts: Addison-Wesley Publishing Co., 1980.
- [3] A. E. Bryson, Jr. and Y. Ho, *Applied Optimal Control*, Waltham, Massachusetts: Balisdehl Publishing Co., 1969.
- [4] H. Kwakernaak and R. Sivan, *Linear Optimal Control Systems*, New York: John Wiley and Sons, Inc., 1972.
- [5] K. J. Astrom and B. Wittenmark, *Computer Controlled Systems: Theory and Design*, Reading, Massachusetts: Addison-Wesley Publishing Co., 1980.
- [6] G. Stein and M. Athans, "The LQG/LTR Procedure for Multivariable Control Design," *IEEE Trans. Automatic Control*, vol. AC-32, no. 2, pp. 105-114, February 1987.

- [7] J. C. Doyle and G. Stein, "Multivariable Feedback Design: Concepts for a Classical/Modern Synthesis." *IEEE Trans. Automatic Control*, vol. AC-26, pp. 4-16, February 1981.
- [8] R. E. Hill, "A Modern Control Theory Based Algorithm for Control of the NASA/JPL 70-Meter Antenna Axis Servos," *TDA Progress Report 42-91*, vol. July-September, Jet Propulsion Laboratory, Pasadena, California, pp. 285-294, November 15, 1987.
- [9] R. E. Hill, "Dynamic Models for Simulation of the 70-M Antenna Axis Servos," *TDA Progress Report 42-95*, vol. July-September 1988, Jet Propulsion Laboratory, Pasadena, California, pp. 32-50, November 15, 1988.

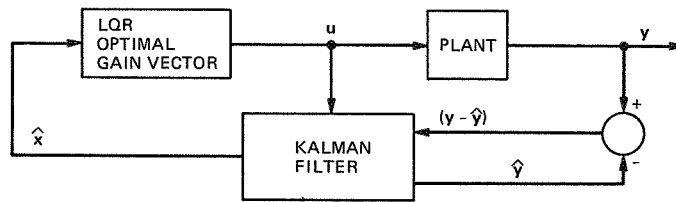


Fig. 1. State feedback with a Kalman estimator for a continuous time regulator.

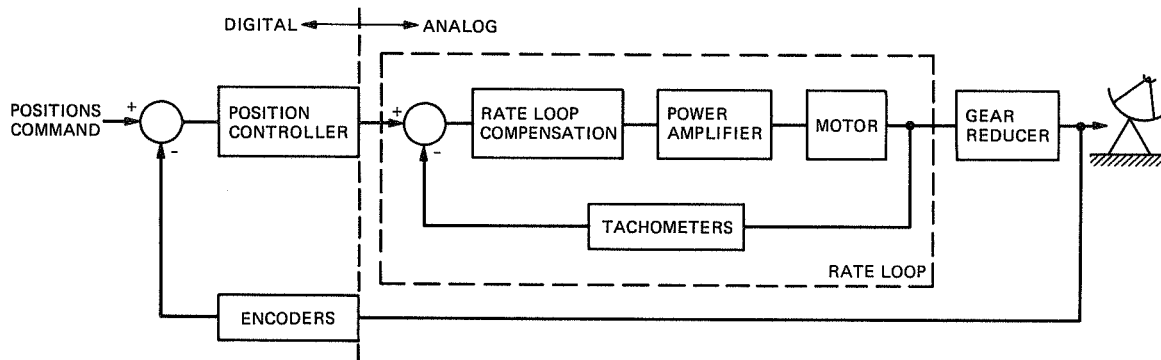


Fig. 2. Rate loop model.

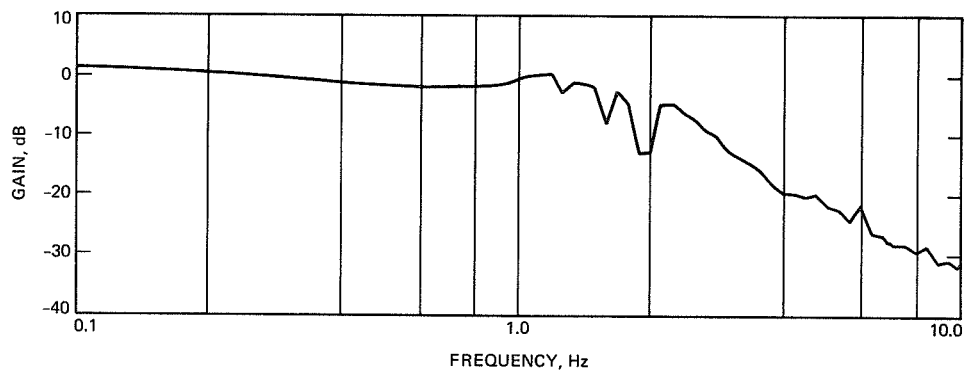


Fig. 3. DSS-14 azimuth rate loop gain response.

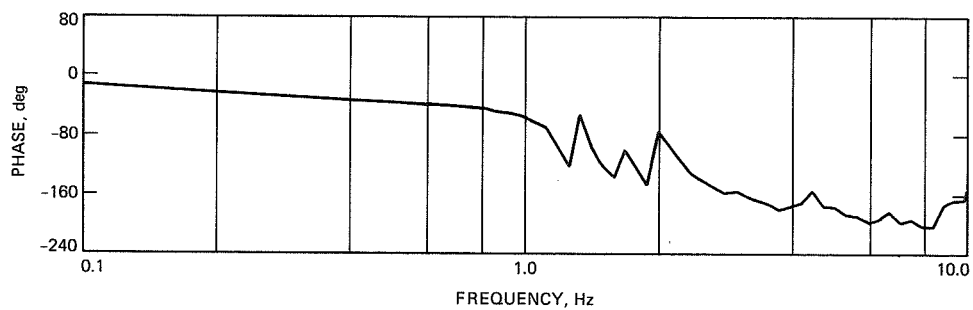


Fig. 4. DSS-14 azimuth rate loop phase response.

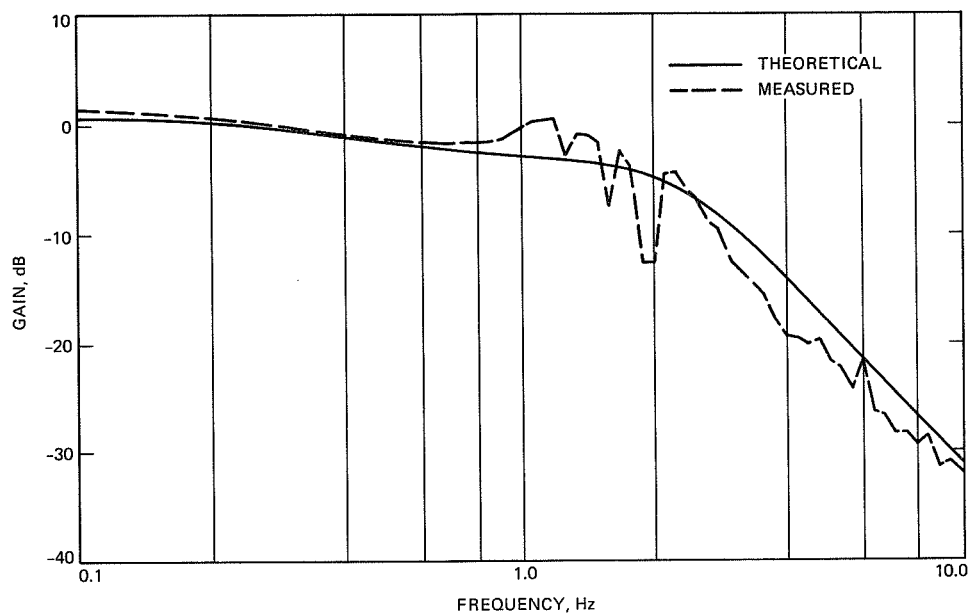


Fig. 5. Comparison of measured and theoretical gain response.

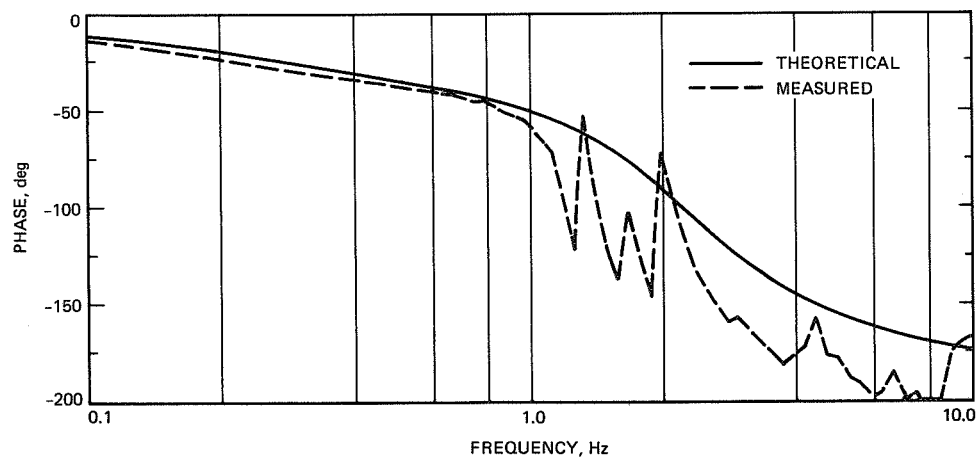


Fig. 6. Comparison of measured and theoretical phase response.

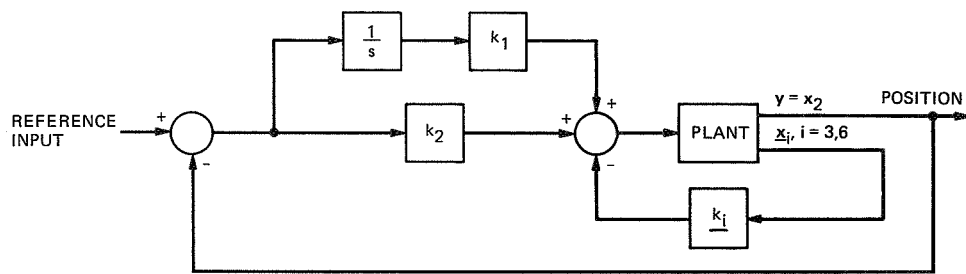


Fig. 7. Visualization of LQ servo.

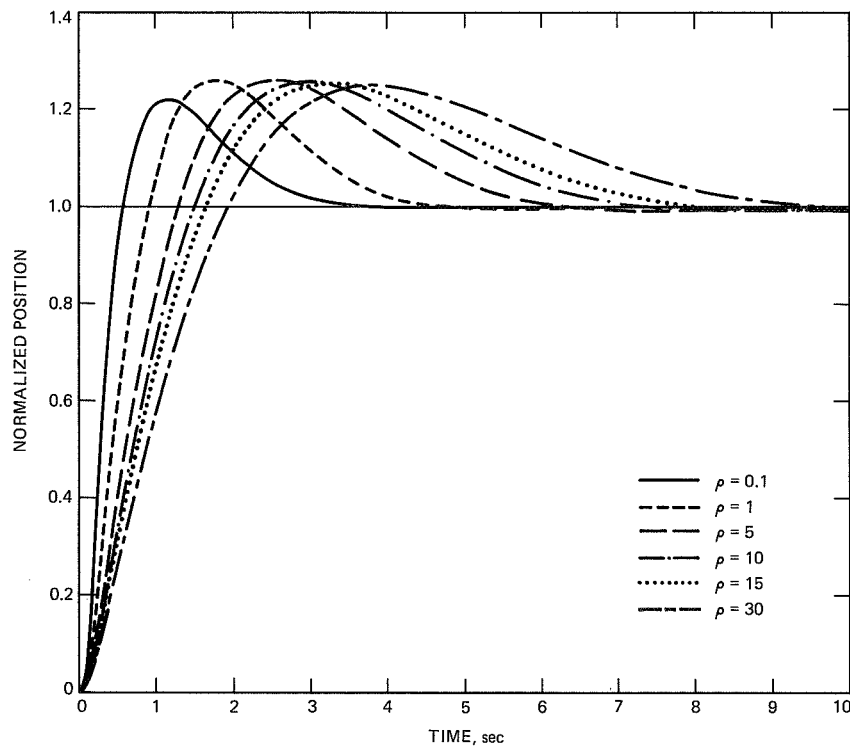


Fig. 8. Normalized step responses for $Q_{11} = 4$.

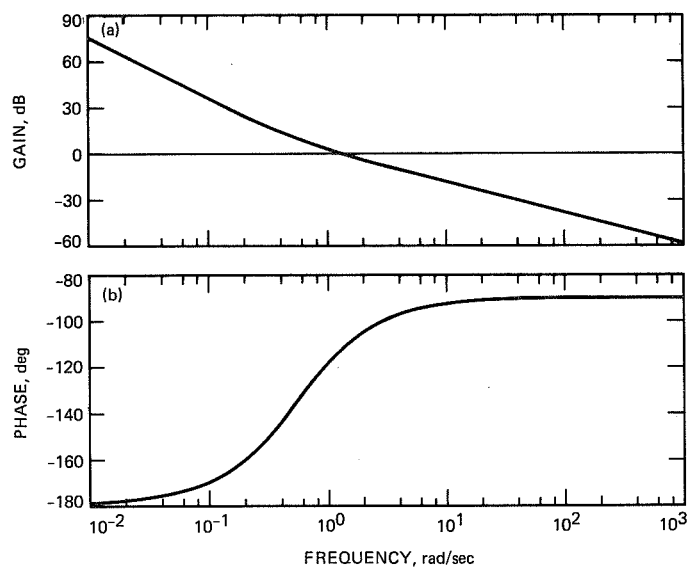


Fig. 9. Open-loop frequency responses for final LQ-servo design: (a) gain, and (b) phase.

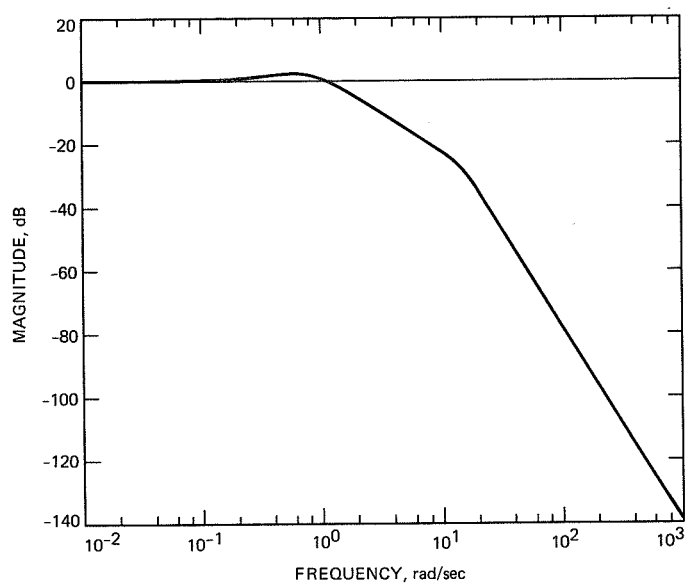


Fig. 10. Closed-loop Bode magnitude plot for final LQ-servo design.

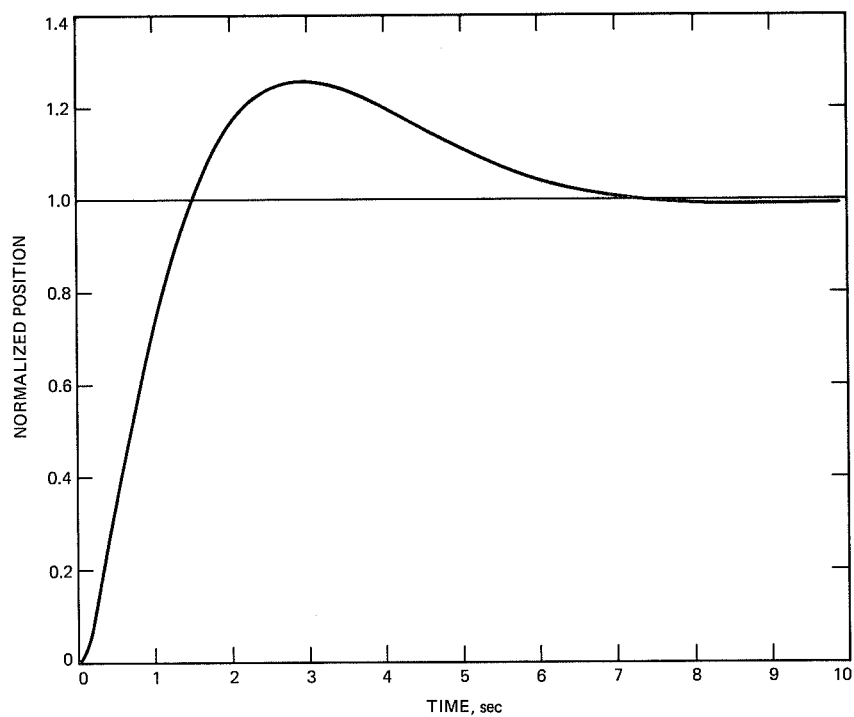


Fig. 11. LQ-servo step response.

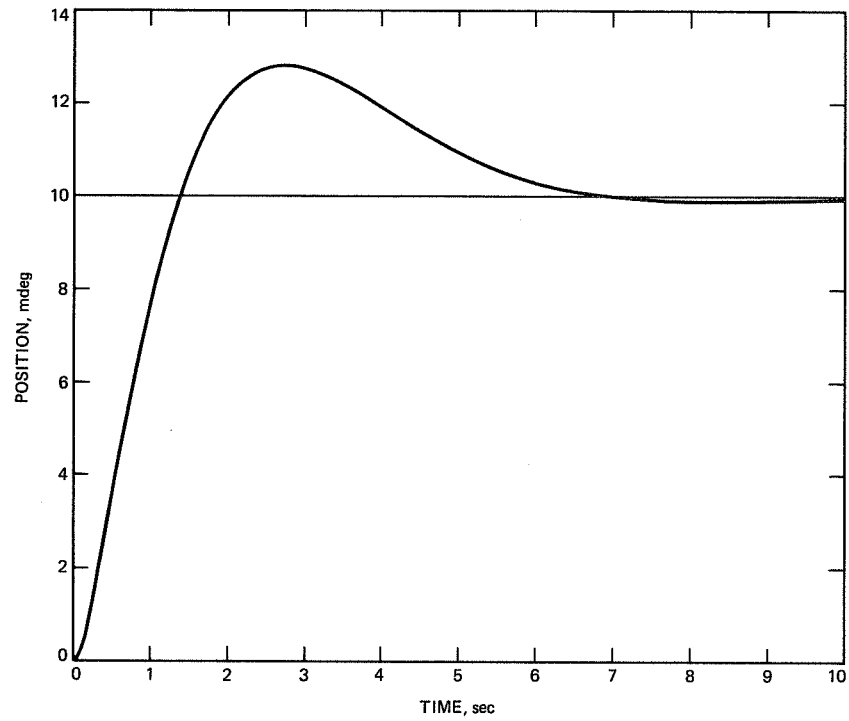


Fig. 12. LQG step response.

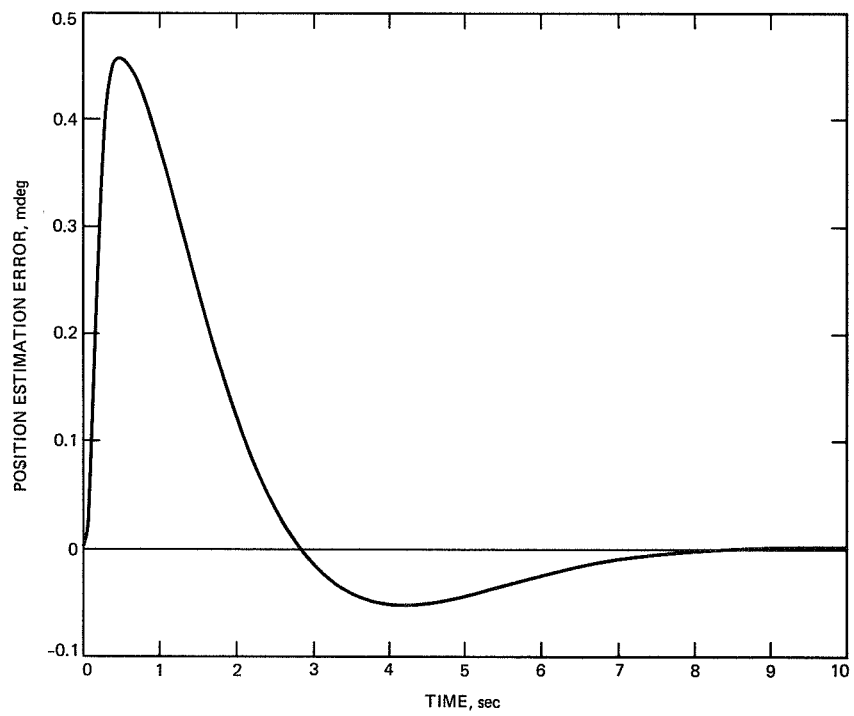


Fig. 13. LQG position estimation error.

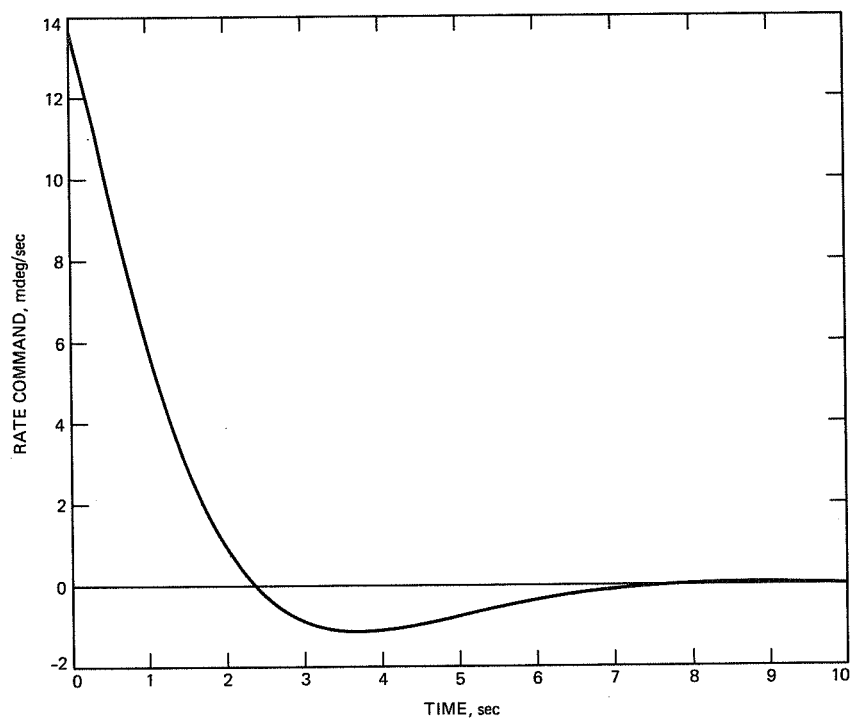


Fig. 14. LQG rate command.

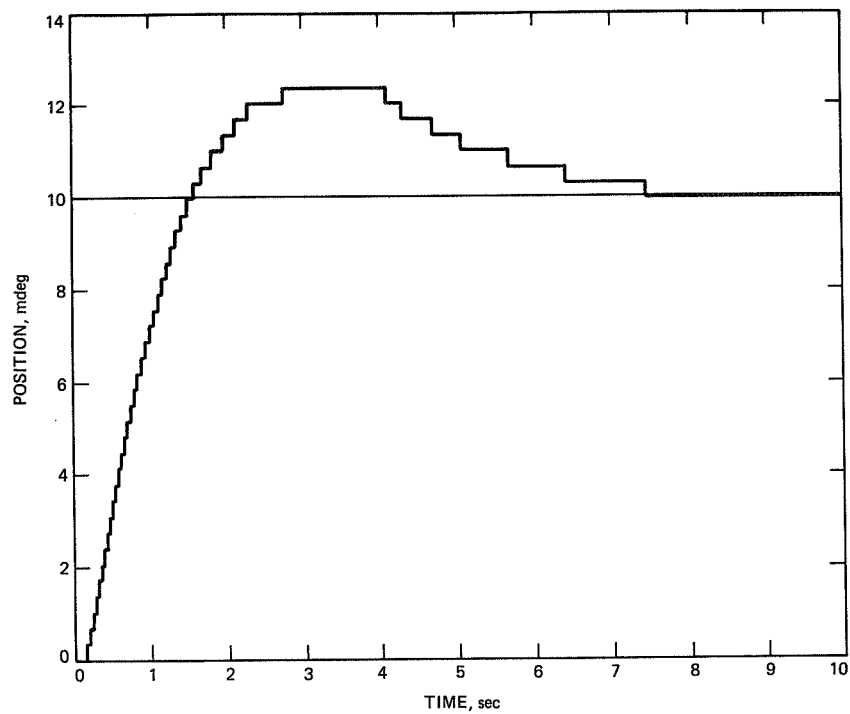


Fig. 15. Nonlinear position response.

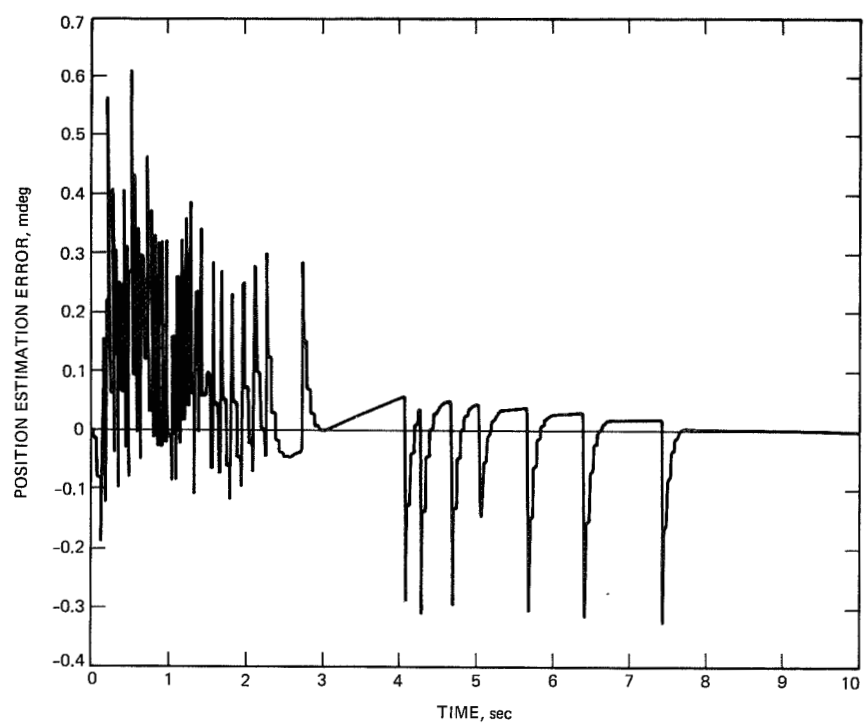


Fig. 16. Nonlinear position estimation error.

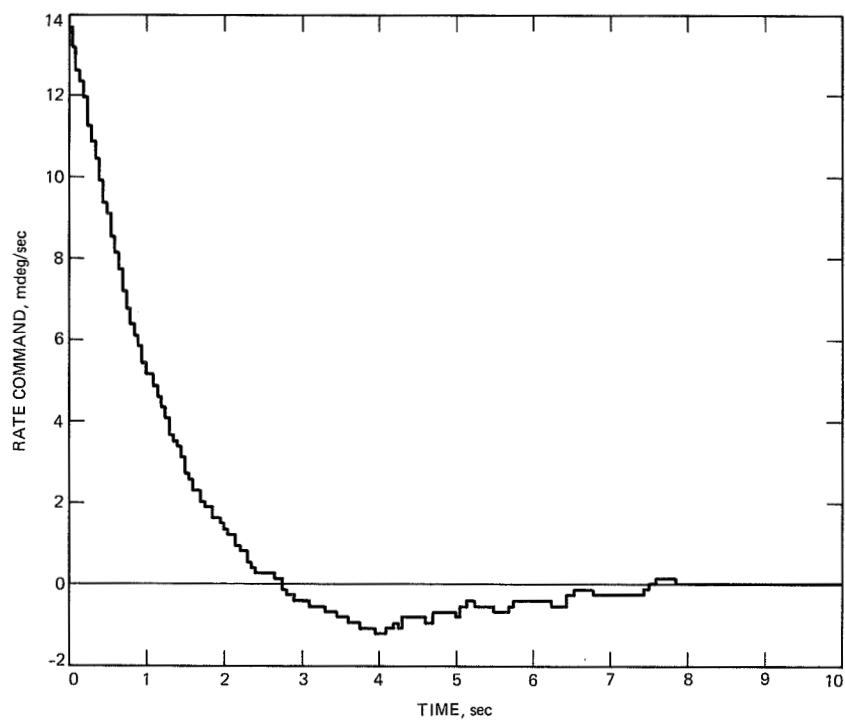


Fig. 17. Nonlinear rate command.

Precision Pointing Compensation for DSN Antennas With Optical Distance Measuring Sensors

R. E. Scheid

Guidance and Control Section

The pointing control loops of DSN antennas do not account for unmodeled deflections of the primary and secondary reflectors. As a result, structural distortions due to unpredictable environmental loads can result in uncompensated boresight shifts which degrade pointing accuracy.

The design proposed here can provide real-time bias commands to the pointing control system to compensate for environmental effects on pointing performance. The bias commands can be computed in real time from optically measured deflections at a number of points on the primary and secondary reflectors. Computer simulations with a reduced-order finite-element model of a DSN antenna validate the concept and lead to a proposed design by which a ten-to-one reduction in pointing uncertainty can be achieved under nominal uncertainty conditions.

I. Introduction

Current pointing system designs for DSN antennas do not incorporate effects beyond some reference plane which separates the control system from the antenna tipping structure, which includes the primary reflector, the secondary reflector, the quadripod, and the feedcone. For example, the DSN 70-meter antenna pointing system determines the main az-el pointing servo-drive error signals from a two-axis autocollimator mounted on the Intermediate Reference Structure (IRS) (see Fig. 1) [1]. By projecting a light beam onto a precision mirror mounted on the Master Equatorial (ME) and measuring the angular deviation of the reflected beam from the nominal orientation, the autocollimator determines an error signal which results from the nonparallelism of the two surfaces.

Because the tipping structure is outside the pointing control loop, uncompensated boresight shifts will typically result from the distortion of the structure due to environmental loads. Self-compensating effects in the structural design of the antenna limit the net peak pointing offset to approximately 100 millidegrees even though structural deformations of the components of the antenna system can individually produce equivalent pointing shifts of nearly 1 degree due to unmodeled environmental loads.

The schematic diagram in Fig. 2 illustrates the effect of structural distortion on pointing capability. According to design specifications, the axes of the main reflector paraboloid and the subreflector hyperboloid lie on an axis normal to the IRS, which passes through the vertex of the paraboloid. As indi-

cated by the broken line, environmental forces which distort the structure prevent rays reflected from different segments of the antenna from being focused onto the IRS reference axis. The design objective of a pointing error compensation system is to bias the pointing command so that the centroid of energy with respect to the target falls along the IRS reference axis. Other DSN antennas also employ compensator designs which do not correct for the effect of distortions due to unmodeled environmental loads on the tipping structure.

The principal environmental factors acting on the antenna are gravity, wind, and thermal effects. Gravity, the largest but most predictable load on the structure, causes sagging in the primary reflector and varies as a function of elevation angle. In addition, the gravitational effects lead to a displacement of the quadripod structure and a resultant displacement of the subreflector. The effects of gravity can be modeled by means of the finite element models which are available for DSN antennas, and, since the effects are predictable, the resulting boresight errors can be offset through a calibration process. The resulting look-up tables then provide an elevation pointing command bias signal to compensate for gravitationally induced pointing errors as a function of elevation angle. Wind and thermal effects on the structure lead to considerably less severe distortions but are also much less predictable.

By using look-up tables to bias the elevation pointing command to compensate for gravitational effects, a blind pointing capability of approximately 10 millidegrees is currently achievable in weather conditions that range from benign to moderately windy. With the recently completed upgrades to enlarge and improve the shape of the large DSN tracking antennas in combination with future plans to quadruple the upper operating frequency, it is desirable to improve pointing precision to 1 millidegree so as to fully realize the benefits of the upgrades for 32-GHz (Ka-band) operation.

The following presents a description and analysis of a real-time optical measurement and processing concept which delivers real-time pointing system bias commands to compensate for the effects of environmentally induced structural distortions. The concept requires optical measurements of the displacements of selected points on the primary and secondary reflectors relative to some reference coordinate system which lies at the base of the feedcone (e.g., the pointing reference plane in Fig. 2).

The Spatial High-Accuracy Position Encoding Sensor (SHAPES) system under development at JPL [2] was taken as the baseline sensor for the measurement system since it is capable of delivering multiple simultaneous high-speed (10 frames per second) ranging measurements with accuracies at the submillimeter level. SHAPES is a time-of-flight laser rang-

ing sensor which measures ranges from multiple sources to retroreflector targets placed at optically unobstructed locations. By means of a system of fiber-optic connections, each SHAPES sensor head can accommodate up to 24 targets, whose actual locations can be physically remote from the head. By means of triangulation, the range measurements taken from sensor heads fixed with respect to a known reference coordinate system can be combined to give two- and three-dimensional displacement coordinates for a given retroreflector. A discussion of the effects on the SHAPES system due to anticipated environmental uncertainties in DSN applications can be found in [3].

The discussion here deals only with the effects of unmodeled structural distortions beyond the reference coordinate plane (i.e., primary reflector, secondary reflector, quadripod, and feedcone) and assumes an a priori spatial knowledge of a reference coordinate system, the determination of which is a subject of current investigations in this technology. While others have approached the problem of real-time compensation by combining SHAPES technology with purely geometrical analysis [4], the treatment here is based on the solution of an underlying structural estimation problem combined with a geometrical synthesis. It is the framework of the estimation problem that provides for a meaningful quantitative evaluation of a given compensator design.

Section II begins with a general description of the proposed compensator design and continues with a more detailed discussion of the resulting structural and geometrical problems. Section III presents the simulation results based on a reduced-order finite-element model of a DSN antenna. Section IV outlines the conclusions of this work.

II. Problem Formulation

A. Compensator Design

The current compensator design is based on a calibration process for the effects of external loads such as gravity which can be predicted by finite-element (FE) modeling analysis (Fig. 3). The result is a tabulation of compensation signals which depends on the current attitude of the antenna tipping structure.

As a starting point for the calibration process, the modeled external forces are taken as static load inputs to a high-order finite-element model, and this results in a predicted estimate for the shape of the main reflector as well as location estimates for the subreflector and the feed. From this a parabolic fit routine is used to obtain a least-squares fit of the main reflector to a parabola of revolution. The effective boresight axis can then be determined as a linear combination of terms

which depends on the parameters of the best-fit parabola and the position of the other rigidly modeled structural components of the system [5]. More precisely, the boresight error is determined as a linear combination of the vertex shift and the rotation of the best-fit parabola, the lateral translation and rotation of the subreflector, and the lateral translation of the feed.

Such a control process is called open-loop in that there is no feedback from the state of the system. The development proposed here is a real-time structural-optical compensator (Fig. 4) which incorporates measurement data into the process of estimating the state of the structural system. The blocks of the design which indicate the parabolic best fit and the boresight determination can be used as before. The crucial block of this real-time compensator design is the structural-optical estimator which combines modeled responses to static loads with real-time measurement data (Fig. 5).

This block has the structure of a predictor-corrector system whereby the difference between the observed data and what can be predicted by a priori modeling leads to a correction which is added to the prediction derived before measurements are taken. Thus the dashed box in Fig. 5 denotes the structural predictor leading to the estimate which conceptually determines the current structural compensator (Fig. 4). The key ingredient in the structural-optical estimator is the filter gain which is determined by the solution to an optimization problem posed in the finite-element space.

In the next subsections, key components of the structural-optical compensator design are discussed in more detail. The structural-optical estimator is derived by means of a shape-determination problem posed in a finite-element space. Next the parabolic fit analysis is discussed and specialized to the two-dimensional case, which was the version used in the simulations subsequently undertaken.

B. Static Shape Determination

A number of important emerging applications in the technology of large space structures can be appropriately analyzed as statically loaded structural systems. This approach is applicable to systems where the time-dependent effects are negligible and where the relevant forces do not significantly excite dynamic behavior in the system. More generally, one can consider problem settings where the stiffness properties dominate the mass properties in determining the energy balances. Then a static response of the structure defines a reference configuration about which motions can be resolved with greater accuracy. In this context one can include applications where the time-varying effects of the model are changing slowly with respect to the scale on which operations must be carried out.

These quasi-static disturbances may, for example, include gravitational and thermal effects.

The introduction of statistical model errors allows the smearing of effects which have been ignored in the modeling or which occur on too fine a scale to be adequately modeled. This treatment of the system error distinguishes this approach from purely dynamic treatments of the problem. As a result the observational data can be statistically referenced to a plant, and questions regarding the validity of the estimates can be treated in a statistical framework which includes modeling errors as well as observational errors. The approach developed here leads to a framework which is suitable for combining a variety of geometric and structural models with a variety of mechanical and electro-optical sensing systems.

Of particular interest are the many large space antenna systems such as the DSN antennas. Performance requirements in communications and radiometry call for antennas with increasingly large diameters and surface-error requirements far beyond current capabilities.

This section summarizes the basic analysis which supports the static shape determination algorithms. This approach to shape estimation is part of an integrated methodology combining the techniques of modeling, identification, and estimation for static control of distributed systems. A more complete discussion of this framework is given in [6] and [7].

Let the state variable be given by \vec{u} . The models considered have the general form

$$A\vec{u} = C\vec{f} + B\vec{\omega} \quad (1)$$

$$\vec{y} = H\vec{u} + F\vec{\eta} \quad (2)$$

Here A is an operator representing the system model. The preliminary analysis can begin with coarse geometric models which are suitable for resolving overall features. More detailed resolutions are then obtained by taking A to be a stiffness matrix. This type of fine-scale resolution can be idealized by taking A to be an invertible self-adjoint elliptic differential operator defined over some spatial domain. The operator A is assumed to be invertible with inverse Φ ; this gives

$$\Phi A = I$$

where I is the identity. The two terms on the right-hand side of Eq. (1) respectively represent the modeled and unmodeled loads on the system. In particular C is an operator that characterizes the relevant deterministic forces, while B is an operator that characterizes the process errors that influence the state.

The vector \vec{y} represents an observation of the system (i.e., a set of measurements). H is an operator that characterizes the state-to-observation map. It is assumed that the observation space has dimension N_s which corresponds to a finite-dimensional sensing scheme. The second term on the right-hand side of Eq. (2) represents the measurement errors present in the observation \vec{y} . The integrated form of the observation equation is given by

$$\vec{y} = H\Phi C\vec{f} + H\Phi B\vec{\omega} + F\vec{\eta}$$

There are three inner-product spaces of primary interest: the input space S_1 to which the process error $B\vec{\omega}$ and the deterministic input $C\vec{f}$ belong; the state space S_2 containing the state \vec{u} ; and the measurement space S_3 where the data \vec{y} and the observation error $F\vec{\eta}$ belong. The inner product between two arbitrary elements u and v in the space S_i is denoted by $\langle u, v \rangle_i$ or by the simpler notation $u * v = \langle u, v \rangle_i$. Similarly, uv^* denotes an outer product. The corresponding norms are given by $\| \cdot \|_i$ or, when the context is clear, by the simpler notation $\| \cdot \|$.

The appropriately dimensioned operators B and F model the statistical influence of the process error and the measurement error; these errors, ω and η , form the model error vector

$$\xi = (\omega, \eta)$$

which represents spatial white noise and is characterized by the covariance operator

$$E(\xi \xi^*) = I$$

where $E(\cdot)$ denotes the expectation operator. More precisely, for $x_1 \in S_1$ and $x_3 \in S_3$, one has

$$E[\vec{\omega}] = 0 \quad E[\langle \vec{x}_1, \vec{\omega} \rangle_1 \vec{\omega}] = \vec{x}_1$$

$$E[\vec{\eta}] = 0 \quad E[\langle \vec{x}_3, \vec{\eta} \rangle_3 \vec{\eta}] = \vec{x}_3$$

The limiting cases $\|B\| \rightarrow 0$ and $\|F\| \rightarrow 0$ respectively represent the assumptions of perfect modeling and perfect measurements.

The abstract quantities in Eqs. (1) and (2) take on relevant physical meanings in the context of the application under consideration. Here the state \vec{u} represents the elastic deformation of the antenna tipping structure as modeled by A , a finite-element stiffness matrix. The modeled forces $C\vec{f}$ are restricted to gravity only while the process-error term $B\vec{\omega}$ represents all unmodeled environmental loads as well as inac-

curacies in the finite-element model. The vector of observations \vec{y} results from the sampling of the state by the measurement system (i.e., SHAPES), which is characterized by the state-to-observation map H and the measurement error term $F\vec{\eta}$.

The preceding assumptions lead to an appropriate framework for the analysis of minimum variance estimators of the state. Here the expected observation \vec{m} is characterized by

$$\vec{m} = H\Phi C\vec{f}$$

$$E[\vec{y}] = \vec{m} \quad E[(\vec{y} - \vec{m})(\vec{y} - \vec{m})^*] = HR_\omega H^* + R_\eta$$

and the expected process and measurement covariances R_ω and R_η

$$R_\omega = \Phi B B^* \Phi^* \quad R_\eta = F F^* \quad (3)$$

The resulting formulas are similar to the typical Kalman gain formulations used in the analysis of dynamical systems [8]. The minimum-variance estimate u_{est} has the form

$$\vec{u}_{est} = \vec{u}_o + g(\vec{y} - \vec{m})$$

$$\vec{u}_o = C\vec{f}$$

where the gain g is given by

$$g = R_\omega H^* (R_\eta + H R_\omega H^*)^{-1}$$

Thus, as illustrated in Fig. 5, the structural-optical estimator acts as a predictor-corrector scheme where the prediction comes from the modeled value of the state and where the correction is determined by the discrepancy between the modeled state and the actual measurements.

The covariance operator associated with the estimation error is given by

$$P = R_\omega - R_\omega H^* (R_\eta + H R_\omega H^*)^{-1} H R_\omega \quad (4)$$

The covariance then can be used to determine the expected error before and after measurements:

$$\begin{aligned} E[\|u - u_o\|^2] &= \text{tr}[R_\omega] \\ E[\|\vec{u} - \vec{u}_{est}\|^2] &= \text{tr}[P] \end{aligned} \quad (5)$$

From Eqs. (3), (4), and (5) it follows that

$$E [\| \vec{u} - \vec{u}_{est} \|^2] < E [\| \vec{u} - \vec{u}_0 \|^2]$$

That is, the incorporation of measurements reduces the expected error in the estimate of the state (i.e., the shape of the antenna tipping structure).

In the case where A represents a finite-element stiffness matrix, a number of static loading problems must be solved in order to approximate the gain and the covariance. For example, when the state-to-observation map H returns point-values of the state, one needs to compute fundamental solutions which correspond to unit static loads at the observed points.

One can also consider possibilities for recursive batch processing of data sets obtained by means of different sensing strategies. For example, Eq. (2) can be replaced by two sets of observations:

$$\begin{aligned} \vec{y}_1 &= H_1 \vec{u} + F_1 \vec{\eta}_1 \\ \vec{y}_2 &= H_2 \vec{u} + F_2 \vec{\eta}_2 \end{aligned}$$

An analysis of the second-order statistics of the related estimation error can also be conducted. Such an approach was implemented in [9] to combine optical measurements with data taken from radiation patterns to obtain optimal estimates for antenna surface deformations.

C. Parabolic Fit Analysis

The problem of fitting a reflector deformation model with many degrees of freedom to a parabola of revolution has been treated for DSN applications elsewhere in detail (see, for example, [10], [11]). The problem is generally treated in a least-squares formulation about the undisturbed dish, and the minimization is carried out with respect to the sums of squares of the pathlength errors associated with each point in the discretization. It can be shown that the pathlength error at a point can be trigonometrically related to the normal component of the surface error (cf. Eq. (7)). Here is a summary of the analysis when specialized to two spatial dimensions. The relevant equation is

$$z = \frac{y^2}{4f}$$

$$-1 \leq y \leq 1$$

where the coordinates y and z and the focal parameter f have been normalized by the radius of the dish.

The grid $G = \{(y_i, z_i)\}$ is chosen so that the deformation can be represented sufficiently accurately by these point values. For this application the y_i -values are the nodal locations of the finite-element model, and the corresponding z_i -values are the displacements at the nodes. The differential distortion of the parabola is represented by the so-called homology parameters $\vec{h} = (h^{(1)}, h^{(2)}, h^{(3)}, h^{(4)})^T$ where

$$\begin{aligned} h^{(1)} &= \text{shift in vertex (y-coordinate)} \\ h^{(2)} &= \text{shift in vertex (z-coordinate)} \\ h^{(3)} &= \text{rotation about origin in the } y/z \text{ plane} \\ h^{(4)} &= \text{relative change in focal length } (\Delta f/f) \end{aligned}$$

The analysis is very similar in the three-dimensional case, where there are two additional homology parameters (one for the shift in vertex, one for the rotation).

Retaining only first-order terms, one can compute the differential distortion at the point (y, z) :

$$\begin{pmatrix} h^{(1)} \\ h^{(2)} \end{pmatrix} + \begin{bmatrix} 1 & -h^{(3)} \\ h^{(3)} & 1 \end{bmatrix} \begin{pmatrix} y \\ z \end{pmatrix} + \begin{pmatrix} 0 \\ -zh^{(4)} \end{pmatrix}$$

where geometrically these three terms respectively represent the translation, rotation, and focal shift of the parabola. Thus the differential displacement of the parabolic point is given by

$$\hat{C}(y, z) \vec{h}$$

where the 2×4 matrix $\hat{C}(y, z)$ is defined by

$$\hat{C}(y, z) = \begin{pmatrix} 1 & 0 & -z & 0 \\ 0 & 1 & y & -z \end{pmatrix}$$

The normal to the surface at (y, z) is given by

$$\vec{n}(y, z) = \frac{1}{\sqrt{\frac{z}{f} + 1}} \begin{pmatrix} -y \\ \frac{z}{2f} \\ 1 \end{pmatrix}$$

Then projecting the deflection onto the normal gives

$$\hat{B}(y, z) = \vec{n}(y, z)^T \hat{C}(y, z) = \frac{1}{\sqrt{\frac{z}{f} + 1}} \left(\frac{-y}{2f}, 1, \left(\frac{yz}{2f} + y \right), -z \right)$$

The deflection at each point is also projected onto the normal direction

$$\rho(y, z) \vec{n}(y, z)$$

where $\rho(y, z)$ is a scalar.

It is now possible to form the normal equations on the grid G by defining the $N \times 4$ matrix

$$\hat{A} = \begin{bmatrix} \hat{B}(y_1, z_1) \\ \hat{B}(y_2, z_2) \\ \vdots \\ \hat{B}(y_N, z_N) \end{bmatrix}$$

and the N -dimensional vector

$$\vec{b} = \begin{pmatrix} \rho(y_1, z_1) \\ \vdots \\ \rho(y_N, z_N) \end{pmatrix}$$

This allows one to form the N -dimensional residual vector for the normal deflections

$$\vec{r} = \hat{A} \vec{h} - \vec{b}$$

The best-fit optimization problem is now posed as a minimization of the residual with respect to the norm

$$\|\vec{r}\|_W^2 = \vec{r}^T W \vec{r}$$

where W is an $N \times N$ symmetric positive definite matrix (see, for example, [12]). The resulting normal equations are given by

$$(\hat{A}^T W \hat{A}) \vec{h} = \hat{A}^T W \vec{b} \quad (6)$$

or equivalently

$$(\tilde{A}^T \tilde{A}) \vec{h} = \tilde{A}^T \vec{\tilde{b}}$$

$$\tilde{A} = W^{\frac{1}{2}} \hat{A}$$

$$\vec{\tilde{b}} = W^{\frac{1}{2}} \vec{b}$$

W can be chosen as a diagonal matrix

$$W = \text{diag} [w_1, w_2, \dots, w_N]$$

where w_i has the form

$$w_i = a_i \left(\frac{f}{f + z_i} \right) \quad (7)$$

Here a_i is the length (or area) associated with each point. The additional factor results in a minimization with respect to path length.

The solution of Eq. (6) is then given by

$$\begin{aligned} \vec{h} &= \hat{T} \vec{b} \\ \hat{T} &= (\hat{A}^T W \hat{A})^{-1} \hat{A}^T W \end{aligned} \quad (8)$$

Here the $4 \times N$ matrix \hat{T} is often called the pseudo-inverse.

III. Model Description and Simulation Results

The functional block diagram in Fig. 6 outlines the conceptual framework in which the boresight determination problem is treated in this article. The relevant synthesis problem focuses on the determination of three antenna boresights:

- (1) A gravitational boresight derived from a model for gravitational deformations combined with a parabolic fit.
- (2) A true boresight derived from a model for gravitational plus unmodeled deformations combined with a parabolic fit.
- (3) An estimated boresight derived from an estimator which integrates structural finite-element models, gravitational deformation models, sampled measurements of the true deformation vector, and a parabolic fit.

As has been previously noted, current boresight pointing technology is based on a calibration with respect to forces whose effects can be adequately predicted (e.g., gravity). However, this calibration process is less successful when the disturbance forces cannot be adequately modeled (e.g., thermal effects, wind, etc.). The subsequent simulations were intended to determine the requirements for a boresight estimator which, under nominal uncertainty conditions, would recover the true boresight to within 1 millidegree, a requirement beyond the capabilities of the current calibration process. The design parameters included the properties of the disturbance forces (modeled and unmodeled) as well as the requirements for the sensing configuration (number, placement, and accuracy). In

order to make the simulations more tractable, simplifications were introduced in the structural, geometrical, and statistical analyses.

For the structural analysis a reduced two-dimensional antenna deformation model was derived from a high-order finite-element model of a 34-meter DSN antenna (DSS-15). More precisely, two ribs were designated as the north and south ribs, and all deformations calculated from the three-dimensional model were projected onto this pair (see Fig. 7). The total number of nodal values retained was 26, and these were evenly divided between the two ribs.

For the geometrical analysis of the parabolic fit, the two-dimensional least-squares formulation given in Section II.B was implemented. In addition, only the third component of the homology vector ($h^{(3)}$) was used in the estimate of the boresight. This component, the rotation about the origin in the y/z plane, is the geometrical boresight of the best-fit parabola and corresponds to the largest term in the computation of the structural boresight [5]. Thus, in the spirit of the analysis of Section II.B this work focuses on the boresight errors associated with the structural deformations of the primary reflector, and attention is restricted to the dominant contribution. The other relevant components of the structural boresight noted in Section II.A (vertex shift of best-fit parabola, lateral translational and rotation of the subreflector, and lateral translation of the feed) could also have been included in the analysis, making the simulations somewhat more complex. Instead, the boresight errors associated with estimating these contributions were acceptably bounded. In particular, it was determined that the SHAPES system when combined with a charge-coupled device (CCD) angle-measuring camera is capable of measuring the subreflector position with sufficient accuracy so that the resulting uncertainty in the boresight is smaller than the errors considered here.

For the statistical analysis the weighting matrices for the process error and the measurement error were taken to be scalar:

$$\begin{aligned} F &= \sigma_\eta I \\ B &= \sigma_\omega I \end{aligned} \quad (9)$$

where I is the identity. More general forms for F and B could be used to characterize such features as a structural finite-element model which is less reliable at some nodes than at others, or a measurement system with some components that are more accurate than others.

The preceding assumptions lead to the following version of the formulations given in Section II:

$$A\vec{u} = C\vec{f} + \sigma_\omega\vec{\omega} \quad (10)$$

$$\vec{y} = H\vec{u} + \sigma_\eta\vec{\eta} \quad (11)$$

$$\beta = \hat{Q}\hat{T}\hat{N}\vec{u} \quad (12)$$

Here Eqs. (10) and (11) are simply Eqs. (1) and (2) combined with the simplification given by Eq. (9). In Eq. (12), \hat{N} is the mapping that projects the state (i.e., the deflection of the structure) onto the normal component. Then \hat{T} is the pseudo-inverse given in Eq. (8) which maps the normal deflections onto the vector of homology parameters \vec{h} . And finally, \hat{Q} maps the homology parameters onto the boresight value. In accordance with the simplifying assumptions outlined here, \hat{Q} is given by

$$\hat{Q} = [0, 0, 1, 0]$$

That is, \hat{Q} is a projection onto the third homology parameter ($h^{(3)}$), which denotes the rotation about the origin in the y/z plane. More generally, the dimension of β could be increased to account for the other rotational degree of freedom which must be treated in the full three-dimensional problem. Also, the input-space could be augmented to include the measured estimates of the subreflector and feedcone positions. By a principle of optimality for linear systems [8], the minimum-variance estimate for β can be written in terms of the minimum-variance estimate for \vec{u} as

$$\beta_{est} = \hat{Q}\hat{T}\hat{N}\vec{u}_{est}$$

The other statistical qualities are similarly transformed. Thus, with the definitions

$$\begin{aligned} \beta_o &= \hat{Q}\hat{T}\hat{N}\vec{u}_o \\ (\sigma_\beta^o)^2 &= E[(\beta - \beta_o)^2] \\ (\sigma_\beta^1)^2 &= E[(\beta - \beta_{est})^2] \end{aligned} \quad (13)$$

one can show the precise relationship between the state covariances (cf. Eqs. (3), (4)) and the boresight covariances as

$$\begin{aligned} (\sigma_\beta^o)^2 &= (\hat{Q}\hat{T}\hat{N})R_\omega(\hat{Q}\hat{T}\hat{N})^* \\ (\sigma_\beta^1)^2 &= (\hat{Q}\hat{T}\hat{N})P(\hat{Q}\hat{T}\hat{N})^* \end{aligned}$$

These quantities can be identified with the outputs of the block diagram in Fig. 6. Thus, the quantities β , β_o , and β_{est} respectively represent the true boresight, the modeled boresight, and the estimated boresight. The expected boresight errors before and after measurements are respectively given by σ_β^o and σ_β^1 . To these one can add a fourth boresight value

$$\tilde{\beta}_{est} = \beta_o + \hat{W} \hat{T}_{fit} \hat{N}_{fit} (\vec{y} - H \vec{u}_o)$$

Here β_o , \vec{y} , \vec{u}_o , and H are as previously given, the matrix \hat{N}_{fit} gives the normal projection at the observed points only, and the matrix \hat{T}_{fit} is the pseudo-inverse (cf. Eq. (8)) which carries out the parabolic fit with respect to the values at the observed points only. The quantity $\tilde{\beta}_{est}$ represent the boresight estimate which is obtainable by purely geometrical analysis. In correspondence to Eq. (13), one also has an expression for the covariance:

$$\begin{aligned} (\tilde{\sigma}_\beta^1)^2 &= E[(\tilde{\beta}_{est} - \beta)^2] \\ &= (\sigma_\omega)^2 (\hat{Q} \hat{T} \hat{N}) R_\omega (\hat{Q} \hat{T} \hat{N})^* \\ &\quad + (\sigma_\omega)^2 (\hat{Q} \hat{T}_{fit} \hat{N}_{fit}) R_\omega (\hat{Q} \hat{T}_{fit} \hat{N}_{fit})^* \\ &\quad + (\sigma_\eta)^2 (\hat{Q} \hat{T}_{fit} \hat{N}_{fit}) (\hat{Q} \hat{T}_{fit} \hat{N}_{fit})^* \\ &\quad - (\sigma_\omega)^2 (\hat{Q} \hat{T} \hat{N}) R_\omega (\hat{Q} \hat{T}_{fit} \hat{N}_{fit})^* \\ &\quad - (\sigma_\omega)^2 (\hat{Q} \hat{T}_{fit} \hat{N}_{fit}) R_\omega (\hat{Q} \hat{T} \hat{N})^* \end{aligned}$$

The simulations focused on the covariance analysis of the estimates. Thus, given the expected boresight error before measurements (σ_β^o), the number and placement of targets where measurements are taken (H), and the accuracy of the measurements (σ_η), one can calculate the expected boresight error of the estimates (σ_β^1 , $\tilde{\sigma}_\beta^1$). For the results presented in Fig. 8, the following specifications were made. First, the model error parameter σ_ω was chosen so that the expected error before measurements σ_β^o would be 10 millidegrees. The observation error parameter σ_η was taken as 50 micrometers, a value consistent with the capability of the SHAPES system [3]. The only additional specifications required are the number and placement of targets where the displacement values are measured. Thus, in Fig. 8 the quantities $\sigma_\beta^1(j)$ and $\tilde{\sigma}_\beta^1(j)$, where j is an even number, refer to the expected boresight errors with $j/2$ optimally located targets on each of the two ribs in the reduced-order antenna model. Here the optimization was carried out by evaluating all possible distinct target locations and choosing the set which gave the lowest values for the expected boresight error.

Thus, with a total of six optimally placed measurement points the structural-optical estimator achieves a ten-to-one reduction in the expected error of the estimated boresight. One should note that the structurally-based estimators are superior to the purely geometrical estimators, but they are not substantially better. This observation may be interpreted as being supportive of compensator designs based on real-time optical measurements. That is, the sophistication of the underlying estimator and the fidelity of the model may not be too important so long as measurements are available. The simulation results presented in Fig. 8 are the main quantitative outcome of this work; they demonstrate that under nominal uncertainty conditions a ten-to-one reduction in the boresight error can be achieved by integrating structural models, geometrical fitting analysis, and a real-time optical measurement system. Even though the underlying structural finite-element model may have a large dimension, the real-time computational requirements involve only matrix and vector operations where the relevant dimensions are determined by the number of measurements taken.

The results of a test case derived from the gravity model at horizon (elevation angle equals zero) are given in Fig. 9. To test the estimator's ability to recover the boresight from the measurement values only, the modeled gravitational boresight before measurements was taken to be zero ($\beta_o = 0$). For this trial the deflection was scaled to correspond to a 10-milli-degree offset in the boresight, and the measurement locations were evenly spaced on each of the two ribs in the model. (The tips of the ribs were always included as measurement locations.) The measurement error was taken to be zero ($\sigma_\eta = 0$). Thus, $\beta_{est}(j)$ and $\beta_{est}(j)$ are the estimated boresight offsets with j evenly spaced measurement locations.

This may be thought of as a worst-case scenario for the structurally-based estimator since the deflection is spatially biased (i.e., distorted in a preferred direction), and the estimators were designed to perform best with all distortion directions equally likely [6], [7]. Nevertheless, a ten-to-one reduction in the error is achieved. Again the geometrical estimators perform well with no structural information incorporated into the design.

Since the simple geometrical fit recovered the spatially biased component so well, this suggests that the two designs might be used in combination. First a simple geometrical fit can be performed to recover the spatially biased component, then a version of the structural-optical estimator can be implemented to obtain a finer resolution about this set point.

While additional simulations with the full three-dimensional model will be necessary to advance the design process, it is

already possible to estimate the number of measurements required to achieve a ten-to-one reduction in the pointing uncertainty. For example, two adequately resolved cross-sections would determine all the relevant parameters of a three-dimensional parabola of revolution (paraboloid). This would lead to a requirement of twelve measurements (six per cross-section). Another proposed baseline would require eighteen targets to similarly cover three cross-sections. This last design is motivated by the observation of three cross-sectional nodal lines on the main reflector of some DSN antennas; these nodal lines apparently lie on or near the best-fit paraboloid derived from the gravitational models (see, for example, [13]).

In Fig. 10 the key locations on the antenna for the measurement system are noted. The proposed design would include approximately three SHAPES sensor heads mounted on the quadripod near the subreflector. These sensor heads would return range measurements from the targets located on the main reflector, and triangulation methods would be used to recover the displacement values relative to the sensor heads. The connection from the sensor heads to the reference plane would be made by taking additional range measurements at targets located near the origin of the reference coordinate system (base of feedcone). Calculated error estimates indicate that an additional angle-measuring camera (CCD array) at the base of the feedcone would adequately measure the angular

displacement of the subreflector and the sensor heads from their nominal positions.

IV. Conclusions

The concept proposed and analyzed in this article combines a real-time measurement system, a structural estimator, and a parabolic fitting algorithm to determine DSN antenna pointing offsets resulting from unmodeled structural distortions. This pointing offset data can be used to generate real-time command biases to correct for pointing errors. Simulations with a reduced-order antenna finite-element model have demonstrated that a ten-to-one reduction in boresight uncertainty can be achieved. The concept requires optical measurements of the displacements of selected points on the primary and secondary reflectors relative to some reference coordinate system at the base of the feedcone.

This work represents one method of improving the pointing capabilities of DSN antennas by using the techniques of the spatially random analysis of static systems. As illustrated in Fig. 11, this approach is suitable for investigating many aspects of antenna analysis related to surface deformations. While this work mainly concerns the justification of algorithms which estimate the structural boresight of an antenna, other relevant problems concerning the analysis of rms surface errors and the synthesis of antenna radiation patterns also can be studied in this framework.

Acknowledgments

The author is indebted to C.-T. Chian for his essential contributions to the finite-element simulations. The author is also grateful to R. Levy and J. Cucchissi for many interesting discussions on the subject of this work.

References

- [1] M. D. Nelson, J. R. Schroeder, and E. F. Tubbs, "Optical Links in the Angle-Data Assembly of the 70-meter Antennas," *TDA Progress Report 42-92*, vol. October-December 1987, Jet Propulsion Laboratory, Pasadena, California, pp. 154-165, February 15, 1988.
- [2] J. McLauchlan, W. Goss, and E. Tubbs, "SHAPES: A Spatial, High Accuracy, Position Encoding Sensor for Space System Control Applications," *American Astronautical Society*, Publication 82-032, January 20, 1983.

- [3] N. Nerheim, "Effect of Atmospheric Turbulence on Precision Optical Measurements Used for Antenna Pointing Compensation," *TDA Progress Report 42-97*, Jet Propulsion Laboratory, Pasadena, California, this issue.
- [4] L. L. Schumacher and H. C. Vivian, "Antenna Pointing Compensation Based on Precision Optical Measurement Techniques," *TDA Progress Report 42-94*, vol. April-June 1988, Jet Propulsion Laboratory, Pasadena, California, pp. 135-144, August 15, 1988.
- [5] R. Levy, "Optimization of Antenna Structure Design," *Eighth Conference on Electronic Computation*, Houston, Texas, February 1983.
- [6] G. Rodriguez and R. E. Scheid, "Modeling, Estimation and Identification Methods for Static Shape Control of Flexible Structures," *AAS/AIAA Astrodynamics Specialists Conference*, Vail, Colorado, August 1985.
- [7] G. Rodriguez and R. E. Scheid, "An Integrated Approach to Modeling, Identification, Estimation and Control for Static Distributed Systems," *Proceedings of the Fourth IFAC Symposium on the Control of Distributed Parameter Systems*, Los Angeles, California, June 1987.
- [8] A. E. Bryson and Y.-C. Ho, *Applied Optimal Control*, Washington, D.C.: Hemisphere Publishing Company, 1975.
- [9] G. Rodriguez and R. E. Scheid, "Kalman-Like Estimation for Static Distributed Systems: Antenna Shape from Radiation Measurements," *Proceedings of the Fifth VPI & SU/AIAA Symposium on Dynamics and Control of Large Structures*, Blacksburg, Virginia, June 1985.
- [10] M. S. Katow, *Antenna Structures: Evaluation of Reflector Surface Distortions*, JPL Technical Report 32-1526, vol. 1, Jet Propulsion Laboratory, Pasadena, California, pp. 76-80, February 15, 1971.
- [11] M. S. Katow and L. W. Schmele, "Antenna Structures: Evolution Techniques of Reflector Distortions," in *Supporting Research and Advanced Development, Space Programs Summary 37-40*, vol. IV, Jet Propulsion Laboratory, Pasadena, California, pp. 176-184, August 31, 1966.
- [12] G. H. Golub and C. F. Van Loan, *Matrix Computations*, Baltimore, Maryland: The Johns Hopkins University Press, 1983.
- [13] Tracking and Data Acquisition Organization (Technical Staff), "The NASA/JPL 64-Meter-Diameter Antenna at Goldstone, California Project Report," *Technical Memorandum 33-671*, Jet Propulsion Laboratory, Pasadena, California, July 15, 1974.

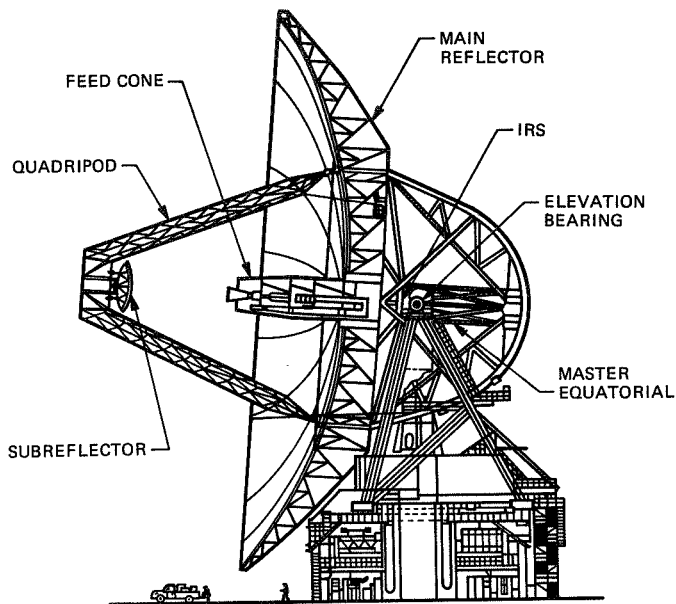


Fig. 1. 70-meter DSN antenna.

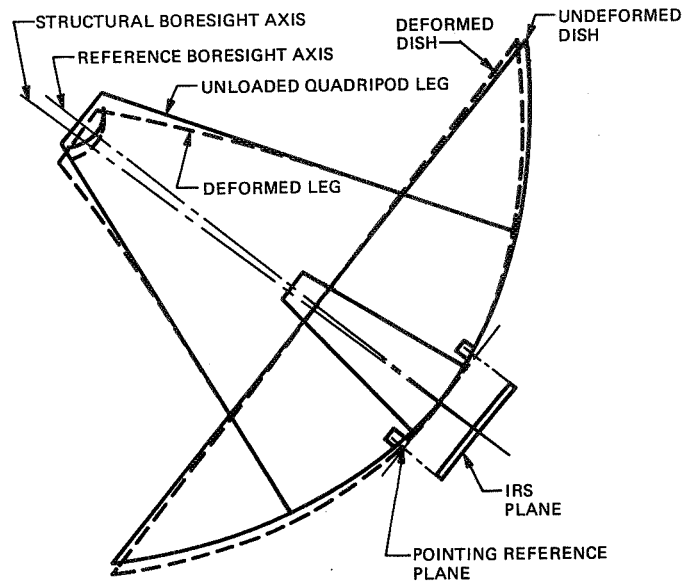


Fig. 2. Antenna deformation under loads.

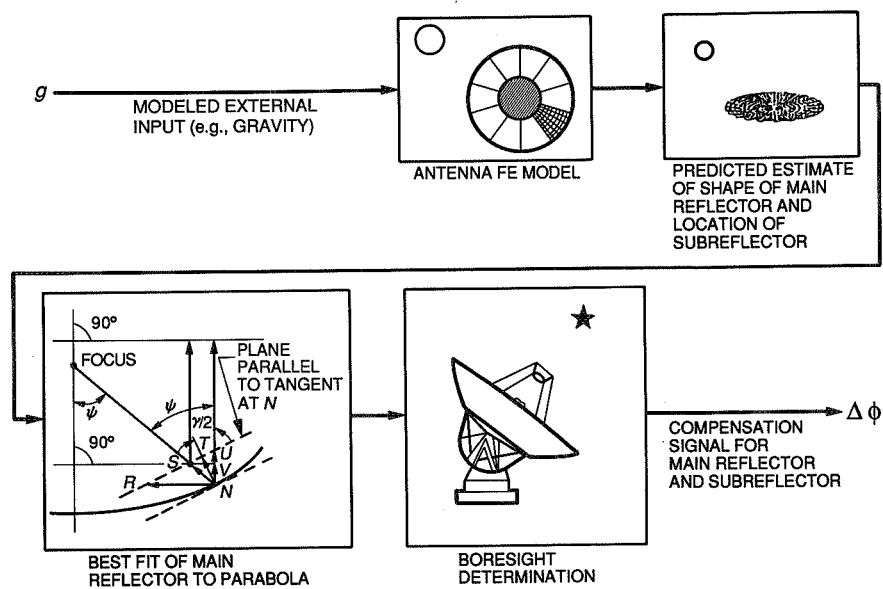


Fig. 3. Current compensator design.

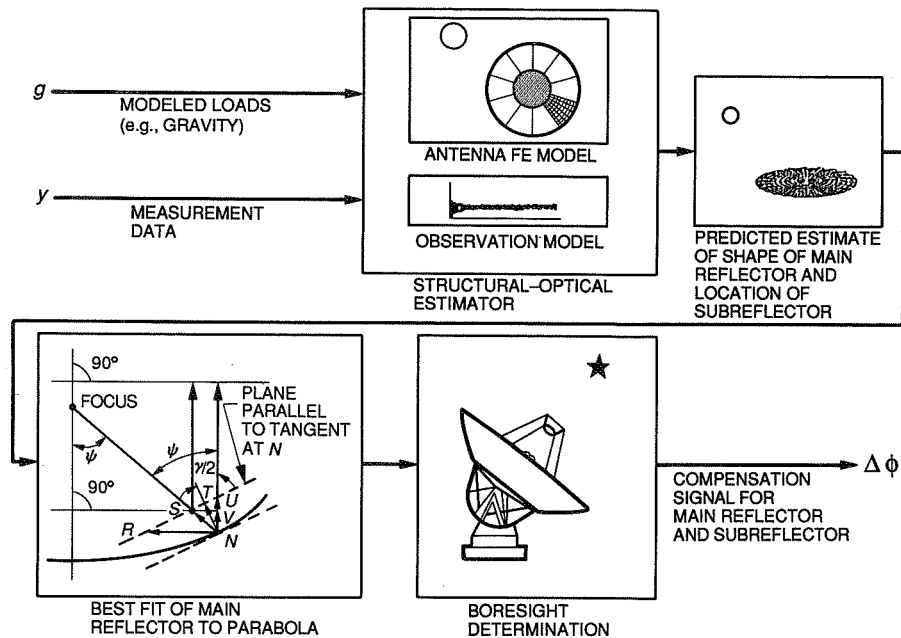


Fig. 4. Structural-optical compensator.

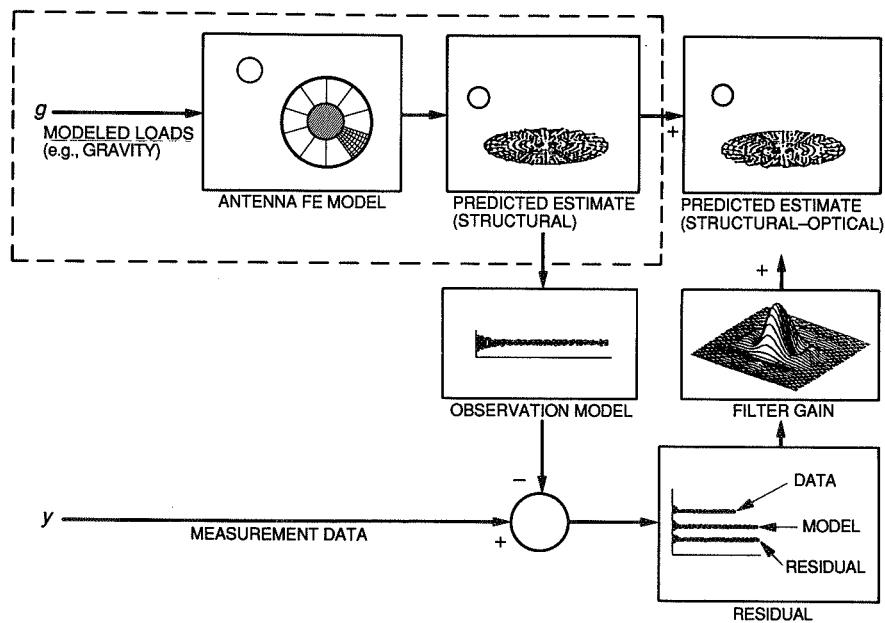


Fig. 5. Structural-optical estimator.

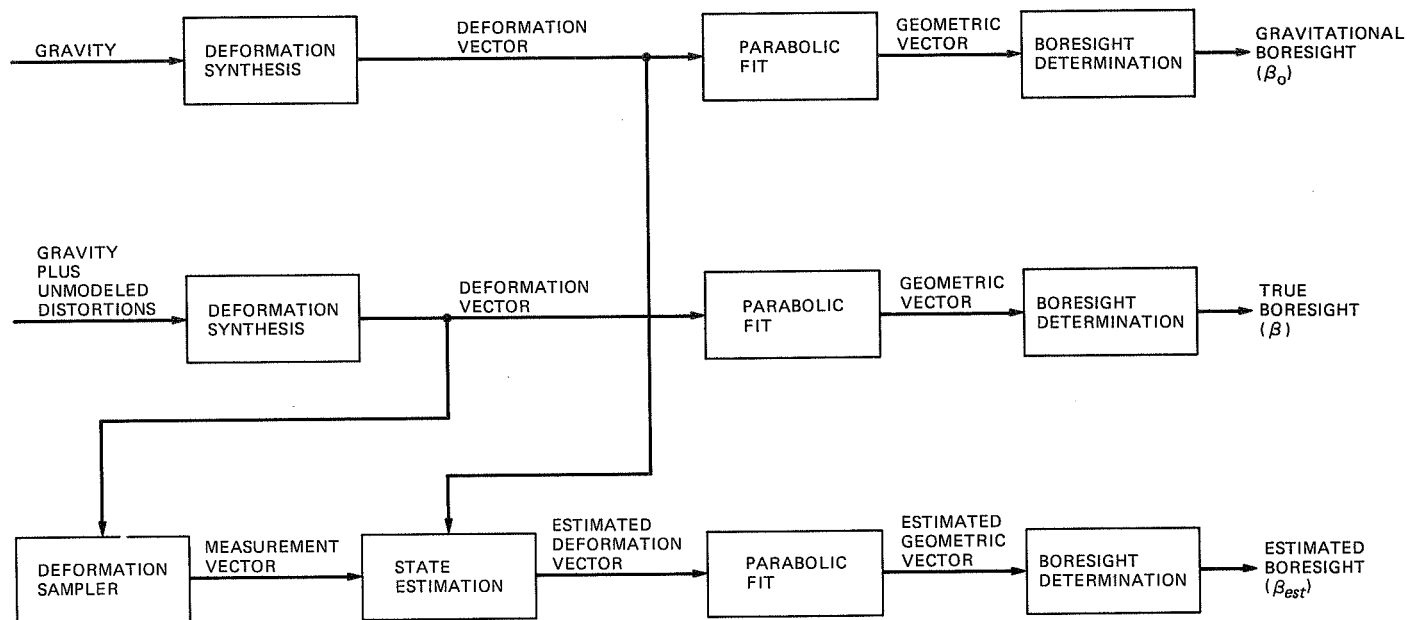


Fig. 6. Analysis of boresight synthesis problem.

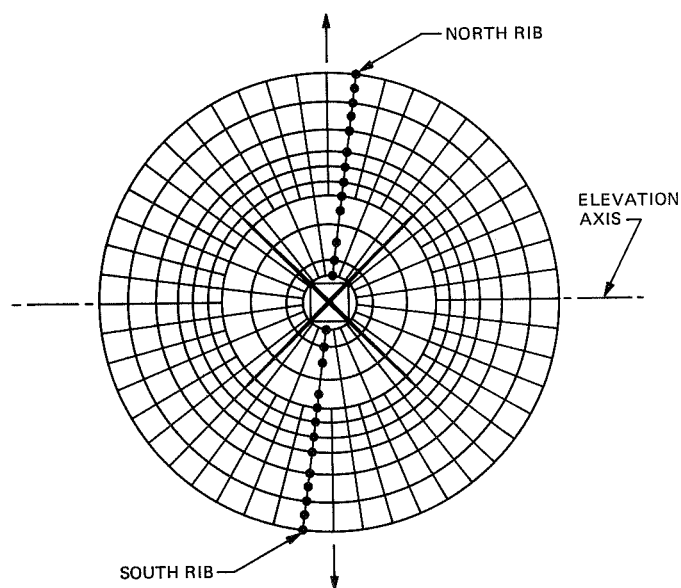


Fig. 7. Reduced-order finite-element model of main reflector.

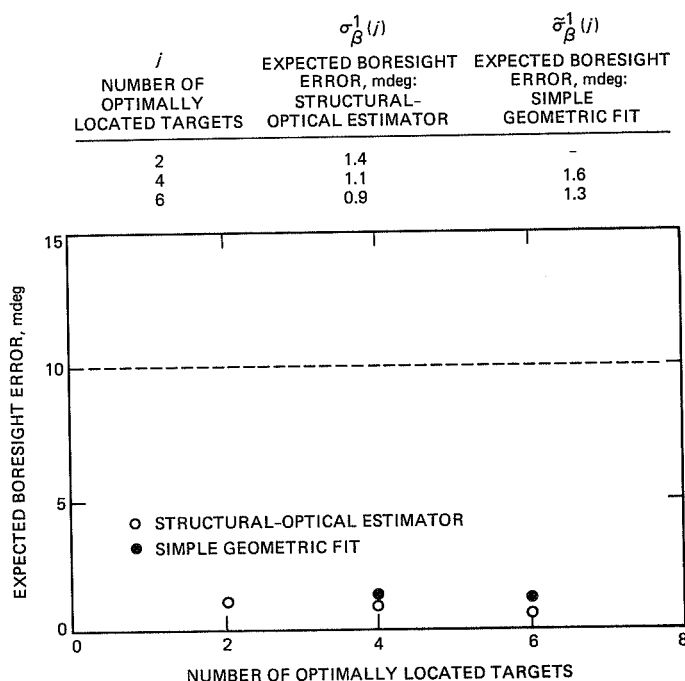


Fig. 8. Expected boresight error ($\sigma_{\beta}^0 = 10$ millidegrees).

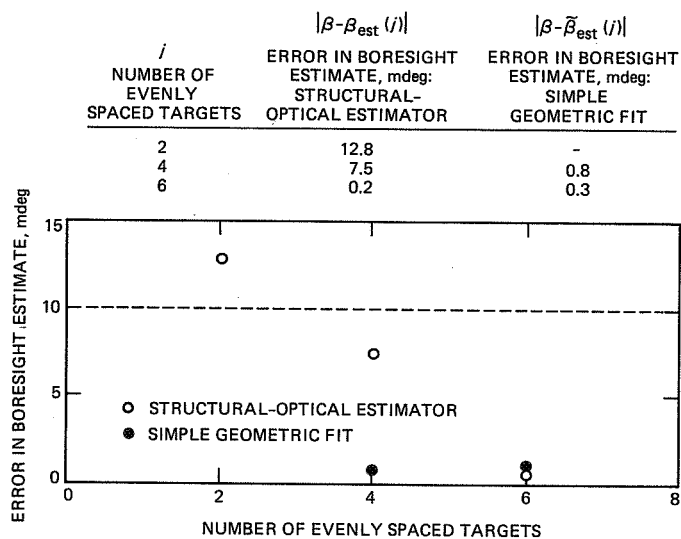


Fig. 9. Boresight error in simulations with gravity model ($\beta = 10$ millidegrees, $\beta_0 = 0$ millidegrees).

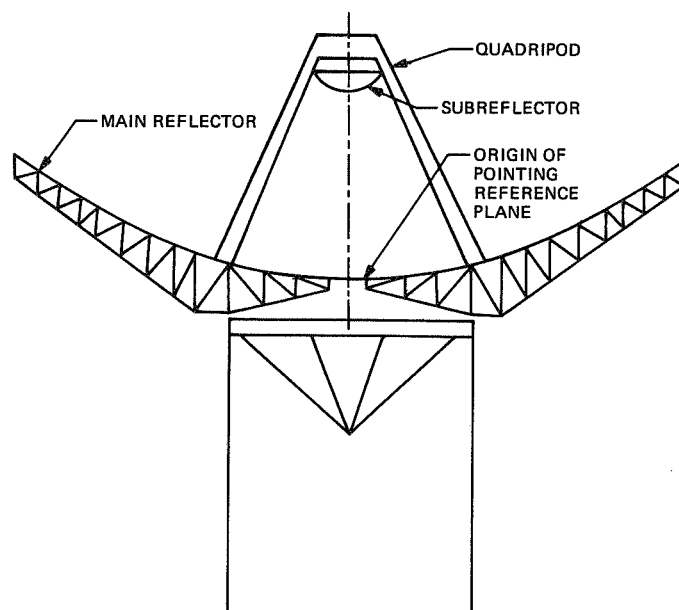


Fig. 10. Key locations on antenna for measurement system.

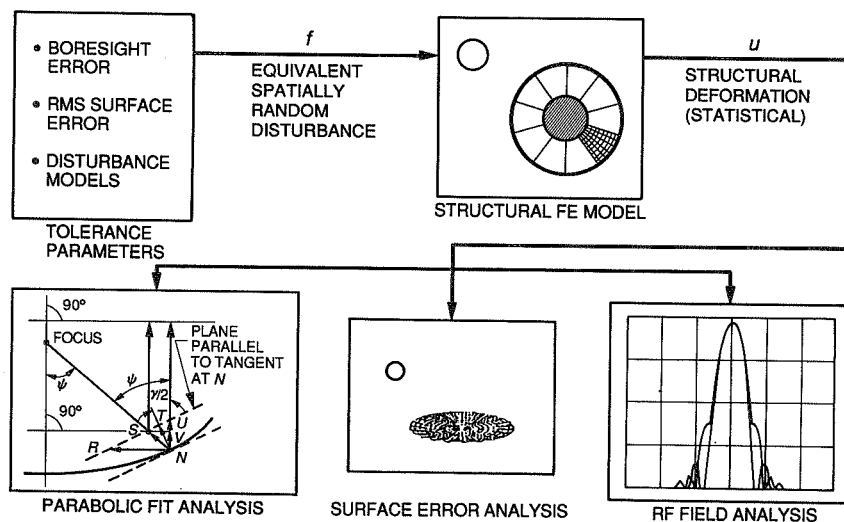


Fig. 11. Antenna estimator design by means of spatially random disturbances.

The Effects of Atmospheric Turbulence on Precision Optical Measurements Used for Antenna-Pointing Compensation

N. Nerheim
Guidance and Control Section

Blind pointing of the Deep Space Network (DSN) 70-meter antennas can be improved if distortions of the antenna structure caused by unpredictable environmental loads can be measured in real-time, and the resulting boresight shifts evaluated and incorporated into the pointing control loops. The measurement configuration of a proposed pointing compensation system includes an optical range sensor that measures distances to selected points on the antenna surface.

This article examines the effect of atmospheric turbulence on the accuracy of optical distance measurements and describes a method to make in-situ determinations of turbulence-induced measurement errors.

I. Introduction

A method has been investigated [1] to improve the pointing accuracy of the DSN antennas. The method uses optical distance measurements to estimate the shape of the antenna surface and the direction of the associated RF boresight axis. At present, a blind pointing error of about 4–6 millidegrees is achievable. The pointing error increases to about 12 millidegrees under moderately windy conditions. If the full benefits of future plans to increase the operating frequency of the 70-meter antennas to 32 GHz are to be realized, it will be necessary to reduce the blind pointing error to 1-millidegree rms. The goal of the precision optical pointing research is to achieve 1-millidegree pointing accuracy by compensating for wind, thermal, and gravity loadings through the use of precision optical distance measurements.

Analytical study results [1] indicate that 1-millidegree geometric pointing accuracy relative to a stable reference base

may be achieved if the distance measurements can be made with an accuracy of about 25–50 μm . The present work examines the effect of atmospheric turbulence on the accuracy of the optical distance measurements and describes a method to make in-situ determinations of turbulence-induced distance errors. The effect of precipitation on optical measurements is discussed briefly.

II. Optical Distance Measurements

The distance measurements will be made with SHAPES (Spatial, High-Accuracy, Position-Encoding Sensor), a JPL-developed time-of-flight range sensor capable of making simultaneous range measurements to multiple targets with submillimeter precision [2].

Optical distance measurements are dependent on the speed of light and therefore on the value of the index of refraction,

n , along the measurement path. If the index does not change with time, an error in the value used for the distance measurement results in a systematic error that has a negligible effect on the pointing accuracy. The presence of turbulence, however, causes random variations in both temporal and spatial values of n that result in random uncertainties in the distance measurements and therefore in the pointing direction.

A. Turbulence and Measurement Errors

The literature concerning the propagation of light through a turbulent atmosphere is extensive. General review articles, of which [3] and [4] are examples, contain long lists of references. Problems associated with turbulence are important for astronomical measurements, laser communication systems, precision optical measurements of distances, and the direction of high-power laser beams. Atmospheric turbulence causes variations of the optical wave amplitude and phase, resulting in beam steering, beam spreading, image blurring, scintillation, and phase fluctuations [5, 6]. Of these effects only phase fluctuations (a 2π -variation of the phase of the optical wave is equivalent to a path-length change of one optical wavelength) affect the accuracy of distance measurements. In [7] and [8] are experimental studies that have a direct bearing on the present work.

Turbulent pressure and humidity fluctuations produce negligible refractive index changes compared to temperature variations; consequently, for optical purposes, "turbulence" refers to atmospheric temperature fluctuations. Nearly all theoretical studies, notably those of Tatarski [9], are based on a model of turbulence proposed by Kolmogorov [10]. The model, which is applicable to both temperature and velocity fluctuations, contains the concept of local isotropy in the fine structure of turbulent flow and justifies the use of statistical methods to study turbulence.

Tatarski's approach to the problem of wave propagation through random media involves the direct solution of a scalar form of the optical wave equation in terms of amplitude and phase fluctuations of the wavefront. Phase variations are formulated in terms of a phase structure function, $D_\phi(\rho)$. For a plane wave of wavelength λ traveling distance L , this structure function is given by

$$D_\phi(\rho) = 2.91 \left(\frac{2\pi}{\lambda} \right)^2 \rho^{5/3} C_n^2 L \quad (\text{radians})^2 \quad (1)$$

where C_n is a measure of the intensity of the turbulence and ρ is the separation of two points on the wavefront normal to the direction of propagation. (For a spherical wave, the constant 2.91 in Eq. (1) is replaced by 1.05.) The phase structure

function is related to the more familiar standard deviation of single path phase σ_ϕ , by

$$D_\phi(\rho) = 2\sigma_\phi^2 [1 - B(\rho)] \quad (2)$$

where $B(\rho)$ is the phase autocorrelation function [11].

The 5/3 power dependence on ρ expressed by Eq. (1) is valid out to some maximum value of ρ which is called the "outer scale of turbulence." The outer scale of turbulence, designated here as ρ_m , is roughly equal to the largest eddies in the turbulence. For $\rho > \rho_m$, $B(\rho) = 0$, the rms phase errors of two paths separated by more than ρ_m are not correlated and the relative phase variation between the two paths is just $2\sigma_\phi^2$. This translates into a relative rms path length variation, σ_L , where

$$\sigma_L^2 = \left(\frac{\lambda}{2\pi} \right)^2 2\sigma_\phi^2 = 2.91 \rho_m^{5/3} C_n^2 L \quad \text{m}^2 \quad (3)$$

The maximum value of $D_\phi(\rho)$ for which Eq. (1) remains valid is not provided by the theory, nor has it been established by experiment. A number of experimental studies of the phase structure function have been made, but none for the condition of very intense turbulence that would cause a problem for the proposed measurements. Consequently, the estimates made below are extrapolated from available experimental data.

The work of Clifford, et al., [8] provides a context for these estimates. The results reported in [8] show excellent agreement with theory (for a spherical wave) up to $D_\phi(\rho) = 100$ (radians)² for $\rho = 30$ cm on a 70-meter propagation path. Temperature measurements were used to determine the turbulence intensity ($C_n^2 = 10^{-13} \text{ m}^{-2/3}$) and to determine the outer scale of turbulence. Over a 24-hour period, ρ_m varied between 1 and 2 m with an average of 1.3 m.

The maximum measured value of $D_\phi(\rho)$ reported by Clifford corresponds to an rms distance error of 1 μm . Extrapolating the experimental results to $\rho_m = 1.3$ m yields $D_\phi(\rho) = 1200$ (radians)² and $\sigma_L = 3.4 \mu\text{m}$.

B. Turbulence-Induced Measurement Errors in SHAPES

SHAPES measures the displacement of selected points on the main reflector relative to a reference point on the sensor optical head. The measurement error includes the intrinsic instrumental error (about 25 μm) and the error due to turbulence. As discussed above, an estimate of the turbulence-induced measurement errors may be obtained from Eq. (3),

provided reliable values of ρ_m and C_n^2 are known. Unfortunately, neither C_n nor ρ_m at the antenna site can be predicted with accuracy. For the present analysis, ρ_m is assumed to be 1.5 m, a value within the range reported in [8], and the value of C_n^2 that would produce a 25- μ m distance error (the approximate SHAPES instrumental error) is calculated. If $L = 80$ m is a typical round-trip optical path length and $\rho_m = 1.5$ m, Eq. (3) becomes $\sigma_L^2 = 458 C_n^2$, and $\sigma_L = 25 \mu\text{m}$ requires $C_n^2 = 1.4 \times 10^{-12} \text{ m}^{-2/3}$.

This value of C_n^2 may be compared with measurements made by a number of workers for various conditions. As an example, a plot [12] of C_n^2 as a function of the time of day is shown in Fig. 1. The measurements were taken on a clear day at a position 2 m above a grassy plain. The figure indicates C_n^2 exceeds $10^{-12} \text{ m}^{-2/3}$ only for short periods of time when the effects of solar heating are most strongly felt. Insofar as the underlying theory remains valid and the cited conditions resemble those above the antenna, it appears that turbulence will only infrequently degrade the nominal 1-millidegree pointing accuracy.

C. Effect of Precipitation

1. Attenuation by Rain and Fog. The effects of clouds, fog, and rain on electromagnetic wave propagation have been studied extensively [13–17]. Rain (but not fog) strongly attenuates microwaves; consequently, the antennas are situated in rather dry climates [14]. Both fog and rain are known to attenuate optical radiation.

The effect of fog at visible wavelengths is generally reported as visibility, which is defined in terms of attenuation [18]. For example, if the visibility is 0.25 miles, an optical signal would be reduced by 3.4 dB over an 80-m path. Attenuation of optical signals degrades the SHAPES measurement accuracy; part of the instrumental error is inversely proportional to the square root of the received signal energy. A 3.4-dB loss of signal would increase the instrument error from a nominal value of 25 μm to about 32 μm .

The effects of rain on the propagation of optical radiation have been measured at a number of wavelengths. It has been shown [15] that the attenuation, α , in heavy rain may be expressed as $\alpha = 0.155 r + 2.66 \text{ dB/km}$ where r is the rate of rainfall in mm/hr. At a rate of 15 mm/hr, which is considered moderate to heavy rainfall, the optical attenuation over an 80-m path is about 0.4 dB, a value that would increase the SHAPES measurement error by only about 2 percent. The impact of such rainfall on microwave antenna performance would be much more severe [14], leading to the observation that rain is a more serious problem for antenna operation than for SHAPES measurements.

2. Average Rain and Fog at Goldstone and Their Impact on SHAPES Operation. Climatological data for airfields have been published by the U.S. Navy [19]. The data for fog applicable to the present problem are expressed as a percentage of weather observations for which visibility was less than one mile for any period of time during 3-hour observation periods. At Daggett, California, (about forty miles south of and climatologically similar to the JPL antenna site at Goldstone), visibility less than one mile was reported for 0.5 percent of the observations.

The annual rainfall at Daggett [19] is 3.6 inches. Studies have shown that the duration of any rainfall rate (e.g., 15 mm/hr) is well-correlated with the total annual rainfall [14]. Based on this correlation, the rate at Goldstone should not exceed 15 mm/hr for more than about 15 minutes per year. One concludes that because of the dry climate at Goldstone, the effects of rain and fog on SHAPES operation are negligible.

III. SHAPES Measurements of Turbulence-Induced Path Length Variations

The following describes a method by which SHAPES can be used to determine the rms magnitude of turbulence-induced variations in optical path length. The method relies on the form of SHAPES measurement errors and the use of two coincident but separable optical paths to isolate turbulence-induced variations.

A. SHAPES Measurement Errors

SHAPES range measurements are based on the time required for a laser pulse to travel the round-trip distance from source to detector, usually via an intermediate retroreflector target. The laser is pulsed at frequency f and the pulses are separated by an effective wavelength λ , given by

$$\lambda = \frac{c}{nf} \quad (4)$$

where c is the speed of light and n is the refractive index at the optical wavelength (0.78 μm) of the laser pulse along the optical path.

The target range relative to a reference position may be written as

$$R = N \frac{\lambda}{2} + \Delta R = \frac{Nc}{2nf} + \Delta R \quad (5)$$

where N is the integer number of wavelengths in the optical path and ΔR is the SHAPES measurement. N may be calcu-

lated exactly from the known geometry of the antenna measurements.

Measurement errors consist of the SHAPES instrument error and errors in λ . Variation of the SHAPES operating frequency is negligible; hence, from Eq. (4), only errors in the atmospheric refractive index contribute to the error in λ and $\sigma_\lambda \approx \lambda \sigma_n$ for $n \approx 1.0$.

Standard error analysis applied to Eq. (5) now yields

$$\sigma_R^2 = \left(\frac{N}{2}\right)^2 \sigma_\lambda^2 + \sigma_{\Delta R}^2 \quad (6)$$

or

$$\sigma_R^2 = R^2 \sigma_n^2 + \sigma_{\Delta R}^2 \quad (7)$$

where $\sigma_{\Delta R}$ is the SHAPES instrument error, and $R^2 \sigma_n^2$ is the portion of the range variance that is due to the random fluctuations of n as given by σ_L of Eq. (3).

B. Evaluation of Turbulence Effects with SHAPES

As noted above, SHAPES range measurements typically involve laser pulses that travel a round trip from a pulsed laser mounted very near the sensor head to a retroreflector and back to the sensor head. However, the tip of an optical fiber may be co-located with the retroreflector and used to direct a train of laser pulses at SHAPES; the optical path length through the air for these pulses is half that for the retro-reflected pulses. Measurements of turbulence-induced range error may then be obtained by comparing the standard deviations of simultaneous measurements made over the fiber and retroreflected paths. The pulse propagation time through the fiber will vary with temperature but this verification has a long time constant and is unaffected by turbulence during the measurement period.

For the fiber-originated path, Eq. (7) becomes

$$\sigma_R^2 = \left(\frac{R}{2}\right)^2 \sigma_n^2 + \sigma_{\Delta R}^2 \quad (8)$$

Because the instrument error is identical for the two simultaneous measurements of the same signal strength, the difference of Eqs. (7) and (8) is

$$\sigma_2^2 - \sigma_1^2 = 0.75 R^2 \sigma_n^2 \quad (9)$$

where the subscripts 2 and 1 refer to the double and single paths respectively. Equation (9) indicates that SHAPES can be used to measure the effects of turbulence on antenna distance measurements provided these effects are sufficiently large compared to the sensor's intrinsic resolution.

IV. Laboratory Demonstration of Turbulence Measurements Using SHAPES

A. Experimental Procedure

The sensitivity of SHAPES to turbulence-induced errors in range measurements has been demonstrated in laboratory experiments. No attempt was made to reproduce the open air turbulence of the antenna site: the measurements merely demonstrate the capability of SHAPES to detect and measure errors due to turbulence.

A sketch of the experimental setup is shown in Fig. 2. Two retroreflector targets, T_r and T_a , located about 10 m from the sensor, were illuminated by laser L_a . A second target, T_b , also located at a distance of 10 m, was illuminated by a second laser, L_b . Turbulence was generated in the optical path between the sensor and target T_b by an electrical heater.

The return from each target ultimately forms an image on the SHAPES CCD. The relative position of the image's centroid, x , is directly related to the target's range. The reference centroid, x_r , is subtracted from each of the other target centroids x_i , to form the quantity $y_i = x_i - x_r$. The standard deviation of each y_i , σ_{yi} , was calculated from 94 consecutive measurements.

The targets T_a and T_r are located at the same range and are illuminated by a single laser; the measurement error σ_{ya} thus consists of only the CCD readout errors, $\sigma_{xa} = \sigma_{xr} = \sigma_x$, of the two centroids,

$$\sigma_{ya}^2 = \sigma_{xa}^2 + \sigma_{xr}^2 = 2\sigma_x^2 \quad (10)$$

Because targets T_b and T_r are illuminated by separate lasers, determination of y_b is subject to an additional error, σ_ϕ , associated with jitter in the relative firing times of the two lasers. Thus, in the absence of turbulence,

$$\sigma_{yb}^2 = 2\sigma_x^2 + A^2 \sigma_\phi^2 \quad (11)$$

where A is a constant proportional to the streak tube drive voltage.

Detection of turbulence depends on the increase in σ_{yb} caused by the turbulence. If the turbulence-induced error is designated by σ_t , the variance of y_b becomes

$$\sigma_{y2}^2 = 2\sigma_x^2 + A^2 \sigma_\phi^2 + \sigma_t^2 \quad (12)$$

The difference of Eqs. (12) and (11) gives the desired turbulence-induced error.

Laboratory measurements were made with and without the heater-generated turbulence, and the difference in the calculated variance with and without turbulence was assigned to σ_t^2 . Measurements of σ_{ya}^2 verified that the turbulence did not affect the optical path of L_a .

The laboratory experiments used to determine σ_t require that both σ_x and σ_ϕ remain constant for all measurements. The method proposed for determining $R\sigma_n$ above the DSN antennas eliminates this requirement by performing simultaneous measurements of single- and double-path values of σ_y .

B. Results and Discussion

The results of one set of experiments are shown in Table 1. The relationship between range and CCD centroid position depends on the amplitude of the streak tube drive voltage: for this experiment, $\sigma_{\Delta R} = 800 \sigma_y \mu\text{m}$ and thus

$$R\sigma_n = 800 \sigma_t \mu\text{m} = \sqrt{\sigma_{\Delta R}^2 - (12 \mu\text{m})^2}$$

where $12 \mu\text{m}$ is the average value of $\sigma_{\Delta R}$ with no turbulence.

The results shown in Table 1 vary with heater power and heater location. Increasing heater power, which was expected to increase the turbulence intensity, caused an increase in the

measurement error. Moving the heater to increase the turbulence path length also produced increased measurement error. The use of a constant value of $12 \mu\text{m}$ for the instrument error is validated by the nearly constant value of $\sigma_{\Delta R}$ ($10\text{--}13 \mu\text{m}$) when the heater was turned off.

The results of the laboratory experiments demonstrate that SHAPES measurements may be used to sense atmospheric turbulence. Although natural turbulence at the antenna site is expected to be very different from that produced in the laboratory, the laboratory experiments suggest that SHAPES may be used to make in-situ measurements of turbulence on the antenna. The results also show that, in the presence of sufficient turbulence intensity, optical range measurements may be in error by an amount that is significant for the proposed compensation scheme.

V. Conclusions

A proposed method to achieve 1-millidegree geometric pointing accuracy of the DSN 70-meter antennas makes use of multi-point optical measurements of high precision. Heavy rain and intense fog degrade optical measurements. However, because of the dry climate at most antenna sites, these events occur infrequently and their effect on antenna operation is negligible. Atmospheric turbulence produces errors in the optical measurements that degrade the derived pointing precision. The results of the present study suggest that turbulence will not seriously degrade the pointing precision except for very limited periods of intense turbulence caused by solar heating of the air above the antenna. The precision pointing system [1] requires knowledge of the measurement error to evaluate the pointing error. During operational periods, the variance of the SHAPES measurements, turbulence-related and otherwise, can be determined and the degradation of the pointing accuracy assessed. Additional measurements allow the part of the error caused by turbulence to be determined.

References

- [1] R. Scheid, "Precision Pointing Compensation for DSN Antennas with Optical Distance Measuring Sensors," *TDA Progress Report 42-97*, vol. April-June 1989, Jet Propulsion Laboratory, Pasadena, California, this issue.
- [2] J. McLaughlan, W. Goss, and E. Tubbs, "SHAPES: A Spatial High-Accuracy, Position-Encoding Sensor for Space-Systems Control Applications," in *Proceedings of the Annual Rocky Mountain Guidance and Control Conference*, January 30-February 3, 1982, Keystone, Colorado, pp. 371-382, 1982.

- [3] R. S. Lawrence and J. W. Strohbehn, "A Survey of Clear-Air Propagation Effects Relevant to Optical Communications," *Proc. IEEE*, vol. 58, no. 10, pp. 1523-1545, 1970.
- [4] A. Ishimaru, "Theory of Optical Propagation in the Atmosphere," *Opt. Eng.*, vol. 20, no. 1, pp. 63-70, 1981.
- [5] J. I. Davis, "Considerations of Atmospheric Turbulence in Laser Systems Design," *Appl. Opt.*, vol. 5, pp. 139-147, 1966.
- [6] K. S. Shaik, "Atmospheric Propagation Effects Relevant to Optical Communications," *TDA Progress Report 42-94*, vol. April-June 1988, Jet Propulsion Laboratory, Pasadena, California, pp. 180-200, August 15, 1988.
- [7] G. N. Gibson, J. Heymay, J. Lugten, W. Fitelson, and C. H. Townes, "Optical Path Lengths in Atmosphere," *Appl. Opt.*, vol. 14, pp. 4383-4389, 1984.
- [8] S. F. Clifford, G. M. B. Bouricius, G. Ochs, and M. H. Ackley, "Phase Variations in Atmospheric Propagation," *J. Opt. Soc. Am.*, vol. 61, pp. 1279-1284, 1971.
- [9] V. I. Tatarskii, *Wave Propagation in a Turbulent Medium*, New York: McGraw-Hill, 1961.
- [10] A. N. Kolmogorov, "The Local Structure of Turbulence in Incompressible Viscous Fluid for Very Large Reynolds Numbers," *Soviet Physics Uspekhi*, vol. 10, no. 6, pp. 734-736, May-June 1968.
- [11] R. E. Hufnagel, "Variations of Atmospheric Turbulence," in *The Infrared Handbook*, Chapter 6, USGPO, Washington, D.C., 1974.
- [12] R. S. Lawrence, G. R. Ochs, and S. F. Clifford, "Measurements of Atmospheric Turbulence Relevant to Optical Propagation," *J. Opt. Soc. Am.*, vol. 60, pp. 826-830, 1970.
- [13] D. C. Hogg and T. S. Chu, "The Role of Rain in Satellite Communications," *IEEE Proc.*, vol. 63, pp. 1308-1331, 1975.
- [14] P. D. Potter, M. S. Shumante, C. T. Stelzried, and W. H. Wells, "A Study of Weather-Dependent Data Links to Deep Space Applications," *JPL Technical Report 32-1392*, Jet Propulsion Laboratory, Pasadena, California, 1969.
- [15] T. S. Chu and D. C. Hogg, "Effects of Precipitation and Propagation at 0.63, 0.35 and 10.6 Microns," *Bell System Tech. J.*, vol. 47, pp. 723-759, 1960.
- [16] G. C. Mooradian, M. Geller, L. B. Stotts, D. H. Stevenson, and R. A. Krautwald, "Blue-Green Pulsed Propagation Through Fog," *Appl. Opt.*, vol. 18, pp. 429-441, 1979.
- [17] G. C. Mooradian, M. Geller, P. H. Levine, L. B. Stotts, and D. H. Stevenson, "Over the Horizon Optical Propagation in a Maritime Environment," *Appl. Opt.*, vol. 19, pp. 11-30, 1980.
- [18] R. G. Fleagle and J. A. Businger, *An Introduction to Atmospheric Physics*, Orlando, Florida: Academic Press, Inc., 1980.
- [19] U. S. Naval Weather Services, *World-Wide Airfield Summaries*, Vol. VIII, Part I, Asheville, North Carolina, 1969.

Table 1. Effect of turbulence on SHAPES measurement error

Test No.	Description	$\sigma_{\Delta R}, \mu\text{m}$	$R\sigma_n, \mu\text{m}$
1	Turbulence	19	14
2	No turbulence	10	—
3	Turbulence (repeat no. 1)	19	14
4	Turbulence (increase heater power)	26	23
5	Turbulence (move heater to increase turbulence)	38	35
6	No turbulence	13	—
7	Turbulence (reduce power)	22	18
8	No turbulence	12	—

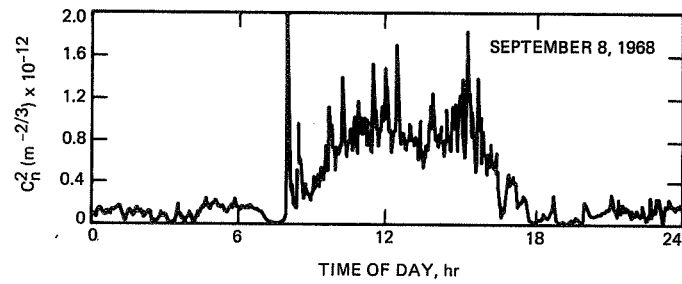


Fig. 1. Refractive index structure parameter versus time of day. The measurements were derived from temperature measurements made on a clear day at an elevation of 2 m above a grassy plain [11].

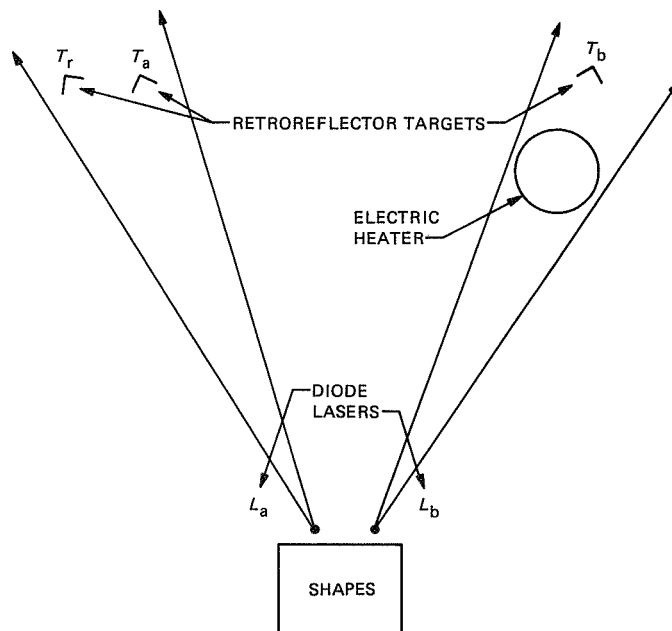


Fig. 2. Sketch of a laboratory experiment to demonstrate the sensitivity of SHAPES to turbulence-induced range errors.

A Multiflare Horn With 1-Megawatt Power Handling Capability

D. J. Hoppe

Radio Frequency and Microwave Subsystems Section

This article describes the design and testing of the prototype horn for the proposed 1-megawatt radar. The unique features of this square horn include a multiflare design in which flare angle changes rather than corrugations are used to generate the required higher-order modes. A five-port combining section is used at the input. The design of this section and the multiflare section are described in this article. Measured radiation patterns are in good agreement with theoretical patterns.

I. Introduction

Deep Space Network (DSN) plans call for increasing the transmitting power of the Goldstone Solar System Radar from the present 365 kW to 1 MW [1]. In the proposed 1-MW configuration, the output from four 250-kW klystron amplifiers must be combined to form the 1-MW signal. This article focuses on the proposed horn for the 1-MW radar, including the input section where the four 250-kW signals will be combined. The horn design closely resembles the design of the horn used at the Haystack Observatory in Westford, Massachusetts [2], with some important simplifications.

The first section of this article describes the input section of the horn and how it interfaces with the four high-power amplifiers and waveguide system. Computer simulation of the combiner section and multiflare sections of the horn are described, and radiation patterns for the final design are presented. The following section compares these theoretical patterns with measured patterns for the prototype horn. Finally, conclusions are drawn and remaining areas of concern are described.

II. Horn Input Section

A. Combiner Section

A simplified block diagram for the proposed 1-MW radar transmitter system is shown in Fig. 1. Four 250-kW klystron amplifiers are fed by a common drive signal and produce the required 1-MW signal. These four signals are carried through a WR125 waveguide to the horn input, where they are further split into eight 125-kW signals. Four of these signals (one pair of klystrons) feed the in-line ports of four orthomode junctions, while the other klystron pair feeds the ortho ports. By correctly adjusting the relative phase of the signals of these klystron pairs, either circular or linear polarization can be generated in the output port of the four orthomodes. For this design, the orthomode output is through 0.95-in. square waveguides rather than the circular waveguides used in the DSN. These four square waveguides then enter the combiner section of the horn, which is described next.

In order to design the combiner section, the possible propagating waveguide modes for a particular dimension of the

square waveguide must be known. The critical dimension a_{max} where a TE_{mn} or TM_{mn} begins to propagate is given by:

$$a_{max} = \frac{\lambda_0 (m^2 + n^2)^{1/2}}{2}$$

For the frequency of interest (8.51 GHz), the critical dimension for several of the most important modes is given in Table 1. It is seen that in the feeding waveguides where $a = 0.95$ in., only the two orthogonally polarized TE_{10} modes propagate. When the four guides are combined as shown in Fig. 2, the output waveguide has an inner dimension of 2.060 in. From Table 1 it is seen that this is just below the critical dimension for the TE_{30} and TE_{03} modes. For symmetric (in-phase) excitation of the four feeding waveguides, this is the first higher-order mode that is excited in the large waveguide. Therefore, for the chosen dimensions, only the TE_{10} and TE_{01} modes exist in the large output waveguide section of the combiner. Since the TE_{30} and TE_{03} modes are strongly excited at the junction but decay away from the edge, a straight section follows the combiner in order to allow these modes to decay at least 30 dB before the horn begins to flare out. A wall thickness of 0.160 in. between the four input waveguides was chosen to allow sufficient room for cooling channels in the web region. Maximum dimensions were chosen to obtain the highest possible power handling capability.

B. Multiflare Section

Next, the horn must be flared out in order to properly illuminate the 70-m dual-reflector antenna. Since the antenna is a dual-shaped system, optimum efficiency is obtained when the feed radiation pattern matches that of the design feed (in this case the DSN standard 22.37-dB corrugated horn) over the 16 degrees of angle subtended by the subreflector. The TE_{10} mode itself has unequal E- and H-plane patterns and is, therefore, not suitable for illuminating the 70-m antenna alone. In order to obtain equal E- and H-plane patterns for a square horn, higher-order modes must be added to the TE_{10} mode. A method for generating the required modes by using changes in horn flare angle rather than steps or corrugations has been described by Cohn [3]. The multiflare horn is ideally suited for high-power applications, as has been shown by the success of the Haystack system.

The required modes were determined by calculating the radiation from square apertures of different sizes with varying mode mixtures. An extensive computer study determined that the mixture given in Table 2 most closely reproduced the 22.37-dB corrugated horn pattern over the 16-degree range. It is evident from the table that three modes must be added to

the TE_{10} mode. These three modes will contain about 17 percent of the propagating power in the ideal design.

The next task was to determine the flare angle changes required to generate such a mode mixture. Initial guesses were made from information in Cohn's original paper, and a more detailed analysis was carried out to fine-tune the horn dimensions. For this part of the analysis, the horn was step-approximated by 200 segments, and the aperture modes were calculated for a TE_{10} mode incident at the input, using a mode-matching method [4]. Two flare angle changes were found to be necessary to generate the required modes. The dimensions of the final horn design are shown in Fig. 3.

Many iterations were required to determine these final dimensions. The mode generation along the length of the horn may be traced by examining the mode content after each of the segments during the analysis. This is only strictly true if reflections from the remainder of the horn are zero, but in this case reflections in the horn are small enough for this to be an excellent approximation. The modes present at various positions along the horn are plotted in Fig. 4. At the input ($z = 0$), only the TE_{10} mode carries power, and this remains the case through the first 6-in. section of straight guide. At the abrupt flare angle change ($z = 6$ in.), three additional modes are excited, and coupling between these four modes takes place continuously during the first flared section. This coupling occurs because the waveguide modes are only independent (uncoupled) in a perfectly straight waveguide, not in a tapered horn. Once the guide straightens out again ($z = 14.75$ in.), the modes propagate independently through the phasing section. The next flare angle change near $z = 32$ in. generates the mode content required in the aperture. Note that the mode amplitudes are plotted on a linear scale, and the power carried by a particular mode is given by the amplitude squared. At each point in the horn, the sum of the squares of the four mode amplitudes is unity, indicating that power is conserved.

C. Radiation Patterns

The theoretical radiation patterns for the horn in the principal planes are shown in Fig. 5. Important characteristics are the nearly perfectly identical E- and H-plane patterns over the 16-degree angle subtended by the subreflector, and the relatively low sidelobe level. When comparing these patterns with the 22.37-dB circular corrugated horn patterns, one notes that they are virtually identical over the required 16-degree angle. The H-plane pattern for this horn has a higher first sidelobe than the 22.37-dB pattern, while the first sidelobe in the E-plane is lower. The 22.37-dB pattern actually has a filled-in first sidelobe that peaks at about -25 dB. Calculated patterns for the multiflare horn are nearly sidelobe free in the 45-degree plane. These effects help to compensate for the higher side-

lobe in the H-plane. Calculated 70-m antenna gain for this multiflare horn and the 22.37-dB horn are within 0.03 dB of agreement.

III. Measured Results

A photograph of the prototype horn for which radiation patterns were measured is shown in Fig. 6. The E-plane and H-plane patterns of this horn were measured and are compared to the theoretical patterns in Fig. 7. Good agreement can be seen throughout the main beam region, with discrepancies of a few dB in the sidelobe levels in both planes. Although the agreement for this horn is not as close as that for circular

horns analyzed using the mode-matching method, the accuracy is adequate for design purposes.

IV. Conclusions

A design for a 1-megawatt feedhorn has been presented, including a review of the design method. Measured patterns for a prototype horn are in good agreement with those predicted by the theory. Before a final high-power version of this horn is fabricated, work must be completed on the matching of the combiner section and also on the specifics of the cooling passages, due to the high power levels involved.

References

- [1] A. M. Bhanji, D. J. Hoppe, B. L. Conroy, and A. J. Freiley, "Conceptual Design of a 1-MW CW X-Band Transmitter for Planetary Radar," *TDA Progress Report 42-95*, vol. July–September 1988, Jet Propulsion Laboratory, Pasadena, California, pp. 97–111, November 15, 1988.
- [2] W. North, "Haystack Hill Long Range Imaging Transmitter," *Proceedings of the 13th Pulse Power Modulator Symposium*, pp. 247–253, 1978.
- [3] S. B. Cohn, "Flare-angle Changes in a Horn as a Means of Pattern Control," *Micro-wave J.*, vol. 13, pp. 41–46, October 1970.
- [4] D. J. Hoppe, "Modal Analysis Applied to Circular, Rectangular, and Coaxial Waveguides," *TDA Progress Report 42-95*, vol. July–September 1988, Jet Propulsion Laboratory, Pasadena, California, pp. 89–96, November 15, 1988.

Table 1. Square waveguide cutoff dimension for lower order modes at 8.51 GHz

Mode	8.51-GHz cutoff dimension, in.
TE _{10,01}	0.69343
TE ₁₁ , TM ₁₁	0.98066
TE _{20,02}	1.38606
TE _{21,12} , TM _{21,12}	1.55056
TE ₂₂ , TM ₂₂	1.96132
TE _{30,03}	2.08029
TE _{31,13} , TM _{31,13}	2.19282
TE _{32,23} , TM _{32,23}	2.50020
TE ₃₃ , TM ₃₃	2.94197

Table 2. Modes required in a 6.1-in. square waveguide to duplicate 22.37-dB corrugated horn pattern

Mode	Mode amplitude	Mode power, percent	Mode phase, deg
TE ₁₀	0.91	83.2	0
TE ₃₀	0.07	0.5	90
TE ₁₂	0.16	2.6	180
TM ₁₂	0.37	13.7	180
		<u>100.0</u>	

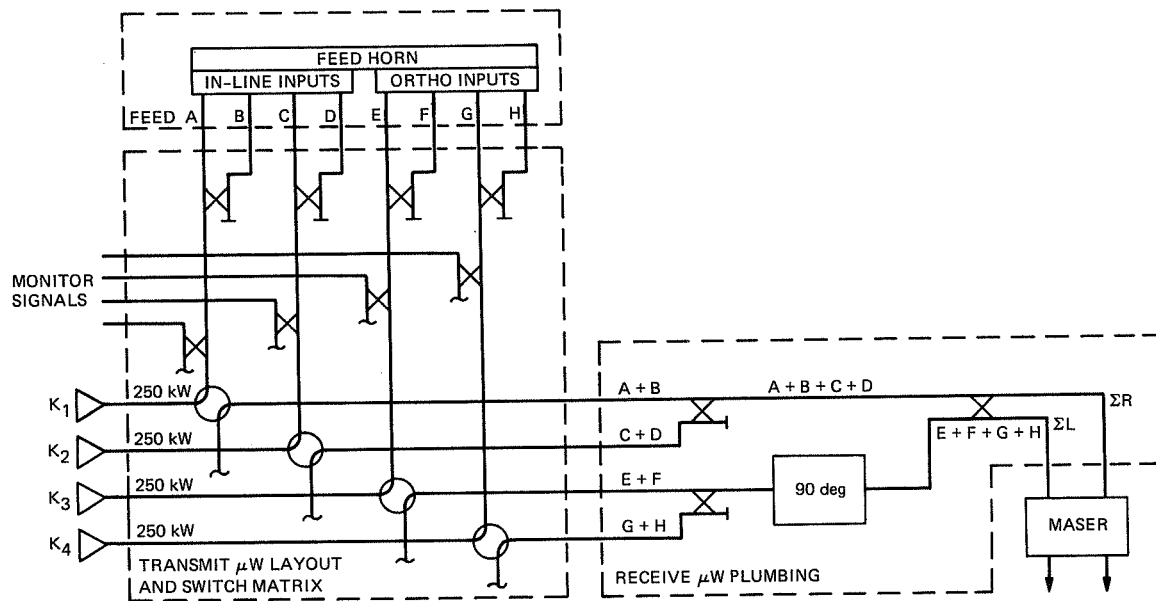


Fig. 1. 1-MW radar transmission line system.

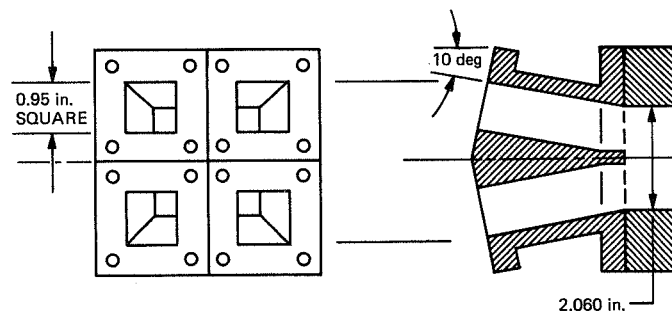


Fig. 2. 1-MW horn combiner section.

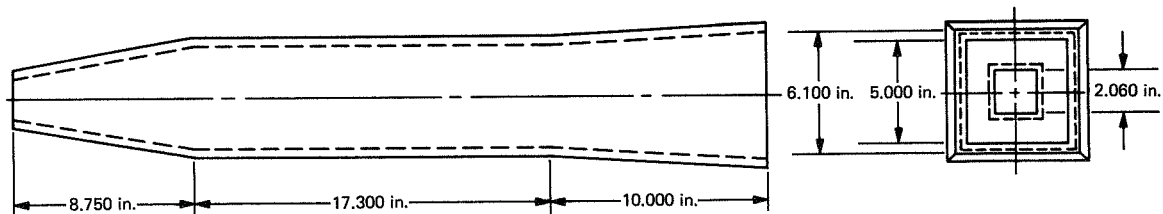


Fig. 3. 1-MW multiflare horn dimensions.

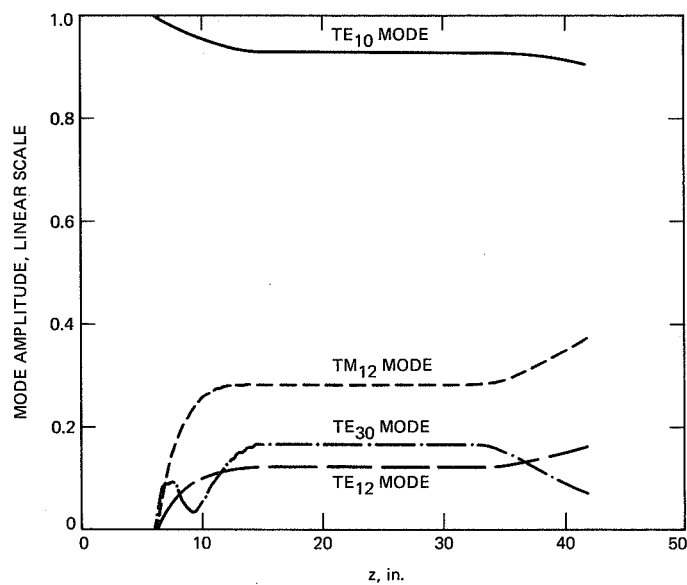


Fig. 4. Mode generation along the multiflare horn.

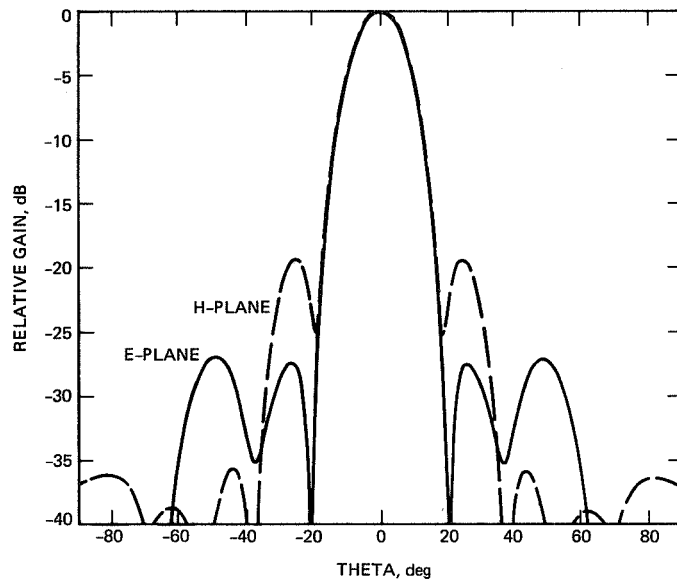


Fig. 5. Theoretical horn patterns.

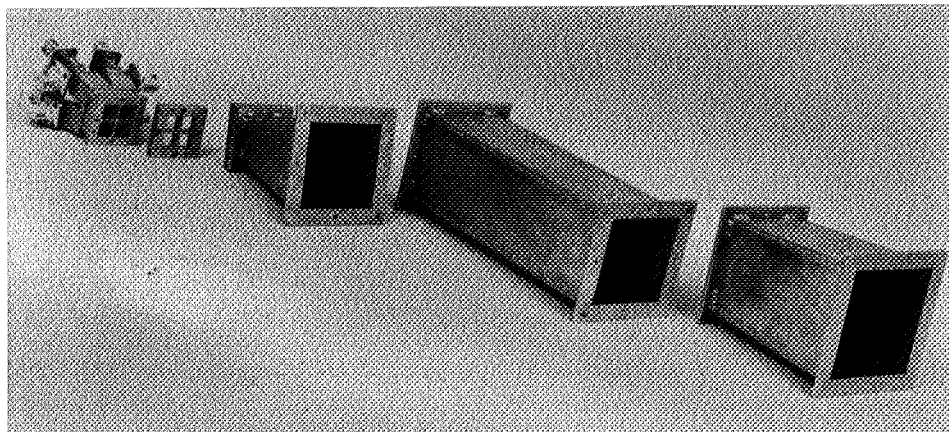
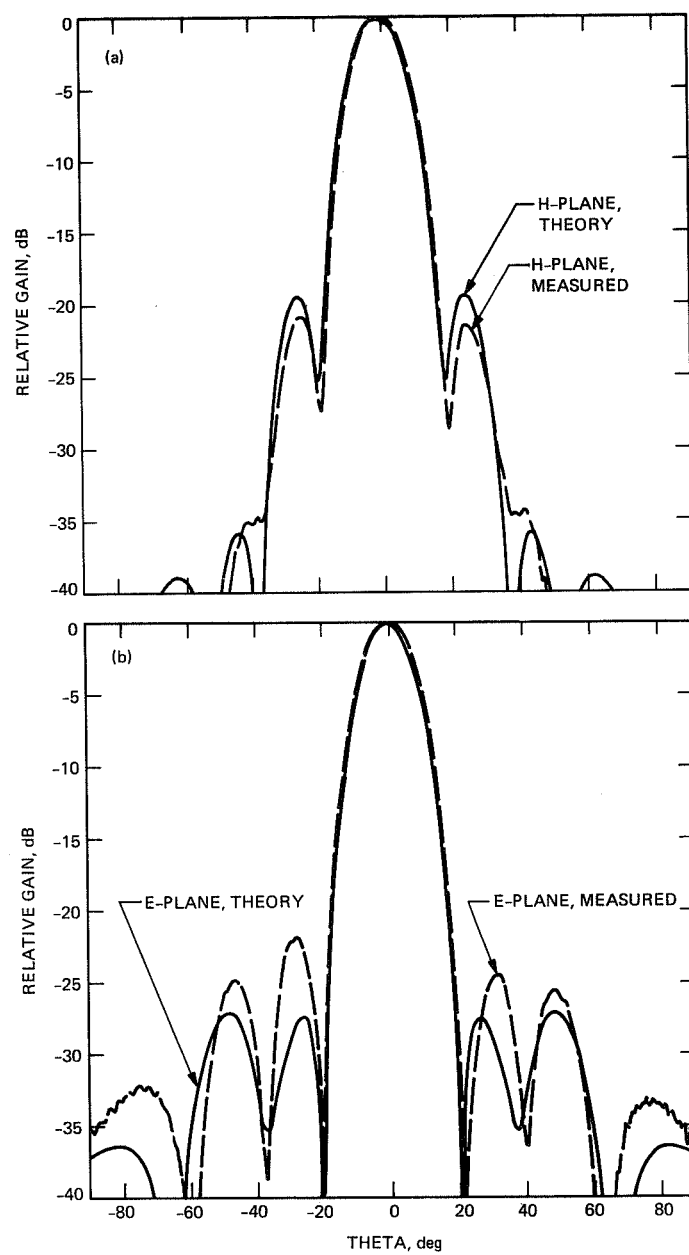


Fig. 6. Prototype horn.

ORIGINAL PAGE
BLACK AND WHITE PHOTOGRAPH



**Fig. 7. Comparison between theoretical and measured patterns:
(a) H-plane; (b) E-plane.**

Thermal Measurements of Microwave Transmitter Feedhorn Window

R. M. Perez and D. J. Hoppe

Radio Frequency and Microwave Subsystems Section

Thermal measurements of microwave transmitter feedhorn windows were performed using an imaging infrared radiometer. The measurement technique is described and results are presented for windows made of 0.001-in. Kapton (trademark of Dupont Chemical Co.) and 0.1-in. HTP-6 (Space Shuttle tile material). Measured and calculated temperatures agree well.

I. Introduction

The use of a nonpermeable cover is required on microwave transmitter feedhorns to prevent rainwater and wind-borne debris from entering the transmitter waveguide. This window must be manufactured of a low-loss material to minimize heating of the window due to the passing Radio Frequency (RF) beam. In addition, the window material must tolerate high temperatures without permanent damage. Heating of the window is caused both by dielectric heating due to the RF beam and by the burning of debris resting on the window surface.

Present transmitters operating at 8.5 GHz employ a Kapton (trademark of Dupont Chemical Co.) window at power levels up to 400 kW. Performance of the Kapton window is adequate, with some failures due to debris burning on the window (insects or oil droplets). Future transmitters at this frequency will be capable of output power levels of 1 MW [1].

Since no temperature data were available for Kapton windows operating at 400 kW, this information was needed to predict the suitability of using a Kapton window at 1 MW. Based on data obtained for Kapton, the use of alternate

window material may be required. Other possible choices include fused quartz and sapphire. Another promising material is High Thermal Performance (HTP), developed by Lockheed and used on the Space Shuttle for heat shield insulation. This material possesses excellent thermal and electrical properties for this application (see Table 1). In order to investigate the actual performance of HTP under the action of intense RF beams, a 0.1-in. thick window was fabricated from HPT-6 (6 lb/ft³).

II. Method

It is exceedingly difficult to make direct temperature measurements of a microwave transmitter feedhorn window. The use of thermocouples and other means of electrical thermometry is not possible due to rapid and intense heating of any metal in the path of the RF beam. Direct viewing of the window by infrared imaging equipment is also not a viable method, as almost any direct optical path to the window will also be in the RF beam path, possibly damaging the instrument, even if remotely controlled. RF reflections from metal on a

measuring instrument could also be potentially harmful to personnel nearby.

In order to overcome these difficulties, a highly-reflective infrared mirror was erected on a nonmetallic stand parallel to the feedhorn, 14 feet away, at an angle of 45 degrees (see Fig. 1). The mirror was fabricated from a 16-in. by 16-in. by 1-in.-thick soda lime float-glass blank with a highly-reflective gold finish electrodeposited on one side. An Inframetrics 600 infrared radiometer with a 3X telescope lens was placed 54 feet away, allowing viewing of the feedhorn window image on the mirror (see Fig. 2). To ensure the safety of the radiometer operator, the power density was calculated in the vicinity of the radiometer assuming reflection from the mirror surface. Using a worst-case analysis, at no time was a power density greater than 1 mW/cm² calculated. In addition, during the performance of the test, a Narda radiation monitor was used to constantly survey the area about the radiometer.

Calibration of the radiometer was accomplished by setting a large tub of hot water on the transmitter window (with no RF present). A metal can, painted flat black, was placed in the water to serve as a black body radiator, and a mercury thermometer was immersed in the water. After calibration, agreement of better than 1 degree C was obtained between the temperature indication of the radiometer and the true water temperature as measured by the mercury thermometer.¹

Measurements of both peak temperature and the temperature profile across the face of the window were then performed for both Kapton and HPT-6 for transmitted power levels in the range of 200–365 kW.

III. Results

The highest temperature observed using the Kapton window was approximately 100 degrees C at a power level of

360 kW. However, due to 45-degree F air temperature with winds gusting at 30 – 35 mi/hr and the very low thermal mass of the 0.001-in. Kapton window, it was not possible to obtain an accurate representation of the typical operating conditions. A retest in the future under calm conditions is required to properly evaluate the performance of the Kapton window.

More stable temperature data were obtained for the HTP-6 window. A peak operating temperature of 475 degrees C was observed at 365-kW transmitted power. The power-temperature relationship for HTP-6 is shown in Fig. 3. Simple calculations were made of the temperature of a 0.1-in. HTP-6 window at 365 kW using two different models. Assuming a uniformly heated disk model, a temperature of 270 degrees C was predicted. Using a model of a Gaussian temperature distribution over the disk, a temperature of 580 degrees C was predicted. Given the Gaussian distribution of the RF beam passing through the window (see Fig. 4), the second estimate was the better one. The lower measured temperature value was due to neglecting conductive cooling through the window mounting surface in the calculations.

As of April 1989, testing using the X-band radiometer of the Radio Frequency and Microwave Subsystems Section produced values for the noise temperature contribution and insertion loss of the 0.1-inch thick HTP-6 feedhorn window. These values are 0.2 Kelvin and 0.003 dB. This measurement was performed by M. Britcliffe.

IV. Conclusion

A high-power microwave transmitter feedhorn window was successfully imaged using an infrared radiometer-mirror technique. Agreement between the measured and actual temperature of a body was excellent with this method, which is also useful in other remote thermal imaging applications. Good data were not taken for a 0.001-in. thick Kapton window due to the weather conditions. A reevaluation of the Kapton window needs to be performed under better conditions. Measurements of low-loss quartz and lower-density HTP windows would also be of interest.

¹For a more detailed explanation of the radiometer usage and calibration, see S. Glazer, "Thermal Infrared Measurements of R. F. Transmitter Feedhorn Windows During High Power Transmitting Operation," JPL IOM 3547-TSE-109 (internal document), June 1988.

Acknowledgments

Special thanks are due to Stuart Glazer for the capable operation of the infrared radiometer and the determination of the infrared radiation characteristics of Kapton and HTP-6. E. W. Stone is also to be thanked for suggesting the evaluation of HTP-6.

Reference

- [1] A. M. Bhanji, D. J. Hoppe, D. L. Conroy, and A. J. Freiley, "Conceptual Design of a 1-MW CW X-Band Transmitter for Planetary Radar," *TDA Progress Report 42-95*, vol. July–September 1988, Jet Propulsion Laboratory, Pasadena, California, pp. 97–111, November 15, 1988.

Table 1. Some physical properties of HTP-6

Density	6 lb/ft ³
Dielectric constant	1.07
Loss tangent	0.0005
Maximum operating temperature	980 degrees C

ORIGINAL PAGE
BLACK AND WHITE PHOTOGRAPH

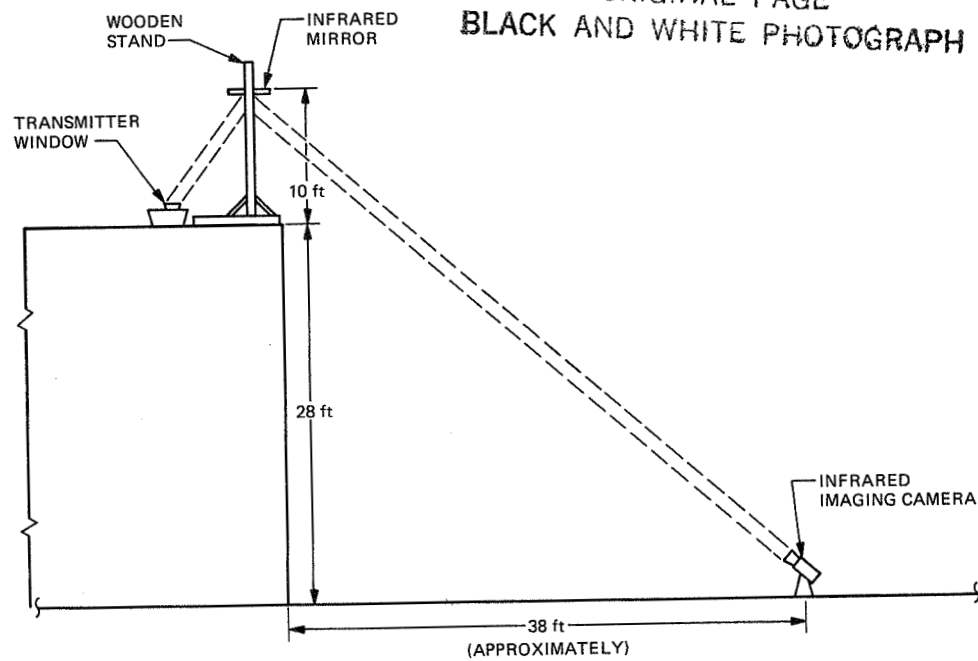


Fig. 1. Microwave window infrared imaging test configuration.

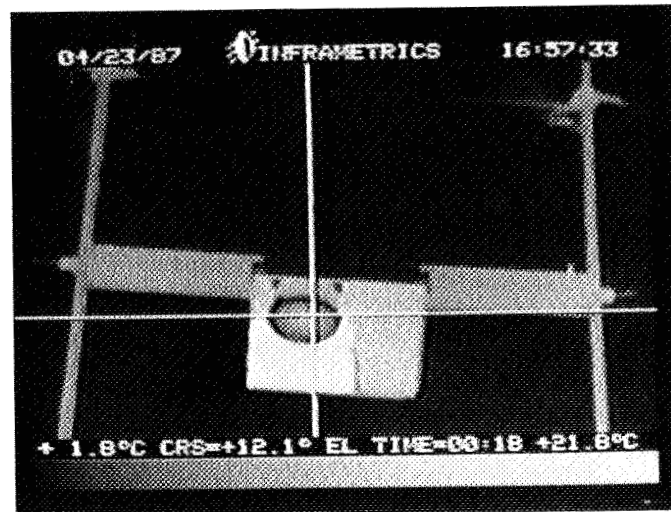


Fig. 2. Infrared image of window in mirror.

ORIGINAL PAGE
BLACK AND WHITE PHOTOGRAPH

ORIGINAL PAGE
BLACK AND WHITE PHOTOGRAPH

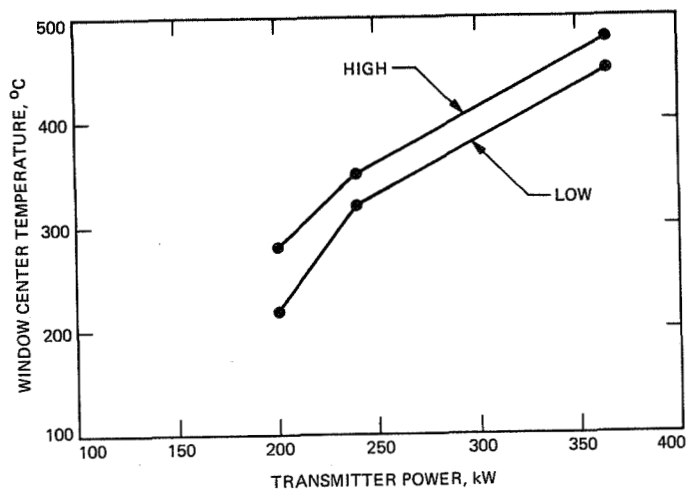


Fig. 3. HTP-6 window temperature versus transmitted power.

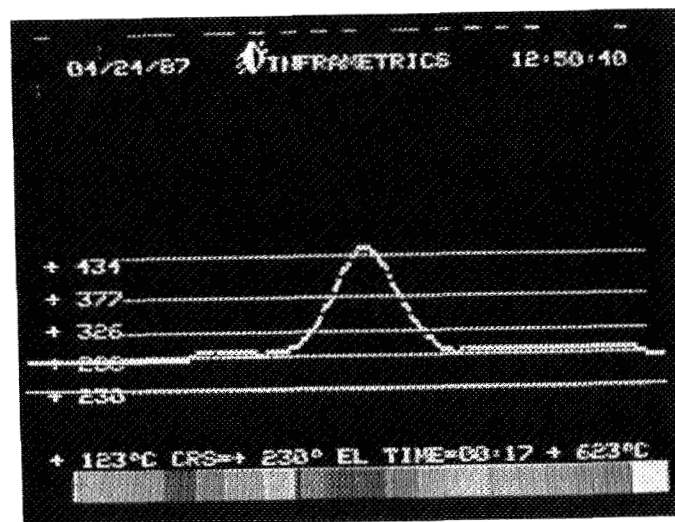


Fig. 4. Temperature distribution across window surface.

ORIGINAL PAGE
BLACK AND WHITE PHOTOGRAPH

515-32
218070

N 8 9 - 2 7 8 8 6

A New Analysis of Beam-Waveguide Antennas Considering the Presence of the Enclosure

A. G. Cha

Ground Antenna and Facilities Engineering Section

Beam-waveguide (BWG) antennas provide multiple frequency band operations and other operational benefits for large ground-station antennas. Present design practices use diffraction analyses that ignore the presence of the BWG enclosure and may be inaccurate at lower frequency bands for ground-station antennas operating over multiple frequency bands. This article introduces a new analysis approach that considers the presence of the BWG enclosure. Results based on the new analysis have revealed new understandings of the performance degradation mechanisms in a BWG antenna and have provided direction for potential design improvements.

I. Introduction

Beam-waveguide (BWG) technology offers wide frequency-band coverages, improved gain/temperature (G/T) performance for ultra-low-noise ground antennas by providing a more stable operating environment for masers, advantages in maintenance and operations, and reduced life-cycle cost for ground-station antennas. For these reasons, there has been a trend towards adopting the BWG design in new ground-station antenna projects. Examples are the Japanese 45-m and 64-m antennas at Nobeyama and Usuda, and various 30-m class Intelsat and Comsat ground antennas. Additionally, the Deep Space Network (DSN) is building a 34-m BWG antenna at Goldstone, California.

The BWG feed operating principle is based on geometric optics (GO). By using a pair of properly shaped and positioned mirrors, the radiation pattern of a feedhorn can be reproduced at a point in space that is some distance away from the physical location of the feedhorn. For finite-size BWG systems and

at finite frequencies, some loss and some pattern distortions are experienced. At present, such effects are predicted from diffraction analysis developed for mirrors in open space. Common analysis techniques are Gaussian mode analysis and physical optics (PO) analysis. In actuality, the BWG mirrors are enclosed by metal walls for safety when transmitting, and for sensitivity (noise temperature) and protection against radio frequency interference (RFI) when receiving. The absence of the metal wall in the current analysis models leads to an error whose magnitude is not well understood, especially at lower frequencies when the wall diameter is 20 wavelengths or less. In practice, this means one is forced to make decisions about, for example, building a 6-ft- or 8-ft-diameter BWG system based on weak assumptions. Such decisions often have major impacts on antenna microwave/structural performances and project cost tradeoffs.

This article presents a new analysis of BWG antennas which considers the presence of the wall. This analysis is based on

replacing the free-space Green's function used in PO analysis with the dyadic Green's function for a cylindrical waveguide, satisfying the boundary condition at the metallic BWG wall. The results from this analysis have revealed some new understandings of the performance degradation mechanisms in a BWG antenna and have pointed to potentially significant design improvements. Some of these ideas are discussed here. Full realization of all benefits from BWG wall analysis and design concepts will take some time. It is hoped that the discussions in this article will induce further innovative ideas and designs.

II. The Optics of BWG Systems

Figures 1(a) and 1(b) show the microwave optics of BWG systems. A basic cell consists of a pair of curved mirrors (reflectors). In practice, a pair of flat mirrors is often added to form a four-mirror system. However, the BWG characteristics are largely determined by the pair of curved mirrors. The conditions for distortionless transmission of feedhorn patterns based on GO are discussed in [1]. It is shown that a paraboloid pair oriented as shown in Fig. 1(a) is one choice that meets the Mizusawa condition. This case is used here to discuss the diffraction effects.

The Mizusawa condition guarantees distortionless transmission of the feedhorn pattern from focus F1 to focus F2 at infinite frequency where GO is valid. The only loss is at the first mirror as it does not collect all the GO rays. In practice, BWG antenna designs must consider diffraction effects which cause further degradations as shown in Fig. 1(b). Figure 1(b) illustrates how the diffraction effects are presently modeled. Mirror 1 is illuminated by the feedhorn and radiates into the whole space. Assuming mirror 2 is in the near-field zone of mirror 1, one can visualize mirror 2 intercepting the bulk of the rays bounced off mirror 1, but there is a small amount of energy loss due to the divergence of the beam of rays. In addition, it can also be expected that the rays reflected from mirror 2 will now not be focused to a single point F2. This implies that the image pattern at F2 compared to the real feedhorn pattern at F1 will have amplitude and phase distortions. If the real feedhorn pattern at F1 is the ideal pattern needed to illuminate a reflector antenna, then the distorted pattern at F2 gives rise to further performance degradations in addition to the spillover loss at each mirror.

Such mechanisms of performance degradation are predicted from present analytical techniques, including Gaussian mode analysis [2], physical optics [3], and geometrical theory of diffraction (GTD). It is generally accepted that these techniques yield good results under the very near-field approximation.

$$L \leq C \left(\frac{D^2}{\lambda} \right) \quad (1)$$

where L is the distance between mirrors 1 and 2, D is the mirror diameter, λ is the wavelength, and C is a constant generally taken as between 0.1 and 0.2 [3]. None of the above analyses recognizes the presence of the wall and thus they are likely to lead to errors in BWG antenna performance analysis when the condition in Eq. (1) is not met. The following introduces a new analytical approach that recognizes the wall presence. The new analysis is theoretically more satisfactory and should in time lead to significantly better analysis and design of BWG antennas.

III. New BWG Antenna Analysis That Considers the Wall Presence

The new BWG wall analysis presented in this article is conceptually similar to the PO analysis used in reflector antenna analysis; Fig. 2 shows this analogy. The PO analysis and the BWG wall analysis can each be conceptualized as a superpositioning process whereby the radiation field of a current distribution is found by integrating the radiation field of point sources. Assuming a time dependence $e^{j\omega t}$, the PO far field is written as

$$\bar{E}(\bar{R}) = I_{\theta} \hat{\theta} + I_{\phi} \hat{\phi} \quad (2)$$

where

$$\bar{I} = -j\omega\mu \int \bar{K}(\bar{R}') g(\bar{R}, \bar{R}') ds' \quad (3)$$

and

$$g(\bar{R}, \bar{R}') = \frac{e^{-jk|\bar{R} - \bar{R}'|}}{4\pi|\bar{R} - \bar{R}'|} \quad (4)$$

In Eqs. (2), (3), and (4), ω is the angular frequency, μ is the permeability, \bar{R} is the position vector of the observer, \bar{R}' is the position vector of a point source, and $g(\bar{R}, \bar{R}')$ is the free-space Green's function. The integration is over the surface current as determined from the PO approximation, i.e.,

$$\bar{K}(\bar{R}') = 2\hat{n} \times \bar{H}^{inc}(\bar{R}')$$

where \hat{n} is the unit normal vector and \bar{H}^{inc} is the incident magnetic field. For BWG analysis, the approach in this article is based on a very elegant dyadic Green's function formulation

discussed in [4]. For the one-mirror BWG system, the field scattered by the BWG mirror in the waveguide can be written as

$$\bar{E} = -j\omega\mu \int \bar{\bar{G}}_1(\bar{R}, \bar{R}') \bar{K} ds' \quad (5)$$

where $\bar{\bar{G}}_1(\bar{R}, \bar{R}')$ is the dyadic Green's function that satisfies Maxwell's equations and the boundary conditions of the BWG metal wall, i.e., no field exists outside the BWG wall. For a cylindrical waveguide, the dyadic Green's function has been derived and is given in Eq. (15) of [4] as

$$\begin{aligned} \bar{\bar{G}}_1(\bar{R}, \bar{R}') &= \frac{-j}{4\pi} \sum_{l=1}^2 \sum_{n=0}^{\infty} \sum_{m=1}^{\infty} (2 - \delta_o) \\ &\times \left[\frac{1}{\mu^2 I_\mu k_\mu} \bar{M}_{o nm}^{(k_\mu)} \bar{M}_{o nm}'^{(-k_\mu)} \right. \\ &+ \left. \frac{1}{\lambda^2 I_\lambda k_\lambda} \bar{N}_{o nm}^{(k_\lambda)} \bar{N}_{o nm}'^{(-k_\lambda)} \right] \\ &- \frac{1}{k^2} z z \delta(\bar{R} - \bar{R}'), \quad z > 0 \end{aligned} \quad (6)$$

where $\delta(\bar{R} - \bar{R}')$ is the Dirac delta function, δ_o is the Kronecker delta, $\delta_o = 0$ if $n \neq 0$ and $\delta_o = 1$ if $n = 0$, and the 1-summation is over even and odd modes. Note that in Eq. (6), $\mu, I_\mu, k_\mu, \lambda, I_\lambda$, and k_λ are understood to have double indices m and n .

$$\bar{M}_{o nm}^{(h)} = \left[\mp \frac{n J_n(\mu r)}{r} \frac{\sin n\phi \hat{r}}{\cos} - \frac{\partial J_n(\mu r)}{\partial r} \frac{\cos n\phi \hat{r}}{\sin} \right] e^{-jhz} \quad (7)$$

$$\begin{aligned} \bar{N}_{o nm}^{(h)} &= \frac{1}{k} \left[-jh \frac{\partial J_n(\lambda r)}{\partial r} \frac{\cos n\phi \hat{r}}{\sin} \right. \\ &\left. \pm \frac{jhn}{r} J_n(\lambda r) \frac{\sin n\phi \hat{r}}{\cos} + \lambda^2 J_n(\lambda r) \frac{\cos n\phi \hat{r}}{\sin} \right] e^{-jhz} \end{aligned} \quad (8)$$

$$I_\lambda = \int_0^a J_n^2(\lambda r) r dr = \frac{a^2}{2\lambda^2} \left[\frac{\partial J_n(\lambda r)}{\partial r} \right]_{r=a}^2 \quad (9)$$

$$I_\mu = \int_0^a J_n^2(\mu r) r dr = \frac{a^2}{2\mu^2} \left(\mu^2 - \frac{n^2}{a^2} \right) J_n^2(\mu a) \quad (10)$$

In Eqs. (9) and (10), a is the radius of the waveguide, k is the free-space wave number, and J_n is the Bessel function of the first kind.

To satisfy the radiation condition, when k_μ and k_λ are real,

$$k_\mu = |(k^2 - \mu^2)^{1/2}|$$

$$k_\lambda = |(k^2 - \lambda^2)^{1/2}|$$

When they are imaginary ($k^2 < \mu^2, k^2 < \lambda^2$),

$$k_\mu = (-j) |(\mu^2 - k^2)^{1/2}|$$

$$k_\lambda = (-j) |(\lambda^2 - k^2)^{1/2}|$$

$$\mu = \mu_{nm} = \frac{q_{nm}}{a} \quad (11)$$

$$\lambda = \lambda_{nm} = \frac{p_{nm}}{a} \quad (12)$$

In Eqs. (11) and (12), q_{nm} and p_{nm} are the m th root of $J_n(x)$ and $J_n'(x)$.

$$J_n(p_{nm}) = 0$$

$$\left. \frac{dJ_n(x)}{dx} \right|_{x=q_{nm}} = 0$$

$$k = \frac{2\pi}{\lambda_0}$$

where λ_0 is the free-space wavelength.

Note that M and N in Eqs. (7) and (8) represent TE and TM waves propagating in the $+z$ direction. Individually, each mode satisfies Maxwell's equation, the boundary conditions at the wall, and the "radiation condition" as $z \rightarrow \infty$. It is clear that Eq. (5) is conceptually the equivalent of PO in the beam-waveguide world. The difference is in Green's functions, which must meet different boundary conditions, including the radiation condition.

IV. Numerical Results and Assessment

The results of the wall analysis of a 34-m antenna under construction (designated DSS-13 in the DSN) are shown in Fig. 3. The projected mirror diameter is approximately 2.4 m, or approximately 19 wavelengths at the analysis frequency of 2.295 GHz. These initial results revealed some exciting potential for BWG antenna design improvement. A very important finding is that there are only a few significant modes propagating between the two curved mirrors. This is despite the facts that the waveguide diameter is 19 wavelengths, and that a large number of modes are theoretically above their cutoff frequencies. As shown in Fig. 3, the electromagnetic (EM) field scattered from mirror 1 consists of mainly TE_{11} and TM_{11} modes. This is not surprising, as the incident field is assumed to be from a horn with a symmetric radiation pattern, similar to that of a corrugated horn. By normalizing the mode power to the TE_{11} mode, the third and fourth significant modes TE_{21} and TM_{21} are already about 30 dB down in power.

Given that hundreds of modes may propagate, this result must be viewed with some caution. It is encouraging that the results described above are in qualitative agreement with some results in [2]. By expanding the reflected field from a curved mirror in Gaussian modes, the field can be represented approximately by just two Gaussian modes, TEM_{00} and TEM_{01} . Note that the field line of the TEM_{00} Gaussian mode bears a striking similarity to that of the aperture field of a dual-mode (TE_{11} and TM_{11}) horn, with the two modes in appropriate amplitude and phase relationships. Furthermore, the TEM_{01} Gaussian mode field lines are similar to the TE_{21} cylindrical waveguide mode. These observations are shown in Fig. 4. Thus the results in [2] are in qualitative agreement with the present analysis with regard to the scattered field from mirror 1 in the immediate neighborhood of mirror 1.

The major difference between a Gaussian mode analysis and the present analysis is that Gaussian modes and cylindrical waveguide modes propagate with distinctly different characteristics between mirrors 1 and 2. One significant difference is that the dominant Gaussian TEM_{00} is seen to be more like two cylindrical waveguide modes. For large mirror separations,

there is phase slippage between the two cylindrical waveguide modes not predicted by the TEM_{00} mode. Clearly, the Gaussian mode analysis is appropriate for BWG systems not enclosed by metal walls. When it is applied to an enclosed BWG system, it is a good approximation only while Eq. (1) is valid. The present analysis is valid when the BWG system is enclosed in metal walls and does not appear to be bound by Eq. (1), at least in principle.

A discussion follows of the mechanisms that cause performance degradation in an enclosed BWG system. These are

- (1) mode generation
- (2) mode dispersion
- (3) spillover loss at each mirror
- (4) multiple scattering between mirrors
- (5) dissipative loss in the wall

Assume that an HE_{11} mode horn or equivalently a dual TE_{11} and TM_{11} mode horn illuminates mirror 1. Each curved mirror may be viewed as a mode generator whose scattered field contains unwanted higher-order modes in the sense that at the output end of the BWG system, only the TE_{11} and TM_{11} modes in the correct complex ratio are desired. It appears that mode dispersion is a limiting factor, i.e., propagation with different phase velocities in the BWG causes the various modes to appear in wrong phases at the output of the BWG system. Undoubtedly, the present analysis provides the correct basis for calculating mode dispersion in an enclosed system compared to existing approaches such as Gaussian mode, PO, GTD, or others. Mechanisms (4) and (5) listed above have not been modeled, although a description of dissipative loss that ignores mechanisms (3) and (4) is within reach in the context of the present analysis. Ignoring the multiple-scattering mechanism nonetheless yields good results, as it appears to be much less important than mode generation and dispersion effects in a first-order analysis.

In terms of design improvements, the greater accuracy of the wall analysis model at lower frequencies should lead to more cost-effective designs of BWG antennas. Specifically, the diameter of the BWG tube is determined by low-frequency performance requirements. A less accurate analysis tends to lead to an unnecessarily large BWG tube, which raises antenna construction costs. Since a section of the BWG tube runs parallel to the antenna elevation axis, a larger tube requires the reflector and its backup structure to be raised higher, increasing the moment of the reflector and backup structure about the elevation axis. This reduces the antenna's pointing performance in wind, which must be compensated for by a

heavier, more expensive design. The alternative is that a reduced antenna wind pointing performance must be accepted. In addition, the analytical results showing that there are only a few significant modes likely between mirrors 1 and 2 suggest some further improvements to the BWG antenna and feed

design. Since most of the power is in the TE_{11} and TM_{11} modes and the differential propagating phase of the modes can be computed, it appears possible to design a dual-mode or multimode horn to compensate for the mode generation and mode dispersion effects discussed above.

Acknowledgments

The author wishes to acknowledge Mr. R. C. Clauss of JPL for many stimulating discussions pertaining to the BWG wall effects and Mr. M. J. Gans of AT&T Bell Laboratories for allowing the use of Fig. 4 in this paper, which is from [2]. Also, J. Schredder has helped tremendously with software development based on the wall analysis.

References

- [1] M. Mizusawa and T. Kitsuregawa, "A Beam Waveguide Feed Having a Symmetric Beam for Cassegrainian Antennas," *IEEE Trans. Antennas and Propagation*, vol. AP-21, pp. 884-886, November 1973.
- [2] M. J. Gans, "Cross Polarization in Reflector Type Beam Waveguides and Antennas," *The Bell System Technical Journal*, pp. 289-316, March 1976.
- [3] K. K. Chan, "Some Aspects of Beam Waveguide Design," *IEE Proc.*, vol. 129, pt. H, no. 4, pp. 203-210, August 1982.
- [4] C. T. Tai, *Dyadic Green's Functions in Electromagnetic Theory*, Scranton, Pennsylvania: Intext Educational Publishers, 1971.

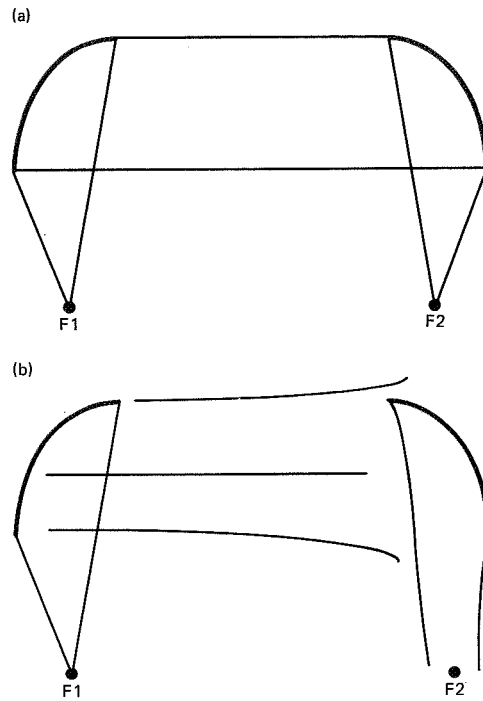


Fig. 1. Optics of BWG systems: (a) geometric optics approximation; (b) diffraction analysis with mirrors in open space.

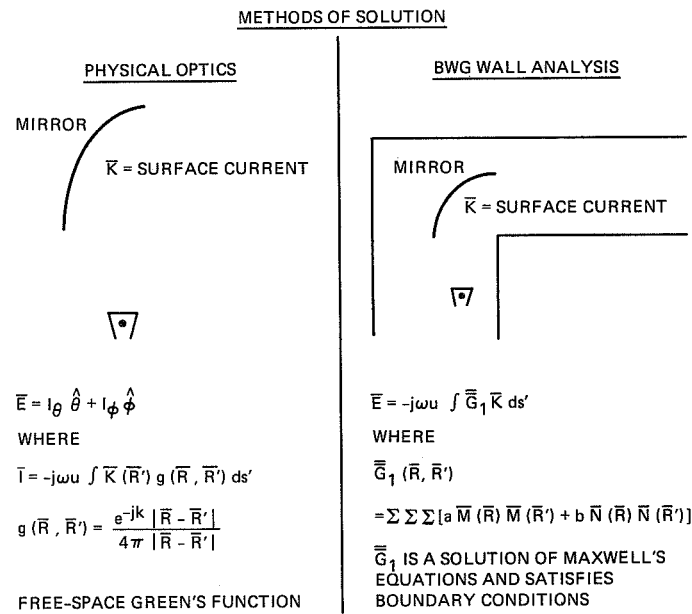
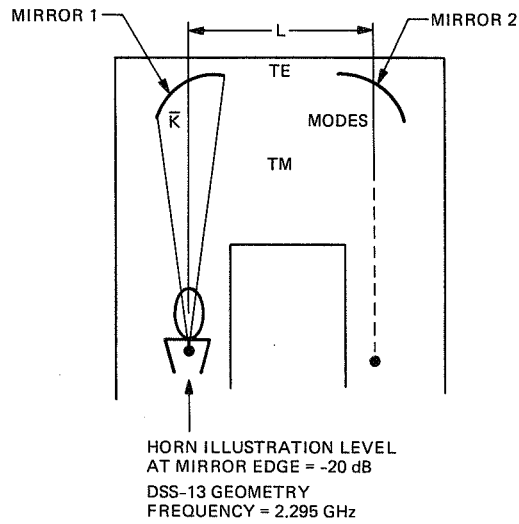


Fig. 2. Enclosed BWG system analysis approaches.



MODE POWER CONTENTS		
MODE	MODE COEFFICIENTS	
TE_{11} EVEN	$0.24 + j 0.88$	0 dB
TM_{11} ODD	$0.25 - j 0.07$	-10.9 dB
TE_{21} EVEN	$-0.01 - j 0.03$	-29.6 dB
TM_{21} ODD	$-0.02 - j 0.0$	-33.2 dB
...		

Fig. 3. Results of one-mirror BWG system wall analysis.

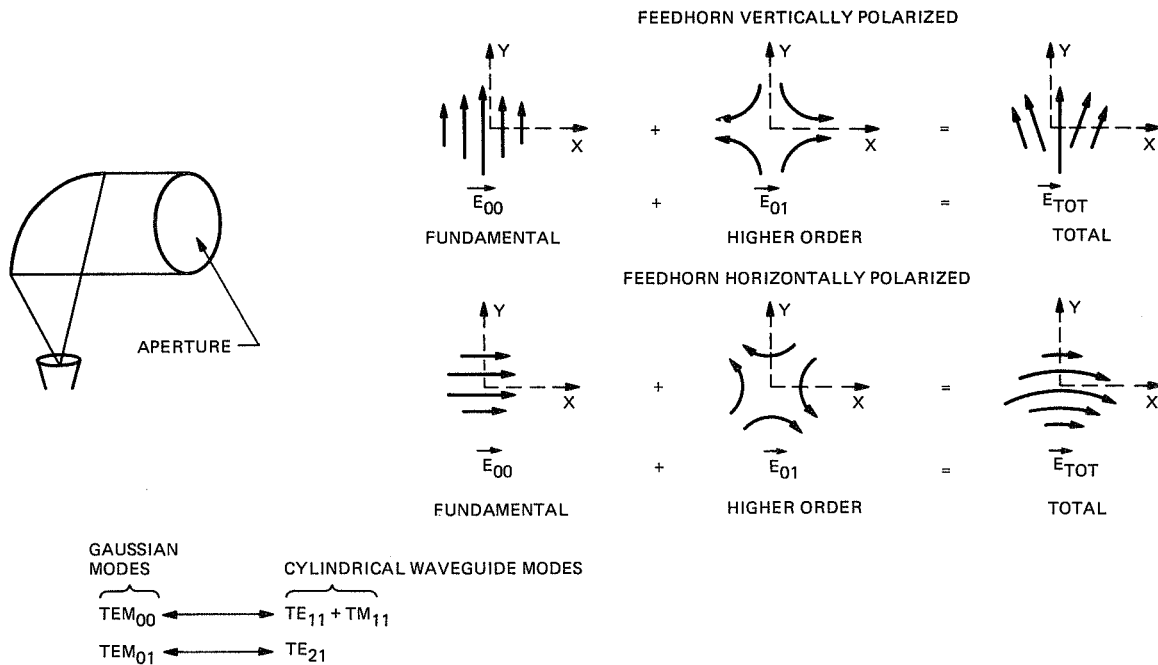


Fig. 4. Two-mode decomposition of aperture field.

516-33
218071

N 89-27887

Multipurpose Exciter With Low Phase Noise

B. Conroy and D. Le

Radio Frequency and Microwave Subsystems Section

This article reports results of an effort to develop a lower-cost exciter with high stability, low phase noise, and controllable phase and frequency for use in Deep Space Network and Goldstone Solar System Radar applications. It includes a discussion of the basic concept, test results, plans, and concerns.

I. Introduction

The advanced exciter development effort arose from a desire to use a high-quality commercial synthesizer to produce a new generation of exciters for the Deep Space Network (DSN) and Goldstone Solar System Radar (GSSR) transmitters. The design is based on the fact that multiplying a frequency also multiplies its phase noise, while translating frequency only adds a fixed amount of phase noise. Since a major part of the phase noise of an exciter is produced by the synthesizer, the synthesizer should not be followed by a frequency multiplier. Frequency translation, however, generates image frequencies that must be filtered. When the synthesizer frequency is above 300 MHz, image filtering is practical for all bands up to 35 GHz. Figure 1 is a block diagram of the translation system [1].

II. Preliminary Design

The Hewlett-Packard (HP) 8662A synthesizer has very low added phase noise in the range of 320 to 640 MHz. Two limitations for exciter applications, however, are that frequency resolution is limited to 0.1 Hz and that phase continuity is not guaranteed when changing frequency. Both these problems are addressed by the factory-supplied option C-03 [2]. This option provides an extra input to the HP 8662A for the injection

of a signal between 10 and 20 MHz, which is added to the output frequency. The range of phase-continuous operation is restricted because the HP 8662A must be reprogrammed if the auxiliary frequency changes by more than 2 MHz. When the signal to be added is derived from an HP 3325A function generator, it provides phase-continuous frequency changes over any 2-MHz range with 0.001-Hz resolution. There is, however, increased phase noise. Figure 2 shows measured phase noise of the HP 8662A at 640 MHz by itself and with the ability to adjust the absolute phase of the output with a precision of 0.1 degree.

Different multiplier configurations were evaluated for long-term stability. Figure 3 shows three such configurations, and Fig. 4 is the resulting Allan variance at X-band of each. In these figures, (a) uses a step recovery diode (SRD) harmonic generator driven by an auxiliary 640-MHz output of the HP 8662; (b) is an SRD harmonic generator driven by 400 MHz derived from the frequency and timing subsystem (FTS); and (c) is a single-frequency multiplier driven by 100 MHz from the FTS. These data indicate that the single-frequency multiplier is preferable to the SRD harmonic generator.

Based on these data, the prototype X-band exciter, shown in Fig. 5, was assembled for further evaluation.

III. Test Data

Figure 6 presents measured phase noise of three X-band exciters. The GSSR exciter was measured at Goldstone by the authors, the current DSN X-band exciter data were published in [5], and the prototype exciter shown in Fig. 5 was measured by the JPL Frequency Standards Test Lab (FSTL).

Figure 7 is a comparison of the Allan variance of the current DSN X-band exciter and the prototype exciter. Data for the DSN system come from [5], and the advanced exciter was measured by the FSTL using the system shown in Fig. 8. The measurement technique is described in [4].

The measured data indicate that the proposed advanced exciter yields a substantial improvement in phase noise and is comparable to the more complex DSN exciter in long-term stability (Allan variance).

IV. Configuration

The first operational test of the prototype advanced exciter will be for the GSSR X-band transmitter. Figure 9 is a block diagram of the intended configuration, with heavy lines indicating new elements and dotted lines for deleted elements. In this test configuration, the advanced exciter can also function as the first local oscillator for the receiver since the transmitter and receiver never operate at the same time. Additional effort will be required on the predicted Doppler interface, however, before this part of the test can be completed.

A rough analytical model of the noise sources in the exciter has been developed. The reason the results of the SRD harmonic generator were so disappointing needs to be learned. The multiplier and filters required to measure phase noise and Allan variance at S-band have been ordered. Tests at Ka-band are also possible.

V. Discussion and Conclusions

The present work has shown the feasibility of producing an advanced exciter using commercial equipment. The exciter will have a number of desirable features, including the following:

- (1) Low phase noise;
- (2) High long-term stability;
- (3) Phase-continuous frequency adjustment with 2-MHz range and 0.001-Hz resolution at any frequency;
- (4) Absolute phase control with 0.1-degree resolution at any frequency;
- (5) Computer-driven frequency and phase control, so that a phase versus time record can be kept and used for digital Doppler extraction;
- (6) Ability to function as the first local oscillator for the receive channel. In this use it can track (remove) predicted Doppler. This function is necessary for GSSR use, and can improve performance in DSN applications by allowing lower receiver bandwidth.

VI. Concerns

Absolute phase accuracy of the advanced exciter still needs to be demonstrated. One factor that affects it is any uncertainty in the time in which frequency changes are executed. Although this is a small effect, it may accumulate to an error in absolute phase. Another factor is that the HP 8662A synthesizer has a reputation for being susceptible to "popcorn noise" or occasional phase steps. This has not been observed in the prototype exciter, but testing of additional units is required to determine if this will be a problem in operational systems.

Acknowledgments

The authors acknowledge the assistance of William A. Diener, Roland E. Taylor, and Charles A. Greenhall of the Communications Systems Research Section in performing the measurements and interpreting the data.

References

- [1] "Low Phase Noise Applications of the HP 8662A and 8663A," *Hewlett-Packard Application Note 283-3*, Palo Alto, California, December 1986.
- [2] *Operating and Service Manual Modification Model 8662A, Option C-03 Synthesized Signal Generator*, Hewlett-Packard Spokane Division, Spokane, Washington, 1984.
- [3] C. E. Johns, "Block III X-Band Receiver-Exciter," *TDA Progress Report 42-89*, vol. January-March 1987, Jet Propulsion Laboratory, Pasadena, California, pp. 83-93, May 15, 1987.
- [4] C. A. Greenhall, "A Method for Using a Time Interval Counter to Measure Frequency Stability," *TDA Progress Report 42-90*, vol. April-June 1987, Jet Propulsion Laboratory, Pasadena, California, pp. 149-156, August 15, 1987.
- [5] C. E. Johns, "X-Band Uplink Ground Systems Development: Part II," *TDA Progress Report 42-91*, vol. July-September 1987, Jet Propulsion Laboratory, Pasadena, California, pp. 265-268, November 15, 1987.

C-3

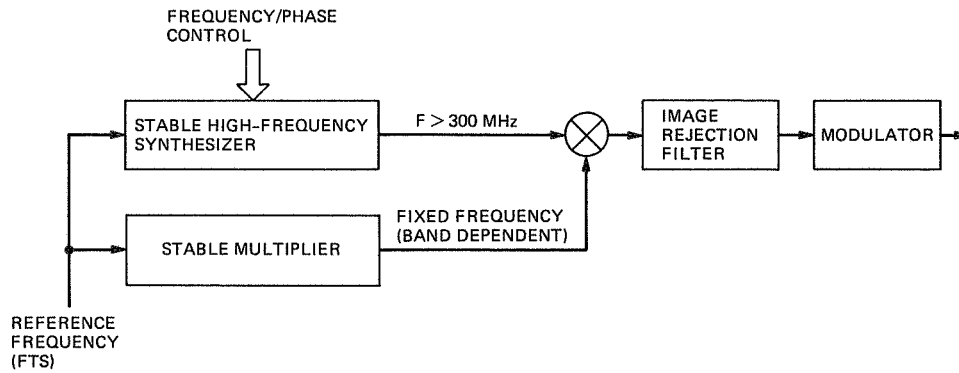


Fig. 1. Frequency translation system.

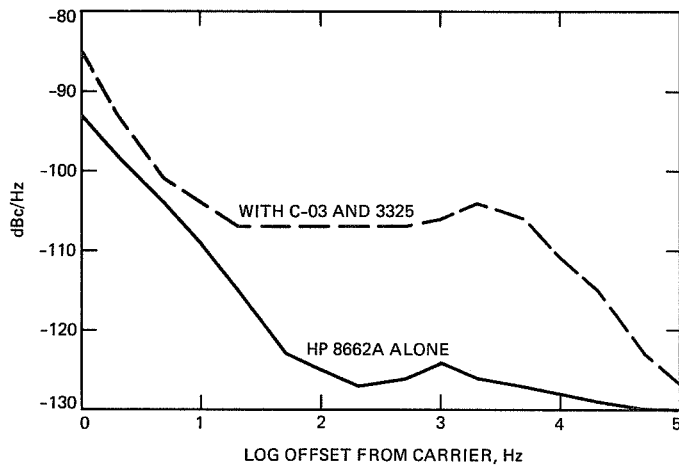


Fig. 2. Added noise from option C-03, single-sideband (SSB) phase noise at 640 MHz.

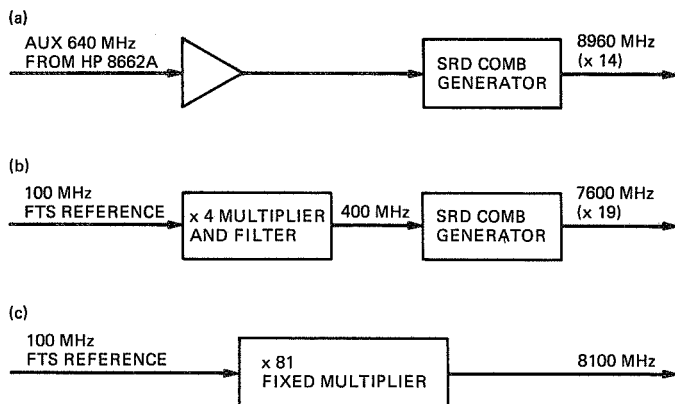


Fig. 3. Multiplier configurations: (a) SRD driven by 640-MHz auxiliary output of HP 8662A; (b) SRD driven by 400 MHz from FTS reference; (c) x81 fixed multiplier.

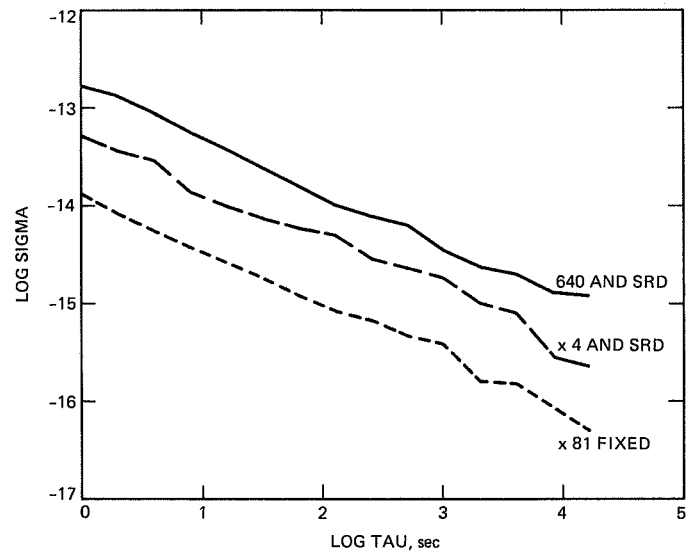


Fig. 4. Allan variance versus multiplier type, measured at X-band.

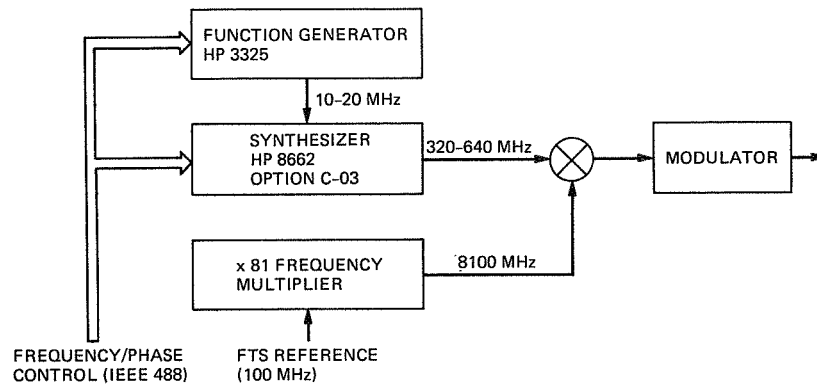


Fig. 5. Prototype X-band exciter.

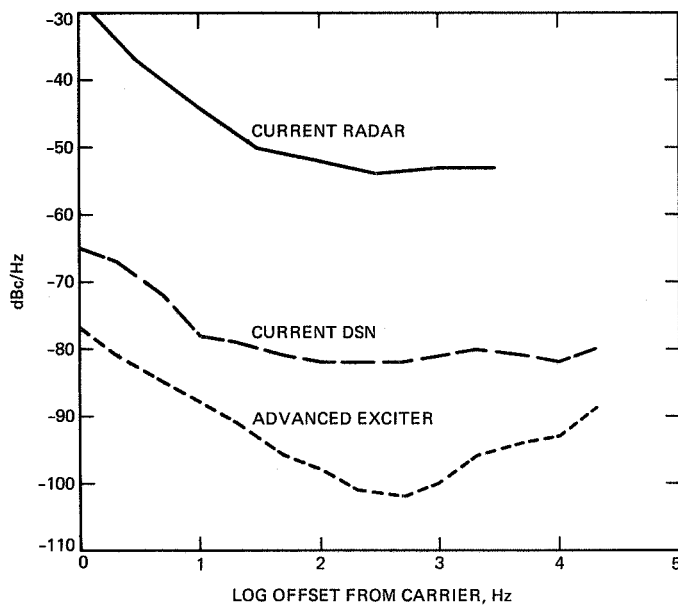


Fig. 6. SSB phase noise, measured at X-band.

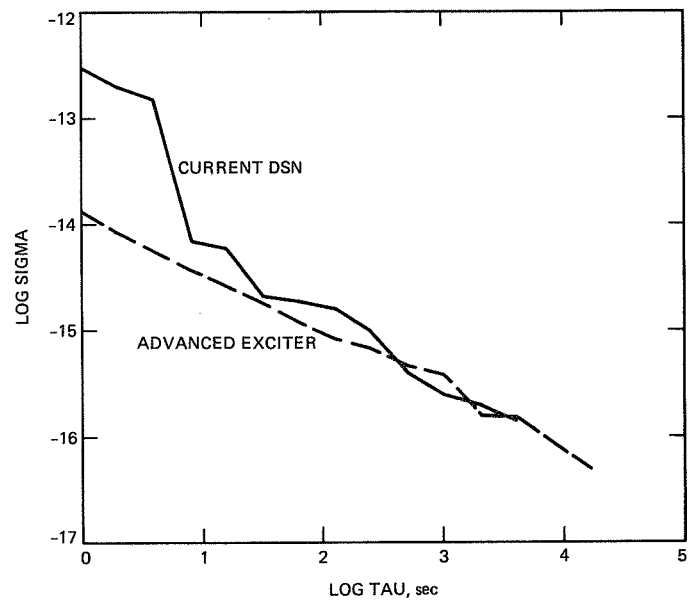


Fig. 7. Allan variance, measured at X-band.

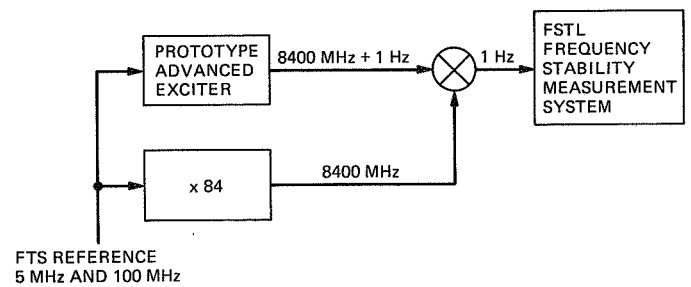


Fig. 8. Allan variance test setup.

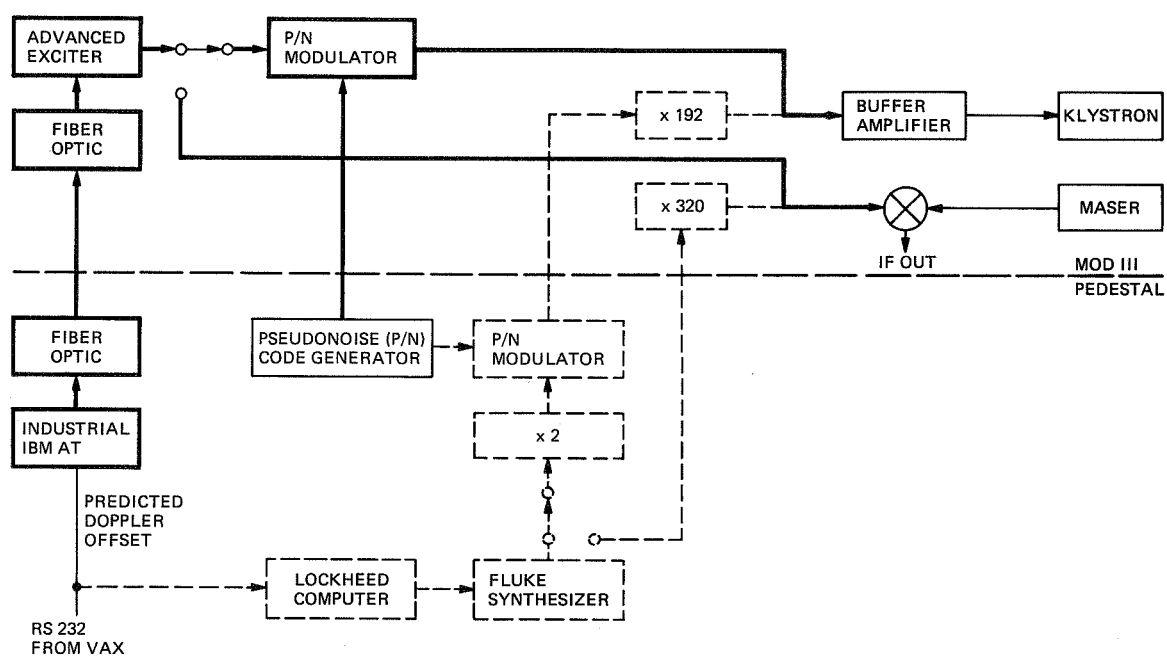


Fig. 9. Block diagram exciter installation, GSSR.

Software Package for Performing Experiments About the Convolutionally Encoded Voyager 1 Link

U. Cheng

Communications Systems Research Section

A software package enabling engineers to conduct experiments to determine the actual performance of long constraint-length convolutional codes over the Voyager 1 communication link directly from JPL has been developed. Using this software, engineers are able to enter test data from the Laboratory in Pasadena, California. The software encodes the data and then sends the encoded data to a personal computer (PC) at the Goldstone Deep Space Complex (GDSC) over telephone lines. The encoded data are sent to the transmitter by the PC at GDSC. The received data, after being echoed back by Voyager 1, are first sent to the PC at GDSC, and then are sent back to the PC at the Laboratory over telephone lines for decoding and further analysis. All of these operations are fully integrated and are completely automatic. Engineers can control the entire software system from the Laboratory. The software encoder and the hardware decoder interface were developed for other applications, and have been modified appropriately for integration into the system so that their existence is transparent to the users. This software provides (1) data entry facilities, (2) communication protocol for telephone links, (3) data displaying facilities, (4) integration with the software encoder and the hardware decoder, and (5) control functions.

I. Introduction

For several years, a goal of TDA Advanced Systems has been to find a convolutional code which, when concatenated with an appropriate outer Reed-Solomon code, would perform 2 dB better than the concatenated code currently used by the Voyager spacecraft [1]. When such a code was found, an "experiment" was planned: data would be encoded, transmitted to a spacecraft (e.g., Voyager 1) on a ranging channel, recovered at Goldstone, and decoded. Because the Galileo mission adopted a coding experiment with a code similar to

this 2-dB code [2], [3], the original experiment is now unlikely to be performed. The software package developed for the experiment may have another use, and hence it is presented here.

The software and hardware configuration is illustrated in Fig. 1. The software package comprises two programs, both running on IBM personal computers (PCs) or compatibles. The first program is run by the engineers at the Laboratory; it is referred to as Program I in this article. The second program,

which runs on a PC at the Goldstone Deep Space Complex (GDSC), is the gateway to the transceiver; it is referred to here as Program II. The software package has eight features:

- (1) menu-driven user interface
- (2) data entry facilities
- (3) interface to the software convolutional encoder
- (4) interface to the hardware convolutional decoder
- (5) stop-and-wait protocol for the telephone link with variable packet size and error detection
- (6) split-screen display for the transmitted and returned data
- (7) command coding with error-correction and error-detection capabilities for software operational control (see the subsequent discussion), and
- (8) dedicated coding protection for the carriage-return byte

Program II has three operational modes: command, receiving, and transmitting. Program II always recognizes the "enter the command mode" command regardless of the current operational mode. For instance, by issuing this command, Program I can interrupt Program II to obtain control during the transmission of the returned data. Program I always puts Program II in the command mode before issuing any further commands. In the command mode, Program II is able to accept other commands from Program I, such as (1) enter the receiving mode, (2) enter the transmitting mode, or (3) clear all buffers. In this manner, the users of Program I can always control Program II remotely. In the receiving mode, Program II receives the encoded data from Program I. In the transmitting mode, Program II sends the returned data to Program I.

The software encoder and the hardware decoder interface were developed by Charles Lahmeyer of the Communications Systems Research Section for other applications. They have been modified appropriately for integration into the system. During transmission, the data entered by the users are first converted into a bit stream which is saved in a file. The software encoder is then invoked to encode the data. During reception, Program I converts the received data into a bit stream which is saved in a file. The decoder interface software is then invoked to decode the data.

The command coding for software operational control is explained in Section II. The stop-and-wait protocol is explained in Section III. The coding protection for the carriage-return byte is described in Section IV.

II. Command Coding

Coding for every operational command is necessary because of the noisy telephone link. Since the data are sent by bytes through the asynchronous telephone link, which has a low byte error rate, the command coding should be designed in bytes (i.e., a 256-symbol alphabet). Let a command code consisting of N bytes be denoted by $\underline{A} = \{a_1, a_2, \dots, a_N\}$. The detection of this command code is done by straight correlation. Let r_1, r_2, r_3, \dots , denote the received bytes and let

$$D(j) = \sum_{i=1}^N \left(1 - W(a_i, r_{j+i}) \right)$$

where $W(x, y)$ is the Hamming distance between two bytes, i.e., $W(x, y) = 0$ if $x = y$, and $W(x, y) = 1$ if $x \neq y$. Then if $D(j) > \delta$, one declares that \underline{A} has been detected at the j th received symbol; otherwise, the symbol stream starting at the next received symbol will be tested. The threshold δ is predetermined, based on the error rate of the asynchronous telephone link.

In this software package, five command codes are provided to trigger the following actions, namely:

- (1) enter the command mode
- (2) enter the receiving mode
- (3) enter the transmitting mode
- (4) clear the operational buffer, and
- (5) acknowledge command acceptance

The same acknowledgment code is also used in the stop-and-wait protocol for acknowledging acceptance of the most recently transmitted data packet. The first four command codes are referred to as the active command codes. They can only be issued by Program I. The acknowledgment code is a passive command code. It is issued by either program upon acceptance of a data packet or a command code. In order to allow Program I to maintain control of Program II even in noisy situations, an active command code must be repeated until an acknowledgment is received from Program II.

III. Stop-and-Wait Protocol

The stop-and-wait protocol is used for both the forward (JPL to GDSC) and the return (GDSC to JPL) telephone links to control the byte error rate. The probability of undetected errors over the telephone links must be made very low compared to the error rate of the Voyager 1 link. Low byte error rate can be accomplished through the addition of an adequate

number of parity-check bytes. In the current design, every data packet is protected by five parity-check bytes. These parity-check bytes are generated as follows:

- (1) one byte derived by the overall bitwise exclusive-OR operation, and
- (2) four bytes derived by the overall long-integer sum [4]

Each packet can be of any size up to 100 bytes. The first two bytes of each packet are the packet length. Two bytes are reserved for packet length out of consideration for software expandability. This allows the software to be usable should packets of length greater than 256 bytes be handled in the future. Each packet is transmitted repeatedly until an acknowledgment is received. On the receiving side, an acknowledgment is sent if a packet is received correctly.

The data transmission session is started by Program I using one of two commands: "enter the receiving mode" or "enter the transmitting mode." The session is terminated by Program I using the "enter the command mode" command. During data transmission, the programs display the number of packets transmitted, the number of packets received, and the length of the current packet. Program I attempts to collect the returned data from Program II whenever possible. For instance, when users are looking at the menu or examining the returned data, Program I will put Program II in the transmitting mode automatically in order to obtain as much returned data as possible. This strategy maximizes the link utilization and minimizes the waiting time for the users.

IV. Coding Protection for the Carriage-Return Byte

An important feature of this software package is to let users send plain-English text. Users can easily compare the transmitted text with the returned text. Errors which are not corrected by the convolutional decoder will be obvious to them.

In displaying the plain-English text, there is a control character of particular importance, the carriage-return character. This character tells when a new line begins. If the carriage-return character is received in error, the received text will have a disturbed format that makes the visual comparison between

the transmitted and the received text more difficult. Therefore, it is worth protecting this character by coding. The codeword must be designed so that when Program I searches for it in the data bit stream, the probability of detecting it is high but that of false alarm is low. The data bit stream has a bit error rate ranging from 10^{-5} to 0.2 (typical of the convolutionally encoded Voyager 1 link). The command coding concept described in Section II can be applied here. In this case, however, the codeword should be over binary alphabets and bitwise correlation should be performed:

$$D(j) = \sum_{i=1}^M \left(1 - W(c_i, b_{j+i}) \right)$$

where b_1, b_2, b_3, \dots , are the received bits, $\underline{C} = (c_1, c_2, \dots, c_M)$ is the carriage-return codeword, and $W(x, y)$ is the Hamming distance between two bits, i.e., $W(x, y) = 0$ if $x = y$, and $W(x, y) = 1$ if $x \neq y$. Then if $D(j) > \delta_1$, one declares that \underline{C} has been detected at the j th received bit; otherwise, the bit stream starting at the next received bit will be tested. The threshold is predetermined based on the bit error rate.

When Program I is transmitting, it examines each byte prior to transmission. If a carriage-return byte is encountered, the carriage-return codeword is sent instead. When Program I is receiving, it examines the received bit stream constantly to detect the carriage-return codeword. If this codeword is found, it is removed from the data and a carriage-return byte is inserted at that position.

V. Conclusion

The software described in this article enables engineers to conduct experiments to determine the actual performance of long constraint-length convolutional codes over the Voyager 1 communication link from the Laboratory. The concept behind this software should also be useful for other applications. Its control features allows engineers to conduct off-lab experiments from the Laboratory. The implemented protocol guarantees nearly error-free transmission of data from the remote sites to the Laboratory over standard telephone lines. High-speed modems can be used if a great amount of data must be transferred.

References

- [1] J. H. Yuen and Q. D. Vo, "In Search of a 2-dB Coding Gain," *TDA Progress Report 42-83*, vol. July–September 1985, Jet Propulsion Laboratory, Pasadena, California, pp. 26-33, November 15, 1985.
- [2] S. Dolinar, "A New Code for Galileo," *TDA Progress Report 42-93*, vol. January–March 1988, Jet Propulsion Laboratory, Pasadena, California, pp. 83–96, May 15, 1988.
- [3] S. Arnold and F. Pollara, "A Software Simulation Study of the Long Constraint Length VLSI Viterbi Decoder," *TDA Progress Report 42-94*, vol. April–June 1988, Jet Propulsion Laboratory, Pasadena, California, pp. 210–221, August 15, 1988.
- [4] *Microsoft C Language Reference Manual*, Microsoft Corporation, Bothell, Washington, 1987.

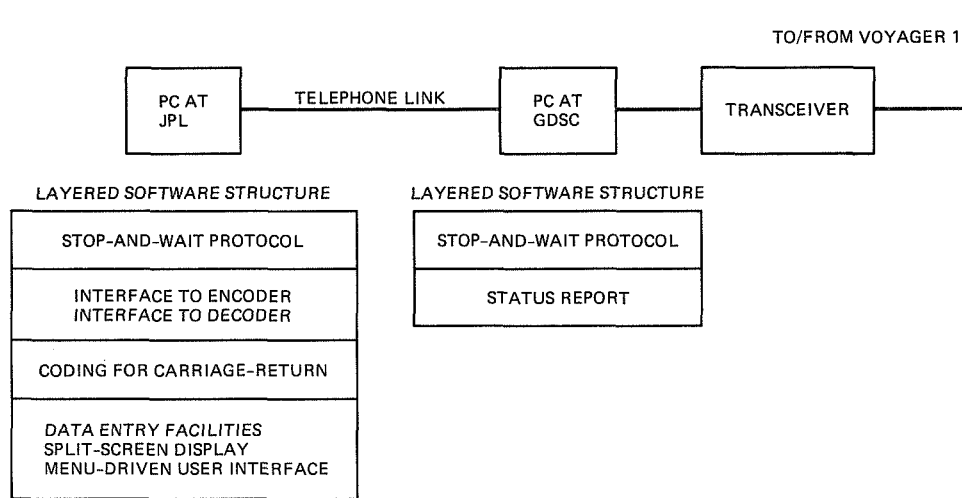


Fig. 1. Software and hardware configuration.

The Use of Interleaving for Reducing Radio Loss in Trellis-Coded Modulation Systems

D. Divsalar

Communications Systems Research System

M. K. Simon

Telecommunications Systems Section

In this article, it is demonstrated how the use of interleaving/deinterleaving in trellis-coded modulation (TCM) systems can reduce the SNR loss due to imperfect carrier demodulation references. Both the discrete carrier (phase-locked loop) and suppressed carrier (Costas loop) cases are considered and the differences between the two are clearly demonstrated by numerical results. These results are of great importance for future communication links to the DSN, especially from high Earth orbiters, which may be bandwidth limited.

I. Introduction

In a previous publication [1], the authors demonstrated how in convolutionally coded BPSK systems, the degradation in signal-to-noise ratio (SNR) performance due to imperfect carrier demodulation references (often referred to as *radio* or *noisy reference loss*) could be reduced by employing interleaving/deinterleaving. Specific closed form results were derived for both discrete and suppressed carrier systems and the differences between the two were discussed and numerically illustrated. Here these former results are generalized to trellis-coded MPSK systems [2]. As a numerical example used for illustration, the case of a rate 1/2 trellis-coded QPSK system with a 2-state trellis shall be considered.

II. Upper Bound on the Average Bit Error Probability Performance of TCM

A. Perfect Carrier Phase Synchronization

In previous work by the authors [3-6] on TCM transmitted over a perfectly phase-synchronized additive white Gaussian

noise (AWGN) channel, an upper bound on the average bit error probability was obtained as

$$P_b \leq \sum_{\underline{x}} \sum_{\hat{\underline{x}} \in C} a(\underline{x}, \hat{\underline{x}}) p(\underline{x}) P(\underline{x} \rightarrow \hat{\underline{x}}) \quad (1)$$

where $a(\underline{x}, \hat{\underline{x}})$ is the number of bit errors that occur when the sequence \underline{x} is transmitted and the sequence $\hat{\underline{x}} \neq \underline{x}$ is chosen by the decoder, $p(\underline{x})$ is the a priori probability of transmitting \underline{x} , and C is the set of all coded sequences. Also, in Eq. (1), $P(\underline{x} \rightarrow \hat{\underline{x}})$ represents the pairwise error probability, i.e., the probability that the decoder chooses $\hat{\underline{x}}$ when indeed \underline{x} was transmitted. The upper bound of Eq. (1) is efficiently evaluated using the *transfer function bound* (generating function) approach [7] applied to TCM.

In general, evaluation of the pairwise error probability depends on the proposed decoding metric, the presence or absence of channel state information (CSI), and the type of detection used, i.e., coherent versus differentially coherent.

For the case of interest here, namely, coherent detection with no CSI and a Gaussian metric (optimum for the AWGN channel), it is well known [7] that the pairwise error probability is given by

$$P(\underline{x} \rightarrow \hat{\underline{x}}) \leq \exp \left\{ -\frac{E_s}{4N_0} d^2(\underline{x}, \hat{\underline{x}}) \right\} \quad (2)$$

where

$$d^2(\underline{x}, \hat{\underline{x}}) = \sum_{n \in \eta} |x_n - \hat{x}_n|^2 \triangleq \sum_{n \in \eta} \delta_n^2 \quad (3)$$

represents the sum of the squared Euclidean distances between the two symbol sequences \underline{x} (the correct one) and $\hat{\underline{x}}$ (the incorrect one) and η is the set of all n for which $\hat{x}_n \neq x_n$. Also, in Eq. (3), E_s is the energy per output coded symbol and N_0 is the single-sided noise spectral density.

B. Imperfect Carrier Phase Synchronization

1. **Discrete Carrier (No Interleaving).** When a carrier phase error $\phi(t)$ exists between the received signal and the locally generated demodulation reference, then the result in Eq. (2) is modified as follows.

Assuming the case where the data symbol rate $1/T_s$ is high compared to the loop bandwidth B_L , then $\phi(t)$ can be assumed constant (independent of time), say ϕ , over a number of symbols on the order of $1/B_L T_s$. Since the decoder has no knowledge of ϕ , the decoding metric can make no use of this information and as such is *mismatched* to the channel. Under these conditions, it can be shown (Appendix A) that using the maximum-likelihood metric for a perfectly phase-synchronized AWGN, one obtains

$$P(\underline{x} \rightarrow \hat{\underline{x}} | \phi; \lambda) \leq \begin{cases} \frac{1}{2} \exp \left\{ -\frac{E_s}{4N_0} \sum_{n \in \eta} 4\lambda (\cos \phi + \alpha_n \sin \phi - \lambda) \delta_n^2 \right\}; \\ \sum_{n \in \eta} \delta_n^2 (\cos \phi + \alpha_n \sin \phi) > 0 \\ 1; \quad \sum_{n \in \eta} \delta_n^2 (\cos \phi + \alpha_n \sin \phi) \leq 0 \end{cases} \quad (4)$$

where

$$\alpha_n \triangleq \sqrt{\frac{4 - |x_n - \hat{x}_n|^2}{|x_n - \hat{x}_n|^2}} = \sqrt{\frac{4 - \delta_n^2}{\delta_n^2}} \quad (5)$$

and $\lambda \geq 0$ is a parameter to be optimized. Note that for $\phi = 0$, the parameter λ can be optimized independent of the summation index n . In particular, the expression $4\lambda(1 - \lambda)$ is maximized by the value $\lambda = 1/2$ which when substituted in Eq. (4) yields Eq. (2) as it should.

Letting $p(\phi)$ denote the probability density function (p.d.f.) of the phase error ϕ , then the average bit error probability is upper bounded by¹

$$P_b \leq \sum_{\underline{x}, \underline{\hat{x}} \in \mathcal{C}} a(\underline{x}, \underline{\hat{x}}) p(\underline{x}) \min_{\lambda} E_{\phi} \{P(\underline{x} \rightarrow \underline{\hat{x}} | \phi; \lambda)\} \quad (6)$$

where $E_{\phi} \{\bullet\}$ denotes statistical averaging over the p.d.f. $p(\phi)$.

To somewhat simplify notation, the Bhattacharyya parameter [7] is introduced

$$D \triangleq \exp \left\{ -\frac{E_s}{4N_0} \right\} \quad (7)$$

in which case

$$E_{\phi} \{P(\underline{x} \rightarrow \underline{\hat{x}} | \phi; \lambda)\} \leq \frac{1}{2} \int_{\mathcal{R}} \left(\prod_{n \in \eta} D^{\delta_n^2} \right)^{[4\lambda(\cos \phi - \lambda)]} \times \left(\prod_{n \in \eta} D^{\alpha_n \delta_n^2} \right)^{[4\lambda \sin \phi]} p(\phi) d\phi + \int_{\mathcal{R}} p(\phi) d\phi \quad (8)$$

where \mathcal{R} is the set of all ϕ in $(-\pi, \pi)$ for which

$$\sum_{n \in \eta} \delta_n^2 (\cos \phi + \alpha_n \sin \phi) > 0 \quad (9)$$

¹ Later on a tighter bound for this case shall be presented by optimizing on λ prior to performing the expectation over ϕ .

and $\overline{\mathcal{R}}$ is the complement of \mathcal{R} , i.e., the remaining values of ϕ in $(-\pi, \pi)$ that do not satisfy Eq. (9). Defining

$$\phi_1 \triangleq \tan^{-1} \frac{\sum_{n \in \eta} \alpha_n \delta_n^2}{\sum_{n \in \eta} \delta_n^2} = \tan^{-1} \frac{\sum_{n \in \eta} \sqrt{\delta_n^2 (4 - \delta_n^2)}}{\sum_{n \in \eta} \delta_n^2} \quad (10)$$

then \mathcal{R} corresponds to the interval $0 \leq |\phi - \phi_1| \leq \pi/2$ and $\overline{\mathcal{R}}$ corresponds to the interval $\pi/2 \leq |\phi - \phi_1| \leq \pi$.

2. Discrete Carrier (With Interleaving). Ordinarily, one thinks of using interleaving/deinterleaving to break up the effects of error bursts in coded communication systems. For example, in TCM systems operating in a multipath fading environment, it has been shown [2] that interleaving/deinterleaving is essential for good performance. To see how it may be applied in systems with noisy carrier phase reference, one can gain an intuitive notion by considering the $\cos \phi$ degradation factor as an "amplitude fade" whose duration is on the order of $1/B_L T_s$ symbols. Thus, if one breaks up this "fade" by interleaving to a depth on the order of $1/B_L T_s$, then, after deinterleaving, the degradation due to $\cos \phi$ and $\sin \phi$ will be essentially *independent* from symbol to symbol. From a mathematical standpoint, this is equivalent to replacing Eq. (4) by

$$P(\underline{x} \rightarrow \hat{\underline{x}} | \underline{\phi}; \lambda) \leq \begin{cases} \frac{1}{2} \exp \left\{ -\frac{E_s}{4N_0} \sum_{n \in \eta} 4\lambda (\cos \phi_n + \alpha_n \sin \phi_n - \lambda) \delta_n^2 \right\}; \\ \sum_{n \in \eta} \delta_n^2 (\cos \phi_n + \alpha_n \sin \phi_n) > 0 \\ 1; \quad \sum_{n \in \eta} \delta_n^2 (\cos \phi_n + \alpha_n \sin \phi_n) \leq 0 \end{cases} \quad (11)$$

where the ϕ_n 's are independent identically distributed (i.i.d.) random variables with p.d.f. $p(\phi)$ and $\underline{\phi}$ refers to the vector whose components are the ϕ_n 's. The expectation required in

Eq. (6) now involves computation of multidimensional integrals over regions of $\underline{\phi}$ corresponding to the inequalities in Eq. (11). Since, in these regions, the intervals of integration per dimension are *dependent* on one another, the expectation required in Eq. (6) is extremely difficult to compute.

Thus, instead a looser upper bound on conditional pairwise error probability is considered, which has the advantage of not having to separate the multidimensional integration required in Eq. (6) into two disjoint regions. Indeed, it is straightforward to see that the right-hand side of Eq. (11) is upper bounded by the exponential in its first line (without the factor of 1/2) over the *entire* domain of $\underline{\phi}$, i.e., $\{\phi_n \in (-\pi, \pi); n \in \eta\}$. Hence,

$$P(\underline{x} \rightarrow \hat{\underline{x}} | \underline{\phi}; \lambda) \leq$$

$$\exp \left\{ -\frac{E_s}{4N_0} \sum_{n \in \eta} 4\lambda (\cos \phi_n + \alpha_n \sin \phi_n - \lambda) \delta_n^2 \right\} \\ = \prod_{n \in \eta} \exp \left\{ -\frac{E_s}{N_0} \lambda (\cos \phi_n + \alpha_n \sin \phi_n - \lambda) \delta_n^2 \right\} \quad (12)$$

which is identically equal to the Chernoff bound. Now, substituting Eq. (12) into Eq. (6) gives the much simpler result

$$E_{\phi} \{P(\underline{x} \rightarrow \hat{\underline{x}} | \underline{\phi}; \lambda)\} \leq$$

$$\prod_{n \in \eta} \int_{-\pi}^{\pi} D^{\delta_n^2 [4\lambda (\cos \phi_n + \alpha_n \sin \phi_n - \lambda)]} p(\phi_n) d\phi_n \quad (13)$$

3. Suppressed Carrier (No Interleaving). When the carrier synchronization loop used to track the input phase is of the suppressed carrier type (e.g., a Costas loop), then the results of Section II.B.1 have to be somewhat modified since the appropriate domain for ϕ is no longer $(-\pi, \pi)$. In fact, for suppressed carrier tracking of MPSK with a Costas-type loop, and assuming perfect phase ambiguity resolution, ϕ takes on values only in the interval $(-\pi/M, \pi/M)$. Thus, the regions \mathcal{R} and $\overline{\mathcal{R}}$ required in Eq. (8) are reduced relative to those defined below Eq. (10), which assume that ϕ is allowed to take on values in $(-\pi, \pi)$. Specifically, \mathcal{R} will now be the intersection of the intervals $0 \leq |\phi| \leq \pi/M$ and $0 \leq |\phi - \phi_1| \leq \pi/2$ where ϕ_1 is defined in Eq. (10). Similarly, $\overline{\mathcal{R}}$ is defined by the intersection of $\pi/M \leq |\phi| \leq \pi/2$ and $\pi/2 \leq |\phi - \phi_1| \leq \pi$.

It can be shown (see Appendix B) that, for any pair of paths \underline{x} and $\hat{\underline{x}}$ (which define the set η), $\pi/2 - \phi_1 \geq \pi/M$. Thus, the intersection of the intervals $0 \leq |\phi| \leq \pi/M$ and $0 \leq |\phi - \phi_1| \leq \pi/2$ is simply $0 \leq |\phi| \leq \pi/M$, which defines \mathcal{R} , and the intersection of $\pi/M \leq |\phi| \leq \pi/2$ and $\pi/2 \leq |\phi - \phi_1| \leq \pi$ is the null set which defines \mathcal{R}^c . In short, for suppressed carrier tracking, the second integral in Eq. (8) disappears and the limits on the first integral become $(-\pi/M, \pi/M)$, i.e.,

$$E_\phi \{P(\underline{x} \rightarrow \hat{\underline{x}}|\phi; \lambda)\} \leq \frac{1}{2} \int_{-\pi/M}^{\pi/M} \left(\prod_{n \in \eta} D^{\delta_n^2} \right)^{[4\lambda(\cos \phi - \lambda)]} \times \left(\prod_{n \in \eta} D^{\alpha_n \delta_n^2} \right)^{[4\lambda \sin \phi]} p(\phi) d\phi \quad (14)$$

The significance of the second integral in Eq. (8) being equal to zero will be mentioned shortly relative to a discussion of *irreducible error probability*.

4. Suppressed Carrier (With Interleaving). Once again, assuming suppressed carrier tracking of MPSK with a Costas-type loop, and perfect phase ambiguity resolution, one obtains, analogous to Eq. (13),²

$$E_\phi \{P(\underline{x} \rightarrow \hat{\underline{x}}|\phi; \lambda)\} \leq \frac{1}{2} \prod_{n \in \eta} \left\{ \int_{-\pi/M}^{\pi/M} D^{\delta_n^2 [4\lambda(\cos \phi_n + \alpha_n \sin \phi_n - \lambda)]} p(\phi_n) d\phi_n \right\} \quad (15)$$

III. Carrier Synchronization Loop Statistical Model and Average Pairwise Error Probability Evaluation

To evaluate Eq. (6) using Eqs. (8), (13), (14), or (15), one must specify the functional form of the p.d.f. $p(\phi)$ of the

modulo- 2π -reduced phase error ϕ . For a discrete carrier synchronization loop of the phase-locked type, $p(\phi)$ is given by the Tikhonov p.d.f. [8]

$$p(\phi) = \begin{cases} \frac{\exp(\rho \cos \phi)}{2\pi I_0(\rho)}; & |\phi| \leq \pi \\ 0; & \text{otherwise} \end{cases} \quad (16)$$

where ρ is the SNR in the loop bandwidth.

In order to allow evaluation of Eq. (6) in closed form, one must recognize that, for the case of no interleaving, Eq. (8) can be further upper bounded by using $(-\pi, \pi)$ instead of \mathcal{R} in the first integral. Then, making this replacement one obtains

$$\min_{\lambda} E_\phi \{P(\underline{x} \rightarrow \hat{\underline{x}}|\phi; \lambda)\} \leq$$

$$\min_{\lambda} \left(\frac{1}{2} \exp \left\{ d^2(\underline{x}, \hat{\underline{x}}) \lambda^2 \frac{E_s}{N_0} \right\} \frac{I_0(\rho')}{I_0(\rho)} + I \right) \quad (17)$$

where

$$\rho' \triangleq \left\{ \left(\rho - d^2(\underline{x}, \hat{\underline{x}}) \lambda \frac{E_s}{N_0} \right)^2 + \left[d_1^2 \lambda \frac{E_s}{N_0} \right]^2 \right\}^{1/2}$$

$$d_1^2 \triangleq \sum_{n \in \eta} \alpha_n \delta_n^2$$

$$I = \frac{1}{2\pi I_0(\rho)} \left[\int_{\pi/2 + \phi_1}^{\pi} \exp(\rho \cos \phi) d\phi + \int_{-\pi}^{-\pi/2 + \phi_1} \exp(\rho \cos \phi) d\phi \right]$$

When Eq. (17) is substituted into Eq. (6), the term I will contribute an *irreducible error probability*, i.e., the system will exhibit a finite error probability when ρ is held fixed and E_s/N_0 approaches infinity.

²Note that the factor of 1/2 can be included here since for $0 \leq |\phi_n| \leq \pi/M$; $n \in \eta$, the condition on the first line of Eq. (11) is always satisfied (see Appendix B) and thus one needs not use the looser upper bound of Eq. (12).

When interleaving is employed, Eq. (15) (minimized over λ) together with Eq. (16) becomes

$$\begin{aligned} \min_{\lambda} E_{\phi} \{P(\underline{x} \rightarrow \hat{\underline{x}} | \phi; \lambda)\} \\ \leq \min_{\lambda} \left\{ \prod_{n \in \eta} \exp \left\{ \delta_n^2 \lambda^2 \frac{E_s}{N_0} \frac{I_0(\rho_n)}{I_0(\rho)} \right\} \right\} \\ = \min_{\lambda} \left\{ \exp \left\{ d^2(\underline{x}, \hat{\underline{x}}) \lambda^2 \frac{E_s}{N_0} \right\} \prod_{n \in \eta} \frac{I_0(\rho_n)}{I_0(\rho)} \right\} \end{aligned} \quad (18)$$

$$\rho_n \triangleq \left(\left(\rho - \delta_n^2 \lambda \frac{E_s}{N_0} \right)^2 + \left(\alpha_n \delta_n^2 \lambda \frac{E_s}{N_0} \right)^2 \right)^{1/2}$$

For suppressed carrier tracking with an M-phase Costas loop, $p(\phi)$ again has a Tikhonov-type p.d.f. which is given by

$$p(\phi) = \begin{cases} \frac{\exp(\rho \cos M\phi)}{(2\pi/M)I_0(\rho)} ; & |\phi| \leq \frac{\pi}{M} \\ 0; & \text{otherwise} \end{cases} \quad (19)$$

Here ρ is the "effective" loop SNR which includes the effects of signal \times signal ($S \times S$), signal \times noise ($S \times N$), and noise \times noise ($N \times N$) degradations commonly referred to as "squaring loss" or, more accurately " M th power loss" [8]. Since suppressed carrier systems of this type derive their carrier demodulation reference from the data-bearing signal, the loop SNR, ρ , is directly proportional to E_s/N_0 ; thus there can be no irreducible error probability since $\rho \rightarrow \infty$ when $E_s/N_0 \rightarrow \infty$. Furthermore, for perfect phase ambiguity resolution, we have previously shown that, for no interleaving, the term I is identically zero since the region \mathcal{R} corresponds to the null set. Thus, the average pairwise error probability results become

$$\begin{aligned} \min_{\lambda} E_{\phi} \{P(\underline{x} \rightarrow \hat{\underline{x}} | \phi; \lambda)\} \\ \leq \min_{\lambda} \left\{ \frac{1}{2} \exp \left\{ d^2(\underline{x}, \hat{\underline{x}}) \lambda^2 \frac{E_s}{N_0} \right\} \frac{f(\rho)}{I_0(\rho)} \right\} \end{aligned} \quad (20)$$

$$\begin{aligned} f(\rho) \triangleq \frac{M}{2\pi} \int_{-\pi/M}^{\pi/M} \exp \left\{ \rho \cos M\phi - \lambda \frac{E_s}{N_0} \right. \\ \left. \times (d^2(\underline{x}, \hat{\underline{x}}) \cos \phi + d_1^2 \sin \phi) \right\} d\phi \end{aligned}$$

for no interleaving and

$$\min_{\lambda} E_{\phi} \{P(\underline{x} \rightarrow \hat{\underline{x}} | \phi; \lambda)\}$$

$$\begin{aligned} \leq \min_{\lambda} \left\{ \prod_{n \in \eta} \exp \left\{ \delta_n^2 \lambda^2 \frac{E_s}{N_0} \frac{f_n(\rho)}{I_0(\rho)} \right\} \right\} \\ = \min_{\lambda} \left\{ \exp \left\{ d^2(\underline{x}, \hat{\underline{x}}) \lambda^2 \frac{E_s}{N_0} \right\} \prod_{n \in \eta} \frac{f_n(\rho)}{I_0(\rho)} \right\} \end{aligned}$$

$$f_n(\rho) \triangleq \frac{M}{2\pi} \int_{-\pi/M}^{\pi/M} \exp \left\{ \rho \cos M\phi \right.$$

$$\left. - \lambda \frac{E_s \delta_n^2}{N_0} (\cos \phi + \alpha_n \sin \phi) \right\} d\phi$$

(21)

for the case of interleaving.

In arriving at Eqs. (17), (18), (20), and (21), the "same type" of Chernoff bound has been assumed, in the sense that in all cases, the minimization over λ was performed *after* the averaging over ϕ . The principal reason for doing this is to allow comparison of performance with and without interleaving using bounds with "similar degrees of looseness." For the case of no interleaving, one can actually achieve a tighter bound than that given above by performing the minimization over λ on the conditional pairwise probability in Eq. (4). When this is done, one obtains

$$\lambda_{\text{opt}} = \frac{1}{2} [\cos \phi + \zeta(\underline{x}, \hat{\underline{x}}) \sin \phi]$$

$$\zeta(\underline{x}, \hat{\underline{x}}) \triangleq \frac{d_1^2}{d^2(\underline{x}, \hat{\underline{x}})} = \frac{\sum_{n \in \eta} \sqrt{\delta_n^2 (4 - \delta_n^2)}}{\sum_{n \in \eta} \delta_n^2}$$

(22)

and Eq. (4) becomes

$$P(\underline{x} \rightarrow \hat{\underline{x}} | \phi) \leq \begin{cases} \frac{1}{2} \exp \left\{ -\frac{E_s}{4N_0} d^2(\underline{x}, \hat{\underline{x}}) \right. \\ \quad \times (\cos \phi + \zeta(\underline{x}, \hat{\underline{x}}) \sin \phi)^2 \Big\}; \\ \sum_{n \in \eta} \delta_n^2 (\cos \phi + \alpha_n \sin \phi) > 0 \\ 1; \quad \sum_{n \in \eta} \delta_n^2 (\cos \phi + \alpha_n \sin \phi) \leq 0 \end{cases} \quad (23)$$

where $d^2(\underline{x}, \hat{\underline{x}})$ is again defined by Eq. (3).³

Unfortunately, the integral of Eq. (23) over the p.d.f.s of Eqs. (16) and (19) cannot be obtained in closed form. Defining the integral

$$L(\beta; J) = \int_{\mathcal{R}} \exp \left\{ -\frac{E_s d^2(\underline{x}, \hat{\underline{x}})}{4N_0} [\cos \phi + \beta \sin \phi]^2 \right\} \\ \times \frac{\exp(\rho \cos J\phi)}{\left(\frac{2\pi}{J}\right) I_0(\rho)} d\phi \quad (24)$$

The average pairwise error probabilities are now as follows:

Discrete Carrier

$$E_\phi \left\{ \min_{\lambda} P(\underline{x} \rightarrow \hat{\underline{x}} | \phi; \lambda) \right\} \leq \frac{1}{2} L(\zeta(\underline{x}, \hat{\underline{x}}); 1) + I \quad (25)$$

where I is defined in Eq. (17).

³Note that Eq. (23) can be obtained directly by applying the bound of Eq. (A-15) to Eq. (A-7) together with Eq. (A-11).

Suppressed Carrier

$$E_\phi \left\{ \min_{\lambda} P(\underline{x} \rightarrow \hat{\underline{x}} | \phi; \lambda) \right\} \leq \frac{1}{2} L(\zeta(\underline{x}, \hat{\underline{x}}); M) \quad (26)$$

where the region \mathcal{R} in the integral of Eq. (24) now corresponds to the interval $(-\pi/M, \pi/M)$.

Using Eqs. (25) and (26) (rather than Eqs. 17 and 20) will result in a smaller improvement in performance due to interleaving/deinterleaving since Eqs. (25) and (26) result in a tighter bound on P_b (no interleaving).

IV. A Trellis-Code Example

Consider a rate 1/2 trellis-coded QPSK using a simple 2-state trellis. The code trellis structure with the appropriate QPSK symbol assignment is illustrated in Fig. 1 and the corresponding pair-state transition diagram is shown in Fig. 2 where a, b, and c are branch label gains to be specified below. The transfer function of the pair-state diagram is

$$T(D, I) = \frac{Iac}{1 - Ib} \quad (27)$$

A. No Interleaving

For the case of no interleaving, one has

$$\left. \frac{dT(D, I)}{dI} \right|_{I=1} = \frac{ac}{(1-b)^2} = \sum_{k=0}^{\infty} (k+1)acb^k \quad (28)$$

where

$$a = D^{16\lambda(\cos \phi - \lambda)} \\ b = c = D^{8\lambda(\cos \phi + \sin \phi - \lambda)} \quad (29)$$

and D is the Bhattacharyya parameter for the ideal AWGN channel, namely

$$D = \exp \left\{ -\frac{E_s}{4N_0} \right\} \quad (30)$$

Using Eq. (28) and the result of Eq. (23), the upper bound on average bit error probability can be represented as

$$P_b \leq \sum_{k=0}^{\infty} (k+1) \int P_k(\phi) p(\phi) d\phi \quad (31)$$

where

$$P_k(\phi) = \begin{cases} \frac{1}{2} D^{2(k+3)} \left(\cos \phi + \frac{k+1}{k+3} \sin \phi \right)^2; \\ \phi - \tan^{-1} \frac{k+1}{k+3} < \frac{\pi}{2} \\ 1; \quad \phi - \tan^{-1} \frac{k+1}{k+3} \geq \frac{\pi}{2} \end{cases} \quad (32)$$

For discrete carrier synchronization, $p(\phi)$ is given by Eq. (16) and for suppressed carrier tracking with a 4-phase Costas loop, $p(\phi)$ is given by Eq. (19) with $M = 4$.

B. Interleaving

When interleaving is employed, then analogous to Eq. (28) one has

$$\left. \frac{dT(D, I)}{dI} \right|_{I=1} = \frac{\bar{a}\bar{c}}{(1-\bar{b})^2} = \sum_{k=0}^{\infty} (k+1) \bar{a} \bar{c} \bar{b}^k \quad (33)$$

where

$$\begin{aligned} \bar{a} &= \int D^{16\lambda(\cos \phi - \lambda)} p(\phi) d\phi \\ \bar{b} = \bar{c} &= \int D^{8\lambda(\cos \phi + \sin \phi - \lambda)} p(\phi) d\phi \end{aligned} \quad (34)$$

For discrete carrier synchronization, Eq. (34) can be represented in closed form as

$$\bar{a} = \exp \left\{ \frac{4\lambda^2 E_s}{N_0} \right\} \frac{I_0(\rho_0)}{I_0(\rho)} \quad (35)$$

$$\bar{b} = \exp \left\{ \frac{2\lambda^2 E_s}{N_0} \right\} \frac{I_0 \left(\sqrt{\left(\rho - \frac{2\lambda E_s}{N_0} \right)^2 + \left(\frac{2\lambda E_s}{N_0} \right)^2} \right)}{I_0(\rho)}$$

where ρ_0 is defined by

$$\rho_0 \triangleq \left| \rho - \frac{4\lambda E_s}{N_0} \right| \quad (36)$$

Using Eq. (33), an expression for the upper bound on average bit error probability, analogous to Eq. (31), is given by

$$P_b \leq \sum_{k=0}^{\infty} (k+1) \min_{\lambda} \gamma \bar{a}(\bar{b})^{k+1} \quad (37)$$

where $\gamma = 1$ for discrete carrier and $\gamma = 1/2$ for suppressed carrier.

The upper bounds of Eqs. (31) and (37) are plotted in Figs. 3 and 4 for discrete carrier tracking and loop SNRs $\rho = 13$ and 15 dB, respectively. In Figs. 5 and 6, the comparable results for the suppressed carrier case are illustrated. Here a 4-phase Costas loop with integrate-and-dump arm filters has been assumed whose equivalent loop SNR is

$$\rho = \frac{1}{16} \left(\frac{S}{N_0 B_L} \right) \mathcal{S}_L = \frac{1}{16} \left(\frac{E_b}{N_0} \right) \left(\frac{1}{B_L T_b} \right) \mathcal{S}_L \quad (38)$$

with \mathcal{S}_L now denoting the "4th power loss" and given by [8]

$$\mathcal{S}_L = \left[1 + \frac{9}{2} \left(\frac{E_s}{N_0} \right)^{-1} + 6 \left(\frac{E_s}{N_0} \right)^{-2} + \frac{3}{2} \left(\frac{E_s}{N_0} \right)^{-3} \right]^{-1} \quad (39)$$

Also, in evaluating the numerical results, the series in Eqs. (31) and (37) has been truncated to 15 terms.

V. Concluding Remarks

It has been shown that by interleaving the transmitted coded symbols in a trellis-coded system, the radio loss can be significantly reduced. The amount of this reduction depends on the particular trellis code used and the region of operation of the system as characterized by such parameters as bit error rate and loop SNR. In this article, a simple example (2-state, rate 1/2 trellis-coded QPSK) has been used strictly for the purpose of illustrating the theoretical results. More complex trellis codes with a larger number of modulation levels and a larger number of states will show even more gain due to interleaving.

In general, whether or not coding and interleaving are employed, suppressed carrier systems have smaller radio losses than discrete carrier systems since they are not subject to

irreducible error probability. This is true despite the fact that for practical passive arm filters (e.g., RC filters) in the suppressed carrier tracking loop (Costas loop), one will experience larger squaring losses and thus larger radio losses than those shown here for active integrate-and-dump arm filters [9]. Thus, if the radio loss is, without interleaving, small (as tends

to be true in suppressed carrier systems), the use of interleaving cannot be of much additional help. Nevertheless, if the system can tolerate the delay associated with the interleaving/deinterleaving process, it is useful to include it in the system design since it also helps to reduce other impairments of a bursty nature such as intersymbol interference, fading, etc.

References

- [1] D. Divsalar, M. K. Simon, and J. H. Yuen, "The Use of Interleaving for Reducing Radio Loss in Convolutionally Coded Systems," *TDA Progress Report 42-96*, vol. October-December 1988, Jet Propulsion Laboratory, Pasadena, California, pp. 21-39, February 15, 1989.
- [2] G. Ungerboeck, "Trellis Coded Modulation with Redundant Signal Sets, Parts I and II," *IEEE Communications Magazine*, vol. 25, no. 2, pp. 5-21, February 1987.
- [3] M. K. Simon and D. Divsalar, *Combined Trellis Coding with Asymmetric MPSK Modulation*, JPL Publication 85-24 (MSAT-X Report No. 109), May 1, 1985. Also see *IEEE Trans. Comm.*, vol. COM-35, no. 2, pp. 130-141, February 1987.
- [4] D. Divsalar and M. K. Simon, *Trellis Coded Modulation for 4800-9600 bps Transmission over a Fading Mobile Satellite Channel*, JPL Publication 86-8 (MSAT-X Report No. 129), June 1, 1986. Also in *IEEE Journal on Selected Areas in Communications, Special Issue on Fading Channels*, vol. SAC-5, no. 2, pp. 162-175, February 1987.
- [5] D. Divsalar and M. K. Simon, *Multiple Trellis Coded Modulation (MTCM)*, JPL Publication 86-44 (MSAT-X Report No. 141), November 15, 1986. Also in *IEEE Trans. Comm.*, vol. 36, no. 4, pp. 410-419, April 1988.
- [6] D. Divsalar and M. K. Simon, "The Design of Trellis Coded MPSK for Fading Channels: Performance Criteria," *IEEE Trans. Comm.*, vol. 36, no. 9, pp. 1004-1012, September 1988.
- [7] A. J. Viterbi and J. K. Omura, *Principles of Digital Communication and Coding*, New York, NY: McGraw-Hill, Inc., 1979.
- [8] W. C. Lindsey and M. K. Simon, *Telecommunications Systems Engineering*, Englewood Cliffs, NJ: Prentice-Hall, Inc., 1978.
- [9] W. C. Lindsey and M. K. Simon, "Optimum Performance of Suppressed Carrier Receivers with Costas Loop Tracking," *IEEE Trans. Comm.*, vol. COM-25, no. 2, pp. 215-227, February 1977.

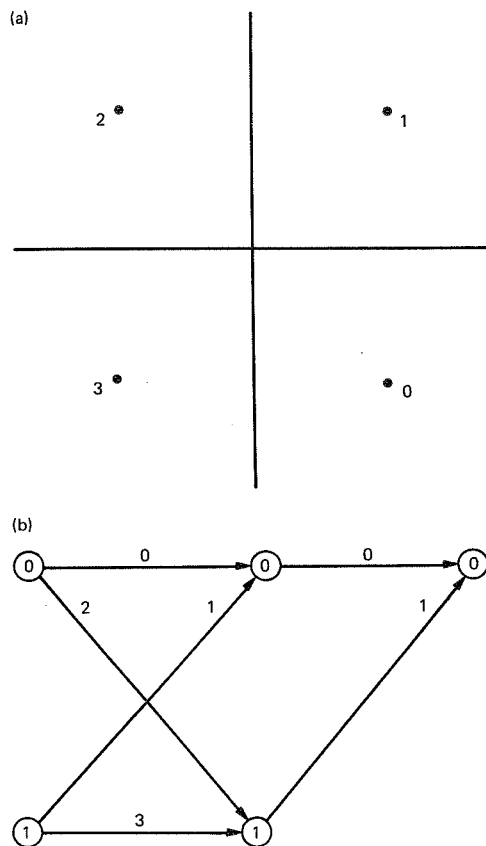


Fig. 1. (a) QPSK signal point constellation and (b) trellis diagram showing QPSK signal assignments to branches.

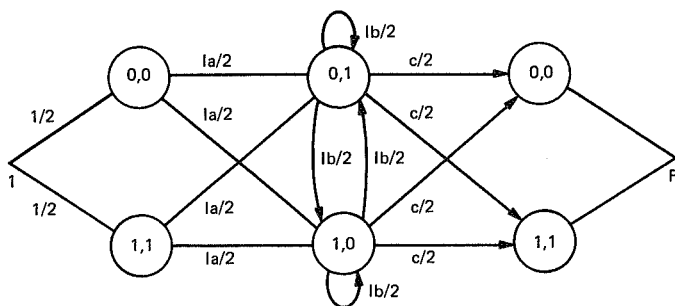


Fig. 2. Pair-state transition diagram for trellis diagram of Fig. 1.

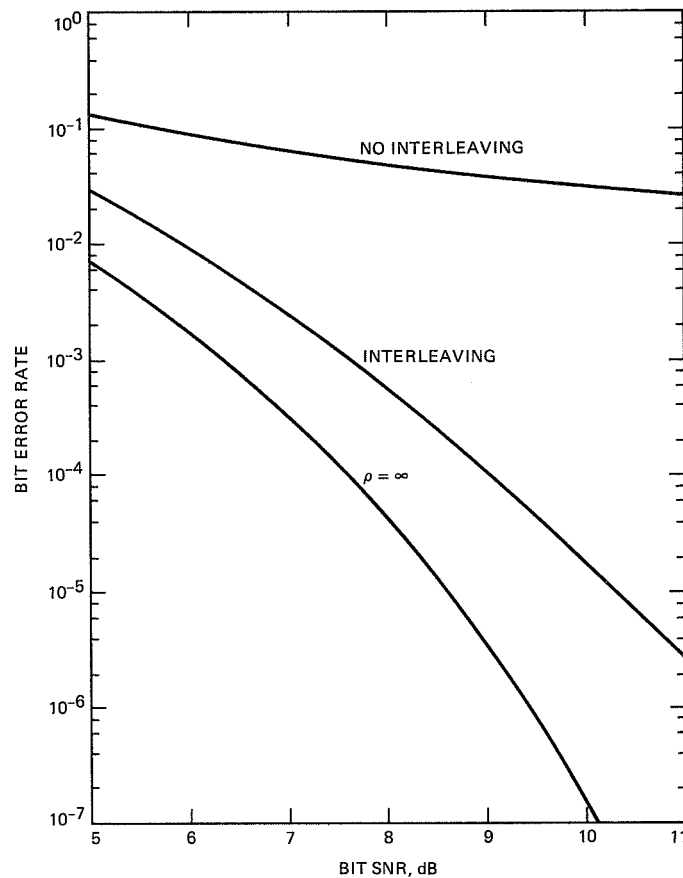


Fig. 3. Upper bound on average bit error probability versus bit energy-to-noise ratio for rate 1/2, trellis-coded QPSK; 2 states; loop SNR = 13 dB; discrete carrier.

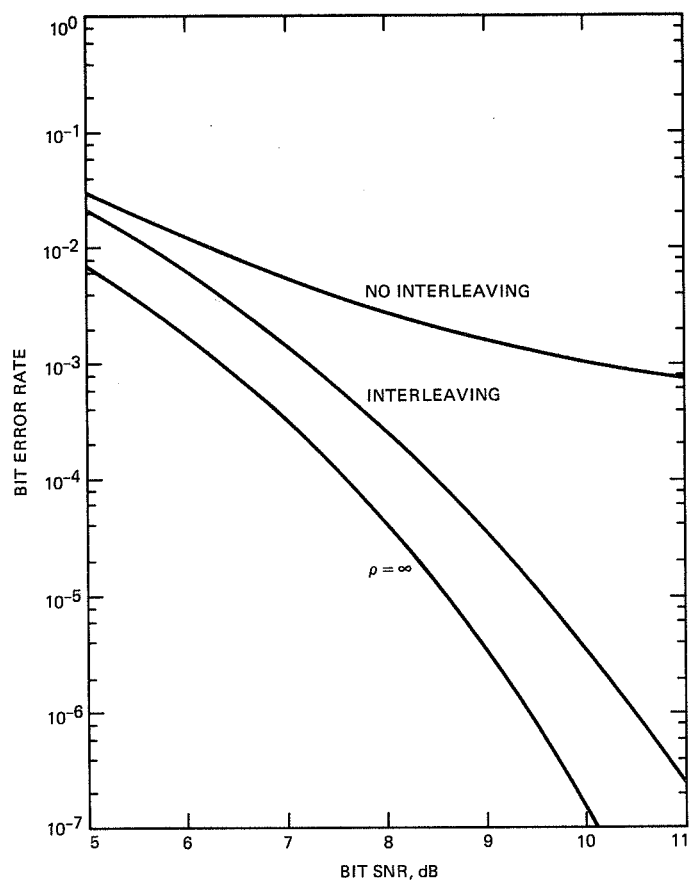


Fig. 4. Upper bound on average bit error probability versus bit energy-to-noise ratio for rate 1/2, trellis-coded QPSK; 2 states; loop SNR = 15 dB; discrete carrier.

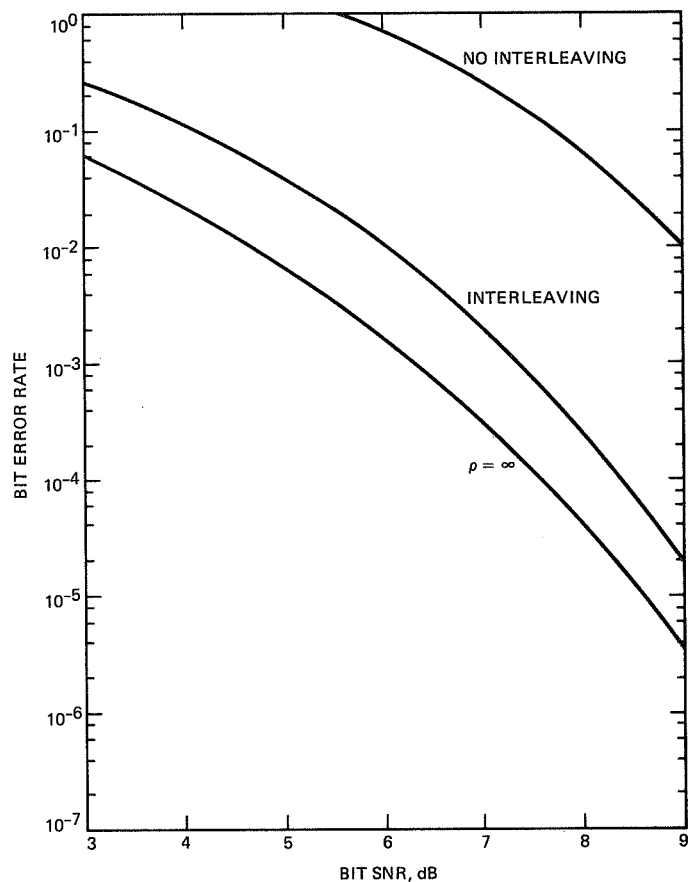


Fig. 5. Upper bound on average bit error probability versus bit energy-to-noise ratio for rate 1/2, trellis-coded QPSK; 2 states; $1/B_L T_b = 10$; suppressed carrier.

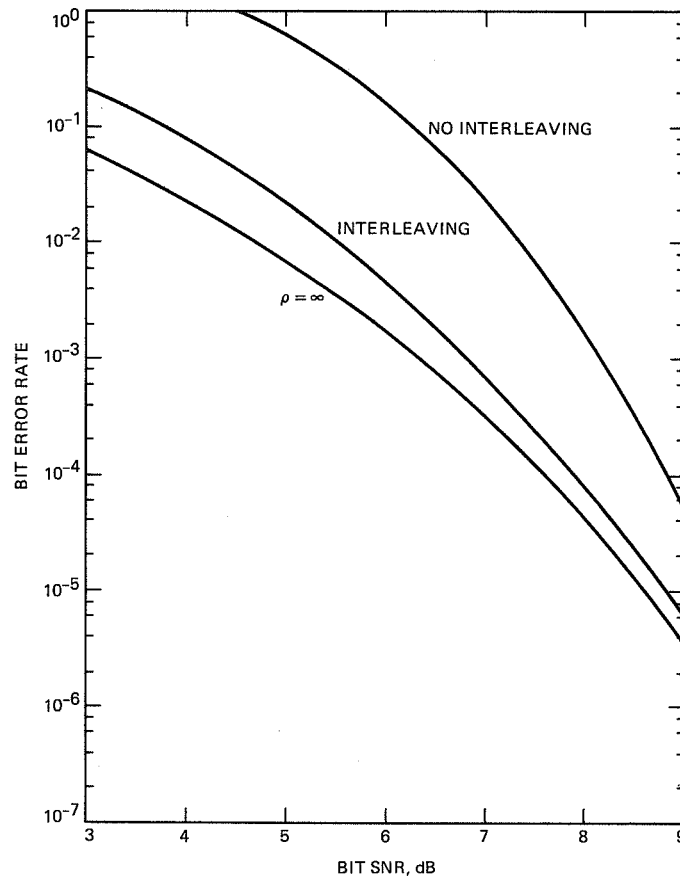


Fig. 6. Upper bound on average bit error probability versus bit energy-to-noise ratio for rate 1/2, trellis-coded QPSK; 2 states; $1/B_L T_b = 20$; suppressed carrier.

Appendix A

Derivation of an Upper Bound on the Pairwise Error Probability for Trellis Coded MPSK with Imperfect Carrier Phase Reference

Let $\underline{y} = (y_1, y_2, \dots, y_N)$ denote the received sequence when the normalized (to unit power) sequence of MPSK symbols $\underline{x} = (x_1, x_2, \dots, x_N)$ is transmitted. A *pairwise error* occurs if $\underline{\hat{x}} = (\hat{x}_1, \hat{x}_2, \dots, \hat{x}_N) \neq \underline{x}$ is chosen by the receiver, which, if the receiver uses a distance metric to make this decision, implies \underline{y} is closer to $\underline{\hat{x}}$ than to \underline{x} . Assuming that distance metric which is maximum-likelihood for ideal coherent detection (perfect carrier phase reference), then such an error occurs whenever

$$\sum_{n=1}^N |y_n - \hat{x}_n|^2 < \sum_{n=1}^N |y_n - x_n|^2 \quad (\text{A-1})$$

Since MPSK is a constant envelope signaling set, one has $|x_n|^2 = |\hat{x}_n|^2 = \text{a constant}$, and Eq. (A-1) reduces to

$$\sum_{n=1}^N \text{Re} \left\{ y_n \hat{x}_n^* \right\} > \sum_{n=1}^N \text{Re} \left\{ y_n x_n^* \right\} \quad (\text{A-2})$$

Letting n_n represent the additive noise in the n th signaling interval, and ϕ_n the phase shift introduced by imperfect carrier demodulation in that same interval, then y_n and x_n are related by

$$y_n = x_n e^{j\phi_n} + n_n; \quad n = 1, 2, \dots, N \quad (\text{A-3})$$

Substituting Eq. (A-3) into Eq. (A-2) and simplifying gives

$$\text{Re} \left\{ \sum_{n \in \eta} (\hat{x}_n - x_n)^* n_n \right\} > \text{Re} \left\{ \sum_{n \in \eta} x_n (x_n - \hat{x}_n)^* e^{j\phi_n} \right\} \quad (\text{A-4})$$

where η is the set of all n such that $x_n \neq \hat{x}_n$.

Since for an AWGN channel, n_n is a complex Gaussian random variable whose real and imaginary components have variance

$$E \left\{ [\text{Re}(n_n)]^2 \right\} = E \left\{ [\text{Im}(n_n)]^2 \right\} \triangleq \sigma^2 \quad (\text{A-5})$$

then

$$\text{var} \left\{ \text{Re} \left[\sum_{n \in \eta} (\hat{x}_n - x_n)^* n_n \right] \right\} = \sigma^2 \sum_{n \in \eta} |x_n - \hat{x}_n|^2 \quad (\text{A-6})$$

and the conditional pairwise error probability $P(\underline{x} \rightarrow \underline{\hat{x}} | \underline{\phi})$ is given by

$$\begin{aligned} P(\underline{x} \rightarrow \underline{\hat{x}} | \underline{\phi}) &= \Pr \left\{ \text{Re} \left[\sum_{n \in \eta} (\hat{x}_n - x_n)^* n_n \right] \right. \\ &\quad \left. > \text{Re} \left[\sum_{n \in \eta} x_n (x_n - \hat{x}_n)^* e^{j\phi_n} \right] \right\} \\ &= Q \left(\frac{\text{Re} \left[\sum_{n \in \eta} x_n (x_n - \hat{x}_n)^* e^{j\phi_n} \right]}{\sigma \sqrt{\sum_{n \in \eta} |x_n - \hat{x}_n|^2}} \right) \end{aligned} \quad (\text{A-7})$$

where $\underline{\phi} = (\phi_1, \phi_2, \dots, \phi_N)$ is the sequence of carrier phase errors and $Q(x)$ is the Gaussian integral defined by

$$Q(x) = \frac{1}{\sqrt{2\pi}} \int_x^\infty \exp \left(-\frac{y^2}{2} \right) dy \quad (\text{A-8})$$

To simplify Eq. (A-7), proceed as follows. Since for constant envelope signals

$$2\text{Re} \left\{ x_n (x_n - \hat{x}_n)^* \right\} = |x_n - \hat{x}_n|^2 \quad (\text{A-9})$$

$$2\text{Im} \left\{ x_n (x_n - \hat{x}_n)^* \right\} = (x_n - \hat{x}_n)^* (x_n + \hat{x}_n)$$

the numerator of the argument of the Gaussian integral in Eq. (A-7) becomes

$$\begin{aligned}
& \sum_{n \in \eta} \operatorname{Re} \{x_n (x_n - \hat{x}_n)^* e^{j\phi_n}\} \\
&= \frac{1}{2} \sum_{n \in \eta} |x_n - \hat{x}_n|^2 \cos \phi_n + j(x_n - \hat{x}_n)^* (x_n + \hat{x}_n) \sin \phi_n \\
&= \frac{1}{2} \sum_{n \in \eta} |x_n - \hat{x}_n|^2 \left\{ \cos \phi_n + j \frac{(x_n + \hat{x}_n)}{(x_n - \hat{x}_n)} \sin \phi_n \right\}
\end{aligned} \tag{A-10}$$

Performing some further trigonometric simplification of Eq. (A-10) gives the desired result

$$\begin{aligned}
\sum_{n \in \eta} \operatorname{Re} \{x_n (x_n - \hat{x}_n)^* e^{j\phi_n}\} &= \sum_{n \in \eta} |x_n - \hat{x}_n| \cos(\phi_n - \eta_n) \\
\eta_n &= \tan^{-1} \alpha_n \\
\alpha_n &\triangleq \sqrt{\frac{4 - |x_n - \hat{x}_n|^2}{|x_n - \hat{x}_n|^2}} = \sqrt{\frac{4 - \delta_n^2}{\delta_n^2}}
\end{aligned} \tag{A-11}$$

The argument of the Gaussian integral in Eq. (A-7) is in the form a/\sqrt{b} . For $a > 0$, one can upper bound this integral by¹

$$Q\left(\frac{a}{\sqrt{b}}\right) \leq \frac{1}{2} e^{-a^2/2b} \tag{A-12}$$

¹Note that for perfect carrier demodulation, i.e., $\phi = 0$, one always has $a > 0$.

Since for any λ , one has $(a - 2\lambda b)^2 > 0$, rearranging this inequality gives the equivalent form

$$\frac{a^2}{b} \geq 4\lambda a - 4\lambda^2 b \tag{A-13}$$

Thus, for $a > 0$,

$$Q\left(\frac{a}{\sqrt{b}}\right) \leq \frac{1}{2} \exp \{-2\lambda[a - \lambda b]\} \tag{A-14}$$

For $a < 0$, one must use the loose upper bound

$$Q\left(\frac{a}{\sqrt{b}}\right) = Q\left(-\frac{|a|}{\sqrt{b}}\right) = 1 - Q\left(\frac{|a|}{\sqrt{b}}\right) \leq 1 \tag{A-15}$$

Finally, using Eq. (A-11) together with Eqs. (A-14) and (A-15) in Eq. (A-7) gives the desired upper bound on pairwise error probability as

$$P(\underline{x} \rightarrow \hat{\underline{x}} | \underline{\phi}; \lambda) \leq \begin{cases} \frac{1}{2} \exp \left\{ -\frac{E_s}{4N_0} \sum_{n \in \eta} 4\lambda(\cos \phi_n + \alpha_n \sin \phi_n - \lambda) \delta_n^2 \right\}; \\ \sum_{n \in \eta} \delta_n^2 (\cos \phi_n + \alpha_n \sin \phi_n) > 0 \\ 1; & \sum_{n \in \eta} \delta_n^2 (\cos \phi_n + \alpha_n \sin \phi_n) \leq 0 \end{cases} \tag{A-16}$$

In Eq. (A-16), use has been made of the fact that for the unnormalized system, $1/2\sigma^2 = E_s/N_0$ where E_s is the symbol energy and N_0 the noise spectral density, and λ has been replaced by the normalized quantity $\lambda\sigma^2$. Also, note that if Eq. (A-16) is minimized over λ , then it is identically in the form of a Chernoff bound.

Appendix B

Derivation of the Integration Region \mathcal{R} for Suppressed Carrier Tracking

First it will be shown that for *any error event path*, the intersection of the intervals $0 \leq |\phi| \leq \pi/M$ and $0 \leq |\phi - \phi_1| \leq \pi/2$, where ϕ_1 is defined in Eq. (10), is indeed $0 \leq |\phi| \leq \pi/M$, which then defines the region \mathcal{R} for the no-interleaving case. This is equivalent to showing that for *any error event path*, $\pi/2 - \phi_1 \geq \pi/M$. From Eq. (10), this inequality can be expressed as

$$\frac{\sum_{n \in \eta} \sqrt{\delta_n^2 (4 - \delta_n^2)}}{\sum_{n \in \eta} \delta_n^2} \leq \cot \frac{\pi}{M} \quad (\text{B-1})$$

or, equivalently,

$$\sum_{n \in \eta} \sqrt{\delta_n^2 (4 - \delta_n^2)} \leq \sum_{n \in \eta} \frac{\delta_n^2}{\tan \frac{\pi}{M}} \quad (\text{B-2})$$

Equation (B-2) will be satisfied if for each $n \in \eta$,

$$\delta_n^2 (4 - \delta_n^2) \leq \frac{\delta_n^4}{\tan^2 \frac{\pi}{M}} \quad (\text{B-3})$$

or, equivalently,

$$\delta_n^2 \geq \frac{4 \tan^2 \frac{\pi}{M}}{1 + \tan^2 \frac{\pi}{M}} = 4 \sin^2 \frac{\pi}{M} \quad (\text{B-4})$$

However, for an MPSK signaling set, the *smallest* squared Euclidean distance occurs between adjacent points in the constellation and has value $4 \sin^2 \pi/M$. Thus, Eq. (B-4) is satisfied for all $n \in \eta$. Q.E.D.

For the interleaving case, it must be shown that for $0 \leq |\phi_n| \leq \pi/M$,

$$\sum_{n \in \eta} \delta_n^2 (\cos \phi_n + \alpha_n \sin \phi_n) \geq 0 \quad (\text{B-5})$$

where, from Eq. (5),

$$\alpha_n = \sqrt{\frac{4 - \delta_n^2}{\delta_n^2}} \quad (\text{B-6})$$

Since, if all the ϕ_n 's are equal to $-\pi/M$, the left-hand side of Eq. (B-5) is most negative, then, equivalently, it must be shown that

$$\sum_{n \in \eta} \delta_n^2 \left(\cos \frac{\pi}{M} - \alpha_n \sin \frac{\pi}{M} \right) \geq 0 \quad (\text{B-7})$$

The inequality in Eq. (B-7) is satisfied if each term in the sum is greater than or equal to zero. Thus, it must be shown that

$$\cos \frac{\pi}{M} - \sqrt{\frac{4 - \delta_n^2}{\delta_n^2}} \sin \frac{\pi}{M} \geq 0 \quad (\text{B-8})$$

or, equivalently,

$$\tan^2 \frac{\pi}{M} \leq \frac{\delta_n^2}{4 - \delta_n^2} \quad (\text{B-9})$$

which is the identical inequality to Eq. (B-3) whose validity was established above. Q.E.D.

Performance of Concatenated Codes Using 8-Bit and 10-Bit Reed-Solomon Codes

F. Pollara and K.-M. Cheung
Communications Systems Research Section

The performance improvement of concatenated coding systems using 10-bit instead of 8-bit Reed-Solomon codes is measured by simulation. Three inner convolutional codes are considered: (7,1/2), (15,1/4), and (15,1/6). It is shown that approximately 0.2 dB can be gained at a bit error rate of 10^{-6} . The loss due to nonideal interleaving is also evaluated. Performance comparisons at very low bit error rates may be relevant for systems using data compression.

I. Introduction

Concatenated codes consisting of an inner convolutional code and an outer Reed-Solomon (RS) code are used in several current and planned deep-space missions. The Voyager spacecraft, for example, employs a concatenated coding system based on a (7,1/2) convolutional code as the inner code and an 8-bit (255,223) RS code as the outer code. The Galileo mission will use an experimental (15,1/4) convolutional code [1] concatenated with the same 8-bit RS code. Future missions may use the recently discovered (15,1/6) convolutional code [2] together with a 10-bit (1023,959) RS code.

The plan to develop a switchable (8-bit and 10-bit) Reed-Solomon decoder¹ suggested a study of the performance

improvement that can be obtained by using the 10-bit RS code in place of the 8-bit RS code. The results of this study are the main subject of this article.

Since maximum-likelihood decoding of convolutional codes generates errors in bursts, a block interleaver is used between the convolutional encoder and the RS encoder to randomize the symbol errors. The deinterleaving operation performed at the receiving station removes most of the dependency among errors that enter the RS decoder, given that the interleaving depth I is sufficiently large. It is important to assess the performance degradation resulting from interleaving at a given depth with respect to ideal interleaving that assumes totally independent errors.

The availability of a hardware Viterbi decoder built by C. Lahmeyer made it possible to generate enough error bursts to compute the performance degradation due to nonideal interleaving, as described in [3]. Simulation results have been stored on disk files in a compressed format which allows for

¹R. Stevens, "Board Report for Risk Assessment Review for a Switchable Reed-Solomon Decoder," JPL Interoffice Memorandum RS-88-024 (internal document), Jet Propulsion Laboratory, Pasadena, California, December 30, 1988.

easy reconstruction of the actual decoded bit stream. The hardware decoder uses the traceback method to compute the decoded bits. Paths are traced back starting from a random state. Traceback is accomplished by three buffers, each 170 bits long, storing the results of comparisons of merging paths. Received symbols are quantized by a uniform 8-bit quantizer. Operations internal to the decoder are performed with 16-bit precision.

II. Results for Convolutional Codes

Three convolutional codes are considered: Voyager's (7,1/2) code, Galileo's (15,1/4) code, and the (15,1/6) code described in [2].

Figure 1 shows the bit error rate (BER) and the symbol error rates (8- to 16-bit symbols) for the (7,1/2) code as a function of the bit signal-to-noise ratio (bit SNR). These are the only results described in this article that were obtained by using software simulation instead of the hardware decoder, since the software decoding speed is reasonable for constraint length 7 codes. The software decoder operates with no quantization of the received symbols and uses a path truncation length of 64 bits. The survivors are updated by the register exchange method, and the decoded bits are taken from the survivor with the lowest accumulated metric. Each data point in Fig. 1 is the result of a simulation run of at least 10 million information bits. Figure 1 has been included primarily for comparison with other more powerful codes.

Figure 2 shows the same performance results for the (15,1/4) code, obtained by hardware simulation. The data points below the bit error rate curve are the results of software simulation [1] with no quantization and a path truncation length of 128 bits.

Similar results are shown in Fig. 3 for the (15,1/6) code. The performance of the (15,1/6) code found by hardware simulation is slightly worse than that previously found in [2] by software simulation. To facilitate the comparison of the (15,1/4) and the (15,1/6) codes, their bit error rates are shown together in Fig. 4.

III. Results for Concatenated Codes

Figures 5 to 13 show the performance of concatenated codes with ideal and nonideal interleaving, and point out the difference in performance between 8-bit and 10-bit RS codes. The bit SNR shown in these figures is the bit signal-to-noise ratio of the concatenated system, which includes a penalty of 0.58 dB due to the rate of the 8-bit RS code, or 0.28 dB for the 10-bit RS code. The bit error rate at the RS decoder out-

put is computed from the bit and symbol error rates of the Viterbi decoder.²

Figures 5 and 6 show the bit error rate of the (7,1/2) code concatenated with the 8-bit and 10-bit RS codes, respectively. Interleaving depths $I = 2$ and $I = 4$ are shown along with ideal interleaving. Higher values of I had nonmeasurable performance degradation relative to ideal interleaving. Larger constraint length codes suffer more from shallow interleaving since the average length of bursts grows with the constraint length. It must be observed that results for nonideal interleaving need very large amounts of data (decoded bits) and are not very accurate even with runs of 10 million or more bits. The 1σ statistical uncertainty for BER estimates lower than 10^{-5} is more than 100 percent for nonideal interleaving, but only approximately 20 percent for ideal interleaving. Figure 7 shows a comparison of the bit error rates of the 8-bit and 10-bit codes concatenated with the (7,1/2) code and ideal interleaving. The advantage of the 10-bit RS code becomes apparent only at very low bit error rates. A different 10-bit RS code specifically optimized for concatenation with the (7,1/2) code could offer a larger improvement over the 8-bit RS code than the (1023,959) RS code, which was optimized for the (15,1/6) code.

Figures 8 and 9 show the bit error rate of the (15,1/4) code concatenated with the 8-bit and 10-bit RS codes, respectively. Figures 5 and 8 appeared in [3], and are repeated for comparison. Figure 10 shows a comparison of the bit error rates of the 8-bit and 10-bit codes concatenated with the (15,1/4) code and ideal interleaving. Now the advantage of the 10-bit RS code over the 8-bit RS code is approximately 0.2 dB at $\text{BER} = 10^{-6}$. This advantage grows to approximately 0.3 dB at $\text{BER} = 10^{-12}$.

Finally, Figs. 11 and 12 show the bit error rate of the (15,1/6) code concatenated with the 8-bit and 10-bit RS codes, respectively. Figure 13 shows a comparison of the bit error rates of the 8-bit and 10-bit codes concatenated with the (15,1/6) code and ideal interleaving. The advantage of the 10-bit code is slightly less than 0.2 dB at $\text{BER} = 10^{-6}$, and approximately 0.3 dB at $\text{BER} = 10^{-12}$.

IV. Conclusions

In summary, the improvement offered by the 10-bit RS code over the 8-bit RS code is approximately 0.2 dB at $\text{BER} =$

²F. Pollara and S. Dolinar, "Concatenated Codes Performance at Low Bit Error Rates," JPL Interoffice Memorandum 331-88.2-043 (internal document), Jet Propulsion Laboratory, Pasadena, California, July 13, 1988.

10^{-6} for both the Galileo system and the new (15,1/6) code proposed for future missions. For systems that transmit heavily compressed data and may have to operate at $\text{BER} = 10^{-12}$, the improvement increases to approximately 0.3 dB.

This improvement is quickly eroded by insufficient interleaving. From our limited results on interleaving losses it is

nevertheless possible to conclude that interleaving depths of eight or higher will produce insignificant losses at $\text{BER} \geq 10^{-6}$.

A comparison of three concatenated systems is shown as a summary in Fig. 14. This figure includes Voyager's coding system, the Galileo experimental code, and a concatenated code available for future missions.

Acknowledgment

The authors acknowledge helpful suggestions by S. Dolinar, who also provided some of the data included in this article.

References

- [1] S. Dolinar, "A New Code for Galileo," *TDA Progress Report 42-93*, vol. January-March 1988, Jet Propulsion Laboratory, Pasadena, California, pp. 83-96, May 15, 1988.
- [2] J. H. Yuen and Q. D. Vo, "In Search of a 2-dB Coding Gain," *TDA Progress Report 42-83*, vol. July-September 1985, Jet Propulsion Laboratory, Pasadena, California, pp. 26-33, November 15, 1985.
- [3] K.-M. Cheung and S. Dolinar, "Performance of Galileo's Concatenated Codes with Nonideal Interleaving," *TDA Progress Report 42-95*, vol. July-September 1988, pp. 148-152, November 15, 1988.

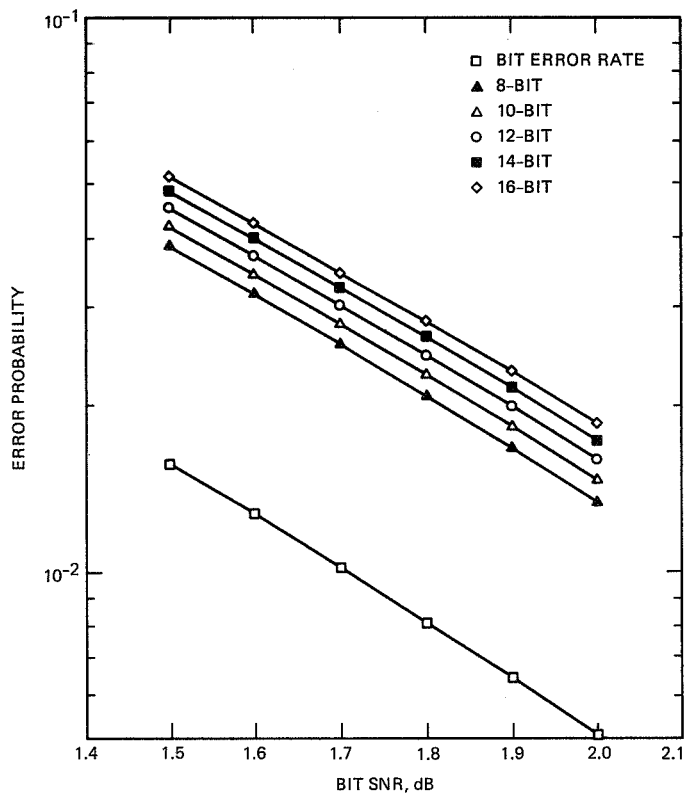


Fig. 1. Convolutional code performance: (7,1/2) code.

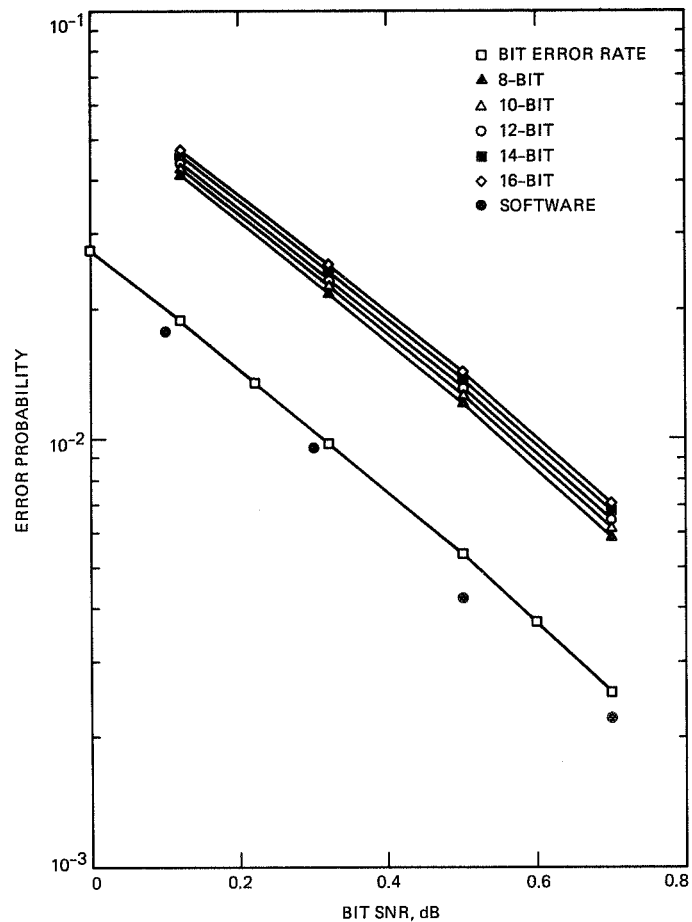


Fig. 2. Convolutional code performance: (15,1/4) code.

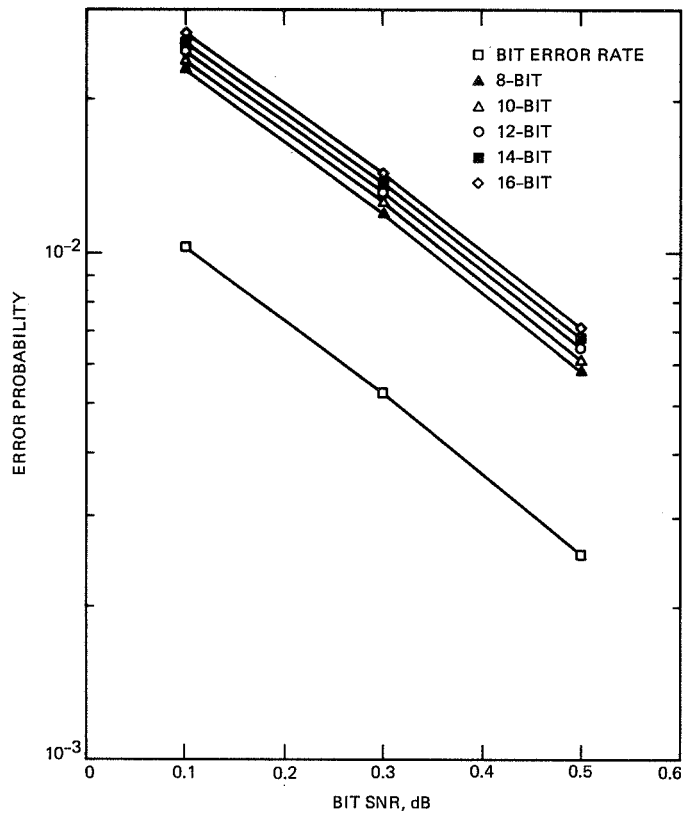


Fig. 3. Convolutional code performance: (15,1/6) code.

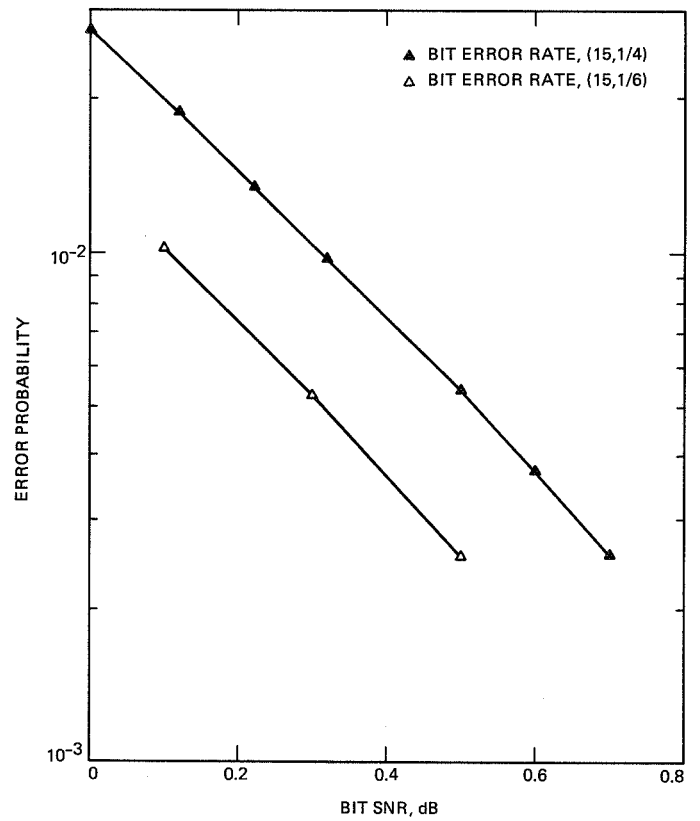


Fig. 4. Convolutional code performance comparison: (15,1/4) and (15,1/6) codes.

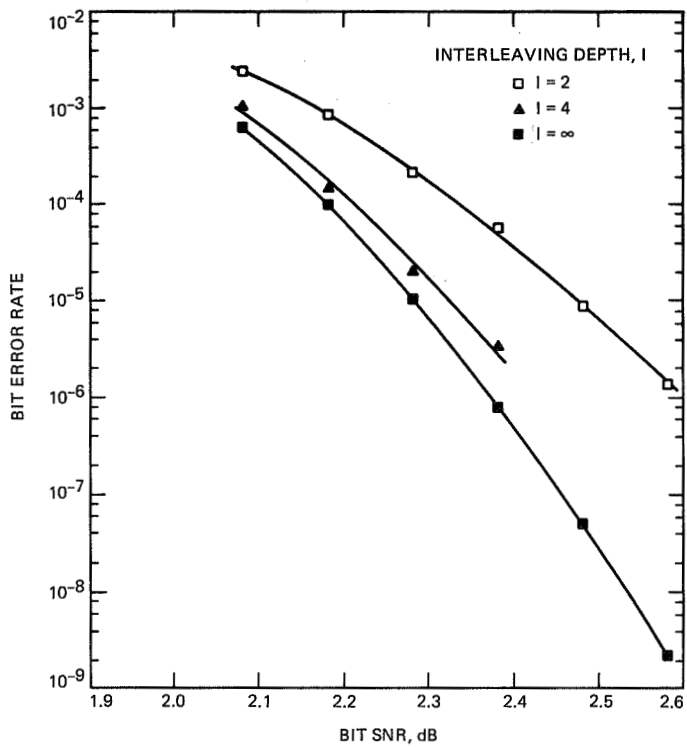


Fig. 5. Concatenated code performance: (7,1/2) convolutional and 8-bit (255,223) RS.

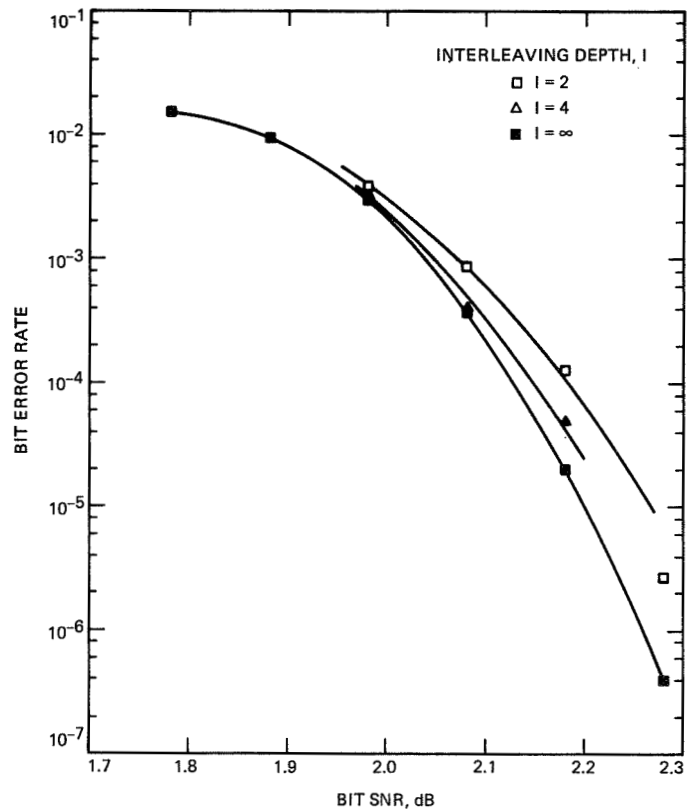


Fig. 6. Concatenated code performance: (7,1/2) convolutional and 10-bit (1023,959) RS.

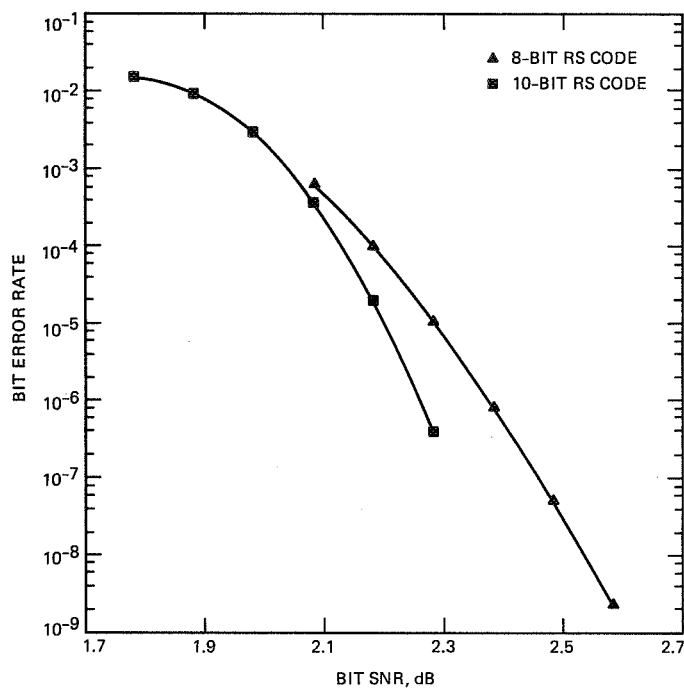


Fig. 7. Concatenated code performance comparison: 8-bit (255,223) and 10-bit (1023,959) RS concatenated with (7,1/2) convolutional.

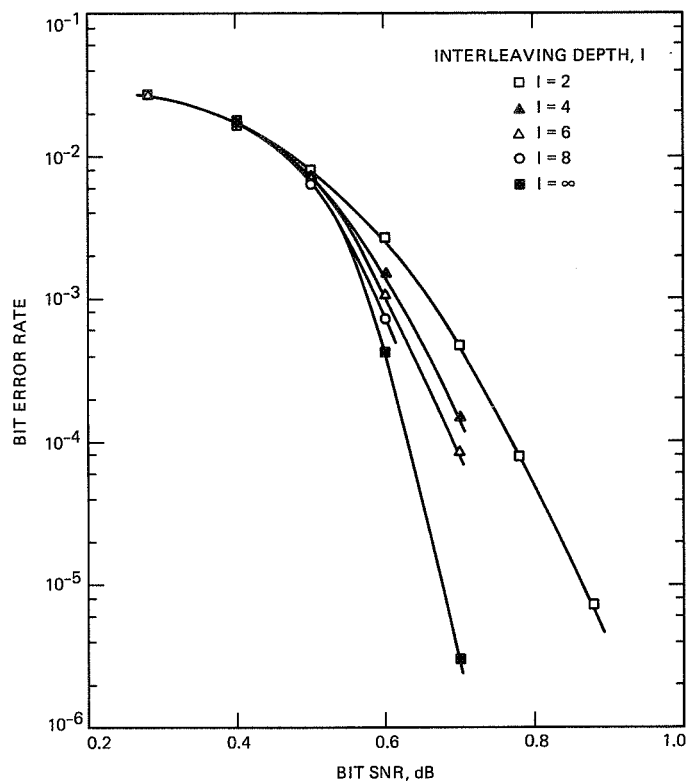


Fig. 9. Concatenated code performance: (15,1/4) convolutional and 10-bit (1023,959) RS.

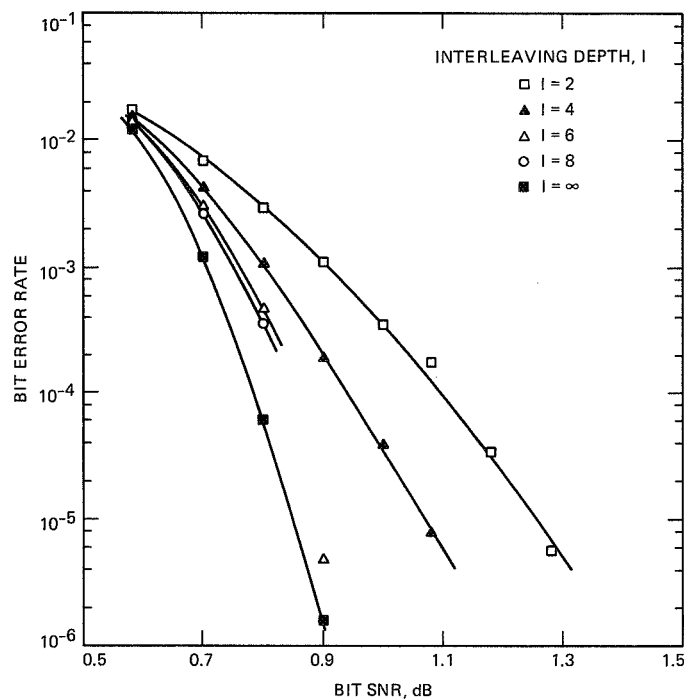


Fig. 8. Concatenated code performance: (15,1/4) convolutional and 8-bit (255,223) RS.

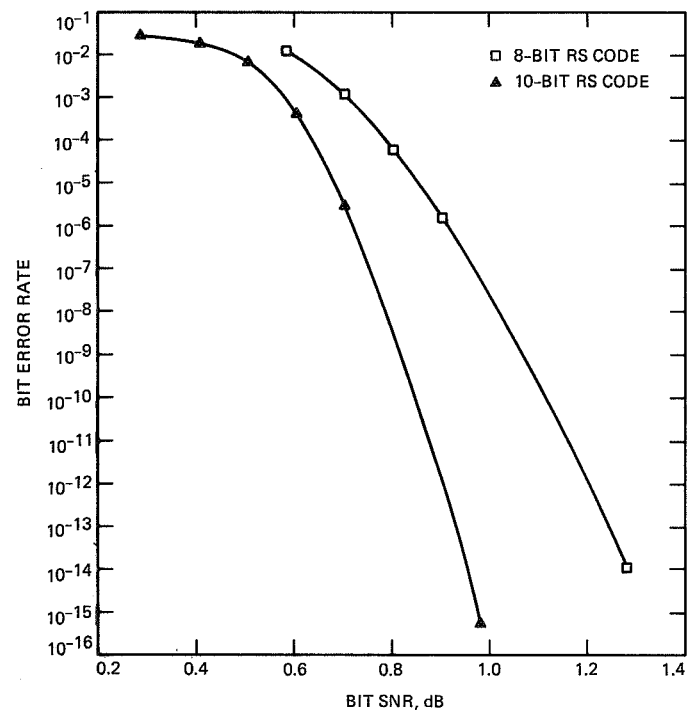


Fig. 10. Concatenated code performance comparison: 8-bit (255,223) and 10-bit (1023,959) RS concatenated with (15,1/4) convolutional.

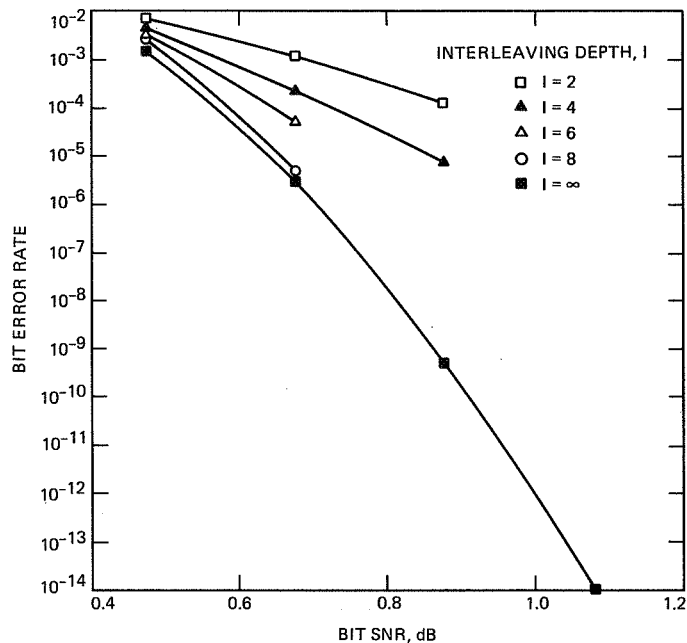


Fig. 11. Concatenated code performance: (15,1/6) convolutional and 8-bit (255,223) RS.

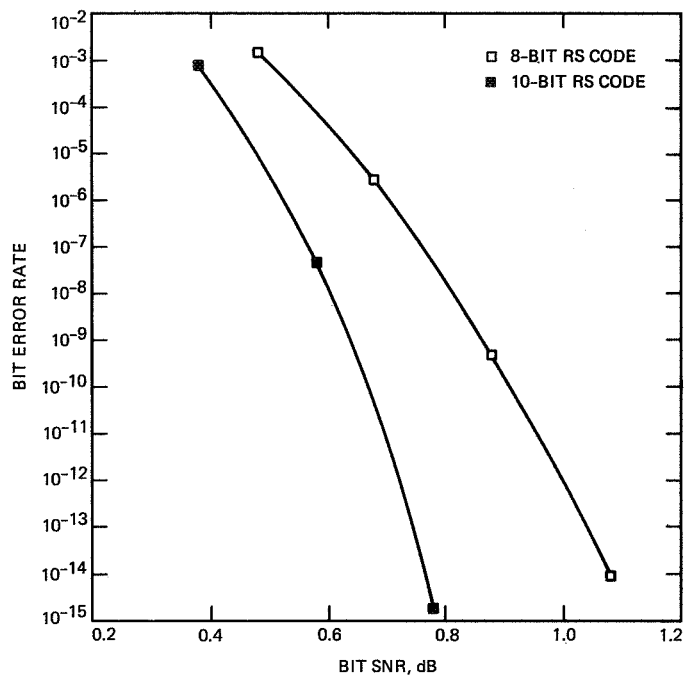


Fig. 13. Concatenated code performance comparison: 8-bit (255,223) and 10-bit (1023,959) RS concatenated with (15,1/6) convolutional.

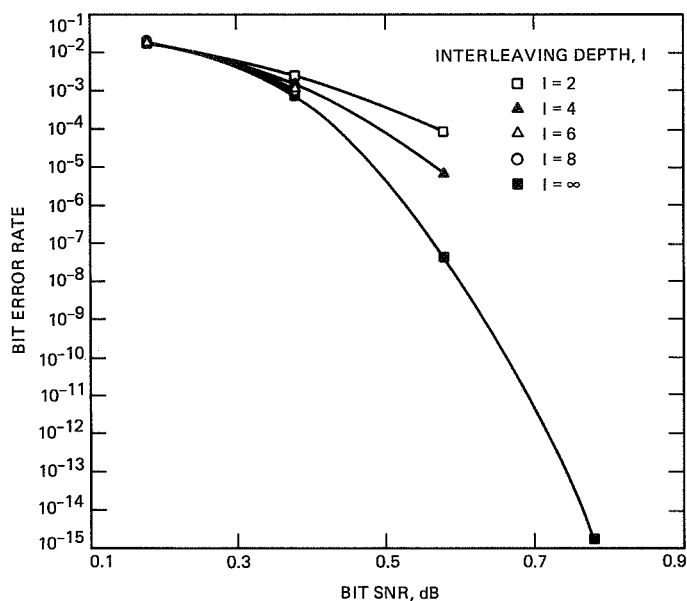


Fig. 12. Concatenated code performance: (15,1/6) convolutional and 10-bit (1023,959) RS.

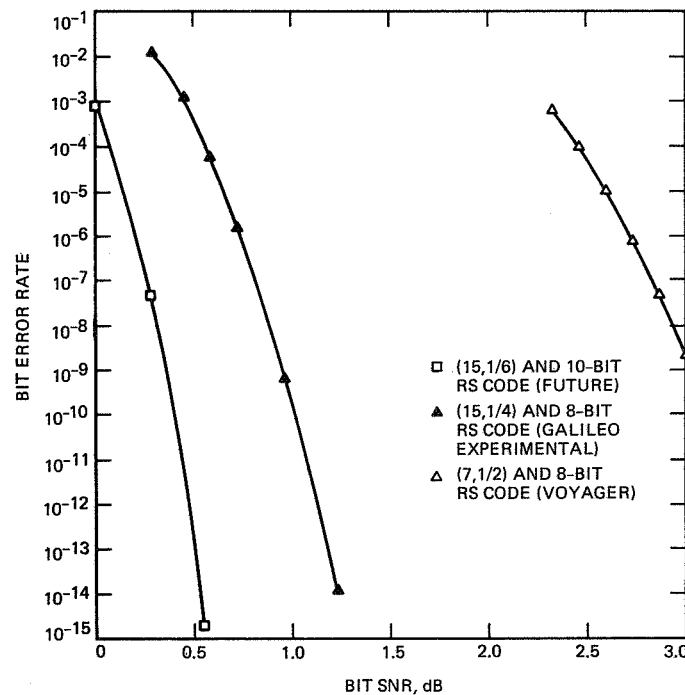


Fig. 14. Comparison of three concatenated codes.

520-61
218075

N 8 9 - 2 7 8 9 1

Decoding of 1/2-Rate (24,12) Golay Codes

T.-K. Truong

Communications Systems Research Section

I. S. Reed and X. Yin

Department of Electrical Engineering, University of Southern California

In this article, a decoding method for a (23,12) Golay code is extended to the important 1/2-rate (24,12) Golay code.

I. Introduction

The 23-bit Golay code is a very useful code, particularly for those applications where a parity bit is added to yield a 1/2-rate code. Recently a simplified procedure was developed for decoding this important (24,12) Golay code [1]. It is shown here that this procedure can be extended to any decoding method which can correct three errors in the (23,12) Golay code.

There are several known decoding procedures for correcting the three possible errors of (23,12) Golay code:

- (1) The minimum-distance method [2]
- (2) The standard-array method [2], [3]
- (3) The majority-logic method, suggested by Goethals [4]
- (4) Kasami's error-trapping algorithm [5]
- (5) The shift-and-search procedure [1]
- (6) Algebraic algorithms which include Berlekamp's method [2], [6] as well as the extended Bose-Chaudhuri-Hocquenghem (BCH) algorithm suggested recently by M. Elia in [7]

In this article, a simple method is given to extend any of these procedures to the 1/2-rate (24,12) Golay code so that three errors can be corrected and four errors can be detected.

II. Theorem for Close-Packed Error-Correcting Codes

The (23,12) Golay code is a close-packed error-correcting code for which the following theorem can be proved:

Theorem: Let C be the set of codewords of a Golay code. Also let E_i be the set of vectors of weight i . Then for any $c \in C$, and any $e_4 \in E_4$, there is a $c' \in C$ such that

$$c + e_4 = c' + e_3$$

where $e_3 \in E_3$.

Proof: See Appendix and [1].

III. The (24,12) Golay Code

A (24,12) Golay codeword can be formed by adding an even or odd parity-check bit to the (23,12) Golay codeword. It is well known that such a (24,12) Golay code has the minimum distance $d_{\min} = 8$. Thus any decoding algorithm can be extended to the (24,12) Golay code with the correction of three or fewer errors and the detection of four errors.

There is no loss in generality to assume that the parity of a (24,12) Golay codeword is even. That is, the sum of the 24 bits modulo 2 is equal to zero. Now assume during transmission that four errors are added to the codeword. There are two cases to consider:

- (1) If the four errors occur in the first 23 bits, then by the Theorem in Section II, the addition of an error vector of Hamming weight 4 to a codeword produces a 23-bit vector that is equal to some other (23,12) Golay codeword plus an error vector of weight 3. Thus if one of the decoding algorithms in Section I is applied to the first 23 bits, an error vector of weight 3 is added to the received codeword. As a consequence the parity of the (24,12) codeword also is changed. Hence by checking the parity of the decoded codeword, the decoder detects the presence of four errors.
- (2) On the other hand, if three errors occur in the first 23 bits, and one error occurs in the parity bit, the decoding algorithm corrects the three errors in the first 23 bits. The parity of the 23-bit decoded codeword now differs from the received parity bit. Hence the decoder detects the presence of four errors.

The extended decoding algorithm for the (24,12) Golay code is summarized as follows:

Apply any decoding algorithm which can correct three errors to the first 23 bits. If the number of errors is less than three, the decoding procedure terminates normally. If the number of errors is greater than or equal to three, the parity of the decoded codeword is compared with the received parity bit. If they are different, the decoder detects four errors. The detailed flowchart of this decoding procedure is shown in Fig. 1.

IV. An Example of Implementation

A complete algebraic decoding algorithm for the (23,12) Golay code was found recently by M. Elia [7]. To illustrate this method, define

$$E(x) = e_{22}x^{22} + e_{21}x^{21} + \dots + e_1x + e_0$$

to be the error polynomial. Then the received codeword has the form

$$R(x) = C(x) + E(x) = q(x)g(x) + E(x)$$

Suppose that three errors occur in the received code word $R(x)$ and assume that $2t \leq d - 1$. Since α, α^3 , and α^9 are the roots of $g(x)$, one has

$$s_1 = E(\alpha) = R(\alpha), s_3 = E(\alpha^3) = R(\alpha^3), s_9 = E(\alpha^9) = R(\alpha^9)$$

where s_1, s_3 , and s_9 are called the syndromes of the code. Assume z_1, z_2 , and z_3 are the positions of the three errors. Then the error-locator polynomial is defined by

$$\sigma(z) = \prod_{i=1}^3 (z - z_i) = z^3 + \sigma_1 z^2 + \sigma_2 z + \sigma_3$$

where $\sigma_1 = z_1 + z_2 + z_3$, $\sigma_2 = z_1 z_2 + z_2 z_3 + z_1 z_3$, and $\sigma_3 = z_1 z_2 z_3$. Then from [7],

$$\sigma_1 = s_1$$

$$\sigma_2 = s_1^2 + D^{1/3}$$

$$\sigma_3 = s_3 + s_1 D^{1/3}$$

where

$$D = \frac{(s_1^3 + s_3)^2 + (s_1^9 + s_9)}{(s_1^3 + s_3)}$$

Hence under different conditions for the syndromes, the error location polynomial has the following forms:

$$\sigma(z) = \begin{cases} 1 & \text{If } s_1 = s_3 = s_9 = 0 \\ & \text{then no error} \\ z + s_1 & \text{If } s_3 = s_1^3 \text{ and } s_9 = s_1^9 \\ & \text{then one error} \\ z^2 + s_1 z + (s_1^2 + D^{1/3}) & \text{If } s_1 \neq s_3 \text{ and } s_3 = s_1 D^{1/3} \\ & \text{then two errors} \\ z^3 + s_1 z^2 + (s_1^2 + D^{1/3}) z + (s_3 + s_1 D^{1/3}) & \text{Otherwise three errors} \end{cases}$$

Note that the cube root $D^{1/3}$ is in $GF(2^{11})$ and can be computed recursively, i.e.,

$$D^{1/3} = D^{1365} = D^{2^{10}+2^8+2^6+2^4+2^2+2^0} =$$

$$D^{2^{10}}D^{2^8}D^{2^6}D^{2^4}D^{2^2}D$$

After using the Chien search to find the error locations, one can apply the decoding procedure in this article to decode the (24,12) Golay code as described in Fig. 2.

A shift-and-search procedure for decoding Golay codes is given in [1]. In a computer simulation, this procedure is com-

pared with the Elia algebraic technique in terms of CPU time. For three and four errors this comparison shows that the algebraic method is more than twice as fast as the shift-and-search method in [1]. These results are shown in detail in Table 1.

V. Conclusion

The procedure given in this article extends the decoding of the (23,12) Golay code to the (24,12) Golay code. This extension generalizes to any close-packed error-correcting code. However, since there is only one other nontrivial multiple-error-correcting perfect code—the (11,6) Golay code over $GF(3)$ —such a generality may be somewhat academic.

Acknowledgment

The authors thank Professor Van Lint, presently visiting at Caltech, for bringing M. Elia's paper to our attention.

References

- [1] T.-K. Truong, J. K. Holmes, I. S. Reed, and X. Yin, "A Simplified Procedure for Decoding the (23,12) and (24,12) Golay Codes," *TDA Progress Report 42-96*, vol. October–December 1988, Jet Propulsion Laboratory, Pasadena, California, pp. 49–58, February 15, 1989.
- [2] J. H. van Lint, *Introduction to Coding Theory*, New York: Springer-Verlag, 1982.
- [3] R. McEliece, *The Theory of Information and Coding*, Reading, Massachusetts: Addison-Wesley, 1977.
- [4] J. J. MacWilliams and W. J. A. Sloane, *The Theory of Error-Correcting Codes*, Amsterdam: North-Holland, 1977.
- [5] S. Lin and D. J. Costello, *Error Control Coding: Fundamentals and Applications*, Englewood Cliffs, New Jersey: Prentice-Hall, 1983.
- [6] E. R. Berlekamp, *Algebraic Coding Theory*, New York: McGraw-Hill, 1968.
- [7] M. Elia, "Algebraic Decoding of the (23,12) Golay Code," *IEEE Trans. Inform. Theory*, vol. IT-33, pp. 150–151, January 1987.

Table 1. Computer CPU time for decoder simulations

CPU time, ms	Number of errors				
	0	1	2	3	4
Algebraic method	15.5	16	20	21	22
Shift-and-search method	15	15.5	20	44.5	47

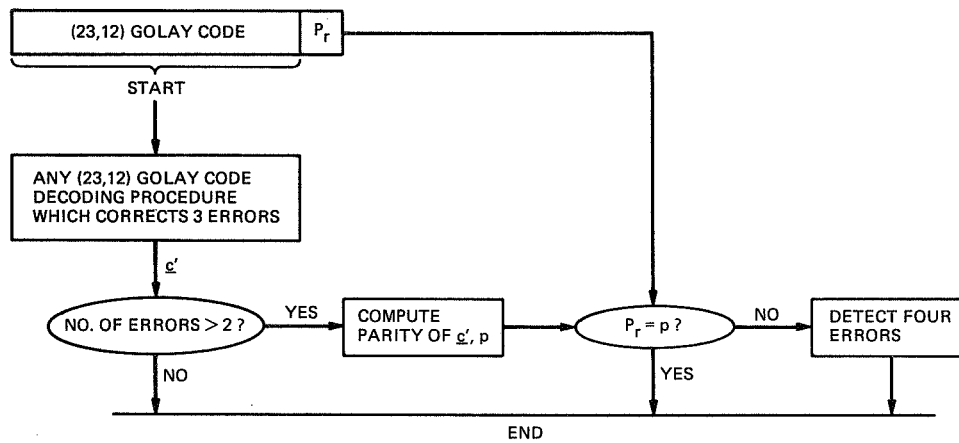


Fig. 1. Flowchart for decoding (24,12) Golay codes.

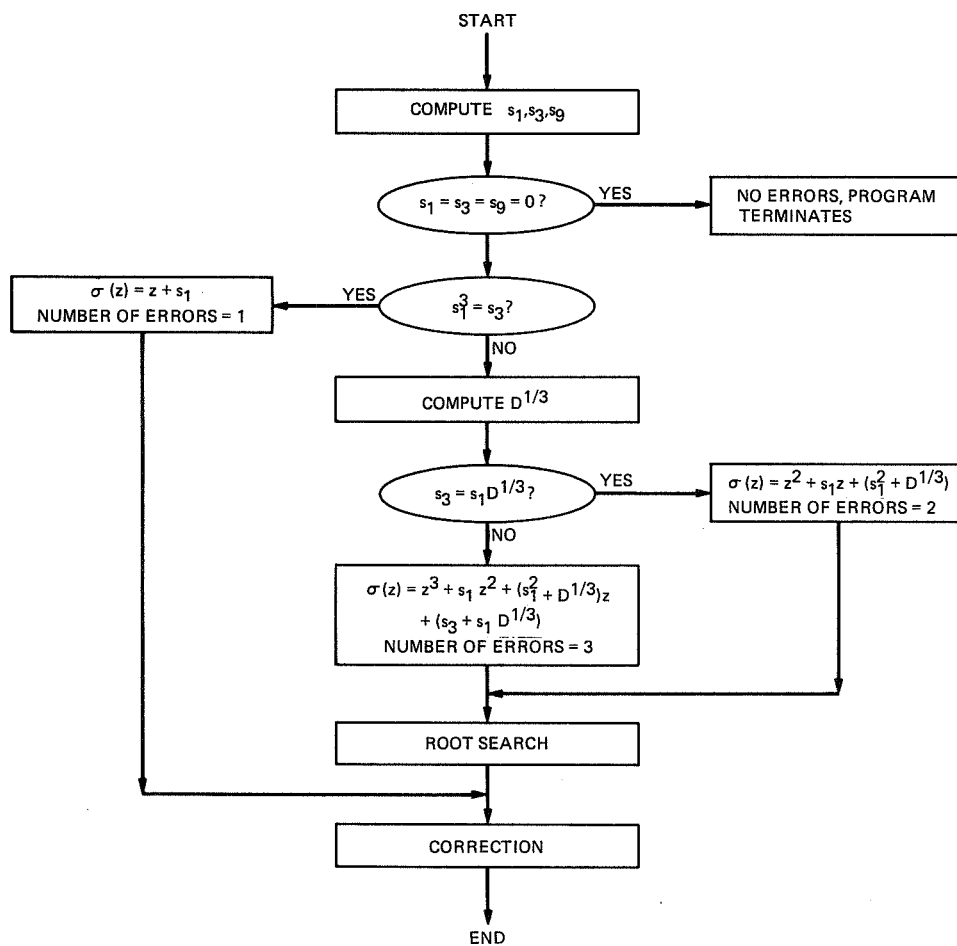


Fig. 2. Flowchart of Elia's algebraic procedure.

Appendix

Proof of Theorem

It is well known that the (23,12) Golay code is a close-packed code, i.e., the following equation holds:

$$2^{23} = \left[1 + \binom{23}{1} + \binom{23}{2} + \binom{23}{3} \right] 2^{12}$$

Let \mathbf{C} be the set of codewords of the Golay code. Also let \mathbf{E}_i be the set of vectors of weight i . Therefore, for any $\underline{c} \in \mathbf{C}$, and

any $\underline{e}_4 \in \mathbf{E}_4$, then $\underline{x} = \underline{c} + \underline{e}_4 = \underline{c}' + \underline{e}$ where weight of \underline{e} satisfies $w(\underline{e}) \leq 3$. Hence $\underline{e} = \underline{x} + \underline{c}'$ so that by property $w(x+y) \geq |w(x) - w(y)|$ one has the inequality

$$w(\underline{e}) = w(\underline{c} + \underline{c}' + \underline{e}_4) \geq |w(\underline{c} + \underline{c}') - w(\underline{e}_4)|$$

where $w(\underline{c} + \underline{c}') = \text{dis}(\underline{c}, \underline{c}')$. Since minimum distance of the code is $d_{\min} = 7$, one has finally that $w(\underline{e}) \geq 3$, and the theorem is proved.

51-61
218076

N89-27892

The Weight Distribution and Randomness of Linear Codes

K.-M. Cheung

Communications Systems Research Section

Finding the weight distributions of block codes is a problem of theoretical and practical interest. Yet the weight distributions of most block codes are still unknown except for a few classes of block codes. In this article, by using the inclusion and exclusion principle, an explicit formula is derived which enumerates the complete weight distribution of an (n,k,d) linear code using a partially known weight distribution. This expression is analogous to the Pless power-moment identities—a system of equations relating the weight distribution of a linear code to the weight distribution of its dual code.

Also, an approximate formula for the weight distribution of most linear (n,k,d) codes is derived. It is shown that for a given linear (n,k,d) code over $GF(q)$, the ratio of the number of codewords of weight u to the number of words of weight u approaches the constant $Q = q^{-(n-k)}$ as u becomes large. A relationship between the randomness of a linear block code and the minimum distance of its dual code is given, and it is shown that most linear block codes with rigid algebraic and combinatorial structure also display certain random properties which make them similar to random codes with no structure at all.

I. Introduction

Finding the weight distribution of block codes is a problem of theoretical and practical interest. When an incomplete decoding algorithm is used (e.g., bounded distance decoding), the probabilities of correct decoding, decoding error, and decoding failure can all be expressed in terms of the code's weight enumerator [2].

Let C be a linear (n,k,d) code over $GF(q)$, and C^\perp be its $(n,n-k,d^\perp)$ dual code. Let G be the generator matrix of C . Let the number of codewords of weight u be denoted by A_u . MacWilliams [3] showed that the weight enumerator of the dual C^\perp of a linear code C is given by a linear transformation

of the weight enumerator of C . Pless [1] introduced the power-moment identities—a system of equations relating the weight distribution of a linear code to the weight distribution of its dual code. In this article, by using the inclusion and exclusion principle, it is shown in Section III that the complete set of A_u 's, $0 \leq u \leq n$, can be generated if only the partial set of A_u 's, $d \leq u \leq n-d^\perp$, is known.

By modifying the techniques used in the above derivation, an approximate formula for A_u of most (n,k,d) nonbinary linear codes is derived. This formula, together with the approximate formula for A_u of binary linear code derived by Kasami et al. [4], shows that the distribution $q^{-(n-k)} \binom{n}{u} (q-1)^u$ is a close approximation to A_u for most (n,k,d) codes over $GF(q)$.

The intrinsic randomness of a linear (n, k, d) block code over $GF(q)$ is implicit in the Pless identities which show that the v th binomial moment, for $v = 0, 1, \dots, d^\perp - 1$, is independent of the code and is equal to that of the whole vector space, i.e., the $(n, n, 1)$ code $(GF(q))^n$. In this article, an explicit relationship between the randomness of a linear block code and the minimum distance of its dual code is given, and it is shown that for large u ,

$$\frac{\text{no. of codewords of weight } u}{\text{no. of vectors of weight } u} \rightarrow \frac{\text{total no. of codewords}}{\text{total no. of vectors}} = q^{-(n-k)} \stackrel{\text{def}}{=} Q \quad (1)$$

Equation (1) states that if the vector space $(GF(q))^n$ is partitioned into weight classes according to the Hamming weights of the vectors, then the ratio of the number of codewords in a weight class to the number of vectors in that weight class approaches a constant Q , where Q is the ratio of the size of the code to the size of the whole vector space $(GF(q))^n$. This remarkable relationship shows that most linear block codes with rigid algebraic and combinatorial structure also display certain intrinsic random properties which make them similar to random codes with no structure at all.

II. Mathematical Preliminaries

In this section combinatorial and coding techniques required to derive the results in later sections are introduced.

A. Principle of Inclusion and Exclusion [5]

Let χ be a set of N objects, and $P(1), P(2), \dots, P(u)$ be a set of u properties. Let $N(i_1, i_2, \dots, i_r)$ be the number of objects with properties $P(i_1), P(i_2), \dots, P(i_r)$. The number of objects $N(\emptyset)$ with none of the properties is given by

$$\begin{aligned} N(\emptyset) = & N - \sum_i N(i) + \sum_{i_1 < i_2} N(i_1, i_2) + \dots \\ & + (-1)^r \sum_{i_1 < i_2 < \dots < i_r} N(i_1, i_2, \dots, i_r) + \dots \\ & + (-1)^u N(1, 2, 3, \dots, u) \end{aligned} \quad (2)$$

There are $u + 1$ terms in the RHS of Eq. (2), with the 0th term representing the total number of objects in χ . If the RHS of Eq. (2) is truncated at the r th term, where r is even, the truncated sum represents a lower bound on $N(\emptyset)$. Similarly, if the

RHS of Eq. (2) is truncated at an odd term, an upper bound on $N(\emptyset)$ is obtained. Thus the maximum error magnitude introduced by the inclusion and exclusion formula by truncating the sum at the r th term does not exceed the magnitude of the r th term. This fact will be used later to upper bound the magnitude of the errors of the approximate weight distribution formula.

B. Facts on Coding Theory

A linear (n, k, d) code over $GF(q)$ can be generated by a $k \times n$ generator matrix G , not necessarily unique and such that $\text{rank}(G) = k$. Let l be the maximum number such that no l or fewer columns of G add to zero. Then

$$l \leq k \quad (3)$$

Equality in Eq. (3) is achieved in the case of *maximum distance separable* (MDS) codes. Since G is the parity-check matrix of C^\perp , $l = d^\perp - 1$. Let $\text{col}_{i_1}, \text{col}_{i_2}, \dots, \text{col}_{i_j}$ be any j particular columns of G , $j \leq l \leq k$. It is obvious that there exists a $k \times n$ generator matrix G' of C and a $k \times k$ non-singular matrix K such that

$$G' = KG \quad (4)$$

and $\text{col}_{i_1}, \text{col}_{i_2}, \dots, \text{col}_{i_j}$ of G' form a $k \times j$ submatrix of the form $\begin{pmatrix} I_j \\ 0 \end{pmatrix}$. This fact guarantees that the number of codewords with zeros on the i_1 th, i_2 th, \dots , i_j th coordinates equals q^{k-j} for $j \leq l$.

III. Derivation of Formula

Let \underline{c} be a codeword of C with Hamming weight u , $u \geq n - l$. Let the coordinates of \underline{c} be indexed by $\{0, 1, \dots, n - 1\}$. Then \underline{c} has v zeros ($v \leq l$), where $v = n - u$. Let V be a set of v coordinates, $|V| = v$. Let $\{i_1, i_2, \dots, i_j\} \subseteq \{0, 1, \dots, n - 1\} - V$ be a set of j coordinates. Define $S(i_1, i_2, \dots, i_j) = \{\underline{c} : \underline{c} \in C \text{ and } \underline{c} \text{ has zeros in } V \cup \{i_1, i_2, \dots, i_j\}\}$. A codeword $\underline{c} \in S(i_1, i_2, \dots, i_j)$ always has at least $v + j$ zeros. Let

$$T_j = \sum_{|V|=v} \sum_{i_1 < i_2 < \dots < i_j} |S(i_1, i_2, \dots, i_j)|$$

That is, T_j is the j th term in the inclusion and exclusion formula. From the discussion in Section II.B, the number of codewords in $S(i_1, i_2, \dots, i_j)$ is

$$|S(i_1, i_2, \dots, i_j)| = q^{k-v-j} \quad \text{for} \quad 0 \leq j \leq l - v \quad (5)$$

There are $\binom{n}{v}$ ways to choose V from $0, 1, \dots, n-1$ and for each choice of V there are $\binom{u}{j}$ ($u = n - v$) ways to choose i_1, i_2, \dots, i_j from the remaining set of $u = n - v$ coordinates. Thus

$$T_j = \binom{n}{v} \binom{u}{j} q^{k-v-j} \quad \text{for} \quad 0 \leq j \leq l - v \quad (6)$$

For $l - v + 1 \leq j \leq n - d - v$, the number of zeros in the codewords of $S(i_1, i_2, \dots, i_j)$ exceeds l and therefore T_j cannot be expressed using Eq. (5). In this case T_j is evaluated by counting the number of $S(i_1, i_2, \dots, i_j)$ each codeword can contribute to. For a given v and j , the codewords that can contribute to T_j are the zero codeword and the codewords of weight $n - m$, $v + j \leq m \leq n - d$. For the zero codeword, there are $\binom{n}{v}$ ways of choosing V and $\binom{u}{j}$ ways of choosing the remaining j zero coordinates. For a codeword of weight $n - m$ (m zeros), $v + j \leq m \leq n - d$, there are $\binom{m}{v}$ ways to choose V and $\binom{m-v}{j}$ ways to choose the j remaining zero coordinates. There are A_{n-m} codewords of weight $n - m$. Thus

$$T_j = \binom{n}{v} \binom{u}{j} + \sum_{m=v+j}^{n-d} \binom{m}{v} \binom{m-v}{j} A_{n-m} \quad \text{for} \quad l - v + 1 \leq j \leq n - d - v \quad (7)$$

For $n - d - v + 1 \leq j \leq n - v$, the number of zeros in the codewords of $S(i_1, i_2, \dots, i_j)$ exceeds $n - d + 1$. Since the code has minimum distance d , $S(i_1, i_2, \dots, i_j) = \{\underline{0}\}$. Thus,

$$|S(i_1, i_2, \dots, i_j)| = 1 \quad \text{for} \quad n - d - v + 1 \leq j \leq n - v \quad (8)$$

As in the case for $0 \leq j \leq l - v$, there are $\binom{n}{v}$ ways to choose V and for each V there are $\binom{u}{j}$ ways to choose i_1, i_2, \dots, i_j . Thus

$$T_j = \binom{n}{v} \binom{u}{j} \quad \text{for} \quad n - d - v + 1 \leq j \leq n - v \quad (9)$$

By the principle of inclusion and exclusion, the number of codewords of weight u (v zeros), which is denoted by A_u , is given as follows:

$$A_u = \sum_{j=0}^u (-1)^j T_j \quad (10)$$

Although the above derivation is based upon the assumption that $u \geq n - l$, it is not hard to show that Eq. (10) is indeed

true for all u , $0 \leq u \leq n$. For $d \leq u \leq n - l + 1$, Eq. (10) is reduced to the identity $A_u = A_u$ (proof omitted).

It is observed from the above that only the derivation of T_j 's in the range $l - v + 1 \leq j \leq n - d - v$ ($l + 1 \leq v + j \leq n - d$, where $v + j$ is the number of zeros in a codeword) requires prior knowledge of A_{n-m} 's (weight enumerator of codewords with m zeros), where $v + j \leq m \leq n - d$. Thus the complete set of A_u 's, $0 \leq u \leq n$, can be generated if only the partial set of A_u 's, $d \leq u \leq n - d^\perp$, is known. An example which generates the weight distribution of the (7,4) Hamming code is given in Appendix A.

The above results are summarized in the following theorem and corollary.

Theorem 1. If C is an (n, k, d) code over $GF(q)$, then

$$A_u = \sum_{j=0}^u (-1)^j T_j \quad \text{for} \quad n - d^\perp + 1 \leq u \leq n$$

where

$$T_j = \binom{n}{v} \binom{u}{j} q^{k-v-j} \quad \text{for} \quad 0 \leq j \leq l - v$$

$$T_j = \binom{n}{v} \binom{u}{j} + \sum_{m=v+j}^{n-d} \binom{m}{v} \binom{m-v}{j} A_{n-m}$$

$$\text{for} \quad l - v + 1 \leq j \leq n - d - v$$

$$T_j = \binom{n}{v} \binom{u}{j} \quad \text{for} \quad n - d - v + 1 \leq j \leq n - v$$

Corollary 1. If A_u , $d \leq u \leq n - d^\perp$, of an (n, k, d) linear code C over $GF(q)$ are given, the remaining A_u 's, $n - d^\perp + 1 \leq u \leq n$, can be evaluated explicitly using the equations given in Theorem 1.

IV. Approximate Formula

Theorem 1 and Corollary 1 in Section III enable one to enumerate the complete weight distribution A_u , $0 \leq u \leq n$, given that the partial set of A_u , $d \leq u \leq n - d^\perp$, is known. This partial set of A_u is required in the calculation of T_j , $l - v + 1 \leq j \leq n - d - v$. In cases in which knowledge of this partial set is not available, one can still derive an approximate formula for A_u as follows. For a given coordinate set V , $|V| = v$, let A'_V denote the number of codewords with exactly v zeros in V .

Using a similar derivation as in Section III, A'_V can be represented by the inclusion and exclusion principle as follows:

$$\begin{aligned}
A'_V &= |S(\emptyset)| + (-1) \sum_{i_1} |S(i_1)| + \dots \\
&+ (-1)^r \sum_{i_1 < i_2 < \dots < i_r} |S(i_1, i_2, \dots, i_r)| + \dots \\
&+ (-1)^{n-v} |S(i_1, i_2, \dots, i_{n-v})| \\
&= \sum_{j=0}^{l-v} (-1)^j \binom{u}{j} q^{k-v-j} \\
&+ \sum_{j=l-v+1}^{n-d-v} (-1)^j \sum_{i_1 < i_2 < \dots < i_j} |S(i_1, i_2, \dots, i_j)| \\
&+ \sum_{j=n-d-v+1}^{n-v} (-1)^j \binom{u}{j} \quad (11)
\end{aligned}$$

If the above inclusion and exclusion formula is truncated at the $(l-v)$ th term, Eq. (7) is reduced to

$$A'_V = \sum_{j=0}^{l-v-1} (-1)^j \binom{u}{j} q^{k-v-j} + E_1 \quad (12)$$

where

$$\begin{aligned}
E_1 &= (-1)^{l-v} \binom{u}{l-v} q^{k-l} \\
&+ \sum_{j=l-v+1}^{n-d-v} \sum_{i_1 < i_2 < \dots < i_j} (-1)^j |S(i_1, i_2, \dots, i_j)| \\
&+ \sum_{j=n-d-v+1}^{n-v} (-1)^j \binom{u}{j}
\end{aligned}$$

From the discussion in Section II.A, $|E_1| \leq \binom{u}{l-v} q^{k-l}$. If

$$E_2 = \sum_{j=l-v}^u (-1)^j \binom{u}{j} q^{k-v-j}$$

is added to and subtracted from Eq. (12), one has

$$A'_V = \frac{(q-1)^u}{q^{n-k}} + E_1 + E_2 \quad (13)$$

If $\binom{u}{l-v} q \geq \binom{u}{l-v+1}$, that is, if $u \geq [(q+1)/q](n-l) - 1$, E_2 is a sum of terms with alternate signs and decreasing magnitude. Then $|E_2| \leq \binom{u}{l-v} q^{k-l}$. Thus

$$A'_V = \frac{(q-1)^u}{q^{n-k}} + E \quad (14)$$

where $E = E_1 + E_2$ and $|E| \leq 2 \binom{u}{l-v} q^{k-l}$. A'_V can thus be approximated by $[(q-1)^u]/q^{n-k}$, and the goodness of approximation depends on how small the ratio $R = E/[(q-1)^u \times q^{-(n-k)}]$ is. By using the upper bound on $|E|$, an upper bound on this ratio is given by

$$R \leq \frac{2 \binom{u}{n-l} q^{k-l}}{(q-1)^u}$$

Since $v \leq l$, there are $\binom{n}{v} = \binom{n}{u}$ ways to choose v zeros from $\{0, 1, \dots, n-1\}$. Then A_u can be approximated by the following expression:

$$A_u = \sum_{|V|=n-u} A'_V \approx q^{-(n-k)} \binom{n}{u} (q-1)^u \quad (15)$$

for $u \geq \max \{n-l, [(q+1)/q](n-l) - 1\}$.

Strictly speaking, the derivation of Eq. (15) is only valid for $u \geq \max \{n-l, [(q+1)/q](n-l) - 1\}$. However, it is observed that in most cases, $q^{-(n-k)} \binom{n}{u} (q-1)^u$ is also a close approximation to A_u for u considerably smaller than $n-l$ (as in the case of Reed-Solomon codes). The upper bound of R derived above has a denominator term $(q-1)^u$ and this indicates that this approximation formula is good for nonbinary linear codes, and is not useful for binary linear codes. The looseness of this approximation for binary linear codes is best illustrated by extended binary codes which only have even weights. However, it is observed that for most extended binary codes, the number of codewords of weight u , where u is even and is not close to 0 or n , can be approximated by the sum of two adjacent binomial coefficients $2^{-(n-k-1)} \binom{n-1}{u-1} + 2^{-(n-k-1)} \binom{n-1}{u}$. This is obvious since an (n, k, d) extended binary code can always be constructed from an $(n-1, k, d-1)$

binary code by appending each codeword with a parity bit. The weight distribution and its approximation for the (128, 113, 6) binary extended BCH code are given in Fig. 1. In the case of binary primitive codes, Kasami et al. [4] generalized Sidel'nikov's approach [6] and showed that the weights of most binary primitive codes have approximate binomial distribution. For nonbinary linear codes, the upper bound on R shows that the approximation in Eq. (11) is particularly good for codes with large alphabet sets. The upper bound on R for the (31, 15, 17) Reed-Solomon code over $GF(32)$ is given in Fig. 2. The weight distribution and its approximation (using Eq. 11) of the (31, 15, 17) Reed-Solomon code are given in Fig. 3.

V. Randomness of a Linear Block Code

In this section, the approximation for the weight distribution of linear codes will be used to investigate the randomness of linear block codes. It was shown in [7] that in the case of MDS codes, where both the weight distribution of the codes and the weight enumerators of decodable words are known, the following relationships are obtained:

$$\frac{\text{no. of MDS codewords of weight } u}{\text{no. of vectors of weight } u} \rightarrow \frac{\text{total no. of MDS codewords}}{\text{total no. of vectors}} = q^{-(n-k)} \quad (16)$$

and

$$\frac{\text{no. of decodable words of weight } u}{\text{no. of vectors of weight } u} \rightarrow \frac{\text{total no. of decodable words}}{\text{total no. of vectors}} = q^{-(n-k)} V_n(t) \quad (17)$$

where $V_n(t)$ is the volume of the Hamming sphere of the codes. In this article, by using the approximation in Eq. (11), Eq. (12) is generalized to all linear block codes. That is, for an (n, k, d) linear code C ,

$$\begin{aligned} \frac{\text{no. of codewords of weight } u}{\text{no. of vectors of weight } u} &\approx \frac{q^{-(n-k)} \binom{n}{u} (q-1)^u}{\binom{n}{u} (q-1)^u} \\ &= q^{-(n-k)} \\ &= \frac{\text{total no. of codewords}}{\text{total no. of vectors}} \end{aligned} \quad (18)$$

for $u \geq \max \{n-l, [(q+1)/q](n-l)-1\}$. As was discussed in Section III, in the case of nonbinary block codes, the goodness of the approximation in Eq. (14) depends upon the ratio $R = E/[(q-1)^u q^{-(n-k)}]$, which is upper bounded by $[2\binom{n}{u} q^{k-l}]/(q-1)^u$. A larger weight u and/or a larger d^\perp of C correspond to a better approximation of the weight distribution of C by the formula $\binom{n}{u} (q-1)^u$. This in turn implies that if d^\perp of C is large, the ratio of the number of codewords of weight u to the number of words of weight u approaches $q^{-(n-k)}$ more quickly as u gets large. This result is, in some way, analogous to Pless power-moment identities [1] which state that for a linear (n, k, d) block code, there are d^\perp (0, 1, ..., $d^\perp - 1$) binomial moments that are independent of the code and are equal to the binomial moments of the whole vector space.

VI. Conclusion

In this article, by using the inclusion and exclusion principle, an explicit formula which enumerates the complete weight distribution of an (n, k, d) linear code using a partially known weight distribution is derived. Using similar combinatoric and coding techniques an approximate formula for the weight distribution of most linear (n, k, d) codes is derived. A relationship between the randomness of a linear block code and the minimum distance of its dual code is given, and it is shown that most linear block codes with rigid algebraic and combinatorial structure also display certain random properties which make them similar to random codes with no structure at all. The results presented can help to simplify the calculations of the probabilities of correct decoding, decoding error, and decoding failure which are all expressed in terms of the code's weight enumerator.

References

- [1] V. Pless, "Power Moment Identities on Weight Distributions in Error Correcting Codes," *Info. and Control*, no. 6, pp. 147–152, 1963.
- [2] E. Berlekamp, *Algebraic Coding Theory*, Laguna Hills, California: Aegean Park Press, 1984.
- [3] F. MacWilliams, *The Theory of Error-Correcting Codes*, Amsterdam: North-Holland, 1977.
- [4] T. Kasami, T. Fujiwara, and S. Lin, "An Approximation to the Weight Distribution of Binary Linear Codes," *IEEE Trans. Inform. Theory*, IT-31, no. 6, pp. 769–780, November 1985.
- [5] R. Stanley, *Enumerative Combinatorics, Vol. I*, Monterey, California: Wadsworth and Brooks-Cole, 1986.
- [6] V.M. Sidel'nikov, "Weight Spectrum of Binary Bose-Chaudhuri-Hocquenghem Codes," *Probl. Peredachi Inform.*, vol. 7, no. 1, pp. 14–22, January–March, 1971.
- [7] K. Cheung, "More on the Decoder Error Probability of Reed-Solomon Codes," to appear in *IEEE Trans. Inform. Theory*.

u	Au (Exact)	A'u (Approx.)
0	1.000e+000	1.000e+000
2	0.000e+000	4.961e-001
4	0.000e+000	6.511e+002
6	3.414e+005	3.310e+005
8	8.729e+007	8.726e+007
10	1.384e+010	1.385e+010
12	1.448e+012	1.448e+012
14	1.061e+014	1.061e+014
16	5.697e+015	5.697e+015
18	2.315e+017	2.315e+017
20	7.303e+018	7.303e+018
22	1.827e+020	1.827e+020
24	3.683e+021	3.683e+021
26	6.070e+022	6.070e+022
28	8.272e+023	8.272e+023
30	9.413e+024	9.413e+024
32	9.020e+025	9.020e+025
34	7.332e+026	7.332e+026
36	5.087e+027	5.087e+027
38	3.029e+028	3.029e+028
40	1.555e+029	1.555e+029
42	6.914e+029	6.915e+029
44	2.672e+030	2.672e+030
46	8.998e+030	8.998e+030
48	2.649e+031	2.649e+031
50	6.834e+031	6.834e+031
52	1.548e+032	1.548e+032
54	3.082e+032	3.082e+032
56	5.406e+032	5.406e+032
58	8.359e+032	8.359e+032
60	1.141e+033	1.141e+033
62	1.374e+033	1.374e+033
64	1.462e+033	1.462e+033

* Au = 0 for odd u.
**Au = A_{128-u} and A'u = A'_{128-u}.

Fig. 1. Weight distribution and its approximation of the (128, 113, 6) BCH code.

u	R
16	2.74943144e-024
17	1.50775270e-024
18	4.37734673e-025
19	8.94296586e-026
20	1.44241389e-026
21	1.95423782e-027
22	2.31146419e-028
23	2.44993596e-029
24	2.37090920e-030
25	2.12446863e-031
26	1.78181347e-032
27	1.41082139e-033
28	1.06190837e-034
29	7.64152968e-036
30	5.28215447e-037
31	3.52143591e-038

Fig. 2. Upper bound on R for the (31, 15, 17) RS code.

u	Au (Exact)	A'u (Approx.)
0	1.000e+000	8.272e-025
1	0.000e+000	7.949e-022
2	0.000e+000	3.696e-019
3	0.000e+000	1.108e-016
4	0.000e+000	2.404e-014
5	0.000e+000	4.024e-012
6	0.000e+000	5.405e-010
7	0.000e+000	5.984e-008
8	0.000e+000	5.565e-006
9	0.000e+000	4.409e-004
10	0.000e+000	3.007e-002
11	0.000e+000	1.780e+000
12	0.000e+000	9.195e+001
13	0.000e+000	4.166e+003
14	0.000e+000	1.660e+005
15	0.000e+000	5.833e+006
16	0.000e+000	1.808e+008
17	8.221e+009	4.946e+009
18	9.591e+010	1.193e+011
19	2.629e+012	2.530e+012
20	4.676e+013	4.705e+013
21	7.646e+014	7.640e+014
22	1.076e+016	1.077e+016
23	1.306e+017	1.306e+017
24	1.349e+018	1.349e+018
25	1.171e+019	1.171e+019
26	8.380e+019	8.380e+019
27	4.811e+020	4.811e+020
28	2.130e+021	2.130e+021
29	6.832e+021	6.832e+021
30	1.412e+022	1.412e+022
31	1.412e+022	1.412e+022

Fig. 3. Weight distribution and its approximation for the (31, 15, 17) RS code over GF(32).

Appendix A

An Example Which Generates the Complete Weight Distribution of the (7,4,3) Hamming Code from an Incomplete Weight Distribution

This example illustrates the use of Theorem 1 to evaluate the complete weight distribution of the (7,4,3) Hamming code C . It is given that C has minimum distance $d = 3$ and C^\perp has minimum distance $d^\perp = 4$. According to Theorem 1 it is also required to know the partial weight distribution A_u , $3 = d \leq u \leq n - d^\perp = 3$. It is given that $A_3 = 7$, A_4 , A_5 , A_6 , and A_7 are now evaluated as follows:

1. $u = 4$ ($v = 3$). In this case T_0, T_1, T_2, T_3 , and T_4 are $\binom{7}{3} \binom{4}{0} 2$, $\binom{7}{3} \binom{4}{1} + \binom{4}{3} 7$, $\binom{7}{3} \binom{4}{2}$, $\binom{7}{3} \binom{4}{3}$, and $\binom{7}{3} \binom{4}{4}$, respectively. Thus,

$$A_4 = 70 - 168 + 210 - 140 + 35 = 7$$

2. $u = 5$ ($v = 2$). In this case T_0, T_1, T_2, T_3, T_4 , and T_5 are $\binom{7}{2} \binom{5}{0} 2^2$, $\binom{7}{2} \binom{5}{1} 2$, $\binom{7}{2} \binom{5}{2} + \binom{4}{2} 7$, $\binom{7}{2} \binom{5}{3}$, $\binom{7}{2} \binom{5}{4}$, and $\binom{7}{2} \binom{5}{5}$, respectively. Thus,

$$A_5 = 84 - 210 + 252 - 210 + 105 - 21 = 0$$

3. $u = 6$ ($v = 1$). In this case $T_0, T_1, T_2, T_3, T_4, T_5$, and T_6 are $\binom{7}{1} \binom{6}{0} 2^3$, $\binom{7}{1} \binom{6}{1} 2^2$, $\binom{7}{1} \binom{6}{2} 2$, $\binom{7}{1} \binom{6}{3} + \binom{4}{1} 7$, $\binom{7}{1} \binom{6}{4}$, $\binom{7}{1} \binom{6}{5}$, and $\binom{7}{1} \binom{6}{6}$, respectively. Thus,

$$A_6 = 56 - 168 + 210 - 168 + 105 - 42 + 7 = 0$$

4. $u = 7$ ($v = 0$). In this case $T_0, T_1, T_2, T_3, T_4, T_5, T_6$, and T_7 are $\binom{7}{0} 2^4$, $\binom{7}{1} 2^3$, $\binom{7}{2} 2^2$, $\binom{7}{3} 2$, $\binom{7}{4} + \binom{4}{0} 7$, $\binom{7}{5}$, $\binom{7}{6}$, and $\binom{7}{7}$, respectively. Thus,

$$A_7 = 16 - 56 + 84 - 70 + 42 - 21 + 7 - 1 = 1$$

522-74
218077

N 8 9 - 2 7 8 9 3

Effective Amplifier Noise for an Optical Receiver Based on Linear Mode Avalanche Photodiodes

C.-C. Chen

Communications Systems Research Section

The rms noise charge induced by the amplifier for an optical receiver based on the linear-mode avalanche photodiode (APD) was analyzed. It is shown that for an amplifier with a 1-pF capacitor and a noise temperature of 100 K, the rms noise charge due to the amplifier is about 300. Since the noise charge must be small compared to the signal gain, APD gains on the order of 1000 will be required to operate the receiver in the linear mode.

I. Introduction

The use of silicon avalanche photodiodes (APDs) in photon detection has been reported by several authors [1-4]. Compared to photomultiplier tubes (PMTs), the APDs offer smaller size and higher quantum efficiency. Since it is a solid state device, the APD is also inherently more reliable than the PMT. Additionally, the APD can be operated at a moderate supply voltage.

In order to apply the APD to photon-counting operation, the APD can be operated in either the Geiger mode [1-4] or the linear mode [5]. Most of the research in APD-based photon counters has been carried out with Geiger-mode APDs. In the Geiger-mode operation, the detector is biased beyond the breakdown voltage and cooled to reduce the number of thermally excited carriers. Since the device is biased beyond its normal breakdown voltage, an easily observable avalanche event will be initiated when a photon is absorbed by the device. Detector gain on the order of 10^5 - 10^6 can be achieved. The principal disadvantage of the Geiger-mode

operation is the requirement to quench the detector after each photon event to stop the avalanche. Both passive [1, 2] and active [3, 4] quenching schemes have been investigated. Since the quenching operation requires a direct feedback from the detector, the operating bandwidth is limited. Device speeds on the order of tens of megacounts per second have been reported. Another disadvantage associated with the Geiger mode operation is the large amount of after-pulsing observed. This is caused by the release of carriers that are trapped by the shallow potential wells during the avalanche. Since the receiver cannot differentiate between a photon event and after-pulsing, the after-pulsing effect must be minimized for reliable photon-counting operation.

An alternative to operating the APD in the Geiger mode is to operate the device in the linear mode, under normal bias condition. Under this mode, the detector is biased at just below the breakdown voltage so that the detection gain is large but finite. Since the detector is biased at below the breakdown voltage, the avalanche action does not persist and

the diode recovers quickly for the next photon event. Furthermore, since the number of carriers flowing through the junction is relatively small compared to the Geiger mode, the effect of after-pulsing is practically negligible. The low detection gain, however, poses a significant problem for the post-detection amplifier design. The amplifier must be designed to have an equivalent noise that is small compared to the total charge developed by the APD. The purpose of this article is to perform the noise analysis of such a detector.

II. Simplified Noise Model

The APD can be modeled as a current source which outputs G electrons for each detected photon. The avalanche gain, G , is random and its statistics depend on the bias voltage. An amplifier is needed to convert the current signal from the APD into a voltage signal. The two amplifier configurations that are most commonly used are the trans-impedance or shunt-feedback configuration, and the high impedance or integrating configuration. The effects of amplifier noise in these configurations are considered separately.

A. Shunt Feedback Configuration

The block diagram for a shunt-feedback receiver circuit is shown in Fig. 1. The output current (charge) from the APD is integrated by the amplifier, which consists of an op-amp and a feedback capacitor. The reset switch with a low resistive load is included so that the charge accumulated by the capacitor can be quickly discharged, thereby improving the response time of the circuit.

The photodiode can be modeled as an ideal current source with a shunt resistor R_D , a shunt capacitor C_D , and a series resistance R_s . The shot noise and the excess noise of the diode are summarized by the current source I_s . The amplifier can be characterized by an input noise voltage v_n , an input noise current i_n , an input impedance Z_i , and an effective gain A . Both the amplifier gain and the input impedance are assumed to be large. Because of the large input impedance of the amplifier, charge flowing from the detector will tend to accumulate over the feedback capacitor C_F , resulting in a voltage signal at the inverting input given by

$$v_- - v_o = \frac{Q_F}{C_F} \quad (1)$$

where Q_F is the amount of charge accumulated across the feedback capacitor, and is related to the amount of charge accumulating over the diode capacitance, Q_D , by

$$(A + 1) \times \frac{Q_D}{C_D} = \frac{Q_F}{C_F} \quad (2)$$

In order to achieve effective charge transfer into the integrating capacitor, the capacitance of the diode must be small compared to the effective feedback capacitance, $(A + 1) C_F$. Current state-of-the-art APDs have capacitance on the order of 1–2 pF. Future devices may have capacitance less than 1 pF. The total charge generated by the APD, or Q , is simply the sum of Q_F and Q_D

$$Q = Q_F + Q_D \quad (3)$$

For a sufficiently large A , it is reasonable to assume that most of the charge developed across the diode is accumulated across the feedback capacitor. In other words, the signal charge accumulated over the integrating capacitor is equal to the avalanche gain, G , of the detector.

The effect of noise on the integrating amplifier can be seen from the noise-equivalent circuit shown in Fig. 2. The rms voltage noise at the input to the amplifier, v_n , will induce an effective charge over the capacitor, $Q_{n,v}$. For an integrating amplifier with integration period T_s , the total noise charge is given by

$$Q_{n,v} = C_F v_n = C_F v_n / \sqrt{T_s} \quad (4)$$

Note that the amplifier noise voltage, v_n , which is generally specified in volts per root hertz, should be multiplied by the root bandwidth ($1 / \sqrt{T_s}$) to provide the rms input voltage.

The effect of current noise can be similarly analyzed. The shunt resistance of the diode, R_D , is typically on the order of several hundred megohms to a few gigohms. Because of its large value, the thermal noise generated by the diode can be practically ignored, and the dominating source of current noise is the amplifier noise current i_n . In general, since the noise current is shunted by C_D and R_D , the effective current noise flowing into C_F will be smaller than i_n . However, since the feedback capacitor is much larger than the diode capacitance for effective charge transfer, most of the noise current will flow across C_F . As a result, the effect of diode shunt is small and will be ignored in subsequent calculations. For a white current noise with power spectral density i_n^2 , the rms charge accumulated during the integrating period can be calculated as

$$Q_{n,i} = \sqrt{\langle \iint i_n(t) i_n(t) dt dt \rangle} = \sqrt{i_n^2 T_s} \quad (5)$$

where the notation $\langle x \rangle$ denotes the expectation of x . By assuming that the current noise and the voltage noise are

uncorrelated, the total rms noise charge sensed by the integrating amplifier is therefore

$$Q_n = \sqrt{\frac{(C_F v_n)^2}{T_s} + i_n^2 T_s} \quad (6)$$

Note that the effective noise charge depends on the noise current and noise voltage of the amplifier. For an amplifier operating at an equivalent noise temperature T_n , the noise charge can be optimized by choosing the noise impedance, R_n , equal to

$$R_n = \frac{v_n}{i_n} = \frac{T_s}{C_F} \quad (7)$$

The resulting optimal amplifier noise charge is given by

$$Q_n = C_F v_n \sqrt{\frac{2}{T_s}} = \sqrt{2kT_n C_F} \quad (8)$$

where we have used the fact that

$$v_n i_n = kT_n \quad (9)$$

In an optical communication receiver using an APD, the detector output should be integrated over the slot time. With a 10-nsec slot time, a 1-pF feedback capacitor, and an amplifier noise temperature of 100 K, the optimum effective noise charge as seen by the amplifier input is equal to 330 electrons. In order to effectively distinguish the detector output from system noise, the total signal charge must be several times the noise charge. In other words, the APD must provide a gain on the order of 1000. In practice, the noise voltage and noise current of an amplifier will not be optimized, and an even larger detector gain will be required.

B. High Impedance Configuration

The block diagram of the high impedance integrating amplifier is shown in Fig. 3. The configuration is simpler than the shunt feedback amplifier in that no feedback impedance is employed to develop the voltage signal. Instead, a high input impedance, Z_i , is used to convert the current signal from the APD into a voltage signal. Since the amplifier does not rely on the closed-loop feedback, the frequency response for the high Z configuration is generally better than that of the shunt feedback configuration.

The noise analysis for this configuration is straightforward. Again, the effect of diode series resistance R_s shall be ignored. The effect of amplifier noises, i_n and v_n , can be analyzed in a similar way to the shunt feedback case. The results are

$$Q_{n,v} = C_D v_n = C_D v_n / \sqrt{T_s} \quad (10)$$

$$Q_{n,i} = \sqrt{i_n^2 T_s} \quad (11)$$

Note that for the high impedance configuration, the device capacitance C_D dominates the voltage noise contribution. In addition to the amplifier current and voltage noises, the thermal noise of the input impedance Z_i , is also important. For a resistive load of R_i , the rms noise charge at the diode capacitor due to the thermal noise can be calculated by substituting into Eq. (5) the spectral density of the thermal noise, $i_T^2 = 4kT/R_i$. The result is

$$Q_{n,T} = \sqrt{\frac{4kT}{R_i} T_s} \quad (12)$$

where T is the operating temperature of the amplifier. Note that T is in general different from the noise equivalent temperature T_n . The total rms noise charge at the amplifier input is the root mean square sum of $Q_{n,i}$, $Q_{n,v}$, and $Q_{n,T}$. For an input impedance of 100 kilohms and an operating temperature of 300 K, the equivalent noise charge is about 250. This number can be reduced significantly, of course, by increasing the amplifier input impedance R_i . For a 10-megohm input impedance, the noise count due to R_i is only about 30. By choosing the high input impedance, therefore, the effect of thermal noise can be ignored compared to the effects of amplifier current and voltage noises, and the optimal rms noise charge can again be approximated by Eq. (8).

III. Limitations

Practical limitations on the application of linear-mode APDs include the following: non-ideal amplifier noise impedance, gain-bandwidth limitation of the amplifier, and stray (parasitic) capacitance and dynamic resistance.

The effect of amplifier noise impedance can be seen as follows: For a system operating with a 1-pF capacitance and 10-nsec slot time, the optimal noise impedance is 10 kilohms. With a 10:1 mismatch, the equivalent noise charge is about 740 electrons rms. This is large compared to the 300 electrons rms of a matched amplifier. The gain-bandwidth product is another factor that limits the application of linear mode APDs. For the shunt feedback configuration, the amplifier gain must be high enough to ensure effective charge transfer from the diode, and yet must be low enough to provide a reasonable bandwidth. In order to achieve an effective integration period of 10-nsec, a closed-loop bandwidth in excess of 1 GHz will be required. The high input impedance configuration, on the

other hand, does not rely on the active feedback to achieve high trans-impedance gain. Consequently, it is easier to achieve the desired frequency response with the high impedance configuration. Finally, the effect of stray capacitance is also important. Excessive capacitance at the input of the amplifier can reduce the charge transfer and increase the effective noise charge. And any stray capacitance at the output can reduce the frequency response of the circuit.

IV. Conclusions

Operating the APD under linear mode removes the need for quenching the detector after each photon event. The large, but finite, charge gain resulting from the avalanche can be integrated by either a shunt-feedback or an integrating amplifier

to generate a detectable signal at the output. The rms noise charge introduced by the amplifier was analyzed. It is shown that for a receiver operating with a 1-pF capacitance and an equivalent amplifier noise temperature of 100 K, APD gain in excess of 300 is required to provide a detectable signal (SNR = 1). The required detection gain can be even higher if the amplifier noise impedance is not perfectly matched. In order to provide a detection threshold that is several times higher than the noise level, a detection gain on the order of 1000 will be required for a matched system. It should be noted, however, that this analysis was carried out only for the two basic amplifier configurations shown in Figs. 1 and 3. Further reduction in amplifier noise at the same noise temperature is possible with other circuit configurations, and more studies are needed to fully understand the lower limit on the amplifier noise.

Acknowledgment

I thank Bill Folkner of the Tracking Systems and Applications Section for his helpful advice and discussions.

References

- [1] R. G. Brown, K. D. Ridley, and J. G. Rarity, "Characterization of Silicon Avalanche Photodiodes for Photon Correlation Measurements. 1: Passive Quenching," *Appl. Opt.*, vol. 25, pp. 4122-4126, 1986.
- [2] D. L. Robinson and B. D. Metscher, "Photon Detection with Cooled Avalanche Photodiodes," *Appl. Phys. Lett.*, vol. 51, pp. 1493-1494, 1987.
- [3] R. G. Brown, R. Jones, J. G. Rarity, and K. D. Ridley, "Characterization of Silicon Avalanche Photodiodes for Photon Correlation Measurements. 2: Active Quenching," *Appl. Opt.*, vol. 26, pp. 2383-2389, 1987.
- [4] S. Cova, A. Longoni, and A. Andreoni, "Towards Picosecond Resolution with Single-Photon Avalanche Diodes," *Rev. Sci. Instrum.*, vol. 52, pp. 408-412, 1981.
- [5] K. Kikuchi, T. Okoshi, and A. Hirose, "Achievement of Shot-Noise Limited Sensitivity and 50 dB Dynamic Range by Photon Counting Receiver Using Si Avalanche Photodiodes," *Elect. Lett.*, vol. 29, pp. 801-802, August 1985.

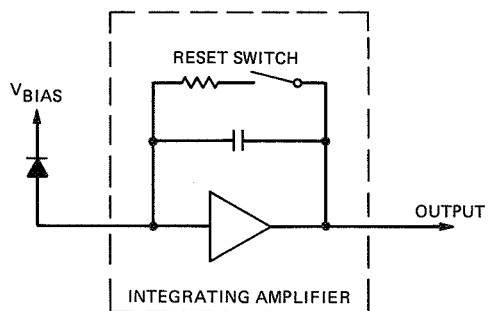


Fig. 1. Configuration of a shunt-feedback integrating amplifier.

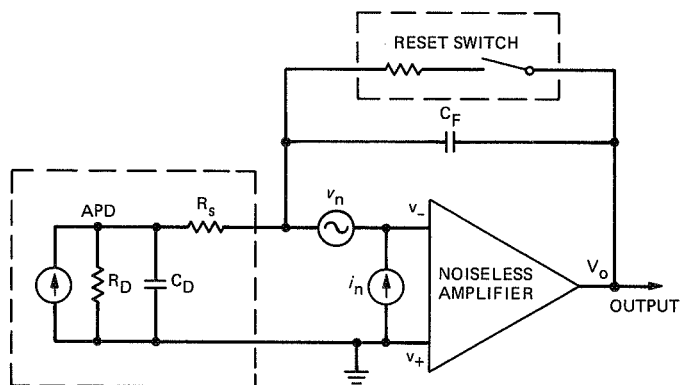


Fig. 2. Noise-equivalent circuit of the integrating amplifier.

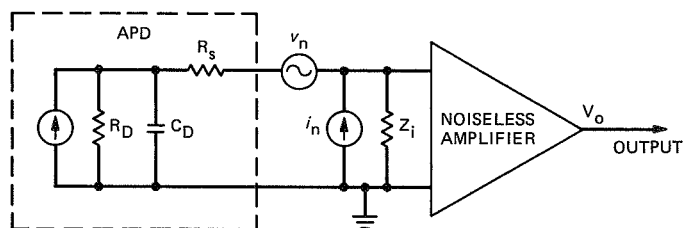


Fig. 3. Noise-equivalent circuit of high impedance trans-impedance amplifier.

A Visibility Characterization Program for Optical Communications Through the Atmosphere

K. Cowles

Communications Systems Research Section

A program is described for characterizing the atmosphere as it affects optical communications from a spacecraft. Cloud cover patterns and optical transmission will be determined by setting up three automated observatories in the Southwestern United States. Methods of site selection and operation of hardware and software components are presented, as well as plans for term deployment.

I. Introduction

Optical communication links to a ground-based station or network from a spacecraft experience degradation from the atmosphere. Cloud cover and other atmospheric effects can greatly attenuate laser signals or prevent transmission. The Atmospheric Visibility Monitoring (AVM) Program has been created to validate models for the effects of the Earth's atmosphere on optical communications. Three automated photoelectric telescopes (APTs) will be deployed in the Southwestern United States to measure atmospheric attenuation and determine cloud cover patterns. The telescopes will be located in areas that exhibit low correlation of weather patterns in order to determine the maximum percentage of time during which at least one area has favorable atmospheric conditions for deep space optical communications.

II. Preliminary Weather Model

A study conducted early in the project found that three sites with low correlation of weather patterns yield a joint visi-

bility probability of 94 percent [1]. Fewer sites do not yield a probability of clear skies sufficient for reliable communications. (Two sites yield an 83 percent probability.) More sites do not provide enough improvement for their additional cost. (Four sites yield a 97 percent probability.) An extensive investigation of sites and site characteristics was then begun to determine what characteristics are most important to the AVM project and which sites possess them.

III. Site Selection Criteria

Only sites in the Southwestern United States were considered since they hold the highest percentage of days with clear skies in the continental United States [2]. For ease of travel, no sites out of the country were considered. Nor were sites in Hawaii considered because they would be too far away from the mainland sites to measure any significant spatial correlation of weather, and because of the higher cost of Hawaiian travel. If only one site were going to be used, or if a "belt" of sites were to be strung around the Earth (experimental or operational), Hawaii would be a prime choice for

a site because of the excellent observing conditions and high probability of clear skies (90 percent on Mauna Kea).

Each site to be considered needs to exhibit other characteristics, such as low probability of cloud cover, fog, smog, and haze; low particle scattering; and low turbulence. These characteristics are discussed in depth in another report [3]. Since the telescopes are to be run remotely, there is also a need to locate them at present observatory sites so that someone can be on-hand to do maintenance and handle emergencies. There needs to be a degree of security to protect the system. Power, telephone lines, and roads also need to be easily accessible. All of the criteria have been weighted according to their importance to the program so that an educated decision can be made about which sites possess the best of the most important qualities [3].

IV. Candidate Sites

A search of sites in the southwest that presently have observatories was conducted, and further research was done to determine which sites possess favorable conditions. These sites include Mt. Hamilton, Table Mountain Observatory (TMO), Mt. Wilson, and Mt. Laguna in California; Mt. Hopkins, Mt. Lemmon, and the Hualapai Indian Reservation in Arizona; South Baldy and Sacramento Peak in New Mexico; and Mt. Locke in Texas. Other sites originally considered but eliminated for various reasons are Anderson Mesa, Mt. Graham, and Kitt Peak in Arizona; and Palomar and Goldstone in California. Goldstone was eliminated at this time because it is a very poor optical site. Its low elevation and location in the desert give rise to large amounts of particle scattering, turbulence, and atmospheric attenuation. Particle scattering is of great importance to the project because with large amounts of scattering, as is found at Goldstone, the number of stars able to be detected during the day is greatly reduced. Turbulence has been measured to be as much as ten times greater at Goldstone than at other sites.

The present sites have been split up into three categories by geographic location and general weather patterns in order to analyze the expected weather correlation factor between sites. The first category includes sites in southern California that experience storms from January to March: Mt. Wilson, TMO, and Mt. Laguna. The second includes sites in southern Arizona that experience storms in July and August: Mt. Hopkins and Mt. Lemmon. Areas in these two categories are known to be quite good for observing and have low correlation of weather patterns.

The question then arises as to where to locate the third telescope system. All the other sites fall into the third cate-

gory. They exhibit some of the same weather as the first two categories, only there might be a time lag, or the storms might not be as severe or as large when they are passing over the site. The site having the lowest correlation with the others while still having a considerable amount of cloud-free hours needs to be determined. The best way to determine this is to analyze satellite data collected over several years, comparing cloud cover at the rest of the sites with the ones in southern California and southern Arizona. These data are being acquired and will be used to determine cloud cover patterns, including the size of an average storm and the time frames in which storms travel, over each site. The site that is clear the most often when both southern California and southern Arizona are cloudy should be the site picked for the third telescope.

The satellite data can also be used after the study has acquired some of its own cloud cover data to determine if the relatively short study is in fact a representative sample of weather conditions or if special conditions apply to the years for which AVM data are collected.

Three of the mountains have been visited, and excellent locations for the telescope systems have been found at each site. These mountains are Mt. Hopkins (Fig. 1), the Hualapai Indian Reservation (Fig. 2), and most recently, Mt. Wilson. The directors of the observatories were interested in this program and felt there would not be any difficulties in acquiring sites for the project should these three mountains be chosen [3].

V. System Hardware

Meade 10-inch Schmidt-Cassegrain telescopes are to be used to monitor starlight transmission through the atmosphere. Optec SSP-3A solid-state photometers are to use different filters mounted on a filter slider to count photons from each star. The mounts for the system, along with roll-off roof enclosures, are being manufactured by Autoscope Corp. The mounts have right ascension and declination drives that can step in increments of 0.46 arcsec. The enclosures have a 1/2 horsepower motor that can open and close the roof in case of inclement weather. Photos of the telescope, mount, and enclosure are shown in Figs. 3 and 4. A weather station is attached to each enclosure to measure wind speed, wind direction, barometric pressure, and temperature, and to detect precipitation. Alarms are set off for conditions of high wind speed, extreme temperature, or precipitation. Uninterruptible power supplies (UPS) supply emergency power in case there is a sudden power outage. If the power goes out, a UPS supplies enough power to close the roof until power is reconnected. All of the equipment is controlled by International Business Machines personal computer (PC)-AT compatibles that are

able to communicate with a MicroVAX II over telephone lines via modems. WWV clocks are connected to the computers to keep accurate time, allowing for faster acquisition of stars. WWV clocks are radios that monitor a satellite clock. A heat exchanger is attached to the enclosure housing the electronics to keep them cool. All of the equipment is being integrated by Autoscope Corp. since they are also writing the software to control the equipment. Each individual observatory is to be assembled and tested on the Mesa at JPL. Since the Autoscope system is only designed for nighttime use, some slight modifications in hardware may be required to allow daytime detection.

To enable more efficient acquisition of the stars, additional hardware, namely a charge-coupled device (CCD) camera for faster nighttime centering, a second photometer modified for daytime use, and an instrument selector to move between these devices, may be added.

VI. System Software

The software that will control the telescope and enclosure and analyze the data received by the photometer and weather sensors is being written by Autoscope Corp. A large portion of this software will need to be rewritten to accommodate the needs of the AVM project. In its present state, the Autoscope software will accommodate typical astronomy applications for nighttime photometry. Some functions of the present software will not be used, and some code will need to be added to do tasks specific to this project, especially daytime photometry. These modifications should not be extensive. The code will be written in Turbo Pascal.

Telescope and enclosure control are to be entirely run by the PCs, although they can be manually run for testing purposes. There are audible alarms for conditions that cause the roof to close or open. Alarm conditions, as well as other operating conditions such as weather, time, zenith angles, etc., are recorded along with the data. The system should be able to run for several months with only short checks by local personnel.

The data that is received from the telescope photometer and the weather sensors will need to be compiled into a data base and analyzed. It will be transferred from the PCs at the sites to a MicroVAX II computer at JPL, where reduction and correlation algorithms will enable presentation of the data in an interpretable form.

VII. Daytime Viewing

Several different techniques that were considered for detecting cloud cover and transmission during the day are discussed in another report [4]. It was decided that the best method is to modify the photometer and software to allow daytime photometry. This makes possible the gathering of the same type of data as is gathered at night and the reception of atmospheric transmission as well as cloud cover data, although it will not be possible to search the sky as finely as at night.

The determination of where to locate the third telescope needs to wait until the satellite data on each area have been analyzed. Once tested and deployed, the telescopes can begin acquiring the data necessary to determine percentage of cloud cover, correlation effects, and atmospheric transmission.

VIII. Conclusions

An experimental data collection program for analysis of optical atmospheric transmission and verification of existing optical communications models has been described. A thorough study to determine the characteristics and locations of the sites for the telescope systems is almost completed. Site selection is an inexact science, as weather and other atmospheric conditions are constantly changing. Past years of satellite data will help to establish common yearly conditions for each location.

The AVM telescope systems have been configured and will be operating on the Mesa after slight modifications to the hardware. There is still a large amount of software that will need to be incorporated for telescope control and data reduction.

References

- [1] K. Shaik, "A Preliminary Weather Model for Optical Communications Through the Atmosphere," *TDA Progress Report 42-95*, vol. July-September 1988, Jet Propulsion Laboratory, Pasadena, California, pp. 212-218, November 15, 1988.
- [2] R. Lynds and J. Goad, "Observatory Site Reconnaissance," *Publications of the Astronomical Society of the Pacific*, vol. 96, pp. 750-766, September 1984.
- [3] K. Cowles, "Site Selection Criteria for the Optical Atmospheric Visibility Monitoring Telescopes," *TDA Progress Report 42-97*, this issue.
- [4] D. Erickson and K. Cowles, "Options for Daytime Monitoring of Atmospheric Visibility in Optical Communications," *TDA Progress Report 42-97*, this issue.

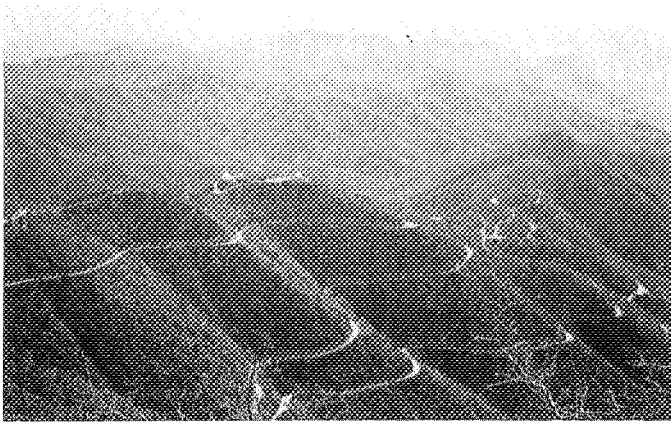


Fig. 1. Mount Hopkins. The AVM systems could be located on the knoll farthest to the left in the foreground.

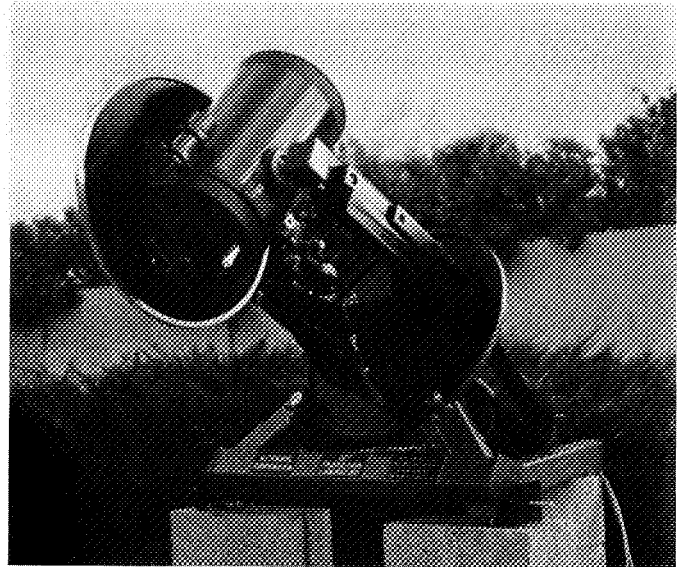


Fig. 3. AVM telescope and mount.



Fig. 2. Hualapai Indian Reservation. The AVM systems could be located on the plateau to the right.

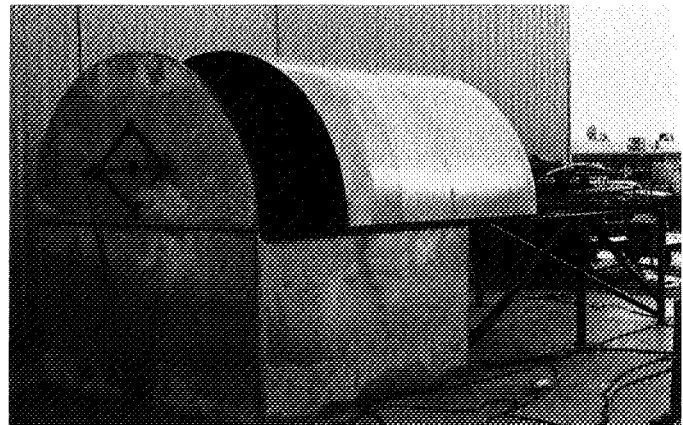


Fig. 4. AVM telescope enclosure with roll-off roof.

ORIGINAL PAGE
BLACK AND WHITE PHOTOGRAPH

524-46

218079

Options for Daytime Monitoring of Atmospheric Visibility in Optical Communications

D. Erickson and K. Cowles

Communications Systems Research Section

Techniques for daytime detection of atmospheric transmission and cloud cover to determine the capabilities of future deep-space optical communications links are considered. A modification of the planned nighttime photometry program will provide the best data while minimizing the need for further equipment. Greater degrees of modification will provide increased detection capabilities. Future testing of the equipment will better define the improvement offered by each level of modification. Daytime photometry is favored at certain wavelengths because of higher transmission and lower background noise, thus giving an increased signal-to-noise ratio. A literature search has provided a list of stars brighter than second magnitude at these wavelengths.

I. Introduction

The Atmospheric Visibility Monitoring (AVM) program will monitor the presence and correlation of cloud cover and transmission through the atmosphere at certain laser wavelengths to determine the feasibility of accommodating a cluster of ground-based optical communications transceivers. The sky must be continuously monitored, 24 hours a day, to detect clouds and transmission at varying zenith angles. At night, starlight will be detected using differential stellar photometry from three automatic photoelectric telescopes (APTs) on mountains in the southwestern United States. Equipment for nighttime photometry has already been purchased. During the day, detection of clouds and measurement of atmospheric transmission using stellar photometry are more challenging because of the background noise caused by scattered sunlight. Several different options were considered for use in monitoring the atmosphere during the day.

II. Criteria

The criteria which need to be met by a daytime AVM detection scheme are as follows:

- (1) Detect the presence of clouds as a percentage of sky cover
- (2) Monitor the entire sky, especially near the ecliptic, throughout the day
- (3) Measure atmospheric transmission at varying zenith angles
- (4) Maintain autonomous operation
- (5) Keep additional equipment costs to a minimum
- (6) Require minimal maintenance (a system could operate for periods of 2-3 months without trained personnel traveling to the site for maintenance)

- (7) Do not point the telescope at the sun because of potential damage

III. Candidate Monitoring Techniques

Several monitoring options were considered, including

- (1) Pyroheliometer mounted on a solar tracker
- (2) A pair of pyranometers, one with a shadow band
- (3) Polaris monitor
- (4) All-sky camera
- (5) Blue-sky monitor
- (6) Modified daytime stellar photometry

A. Pyroheliometer

This technique uses a simple solar radiation sensor mounted on a solar tracker. The sensor measures normally incident solar radiation [1]. The advantages of this technique are that it is capable of measuring atmospheric transmission as a function of solar intensity, is simple, needs very little direct maintenance, and eliminates the need to use the telescope when the sun is up.

However, several disadvantages arise from the fact that only normally incident radiation is measured. Cloud and transmission information would only be measured from a direct line to the sun. Broadband transmission would be measured instead of transmission at specific wavelengths. Cloud cover would not be measured as a percentage of the whole sky, but only if a cloud was between the sun and the detector. Changing solar zenith angle and solar magnitude would complicate the data processing and make the results less well-defined. Also, new equipment would have to be purchased. The added hardware expense would be approximately \$10,000 per station.

B. Pyranometers

This is also a passive solar radiation system. This technique uses two all-sky, solar radiation sensors [1]. One sensor is exposed to the whole sky. The other sensor has a shadow band that blocks the sun's path. By comparing the measurements of the two pyranometers, direct solar radiation can be calculated.

This system is simpler than the pyroheliometer because it has no moving parts. The cost is approximately the same. It has basically the same advantages and disadvantages as a pyroheliometer, but would make it slightly easier to process the data. This is because changes in solar magnitude will cancel out.

C. Polaris Monitor

A Polaris monitor uses a smaller telescope system to monitor the star Polaris throughout the day. This has the advantage of being simple. Polaris, also known as the North Star, moves approximately 90 arc minutes during a 24-hour period. The Polaris monitor also has the advantage of obtaining atmospheric transmission data. This technique's major disadvantage is that it is not an all-sky technique. In fact, it looks at the sky as far away from the ecliptic as possible. It would also require purchasing a second telescope and controller for each site at a cost of approximately \$10,000 apiece.

D. All-sky Camera

Two institutions are using a camera with a wide-angle lens (170-deg FOV), to obtain cloud-cover information. One institution uses film and the other uses a charge-coupled device (CCD) camera [2,3]. Of the six options studied, these cameras have the best all-sky capabilities. However, they both have the disadvantage of being difficult to run remotely for long periods of time. The film camera must have its film changed regularly. The CCD system gathers approximately 150 megabytes of data in a 12-hour day. Transferring this data over a modem would be time- and cost-prohibitive. Storage of the data for long periods would also be very difficult. Another major disadvantage of this technique is that it would not gather any atmospheric transmittance data. It can only describe where the clouds are at any given time. The CCD systems cost approximately \$25,000 each.

E. Blue-sky Monitor

By using the photometer on the APT, the sky could be monitored for clouds. This idea calls for the telescope to sweep periodically across the daytime sky and take photometric measurements using red and blue filters. The data received would be nearly identical to the all-sky camera data. The hardware cost would be minimal. However, developing the data-reduction algorithm and filter design might be difficult.¹ Like the all-sky camera, this scheme would not obtain any atmospheric transmittance data. A worrisome aspect of this technique is the potential damage to the telescope and photometer if the telescope sweeps across the sun. This problem should be solved if the control software is written with enough care.

F. Modified Daytime Stellar Photometry

Using the same methods day and night would be highly convenient when processing and comparing data. Just as it

¹ According to R. W. Johnson, manager of the CCD All-sky Camera project at the Scripps Institution in San Diego, California, the blue-red filter techniques they use were difficult to develop.

would at night, photometry used during the day will yield the most interesting transmission and cloud cover data. Performing standard UBV-differential photometry in the daytime would be difficult with the present system. UBV photometry measures starlight at three spectral bands: ultraviolet or U (centers at 350 nm), blue or B (Centers at 435 nm), and visible or V (Centers at 550 nm). The background noise caused by solar irradiance is too high at these wavelengths to perform daytime photometry. Two ways in which daytime photometry could be modified using the APT are selecting the correct band-pass filters and optically modifying the photometer.

Five issues need to be considered for selecting the correct band-pass filters for use during the day. They are as follows:

1. Photometric Standards. Doing stellar photometry would be simplified and more accurate if the system monitors wavelengths that have well-documented intensities. Some possible photometric standards that are within the range of the existing photometer are ultraviolet/blue/visible/red/infrared (UBVRI) filters, as established by Johnson [4, 5]. The UBVRI bands center near 350 nm, 435 nm, 555 nm, 700 nm, and 860 nm, respectively. They have bandwidths that range from 90–140 nm. The Wing MA, MB, and MI filters, a fairly new standard, center at 712 nm, 754 nm, and 1025 nm, respectively [5]. Their bandwidths are 10–40 nm.

2. Photometer Range. The photometer uses a Hamamatsu silicon PIN-photodiode with a usable spectral range of 320–1050 nm [5].

3. Solar Radiation. Solar irradiance peaks around 500 nm and then decreases sharply with increasing wavelength. Figure 1 shows that at 1000 nm the solar irradiance is at about one-third of the irradiance at 500 nm. The signal-to-noise ratio will improve at longer wavelengths.

4. Atmospheric Absorption. Certain wavelengths will not transmit as well through the atmosphere because of molecular absorption bands; however, in general the atmospheric transmission increases with wavelength, as shown in Fig. 2.

5. Communication Wavelengths. The most likely wavelengths to be used for future deep-space optical communication links are 532 nm, 810 nm, and 1064 nm.

After considering these five variables, it has been determined that the best filters to use for daytime photometry in the AVM project are the MI filter at 1025 nm and the I filter at 860 nm.

Daytime photometry can also be optimized by optically modifying the photometer. Decreasing the photometer's dia-

phragm diameter by one-half can improve the signal-to-noise ratio by a factor of four. The standard photometer has a diaphragm diameter of 1 mm, producing a 90-arc-second field of view. A simple Barlow lens mounted in the telescope's optical path, normally used as an image magnifier, will decrease the field of view of the telescope by the power of the lens. This can also increase the signal-to-noise ratio. Making these modifications will enable the detection of stars 1.5 to 3 magnitudes dimmer than possible with an unmodified APT. This will more than double the number of stars that can be observed.

Decreasing the diaphragm and using a Barlow lens does create some difficulties. The APTs search and centering function will be slowed down substantially since the field of view is decreased. This slowdown will decrease the number of stars the system can monitor in a given period of time. In the day, this may not present a problem because of the limited number of bright stars. At night, however, the longer search and centering function will greatly limit the quantity of stars observed. Adding an instrument selector with day and night photometers will increase the day performance without limiting the night program. An instrument selector and a second photometer will cost approximately \$7,000 for each system.

A dew cap will be used at night to prevent dewing problems. During the day the dew cap will act as a simple sunshade, preventing some scattered sunlight from entering the aperture of the telescope.

Modified daytime stellar photometry meets all the criteria. It has the advantage of requiring minor equipment changes. It will provide daytime data in the same form as nighttime data, thus simplifying data analysis.

There is the possibility of damage to the telescope and photometer if the telescope sweeps across the sun. The control software can be written to avoid this problem. Some modifications will slow down the search and centering of stars. Modifying the APTs could cost as much as \$7,000 each. Despite these disadvantages, the best daytime technique appears to be modified daytime photometry.

IV. Estimated Capabilities of Daytime Photometry

Some daytime measurements have been made using manual location techniques on an amateur mount. Conditions present during the measurements were as follows:

- (1) Date: September 17, 1988
- (2) Time: 9:30 a.m. PST
- (3) Location: Chilao, Angeles National Forest

- (4) Elevation: approximately 6000 ft
- (5) Weather conditions: hazy skies
- (6) Telescope: 10-inch Meade Cassegrain
- (7) Detector: Optec SSP-3 Solid State Photometer
- (8) Filter: MB (centers at 754 nm, 10-nm bandwidth)

The star 19 β Orion (HD 34085) was monitored at an approximate zenith angle of 60 deg. The photometer measured 2800 counts/sec with the star in the field of view and 1400 counts/sec for the sky near the star. The starlight can thus be calculated as 1400 counts/sec. This reading yielded a signal-to-noise ratio of two. To make searching and centering of stars accurate, a signal-to-noise ratio of ten or greater is desirable. It is useful to calculate what is expected from a star of comparable magnitude in the MI band. Using this observation as a simple performance baseline for the APTs, some broad assumptions can be made. In the MB band used in the above observation, β Orion is 0.6 magnitude. The solar irradiance, which comprises most of the daytime background noise, is approximately $9000 \text{ Wm}^{-2}\mu\text{m}^{-1}$ in the MB band. If the measurements were made in the MI band, the solar irradiance would be $5500 \text{ Wm}^{-2}\mu\text{m}^{-1}$. The solar irradiance of the MI band is 0.6 times that of the MB band (see Fig. 1). The atmospheric transmission would improve from approximately 43 percent to 57 percent (see Fig. 2). This will increase the light from the star 1.33 times. From this one can see that when using the APT at 1025 nm, the signal-to-noise ratio is roughly equal to

$$\frac{1.33 \times \text{Starlight} + 0.6 \times \text{Background light}}{0.6 \times \text{Background light}} =$$

$$\frac{1.33 \times (1400) + 0.6 \times (1400)}{0.6 \times (1400)} = 3.2$$

A star 3.1 times brighter than the above example (or -0.5 magnitude in the MI band) has a signal to noise ratio of ten. There are thirteen stars brighter than -0.5 magnitude at 1025 nm (see Table 1). By allowing the telescope to view down to a zenith angle of 60 deg, eight hours of right ascension can be viewed. Any given eight hours of right ascension will provide a minimum of three, a maximum of seven, and an average of four-and-a-half observable stars brighter than -0.5 at 1025 nm (MI band). If the field of view is decreased by using a smaller, 0.5-mm diaphragm or a 2X Barlow lens, one can see stars as dim as first magnitude. There are 61 stars brighter than first magnitude at 1025 nm. With both a smaller diaphragm and a

2X Barlow lens, stars of the second magnitude would be obtainable. There are 105 stars that are brighter than second magnitude at 1025 nm.

A search has been conducted of possible daytime stars brighter than second magnitude between 1000 nm and 1200 nm [8, 9, 10]. Table 1 lists those stars visible from the southwestern United States (at least 20 deg above the horizon from a latitude of 34 deg). Figure 3 shows how these stars are distributed across the heavens. Many of the brightest of these stars are late-type stars. The blackbody curves of these older stars peak in the red and infrared. Quite a few of these late-type stars are variables [10]. The project will be able to accommodate variables with long periods or small variations (less than 0.2 magnitude). Stars with long periods will have predictable small daily variations. Small variations will not be significant in measurements. Less than seven percent of the stars listed in Table 1 are variables that cannot be used [10].

With minor equipment modifications to the APTs, daytime stellar photometry in the near infrared can produce daytime cloud cover and atmospheric transmission information.

V. Conclusions

Only one of the evaluated techniques, the modified photometry technique, is able to meet all the monitoring criteria. The degree of optimization will determine the quantity of stars the system can acquire during the day and thus how finely the sky will be monitored.

By simply using an MI filter, this technique can produce limited daytime atmospheric information. By using a single photometer and modifying it with a smaller diaphragm and/or a Barlow lens, the daytime performance will be improved. However, there will be a decrease in the number of stars obtained at night since the search routine will take longer to cover the same area. How the various daytime photometry techniques affect the project can be evaluated after the APTs are tested. The first of the APTs should have been delivered about March 1989.

By using an instrument selector and a second photometer, the systems can be modified to increase the number of stars that are seen in the day without changing the performance at night. With this minor equipment change, daytime stellar photometry can provide atmospheric transmission data derived from an average of 30 evenly distributed stars at any given time.

Acknowledgment

The authors would like to acknowledge M. Rayman for stimulating discussions and for his help in the field experiment.

References

- [1] *Geophysical Instruments and Systems Catalog 1987*, Qualimetrics Inc., Sacramento, California, pp. 27–28, 192–193, 1987.
- [2] K. McGuffie, A. Henderson-Sellers, "Observations of Oceanic Cloudiness," *EOS Transactions*, American Geophysical Union, vol. 69, no. 28, pp. 714–715, July 1988.
- [3] R. W. Johnson, W. S. Herin, "Automated Cloud Cover Measurements with a Solid-State Imaging System," In House Technical Note No. 206, University of California, San Diego, Scripps Institution of Oceanography, Visibility Laboratory, La Jolla, California, July 1987.
- [4] A. W. F. Cousins, "VRI Standards in the E Regions," *Memoirs of the Royal Astronomical Society*, vol. 81, pp. 25–36, 1976.
- [5] *Model SSP-3 Solid-State Stellar Photometer, Technical Manual*, Optic Inc., Lowell, Michigan, October 1988.
- [6] P. R. Gast, "Solar Irradiance," in *Handbook of Geophysics and Space Environments*, Section 16.1, Cambridge, Massachusetts: S. L. Valley, 1965.
- [7] D. E. Novoseller, "Use of Lowtran in E Transmission Calculations," *Applied Optics*, vol. 26, pp. 3185–3186, 1987.
- [8] G. Neugebauer, R. B. Leighton, "Two-Micron Sky Survey, A Preliminary Catalog," National Aeronautics and Space Administration Special Publication SP-3047, Washington D.C., 1969.
- [9] D. Y. Gezari, M. Schmitz, J. M. Mead, *Catalog of Infrared Observations*, 1st ed., National Aeronautics and Space Administration Reference Publication RP-1118, Washington D.C., 1984.
- [10] D. Hoffleit, C. Jaschek, *The Bright Sky Catalogue*, 4th ed., Yale University Observatory, New Haven, Connecticut, 1982.

Table 1. Stars brighter than second magnitude (1000 nm to 1200 nm)

Henry Draper (HD) no.	Right Ascension	Declination	Magnitude	Type
432	00 07 47.5	+59 08 59	1.65	F2III-IV
1760	00 21 46.3	-20 03 28	1.02	M5IIe
3627	00 39 19.6	+30 51 40	1.24	K3III
3712	00 40 30.4	+56 32 15	0.42	K0IIIa
4128	00 43 35.3	-17 59 12	0.39	K0III
6860	01 09 43.8	+35 37 14	-0.25	M0IIIa
12533	02 03 53.9	+42 19 47	0.26	K3-IIb
12929	02 07 10.3	+23 27 45	0.28	K2IIIab
14386	02 19 20.7	-02 58 39	-1.70	M7IIIa
17506	02 50 41.8	+55 53 44	1.05	M3Ib-IIa
18884	03 01 40.6	+04 05 23	-0.29	M1.5IIIa
18925	03 03 47.7	+53 30 23	1.70	G8III+A2V
19058	03 05 10.5	+38 50 25	-0.10	M4II
20720	03 19 30.9	-21 45 28	0.00	M2III
20902	03 24 19.3	+49 51 41	0.87	F5Ib
23475	03 49 31.2	+65 31 34	0.51	M2IIab
25025	03 58 01.7	-13 30 31	0.35	M0.5III
29139	04 35 55.2	+16 30 33	-1.16	K5III
29755	04 40 26.4	-19 40 18	0.69	M4III
31398	04 56 59.6	+33 09 58	-0.74	K3II
32068	05 02 28.6	+41 04 33	1.10	K4IIB8V
32887	05 05 27.6	-22 22 16	1.48	K5IIIV
33664	05 11 22.8	-11 50 57	-0.10	M6III
34085	05 14 32.2	-08 12 06	1.15	B8Iae
34029	05 16 41.3	+45 59 53	-1.17	G5IIIe
35497	05 26 17.5	+58 36 27	1.96	B7III
36079	05 28 14.7	-20 45 34	-1.33	G5II
36389	05 32 12.7	+18 35 39	0.82	M2Iab-Ib
37128	05 36 12.7	-01 12 07	2.00	B0Iae
39801	05 55 10.3	+07 24 25	-2.68	M2Ia-Iab
40183	05 59 31.7	+44 56 51	1.85	A2IV
40239	05 59 56.1	+45 56 13	0.30	M3III
42995	06 14 52.6	+22 30 24	-0.23	M3III
44478	06 22 57.6	+22 30 49	-0.28	M3IIIab
47105	06 37 42.7	+16 23 57	1.91	AOIV
48329	06 43 55.9	+25 07 52	0.99	G8Ib
48915	06 45 08.9	-16 42 58	-1.33	AIVm
52089	06 58 37.5	-28 58 20	1.97	B2II
52877	07 01 43.1	-27 56 06	0.93	K7Ib
54605	07 08 23.4	-26 23 35	0.07	F8Ia
60179	07 34 35.9	+31 53 18	1.55	AIV
61421	07 39 18.1	+05 13 30	-0.41	F5IV-V
62509	07 45 18.9	+28 01 34	-0.35	K0IIIb
69267	08 16 30.9	+09 11 08	1.09	K4III
76294	08 55 23.6	+05 56 44	1.48	G9-II-III
80493	09 21 03.2	+34 23 33	0.65	K7IIIab
81797	09 27 35.2	-08 39 31	-0.36	K3II-III
84748	09 47 33.4	+11 25 43	-0.40	M8IIIe
87901	10 08 22.3	+11 58 02	1.47	B7V
89484	10 19 58.3	+19 50 30	-0.67	KI-IIIb
89758	10 22 19.7	+41 29 58	0.60	M0III
93813	10 49 37.4	-16 11 37	1.06	K2III
95689	11 03 43.6	+61 45 03	0.05	K0IIIa
100029	11 31 24.2	+64 19 52	1.62	M0III
102647	11 49 03.5	+14 34 19	1.99	A3V
105707	12 10 07.4	-22 37 11	1.61	K2.5IIIa
109379	12 34 23.2	-23 23 48	1.23	G5II

Table 1 (contd)

Henry Draper (HD) no.	Right Ascension	Declination	Magnitude	Type
112300	12 55 36.1	+03 23 51	0.08	M3III
113226	13 02 10.5	+10 57 33	1.52	G8IIIab
116658	13 25 11.5	-11 09 41	1.50	B1III-IV
120315	13 47 32.3	+49 18 48	-0.19	B3V
120285	13 49 02.0	-28 22 03	-1.12	M7.5-M9pe
121370	13 54 41.0	+18 23 51	1.65	GOIV
124897	14 15 39.6	+19 10 57	-1.95	KIIIb
127665	14 31 20.1	+30 22 17	1.46	K3III
129988	14 44 29.1	+27 04 27	0.65	KOII-III
131873	14 50 42.2	+79 09 19	1.47	K4III
132813	14 57 34.8	+65 55 56	0.73	M5III
133216	15 04 04.1	-25 16 55	0.02	M3IIIa
140573	15 44 16.0	+06 25 32	1.99	K2 III
146051	16 14 20.6	-03 41 39	0.54	M0.5III
148387	16 23 59.3	+61 30 51	1.17	G8IIIab
148478	16 29 24.3	-26 25 55	-2.69	M1.5Iab-Ib
148783	16 28 38.4	+41 52 54	-0.20	M6III
148856	16 30 13.1	+21 29 22	1.21	G7IIIa
150680	16 41 17.1	+31 36 10	1.70	GOIV
156014	17 14 38.8	+14 23 25	-2.11	M5Ib-II
156283	17 15 02.6	+36 48 33	0.80	K3IIab
159181	17 30 25.8	+52 18 05	1.29	G2Ib-IIa
159561	17 34 55.9	+12 33 36	1.71	A5III
164058	17 56 36.2	+51 29 20	-0.39	K5III
168454	18 20 59.5	-29 49 42	1.20	K3IIIa
169916	18 27 58.1	-25 25 18	1.72	KIIIb
172167	18 36 56.2	+38 47 01	-0.02	A0Va
175865	18 55 19.9	+43 56 46	-0.32	M5III
180711	19 12 33.1	+67 39 41	1.43	G9III
183912	19 30 43.1	+27 57 35	+1.13	K3II
186791	19 46 15.4	+10 36 48	0.24	K3II
187076	19 47 23.0	+18 32 03	0.37	M2II+AOV
187642	19 50 46.8	+08 52 06	0.39	A7V
189319	19 58 45.3	+19 29 32	1.79	M0III
192909	20 15 28.1	+47 42 51	1.19	K3Ib+B3V
194093	20 22 13.5	+40 15 24	1.22	F8Ib
197345	20 41 25.8	+45 16 49	0.91	A2Iae
197989	20 46 12.5	+33 58 13	0.91	K0III
200905	21 04 55.7	+43 55 40	1.26	K4-5Ib-II
204867	21 31 33.3	-05 34 16	1.61	G0Ib
205730	21 36 02.2	+45 22 29	-1.41	M5IIae
210745	22 10 51.1	+58 12 05	0.97	K1.5b
213310	22 29 31.7	+47 42 25	1.65	MOII+B8V
216386	22 52 36.6	-07 34 47	0.92	M2.5IIIa
216956	22 57 38.9	-29 37 20	1.99	A3V
217906	23 03 46.3	+28 04 58	-0.64	MK2.5II-III
224935	00 01 57.5	-06 00 51	1.44	M3III

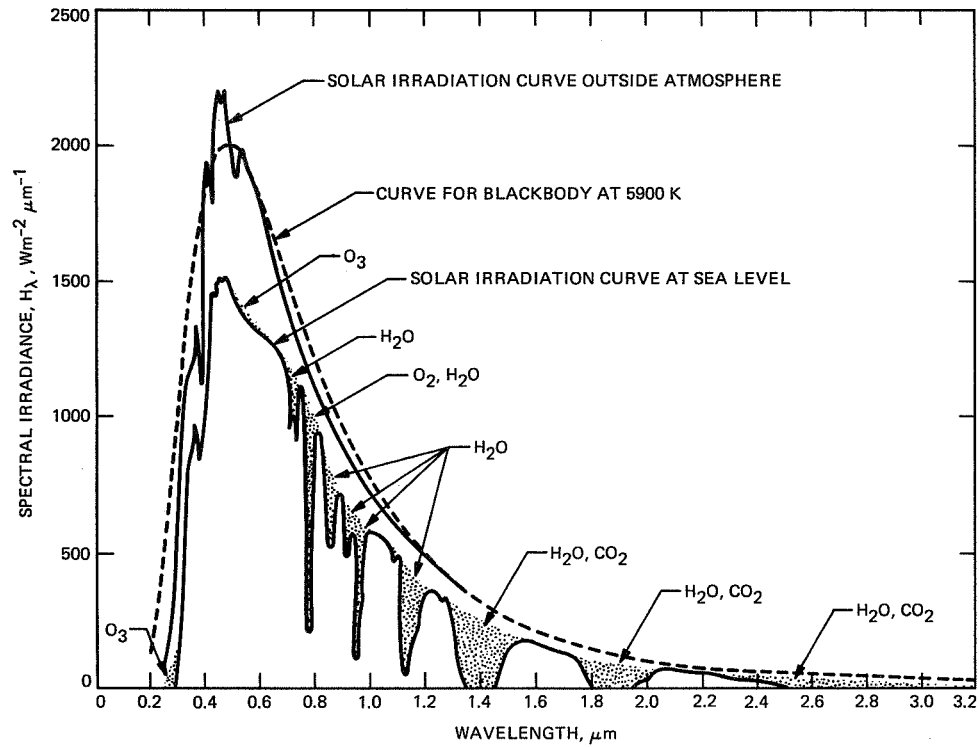


Fig. 1. Solar spectral irradiance with the sun at zenith. Absorption bands are shown shaded [6].

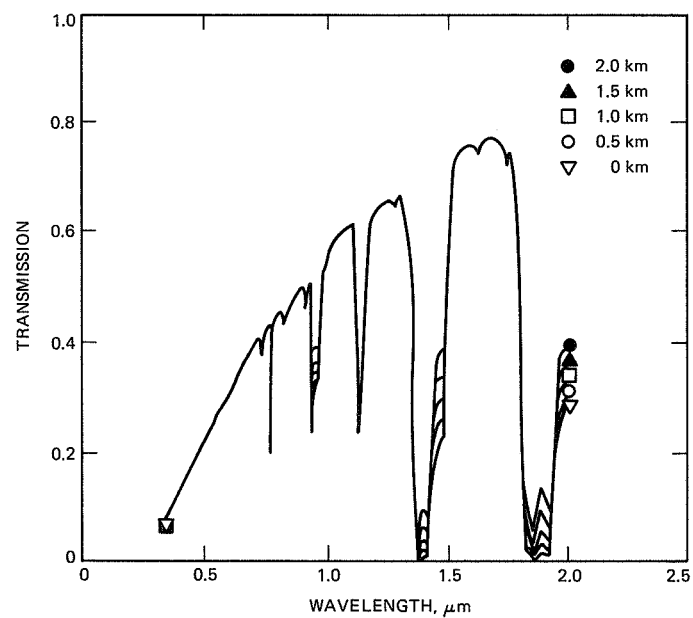


Fig. 2. LOWTRAN6 calculation of space-to-ground transmission as a function of wavelength in the presence of mid-latitude winter haze. The curves correspond to transmitter altitude [7].

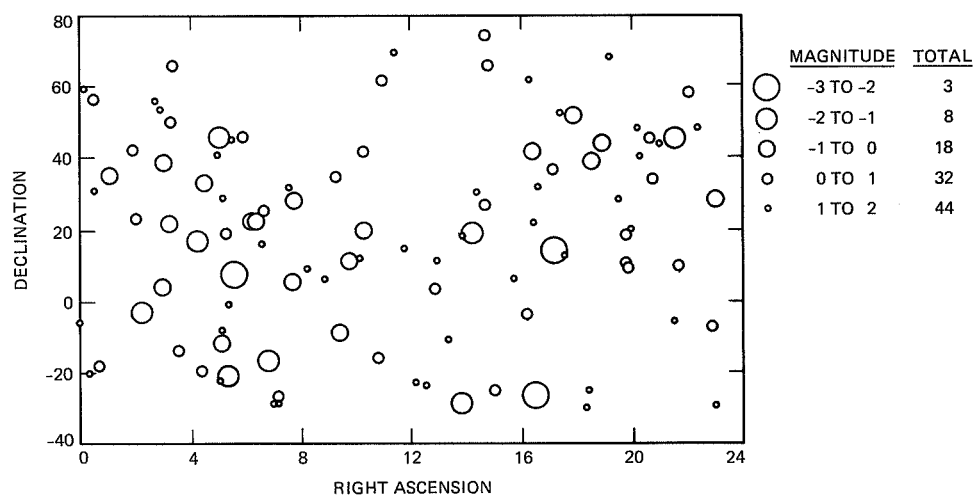


Fig. 3. Stars brighter than second magnitude at 1025 nm.

Site Selection Criteria for the Optical Atmospheric Visibility Monitoring Telescopes

K. Cowles

Communications Systems Research Section

A description of each of the criteria used to decide where to locate the Atmospheric Visibility Monitoring (AVM) telescope systems is given, along with a weighting factor for each of them. These criteria include low probability of clouds, fog, smog, haze, low scattering, low turbulence, availability of security and maintenance, and suitability of a site for a potential optical reception station. They will be used to determine which three of several sites under consideration will be used for monitoring visibility through the atmosphere as it applies to an optical ground-based receiving network as may be used in NASA space missions in decades to come.

I. Introduction

The Atmospheric Visibility Monitoring (AVM) program is designed to set up three optical telescope systems on mountains in the southwestern United States to observe atmospheric transmission at possible laser communication wavelengths and monitor cloud cover correlation between the three different locations. A goal is to find three sites which experience a low correlation of weather patterns such that at least one of the sites is clear at any given time. A previous study has determined that with three such sites there is a joint probability of visibility of 94 percent [1]. Since this project will only use three telescope systems, to attempt to determine the actual amount of time in which at least one site is operational it is crucial to carefully consider the characteristics of each candidate observatory site.

II. Criteria

The criteria being considered for selection of AVM telescope sites are low probability of clouds, fog, smog, and haze;

low particle scattering; low turbulence; availability of security and maintenance; and suitability of the site for a potential deep-space optical reception station. Also, the sites must exist in locations which exhibit low correlation of weather patterns. Each site being considered already has available roads, power, and telephone lines.

Each site will be rated on a 1-10 basis in each category. This rating will be multiplied by a weighted percentage (each weight based on the relative importance of that criteria to the project), and all the weighted ratings will be summed. Each site will then be judged based on this weighted comparison of conditions.

A. Low Probability of Cloud Cover, Fog, Smog, and Haze

Many factors go into the evaluation of the rating of each site for a particular characteristic. Sites are judged for their low probability of cloud cover, fog, smog, and haze based on

a history of annual percentage of sunshine, orographic effects, the height of the temperature inversion, and low correlation with other sites in question.

In [2] is a study of annual percentage of sunshine for the continental United States, however, it is unclear how exact the estimates are in some areas because the amounts of annual sunshine can differ by several hundred hours in a distance of fifty miles (see Fig. 1). A minimum number of sunshine hours has been set at 3,200 hours, and the corresponding areas are shown in the figure. The number of sunshine hours does not take into consideration orographic effects, i.e., clouds "clinging" to some mountains. These effects vary with the altitude of the mountain. Generally, mountains and ridges above 9,000 feet will exhibit more of this behavior, although if the peak is above 12,000 feet, it may rise above the cloud line, as is the case with Mauna Kea. Another consideration is the height of the temperature inversion in relation to the elevation of the observatory. Fog and smog tend to stay below the inversion, so if the site is a few hundred feet above the inversion layer it should not generally be affected. The fourth item considered is the low correlation of weather patterns with other possible sites. The sites have already been broken down into three different areas, but some areas in Arizona, California, New Mexico, and Texas suffer from the same weather patterns, possibly to a smaller degree. For example, northern Arizona falls prey to some of the winter storms from California as well as some of the summer storms that are known to attack southern Arizona. New Mexico experiences the same summer storms as southern Arizona, but sometimes there is a time delay between sites if the storm is not too large. Several such relationships exist.

Lack of cloud cover is the most important criterion because the basis of this study is to find clear skies in at least one of three places as often as possible. Some astronomical observers look for other characteristics which are also considered here, but they are usually trying to find the best "seeing," even if it only happens for a small fraction of the time. "Seeing" refers to image quality, which is enhanced when atmospheric turbulence is low. Since the goal here is counting photons, not imaging, clear skies are needed as often as possible and atmospheric turbulence is a lesser consideration.

B. Low Particle Scattering

Low scattering is important to atmospheric visibility because as many photons as possible need to be detected. Future missions may require detection of extremely weak signals, thus locating a receiving station away from areas exhibiting large amounts of aerosols and larger particles (i.e., sand blowing from a desert area) would be desirable. Aerosol content diminishes with elevation, improving visibility with higher

elevation. A shorter path through the atmosphere will decrease scattering making it possible to receive weaker signals since the amount of atmospheric attenuation will be lower. Vegetated areas tend to decrease the amount of dust by holding down the soil. Desert areas would cause problems with even the slightest wind. A small amount of wind is usually beneficial for turbulence effects, but larger amounts will cause scattering. Sites should therefore be located away from sources of aerosols and dust, and at elevations above 5,000 feet.

Scattering will be a larger problem during the daytime because signals will already be very weak compared to the background. Solar observatories are very concerned with scattering and daytime conditions, so choosing sites near solar observatories will prove beneficial for daytime studies.

C. Low Turbulence

Turbulence is caused by microthermal fluctuations in the atmosphere. It can cause effects such as scintillation, beam broadening, loss of spatial coherence, and phase distortions [3]. Astronomers characterize turbulence by rms image motion, a characteristic which has been measured at most of the observatories under consideration. Turbulence will degrade an optical communications signal by creating a larger blur circle at the receiver detector. Complete signal detection (capture) can still be accomplished in operational systems by opening up the detector field-of-view, although with an increase in system background noise susceptibility. Although cost considerations will not permit monitoring of the atmospheric turbulence at this time with the AVM project, published values of turbulence will be included in the site evaluation criteria. Because of its secondary impact on future possible operational systems, the turbulence criterion will be given a reduced weighting factor.

D. Availability of Security and Maintenance

The automated telescopes are designed to operate remotely, so there will be no operator present at the telescope to keep an eye on the equipment or to fix any problems that may arise. It is therefore important to locate the telescopes at a present observatory site, where someone familiar with the system could periodically check up on it for a small fee. If anything went wrong he or she could fix it, or at least make sure the roof was closed in inclement weather until JPL personnel could arrive and make repairs.

Some observatories are open to the public. People can walk around and look at the different telescopes and viewing galleries. In such a case a fence may have to be built around the telescope enclosure to make sure no one interferes with its operation or gets injured by a moving roof or telescope.

E. Suitability of a Site for a Potential Optical Reception Station

The results of the AVM research will provide knowledge of transmission, daytime conditions, and weather conditions at three different locations. If a ground-based optical receiver is developed in the future, it would be a great advantage to locate it at one of these sites providing the site proved to be favorable. Therefore, the feasibility of this potential future need is being taken into consideration. Any site under consideration for the AVM study should also be able to accommodate a larger transceiver station. The people who manage the land where the receiver would be located need to accept this idea and be willing to have a large facility operating there. Also, there needs to be enough space on the mountain to expand to a larger facility. Security and safety become an added issue for a large photon bucket and an earth-to-space laser system. Weighting for this criterion applies to how *well suited* a site would be for a potential station; however, for a site to be considered in the first place, it must be possible to locate a potential station at the site.

III. Rating

After consideration of all of the factors, it has been decided to weight the criteria in the following manner, as a percentage according to what is most important to the project:

	Percent
Low probability of cloud cover, fog, smog, haze	30
Low particle scattering	20
Suitability of the site for a potential optical reception station	20
Low turbulence	15
Availability of security and maintenance	15
	100

Each location will be rated on a 1 – 10 basis for each criterion. Then each criterion value will be multiplied by its corresponding percentage, and the weighted ratings will be summed. Site selection is a very inexact science, so the percentages and ratings chosen are loosely defined. However, they are the best estimates that can be given at this time. The benefits need to be weighted individually, while still producing a result which has some general meaning. Site selections for other telescopes have faced similar difficulties in determining what is important as the problem becomes more complex with logistical, financial, and technical factors [4].

These weighting factors are being used to rate sites which have not been already eliminated by other factors. Examples include Mt. Graham, where environmentalist opposition has limited new construction, or Kitt Peak, where there is no space to put another telescope.

Sites still under consideration include Mt. Hamilton, Table Mountain Observatory (TMO), Mt. Wilson, and Mt. Laguna in California; Mt. Hopkins, Mt. Lemmon, and the Hualapai Indian Reservation in Arizona; South Baldy and Sacramento Peak in New Mexico; and Mt. Locke in Texas. Data is presently being gathered which will allow the rating system to be applied to these sites.

IV. Conclusions

In weighting the criteria for the site selection, it has been determined that the most important factor is a low probability of cloud cover, fog, smog, and haze. If a site does not have clear skies to allow communications, none of the other factors matter. The criteria take into account the needs of the visibility monitoring telescopes as well as general considerations for a ground-based optical receiving station. A full list of criteria for a possible future optical transceiver is not known at this time, although a minimal set of criteria has been determined. These future needs are also given a fairly large weighting in the present criterion list.

References

- [1] K. Shaik, "A Preliminary Weather Model for Optical Communications Through the Atmosphere," *TDA Progress Report 42-95*, vol. July–September, Jet Propulsion Laboratory, Pasadena, California, pp. 212–218, November 15, 1988.
- [2] R. Lynds and J. Goad, "Observatory Site Reconnaissance," *Publications of the Astronomical Society of the Pacific*, vol. 96, pp. 750–766, September 1984.
- [3] K. Shaik, "Atmosphere Propagation Effects Relevant to Optical Communications," *TDA Progress Report 42-94*, vol. April–June, Jet Propulsion Laboratory, Pasadena, California, pp. 180–200, August 15, 1988.
- [4] N. J. Woolf, "Out of Site-Out of Mind, the Common Sense of Site Selection," in *Identification, Optimization and Protection of Optical Telescope Sites*, Flagstaff, Arizona: Lowell Observatory, p. 119, 1987.

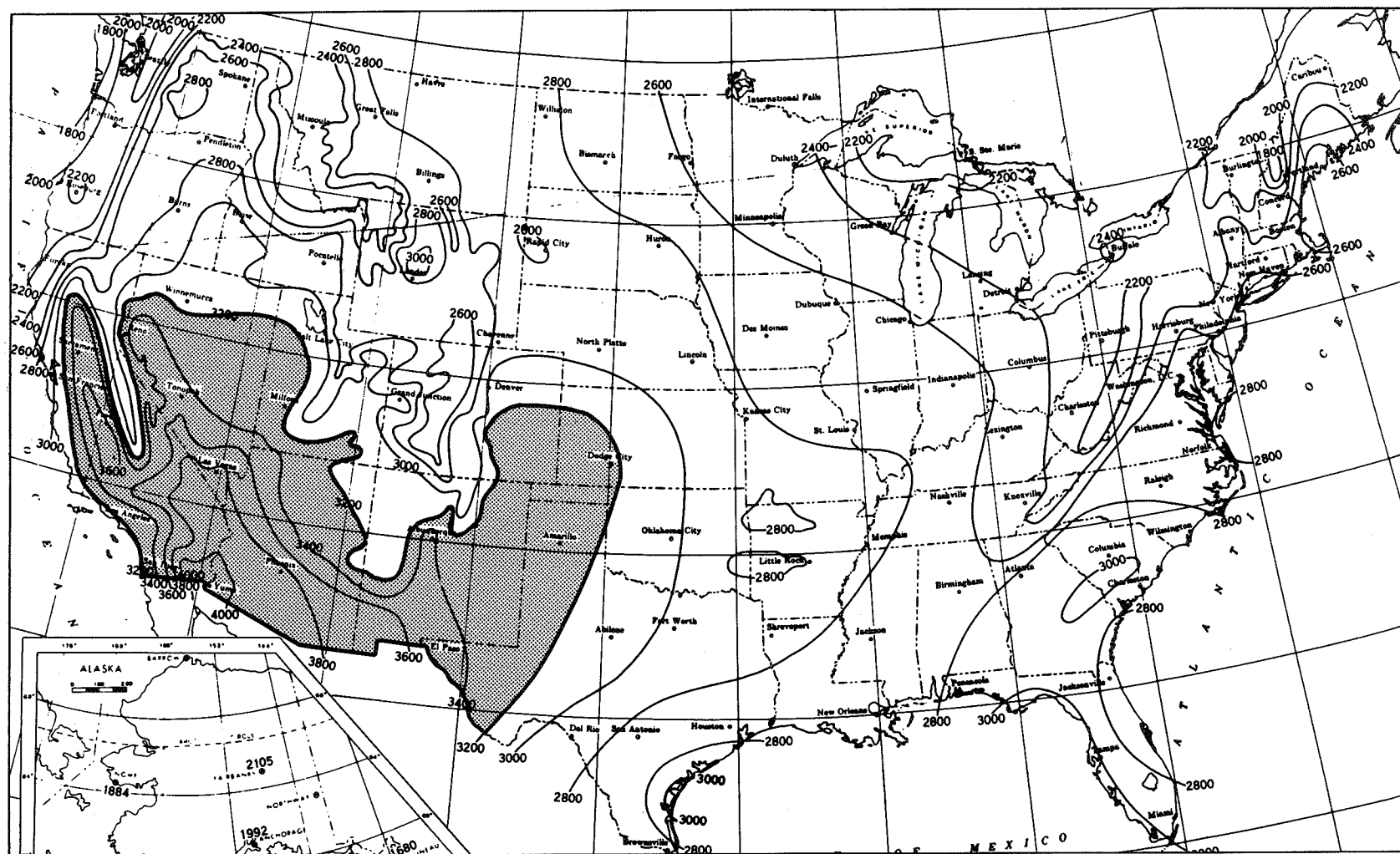


Fig. 1. Annual mean total hours of sunshine ≥ 3200 ; from [2].

A Novel Approach to a PPM-Modulated Frequency-Doubled Electro-Optic Cavity-Dumped Nd:YAG Laser

D. L. Robinson

Communications Systems Research Section

This article describes a technique which can provide frequency doubling, with high efficiency, while cavity dumping a laser for pulse position M-ary modulation while being used for an optical communication link. This approach uses a secondary cavity that provides feedback of the undoubled fundamental light, which is normally lost, into the primary cavity to be recirculated and frequency doubled. Specific operations of the electro-optic modulator and frequency-doubling crystal are described along with the overall modulation scheme and experimental setup.

I. Introduction

For deep space communication, optical frequencies provide many advantages over presently used technologies. Higher data rates, less power and mass consumption, and smaller beam divergence are some of the benefits provided by laser communications. Current link analyses incorporate either a ground-based station or an Earth-orbiting spacecraft to send to, and receive optical signals from, the mission spacecraft. Design considerations require the transmitter on the spacecraft to consist of a pulse position M -ary (PPM) modulated frequency-doubled Nd:YAG laser operating at $0.532 \mu\text{m}$. The anticipated range of communication rates for deep space is between 20 kbits/sec and 50 Mbits/sec (dependent on the range of the mission). If we assume $M = 256$, this corresponds to nominal laser repetition rates between 2.5 kHz and 6.3 MHz. To achieve these rates of modulation, Q-switching is utilized at the lower rates and cavity dumping is utilized for the higher rates. In this article, a unique design, which efficiently incorporates both cavity dumping and frequency doubling for deep space optical communication is described.

II. Technical Background

In laser Q-switching, lasing is held off by introducing loss into the resonator cavity while energy is pumped into and stored in the atomic population inversion. Once the desired inversion is attained, cavity losses are reduced to allow lasing. In this mode, it is possible to attain a single large pulse output from the laser. The frequency range of Q-switching extends up to 50-100 kHz [1], with no lower boundary. The upper repetition rate is limited by the finite time to repump the inversion in the gain medium of the laser. To extend the frequency further, cavity dumping must be used. In cavity dumping, energy is stored in the photon field instead of the atomic inversion. The photon field is generated between two mirrors of maximum reflectivity. To extract a pulse from the resonator, the beam is electro-optically or acousto-optically switched out of the main resonator. Repetition rates achievable with cavity dumping have been demonstrated between 125 kHz and 10 MHz [1]. The lower limit is reached when the photon field within the resonator is reduced to one photon after dumping the field. At this point, the beginning of the

buildup is dependent on the statistical variance of spontaneous emission. Hence, if the cavity is dumped of all its energy, cavity dumping becomes unstable [1]. If the cavity is not dumped of all its energy, for example by inducing an incomplete polarization flip with the electro-optic modulator, this lower limit can be extended. The upper limit of cavity dumping is limited by the switching time of the modulator. To extend pulse rates beyond 10 MHz, a mode-locked laser must be used.

Additionally, frequency doubling of the laser radiation is often desired for efficient detection at the receiver. The frequency-doubling conversion efficiency is a function of the intensity in the nonlinear doubling crystal. As the intensity increases, the conversion efficiency also increases. Therefore, to maximize efficiency, intra-cavity doubling is desirable because photon flux levels are much higher inside the laser resonator. Techniques for intra-cavity doubling of Q-switched lasers are well known. However, intra-cavity frequency doubling/cavity dumping is less desirable since placing a frequency-doubling crystal in the primary cavity would reduce the stored energy in the laser resonator. Once the energy is frequency doubled it can no longer stimulate emission in the gain medium and, therefore, will not experience gain in the laser resonator. On the other hand, in external frequency doubling the fundamental wavelength that is undoubled is lost, resulting in lower conversion efficiency. Therefore, a scheme has been conceived that efficiently frequency doubles while cavity dumping. The doubling crystal is placed outside the resonator and a third mirror is used to recycle the undoubled light back into the primary resonator. Since output beam losses are low in cavity dumping, switching light electro-optically or acousto-optically out of the primary cavity maintains a high-intensity beam, resulting in efficient frequency doubling. The third mirror, M_3 , placed at a right angle to the primary cavity and used in conjunction with a polarizing beam splitter (other angles with other types of polarizing prisms may be used), forms a secondary cavity with M_1 , which reflects the undoubled $1.06\text{-}\mu\text{m}$ light back into the primary cavity (see Fig. 1). Care must be taken to match the spatial modes of both resonators. The following section describes, in more detail, this technique for semi-intra-cavity doubling while cavity dumping.

III. Design Configuration

A unique design has been conceived to incorporate both cavity dumping and frequency doubling while reusing the undoubled light. This scheme incorporates an electro-optic modulator; however, the overall concept can be applied to cavity dumping with an acousto-optic modulator as well. Two schematics of the optical design are illustrated in Figs. 1(a) and (b). As is normal for cavity dumping, a photon field is built

up between two resonator mirrors, M_1 and M_2 . As seen in Figs. 1(a) and (b), a polarizing beam splitter (PBS) is inserted in the primary optical path to polarize the initial beam horizontally. When the appropriate field has been realized, a transverse electric field is applied to the electro-optic modulator (EO) to induce a quarter-wave phase retardation to the beam. A double pass through the electro-optic modulator creates a half-wave phase shift resulting in a 90-degree rotation of the polarization which is then reflected by the PBS. Upon reflection, the beam is directed through a frequency doubler (FD) and reflected by M_3 . By utilizing a type-I frequency doubler,¹ that portion of the beam that is doubled will be rotated 90 degrees, resulting in horizontally polarized light which will be transmitted through the polarizing beam splitter and coupled out of the resonator. If instead a type-II frequency doubler is utilized, the doubled portion of the beam is rotated only 45 degrees. Since part of this beam would be reflected back into the cavity, a dichroic beam splitter must be used to efficiently couple out the $0.532\text{-}\mu\text{m}$ portion of the beam. In either case, the undoubled light remains in the vertical polarization and is reflected back into the primary cavity. As long as an electric field is applied to the electro-optic modulator, this returned $1.06\text{-}\mu\text{m}$ light will be preserved and rotated back to the original horizontal polarization. When the desired output pulse width has been attained, typically 10–20 nsec, the electric field applied to the modulator is switched to zero allowing the photon field in the original cavity to build up once again to accommodate a second pulse.

IV. Experimental Setup

A standard 2-watt $1.06\text{-}\mu\text{m}$ laser was procured from General Photonics to provide the basic resonator cavity: pump cavity, Nd:YAG rod, mirror-mounting hardware, and overall structural support. Modifications to the basic laser design were necessary to obtain appropriate beam waists and mirror reflectivities within the laser cavity for frequency doubling and cavity dumping. Since the efficiency of frequency doubling increases proportionately with the optical intensity, a tightly focused beam within the doubling crystal is desirable. A second design limitation was the aperture size of the electro-optic modulator. To aid in the determination of the modifications, a computer program was written to analyze the spatial mode size within the laser resonator. Mirror curvatures were optimized until desired beam waists within the cavity were formed. In Fig. 2, a typical output from the optimizing pro-

¹Type-I frequency doubling converts two horizontally (or two vertically) polarized photons to one vertically (or one horizontally) polarized photon. Type-II frequency doubling converts one vertically and one horizontally polarized photon to one vertically (or horizontally) polarized photon.

gram is shown. The diameter of the spatial mode is plotted versus the length of the resonator cavity. Labels M_1 and M_2 designate the two mirrors of the primary laser resonator, while R and EO denote the rod and the electro-optic modulator, respectively. Between the rod and the front mirror, M_2 , a tight focus is formed. Likewise, when the modulator rotates the field's polarization causing the beam to be reflected by the PBS into the secondary cavity formed by M_3 , the beam will be tightly focused in the doubling crystal.

To maintain a low half-wave voltage on the electro-optic modulator, a LiNbO_3 or LiTaO_3 crystal is used. These crystals require lower half-wave voltages than traditionally used crystals like KDP. The KDP crystal requires half-wave voltages of approximately 3 kV and is hygroscopic. Both LiNbO_3 and LiTaO_3 are trigonal, 3m-symmetry, non-hydroscopic-class crystals that require half-wave voltages between 500 and 900 volts, resulting in power consumptions between 0.5 and 2.5 watts. Appendix A describes specific calculations and theory pertinent to electro-optic modulation with LiNbO_3 and LiTaO_3 crystals.

A crystal of KTiOPO_4 (KTP) will be used to frequency double the laser. KTP is a fairly new crystal which exhibits a very high frequency-doubling efficiency at $1.06 \mu\text{m}$. Furthermore, KTP is a non-hydroscopic crystal, has a high damage threshold, and is thermally stable with wide angular and thermal bandwidths when phase matched in a type-II con-

figuration. These physical properties make KTP one of the best available materials for frequency doubling [2]. Conversion efficiencies between 30 and 45 percent can be achieved with KTP. Specific calculations and relevant theory for frequency doubling with KTP are included in Appendix B.

Equipment for the above design has been ordered and received. However, failures of the commercially procured laser resulting from a design flaw in that unit have necessitated the return of the laser to the manufacturer. Upon receipt of the repaired laser, the dual-cavity design will be reassembled and tested.

V. Conclusion

In conclusion, a method has been described for efficiently frequency doubling while cavity dumping a solid-state laser. Using this technique provides a means for PPM modulating an optical communications link for deep space exploration at data rates between 1 Mbit/sec and 80 Mbit/sec (this assumes nominal laser repetition rates of 126 kHz — 10 MHz with $M = 256$). Lower data rates, up to approximately 500 kbits/sec, however, can be achieved by Q-switching the laser. The region between 500 kbits/sec and 1 Mbit/sec is considered an unstable region [3]; however, it is believed that by using some techniques as described above, either Q-switching or cavity dumping may be used to achieve these data rates for optical communication.

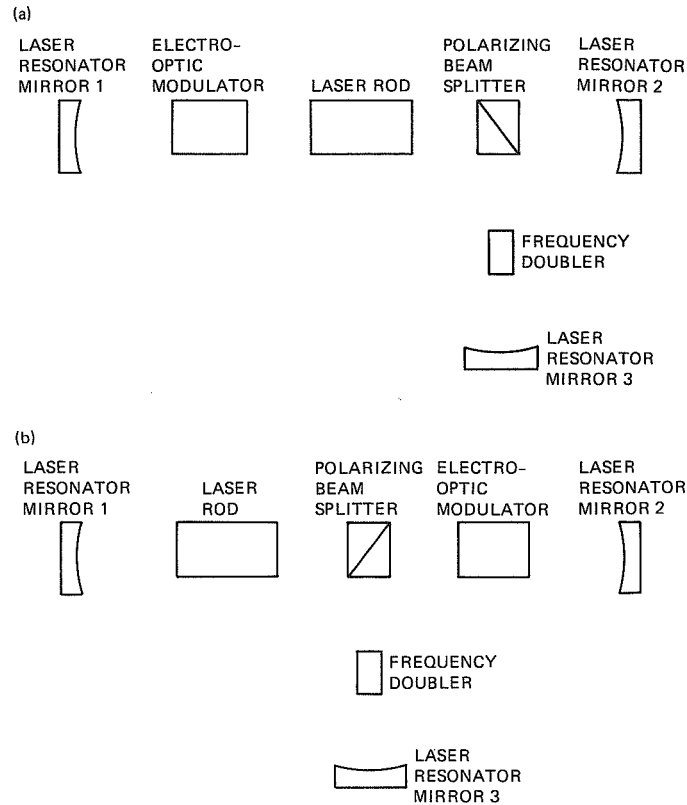


Fig. 1. Two overall optical schematics used for efficient frequency doubling while cavity dumping.

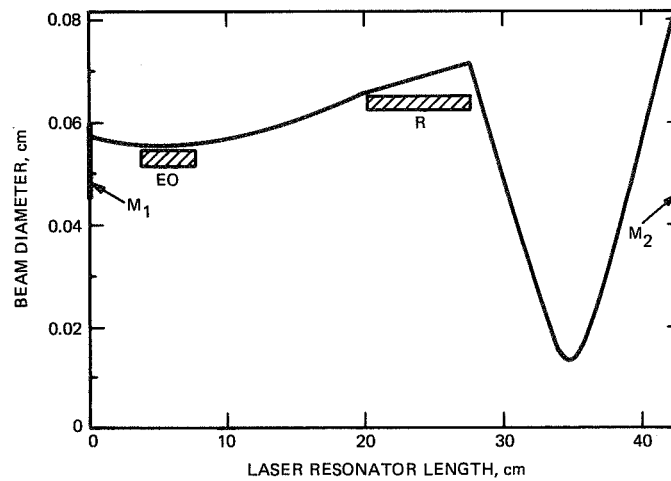


Fig. 2. A typical spatial spot size within the laser resonator where diameter of the beam is plotted as a function of the length of the laser cavity.

Appendix A

Electro-Optic Modulation with LiNbO₃ and LiTaO₃ Crystals

The following analysis describes electro-optic modulation using LiNbO₃ and LiTaO₃. Both LiNbO₃ and LiTaO₃ are trigonal, 3m-symmetry-class crystals. The electro-optic coefficients of a 3m crystal in tensor notation are of the form

$$\begin{pmatrix} 0 & -r_{22} & r_{13} \\ 0 & r_{22} & r_{13} \\ 0 & 0 & r_{33} \\ 0 & r_{51} & 0 \\ r_{51} & 0 & 0 \\ -r_{22} & 0 & 0 \end{pmatrix}$$

The specific values of the coefficients for LiTaO₃ and LiNbO₃ at 0.633 μm are as given for high-frequency operation [4]:

$$\text{LiNbO}_3 \begin{cases} r_{13} = 8.6 \times 10^{-12} \text{ m/V} \\ r_{22} = 3.4 \times 10^{-12} \text{ m/V} \\ r_{33} = 30.8 \times 10^{-12} \text{ m/V} \\ r_{51} = 28.0 \times 10^{-12} \text{ m/V} \end{cases}$$

$$\text{LiTaO}_3 \begin{cases} r_{13} = 7.5 \times 10^{-12} \text{ m/V} \\ r_{33} = 33.0 \times 10^{-12} \text{ m/V} \\ r_{22} = -1.0 \times 10^{-12} \text{ m/V} \\ r_{51} = 20.0 \times 10^{-12} \text{ m/V} \end{cases}$$

These values are dependent on the resonant frequencies of the crystal and will vary according to pulse rise time, crystal size, and frequency of operation. Given a specific crystal, these values must be calculated from the experimentally determined half-wave voltage. In the presence of an electric field $E(E_x, E_y, E_z)$ the equation of the index ellipsoid for the 3m crystal is as follows:

$$\begin{aligned} & \left(\frac{1}{n_o^2} - r_{22} E_y + r_{13} E_z \right) x^2 + \left(\frac{1}{n_o^2} + r_{22} E_y + r_{13} E_z \right) y^2 \\ & + \left(\frac{1}{n_e^2} + r_{33} E_z \right) z^2 + 2(-r_{22} E_x) xy + 2(r_{51} E_y) yz \\ & + 2(r_{51} E_x) zx = 1 \end{aligned} \quad (1)$$

where n_o denotes the ordinary and n_e denotes extraordinary indices of refraction.

Generally, in electro-optic modulation an electric field is only applied along one axis of the crystal, so this equation can be simplified to some extent. Since we are interested in transverse electro-optic modulation (as opposed to longitudinal electro-optic modulation) to rotate the polarization, we can eliminate cases where the axis of propagation is parallel to the electric field. Since highly efficient systems are needed for deep space optical communications, maximum phase retardation with the minimum amount of applied voltage is desirable. By applying an E field parallel to the z -axis, maximum phase retardation results with light propagating parallel to the x - or y -axis. Phase retardation for the case of x -axis propagation is given in Eq. (2) [5].

$$\Gamma = \left(\frac{\pi \ell_x V_z}{\lambda_o d_z} \right) (n_e^3 r_{33} - n_o^3 r_{13}) \text{ rad} \quad (2)$$

However, when used in this orientation, the indices of refraction are strongly dependent on temperature [6]. By applying an E -field parallel to the x - or y -axis, the temperature dependence can be eliminated for light propagating parallel to the z -axis. Phase retardation for this case of propagation, specifically for E_x , is given in Eq. (3). This is typically the orientation used with 3m crystals.

$$\Gamma = \frac{2\pi \ell_z V_x n_o^3 r_{22}}{\lambda_o d_x} \text{ rad} \quad (3)$$

In order to quantitatively compare Eqs. (2) and (3) for crystals of interest, we solve for the half-wave voltage and substitute appropriate electro-optic coefficients. The half-wave voltage is defined as the voltage required to induce a phase retardation of π . Half-wave voltages for LiNbO₃ and LiTaO₃

are summarized below for the indicated orientations. The length of the crystal is ℓ and d is the crystal thickness.

	V	(E field x or y) propagation z	V	(E field z) propagation x or y
LiNbO ₃	$\frac{d}{\ell}$	1.3×10^4	$\frac{d}{\ell}$	4706.5
LiTaO ₃	$\frac{d}{\ell}$	5.0×10^4	$\frac{d}{\ell}$	4005.9

When applying a field parallel to the x - or y -axis and propagating light parallel to the z -axis, LiNbO₃ is the preferred material to obtain lower required voltages. Even lower voltages can be obtained, however, by propagating in the x - or y -direction with an electric field parallel to the z -axis for both LiNbO₃ and LiTaO₃. In this crystal orientation the indices of refraction are more dependent on temperature, and thermally induced birefringence becomes a problem. This effect can be eliminated for uniform temperature variations across the crystal by utilizing two crystals with optic axes rotated 90 degrees. However, any temperature-induced gradient will be uncorrected by this technique. Since temperature gradients can result from nonuniformities in the laser beam or the applied electric field, the advantages of reduced required voltages are offset by thermally induced birefringence¹ Furthermore, it is difficult to obtain good optical quality LiTaO₃ with a high damage threshold appropriate for intra-cavity modulation. Further investigation is planned to quantitatively determine thermal birefringent effects since required voltages are less in the crystal orienta-

tion with the E -field applied parallel to the x - or y -axes. If thermal effects can be tolerated and good optical quality can be obtained, using LiTaO₃ would further reduce the half-wave voltage.

For a spacecraft optical communication link, the overall power consumption of the modulator is important. In order to calculate this, the modulator can be treated as a capacitor. The capacitance, C , may be written as

$$C = \bar{\epsilon} \epsilon_o \frac{A}{d}$$

where A = electrode area, d = modulator thickness, ϵ_o = the free space permittivity constant, 8.85 pf/m, $\bar{\epsilon}$ = the dielectric constant. For LiNbO₃, $\bar{\epsilon} = 78.2$. The resistance of the modulator is very small and can be neglected. However, the load resistance due to capacitance must be accounted for. Using well-known equations, the overall power consumption can be calculated

$$R_c = \frac{1}{(2\pi\omega C)} \quad P = \frac{V^2}{R_c}$$

For a LiNbO₃ modulator of dimensions $30 \times 2 \times 2$ mm ($\ell \times d \times d$), $C = 20.7$ pf. Using a pulse width of 20 nsec ($\omega = 50$ MHz), $R_c = 153.8$ ohms. For a quarter-wave voltage of $V = 433.3$ volts, peak power consumption is 1.2 kW. Assuming an average modulation rate of 100 kHz and a pulse width as given above, average power consumption is 2.4 watts.

¹T. Noricky, private communication, Engineering Manager, Inrad Corp.

²Ibid.

Appendix B

Frequency Doubling With KTP Crystals

The following analysis describes frequency doubling with KTiOPO_4 (KTP). KTP is a biaxial orthorhombic crystal of symmetry class mm2. The nonlinear optical tensor for the mm2 crystal is as follows:

$$\begin{pmatrix} 0 & 0 & 0 & d_{15} & 0 \\ 0 & 0 & 0 & d_{24} & 0 \\ d_{31} & d_{32} & d_{33} & 0 & 0 \end{pmatrix}$$

where

$$d_{15} = 5.40 \times 10^{-23} \text{ m/V}$$

$$d_{31} = 5.75 \times 10^{-23} \text{ m/V}$$

$$d_{32} = 4.43 \times 10^{-23} \text{ m/V}$$

$$d_{33} = 12.12 \times 10^{-23} \text{ m/V}$$

$$d_{24} = 6.73 \times 10^{-23} \text{ m/V}$$

for KTP (including ϵ_o) [2]. Multiplying this tensor by the E^2 column tensor leads to the following optical polarizations for KTP

$$P_x(2\omega) = 2d_{15}E_x(\omega)E_z(\omega)$$

$$P_y(2\omega) = 2d_{24}E_y(\omega)E_z(\omega)$$

$$P_z(2\omega) = d_{31}E_x^2(\omega) + d_{32}E_y^2(\omega) + d_{33}E_z^2(\omega)$$

By applying various axis rotations, these expressions can be simplified to an expression of the form

$$P = d_{\text{eff}} \mathcal{E}(\omega_1) \mathcal{E}(\omega_2)$$

where d_{eff} is an effective nonlinear coefficient obtained from the axis of rotation of the crystal and $\mathcal{E}(\omega_1)$ and $\mathcal{E}(\omega_2)$ are the electric fields applied at the respective frequencies.

Since KTP is a biaxial crystal, coordinate axis rotation is not a trivial problem and has been treated elsewhere [7]. Upon attaining the form of the above equation, Yao and Fahlen [7] have determined d_{eff} to be of the following form:

$$\begin{aligned} d_{\text{eff}} &\approx 0.974 d_{24} = 17.7 \times 10^{-9} \text{ e.s.u.} \\ &= 6.51 \times 10^{-23} \text{ m/V} \end{aligned}$$

(MKS, where ϵ_o is included in the coefficient)

There is some variance in the literature as to the experimental agreement with this value. Experimental values of d_{eff} range between $16.8 \times 10^{-23} \text{ m/V}$ [8] and $1.5 \times 10^{-23} \text{ m/V}$ [9]. These discrepancies from the theoretical d_{eff} values are most likely due to varying methods of crystal growth, material impurities, and phase matching techniques.

Knowing d_{eff} , the power conversion efficiency can be calculated with the following equation, assuming a depleted input source and complete phase matching [10, 11]

$$\eta = \frac{P(2\omega)}{P(\omega)} = \tanh^2 \left(\frac{1}{2} K A(0)z \right)$$

where

$$K = d_{\text{eff}} \sqrt{\frac{\mu_o \omega_1^2 \omega_2}{\epsilon_o n_1^2 n_2}} \quad \text{for } 2\omega_1 = \omega_2$$

and $A_1(0)$ can be derived from the following:

$$I = \frac{P}{A'} = \frac{1}{2} \sqrt{\frac{\epsilon_o}{\mu_o}} \omega |A|^2$$

where

$$A = \sqrt{\frac{n}{\omega}} E$$

and ω_1 , ω_2 , n_1 , and n_2 are the frequencies and indices of refraction at the fundamental and second harmonic, respectively. The length of the crystal is Z , I is the incident intensity, P is the incident power, and A' is the area of the incident beam.

Since the power conversion efficiency is directly proportional to the length of the crystal and the intensity within the crystal, trade-offs result. As the beam is focused tighter, the

beam diverges faster, resulting in less efficient frequency conversion at the entrance and exit faces of the crystal. The confocal parameter [10], z_o , gives guidance as to a reasonable crystal length

$$z_o = \pi \omega_o^2 \frac{n}{\lambda}$$

where ω_o = beam waist radius, n = index of refraction, and λ = the fundamental wavelength. As long as $\ell < 2 z_o$, accept-

able conversion efficiency occurs. Therefore, the beam radius must be greater than

$$\omega_o > \sqrt{\frac{\lambda \ell}{2\pi n}}$$

Staying within this criterion, frequency-doubling efficiencies between 30 and 45 percent can be achieved. See [11] for a more detailed analysis of frequency doubling.

References

- [1] W. Koechner, *Solid State Laser Engineering*, New York: Springer-Verlag, pp. 444–446, 1976.
- [2] Y. S. Liu, L. Drafall, D. Dentz, and R. Belt, "Nonlinear Optical Phase-Matching Properties of KTiOPO_4 ," *G.E. Technical Information Series Report*, 82CRD016, February 1982.
- [3] D. Maydan and R. B. Chesler, "Q-Switching and Cavity Dumping of Nd:YAG Lasers," *Journal of Applied Physics*, vol. 43, no. 3, pp. 1031–1034, March 1, 1971.
- [4] A. Yariv and P. Yeh, *Optical Waves in Crystals*, New York: Wiley, pp. 220–270, 1984.
- [5] P. V. Lenzo, E. G. Spencer, and K. Nassau, "Electro-Optic Coefficients in Single-Domain Ferroelectric Lithium Niobate," *Journal of the Optical Society of America*, vol. 56, no. 5, pp. 633–635, May 1966.
- [6] J. D. Zook, D. Chen, and G. N. Otto, "Temperature Dependence and Model of the Electro-Optic Effect in LiNbO_3 ," *Applied Physics Letters*, vol. 11, no. 5, pp. 159–161, September 1967.
- [7] J. Q. Yao and T. S. Fahlen, "Calculations of Optimum Phase Match Parameters for the Biaxial Crystal KTiOPO_4 ," *Journal of Applied Physics*, 55 (1), pp. 65–68, January 1, 1984.
- [8] Y. S. Liu, D. Dentz, and R. Belt, "High-Average-Power Intracavity Second-Harmonic Generation Using KTiOPO_4 in an Acousto-Optically Q-Switched Nd:YAG Laser Oscillator at 5 kHz," *Optics Letters*, vol. 9, no. 3, pp. 76–78, March 1984.
- [9] T. A. Driscoll, H. J. Hoffman, R. E. Stone, and P. E. Perkins, "Efficient Second-Harmonic Generation in KTP Crystals," *Journal of Optical Society of America B*, vol. 3, no. 5, pp. 683–686, May 1986.
- [10] A. Yariv, *Quantum Electronics*, New York: Wiley, pp. 421–436, 1976.
- [11] D. L. Robinson and R. L. Shelton, "Frequency Doubling Conversion Efficiencies for Deep Space Optical Communications," *TDA Progress Report 42-91*, Jet Propulsion Laboratory, Pasadena, Calif., pp. 112–123, July–September 1987.

527-33
218082

N 8 9 - 2 7 8 9 8

Microwave Time Delays for the X/S-Band Feed System at X-Band

J. Chen

Ground Antenna and Facilities Engineering Section

The X-band time delays for the X/S feed system of the 34-meter high efficiency antenna are required to refine current X-band downlink (8450 ± 50 MHz) calibrations and prepare for the Magellan uplink (7190 ± 45 MHz). The time delays of elements in the X-band feed system are obtained mostly via computer calculation and partly via measurement. The methods used and results obtained are presented in this article. There is good agreement with theory.

I. Introduction

The X/S feed is a large corrugated horn with extremely deep corrugations that are suitable for both the X-band and S-band (Fig. 1). In order to have the two very similar radiation patterns at X- and S-band, the feed operates in a "beamwidth saturation" mode at X-band. In other words, the beamwidth for this saturated condition depends only on the horn flare angle, and not on the aperture size. As a result, the pattern phase center is moved back into the throat of the horn, instead of its usual position near the horn aperture [1].

II. Time Delay for X/S Feedhorn

The X/S corrugated feedhorn, which is 74.397 inches long with an aperture size of 42.061 inches, is analyzed using a mode matching method [2]. In order to apply the circular waveguide computer program, the feedhorn is broken up into 230 circular waveguides with different radii. The program calculates the modes propagating from each discontinuity between

circular sections from the feed throat to the radiating aperture of the X/S feedhorn. Since the aperture is about 30 times the X-band wavelength, many modes are generated at the aperture surface. The radiation pattern of the X/S feedhorn at X-band is calculated using the amplitude and phase of the transmission coefficients for the aperture modes calculated by the circular waveguide program. The phase of the X-band radiation pattern at 0 degree from the center line of the horn changes as the X-band frequency changes. The time delay of the X/S feedhorn was obtained according to the following equation:

$$t_g = \frac{d\phi}{2\pi df}$$

where ϕ is the phase of the radiation pattern at 0 degree from the center line of the horn and f is the frequency.

The time delays of the X/S feedhorn from the throat to the aperture are 6.520 nsec at 8.45 GHz and 6.723 nsec at 7.19 GHz. The phase center is in the center of the X/S feed throat

and 67.5 inches behind the X/S feed aperture. By using the same method, the time delays from the feed throat to the phase center are found to be 0.769 nsec at 8.45 GHz and 0.869 nsec at 7.19 GHz.

III. Time Delay for Orthomode Junction and Quarter-wave Plate Polarizer

The time delays of the orthomode junction and the quarter-wave plate polarizer were measured with a Hewlett-Packard (HP) 8510 network analyzer. The orthomode junction is a three-way junction with one side connected to circular waveguide WC137, one straight path to rectangular waveguide WR125, and the other orthogonal path to WR125. The time delays of the orthomode junction are 0.947 nsec and 0.961 nsec at 8.45 GHz, and 1.253 nsec and 1.279 nsec at 7.19 GHz for the orthogonal path and straight path, respectively. A quarter-wave plate polarizer is a piece of WC137 waveguide with fins inside. The measured time delay of the quarter-wave plate is 0.457 nsec at 8.45 GHz and 0.525 nsec at 7.19 GHz.

The time delays of the rest of the elements are calculated using the group velocity of straight waveguides [3]. The H-plane bend waveguide and the E-plane bend waveguide, which are 3.5 inches by 3.5 inches by 90 degrees, are consid-

ered for this purpose to have an equivalent length (arc length) of 5.498 inches.

IV. Results

The time delays of all of the elements in the X/S feed system at X-band are shown in Table 1. The total time delays from the X/S feedhorn aperture to the ranging coupler are 10.689 nsec at 8.45 GHz and 11.567 nsec at 7.19 GHz. These values are adjusted for the distance to the phase center, which is 67.5 inches behind the feedhorn aperture. The total time delays from the phase center of the X/S feedhorn to the ranging coupler are 4.938 nsec at 8.45 GHz and 5.713 nsec at 7.19 GHz.

A simple experiment was made to measure the total time delay from the X/S feedhorn to the orthomode junction through the straight path using the time-domain feature of an HP 8510 network analyzer. A reflector was put in front of the feedhorn to obtain the round-trip time delay. The measured time delay was about 9.0 nsec at 8.4 GHz, which is close to the calculated value of 8.836 nsec at 8.45 GHz with an error of less than 1.8 percent. Although the experimental technique is not yet mature, good agreement with theory has been obtained in this case.

Acknowledgment

The author would like to acknowledge Phil Stanton for providing the round-trip time-delay experiment data.

References

- [1] W. F. Williams, "A Prototype DSN X/S-Band Feed: DSS 13 First Application Status," *DSN Progress Report 42-44*, vol. January and February 1978, Jet Propulsion Laboratory, Pasadena, California, pp. 98-103, April 15, 1978.
- [2] D. Hoppe, "Modal Analysis Applied to Circular, Rectangular, and Coaxial Waveguides," *TDA Progress Report 42-95*, vol. July-September 1988, Jet Propulsion Laboratory, Pasadena, California, pp. 89-96, November 15, 1988.
- [3] J. Chen, "Microwave Time Delays for the Dual L-C-Band Feed System," *TDA Progress Report 42-96*, vol. October-December 1988, Jet Propulsion Laboratory, Pasadena, California, pp. 126-131, February 15, 1989.

Table 1. Time delay of each element in the X/S feed system from feedhorn aperture (or the phase center) to the ranging coupler at 8.45 GHz and 7.19 GHz

Element	t_g , ns	
	Downlink, 8.45 GHz	Uplink, 7.19 GHz
Feedhorn (from aperture)	6.51977	6.72339
(from phase center)	0.76855	0.86898
Bethe hole coupler (4.500 in.)	0.47567	0.53591
Rotary joint (2.000 in.) \times 2	0.21141×2	0.23818×2
Quarter-wave plate polarizer	0.45661	0.52526
Orthomode junction	0.9475	1.25335
Spacer (0.280 in.)	0.02860	0.03145
H-plane bend (3.500 in. \times 3.500 in. \times 90 degrees)	0.56163	0.61760
E-plane bend (3.500 in. \times 3.500 in. \times 90 degrees)	0.56163	0.61760
54-dB ranging coupler (7.000 in.)	0.71510	0.78635
Total time delay		
(from aperture)	10.689	11.567
(from phase center)	4.938	5.713

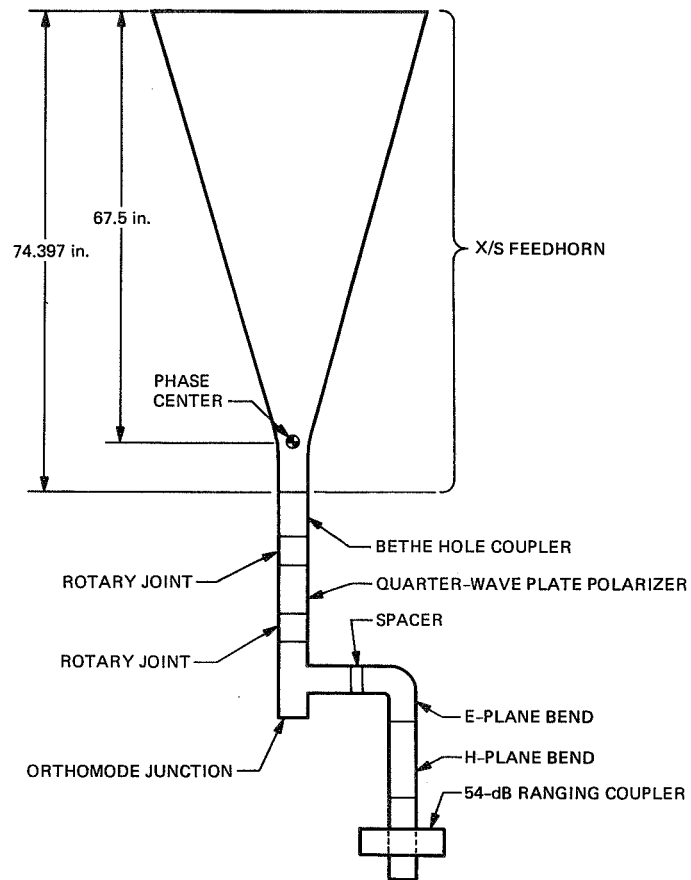


Fig. 1. X/S feed system of 34-meter high-efficiency antenna.

228-32
218083

N 8 9 - 2 7 8 9 9

DSN Radio Science System Design and Testing for Voyager-Neptune Encounter

N. C. Ham, T. A. Rebold, and J. F. Weese
Telecommunications Systems Section

The DSN Radio Science System presently implemented within the Deep Space Network was designed to meet stringent requirements imposed by the demands of the Voyager-Neptune encounter and future missions. This article elaborates on one of the initial parameters related to frequency stability. It describes the requirement, specification, design, and methodology for measuring this parameter. It also includes the description of special instrumentation that was developed for the test measurements and initial test data resulting from the system tests performed at Canberra, Australia and Usuda, Japan.

I. Introduction

The Voyager-Neptune encounter and new deep space missions have imposed very stringent requirements upon the Deep Space Communications Complex (DSCC) Radio Science System, and have prompted a new design to meet these demands. The design requirements apply not only to the basic system, but also to the test methodology and instrumentation necessary to test and verify the system's performance at the complexes. This article describes some of the parameters that were critical to the design, the design configuration, and the test methodology and instrumentation. Presented are results of initial measurements performed at the Canberra Deep Space Communications Complex (CDSCC) and the Deep Space Tracking Complex in Usuda, Japan. The Usuda facility consists of the associated 64-meter antenna, which will gather radio science data from the Voyager 2 spacecraft for post-encounter data correlation with the CDSCC 70-meter antenna. The CDSCC antenna receives S-/X-band data and Usuda receives data at S-band.

Short-term and long-term frequency stability are two of the critical parameters that demanded extra attention. The long-term stability is important to enhance the correlation efficiency of the received data from the separate facilities as one factor and for spacecraft orbit tracking measurements as another. The short-term or phase-noise spectral density characteristics of the receiving system are important to permit the reception of the spacecraft's radio-frequency carrier signal which contains basic scientific information after occulting the medium. This phase-noise parameter is related to the Radio Science System's inherent reference frequency source and the complementary active circuit elements which process and utilize this signal.

It is important that the received carrier signal which contains radio science data in the form of its amplitude, phase, and frequency perturbations not be contaminated, degraded, or masked by the receiving and data acquisition system. Analysis of the carrier used by some of the spacecraft radio science

experiments utilizes the perturbation of the dual radio frequency (RF) signals (S-/X-band) traveling between the spacecraft and the ground tracking antennas to study the aspects of the planetary system visited, as well as other nonplanetary phenomena of interest.

Spacecraft radio science comprises two broad categories of investigation:

1. Occultation measurements of the radio signal as it passes through and probes the media of interest (planetary atmosphere, ionosphere, and rings) while the spacecraft is on the far side of the planet.
2. Tracking measurements wherein the perturbations of the spacecraft orbit are analyzed for information on gravity or other effects [1].

A stabilized frequency reference source on board Voyager 2, called an ultra-stabilized oscillator (USO), is used for generating the dual S- and X-band RF signals and achieves its maximum stability over time intervals of 1 to 600 seconds. This permits the use of a one-way downlink mode of transmission and reduces any discontinuity in the transmitted signal versus time. It is apparent that the ground radio science receiving and data acquisition system must possess greater stability than the USO, both in the short and long term, to maintain suitable accuracy in the radio science measurements. The use of hydrogen-maser frequency standards in the ground systems provides long-term frequency stability; however, careful design and special emphasis are required to maintain this long-term capability and to ensure good short-term stability as well.

The short-term stability can also be defined in the frequency domain as the phase-noise spectral density distribution (or spectrum) about the carrier signal. The Voyager 2 USO possesses good phase-noise spectral density for frequencies offset from the carrier 1 Hz to 10,000 Hz. These good characteristics aided the collection of Saturn ring data [1].

As a result of differential frequency shifts from different parts of the rings, ring occultation signals arrive at the Earth receivers with a frequency spectrum which is broadened by this interaction. Figure 1(a) shows the relative positions and motion of the spacecraft, planetary ring, and Earth, with the resulting spectrum of the received signal. The geometry of ring occultation is shown, with the signal on a direct and indirect path to Earth. Figure 1(b) displays the power spectrum of the received X-band signal when Voyager 1 was behind the mid-point of Saturn's Ring A. Primary features of this spectrum are the well-defined spectral line at the free-space frequency, corresponding to the direct spacecraft-to-Earth ray path, the broad irregular distribution of energy over a range of frequencies, corresponding to scattered waves, and the noise floor [1].

II. Ground System Design Requirements

The noise-power spectral density characteristics of the Earth receiving and data acquisition system should be considerably better than the spacecraft signal, so that the system's contributing noise floor does not mask the spectrum of the received signal during the process of frequency downconverting the carrier to a low-frequency video-band signal for digitization and data acquisition by tape recording.

Similarly, the long-term frequency stability should be adequate to maintain accuracy in the radio science measurements. The Voyager-Neptune encounter requirement for this is specified in terms of the square root of the Allan variance as 6×10^{-13} for 1-second integration time (τ) reducing to 3×10^{-13} as a function of $1/\tau$ at 10 seconds and remaining at this value out to 1000 seconds.

The ground receivers produce two basic noise sources which compete against the received spacecraft signal. One is the thermal noise source and the other is the previously discussed phase noise. The thermal noise is due mainly to the RF-input low-noise amplifier (LNA) with additional contributions by the antenna microwave losses and atmospheric elements. The phase noise is contributed largely by the receiver's first local oscillator (LO), which is derived from the hydrogen-maser frequency standard of the frequency and timing subsystem (FTS).

Figure 2 is a model of the spacecraft signal and the noise sources and illustrates the manner in which the spacecraft signal-to-noise ratio (SNR) is degraded before the final data acquisition process by the radio science receiving system.

The spacecraft transmits a carrier signal, P_c , with an inherent short-term stability phase noise, $\sigma_{\phi_{sc}}$. The term widely used for describing and quantifying this parameter is the phase-noise spectral density as a function of the sideband frequencies offset from the carrier $\mathcal{L}(f_m)$ in the frequency domain. Its magnitude is expressed as the single-sideband (SSB) phase-noise power density divided by the carrier power in dBc/Hz, or

$$\mathcal{L}(f_m) = \frac{\text{Power Density (SSB)}}{P_c} \quad (\text{dBc/Hz})$$

where f_m is the offset frequency away from the carrier.

This is an indirect measure of the noise energy easily related to the RF power spectrum on a spectrum analyzer. $\mathcal{L}(f_m)$ is defined as the ratio of the power in one phase-modulation sideband on a per-hertz basis to the total signal power. Phase noise can also be viewed as a continuous spectrum of infinitely

close phase-modulation sidebands and can be derived from the spectral density of phase fluctuations using phase modulation theory.

As shown in Fig. 2, the carrier power is reduced by the space loss to the ground receiver; however, the inherent phase-noise density to carrier power ratio remains the same as it appeared at the spacecraft's transmitter output except for perturbations created by the media intervening between the spacecraft and the receiver. The resultant carrier power thermal SNR referenced to the receiver input is related to this resultant carrier power and the thermal-noise spectral density N_o of the receiving system, or

$$\text{SNR}_T = \frac{P'_c}{N_o}$$

This thermal-noise spectral density in first-order terms is related to the receiver elements by the expression

$$N_o = kT_{op} = k \left[T_{\text{LNA}} + \frac{T_{\text{MIXER}}}{\text{POWER GAIN}_{\text{LNA}}} \right]$$

ignoring antenna microwave noise/losses and follow-on receiver noise contributors appearing as additive noise. However, the phase-noise contribution to the received signal by the receiver is a multiplicative effect. Since the phase noise was considered to be random phase fluctuation modulation, the spacecraft signal can be expressed as

$$A_c \sin [\omega_c t + \Delta\phi_c(t)]$$

where $\Delta\phi_c(t)$ represents random phase fluctuations. Similarly, the receiver first LO signal can be expressed as

$$V_{\text{LO1}}(t) = A_{\text{LO}} \sin [\omega_{\text{LO1}} t + \Delta\phi_{\text{LO1}}(t)] \quad (1)$$

with $\Delta\phi_{\text{LO1}}(t)$ representing random phase fluctuations of the receiver LO.

These signals are multiplied at the receiver first mixer to produce the first intermediate frequency (IF):

$$V_{\text{IF}}(t) = A_{\text{IF}} \cos [\omega_{\text{IF}} t + \Delta\phi_c(t) + \Delta\phi_{\text{LO1}}(t)] \quad (2)$$

where the phase fluctuations are assumed Gaussian and are independent.

Equation (1) shows that the phase fluctuation modulation of the first LO signal creates sideband variance in proportion to its magnitude A_{LO1} . When multiplied to the car-

rier signal, as shown by Eq. (2), the resultant IF magnitude $A_{\text{IF}} = A_c A_{\text{LO1}}/2$ to sideband variance ratio will be in the same relative ratio as the LO signal to its sideband variance. The overall resultant ratio, however, will be the root-sum-square (RSS) of the carrier and LO sideband variances. Stated another way this means that the receiver phase-noise spectral-density $\mathcal{L}(f_m)$ value contributed by the first LO is transferred to the resultant IF signal in the same ratio independent of the carrier magnitude A_c and the resultant IF signal phase noise is the RSS of the spacecraft carrier and first LO variances. Analogous to an amplitude SNR, the phase-noise spectral density SNR of the output signal can be expressed as

$$\sigma_{\text{SNR(PHASE)}} = \frac{\frac{\sigma_{\phi_{sc}}^2}{P_c}}{\frac{\sigma_{\phi_{RS}}^2}{P_{\text{LO}}}} = \frac{\mathcal{L}_{sc}(f_m)}{\mathcal{L}_{RS}(f_m)}$$

and ideally then

$$\mathcal{L}_{RS}(f_m) \ll \mathcal{L}_{sc}(f_m)$$

Other important continuous noise and unwanted line-spectral signal effects due to the local oscillator are the random amplitude fluctuations and line-spectral interference (or spurious sideband signals). Extending Eq. (1), the instantaneous output voltages of the first LO signal can be written as

$$V_{\text{LO1}}(t) = [A_{\text{LO1}} + \delta\epsilon(t)] \sin [\omega_{\text{LO1}} t + \Delta\phi_{\text{LO1}}(t)]$$

where $\delta\epsilon(t)$ is the instantaneous amplitude fluctuation of the signal. The spectral density $S_{\delta\epsilon}(f)$ of the signal amplitude fluctuations follows the same derivation as the spectral density of phase fluctuations. The amplitude modulation (AM) noise components are typically much less than the phase-noise components; however, it is important that the AM noise be measured or verified to ensure that it is not a major contributor. The amplitude-noise modulation is in phase to LO signal phase while the phase-noise modulation is in quadrature phase to the LO signal phase.

The unwanted line-spectra sideband signals are more deterministic compared to the continuous random noise fluctuations. These are commonly defined as spurious frequencies and will also appear as both amplitude and phase-modulation sidebands. These line-spectra spurious frequencies can generally be identified, but it is difficult to locate their source. They are largely related to power-line frequency and are intermodulation products of the various mixers and frequency-multiplier circuits.

If the spurious sideband signals are at the power-line frequency fundamental they are probably intruded into the receiving system by magnetic coupling via a power transformer to unshielded components and by electrostatic-type coupling, and also via ground-loop currents due to improper grounding of sensitive and weak signal paths.

If the spurious signals appear as harmonics of the power-line frequencies, they can be traced to the DC power supply if they are of the straightforward line-frequency rectification and filtering type.

As opposed to the RSS combination of the random noise fluctuations, these line-spectra spurious sidebands combine directly in all of the various possible LO paths and appear at the final video-frequency output terminal as the aggregate net summation of their amplitude and phases. It is obvious that every LO signal path could potentially be the carrier of these spurious sideband signals; however, since the first LO chain possesses the highest frequency-multiplication factor, this is the first suspected path of spurious frequency intrusion.

For example, the reference signal for the first LO chain which contains spurious frequency intrusion creates an equivalent phase modulation which can be expressed as

$$V_{\text{LO_REF}}(t) = A_{\text{LO_REF}} \sin \left[\omega_{\text{LO_REF}} t + m_p \sin \omega_{\text{SPUR}} t \right] \quad (3)$$

where $\omega_{\text{LO_REF}} t$ is the reference input signal to the first LO chain, $\omega_{\text{SPUR}} t$ is the spurious modulating signal, and m_p is the equivalent modulation index of the spurious intrusion. Expanding Eq. (3) and expressing in terms of the Bessel functions, it can be shown that the spectrum consists of the LO signal acting as the carrier plus sidebands related to the sum and differences of the spurious signal to the LO carrier, whose amplitudes are various-order Bessel functions of m_p . As this phase-modulated wave is frequency multiplied to a higher frequency (to the desired first LO injection frequency), the effect is to increase the modulation index by a factor equal to the frequency-multiplication value. If the first-order sideband spurious signal has a specific value of $\mathcal{L}(f_m)$ dBc/Hz, its value after multiplication will change by the factor $20 \log N$. For example, if the reference signal contains a spurious signal of -90 dBc/Hz and is frequency multiplied by $\times 81$, then the resultant first-order sideband spurious value at the multiplier output is degraded by 38 dB or to a value of $\mathcal{L}(f_m)_{\times 81} = -52$ dBc/Hz due to the frequency multiplication only. The frequency-multiplier circuits themselves can also develop spurious signal intrusion which would modify the output value

depending upon the effective m_p and the relative phase of the spurious signals.

This is similarly applicable to the random or continuous spectrum modulation signal (phase noise) in that the $\mathcal{L}(f_m)$ value is degraded proportional to the multiplication factor N .

Thus, Eq. (3) can be written with a multiplication factor N as

$$V_{\text{LO_REF}}(t) = A_{\text{LO_REF}} \sin N \left[\omega_{\text{LO}_1} t + m_p \sin \omega_{\text{SPUR}} t \right]$$

and the effective modulation index is increased by Nm_p resulting in an increased sideband amplitude proportional to N at the multiplied output frequency $\sin \omega_{\text{LO}_1} t$.

The system specification for the Voyager-Neptune encounter phase-noise spectral density and spurious signal magnitude is -53 dBc/Hz at $f_m = 1$ Hz and -60 dBc/Hz at 10 Hz continuous from 1 Hz to 10 kHz for the X-band channels, and -45 dBc/Hz at $f_m = 1$ Hz continuous to 10 kHz for the S-band channels. The lower value specifications of -60 and -45 dBc/Hz were limited by the expected received spacecraft carrier power to thermal-noise SNR for the respective channels.

III. System Design and Configuration

This section describes the implemented Radio Science Systems for the DSCC and Usuda, Japan configurations in support of the Voyager-Neptune encounter.

A. Deep Space Communications Complex Configuration

Figure 3 is the block diagram of the Radio Science System configuration for DSCC-10, DSCC-40, and DSCC-60. The system has the capability to receive simultaneously S- and X-band frequencies from a spacecraft at the normal DSN RF-assigned channels at the $11/3$ S-/X-band frequency ratio, or either channel individually from a 70-meter antenna. Similarly, right circular polarization (RCP) and left circular polarization (LCP) of RF or individual channels can be received simultaneously. Not shown in the diagram is the capability to receive simultaneously a single X-band and a single S-band RF channel from the 34-meter High-Efficiency Antenna at each DSCC by switching the IF signal into the RF-IF converter via the IF distribution and gain-normalizer assembly shown in the diagram.

The output of the 70-meter antenna S-/X-band polarizers feeds two RF X-band and two S-band LNAs comprising traveling-wave masers (TWMs), which in turn drive the RF-IF converters of the Radio Science System. This converter assembly converts the RF signal to the IF by the first LO frequencies

of 8100 and 2000 MHz. This X-band first LO signal path with the $\times 81$ and $\times 5$ frequency multiplication from the phase calibration generator (PCG) 20-MHz output signal and the PCG reference signal from the FTS hydrogen-maser primary frequency standard are critical in meeting the previously mentioned frequency-stability parameter requirement.

The PCG is a phase-conjugation circuitry which stabilizes the phase characteristics of the long transmission line from the FTS to the antenna and essentially transfers the long-term frequency stability of the hydrogen maser to the antenna cone area. The normal function of the PCG circuitry is to provide a comb of very stable frequencies at the input to the TWMs for very-long-baseline interferometry (VLBI) phase calibration [2]. Thus it can provide a stable reference to the first LO multiplier chain to meet the long-term frequency stability requirements. The $\times 5$, which was to provide the 100-MHz reference to the LO frequency multipliers, was not available for the initial installation; thus, the 100-MHz signal was obtained via a long coaxial cable from the FTS for the initial frequency stability measurements. The long-term frequency-stability measurement using Allan variance methodology resulted in the system meeting the requirements for the Voyager-Neptune encounter; therefore, this will be the configuration at the DSCC. For the Galileo mission, which requires a greater frequency stability, the reference from the PCG or another circuitry concept may be used.

To meet the phase-noise spectral density requirements, the 100-MHz input signal to the above coaxial cable was obtained via a 5-MHz phase-locked loop (PLL) located in the FTS. This phase-locked clean-up loop (CUL) contains a very narrow loop bandwidth which improves the phase-noise spectral density at low offset frequencies of the hydrogen-maser output.

The IF signals from the antenna are sent to the Signal Processing Center (SPC) via long coaxial cable transmission lines, buried between the antenna and the SPC and terminated into the IF distribution assembly, which direct the IF signals to the proper IF channels of the radio science IF-VF (RIV) converter or to the VLBI System, which is not shown in Fig. 3. The RF LNA and RF-IF converters are also used for the VLBI system.

The buried IF cables from the antennas and the SPC vary in length due to the physical locations of the antennas from the SPC, which are not standard for the various DSCCs; consequently, the attenuation of the IF signals from the RF-IF converters to the IF distribution and gain-normalizer assembly are of different values around the network. The gain-normalizer function was inserted at this point so that the resultant IF signal amplitude is the same value for all complexes regardless of

the antenna signal origin. This standardized the design and the gain profile of the RIV for all the complexes.

The output IF signal from the gain-normalizer assembly is sent to the RIV which heterodynes it to another IF, and finally to an IF of 10 MHz where band-pass filters (BPFs) narrow the bandwidth to the desired value prior to the final downconversion to video-band frequency (VF) for digitization and magnetic tape recording. The heterodyning of the second IF to the RIV is accomplished via a programmable local oscillator (PLO) whose output frequency is programmed by the DSCC processor assembly (DPA) through the programmed oscillator control assembly (POCA). The PLO follows a predicted spacecraft Doppler frequency versus time profile to maintain the received carrier frequency centered within the BPF bandwidth. The PLO is an existing assembly within the DSN with phase-noise spectral density and long-term frequency stability characteristics which meet the error-budget allocation in this function and alleviate the burden to the first LO in meeting the overall system requirement. The PLO was modified to meet the spurious-frequency requirements which were largely related to power-line frequency. The frequency-multiplication and bias-frequency mixers for the PLO normalize the final IF to correspond to the input-RF 11/3 ratio.

Each RIV IF channel contains a set of BPFs which can be selected to meet the particular mission requirements. Four are located at the 10-MHz IF with nominal bandwidths from 2000 to 45,000 Hz, and there are two very narrow-bandwidth BPFs in a 100-kHz IF presently at 82 and 415 Hz. Only one filter can be selected for operation at a time in any of the IF channels, in either a single or paired operational mode. These filters are easily removed and replaced if a mission requires different bandwidths than those initially inserted. The band-pass filtered signal is finally downconverted to a video-band frequency (VF) and sent to the DSCC spectrum processor (DSP) for digitization and tape recording. Each IF channel contains an isolated VF output-signal port available for monitoring or testing.

The DSP utilizes a 24-MHz quartz-crystal PLL for converting an FTS 10-MHz reference signal to the desired analog-to-digital converter (ADC) sampling signals that digitize the VF input signals. The digitized signals are then formatted, multiplexed, etc., and recorded on magnetic tape for the final data acquisition. Any digitized signal that enters the DPA can be converted back to an analog form via a digital-to-analog converter (DAC) which is used for monitoring purposes by the spectral signal indicator (SSI). Similarly, the SSI can output a signal that can be transmitted back to JPL for remote monitoring of the received VF signal. The DAC also provides a 12-parallel data-plus-clock output interface jack for connection to

the digital stability analyzer test instrumentation, which is used at the complex for measuring the total Radio Science System phase-stability performance characteristics.

B. Usuda Configuration

The radio science equipment configured at the Usuda Deep Space Center in Usuda, Japan is the result of a combined effort between JPL and the Japanese Institute of Space and Astronautical Sciences (ISAS). Originally developed to support the Japanese Planet-A spacecraft launched toward Halley's Comet, the Usuda Deep Space Center operates a 64-meter Cassegrainian antenna with a beam waveguide feed. In addition to the antenna, ISAS is also providing the RF-IF converter, the primary data acquisition subsystem (DAS), and the hydrogen-maser frequency standard. JPL is providing the TWM, the Global Positioning Satellite (GPS) receiver, a secondary DAS, and several FTS assemblies.

A block diagram of the Usuda Radio Science System is shown in Fig. 4. Unlike the DSCC implementation, the Usuda system is capable of receiving S-band signals only, although ISAS is planning to upgrade to X-band. Also, the receiver does not decompose the signal into its RCP and LCP components. It is strictly a single-channel system.

The antenna beam waveguide feeds into the JPL TWM which is the primary LNA. Not shown in the figure is the ISAS-provided parametric amplifier (paramp), which is to be used as a backup to the TWM. The system noise temperature using the JPL TWM is about 16.5 kelvins, while the corresponding temperature using the paramp is about 30 kelvins.

The output of the TWM is sent to the ISAS RF-IF converter, which translates the RF center frequency of 2295 MHz down to the IF center frequency of 70 MHz. The RF-IF converter works in two steps, mixing the signal with a first LO of 1880 MHz, then with a second LO of 485 MHz. Since the second LO is higher than the corresponding IF, the polarity of the 70-MHz IF spectrum is inverted with respect to the RF input spectrum.

Following the RF-IF downconversion, the 70-MHz output is sent from the antenna building over a frequency-stable fiber-optic link to the control-room building. Once inside the building the IF signal is filtered to a bandwidth of 7.5 MHz, amplified, and distributed to the two data acquisition subsystems—one supplied by JPL, the other by ISAS.

1. JPL Data Acquisition Subsystem. The JPL DAS consists of a RIV and a Mark III occultation data assembly (ODA) that digitizes the video signal, tape records the signal, and controls the LO frequency. The ODA is made up of a Mark III narrow-band occultation converter (NBOC), a Modcomp II

computer with an IBM PS/2 computer to provide terminal input, and two Wanco tape drives for recording and storing digitized data. For frequency tuning purposes, the Modcomp II computer accepts and stores 14 point-predict sets entered through the PS/2.

The 70-MHz IF signal enters the JPL RIV, is sent through a 0- to 60-dB variable attenuator (referred to as the RIV attenuator), is then further amplified by 20 dB, and down-converted to the video band of 0 to 40 kHz by a single side-band converter. The local oscillator used is tunable by the ODA computer so that the received spacecraft carrier containing Doppler shift can be kept within the 35-kHz video-frequency filtered bandwidth. The LO mixer injection frequency is derived by frequency multiplying the output of the computer-controlled Dana frequency synthesizer by $\times 4$ and then mixing it down with a fixed-frequency 100-MHz signal derived from FTS. This scheme translates the Dana output frequency range of 42 to 43 MHz to cover the desired LO range of 68 to 71 MHz. The tuning capability is provided by the POCA, which takes frequency and ramp-rate commands from the Modcomp II computer and controls and monitors the Dana synthesizer accordingly. In this IF-VF downconversion the local oscillator is again higher in frequency than the IF signal so that the spectrum is inverted once more. Therefore, the spectrum of the video signal, which is recorded onto magnetic tape, is non-inverted with respect to the input RF signal.

At the video level, the signal is further amplified, low-pass filtered to a resultant bandwidth of 35 kHz, and then digitized by the NBOC. The video signal can be monitored on a spectrum analyzer at a point just prior to its digitization. Also, a RMS voltmeter is included to measure the level of the signal going into the ADCs in the NBOC. During system pre-calibrations, the RIV attenuator is adjusted to achieve a video level of about 1 volt RMS in order to avoid saturating the ADCs.

The NBOC digitizes the video signal and sends the data to the Modcomp II computer. It contains four ADCs which are configured to sample the same input signal one at a time each with a phase-shifted sampling signal. Thus, the data stream coming from the four converters is effectively the same as what would come from one converter sampling at four times the rate. To reduce sampling jitter, the sampling signals are derived from a 24-MHz quartz-crystal voltage-controlled oscillator phase locked to an FTS 10-MHz reference signal.

After sampling, the NBOC sends the digitized data to the Modcomp II for magnetic tape recording. The Modcomp II reads each byte immediately after it has been written to the tape and sends the data back to the NBOC. The NBOC then converts the digital data back to an analog signal that can be

monitored with a spectrum analyzer to verify that the desired data are being tape recorded.

2. ISAS Data Acquisition Subsystem. The ISAS-provided DAS is the prime recording system, with the JPL subsystem provided as backup. Both subsystems will run concurrently during the encounter.

The two subsystems are functionally equivalent. The ISAS IF-VF converter performs a tuned downconversion with a computer-controlled frequency synthesizer and tape records the signal after digitization. An HP1000/A900 provides the frequency control and data handling, and two Hewlett-Packard tape drives are used for data recording and storage.

The ISAS IF-VF converter differs from the JPL converter in that the first tuned conversion converts the signal to a 20.02-MHz third IF where it is band-pass filtered rather than converted directly to video-band frequency. An additional downconversion translates the carrier to video band, where it is low-pass filtered and amplified prior to digitization. A fast-Fourier-transform (FFT) analyzer monitors the video signal, and a RMS voltmeter facilitates setting the IF attenuator to adjust the video frequency (carrier) to the proper signal level into the ADC.

3. Frequency and Timing Subsystem. The frequency and timing subsystem used at Usuda will rely on a hydrogen-maser frequency standard provided by ISAS, which is to be implemented prior to the Neptune encounter. Currently the station reference can be switched between two cesium-beam standards and one rubidium standard. The output of the standard, regardless of type, is sent through a 5-MHz phase-locked CUL to improve the phase-noise spectrum.

The first and second LOs are derived from this 5-MHz output. The 5-MHz signal is frequency multiplied to 100 MHz followed by frequency synthesizers which form 94- and 97-MHz signals that are sent over the fiber-optic link to the RF-IF converter in the antenna building. There the 94-MHz signal is frequency multiplied by 20 and the 97-MHz signal by 5 to provide the first and second LO mixer injection signals.

It can be seen in the block diagram that there are two 5- to 100-MHz $\times 20$ assemblies, one from ISAS and one from JPL. The JPL $\times 20$ was to provide only a 100-MHz reference signal to the JPL Dana synthesizer third LO chain. The ISAS $\times 20$ was the primary 100-MHz source for the first and second LOs; however, during system testing the Allan variance performance was marginal using the ISAS $\times 20$, and improved when the 100-MHz reference was derived from the spare JPL $\times 20$ assembly. Efforts are underway to modify the JPL $\times 20$ assemblies to provide another output port and to improve

the ISAS $\times 20$ stability. Following final corrections and tests, one $\times 20$ reference will be chosen as prime and the other as backup. This is described in more detail in Section V.

IV. System Test Methodology and Plan

The system test plan included the test hierarchy of performing assembly-level tests by the various Cognizant Development Engineers to verify meeting their level of performance requirements and allocated error budget. Similarly, the subsystem was tested at its level to verify the error budget and functional requirements, followed by complete system testing by the System Cognizant Development Engineer.

Figure 5 illustrates the system test concept for measuring the critical phase-noise spectral density and spurious-frequency parameters. Also shown are the special Test Transmitter and phase-noise instrumentation (Digital Stability Analyzer) developed and provided for the system testing. The Stability Analyzer uses digital signal-processing techniques, and in addition to measuring the two parameters, it is capable of measuring the amplitude spectrum, the power spectrum, and the differential phase between any two RIV output channels.

Similarly, the Stability Analyzer has the capability of measuring the long-term frequency stability of both the hydrogen masers and the Radio Science System using Allan variance methodology, which has been universally accepted as a meaningful quantitative measure of fractional frequency deviation [3, 4].

Figure 6 illustrates the relative phase-noise spectral densities of a typical future spacecraft USO, the DSCC Radio Science System, and the special Test Transmitter that formed the basis and concept of testing the Radio Science System for the phase-noise parameter. These values exceed the Voyager-Neptune encounter specifications and illustrate the anticipated requirements for future missions. The Radio Science System was specified as shown to provide ample margin in its performance such that neither the received spacecraft phase-noise floor nor the signal perturbed by the intervening media (or experiment signal) was masked. Similarly, the Test Transmitter must possess better phase noise characteristics than the Radio Science System specification in order to reliably measure the performance.

Figure 7 is the block diagram of the Test Transmitter, which provided phase-coherent S-/X-band output signals with exceptional phase-noise spectral density characteristics. The Test Transmitter was also used for performing long-term frequency-stability tests using Allan variance methodology, whereby a 5-MHz reference signal from the FTS was used to phase-lock the internal primary 5-MHz PLL oscillator. This 5-MHz prime

signal was then allowed to free-run for performing the short-term (phase-noise) frequency-stability tests in the switch position, as shown, to provide the best phase-noise performance. The phase-coherent output signals also permitted measuring the differential phase-stability parameter of the Radio Science System.

Figure 8 is the block diagram of the Usuda test methodology and test instrumentation that were developed and used for the subsystem and system tests. A 10-MHz stable quartz-crystal oscillator (with good phase-noise characteristics) and $\times 7$ multiplier provided the test signal to the DAS at the 70-MHz IF input frequency for measuring the phase-noise spectral density parameter.

A 10-MHz reference signal from the FTS was then switched into the $\times 7$ multiplier to perform the Allan variance measurement. This method was used to test the subsystem at JPL to verify the subsystem performance prior to its installation at Usuda. The instrument for measuring the phase noise/spurious signals is composed of a PLL and an FFT-type commercial spectrum analyzer, while a combination of zero-crossing detector, time-interval counter, and computer processor was used to measure the Allan variance.

Following the installation at Usuda, the subsystem was retested by the same test instrumentation and methodology as performed at JPL prior to its interfacing with the ISAS RF-IF converter. Next, the complete system was tested with the use of the special Test Transmitter as the RF test input signal.

V. System Test Results

This section describes some of the initial system test measurements and results performed at the CDSCC and the Usuda Tracking Station. The Radio Science System measurements were performed at X- and S-band at CDSCC and at S-band at Usuda.

A. DSCC Initial Test Results

Described below are the initial test results performed at CDSCC beginning with the short- and long-term frequency stability data.

Figure 9 shows the Allan variance measurement of the two hydrogen-maser frequency standards. Figures 10(a), 10(b), and 10(c) compare the noise-power spectral density spectra of the two hydrogen masers relative to 10 GHz with the fractional frequency deviation as a function of integration time and spectral density versus offset frequency. The noise-power spectrum plot scales are normalized for phase noise and corrected for sine-wave line-spectra magnitudes. These masers meet the total

system Allan deviation specification for the encounter. For the phase-noise spectral density, the system specification is shown corrected for the noise factor and referenced to the 8.4-GHz frequency (the plot is referenced to 10 GHz because of the instrumentation design, and the resultant is for the sum of the two masers; hence, each maser at 8.4 GHz would be approximately -4 dB better than plotted).

Figure 11 shows the Allan variance measurement results at X-band of the total DSS-43 Radio Science System where the Test Transmitter was located within the X-band cone with its 5-MHz reference input obtained from the PCG 20-MHz output via a $\times 1/4$ frequency multiplier. The input 100-MHz signal to the first local oscillator $\times 81$ was obtained from an FTS 100-MHz source fed up to the cone through a hardline coaxial cable. The figure shows that the Voyager system requirement is met with a comfortable margin. If the 100-MHz reference to the $\times 81$ were obtained from a stabilized transmission line (fiber optics, for example), it would shift the plot downward to greater stability and could meet the Galileo requirements of 2.5×10^{-15} for 1000-sec integration. Figure 12 shows the time-residual plot associated with Fig. 11. These plots show only the Radio Science System results since the contribution of the frequency standard is cancelled in the measurement methodology; hence, the total system characteristics must include the sum of these two components.

Figure 13 shows the phase-noise spectral density spectrum of the RIV using a good-quality spectral IF signal input of 300 MHz and the normal Dana POCA as the RIV oscillator. This figure shows the characteristic 60 Hz plus harmonics of the power-frequency spurious signal that had been previously identified during system testing at JPL and Goldstone due to the Dana-POCA combination. These spurious signals were being corrected at the time of these tests by modifications to the Dana-POCA local oscillator.

In the overall Radio Science System, the first and second LOs were identified as the two major contributors to the phase-noise spectral density and spurious signals that appear adjacent to the received spacecraft carrier signal. The first LO and its entire frequency distribution and multiplier chain, originating from the FTS 100-MHz reference signal, is the most dominant of the two sources because of its larger multiplication factor of $\times 81$. The multiplication factor for the second LO is $\times 11$; however, the second LO, comprising the programmable frequency synthesizer (Dana POCA) for tracking the Doppler shift of the spacecraft signal contained large-magnitude power-line spurious signals that required magnetic shielding to meet specifications. The first LO injection signal, occurring at microwave frequencies, was allocated the major portion of the error budget for the phase-noise spectral density. To permit this, an error budget of more than 10 dB below the overall sys-

tem specification was allocated to the second LO. It was seen that the spurious signals of the RIV Dana-POCA combination were above the error budget as shown in Fig. 13; hence, it was necessary to substitute another frequency synthesizer with a better spurious signal response but similar noise-power spectral density characteristics in place of the above combination to better measure and evaluate the first LO contribution to the system phase-noise spectral density and spurious signals. Figure 14 shows the resultant RIV noise-power spectral density/spurious signal characteristics using the Fluke 6160 substitute synthesizer, which was used for the majority of the system tests for determining the first LO contribution.

After considerable system testing, including detailed investigative and probing experiments to isolate the sources of many spurious signal contributors and noise-spectral density degradations, final noise-power spectral density measurements were made. These measurements of the noise-power spectral density were not the desired phase-noise spectral density measurements because the stability analyzer's processing program was erratic in its operation during this time period; the measurements were made with the alternate CDSCC test instrumentation. The stability analyzer was still capable of measuring the Allan variance and differential S-/X-band channel phase-stability parameters, and the results are included in this article.

Figure 15 depicts the total DSS-43 Radio Science System noise-power spectral density results with the X81 first LO input obtained from a hardline coaxial cable, using the substitute second LO, and operating the Test Transmitter on its DC power supply with output at X-band. The Voyager phase-noise specification is also shown, and since the noise-power spectral density is greater in magnitude than the phase-noise spectral density, the system meets the specification. It was determined that the 180-Hz spurious signal was contributed by the Fluke 6160 substitute synthesizer via the 5-MHz FTS reference signal; since the normal configuration utilizes the Dana which uses a 100-MHz reference signal, this spurious signal will not be present in the final system. Also shown in Fig. 15 is a broad-band spurious signal at 120 Hz.

Figure 16 is complementary to Fig. 15 and shows the spurious 120-Hz signal on an expanded horizontal axis. The figure shows a peculiar modulation-type signature which is unique to DSS-43 since this type of spurious signal was not visible in the DSS-45 spectrum. Figure 17 shows a similar noise-power spectral density measurement of the total Radio Science System at DSS-45. It lacks the 120-Hz spurious signal and meets the Voyager phase-noise specification. Figure 18 shows the DSS-45 Radio Science System noise-power spectral density measurements at S-band, which meet the phase-noise specifications.

Figure 19 depicts the initial test of the differential phase stability between the DSS-43 Radio Science System S- and X-band channels for a duration of one hour from 1430 to 1530 hours local time. The Test Transmitter was located within the X-band cone for connection to the X-band TWM, and the S-band output signal from the transmitter was connected via a sun-exposed coaxial cable to the S-band cone for connection to the TWM. The phase variation of approximately 16.5 degrees peak per hour is believed to be due to the sun-exposed cable since most of the phase-sensitive elements are the microwave assemblies of this experiment. For example, Fig. 20 shows the S-/X-band differential phase stability measurement conducted at DSS-45 where the transmitter and all connecting cables were located within the controlled environment of the cone. The measurement shows a 7-degree peak-per-hour variation for the same time duration.

Figure 21 depicts DSS-43 S-/X-band differential phase stability with the test signal radiated from the transmitter located on the roof of SPC-40 to the input of the DSS-43 antenna. The high, rapid phase variations are believed to be due to multipath effects. Only 10 minutes were available for this experiment and the variation of the mean of the plot is a 12-degree peak.

B. Usuda Tracking Station Test Results

After the JPL DAS was installed at Usuda, initial tests were performed to verify that the subsystem met pre-shipment acceptance test results. Figure 22 shows a performance shortfall that occurred immediately after installation. Here the phase-noise spectrum of the JPL DAS as measured with a 70-MHz IF test signal shows numerous 60-Hz harmonics spread beyond 2 kHz. This was a concern, even though the harmonics were below the S-band system specification of -45 dBc. The problem was traced to an improperly wired connection from the ISAS station 240/120-volt step-down power transformer to the JPL equipment; some power sockets were wired with reverse phase polarity. After correction of this anomaly, the JPL DAS repeated the acceptance test results. The extreme sensitivity of these radio science receivers required that the spurious signals be eliminated before performing further system tests.

While the correction of the improper wiring required considerable time, the majority of the test time was devoted to correcting the system to meet the Allan variance specification. The very long-term nature of the Allan variance test (1000-sec integration times) requires long test periods to obtain data with an acceptable confidence level. A typical test required 10 hours. The duration of the tests plus sensitivity of the system (even touching an exposed RF test cable affects

the results) meant that many days were required to isolate and correct the system before the specifications were finally achieved.

One major problem was the 5- to 100-MHz $\times 20$ frequency multipliers discussed previously. Initial and repeated measurements made with the ISAS $\times 20$ revealed a varying system performance in meeting the specification at 1-sec integration times. Figure 23 shows the typical performance of these units. The test configuration utilized the Test Transmitter and TWM provided by JPL, the ISAS RIVs and the ISAS DAS.

The spare $\times 20$ unit met the specification as shown in Fig. 23 with little margin; however, it was connected externally with extra cable lengths for testing, not installed in the normal cabinet drawer of the ISAS DAS. These tests indicated that the ISAS units produce marginal performance. The units use a 100-MHz quartz-crystal oscillator phase-locked to the 5-MHz reference input, and it is possible that they are susceptible to temperature fluctuations in the long term and induced vibrations in the short term.

The ISAS frequency-multiplier drawer was designed to accept either a 100-MHz reference signal directly or the normal 5-MHz reference signal. Thus, substituting the 100-MHz signal generated by the JPL unit was easy to accomplish for these tests. The JPL $\times 20$, located in the remote FTS room, consistently performed better than the two ISAS units which were located in the main control room together with the two data acquisition subsystems. The Allan variance of the JPL unit is shown in Fig. 24 using the JPL DAS. It was found during these tests that the use of either DAS had virtually no effect on the system Allan-variance results. The figure also shows a curve indicating the system Allan variance measured at the output of the NBOC digitizer's DAC. At this output test port the video signal has been sampled and represents the final level of degradation to the input RF signal. The curve indicates a small degradation relative to the NBOC input plot as expected from the sampling, and the entire system meets the specification with adequate margin.

A phase variation versus time plot of the downconverted test signal can be extracted from the measured raw Allan-variance data. Since the phase of the video signal depends on the phase of the local oscillators and the phase of the RF test signal, the data can be used to determine the phase performance of the LOs. Figure 25 shows the phase plot of the data used to construct Fig. 24, i.e., the system Allan variance using the JPL $\times 20$. The periodic nature of this curve suggests a strong temperature sensitivity in the LO chain. Note that the effect of a phase oscillation with period T is to increase the Allan variance at integration times on the order of T . In

other words, the "plateau" on the Allan variance curve at 1000 seconds is due to the periodic fluctuations shown on the phase plot.

Figure 26 shows the Allan variance of the Usuda system taken with the ISAS $\times 20$. This is the same configuration used for Fig. 23, with the poorer of the two ISAS units. However, during this test a temperature probe was placed inside the ISAS DAS frequency-multiplier drawer. In Fig. 27, the recorded temperature results are compared with the phase plot derived from the Allan variance data, showing a strong correlation between temperature fluctuations in the LO frequency-multiplier drawer and the system phase. A change in temperature of 1 degree centigrade yields a change in phase of about 45 electrical degrees. However, this does not completely indicate that the ISAS $\times 20$ is the source of the temperature sensitivity, since the $\times 97/100$ and $\times 94/100$ modules are also present in this drawer. The first LO has a larger multiplication factor than the second LO and should be the major contributor. To isolate the source, additional testing will be necessary.

The plots described above demonstrate that a temperature sensitivity exists in the LO chain. This sensitivity causes an increase in the Allan variance at long integration times but does not degrade the system past the specified level. What has not been determined is the cause of the instability of the ISAS $\times 20$ at low integration times, and this is currently being investigated by ISAS personnel.

The Allan variance proved to be a more difficult parameter to meet than the phase-noise spectral density. This is mainly due to the relaxed specification for S-band systems (-45 dBc/Hz from 1 Hz to 10 kHz) because of the lower received SNR at S-band. The anticipated problems with power-line spurious signals did not materialize after the power connections were wired correctly.

Figures 28(a), 28(b), and 28(c) show the system phase noise measured using the JPL test transmitter and TWM, the ISAS RF-IF converter, and the JPL DAS. In this configuration, the original ISAS $\times 20$ was used. The plots are taken from an FFT spectrum analyzer and show the phase noise on the downconverted 20-kHz carrier over three different video-band frequencies: 0 to 50 Hz, 0 to 0.5 kHz, and 0 to 10 kHz. These frequencies correspond to the modulation frequency of the phase-noise component; thus, 0 Hz is right on the carrier. However, any DC component showing in the plots is purely an artifact of the phase-locking instrumentation used to demodulate the phase noise from the carrier. In general, the data on the plots are valid from the third or fourth FFT frequency bin and higher.

Figure 28(a) shows the phase noise to be about -55 dBc/Hz at $f_m = 1$ Hz and diminishing at higher frequencies. Figure 28(b) shows several 60-Hz and harmonically related spurious signals that reach a maximum of -56 dBc at 60 Hz, while the noise-spectrum magnitude levels off at about -75 dBc/Hz. Figure 28(c) shows the phase noise out to 10 kHz dropping to about -80 dBc/Hz. Because the resolution bandwidth is so high at 10 kHz, it is necessary to step across the 10-kHz band using smaller frequency spans to make sure no spurious signals are buried in the noise. In summary, the phase noise using the ISAS $\times 20$ meets specification with a margin of greater than 10 dB.

Because the JPL $\times 20$ is used as the backup to provide the 100-MHz signal for the LO chain, the system phase noise was measured using this unit. Figures 29(a), 29(b), and 29(c) show the phase noise over the video band of 0 to 50 Hz, 0 to 0.5 kHz, and 0 to 10 kHz. In Fig. 29(a), the phase noise at 1 Hz is approximately -63 dBc/Hz, dropping to about -79 dBc/Hz at 50 Hz. The 60-Hz spur shown in Fig. 29(b) is at about -61 dBc, with the noise-spectrum remaining flat at a level of -83 dBc/Hz. Finally, the noise in Fig. 29(c) is seen to decrease to -95 dBc/Hz at 10 kHz and level off.

Caution should be used if any conclusion is to be derived in comparing the merits of these two $\times 20$ s from the sets of data since the RF test signal level used in the JPL $\times 20$ measurement was 14 dB higher than the level used for the ISAS unit. This was not deliberate, but resulted from a procedural error and explains the approximately 15-dB difference in the noise spectra levels in the region near 10 kHz (Fig. 28c compared to Fig. 29c).

These plots illustrate the combination of the phase-noise spectral density, resulting from the LO chain dominating at the low offset frequencies which are independent of the input RF test amplitude and exhibit a decreasing magnitude versus

increasing offset-frequency spectrum distribution characteristic, and the input thermal-noise temperature spectral density which exhibits a nearly flat distribution and is dependent upon the test signal amplitude. This can be seen when comparing Fig. 28(c) to Fig. 29(c) near 6 kHz where the thermal noise is flat beyond 6 kHz and is the dominant contributor, since the phase noise due to the LO is gradually decreasing in this higher frequency region. Below 6 kHz the phase noise becomes the dominant contributor and increases in magnitude towards the low offset frequencies; thus, the plots of Fig. 28(a) and Fig. 29(a) can be considered mainly phase noise due to the LOs. The relative magnitudes of the phase noise shown in Figs. 28(a) and 29(a) can be used to compare the merits of the two $\times 20$ s. The ISAS unit develops phase noise 8 dB higher at 1 Hz and tends to correlate with the degraded Allan variance performance at the 1-sec integration time relative to the JPL unit.

In summary, the Usuda Radio Science System meets the phase noise specification regardless of which $\times 20$ frequency multiplier is used. However, both the Allan variance and phase noise data indicate that the ISAS $\times 20$ is less stable than the JPL unit at integration times of about 1 sec. In order to meet the system Allan variance specification, the ISAS $\times 20$ needs to be improved. The JPL $\times 20$ s are to be used as backups.

VI. Conclusion

The Voyager-Neptune encounter has levied very stringent requirements on the phase-noise spectral density characteristics and frequency stability of the DSN Radio Science Systems at Canberra and Usuda to ensure high performance at Neptune. The DSN has met these requirements with new designs in the signal-acquisition system and in test instrumentation. The results of tests conducted at Canberra and Usuda indicate that the design indeed meets the performance requirements.

References

- [1] G. L. Tyler, "Radio Propagation Experiments in the Outer Solar System with Voyager," *Proceedings of the IEEE*, vol. 75, no. 10, pp. 1404–1430, October 1987.
- [2] E. H. Sigman, "Phase Calibration Generator," *TDA Progress Report 42-92*, vol. October–December 1987, Jet Propulsion Laboratory, Pasadena, California, pp. 89–104, February 15, 1988.
- [3] D. W. Allan, "Time and Frequency (Time-Domain) Characterization, Estimation, and Prediction of Precision Clocks and Oscillators," *IEEE Trans. on Ultrasonics, Ferroelectric and Frequency Control*, vol. UFFC-34, no. 6, November 1987.
- [4] C. A. Greenhall, "A Method for Using a Time Interval Counter to Measure Frequency Stability," *TDA Progress Report 42-90*, vol. April–June 1987, Jet Propulsion Laboratory, Pasadena, California, pp. 149–156, August 15, 1987.

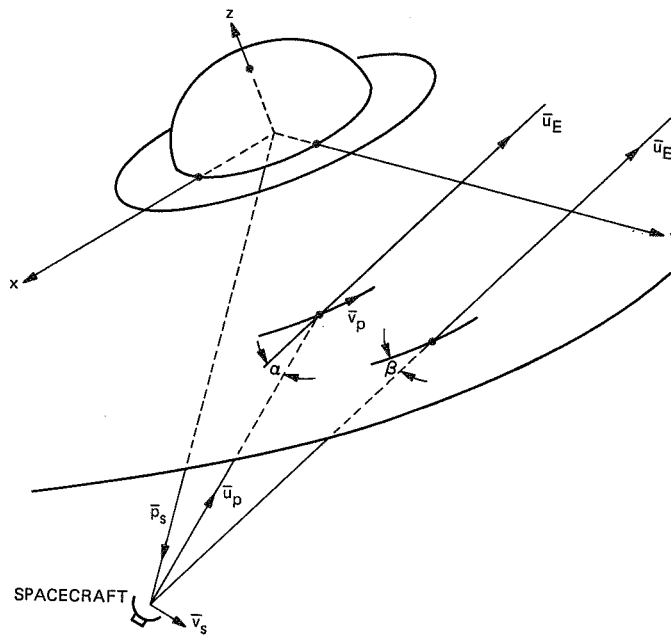


Fig. 1(a). Geometry of ring occultation, signal on direct and indirect path to Earth.

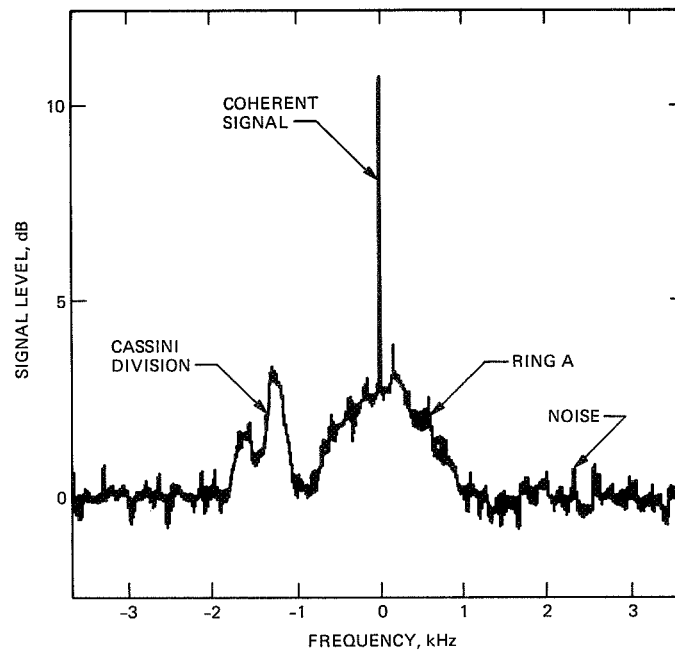


Fig. 1(b). Spectrum of received signal when Voyager 1 was behind Saturn's Ring A. Central spike is the coherent direct path signal. Symmetrical broad spectrum ± 1 kHz about spike is from ring-particle scattering; separate broad feature is from Cassini Division particles.

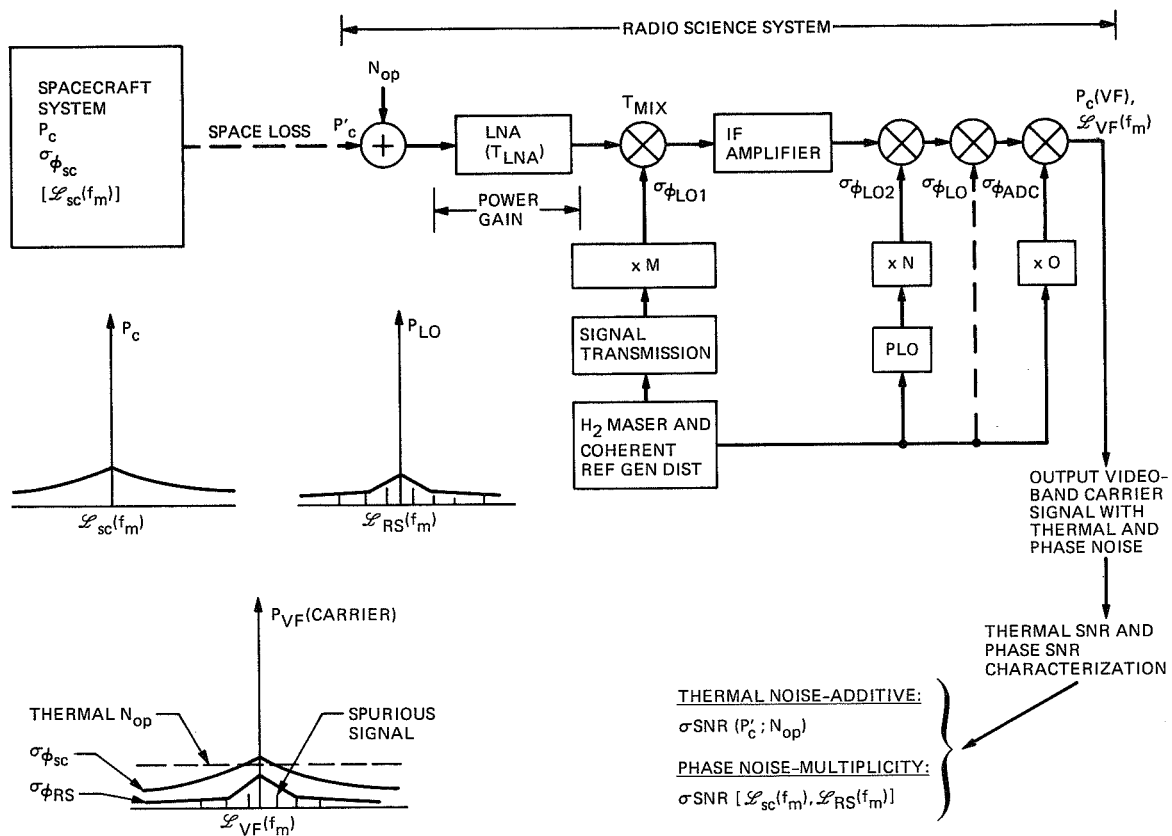
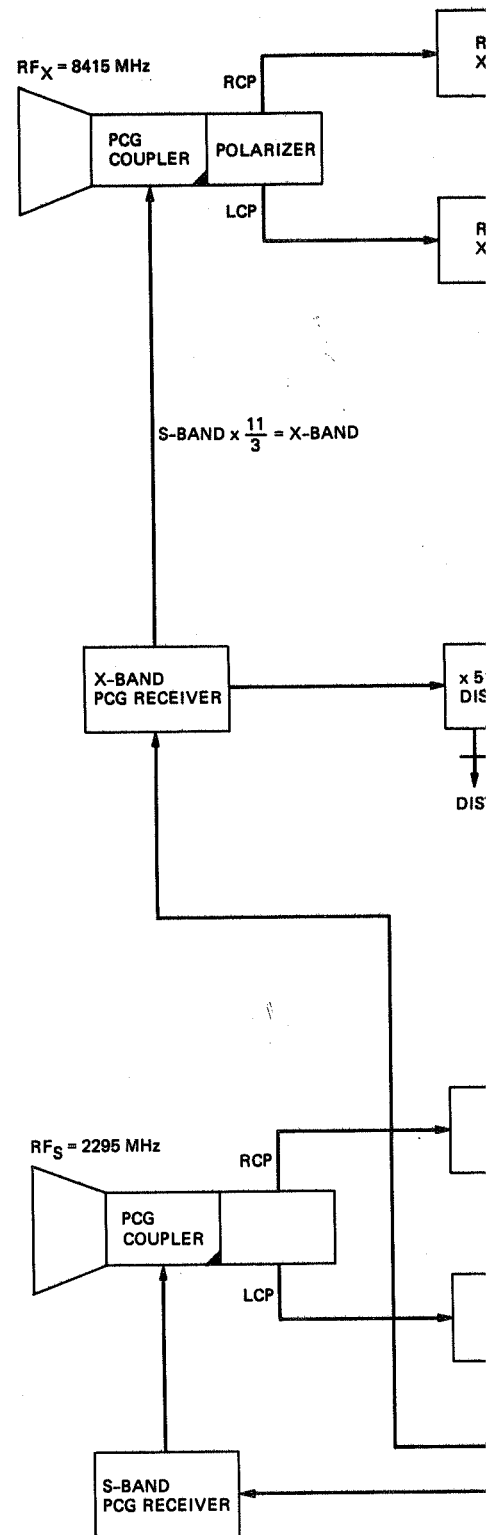
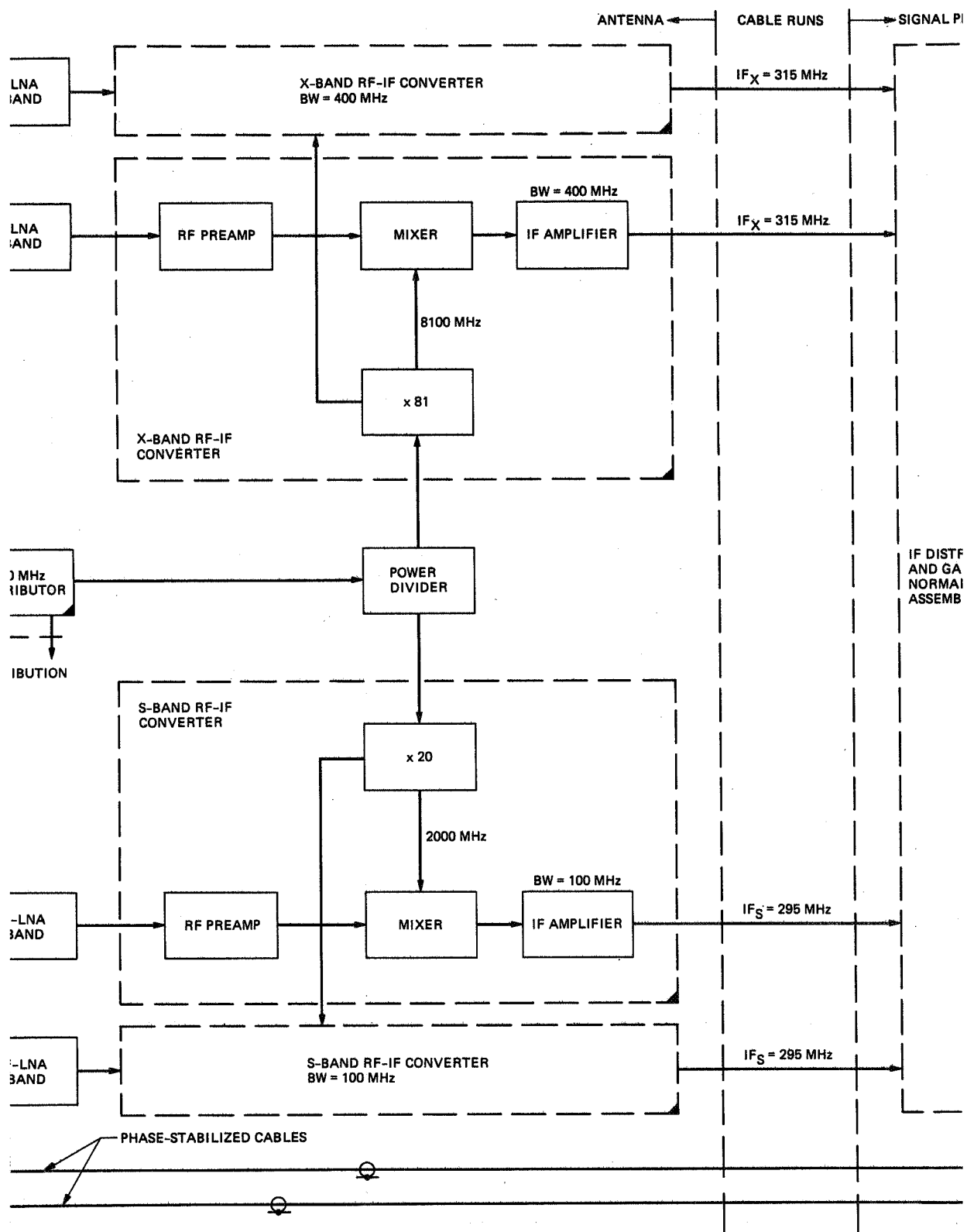


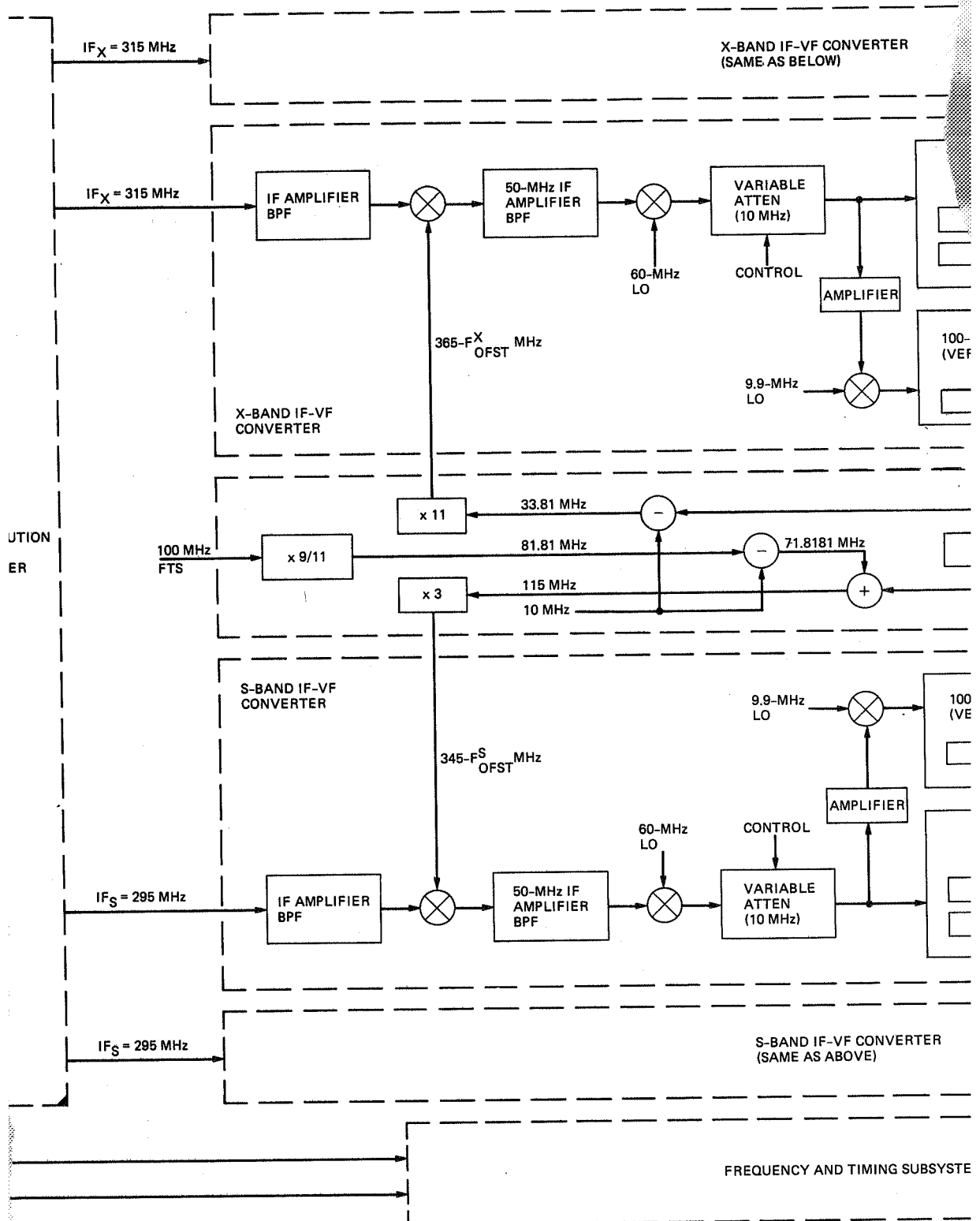
Fig. 2. Model of thermal and phase noise for the spacecraft and Radio Science System.



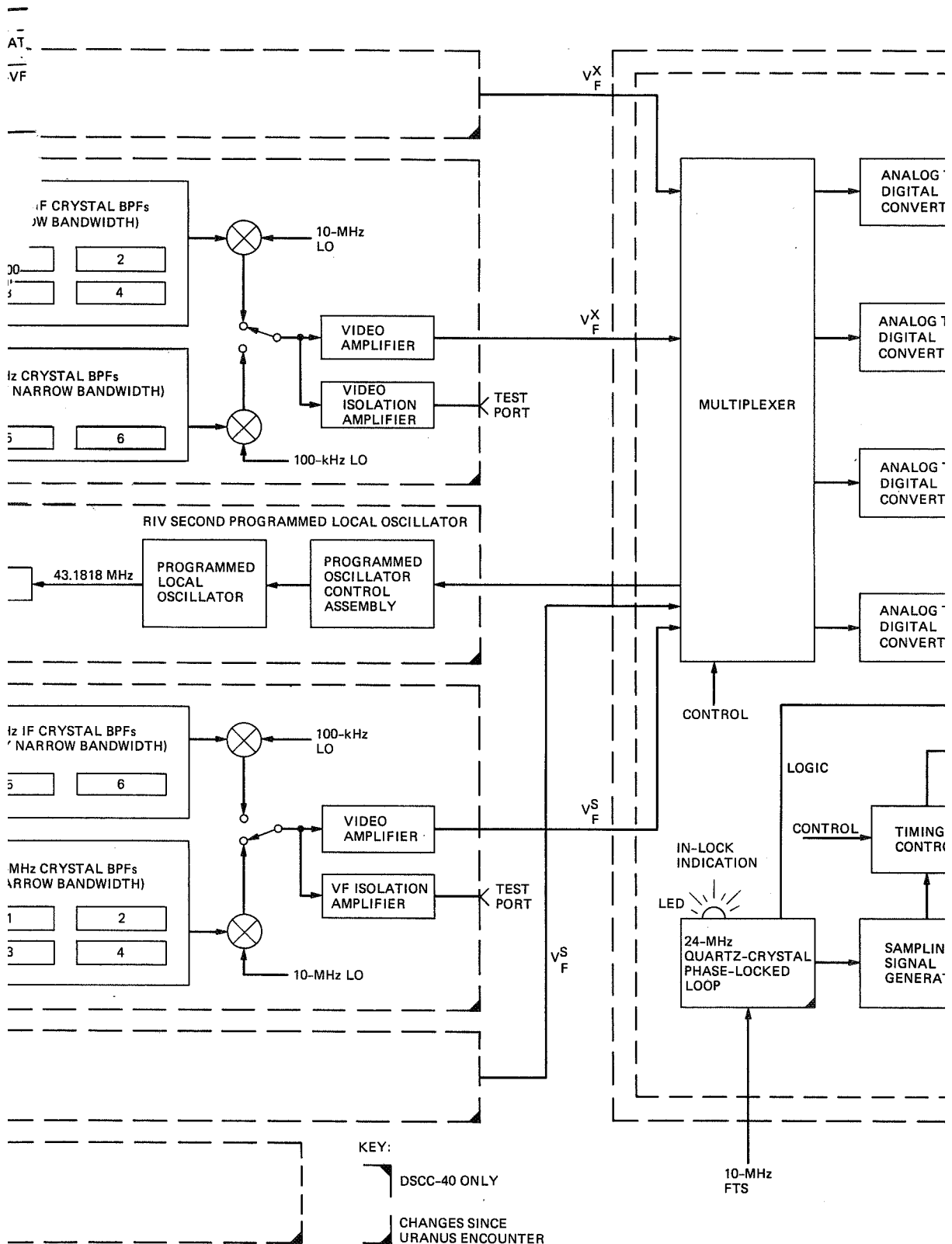
FOLDOUT FRAME



PROCESSING CENTER



2 FOLDOUT FRAME



3 BOLDOUT FRAME

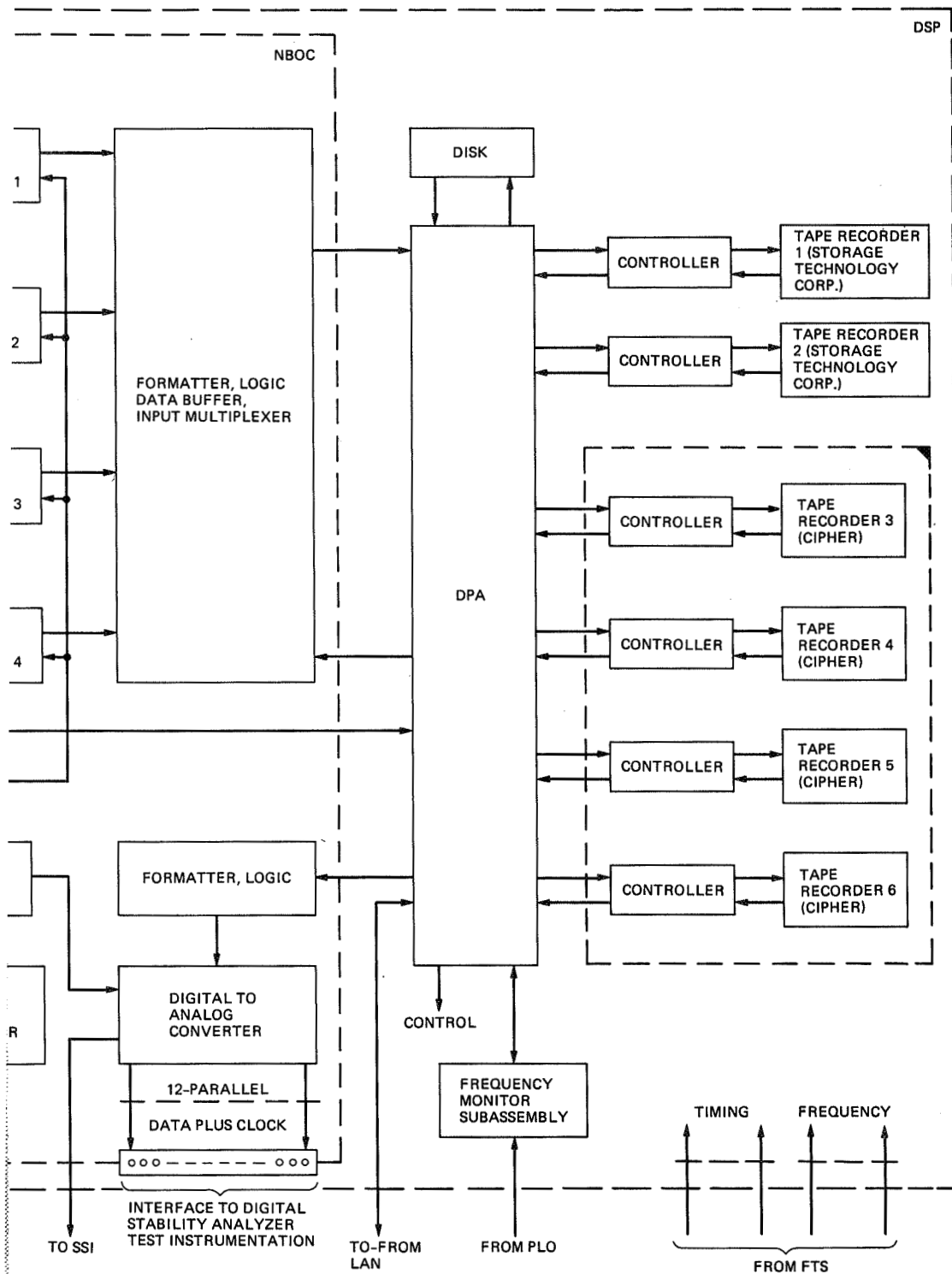
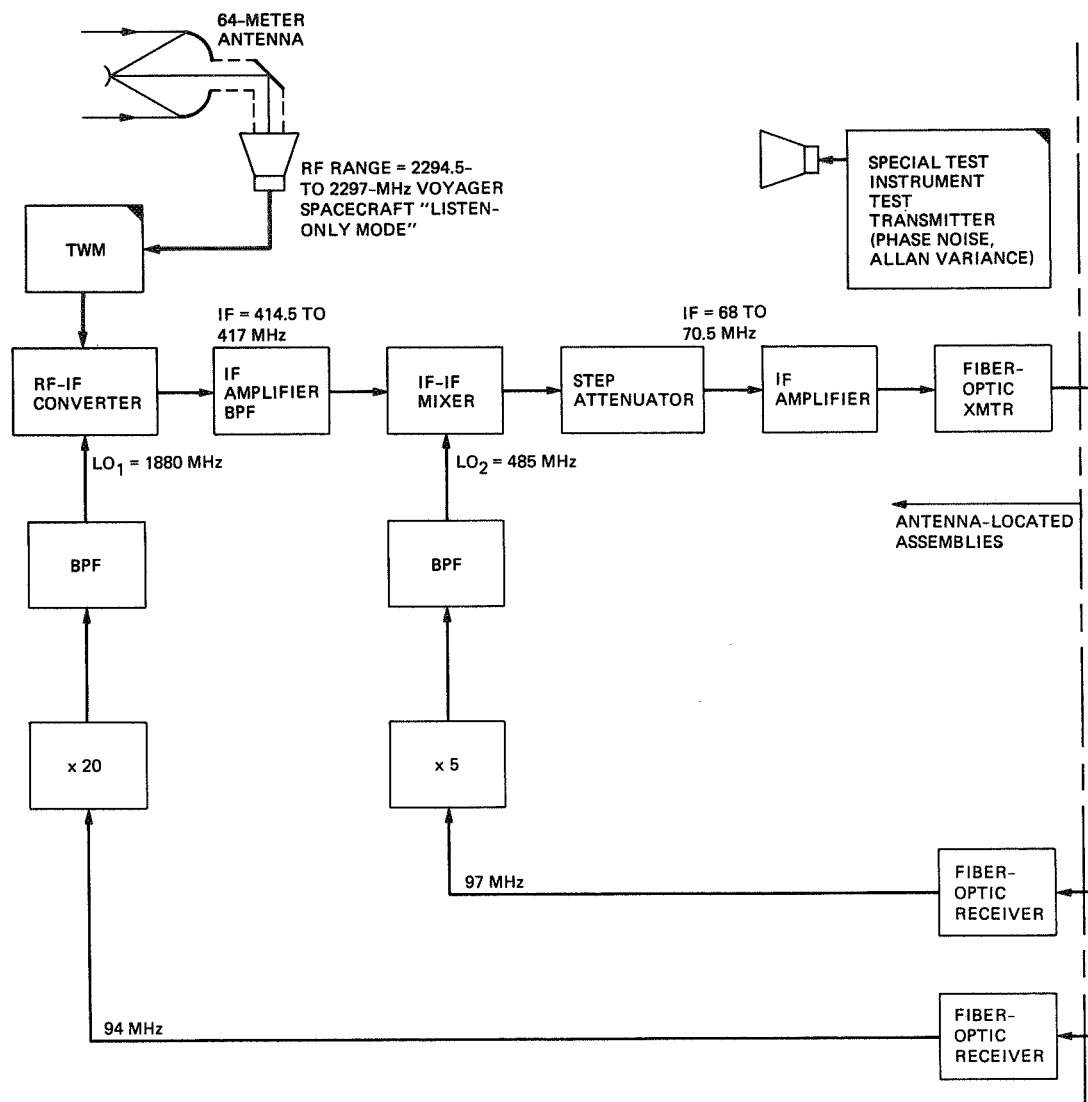


Fig. 3. Block diagram of DSCC Radio Science System, 70-m antenna (DSCC-10, DSCC-40, and DSCC-60).

4/ EOLDOUT FRAMM



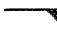
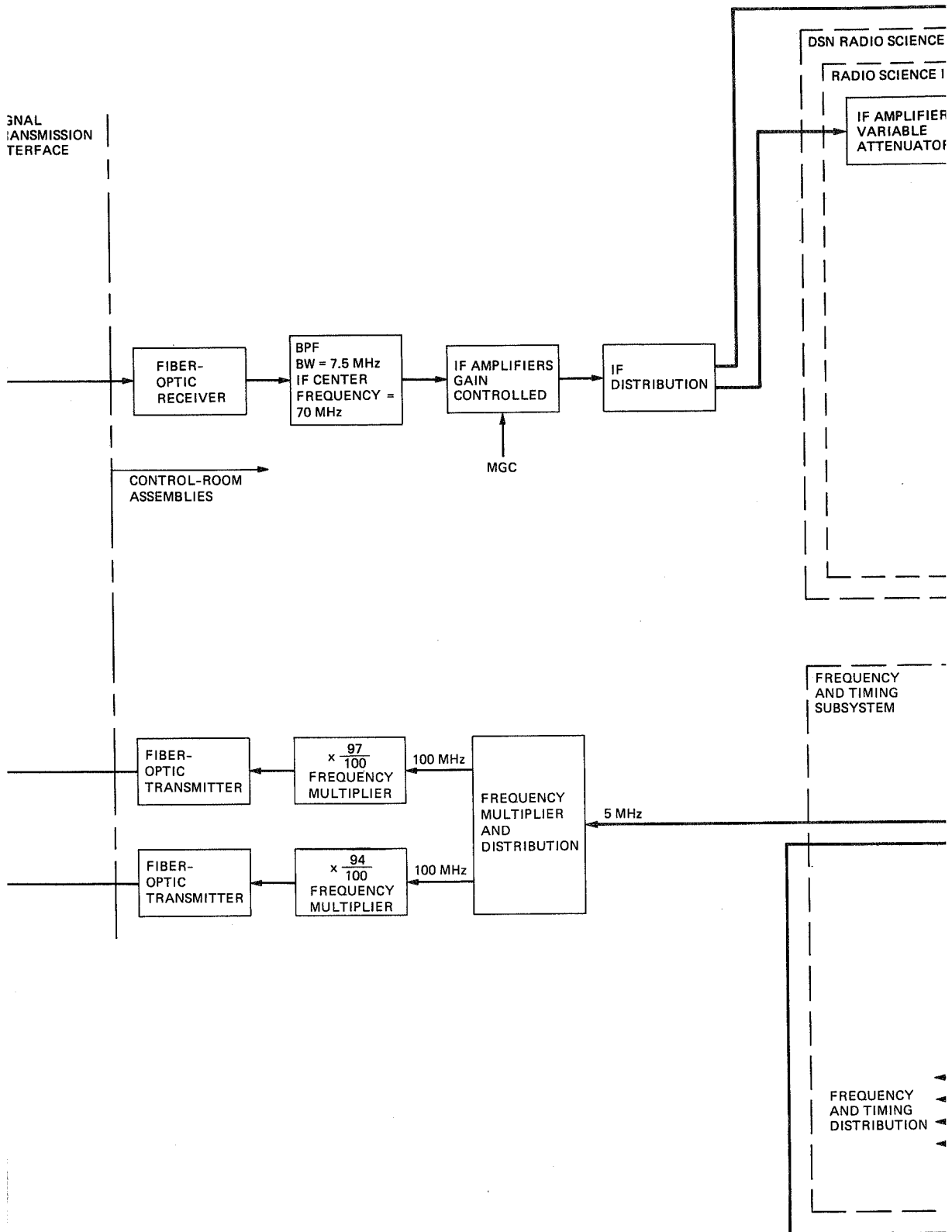
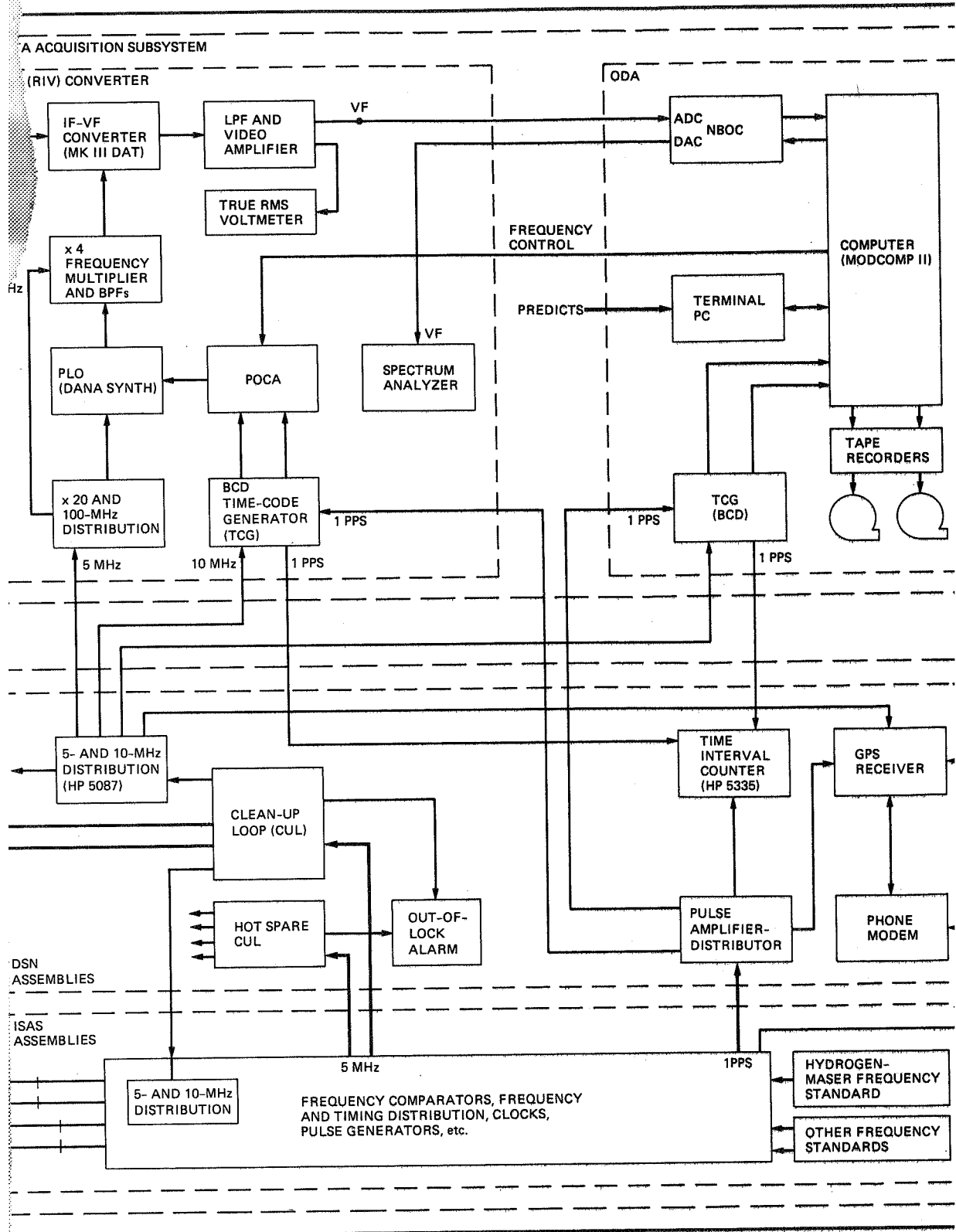
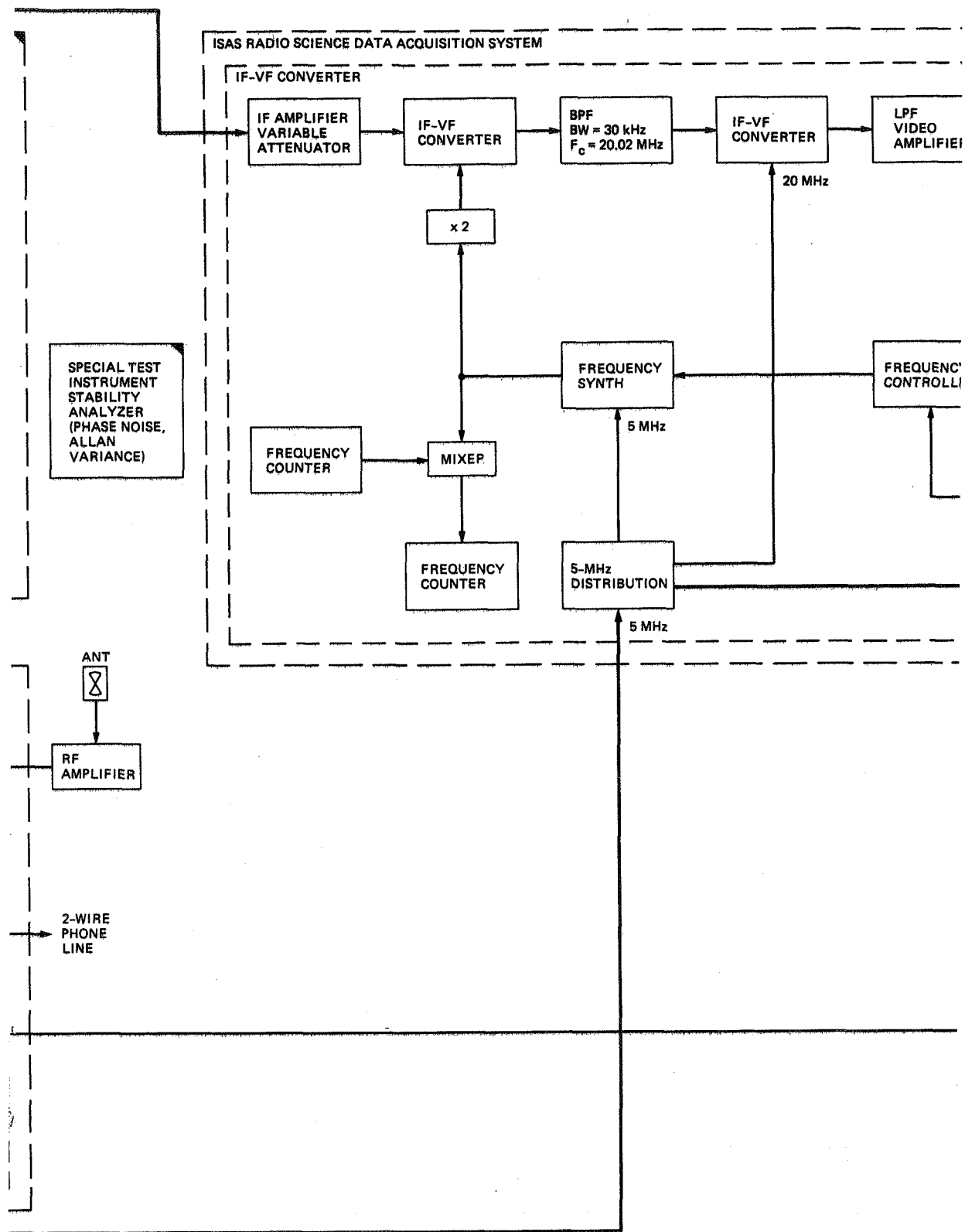
KEY:  DSN-SUPPLIED EQUIPMENT

Fig. 4. Block diagram of Radio Science System, Usuda, Japan.

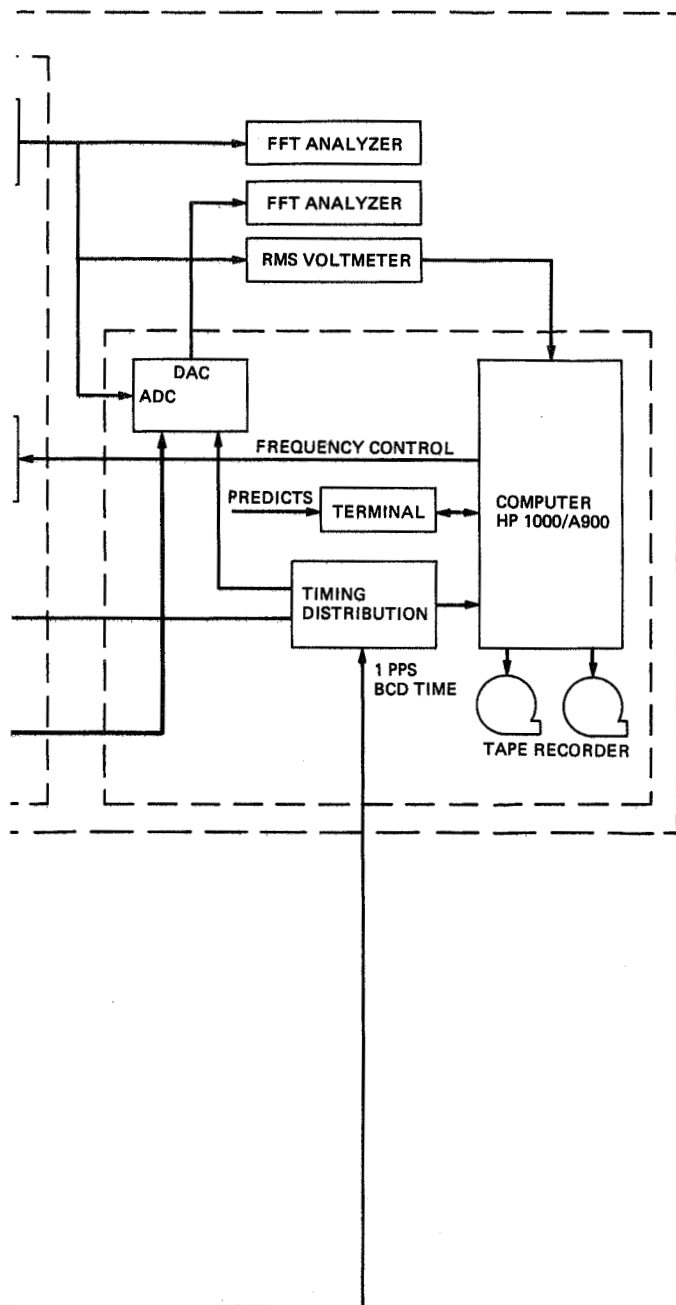




2 FOLDOUT FRAME



3 FOLDOUT FRAME



U FOLDOUT FRAME

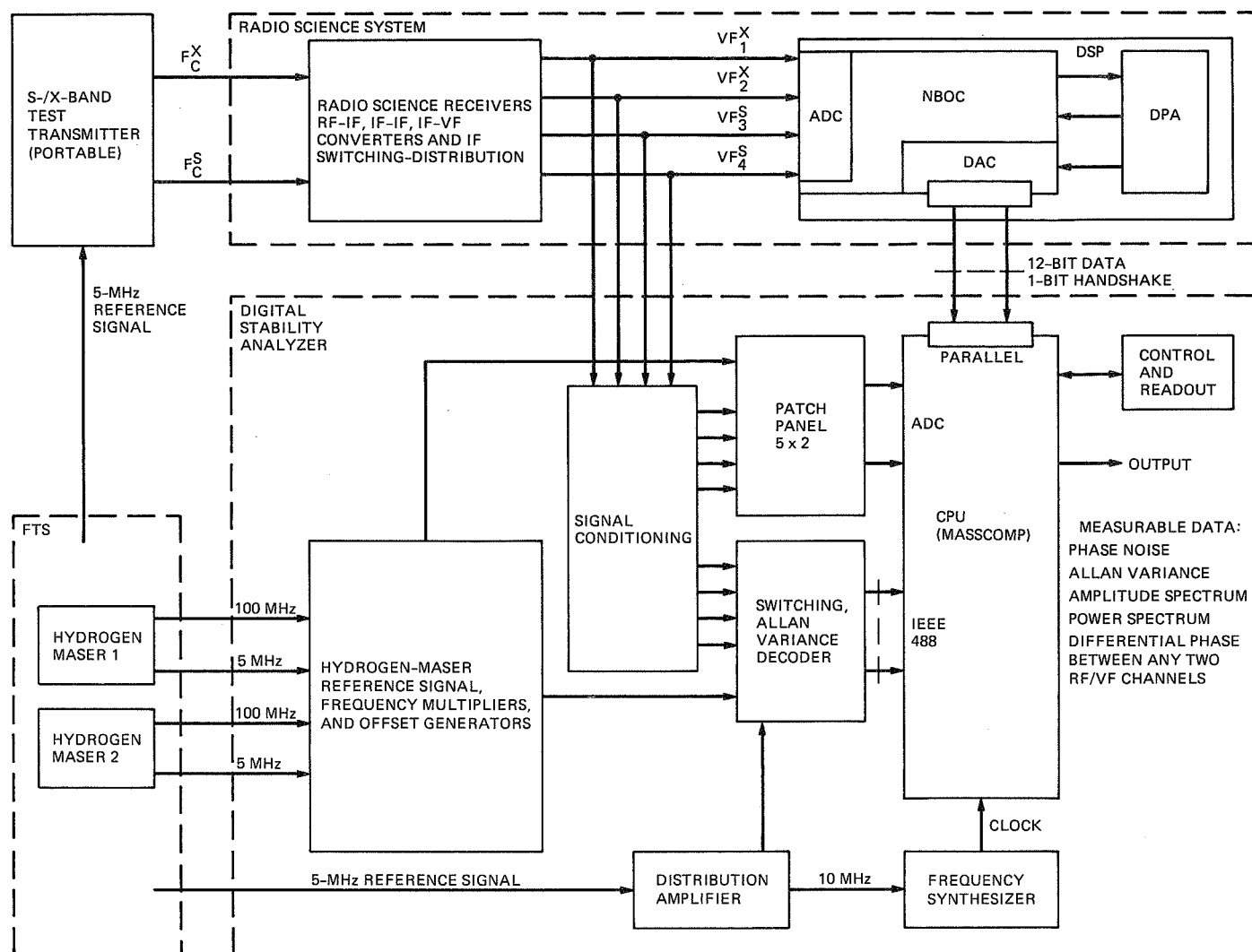


Fig. 5. Block diagram of Digital Stability Analyzer illustrating test methodology.

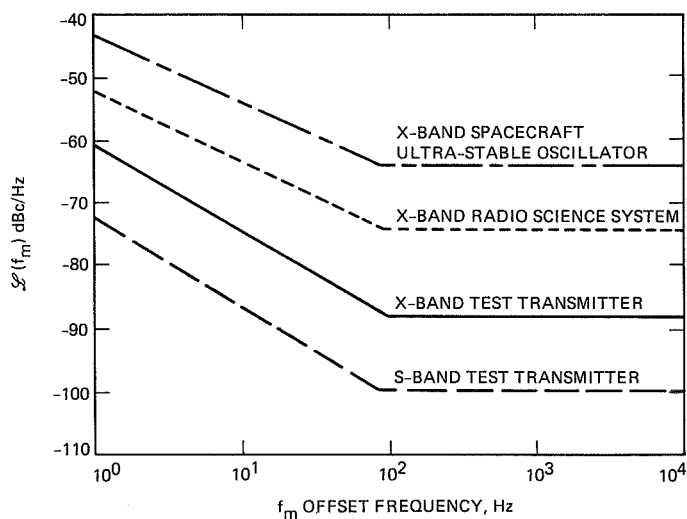


Fig. 6. Relative phase-noise spectral densities of future spacecraft USO, DSCC Radio Science System, and S-/X-band Test Transmitter.

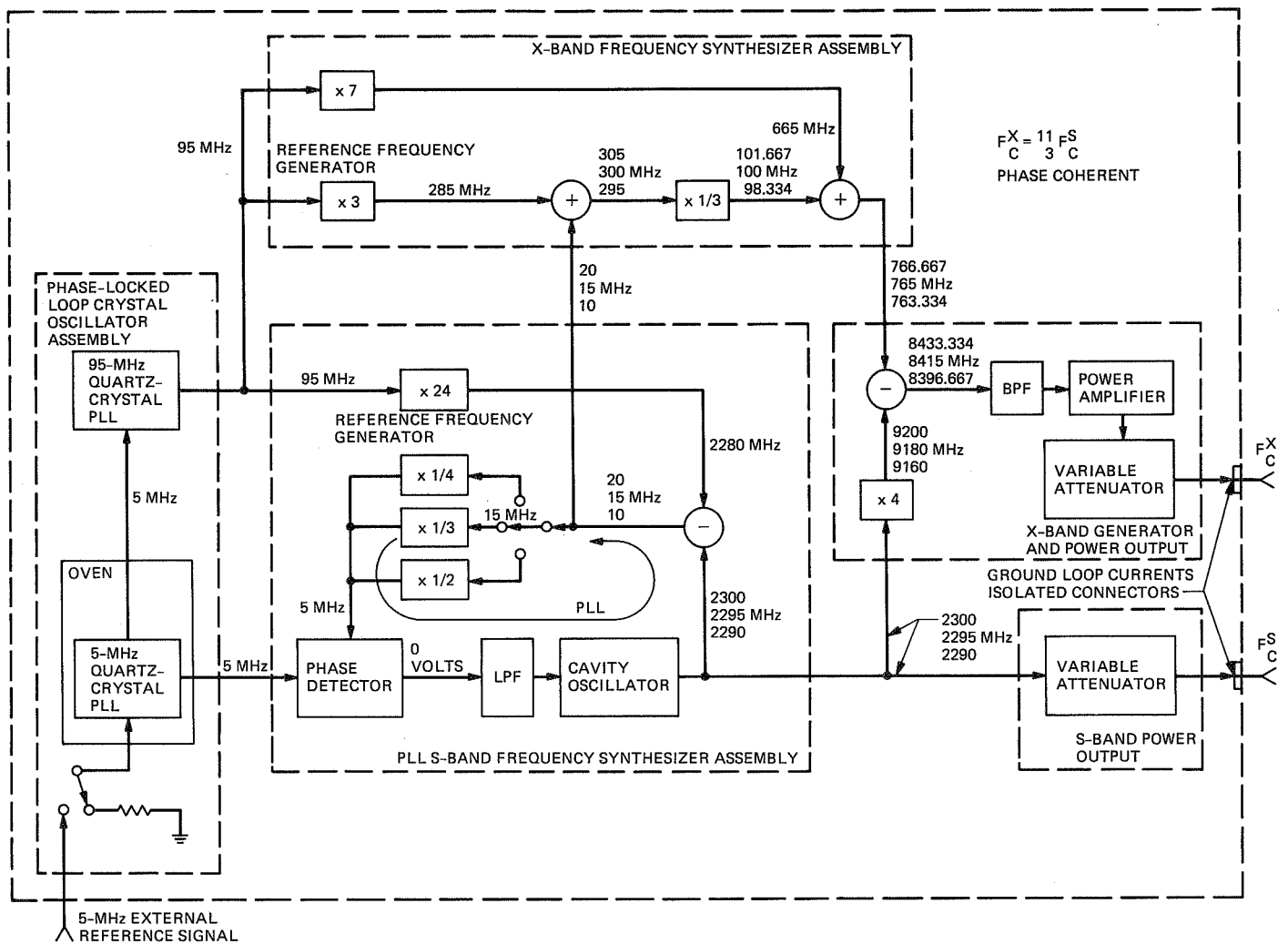


Fig. 7. S-/X-band Test Transmitter test instrumentation.

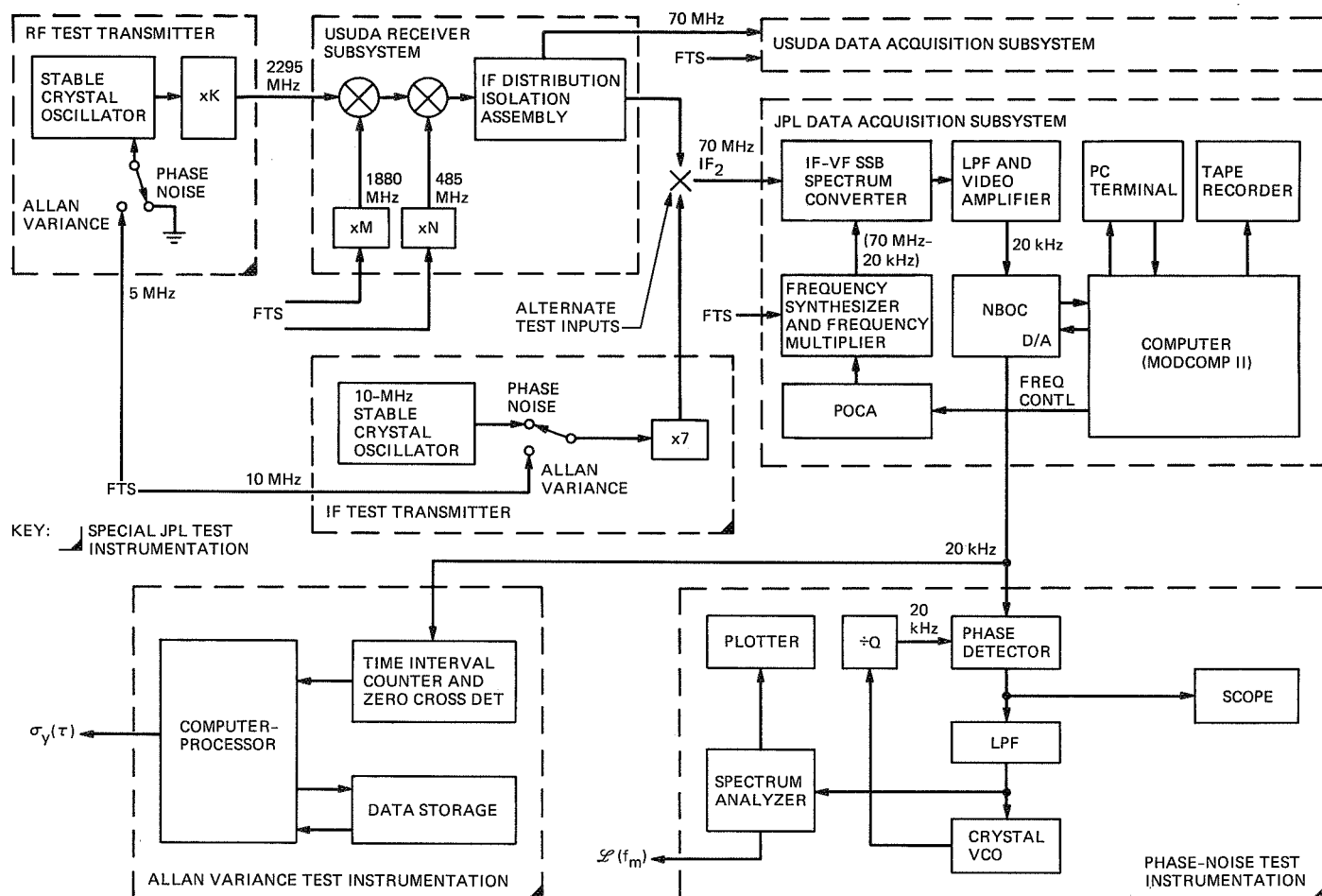


Fig. 8. Usuda test methodology and instrumentation.

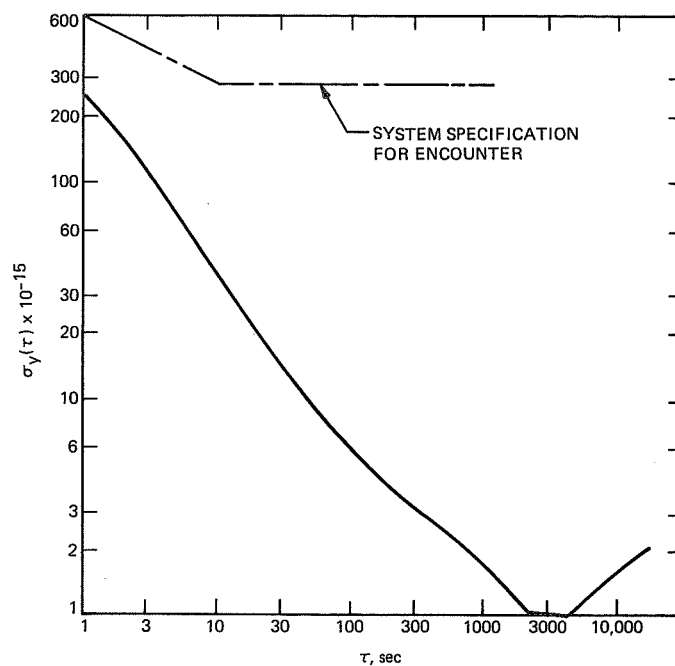


Fig. 9. Allan variance measurement of two hydrogen-maser frequency standards at CDSCC.

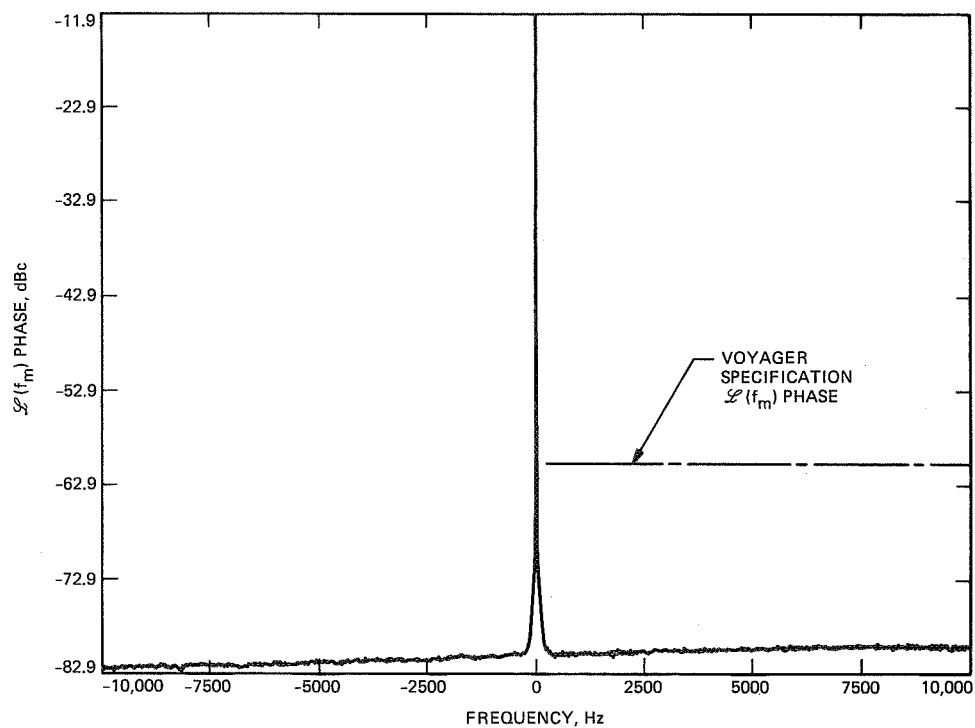


Fig. 10(a). Noise-power spectral density of two hydrogen masers at CDSCC, -10,000 to +10,000 Hz (center frequency = 10 GHz).

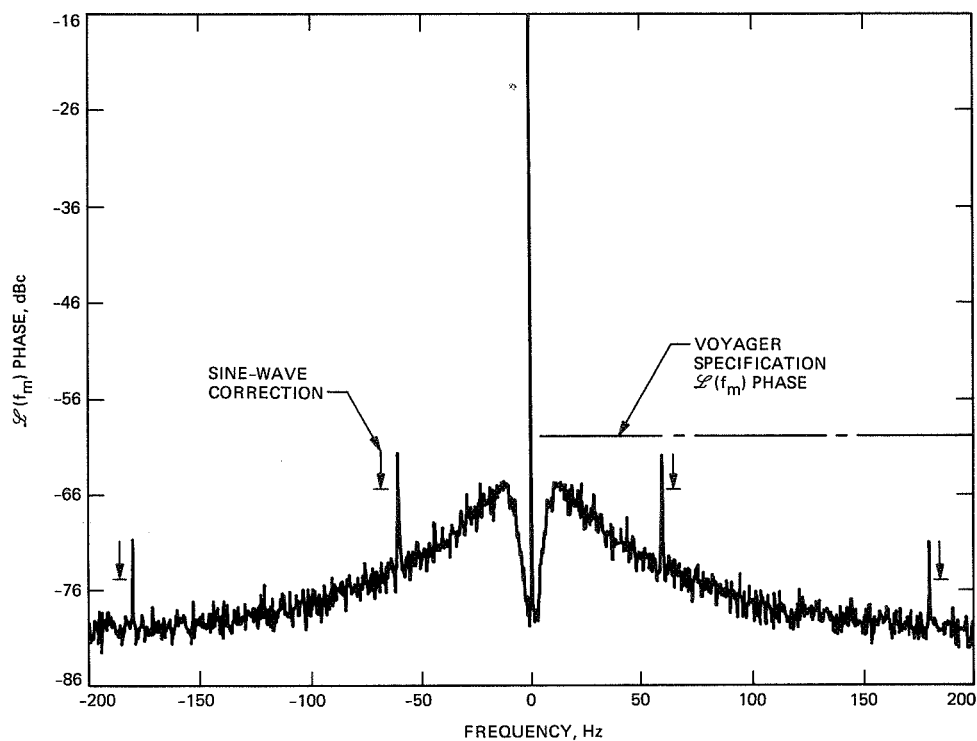


Fig. 10(b). Noise-power spectral density of two hydrogen masers at CDSCC, -200 to +200 Hz (center frequency = 10 GHz).

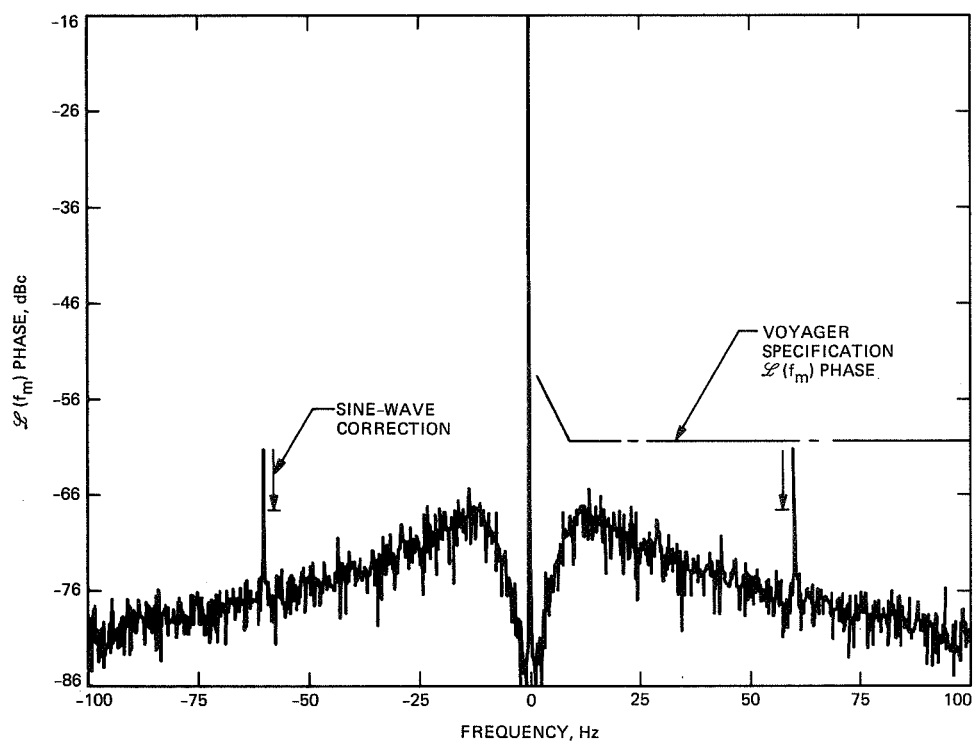


Fig. 10(c). Noise-power spectral density of two hydrogen masers at CDSCC, -100 to +100 Hz (center frequency = 10 GHz).

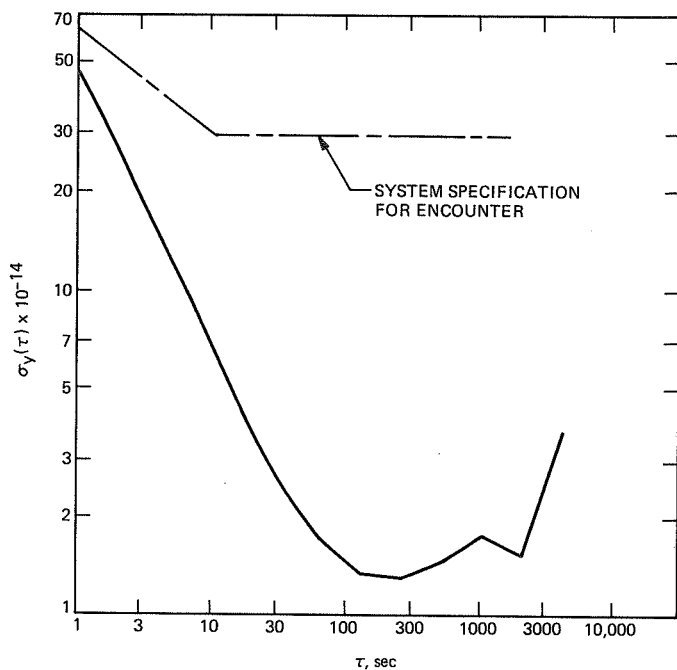


Fig. 11. Allan variance measurement of DSS-43 Radio Science System at X-band (Test Transmitter locked to PCG, 20 MHz \times 1/4).

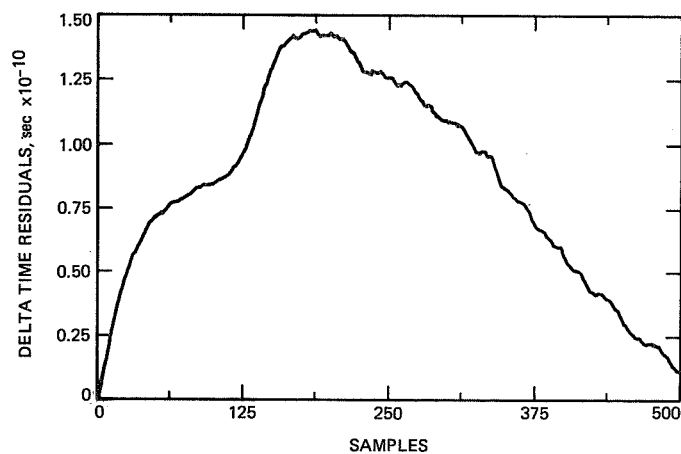


Fig. 12. Allan variance time-residual plot of CDSCC hydrogen masers.

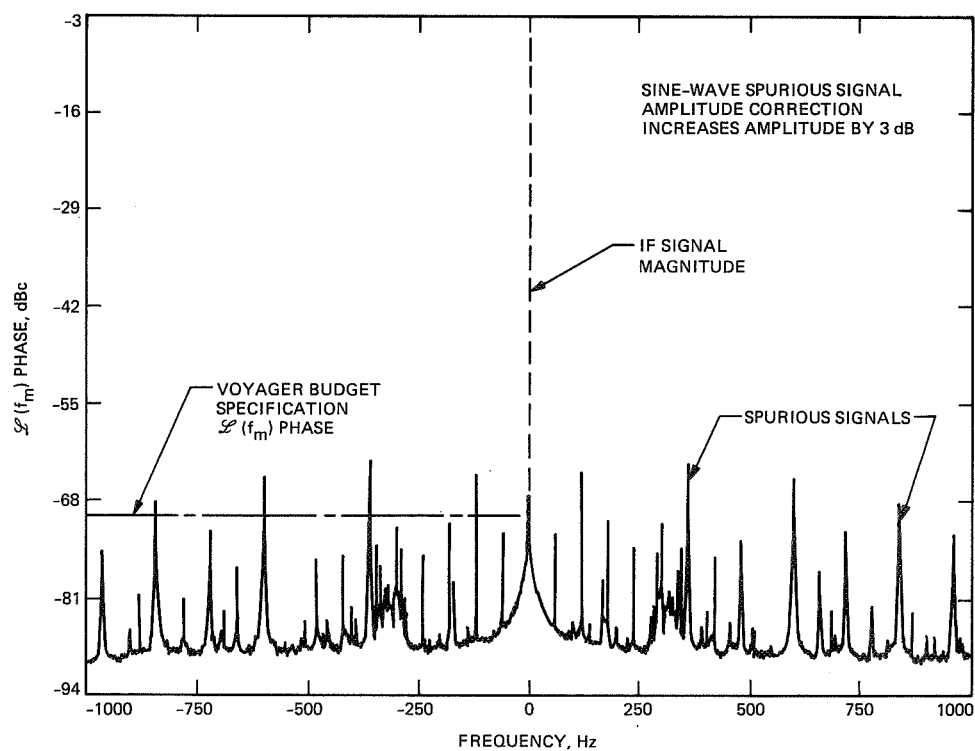


Fig. 13. Phase-noise spectral density of SPC-40 radio science IF-VF converter (Dana POCA as second LO).

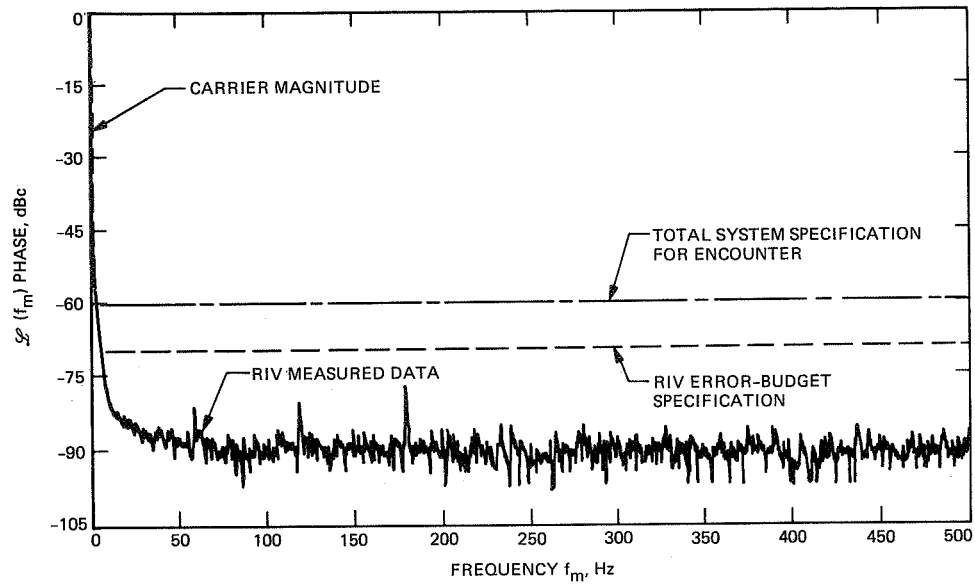


Fig. 14. Noise-power spectral density of CDSCC radio science IF-VF converter (Fluke 6160 as substitute second LO).

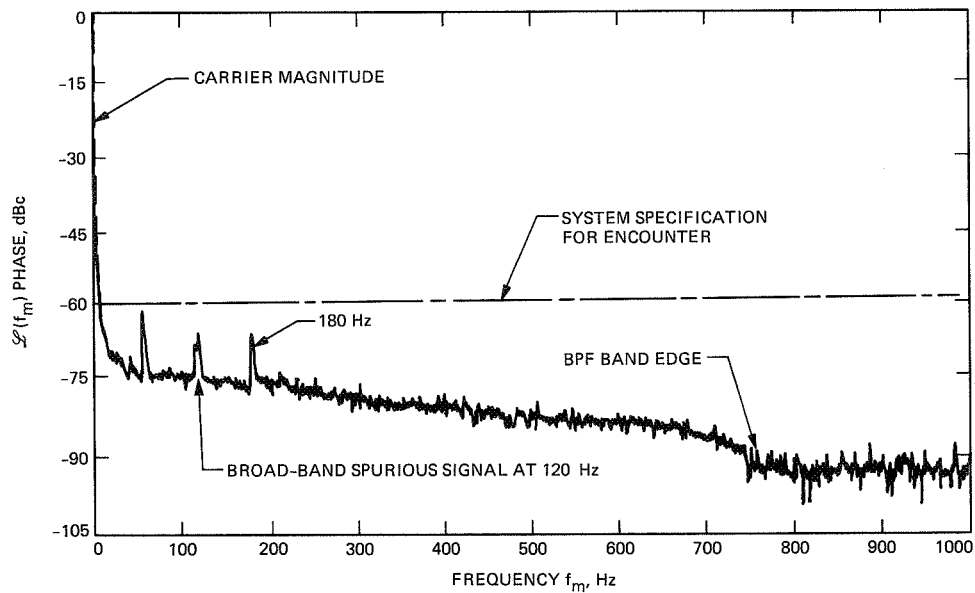


Fig. 15. Noise-power spectral density at X-band, DSS-43 Radio Science System (Fluke 6160 as second LO).

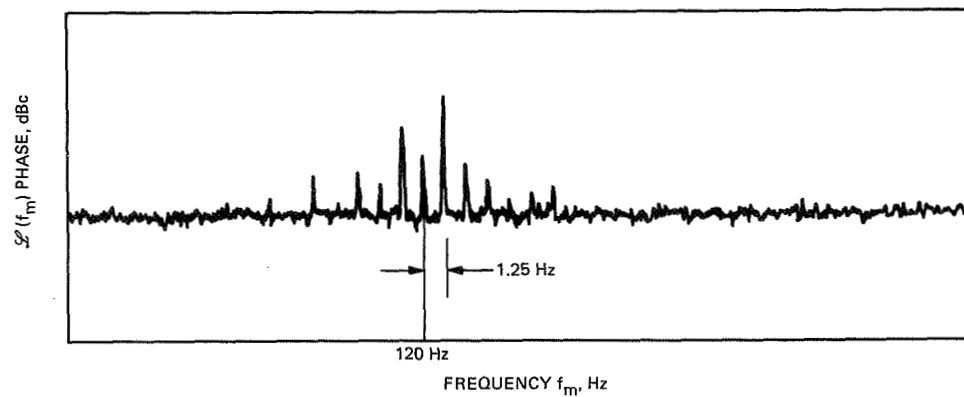


Fig. 16. Unique spurious signal at about 120 Hz, DSS-43 Radio Science System.

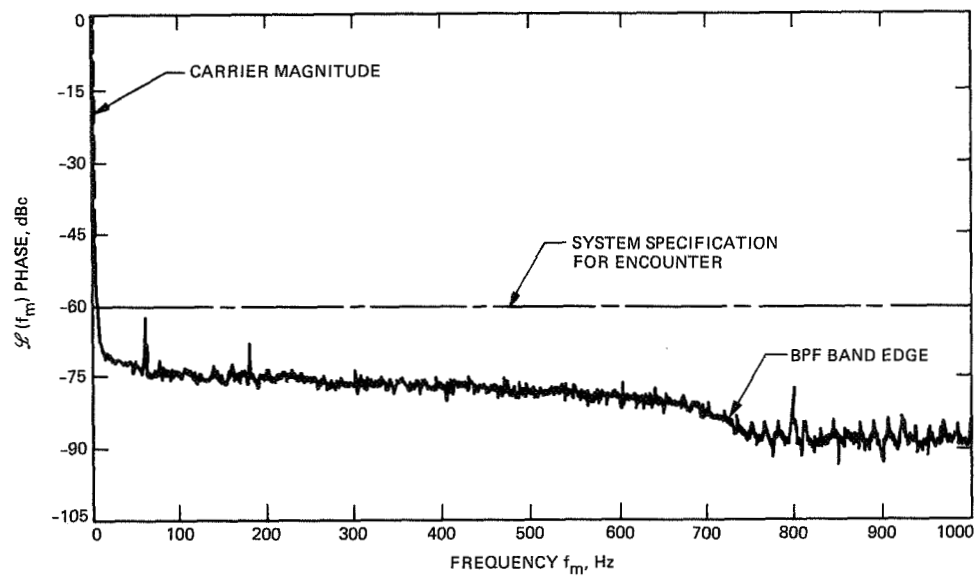


Fig. 17. Noise-power spectral density at X-band, DSS-45 Radio Science System (Fluke 6160 as second LO).

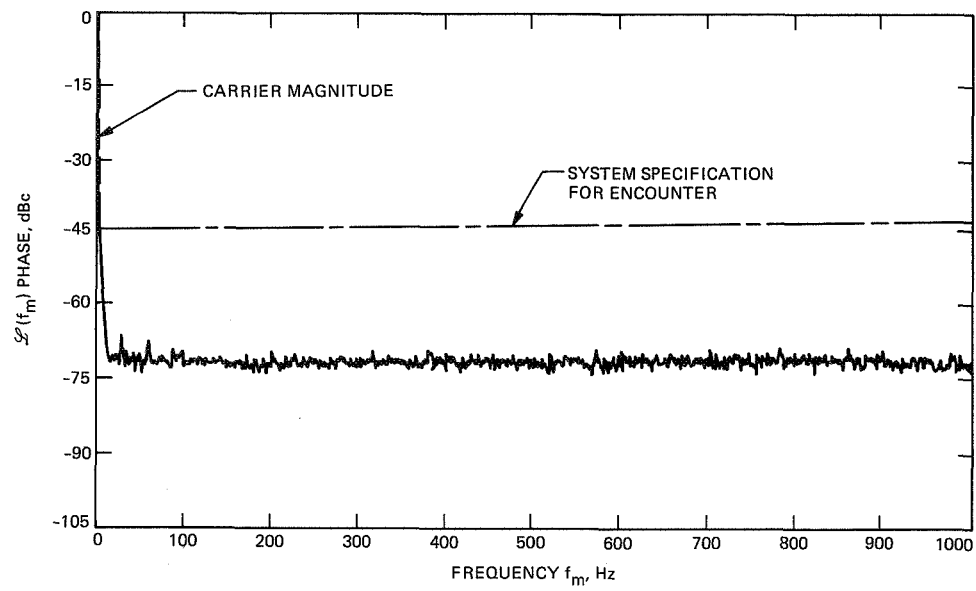


Fig. 18. Noise-power spectral density at S-band, DSS-45 Radio Science System (Fluke 6160 as second LO).

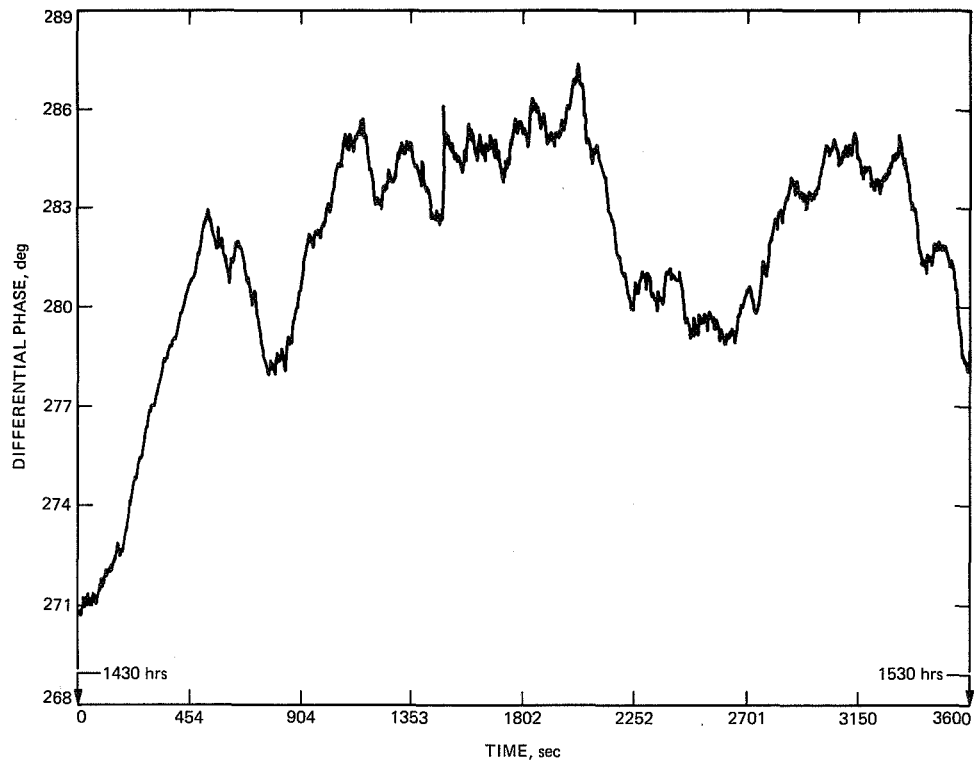


Fig. 19. S-/X-band differential phase stability, DSS-43 Radio Science System.

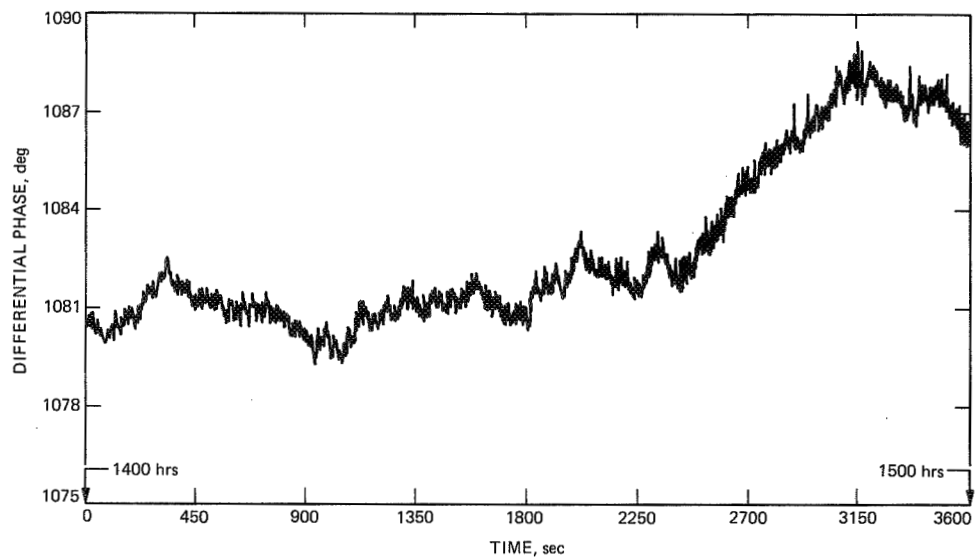


Fig. 20. S-/X-band differential phase stability, DSS-45 Radio Science System.

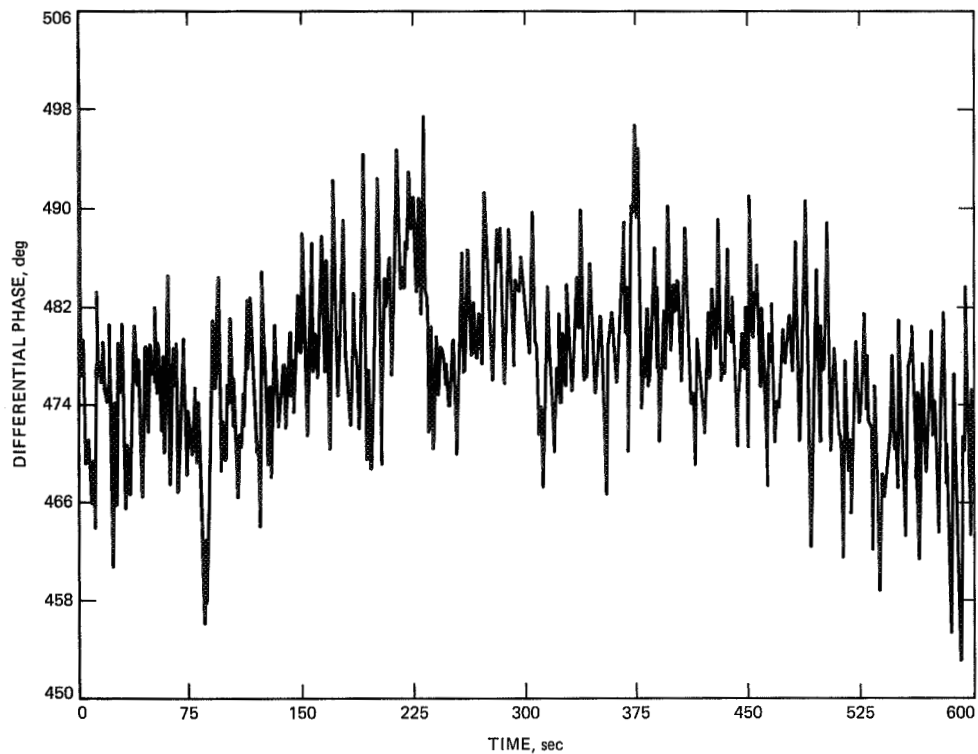


Fig. 21. S-/X-band differential phase stability of DSS-43 Radio Science System with test transmitter signals radiated to the antenna.

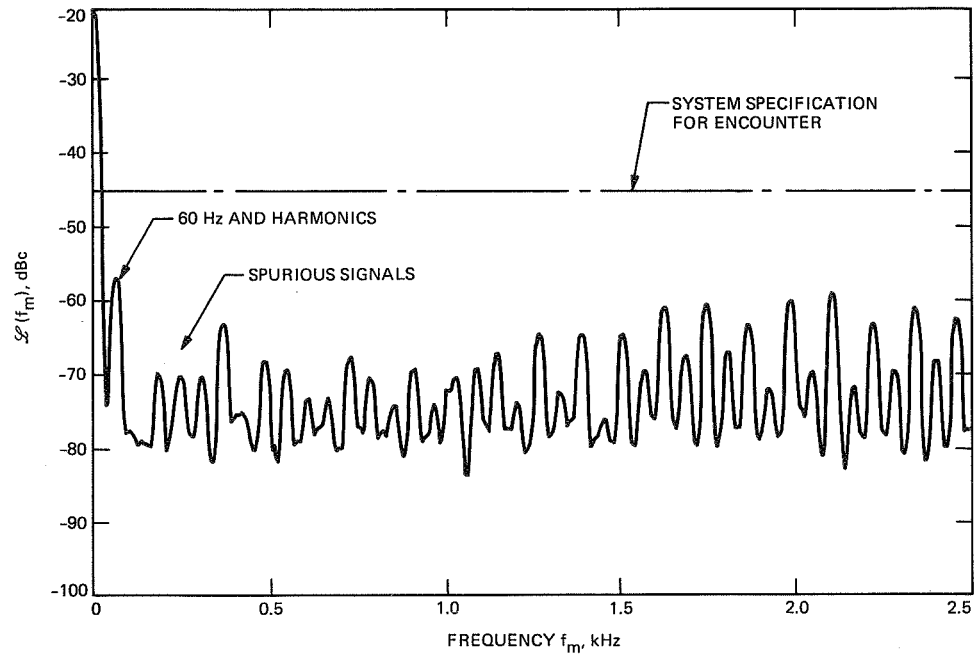


Fig. 22. Spurious signals in phase noise of the JPL DAS at Usuda due to improperly wired power connections.

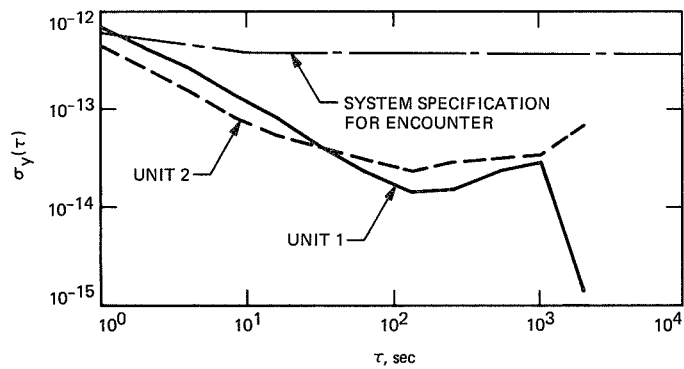


Fig. 23. Allan variance of the Usuda system using two $\times 20$ frequency-multiplier units provided by ISAS.

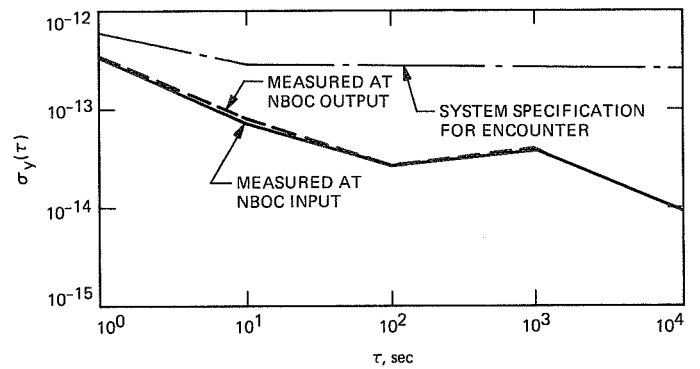


Fig. 24. Allan variance of the Usuda system using the JPL $\times 20$ frequency-multiplier unit, measured at the NBOC input and NBOC output.

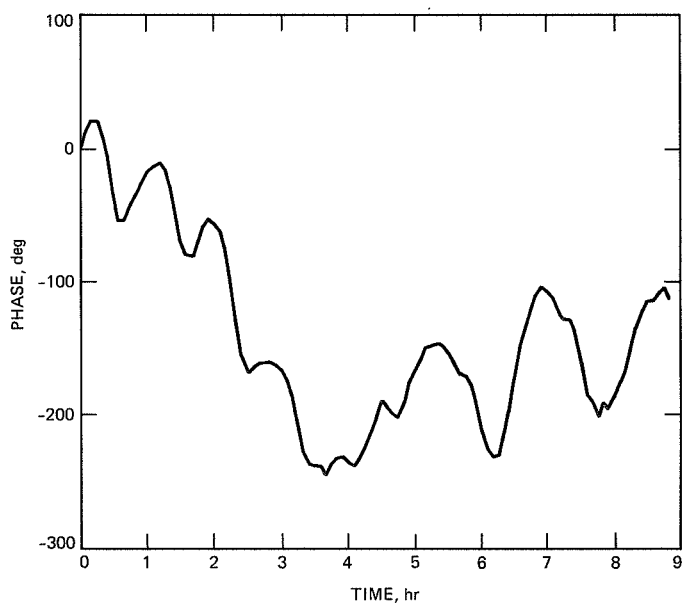


Fig. 25. Phase variation versus time plot, Usuda system, using the JPL $\times 20$ frequency-multiplier unit.

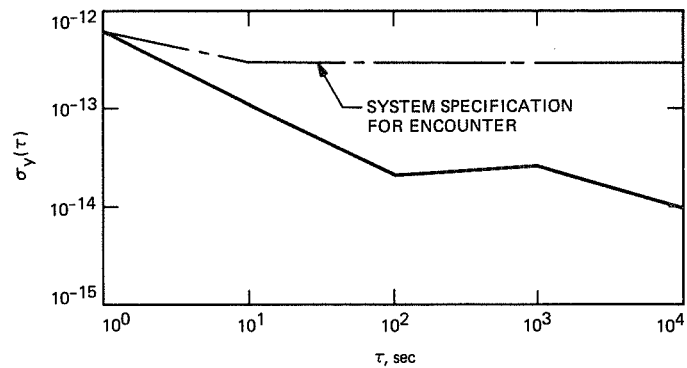


Fig. 26. Repeat measurement of Allan variance, Usuda system, using ISAS Unit 1 $\times 20$ frequency-multiplier unit with temperature measurement.

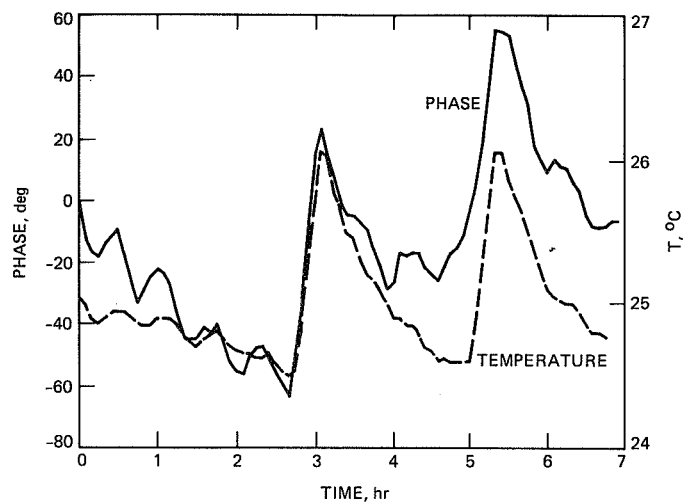


Fig. 27. Phase variation versus time compared to the ISAS $\times 20$ frequency-multiplier unit temperature measurement, Usuda system.

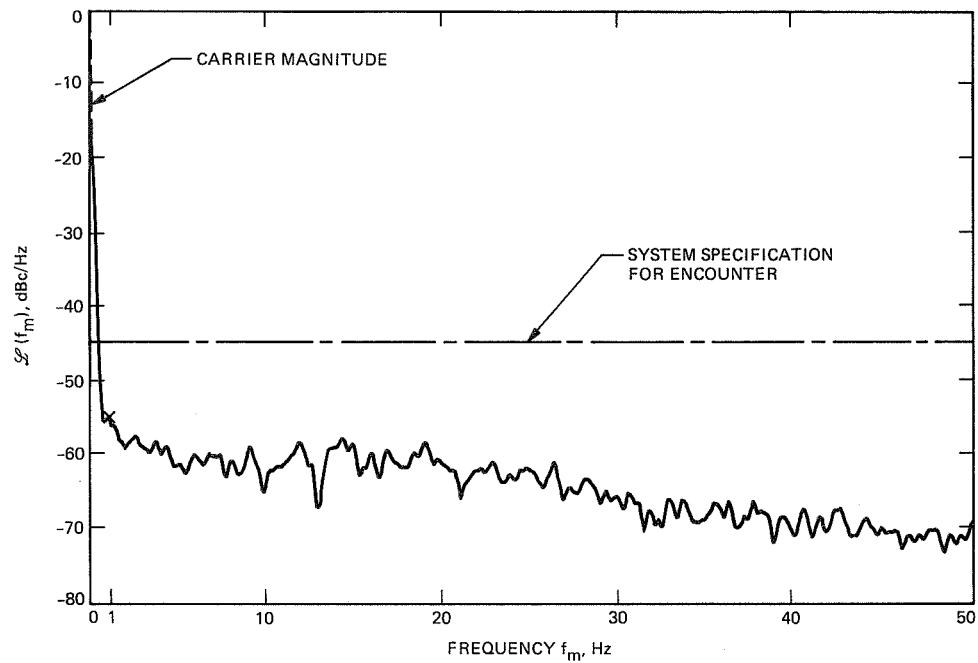


Fig. 28(a). Phase-noise spectral density of the Usuda Radio Science System (0 to 50 Hz, ISAS \times 20 assembly in LO chain).

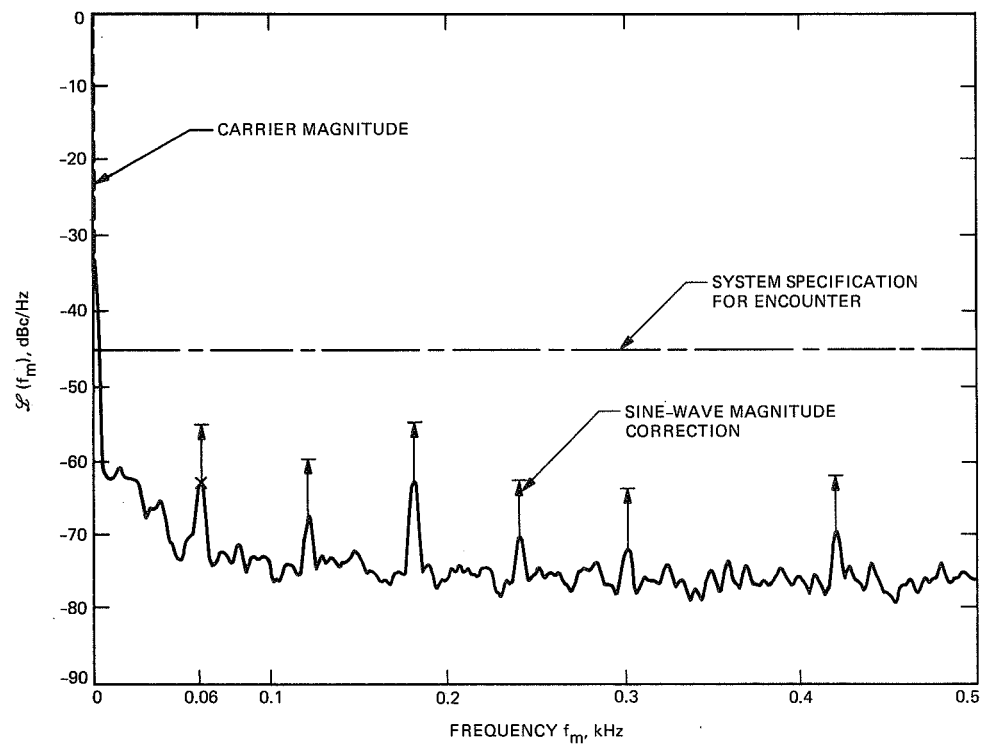


Fig. 28(b). Phase-noise spectral density of the Usuda Radio Science System (0 to 0.5 kHz, ISAS \times 20 assembly in LO chain).

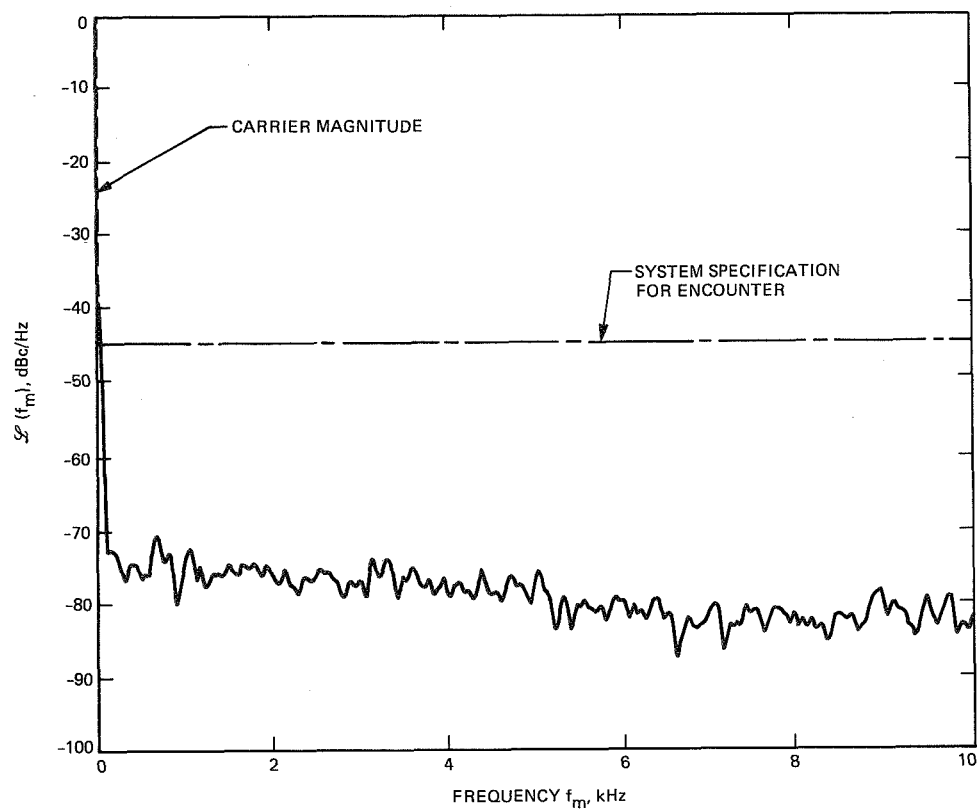


Fig. 28(c). Phase-noise spectral density of the Usuda Radio Science System (0 to 10 kHz, ISAS \times 20 assembly in LO chain).

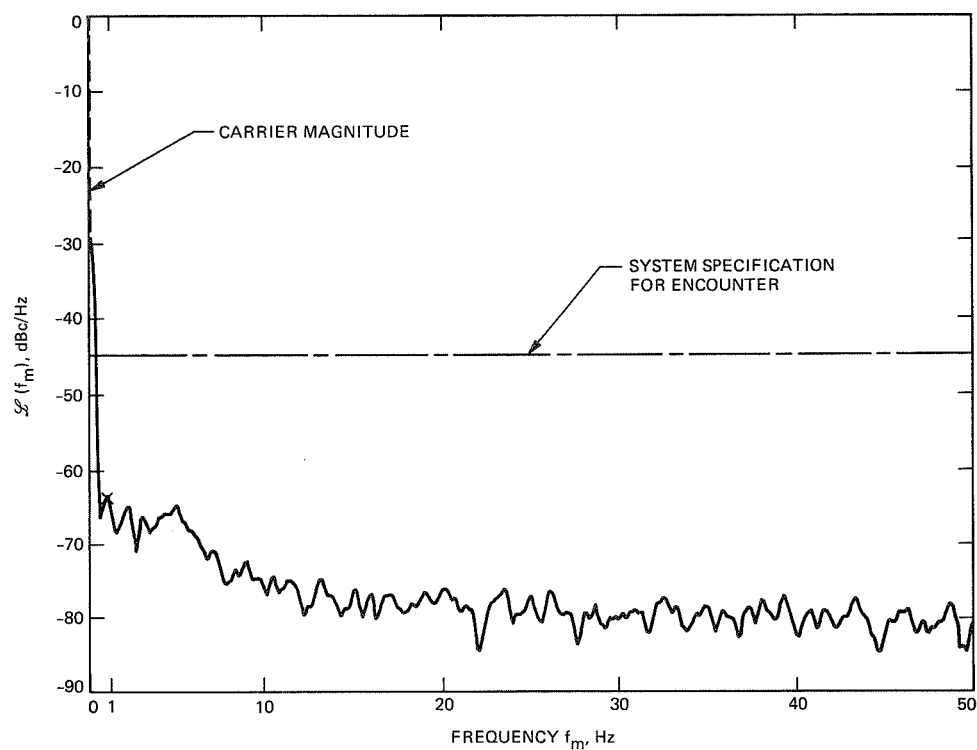


Fig. 29(a). Phase-noise spectral density of the Usuda Radio Science System (0 to 50 Hz, JPL \times 20 assembly in LO chain).

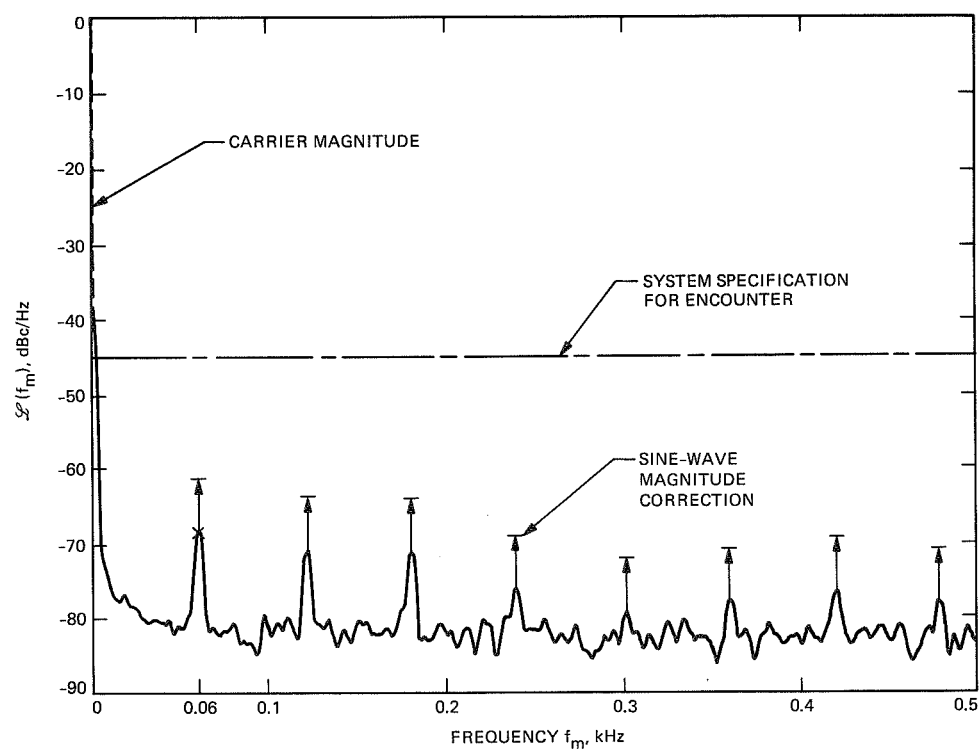


Fig. 29(b). Phase-noise spectral density of the Usuda Radio Science System (0 to 0.5 kHz, JPL \times 20 assembly in LO chain).

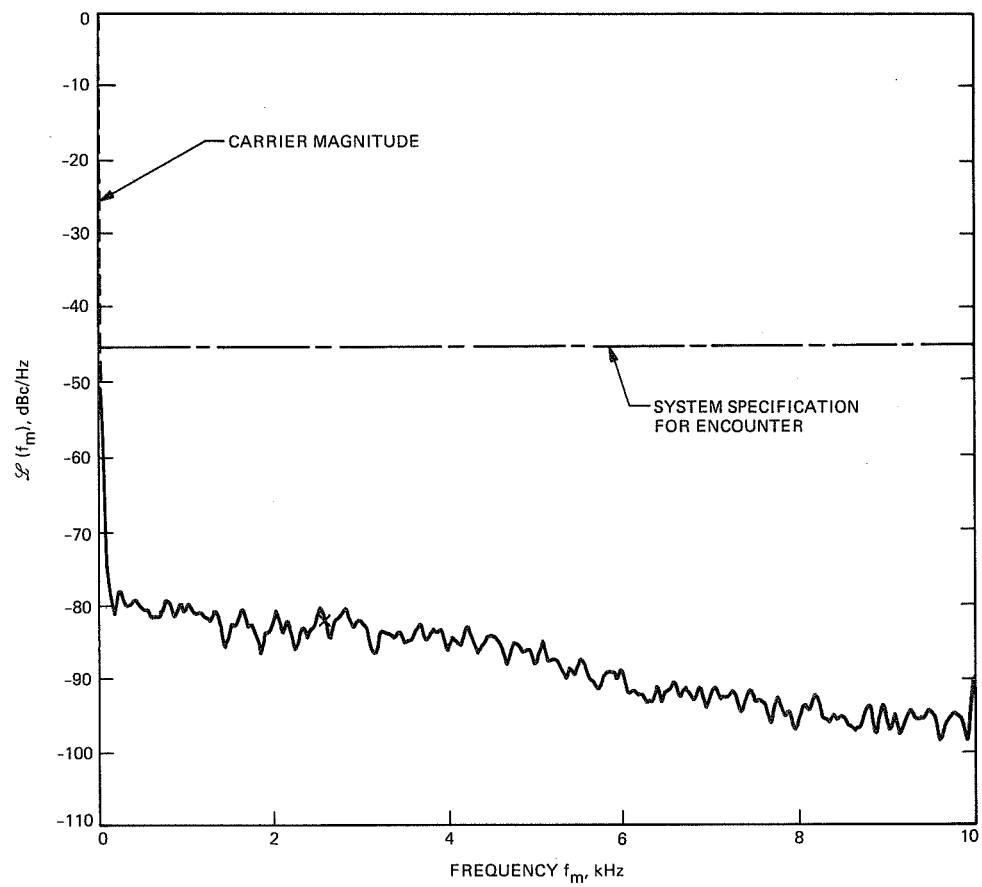


Fig. 29(c). Phase-noise spectral density of the Usuda Radio Science System (0 to 10 kHz, JPL \times 20 assembly in LO chain).

529-17
218084
13

N 8 9 - 2 7 9 0 0

Accuracy of Telemetry Signal Power Loss in a Filter as an Estimate for Telemetry Degradation

M. A. Koerner

Telecommunications Systems Section

When telemetry data is transmitted through a communication link, some degradation in telemetry performance occurs as a result of the imperfect frequency response of the channel. The term telemetry degradation as used in this article is the increase in received signal power required to offset this filtering. The usual approach to assessing this degradation is to assume that it is equal to the signal power loss in the filtering, which is easily calculated. However, this approach neglects the effects of the nonlinear phase response of the filter, the effect of any reduction of the receiving system noise due to the filter, and intersymbol interference. This article compares an "exact" calculation of the telemetry degradation, which includes all of the above effects, with the signal power loss calculation for RF filtering of NRZ data on a carrier. The signal power loss calculation is found to be a reasonable approximation when the filter follows the point at which the receiving system noise is introduced, especially if the signal power loss is less than 0.5 dB. The signal power loss approximation is less valid when the receiving system noise is not filtered.

I. Introduction

When telemetry data is transmitted through a communication link, some degradation in telemetry performance occurs as a result of the imperfect frequency response of the channel. The term telemetry degradation as used in this article is the increase in received signal power required to offset this filtering. The usual approach to assessing this degradation is to assume that it is equal to the signal power loss in the filtering, which is easily calculated.

The disadvantage of this approach is that it neglects some potentially significant effects. First, it neglects the effect of the nonlinear phase response of the filtering. Second, it neglects

the reduction in the effective noise bandwidth of the telemetry detector caused by the filtering when the filtering follows the point at which the receiving system noise is introduced. This reduction in effective noise bandwidth normally offsets a portion of the telemetry degradation caused by the signal distortion. Finally, it neglects the intersymbol interference which occurs when the duration of the channel impulse response is greater than the duration of a telemetry symbol.

This article assesses the accuracy of approximating telemetry degradation by signal power loss for a telemetry channel in which uncoded non-return-to-zero (NRZ) data directly phase-modulate a carrier at a modulation level less than 90

degrees, and the resulting signal is distorted by a band-pass filter. In the receiving system a discrete carrier-tracking phase-locked loop tracks the carrier component of the received signal and coherently demodulates the telemetry data stream. The bits in the telemetry data stream are detected by an integrate-and-dump circuit, which would be a matched filter for undistorted bits, followed by a decision device which decides a 0 was transmitted if the integrate-and-dump circuit output is positive at the end of a bit transmission and a 1 was transmitted if the integrate-and-dump circuit output is negative at the end of a bit transmission. An analysis of such a system was described previously in [1]. For this article, the analysis of [1] is considered "exact"; however, that analysis does contain some approximations. The most important of these is the assumption that the bit-synchronizer timing is always adjusted to minimize the telemetry degradation.

This article compares the telemetry degradation calculated using the "exact" method of [1] with the corresponding signal power loss in the band-pass filter as a function of the band-pass filter 3-dB bandwidth. Results are presented here for band-pass filters whose low-pass equivalents are

- (1) a single-pole filter
- (2) a five-pole Butterworth filter
- (3) a five-pole Tchebychev filter with 0.5-dB ripple factor, and
- (4) a five-pole Bessel or linear-phase filter

In each case the filter resonant frequency is equal to the carrier frequency and the 3-dB bandwidth of the band-pass filter is varied between one and seven times the telemetry channel data rate. For each filter, the signal power loss is compared with the "exact" telemetry degradation, calculated using the analysis of [1], for the four possible combinations of

- (1) telemetry degradation considering only signal distortion,
- (2) telemetry degradation considering both signal distortion and noise bandwidth reduction,

and

- (1) a 10^{-3} allowable bit error probability, and
- (2) a 10^{-5} allowable bit error probability

Note that the telemetry degradation estimate which considers only signal distortion is the valid estimate when the filtering precedes the point at which the receiving system noise is introduced, while the telemetry degradation estimate which considers both the signal distortion and the noise bandwidth

reduction is appropriate when the filtering follows the point at which the receiving system noise is introduced.

II. Calculation of Signal Power Loss in a Filter

The normal approach to calculating the power loss in a filter is to integrate the product of the power spectral density of the input signal and the square of the filter amplitude response over all frequencies. The ratio of this integral to the input signal power is the factor by which the filter reduces the available signal power. As this integration is usually performed numerically, errors occur as a result of the finite step size and limits of the integration.

For the types of filters considered in [1], a closed-form solution for the signal power loss in the filter can be obtained. This approach avoids the problem of selecting an integration step size and integration limits that reduce the integration error to an acceptable value. The analysis of [1] assumes that the filter has only N simple poles and a finite response Q_0 at infinite frequency, and that the filter pole locations and the residues at these poles are known. P_k was the k th pole and Q_k was the residue at that pole. Under these circumstances, the filter impulse response will be

$$h(\tau) = Q_0 \delta(\tau) + \sum_{k=1}^N Q_k \exp(P_k \tau) \quad (1)$$

where $\delta(\tau)$ is the Dirac delta function.

For NRZ telemetry data directly phase modulated on a carrier, the input to the filter will have the form

$$x(t) = d(t) 2^{1/2} \sin(\omega t + \phi)$$

where $d(t)$ is a sequence of statistically independent, equiprobable ± 1 -valued symbols of equal duration T , and ω and ϕ are the carrier frequency and phase. As long as ϕ is statistically independent of $d(t)$, the autocorrelation function of the input signal will be

$$R_x(\tau) = R_d(\tau) \cos(\omega \tau) \quad (2)$$

where

$$R_d(\tau) = \begin{cases} 1 - \frac{|\tau|}{T}, & |\tau| < T \\ 0, & |\tau| > T \end{cases} \quad (3)$$

is the autocorrelation function of the NRZ symbol stream. As the filter input signal has unit power, the factor by which the filter reduces the signal power will be

$$\overline{y^2(t)} = \int_0^\infty \int_0^\infty d\tau_1 d\tau_2 h(\tau_1) h(\tau_2) R_x(\tau_2 - \tau_1) \quad (4)$$

where

$$y(t) = \int_0^\infty h(\tau) x(t - \tau) d\tau$$

is the filter output.

Now define $g(\tau)$ such that

$$h(\tau) = Q_0 \delta(\tau) + g(\tau) \quad (5)$$

where

$$\lim_{\tau \rightarrow \infty} g(\tau) = 0 \quad (6)$$

Then, using Eq. (5) in Eq. (4) and simplifying where possible,

$$\begin{aligned} \overline{y^2(t)} &= Q_0^2 R_x(0) + 2Q_0 \int_0^\infty g(\tau) R_x(\tau) d\tau \\ &\quad + 2 \int_0^\infty d\tau_1 \int_{\tau_1}^\infty d\tau_2 g(\tau_1) g(\tau_2) R_x(\tau_2 - \tau_1) \end{aligned}$$

Now, using Eqs. (2) and (3) and again simplifying where possible,

$$\begin{aligned} \overline{y^2(t)} &= Q_0^2 + 2Q_0 \int_0^T g(\tau) \left(1 - \frac{\tau}{T}\right) \cos(\omega\tau) d\tau \\ &\quad + 2 \int_0^T du \int_0^\infty d\tau g(\tau) g(\tau + u) \left(1 - \frac{u}{T}\right) \cos(\omega u) \end{aligned} \quad (7)$$

Note that in Eq. (7) the only restriction on $g(\tau)$ is that of Eq. (6).

At this point, examining Eqs. (1) and (5), it is found that

$$g(\tau) = \sum_{k=1}^N Q_k \exp(P_k \tau) \quad (8)$$

is the form of $g(\tau)$ of interest here. Substituting Eq. (8) in Eq. (7) yields, after some algebraic manipulation,

$$\begin{aligned} \overline{y^2(t)} &= Q_0^2 - \sum_{h=1}^N Q_h \left[Q_0 - \sum_{k=1}^N \frac{Q_k}{(P_h + P_k)} \right] \\ &\quad \times \left[\frac{1}{P_h + i\omega} \left(1 + \frac{1 - \exp[(P_h + i\omega)T]}{(P_h + i\omega)T} \right) \right. \\ &\quad \left. + \frac{1}{P_h - i\omega} \left(1 + \frac{1 - \exp[(P_h - i\omega)T]}{(P_h - i\omega)T} \right) \right] \end{aligned} \quad (9)$$

Examining Eq. (2), one notes that by setting ω equal to zero in Eq. (9) one obtains the signal power loss factor for direct filtering of the baseband telemetry stream. Setting ω equal to zero in Eq. (9) yields

$$\begin{aligned} \overline{y^2(t)} &= Q_0^2 - 2 \sum_{h=1}^N \left(\frac{Q_h}{P_h} \right) \left[Q_0 - \sum_{k=1}^N \frac{Q_k}{(P_h + P_k)} \right] \\ &\quad \left[1 + \frac{1 - \exp(P_h T)}{P_h T} \right] \end{aligned} \quad (10)$$

For particular cases Eqs. (9) or (10) can be simplified further. For example, for baseband filtering of the telemetry stream by a single-pole filter with unit response at zero frequency and 3-dB bandwidth, $f_0 = \omega_0/(2\pi)$, $N = 1$, $Q_0 = 0$, $Q_1 = \omega_0$, and $P_1 = -\omega_0$, and Eq. (10) simplifies to

$$\overline{y^2(t)} = \frac{\exp(-\omega_0 T) - 1 + \omega_0 T}{\omega_0 T}$$

However, for more complex cases it is usually simpler to evaluate Eqs. (9) or (10) numerically using complex arithmetic.

III. Numerical Results

Figures 1 through 4 of this article show telemetry degradation for a 100-kbps telemetry channel as a function of the band-pass filter 3-dB bandwidth for four different types of band-pass filters.

- (1) Figure 1 shows results for a band-pass filter whose low-pass equivalent is a single-pole filter.
- (2) Figure 2 shows results for a band-pass filter whose low-pass equivalent is a five-pole Butterworth filter.
- (3) Figure 3 shows results for a band-pass filter whose low-pass equivalent is a five-pole Tchebychev filter with 0.5-dB ripple factor.
- (4) Figure 4 shows results for a band-pass filter whose low-pass equivalent is a five-pole Bessel or linear-phase filter.

In each case the number of band-pass filter poles is twice the number of poles in its low-pass equivalent.

In Figs. 1 through 4, telemetry degradation is plotted as a function of the band-pass filter 3-dB bandwidth for five different methods of calculating the degradation. For the curve labeled SIGNAL POWER LOSS the telemetry degradation is assumed to be the factor by which the band-pass filter reduces the available signal power. This was calculated using the equations derived in the preceding section. The other four telemetry degradation curves in these figures were calculated using the analysis described in [1]. The curves labeled $P_B = 10^{-3}$, SIGNAL FILTERED and $P_B = 10^{-5}$, SIGNAL FILTERED assume the band-pass filter precedes the point at which the receiving system noise is introduced. Thus, the filter distorts the signal, but does not affect the receiving system noise. These curves are appropriate for band-pass filtering in the transmit section of a communication link. The curves labeled $P_B = 10^{-3}$, SIGNAL AND NOISE FILTERED and $P_B = 10^{-5}$, SIGNAL AND NOISE FILTERED assume the band-pass filter follows the point at which the receiving system noise is introduced and therefore filters both signal and noise. These curves are appropriate for band-pass filters within the receiving system. In each case the 10^{-3} or 10^{-5} refers to the allowable bit error probability.

The results in Fig. 1 are for a band-pass filter whose low-pass equivalent has a single pole. For small degradations the SIGNAL POWER LOSS curve lies between the two SIGNAL FILTERED curves and the two SIGNAL AND NOISE FILTERED curves. The choice of allowable bit error probability makes some difference, but not a large difference. At 700-kHz 3-dB bandwidth, seven times the bit rate, the SIGNAL AND NOISE FILTERED curve degradations are about 0.1 dB, the SIGNAL POWER LOSS curve degradation is about 0.2 dB, and the SIGNAL FILTERED curve degradations are about 0.3 dB. The degradation estimate based on signal power loss is conservative for band-pass filtering in the receiver, but is optimistic for band-pass filtering in the transmitter.

The results in Fig. 2 are for a band-pass filter whose low-pass equivalent is a five-pole Butterworth filter. In this case the SIGNAL POWER LOSS curve agrees reasonably well with the SIGNAL AND NOISE FILTERED curves for small degradations. The degradations for the SIGNAL FILTERED curves are appreciably worse than that for the other curves. At 700-kHz 3-dB bandwidth, seven times the 100-kbps bit rate, the degradations for the SIGNAL POWER LOSS and SIGNAL AND NOISE FILTERED curves are about 0.15 dB, while those for the SIGNAL FILTERED curves are more than 0.1 dB worse.

The results in Fig. 3 are for a band-pass filter whose low-pass equivalent is a five-pole Tchebychev filter with 0.5-dB ripple factor. As in the five-pole Butterworth case, the agreement between the SIGNAL POWER LOSS and SIGNAL AND NOISE FILTERED curves appears reasonable for small degradations. However, the absolute degradations and the difference between the SIGNAL FILTERED curves and the other three curves are greater for the Tchebychev case than the Butterworth case shown in Fig. 2. At 700-kHz 3-dB bandwidth, seven times the 100-kbps bit rate, the degradations for the SIGNAL POWER LOSS and SIGNAL AND NOISE FILTERED curves are 0.2 to 0.25 dB, while those for the SIGNAL FILTERED curves are about 0.45 dB.

The results in Fig. 4 are for a band-pass filter whose low-pass equivalent is a five-pole Bessel or linear-phase filter. The data in Fig. 4 resemble those in Fig. 1, the single-pole case, much more than the data in Figs. 2 and 3 for the five-pole Butterworth and Tchebychev cases. For small degradations, the SIGNAL POWER LOSS curve lies about halfway between the SIGNAL AND NOISE FILTERED and SIGNAL FILTERED curves. At 700-kHz 3-dB bandwidth, seven times the 100-kbps bit rate, the degradations are about 0.1 dB for the SIGNAL AND NOISE FILTERED curves, 0.2 dB for the SIGNAL POWER LOSS curve, and 0.3 dB for the SIGNAL FILTERED curves.

IV. Conclusion

Figures 1 through 4 show that, for situations where the filtering follows the point at which the receiving system noise is introduced, the signal power loss is a reasonable estimate of the telemetry degradation. The approximation is most appropriate when the signal power loss is less than 0.5 dB. The approximation is also better for filters whose low-pass equivalent is a five-pole Butterworth or Tchebychev filter than for a filter whose low-pass equivalent is a single-pole or five-pole Bessel filter. When the filtering occurs before the point at which the receiving system noise is introduced, such as filtering in the transmitter, the signal power loss is a less accurate estimate of the telemetry degradation.

Reference

- [1] M. A. Koerner, "Effect of RF Filtering on the Performance of Uncoded PCM/PM Telemetry Channels," *TDA Progress Report 42-77*, vol. January-March 1984, Jet Propulsion Laboratory, Pasadena, California, pp. 104-125, May 15, 1984.

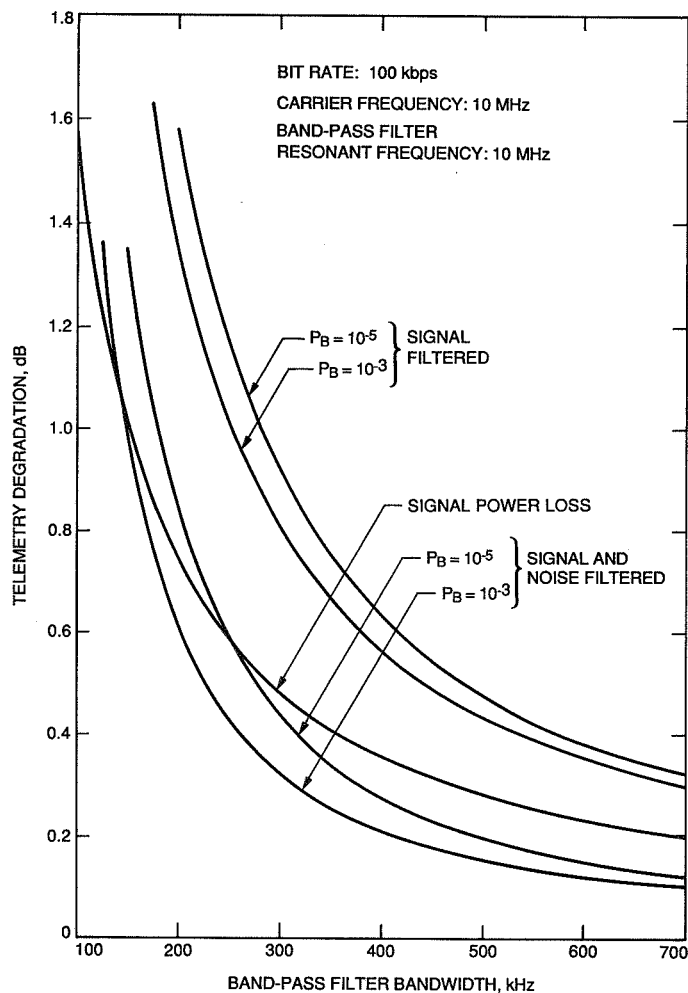


Fig. 1. Comparison of "exact" telemetry degradation and signal power loss for a band-pass filter whose low-pass equivalent is a single-pole filter.

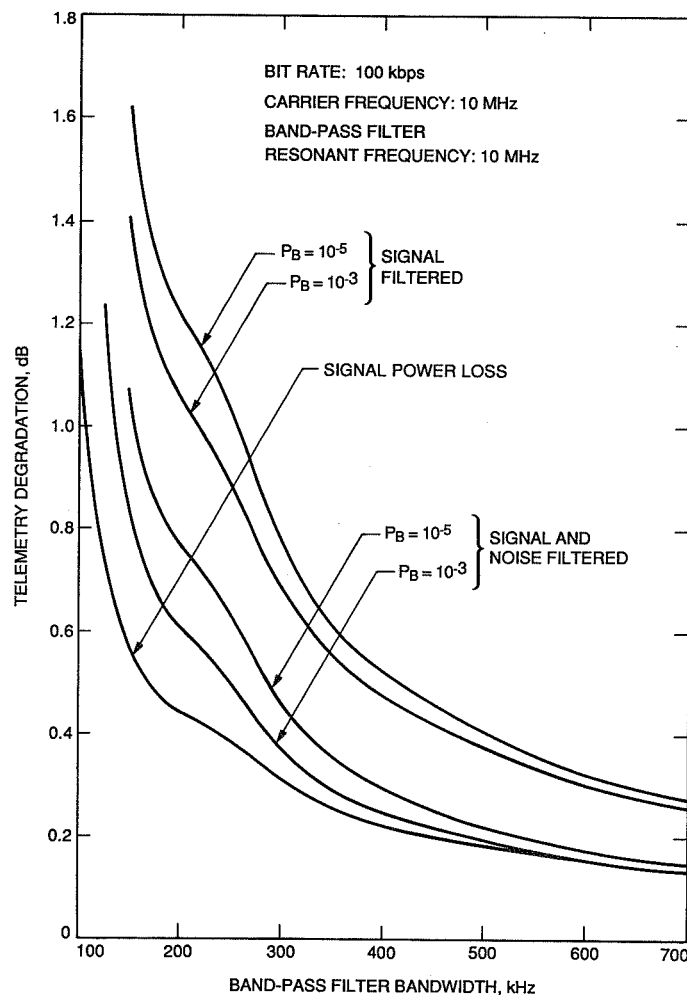


Fig. 2. Comparison of "exact" telemetry degradation and signal power loss for a band-pass filter whose low-pass equivalent is a five-pole Butterworth filter.

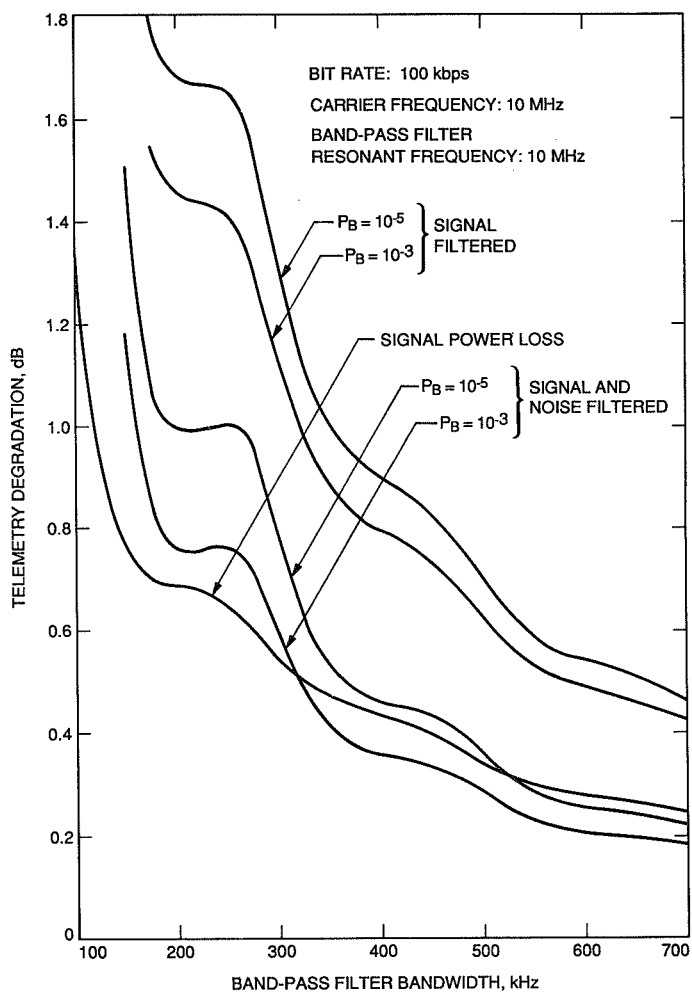


Fig. 3. Comparison of "exact" telemetry degradation and signal power loss for a band-pass filter whose low-pass equivalent is a five-pole Tchebychev filter with a 0.5-dB ripple factor.

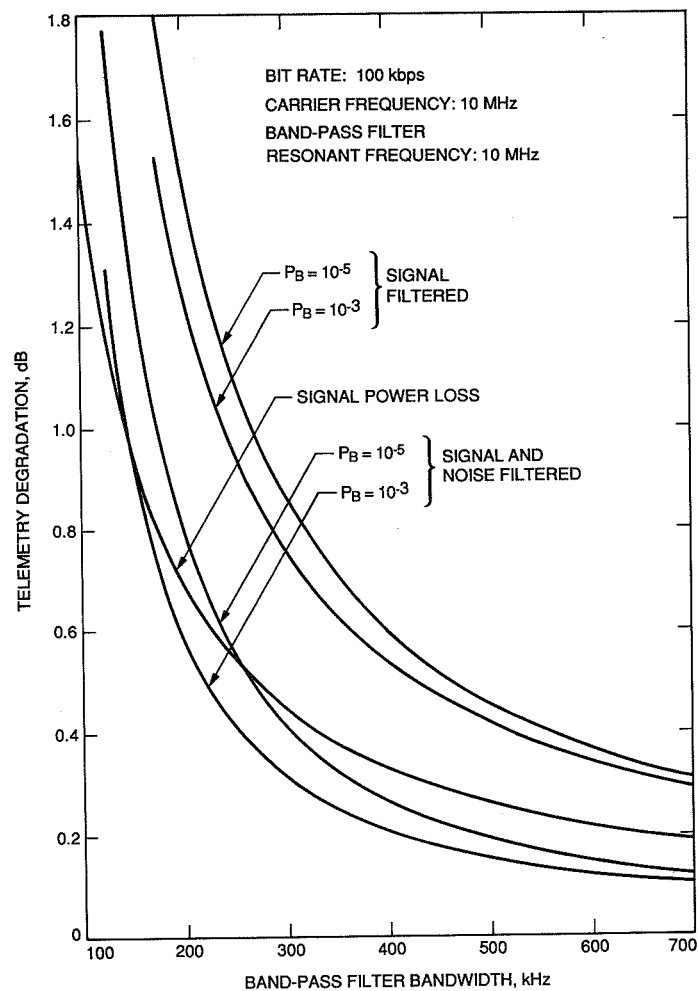


Fig. 4. Comparison of "exact" telemetry degradation and signal power loss for a band-pass filter whose low-pass equivalent is a five-pole Bessel or linear-phase filter.

530-33
218085

N 8 9 - 2 7 9 0 1

The DSS-14 C-Band Exciter

D. R. Rowan

Radio Frequency and Microwave Subsystems Section

The development and implementation of a C-band exciter for use with the Block IV Receiver-Exciter Subsystem at Deep Space Station 14 (DSS-14) has been completed. The exciter supplements the standard capabilities of the Block IV system by providing a drive signal for the C-band transmitter while generating coherent translation frequencies for C-band (5-GHz) to S-band (2.2- to 2.3-GHz) Doppler extraction, C-band to L-band (1.6-GHz) zero delay measurements, and a level calibrated L-band test signal. Exciter functions are described, and a general explanation and description of the C-band uplink controller is presented.

I. Introduction

The C-band (5-GHz) exciter was developed to function with the Block IV Receiver-Exciter Subsystem and L-band (1.6-GHz) to S-band (2.2- to 2.3-GHz) upconverter to provide two-way C/L-band Doppler and ranging capabilities. Additional requirements concerning ranging calibration and antenna pointing were met with the development of a C- to L-band portable zero delay device and a C-band downconverter assembly.

The overall functionality of the C-band exciter as it interfaces with the Block IV equipment is discussed in Section II and the detailed hardware designs are explained in subsequent sections.

II. C-Band/Block IV Interfaces and Functional Relationships

The C-band exciter was designed to make use of as much of the Block IV capabilities and hardware as possible. Modifications were performed to the various Block IV assemblies

to allow the C-band interfaces to be installed as shown in Fig. 1. These interfaces allow the following Block IV components to be used by the C-band exciter: S-band exciter reference synthesizer, range phase modulator, S-band exciter multiplier chain, S-band Doppler extractor, and programmable attenuator assembly.

The output of the Block IV exciter reference synthesizer, located in the RCV-421 exciter rack, has been routed to the RF drawer assembly (RCV-492) in the combined uplink control rack (TXR-191). During the Block IV mode of operation, the reference signal is passed through a transfer relay and sent back to the Block IV exciter to resume its normal path. During the C-band mode of operation, the reference signal is sent to a distribution amplifier in the RF drawer assembly, which distributes the reference signal to the C-band uplink components and sends the reference back to the Block IV exciter to be multiplied up to S-band. These control relays are activated by the combined C-band uplink controller and are independent of the Block IV receiver-exciter controller.

The Block IV Doppler translator assembly has been modified to route the S-band Doppler reference signal to the C-band

exciter assembly. During Block IV mode, a relay in the C-band exciter returns the signal to the Block IV Doppler translator, where it continues on its normal path. During the C-band mode, the C-band exciter provides a substitute S-band Doppler reference that is coherently derived from the C-band exciter drive signal. The resulting Doppler that is extracted by the Block IV Subsystem is therefore C- to L-band Doppler.

The Block IV programmable attenuator assembly (RCV-481) has been modified to provide input and output switching relays on the S-band attenuator. These relays are controlled by the C-band uplink controller and allow the S-band attenuator to be used to attenuate the L-band coherent test signal from the C-band exciter. During the Block IV mode, the relays are set to allow the normal S-band translator signal from the Block IV Doppler translator to pass through the programmable attenuator. During the C-band mode, the relays pass the L-band test signal through the S-band attenuator before the signal is sent to the Microwave Subsystem. It should be noted that although the control relays are configured via the C-band controller, the attenuation level of the S-band attenuator is controlled via the Block IV receiver-exciter controller and the desired attenuation level must be set through the LMC console or a local terminal attached to the receiver-exciter controller.

The S-band exciter assembly (RCV-441) has been modified to provide an S-band exciter drive output to the C-band exciter. This signal, along with the exciter reference signal from the RF drawer assembly (RCV-492), is used to synthesize the C-band exciter drive signal. Due to the shared configuration between the Block IV and C-band equipment, the S-band drive signal was arranged so that only one exciter (either S-band or C-band) could be operated at a time. This was accomplished by using an existing Block IV control relay in the S-band exciter assembly (RCV-441K3) that functions to turn the S-band exciter drive on and off. In the OFF position, the relay normally terminates the S-band drive signal into a 50-ohm load. The load was removed and the output was routed through an isolator to a port on the side of the S-band exciter assembly. This output feeds the C-band exciter assembly when the S-band exciter drive is turned off at the Block IV controls. It should be noted that this is the only Block IV/C-band interface relay that is not controlled by the C-band controller. It then becomes an operational responsibility to ensure that the S-band exciter drive is in the OFF state before the C-band mode is entered.

III. C-Band Exciter Drive Generation

The C-band exciter uses the Block IV S-band exciter frequency reference, which is $1/116$ the desired C-band exciter frequency (F_c). The frequency multiplication is accomplished

using hardware in both the Block IV and C-band exciter assemblies as shown in Fig. 2.

In the C-band mode, the exciter reference frequency ($F_c/116$) is directed along two paths to the C-band exciter assembly (RCV-130). The first path is through the RF drawer assembly (RCV-492) in the C-band control rack (TXR-191). The exciter reference is passed through a distribution amplifier and sent to the C-band exciter assembly, located in the antenna. The second path is through the S-band exciter multiplication path, where the reference is multiplied by 48 ($48 F_c/116$).

The C-band exciter assembly then takes the reference frequency from the RF drawer assembly, multiplies it by 68, and mixes the results ($68 F_c/116$) with the output from the S-band exciter ($48 F_c/116$), with the sum of the two frequencies (F_c) being selected at the output. The C-band exciter frequency is then passed through several stages of amplification to achieve the desired output.

IV. C-Band Exciter Functions

A. Coherent L-Band Test Signal

The C-band exciter provides a coherent C- to L-band test signal at a fixed level that is subsequently passed through the RCV-481 programmable attenuator assembly, allowing level control. The L-band test signal is generated by mixing the C-band exciter frequency (F_c) with a coherently generated conversion frequency ($453 F_c/681$) to create the desired output ($228 F_c/681$).

The RCV-130A4 coherent translator module in the C-band exciter provides the mixing and selection of the frequencies. Two sources of C-band (F_c) signal are provided for conversion, and selection is determined by the operator at the uplink control rack (TXR-191). A sample of the exciter output drive is provided by a coupler in the A3 exciter mixer module, and a sample of the C-band transmitter output is provided by a high-power coupler in the Microwave Subsystem. Either of these sources may be selected to be converted to L-band.

The conversion frequency ($453 F_c/681$) is generated in the C-band exciter using the exciter reference ($F_c/116$) as shown in Fig. 2. The reference is first passed through the A6 frequency shifter module, where it is multiplied by $4379/681$. This output is multiplied by the X12 frequency multiplier in the A7 module to achieve the $453 F_c/681$ required. This output is sent to the A4 coherent translator module, where the C- to L-band conversion occurs.

B. Zero Delay Reference Signal

To provide an external C- to L-band conversion frequency to be used by the C- to L-band portable zero delay device

(C-PZDD), an additional output of the A7-X12 frequency multiplier module is provided to a port on the C-band exciter assembly. The conversion frequency ($453 F_c/681$) is used by the C-PZDD to convert the output of the C-band transmitter signal to L-band in the same manner as the coherent translator in the C-band exciter. The C-PZDD is a calibrated device that is used to determine the equipment delays in the C-band uplink/L-band downlink for ranging calibrations.

C. C- to S-Band Doppler Reference Signal

During the Block IV mode of operation, the S-band Doppler reference from the Block IV Doppler translator assembly (RCV-431) is routed through the C-band exciter assembly (RCV-130) as shown in Fig. 1. During the C-band mode of operation, the Block IV Doppler reference signal is eliminated and a coherent C- to S-band Doppler reference is generated by the C-band exciter and sent to the Block IV Doppler translator assembly.

The L- to S-band upconverter assembly (RCV-103) is used to translate incoming L-band receive frequencies to S-band (Fig. 3); the S-band signal is sent to a Block IV receiver. With the receiver locked to the L- to S-band signal, the local oscillator from the receiver can then be used by the Block IV Doppler translator assembly (RCV-431) to extract the C- to L-band Doppler from the C- to S-band Doppler reference.

The C- to S-band Doppler reference is generated in the C-band exciter using the exciter reference frequency ($F_c/116$) as shown in Fig. 2. The exciter reference is split by the A6 frequency shifter module and sent to several outputs. An output ($F_c/116$) is provided to the A8-X116 frequency multiplier, which creates an equivalent C-band exciter frequency (F_c). The C-band output is sent to the A9 Doppler reference generator, where it is mixed with a C- to L-band conversion frequency ($453 F_c/681$) from the A7-X12 frequency multiplier. The L-band output ($228 F_c/681$) is mixed with the output of the A11-X31 frequency multiplier (620 MHz) to create the S-band Doppler reference signal.

V. Portable Zero Delay Device

To provide a method of measuring the ranging equipment delays in the C- to L-band link, a calibrated zero delay device was constructed. The device performs essentially the same task as the C- to L-band test translator in the exciter by taking a sample of the uplink C-band signal and coherently translating the signal to L-band, where it is injected into the receive path. Since the delays of the C-PZDD have been measured and are known, its contribution to the overall delay of the link can be eliminated, with the remaining delay being attributed to the station equipment.

The C-PZDD is connected into the C-band exciter/Block IV receiver-exciter as shown in Fig. 4. A sample of the transmitter's C-band output (F_c) is taken off a high-power coupler and mixed with the zero delay output ($453 F_c/681$) from the C-band exciter. The difference of the two inputs ($228 F_c/681$) is selected by a filter and sent to a coupler that injects the signal into the L-band receive path.

VI. C-Band Converter Assembly

To help refine the pointing accuracy of the antenna during C-band operations, a C-band converter assembly was provided to allow the antenna pointing to be evaluated at C-band frequencies. The converter accepts a C-band spectrum and down-converts the signals to an IF centered around 200 MHz. This 200-MHz IF is sent to a square law detector, where the noise power in the spectrum is measured. This allows the antenna to be trained upon a known C-band noise source using the square law detector to fine tune the pointing of the antenna by maximizing the signal strength. The antenna position coordinates can then be interpreted using the known location of the celestial source.

VII. Controller

The C-band uplink controller (HP Vectra Computer) was conceived as a stand-alone system providing monitor and control functions from a combined C-band uplink control rack (TXR-191) located in the SPC-10 area. The controller was designed to configure all the new C-band equipment as well as provide status indications. The C-band controller manipulates the exciter, microwave, and transmitter components of the C-band uplink (Fig. 5), but cannot monitor or control any of the subsystems interfacing with those assemblies due to the lack of an LMC/CMC interface.

The subassemblies of the C-band uplink are designed to interface with a commercial Hewlett-Packard data acquisition unit (DAU) that provides monitor and control of the assemblies. A DAU is located in the antenna and relays information to and from the controller in the SPC area via a fiber optic system. An additional DAU in the control rack provides monitor and control of the SPC-located equipment.

VIII. Physical Configurations

The C-band exciter assembly (RCV-130) is housed in a single wall-mounted Hoffman enclosure that measures approximately 30 in. by 24 in. by 9 in. The enclosure contains the RF modules, and associated monitor, control, and power supply hardware as shown in Fig. 2. Interfaces to the box are made

via feedthrough connectors mounted through an interface plate in the side of the box. Multi-pin connectors provide monitor and control interfaces and N-type connectors provide RF ports.

The RF drawer assembly (RCV-492) and the power supply drawer assembly (RCV-493) are both mounted in the combined uplink control rack (TXR-191). The RF connections to the RF drawer assembly are accomplished through an interface plate on the bottom of the TXR-191 rack assembly.

The C-band converter assembly (RCV-129) consists of a single wall-mounted Hoffman enclosure that measures approximately 16 in. by 15 in. by 6 in. The enclosure contains the RF downconverter module and power supply. The RF ports and monitor connections are provided through an interface plate on the side of the assembly.

The C-band portable zero delay device is housed in a weather-tight portable box that contains the RF hardware and a set of three cables for use during the calibration tests. During the use of the device, the assembly is placed in the proximity of the C-band exciter so that connections between the exciter, microwave couplers, and the C-PZDD can be made using the provided cables.

IX. Conclusions

The C-band exciter assemblies were installed at DSS-14 during late December 1988 and are presently undergoing engineering tests. Due to the shared configuration of the C-band uplink controller, the overall C-band uplink assemblies will be tested together when the final acceptance tests are performed. Several tracks of the Phobos spacecraft have been accomplished and the system has met its functional requirements.

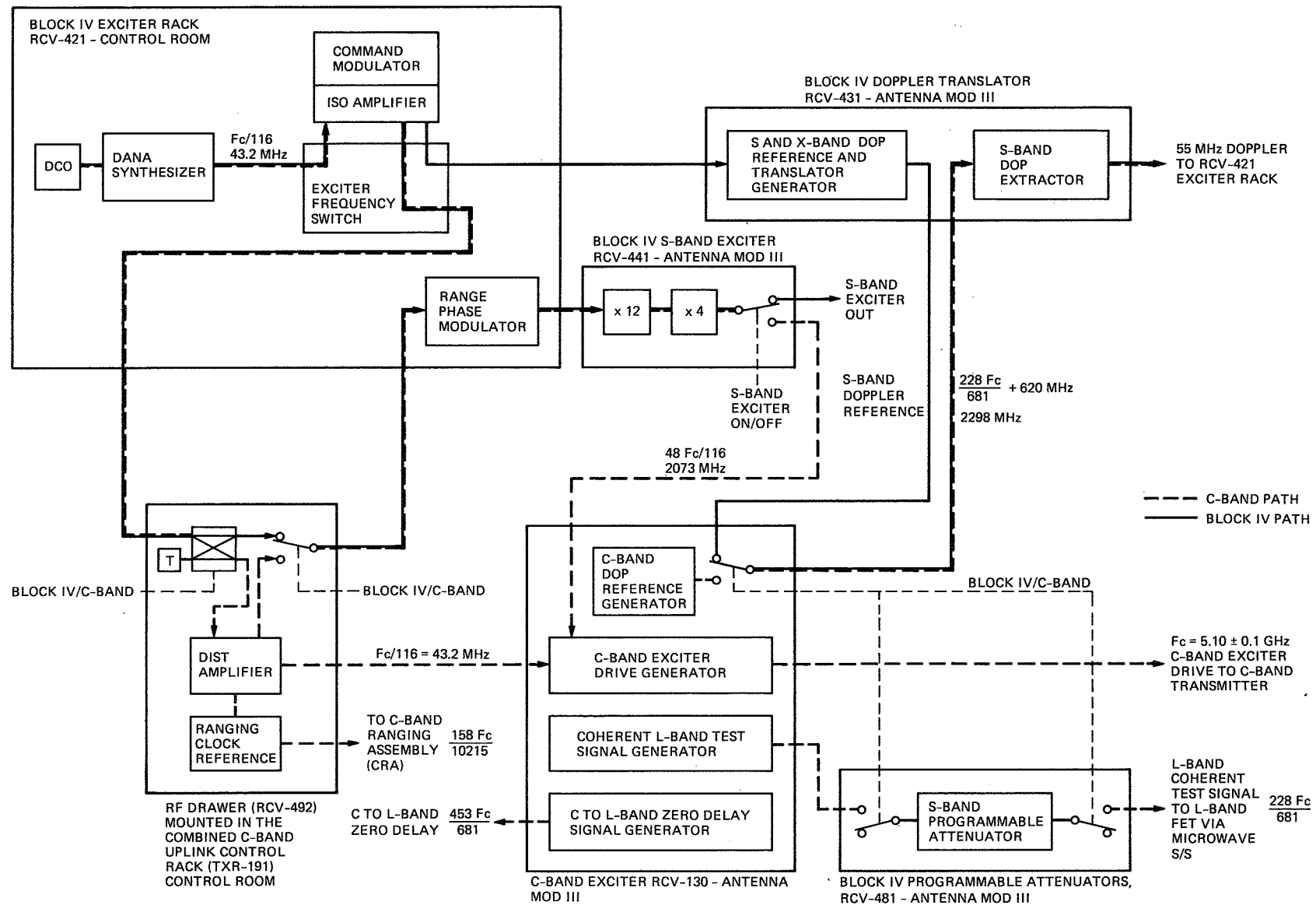


Fig. 1. Block IV receiver-exciter and C-band exciter interfaces.

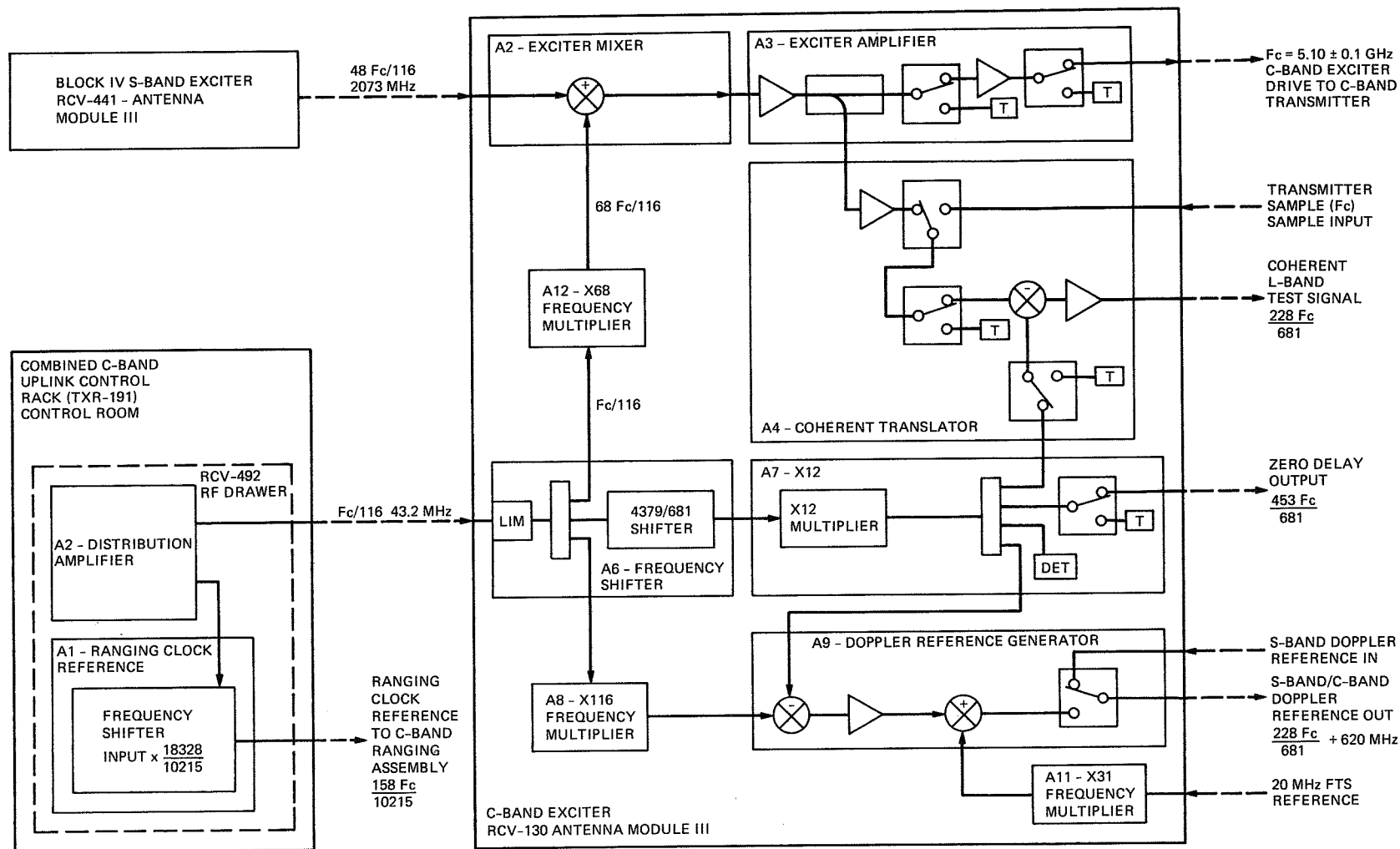


Fig. 2. C-band exciter signal generation.

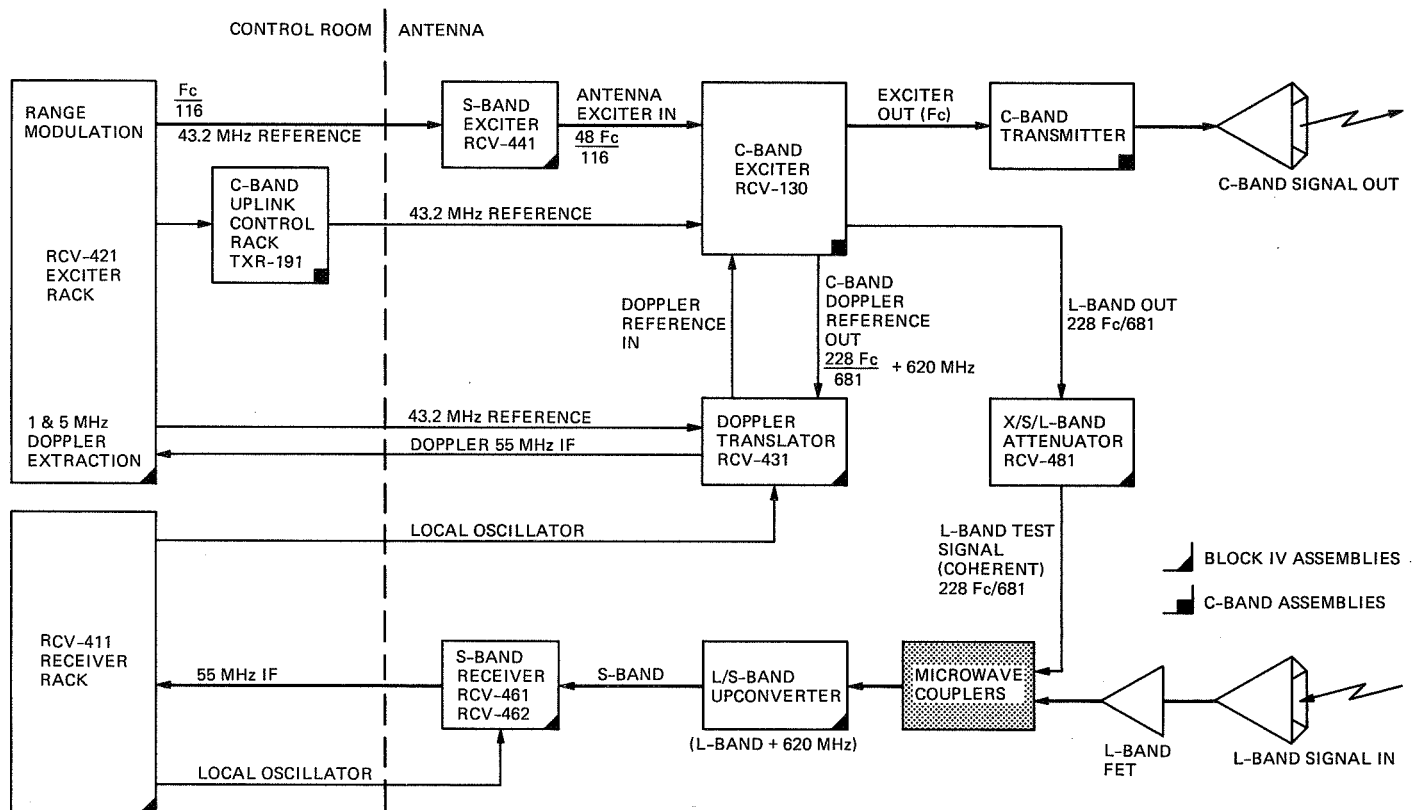


Fig. 3. C-band uplink and L-band downlink signal path.

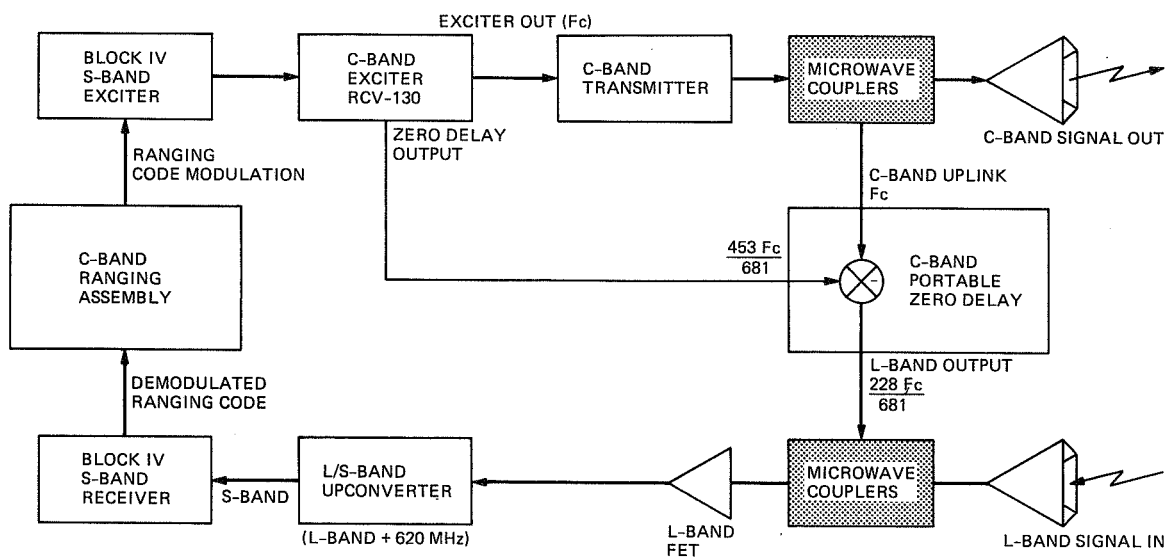


Fig. 4. C-band portable zero delay ranging.

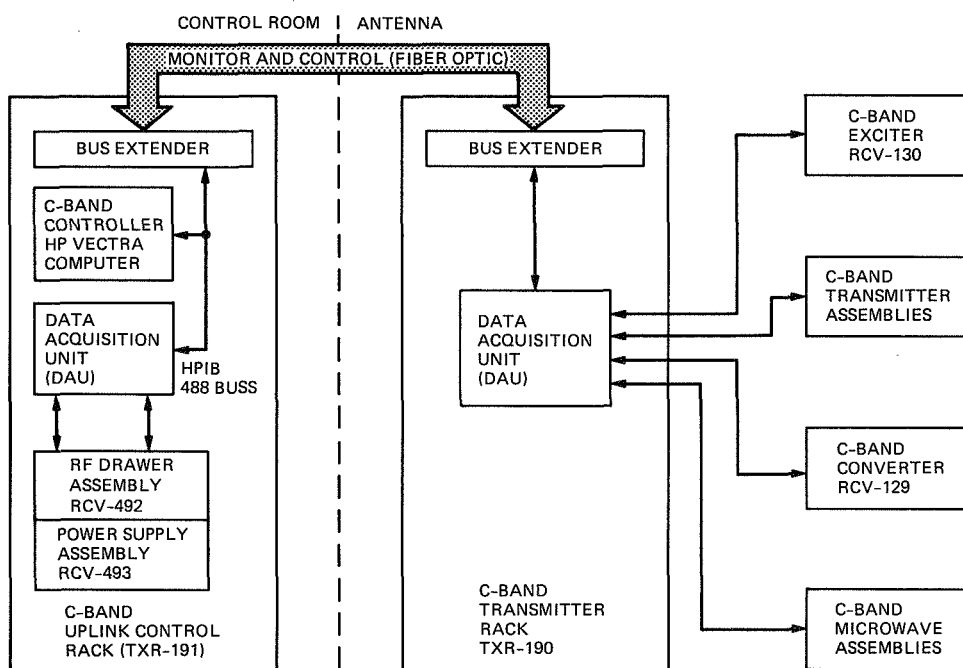


Fig. 5. C-band controller block diagram.

Orthogonal Sets of Data Windows Constructed From Trigonometric Polynomials

C. A. Greenhall

Communications Systems Research Section

This article gives suboptimal, easily computable substitutes for the discrete prolate-spheroidal windows used by Thomson for spectral estimation. Trigonometric coefficients and energy leakages of the window polynomials are tabulated.

I. Motivation

In a paper [1] on precise time and time interval (PTTI) applications, D. Percival argued as follows for the increased use of frequency domain methods for studying PTTI data:

In contrast to common practise in many other physical sciences, the statistical analysis of PTTI data is often based directly on time domain techniques rather than on frequency domain (spectral analysis) techniques. The predominant analysis technique in the PTTI community, namely, the two-sample (or Allan) variance, is often used to indirectly infer frequency domain properties under the assumption of a power-law spectrum. Here we argue that direct use and estimation of the spectrum of PTTI data have a number of potential advantages. First, spectral estimators are typically scaled independent chi-square random variables with a known number of degrees of freedom. These properties allow easy computation of the variance of estimators of various quantities that are direct functions of the spectrum. Second, the effect of detrending data can be quantified more easily in the frequency domain than in the time domain. Third, the variance of estimators of the two-sample variance can be expressed in terms of readily estimated

spectral density functions. This allows one to generate confidence intervals for the two-sample variance without explicitly assuming a statistical model. Fourth, there exist tractable statistical techniques for estimating the spectrum from data sampled on an unequally spaced grid or from data corrupted by a small proportion of additive outliers. The two-sample variance cannot be readily generalized to these situations.

In the course of testing frequency standards and distribution equipment for the Deep Space Network, the JPL Frequency Standards Laboratory generates computer files containing records of phase residuals of pairs of frequency sources. The statistical properties of these time series are routinely summarized by estimating the two-sample variance [2]. This article is a step toward the goal of supplementing this current ability with the ability to generate estimates of power spectral density of phase for Fourier frequencies f below the Nyquist frequency of these records, typically 0.5 Hz. These estimates, together with measurements of spectral density for higher f provided by commercial real-time spectrum analyzers, could characterize the phase noise of frequency sources over many decades of f extending from microhertz to kilohertz. Periodic disturbances, which are now detected haphazardly by visual

inspection of the residuals or by noticing steps or oscillations in the plots of two-sample variance, could be detected unambiguously by statistical procedures based on spectral estimators or periodograms.

In [1] quoted above, Percival recommends a new method of spectral estimation, due to Thomson [3], that is especially suited to situations in which the range of spectral densities to be estimated is large. The method uses multiple orthogonal data windows (also called weights or tapers), the approximate computation of which is the main subject here.

II. The Thomson Spectral Estimation Method

In the Thomson method for estimating the power spectrum of a stationary time series $x[n]$ given N samples $x[0], \dots, x[N-1]$, a frequency band $[f_0 - W, f_0 + W]$ is chosen, and an estimate for the spectral density value $S(f_0)$ is computed as an average of the windowed periodograms, namely,

$$\hat{S}(f_0) = \frac{1}{K} \sum_{k=0}^{K-1} |y_k(f_0)|^2 \quad (1)$$

where

$$y_k(f) = \sum_{n=0}^{N-1} x[n] v_k[n; N, W] e^{-i2\pi f n} \quad (2)$$

The window sequences v_0, \dots, v_{N-1} are the discrete prolate-spheroidal sequences (DPSS) of Slepian [4]. They are orthonormal and are *leakage-optimal* over the space of sequences index-limited to $0, \dots, N-1$, in the sense that

- (1) v_0 has the smallest leakage of all nonzero elements
- (2) for $k > 0$, v_k has the smallest leakage of all nonzero elements orthogonal to v_0, \dots, v_{k-1}

For a given bandwidth W , the *leakage* $L(g, W)$ of a function g of discrete or continuous time is defined here as the fraction of its total energy contained in frequencies outside $[-W, W]$. The leakage $L(v_k, W)$ increases with k and decreases with W . By virtue of the orthogonality of the v_k , the estimate of Eq. (1) has approximately $2K$ degrees of freedom if x is Gaussian, $S(f)$ is nearly constant for $|f - f_0| \leq W$, and the leakage of v_{k-1} is small. Thus, by adjusting W and K , one can achieve a tradeoff in Eq. (1) among variance, resolution, and the influence of frequencies outside $[f_0 - W, f_0 + W]$ (the usual meaning of "leakage").

Since the computation of the DPSS requires the solution of the eigensystem of an $N \times N$ matrix (or of an integral operator if N is large), the design of easily computable suboptimal substitutes for them may be of value. In view of Nuttall's constructions of windows from cosine polynomials of low degree [5], one might expect trigonometric polynomials with both sines and cosines to make attractive materials for construction of DPSS substitutes. In fact, this idea has already been realized by Bronez ([6], p. 1869) in his recent extension of the Thomson method to the more general situation of unevenly spaced and multidimensional data. The coefficients of his polynomials and their leakages are respectively the eigenvectors and eigenvalues of a certain matrix whose coefficients depend on N , the number of data. The aim of this article is to simplify the situation further for evenly spaced one-dimensional data by deriving the coefficients and leakages of an orthonormal set of continuous-time trigonometric polynomials that do not depend on N . They are converted to discrete-time data windows by sampling them at N properly chosen points.

III. Continuous-Time Windows

In this article, w is used to denote bandwidth in terms of the fundamental frequency unit, which is $1/N$ for windows on $0, \dots, N-1$, and 1 for windows on $[-1/2, 1/2]$, as constructed below. It is assumed that w is an integer (for the author's convenience only). Consider a time-limited trigonometric polynomial

$$\begin{aligned} \phi(x) &= \sum_{\nu=-M}^M c[\nu] e^{i2\pi\nu x} & |x| \leq 1/2 \\ &= 0 & |x| > 1/2 \end{aligned}$$

of degree $\leq M$. Its Fourier transform is

$$\Phi(y) = \sum_{\nu=-M}^M c[\nu] s(y - \nu) \quad (3)$$

where

$$s(y) = \frac{\sin \pi y}{\pi y} \quad (4)$$

The polynomials sought can be defined immediately: their coefficient arrays are normalized eigenvectors of the positive-definite matrix

$$A[i, j] = \int_{|y| > w} s(y - i) s(y - j) dy, \quad i, j = -M \text{ to } M$$

and their leakages are the eigenvalues. Denote the resulting polynomials by $\phi_k(x; w, M)$, $k = 0$ to $2M$, and their coefficients by $c_k[\nu]$, $\nu = -M$ to M , where the leakages $L(\phi_k, w)$ are taken in increasing order. The polynomials are orthonormal and leakage-optimal over the space of polynomials of degree $\leq M$. They are called *trig prolates* for short, because they can be regarded as finite-dimensional analogs of the prolate-spheroidal wave functions (PSWF) [7]. The symmetry of A about its reverse diagonal forces the eigenfunctions to be either even or odd (the odd ones are multiplied by $\pm i$ to make them real), and empirically the above indexing gives ϕ_k the parity of k . The trig prolates share with the PSWF the property of double orthogonality: their transforms $\Phi_k(y; w, M)$ are orthogonal over $[-w, w]$ as well as over $(-\infty, \infty)$.

The entries of A were computed as linear combinations of the integrals

$$\int_0^1 \left[\frac{\sin \pi y}{\pi(n+y)} \right]^2 dy, \int_0^1 \left[\frac{\sin^2 \pi y}{\pi^2(n+y)} \right] dy, \quad n = 0 \text{ to } w + M - 1$$

which were computed by Romberg quadrature. The eigenvalues and eigenvectors were computed by EISPACK routines [8], [9]. Although the leakages decrease if M increases, setting $M = w$ gives adequate performance (Section V).

Table 1 gives the coefficients and leakages of the trig prolates for $w = 2$ to 5 , $M = w$, and for all k such that $L(\phi_k, w) < 0.01$. Figure 1 shows the frequency response $|\Phi_k(y; 4, 4)|^2$ for $k = 0$ and 4 . Comparing these with Thomson's graphs of the frequency responses of the DPSS for large N ([3], Fig. 2), one can see that the maximum sidelobes of the trig prolates are at most 2.5 dB above those of the corresponding DPSS, although the sidelobe structure of the trig prolates is less regular.

IV. Discrete-Time Windows

An orthogonal set of windows for data on $0, \dots, N-1$ and bandwidth $W = w/N$ is constructed by sampling the ϕ_k as follows:

$$u_k[n; N, W, M] = \phi_k\left(\frac{n - (N-1)/2}{N}, w, M\right), \quad n = 0 \text{ to } N-1, k = 0 \text{ to } 2M \quad (5)$$

Notice that the denominator is N instead of $N-1$. This has two beneficial effects:

- (1) the basis functions $e^{i2\pi\nu x}$ remain orthogonal when so sampled

- (2) their discrete-time transforms are more closely related to their continuous-time transforms (see below)

The discrete-time windows u_k are called *sampled trig prolates*. Orthogonality is preserved, namely,

$$\sum_{n=0}^{N-1} u_i[n] u_j[n] = N\delta_{ij}$$

Their discrete-time Fourier transforms are

$$U_k(f; N, W, M) = e^{-i\pi(N-1)f} \sum_{\nu=-M}^M c_k[\nu] s(Nf - \nu; N)$$

where

$$s(y; N) = \frac{\sin \pi y}{\sin(\pi y/N)}$$

(compare with Eqs. (3) and (4)). A spectral estimate of Thomson type is obtained by using $(1/\sqrt{N}) u_k[n; N, W, M]$ in place of $v_k[n; N, W]$ in Eqs. (1) and (2).

V. Comparison with Optimal Windows

How much leakage performance is lost by the use of these suboptimal windows? Let $L(\phi_k, w)$, $L(u_k, N, W)$, and $1 - \lambda_k(N, W)$, where $NW = w = M$, be the leakages of the trig prolates, the sampled trig prolates, and the optimal DPSS respectively. Evaluating $L(u_k)$ by means of the quadratic form in the numerator of Eq. (32) of [6], it is found that $L(u_k)$ is between 0 dB and 1.2 dB less than $L(\phi_k)$ for the instances of w and k given in Table 1 and for $N = 8w$. For $N = 16w$, replace 1.2 dB by 0.6 dB. Thus, the sampled trig prolates have slightly less leakage than the trig prolates. Table 2 gives the ratio of sampled trig prolate leakage to DPSS leakage, which was computed by solving the eigensystem given by Eq. (2.9) of [3]. For $N = 8w$, the leakages of the trig prolates are 1.2 dB to 5.4 dB greater than those of the optimal DPSS; for $N = 16w$, the range is 1.2 dB to 2.6 dB. The leakages of the corresponding Bronez discrete polynomial windows, which form the leakage-optimal set of discrete-time polynomials of degree $\leq M$, necessarily lie between those of the sampled trig prolates and those of the DPSS.

VI. Conclusions

This article has described several orthonormal systems of data windows, called the sampled trig prolates, that can be used in the Thomson method of spectral estimation. For $w =$

$NW = 2$ to 5, and $4W$ not greater than the Nyquist frequency (i.e., $N \geq 16w$), the user of these windows pays a leakage penalty of at most 2.6 dB for not using the optimal DPSS windows. In return, one merely needs to evaluate certain trigonometric polynomials of degree w , with coefficients given in Table 1, at N points according to Eq. (5). By contrast, the evaluation of the DPSS windows requires the solution of an $N \times N$ symmetric Toeplitz matrix eigensystem. If

N is large, one can proceed by solving a symmetric $J \times J$ eigensystem obtained from the approximation of a certain integral operator by Gaussian quadrature, in which the required number of knots J depends on the details of floating-point hardware and mathematical software ([3], pp. 1090–1091). The prospective user of the Thomson method might regard the 2.6-dB penalty as an attractive tradeoff for avoiding these complexities.

References

- [1] D. B. Percival, "A Reappraisal of Frequency Domain Techniques for Assessing Frequency Stability Measurements," *Proc. 19th Precise Time and Time Interval Applications and Planning Meeting*, U.S. Naval Observatory, Washington, D.C., 1987.
- [2] C. A. Greenhall, "Frequency Stability Review," *TDA Progress Report 42-88*, vol. October–December 1986, Jet Propulsion Laboratory, Pasadena, California, pp. 200–212, February 15, 1987.
- [3] D. J. Thomson, "Spectrum Estimation and Harmonic Analysis," *Proc. IEEE*, vol. 70, pp. 1055–1096, 1982.
- [4] D. Slepian, "Prolate Spheroidal Wave Functions, Fourier Analysis, and Uncertainty — V: The Discrete Case," *Bell System Tech. J.*, vol. 57, pp. 1371–1430, 1978.
- [5] A. H. Nuttall, "Some Windows With Very Good Sidelobe Behavior," *IEEE Trans. on Acoustics, Speech, and Signal Processing*, vol. ASSP-29, pp. 84–91, 1981.
- [6] T. P. Bronez, "Spectral Estimation of Irregularly Sampled Multidimensional Processes by Generalized Prolate Spheroidal Sequences," *IEEE Trans. on Acoustics, Speech, and Signal Processing*, vol. 36, pp. 1862–1873, 1988.
- [7] D. Slepian, "Some Comments on Fourier Analysis, Uncertainty, and Modeling," *SIAM Review*, vol. 25, pp. 379–393, 1983.
- [8] B. T. Smith et al., *Matrix Eigensystem Routines—EISPACK Guide*, Lecture Notes in Computer Science 6, Berlin: Springer-Verlag, 1976.
- [9] B. S. Garbow et al., *Matrix Eigensystem Routines—EISPACK Guide Extension*, Lecture Notes in Computer Science 51, Berlin: Springer-Verlag, 1977.

Table 1. Sine-cosine coefficients $a_k[\nu]$ and leakage $L(\phi_k, w)$ for trig prolate $\phi_k(x; w, w) = a_k[0] + 2 \sum_{\nu=1}^M a_k[\nu] \cos 2\pi\nu x$ (k even)
or $2 \sum_{\nu=1}^M a_k[\nu] \sin 2\pi\nu x$ (k odd)

$w = M = 2$			$w = M = 3$				
k	0	1	k	0	1	2	3
L	0.8901E-04	0.3254E-02	L	0.2113E-06	0.1520E-04	0.4394E-03	0.6810E-02
ν	$a_k[\nu]$		ν	$a_k[\nu]$			
0	0.8202108	0.0	0	0.7499700	0.0	0.4969513	0.0
1	0.4041691	0.7007932	1	0.4596063	0.6507499	-0.3050683	0.2731233
2	0.0165649	0.0942808	2	0.0867984	0.2765560	-0.5312499	-0.6397174
			3	0.0007513	0.0064282	-0.0350227	-0.1271430

$w = M = 4$					
k	0	1	2	3	4
L	0.4376E-09	0.4203E-07	0.1965E-05	0.5382E-04	0.9029E-03
ν	$a_k[\nu]$				
0	0.6996910	0.0	0.4783016	0.0	-0.3862293
1	0.4830013	0.5927723	-0.1666510	0.3540569	0.3223025
2	0.1473918	0.3805986	-0.5724443	-0.4929565	-0.0856254
3	0.0141997	0.0613650	-0.1736202	-0.3626279	-0.5584413
4	0.0000368	0.0003329	-0.0022015	-0.0117722	-0.0484379

$w = M = 5$							
k	0	1	2	3	4	5	6
L	0.1056E-11	0.1148E-09	0.6265E-08	0.2307E-06	0.6065E-05	0.1112E-03	0.1411E-02
ν	$a_k[\nu]$						
0	0.6632850	0.0	0.4560698	0.0	-0.3821638	0.0	0.3246026
1	0.4915713	0.5401300	-0.0704481	0.3866087	0.2527019	-0.2216043	-0.2957322
2	0.1927963	0.4383060	-0.5519198	-0.3363930	0.1138304	0.3885522	0.1964585
3	0.0347859	0.1266343	-0.2915206	-0.4760267	-0.5457777	-0.3657298	0.0266965
4	0.0019243	0.0105462	-0.0379143	-0.1037856	-0.2286313	-0.4072901	-0.5631039
5	0.0000018	0.0000191	-0.0001319	-0.0007467	-0.0037712	-0.0165910	-0.0588589

Table 2. Ratio (dB) of sampled trig prolate leakage to optimal DPSS leakage^a

k	0	1	2	3	4	5	6
w							
2	2.1, 1.9	1.2, 1.2					
3	2.7, 2.0	2.4, 2.2	2.0, 1.9	1.3, 1.3			
4	3.7, 1.8	2.8, 1.7	2.6, 2.1	2.4, 2.2	1.9, 1.9		
5	5.4, 2.6	4.2, 2.1	3.3, 1.9	2.7, 2.0	2.6, 2.2	2.4, 2.2	1.9, 1.8

^aThe first entry is for $N = 8w$; the second entry is for $N = 16w$.

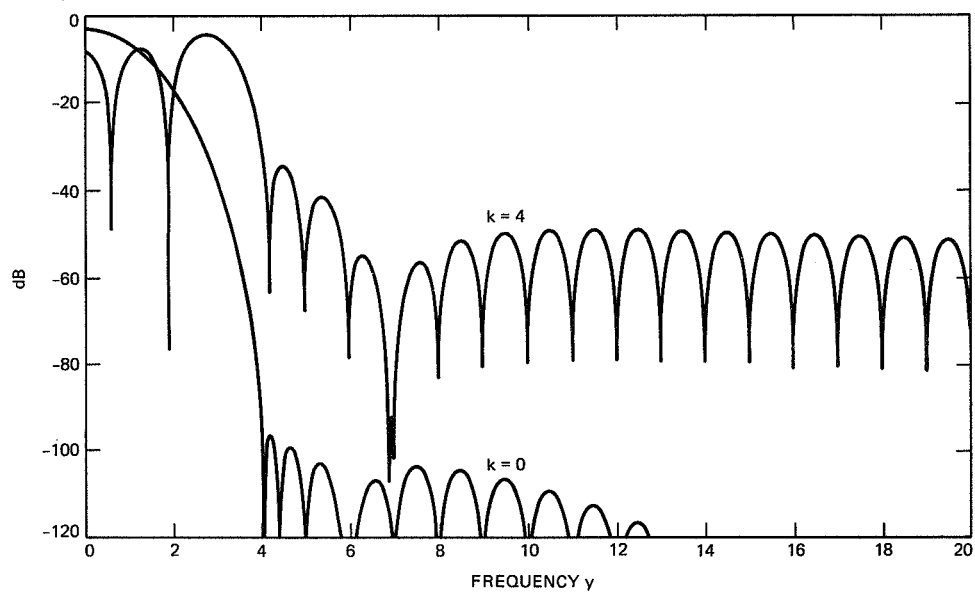


Fig. 1. Frequency response of trig prolate windows for bandwidth $w = 4$, degree $M = 4$. The total energy of each window is 1.

532-74
518087

N 8 9 - 2 7 9 0 3

TDA Progress Report 42-97

January–March 1989

DSN 70-Meter Antenna Microwave Optics Design and Performance Improvements Part I: Design Optimization

D. A. Bathker

Ground Antenna and Facilities Engineering Section

S. D. Slobin

Telecommunications Systems Section

This article reviews the design optimizations associated with the microwave and structural upgrade of the DSN 64-m antennas. Expected area efficiency/gain performances at S- and X-band are given for both the original 64-m systems and the upgraded 70-m systems, and error estimates are developed. The DSN 70-m Upgrade Project specifications, based on predesign estimates, were 1.4-dB gain at S-band and 1.9-dB at X-band, with no degradation to critical receiving system noise temperatures. The measurements show an S-band gain increase of 1.9 dB and an average increase of 2.1 dB at X-band. The Project also delivered small receiving system noise decreases at both frequency bands. The three DSN 70-m antennas, in the initial state of mechanical adjustment as of the end of calendar year 1988, are performing with very high peak microwave area efficiencies at very nearly the engineering design expectations of 76 percent at S-band and 71 percent at X-band.

I. 70-m Microwave Optics Design

A 1975 engineering study identified several technical options for significantly increasing the microwave performance of the DSN 64-m antennas.¹ Between 1975 and 1985, many of those options were implemented, providing improved X-band reception for the Voyager Jupiter, Saturn, and Uranus encounters. Those options included improved structural bracing of the main reflector to reduce the effects of gravity distortion,

improved feedhorn design to obtain better aperture illumination, automated two-axis subreflector focusing for improved gain with elevation angle changes, and improved preamplifiers.

After these initial improvements, three options from the 1975 report remained unincorporated—increasing the physical diameter of the antenna, increasing the antenna aperture efficiency, and improving panel manufacturing and setting. Predesign work estimated that approximately 0.6 dB (15 percent) gain increase could be obtained from uniform illumination and an 0.8-dB (20 percent) increase could be obtained from the greater physical area (at S- and X-bands). In addition, improved manufacturing and panel setting precisions for the individual main reflector panels and subreflector would provide an addi-

¹Radio Frequency Figure of Merit Enhancement Study, DSN 64-M Antennas, JPL 890-47 (internal document), Jet Propulsion Laboratory, Pasadena, California, June 1, 1975.

tional 0.5-dB (12-percent) improvement at X-band. Thus the 64-70-m Upgrade Project was established, with goals of 1.4-dB and 1.9-dB increases at S- and X-band, respectively. To achieve 1.9-dB gain increase over the 64-m antenna by physical area alone would require a conventional 80-m antenna. Alternatively, for the same performance level, the 64-m antenna could be augmented by arraying it with a conventional 47-m antenna.

The 64-m DSN antennas had conventionally profiled paraboloidal main reflectors and hyperboloidal subreflectors. These Cassegrainian systems were characterized by tapered aperture illumination intensity. It was expected that application of the modern dual-reflector contour shaping technique, which achieves uniform aperture illumination intensity and phase, could be successfully applied to the asymmetric feed geometry in place on the 64-m antennas. The asymmetric feed geometry provides multiple frequency feeding from a Cassegrain feed tricone. The tricone and associated rotatable subreflector effectively form a large, efficient bandswitch. For perfect main reflector axis pointing from such asymmetrically fed systems, a subreflector that is not a simple figure of revolution is required.

Designing the microwave optics for specially contoured surfaces begins with the selection of the feedhorn radiation pattern. A key design constraint was to retain the 64-m antenna tricone subassembly, which includes the receivers and transmitters, the feedcone housings containing the feedhorns, associated microwave plumbing, and connections to the low-noise preamplifiers. By retaining this 44-ft-high subassembly, standard DSN feedhorns critical to design and resulting microwave performances were economically retained. However, this constrained the microwave optics design in terms of the feedhorn beamwidth (which influences forward spillover based on subreflector diameter), and Cassegrain optics focal length (feed magnification factor). Despite this constraint, an excellent overall microwave optics design was obtained. The primary tradeoffs were to balance forward spillover against subreflector cost (a function of subreflector diameter), and selection of the rear spillover level past the main reflector rim (which influences critical reception noise). The design balance achieved about a 4-percent forward spillover (96-percent spillover efficiency). Although one might do somewhat better in an unconstrained design, the tricone retention and the savings in subreflector cost clearly established the acceptability of 96-percent forward spillover efficiency with standard feedhorns. In the future, slightly larger feedhorns might improve forward spillover efficiency by an additional 2 percent.

A very slight imbalance in illumination intensity results from the inherent asymmetric feed geometry. This amounts

to about 2-dB amplitude ramping, occurring near the main reflector edges, on a diameter including the asymmetric plane. However, the design is phase perfect; loss due to the slight intensity ramp is less than 0.5 percent at X-band.

The microwave optics design was optimized for X-band (8420-MHz) area efficiency (gain) and noise, which constitute the G/T receiving system performance index. This was done for an operating elevation angle of 30 deg and a total receiving system noise level of 15 kelvins, since for nearly half of all tracking hours, the DSN antennas operate below 30-deg elevation. A total receiving system noise level of 15 kelvins at 30-deg elevation at X-band is an optimistic goal and difficult to achieve; the optimization is therefore conservatively biased in the low-noise direction. It should be pointed out that optimum G/T-balanced very-low-noise antennas sacrifice some gain in order to maintain very low rear spillover. Higher noise antennas, properly G/T balanced for the higher attendant receiving noise, are capable of slightly higher gain, but do not achieve the overall better G/T performance. A clear way to envision a very-low-noise optimized reflector antenna is to view the outer main reflector as intentionally not well illuminated, therefore not instrumental in developing overall system main-beam gain. Alternatively, in signal reception, the feed is purposefully not responsive to signal or noise from the rim regions and beyond; rather, the reflector edge region functions as an earth-noise shield, keeping the other critical factor (total system noise) controlled. This was accomplished in the 70-m DSN design by synthesizing the dual-shaped surfaces for a 69-m (approximately) system, then adding a simple slope-matched paraboloid noise-shield annulus.

At wavelengths shorter than X-band (e.g., 15-, 22- and future 32-GHz) the 70-m DSN antennas will slowly tend, as a function of frequency increase, toward lower rear spillover noise, a consequence of the physics of subreflector edge diffraction. Conversely, at longer wavelengths (e.g., S-band) these antennas will unavoidably have slowly increasing rear spillover and attendant receiving noise.

Another consequence of increased longwave rear spillover arises when transmitting—a concern for transmit radiation power density safety. This issue was studied and it was concluded that in the environment of additional radiation sources beyond direct rear spillover, especially scatter due to the quadripod structure, the 70-m design, despite slightly increased S-band direct rear spillover, would not be a problem. The increased S-band direct spillover when transmitting remained numerically submerged below the scatter term, and radiation safety was not compromised. However, in the event that an ultra-low-noise S-band receiving system or an ultra-high-power S-band transmitting system is required on the 70-m antennas, a fresh look at the adequacy of the X-band optimized optics

operated at S-band will be necessary. In the event that additional main reflector annular rim shielding for S-band is required, such an addition would be straightforward. Alternatively, a slightly larger S-band feedhorn or beamwidth-changing ellipsoidal reflector might suffice.

II. 64/70-m S-Band Design-Expected Performances

Although the 70-m microwave optics are X-band G/T optimized, considerable effort was expended to predict S-band performance to meet the ongoing tracking requirements of a number of S-band deep-space spacecraft at remarkable and increasing distances. Tables 1 and 2 show the S-band design efficiency predictions for the 64-m and 70-m antennas, respectively. These predictions are the result of a consistent computational method. In Table 1, the four-reflector S-band 64-m system is rigorously analyzed [1]. The analysis considers the S-band feedhorn radiation pattern as scattered from the S/X reflex-dichroic ellipsoidal and dichroic reflectors, and the conventional subreflector and main reflector. This analysis provides an efficiency subtotal as well as a pointing loss (squint). Pointing squint is an endemic effect in asymmetrically fed circular polarized antennas, and arises due to subtle cross-polarization field summations. The result is that the DSN antennas do not produce perfectly coaxial simultaneous S/X beams. Rather, in the usual operating configuration, the X-band beam peak is aimed as perfectly as possible and the simultaneous S-band beam peak is unavoidably displaced a few millidegrees. Tables 1 and 2 account for this operating configuration by including a small S-band squint loss term. In Table 1 the illumination amplitude efficiency is, notably, 82 percent, representing the tapered illumination characteristics of paraboloid/hyperboloid RF optics. Other small terms in Table 1 lead to an overall 64-m S-band prediction of 60.3-percent aperture efficiency (61.51-dBi absolute gain) at 2285 MHz.

In Table 2, the 70-m S-band performance increase due to dual-reflector shaping for uniform illumination is apparent in the illumination amplitude term — nearly 96 percent and fully 0.66 dB above the 64-m in Table 1 [2]. Additional 70-m improvements occur due to improved quadripod blockage and subreflector blocking terms. The subreflector is designed for reduced X-band backscatter over the angular range subtending the Cassegrain feedcones. At S-band, some backscatter improvement is realized. The S-band pointing squint effect is actually less for the shaped reflector 70-m system than it was for the 64-m. Table 2 shows an overall 70-m S-band prediction of 75.8-percent aperture efficiency (63.28-dBi absolute gain) at 2285 MHz. If the S-band beam is peaked, in instances where simultaneous S/X operation is not required, a small increase

to 76.1 percent is predicted. The design-expected 64–70-m Upgrade Project S-band gain performance increase is therefore 1.77 dB, which is comfortably above the Project goal of +1.4 dB.

III. 64/70-m X-Band Design-Expected Performances

A previous modification to the 64-m X-band system, employed for the Voyager Jupiter and subsequent encounters, was the dual-hybrid mode feedhorn [3]. At X-band, this modification provided 0.36 dB overall gain improvement over a conventional feed. Thus the 64-m X-band systems were already partially shaped by the use of the special, but somewhat narrowband dual hybrid mode feedhorn. In Table 3 this is reflected in the quite respectable 90-percent illumination amplitude term. Also in Table 3, the 64-m quadripod blockage term is treated the same as at S-band. Finally, Table 3 accepts the 64-m initial construction surface tolerances (main reflector panel manufacturing, setting, and hyperboloid manufacturing), even though 20 years have elapsed since the antennas were constructed, and with near certainty, the initial value (1.14-mm normal rms) used in Table 3 is too low. The overall 64-m X-band design-expected efficiency with initially specified surface tolerance remains high at 56.5 percent (72.55-dBi absolute gain) at 8420 MHz.

Table 4 gives the detailed X-band breakdown for the 70-m. Notably, the illumination amplitude efficiency is increased to a remarkable 98.2 percent when using an ordinary wide-band single-hybrid mode (corrugated) feedhorn (JPL standard, 22.37-dBi gain). The 70-m subreflector blockage is improved over the 64-m, as is the quadripod blockage.

Additional and most valuable information became available for the 70-m antennas based on 12-GHz holographic imaging performed under contract by Eikontech, Ltd., of Sheffield, U.K. High-resolution aperture surface current (intensity) mapping revealed slightly wider quadripod shadowing than initially expected. An adjustment for 70-m quadripod blockage based on holography is included in Table 4 as well as in Table 2. The adjustment combined with the original estimate still predicts a 70-m quadripod efficiency improvement from 64-m (85.6 percent to 90.1 percent), a result of considerable care with quadripod structural design. While it might be argued that the 12-GHz-based adjustment considered applicable at X-band should be further increased in the 70-m S-band estimate due to wavelength, this has not been done in Table 2 due to lack of quantitative information. Lastly, in Table 4, an as-built adjustment for the stovepipe feed is made [4]. The stovepipe feed is a compromise design to avoid repackaging the 64/70-m X-band feedcones. Dual reflector

shaping for uniform aperture illumination is not compatible with the previous 64-m dual-hybrid mode feedhorn. Rather, the JPL standard X-band feedhorn pattern (22.37 dBi) was selected to synthesize the shaped reflector contours and to provide detailed performance estimates.

The stovepipe compromise allowed minimal mechanical changes within the three X-band operational feedcones, but unfortunately results in a slightly greater forward spillover. The overall 70-m design-expected X-band efficiency is therefore 70.8 percent (74.32-dBi absolute gain) at 8420 MHz. Conceivably, the 70-m feedcones may eventually be upgraded, resulting in an increase in the (design potential) efficiency to 72.6 percent. A hypothetically perfect surface X-band 70-m antenna with the design feedhorn would provide 76.5-percent efficiency, which is considered excellent for a very-low-noise centerline-symmetric main reflector antenna optics design with offset and dichroic feeding.

The design-expected 64–70-m Upgrade Project X-band gain performance increase is therefore 1.77 dB, based on the originally specified 64-m surface tolerance. The Project goal of 1.9 dB was based on earlier predesign estimates, which used a somewhat larger value for the 64-m surface tolerance.

IV. Accuracy of Design Expectations

The procedure adopted herein is to identify what are believed to be the top four uncertainties in the predictions described above, and by calculations or judgment attempt to estimate high confidence limits (peaks). The peaks are first simply added, which is of course unduly conservative. It is argued here that one-third of such peaks may be considered the likely or approximate probable error.

The estimating processes (P.O. or physical optics and GTD or geometrical theory of diffraction) that cover the computed subtotals seen in Tables 1 through 4 are considered accurate to about one percent (± 0.04 dB) for P.O., and in this instance ± 0.10 dB for GTD, at X-band. An analytic surface description of the shaped subreflector profile is used in GTD and is known to be a poor fit (at the 1-percent efficiency level) at X-band. The 64-m quadripod blockage efficiency is a poorly known factor. The likely performance is no better than the simple estimate, and could be 0.18 dB worse, based on recent 70-m experience discussed below. The 70-m quadripod is now better known due to holographic imaging, and the performance is not likely to be better than the simple estimate, and could be 0.07 dB worse.

Uncertainty about the effective surface tolerance, especially for the large main reflectors, not surprisingly makes the top four error list. For S-band this is not of significance, but the

X-band estimating is very sensitive to surface tolerances. For the 64-m the likely surface tolerance performance is certainly not better than that stated in Table 3, and could be 0.3 dB worse in the DSS-14 case and 0.5 dB worse in the DSS-43/63 case, based on limited holographic imaging. Limited holographic imaging on one of the 64-m antennas indicates that 1.6- to 1.7-mm rms (normal measure) was the likely condition just prior to decommissioning for the 70-m upgrade. For the 70-m antennas there is fairly clear and repeatable holographic imagery to support the estimated effective 0.7-mm rms (normal) at all three stations. Analysis of holographic imaging indicates that additional adjustment to 0.3 mm is possible as a theoretical limit; in practice, 0.4-mm rms may be achievable. It is considered that the 70-m surface performance at X-band cannot be better than quoted in Table 4, and could conceivably be 0.2 dB worse. Finally, all four antenna/band combinations estimated in Tables 1–4 undoubtedly suffer unmodeled factors: imperfect static focus alignment at the rigging angle, small losses due to panel gaps, mechanical hysteresis, and many other details. Included in the top four error estimating elements is another ± 1 percent (± 0.04 dB) to include at least some accounting for the many unmodeled small factors.

Table 5 summarizes results of the error estimating for DSN 64/70-m efficiency/gain design expectations. Both the conservative simple peak sums and the adopted likely one-third values are shown.

Taking the Table 5 low-end likely errors, Table 6 values are summarized as the design-expected (minimum-likely) area efficiencies to be expected from the various historic and present systems.

Tables 1 through 4 (design-expected) and Table 6 (design-expected minimum-likely) values need to be compared with field measured values. It is expected that the new 70-m antennas may achieve essentially 75-percent area efficiency at S-band, and nearly 70-percent at X-band.

V. Conclusion

On the basis of a very careful and complete analysis of the numerous parameters involved in the makeup of the 64- and 70-meter antenna efficiencies, updated design estimates of gain and aperture efficiency have been developed at both S- and X-band. The final predicted S- and X-band gain improvements were both 1.77 dB (coincidentally), whereas the very early pre-Project goals (based on poor knowledge of “component” efficiencies) were 1.4 dB and 1.9 dB, respectively. These design-gain improvements result from both larger antenna size (0.78 dB) and an increase of efficiency (0.99 dB), from 60 to 76 percent (S-band) and from 57 to 71 percent (X-band).

References

- [1] A. G. Cha, "Physical Optics Analysis of a Four-Reflector Antenna: Part I," *TDA Progress Report 42-84*, vol. October–December 1985, Jet Propulsion Laboratory, Pasadena, California, pp. 94–100, February 15, 1986.
- [2] A. G. Cha, "Physical Optics Analysis of a Four-Reflector Antenna: Part II," *TDA Progress Report 42-86*, vol. April–June 1986, Jet Propulsion Laboratory, Pasadena, California, pp. 231–243, August 15, 1986.
- [3] R. F. Thomas and D. A. Bathker, "A Dual-Hybrid Mode Feedhorn for DSN Antenna Performance Enhancement," *DSN Progress Report 42-22*, Jet Propulsion Laboratory, Pasadena, California, pp. 101–108, August 15, 1974.
- [4] F. Manshadi and R. Hartop, "Compound-Taper Feedhorn for the DSN 70-M Antennas," *TDA Progress Report 42-90*, vol. April–June 1987, Jet Propulsion Laboratory, Pasadena, California, pp. 81–88, August 15, 1987.

Table 1. Design-expected 64-m S-band efficiency

Item	Value	Notes
P.O. computed subtotal	0.7752	[1]
Includes:		
Rear spillover		0.998
Forward spillover		0.970
Illumination amplitude		0.824
Illumination phase		0.984
Cross polarization		0.999
m ≠ 1 modes		0.980
Central blockage	0.9616	
Quadripod blockage	0.8556	6.25 percent, 1.2 opacity
Dichroic reflectivity	0.9993	Relative to plane reflector
Surface reflectivities (4)	0.998	Painted aluminum alloy
Surface tolerances (4)	0.9875	1.26 mm normal (−0.055 dB)
Pointing squint	0.9897	X-band beam peaked
Waveguide dissipation	0.9795	
VSWR	0.9908	
TOTAL	0.603	(61.51 dBi at 2285 MHz)

Table 2. Design-expected 70-m S-band efficiency

Item	Value	Notes
P.O. computed subtotal	0.8925	[2]
Includes:		
Rear spillover		0.994
Forward spillover		0.959
Illumination amplitude		0.959
Illumination phase		0.994
Cross polarization		1.00
m ≠ 1 modes		0.980
Central blockage	0.983	
Quadripod blockage	0.9196	3.42 percent, 1.2 opacity
Holography adjustment	0.9795	5.1 percent effective
Dichroic reflectivity	0.9993	Relative to plane reflector
Surface reflectivities (4)	0.998	Painted aluminum alloy
Surface tolerances (4)	0.9946	0.86 mm normal (−0.024 dB)
Pointing squint	0.996	X-band beam peaked
Waveguide dissipation	0.9795	
VSWR	0.9908	
TOTAL	0.758	(63.28 dBi at 2285 MHz)

Table 3. Design-expected 64-m X-band efficiency

Item	Value	Notes
P.O. computed subtotal	0.8226	[3]
Includes:		
Rear spillover		0.995
Forward spillover		0.9577
Illumination amplitude		0.9008 Dual-hybrid horn
Illumination phase		0.967
Cross polarization		0.999
$m \neq 1$ modes		0.992
Subreflector blockage	0.9616	
Quadripod blockage	0.8556	6.25 percent, 1.2 opacity
Dichroic dissipation	0.9954	
Dichroic VSWR	0.99	
Surface reflectivities (2)	0.998	Painted aluminum alloy
Surface tolerances (2)	0.8702	1.14 mm normal (-0.604 dB)
Pointing squint	1.000	X-band beam peaked
Waveguide dissipation	0.984	
VSWR	0.9908	
TOTAL	0.565	(72.55 dBi at 8420 MHz)

Table 4. Design-expected 70-m X-band efficiency

Item	Value	Notes
GTD computed subtotal	0.8974	
Includes:		
Rear spillover		0.997
Forward spillover		0.964
Illumination amplitude		0.982 Standard feedhorn
Illumination phase		0.989
Cross polarization		~1.000
$m \neq 1$ modes		0.996
Subreflector blockage	0.988	
Quadripod blockage	0.9196	3.42 percent, 1.2 opacity
Holography adjustment	0.9795	5.1 percent effective
Dichroic dissipation	0.9954	
Dichroic VSWR	0.99	
Surface reflectivities (2)	0.998	Painted aluminum alloy
Surface tolerances (2)	0.9489	0.7 mm normal (-0.228 dB)
Pointing squint	1.000	X-band beam peaked
Waveguide dissipation	0.984	
VSWR	0.9908	
Stovepipe feed compromise	0.975	-0.11 dB
TOTAL	0.708	(74.32 dBi at 8420 MHz)

Table 5. Estimated errors for 64/70-m design expectations

Antenna/Band	Estimated peak sum error, dB	Estimated likely error, dB	Reference
64-m/S-band	+0.08	+0.03	Table 1
	-0.26	-0.09	
70-m/S-band	+0.08	+0.03	Table 2
	-0.15	-0.05	
64-m/X-band (DSS-14)	+0.08	+0.03	Table 3
	-0.56	-0.19	
64-m/X-band (DSS-43/63)	+0.08	+0.03	Table 3
	-0.76	-0.25	
70-m/X-band	+0.14	+0.05	Table 4
	-0.41	-0.14	

Table 6. Estimated minimum-likely efficiencies for 64/70-m systems

DSN system	Antenna	Design-expected (estimated minimum-likely) efficiency
64-m S-band	All antennas	0.591
70-m S-band	All antennas	0.749
64-m X-band	DSS-14	0.541
64-m X-band	DSS-43/63	0.533
70-m X-band	All antennas	0.686

DSN 70-Meter Antenna X- and S-Band Calibration

Part I: Gain Measurements

P. H. Richter and S. D. Slobin
Telecommunications Systems Section

Aperture efficiency measurements made during 1988 on the three 70-m stations (DSS-14, DSS-43, and DSS-63) at X-band (8420 MHz) and S-band (2295 MHz) have been analyzed and reduced to yield best estimates of antenna gain versus elevation. The analysis has been carried out by fitting the gain data to a theoretical expression based on the Ruze formula. Newly derived flux density and source-size correction factors for the natural radio calibration sources used in the measurements have been used in the reduction of the data. Peak gains measured at the three stations were 74.18 (± 0.10) dBi at X-band, and 63.34 (± 0.03) dBi at S-band, with corresponding peak aperture efficiencies of 0.687 (± 0.015) and 0.762 (± 0.006), respectively. The values quoted assume no atmosphere is present, and the estimated absolute accuracy of the gain measurements is approximately ± 0.2 dB at X-band and ± 0.1 dB at S-band (1- σ values).

I. Introduction

Aperture efficiency measurements made on the newly completed and holographically adjusted DSN 70-m antennas at both X- and S-band were completed in the latter half of 1988. The last set of data taken was at DSS-63 after the rebolting of the major structural brace in September of that year.

Analysis of these measurements has now been completed, and a pair of gain versus elevation curves has been generated for each station at each frequency corresponding to antenna performance with and without the Earth's atmosphere under normal, clear, dry conditions.

These best estimates of antenna performance have been arrived at by fitting the data to a theoretical gain versus elevation profile based on the Ruze formula, and applying recently derived corrections to a number of natural radio source flux

density and source-size correction factors used to convert source temperature measurements to aperture efficiency. These corrections have been necessitated by the publication of more recent flux density measurements for the source 3C274, especially at higher frequencies (up to 90 GHz), and the use of a new and more accurate numerical convolution procedure for calculating source-size correction factors from high-resolution radio maps.

The use of a fitting procedure based on the Ruze formula rather than the usual polynomial expansion was suggested by the somewhat unusual shapes of many of the individual gain versus elevation curves obtained at the stations. At X-band in particular, the new antennas' behavior is not easily expressed by low-order polynomials, whereas the fit to the theoretical Ruze expression is excellent. A further advantage to this method of analysis is that the fitting parameters have direct

physical significance related to the gravity-induced distortion of the main reflector, and may thus be compared with calculations based on modeling of the reflector structural performance.

The following sections of this article provide a summary of the measurements at each DSS, and describe the curve fitting and calibration procedures used to analyze these measurements and obtain best estimates of the gain characteristics for the 70-m antennas.

II. Summary of 70-m X-Band Gain versus Elevation Measurements for DSS-14, DSS-43, and DSS-63

Figures 1-3 show the gain versus elevation curves for DSS-14, -43, and -63 respectively, as measured at each station, i.e., including the effects of atmospheric attenuation. For each station, individual curves are identified according to the day of year (DOY) on which the measurements were made and the source used for the measurements. DOY refers to 1988 in all cases.

Figures 4-6 present the same set of data, except that for each curve the effects of atmospheric absorption have been removed (see Section III.A for a discussion of the procedure used).

For all cases shown in these figures, except for DSS-63 DOY 207 (source 3C274), the fit is within ± 0.040 dB ($1-\sigma$), and in many cases is approximately half this value (see Appendix A for details). The data for DSS-63 taken on this date are sparse and show considerable scatter so that the $1-\sigma$ error is 0.088 dB. The curve is nevertheless included in the analysis since it provides the only comparison at this station of this important source with the more commonly used source 3C123.

It can be seen from Figs. 1-6 that there is considerable variation between the 70-m antennas, and that different sources in general give different results. On the other hand, agreement between different runs at a given station using a given source is quite good.

The question of different results for a given antenna with different sources centers on the correctness of the flux densities and source-size correction factors given in *DSN Radio Source List for Antenna Calibration*, rev. B.¹ Analysis of this

question, given in Section IV, shows that as a result of the limitations inherent in previously available methods of computing the source-size correction factor, C_s , significant errors have existed in the values of both flux density S , and C_s for certain sources such as 3C274. Additionally, more recent measurements of various calibration sources at higher frequencies have resulted in a slightly revised flux density scale which results in yet another contribution to the systematic differences apparent in Figs. 1-6.

When all of these effects are taken into account, the gain versus elevation curves shown in Figs. 7 and 8 result (see Section IV.E for details). These are based on all of the data used to generate Figs. 1-6, and the fits are very good in each case ($0.029 \text{ dB} < \sigma < 0.040 \text{ dB}$). Also shown in Fig. 8 is a theoretical curve based on design expectations, indicating that the actual performance at the three stations is somewhat poorer than anticipated both in terms of the maximum gain and the fall-off in gain with elevation angle [1, 4].

III. Analysis of Gain Measurements

A. Curve Fitting

As mentioned above, the gain versus elevation data for each run were fitted to a theoretical curve based on the use of the Ruze formula [2],

$$\epsilon_0(\alpha) = \epsilon_m \exp \left[- \left(\frac{4\pi \Sigma(\alpha)}{\lambda} \right)^2 \right] \quad (1)$$

where

$\epsilon_0(\alpha)$ = aperture efficiency at elevation angle α

ϵ_m = maximum aperture efficiency

$\Sigma(\alpha)$ = rms half-pathlength deviation of antenna surface from best fit design surface (inches)

λ = wavelength (inches)

The rms half-pathlength deviation, $\Sigma(\alpha)$, may be expressed in terms of geometrical factors and the deviations for gravity loadings applied parallel to the reflector y- and z-axes respectively [3]

$$\Sigma^2 = S_y^2 \eta^2 + S_z^2 \zeta^2 + 2CS_y S_z \eta \zeta \quad (2)$$

where

S_y = rms half-pathlength deviation for y-axis load ($\alpha = 0 \text{ deg}$) (inches)

¹ *DSN Radio Source List for Antenna Calibration*, rev. B, JPL internal document D-3801, September 25, 1987. In the remainder of this article, JPL D-3801 will be used to refer to this document.

S_z = rms half-pathlength deviation for z-axis load ($\alpha = 90$ deg) (inches)

$$\eta = \cos \gamma - \cos \alpha$$

$$\xi = \sin \gamma - \sin \alpha$$

C = correlation coefficient between y- and z-axis load deviations

In the above, γ is the angle for which the aperture efficiency is maximum, so that the rms deviation Σ is relative to that at $\alpha = \gamma$.

Using Eqs. (1) and (2) the antenna gain may be expressed as

$$G_0(\alpha) = G_m + G_1 X_1(\alpha, \gamma) + G_2 X_2(\alpha, \gamma) + G_3 X_3(\alpha, \gamma) \quad (3)$$

where

$G_0(\alpha)$ = gain in dBi at elevation angle α

$G_m = G_{100} + 10 \log \epsilon_m$ = maximum gain ($\alpha = \gamma$)

$$G_1 = -KS_y^2$$

$$G_2 = -KS_z^2$$

$$G_3 = -2KCS_y S_z$$

$$X_1 = \eta^2$$

$$X_2 = \xi^2$$

$$X_3 = \eta \xi$$

$G_{100} = 20 \log(\pi D / \lambda) = 75.815$ dBi at X-band ($\nu = 8420$ MHz)

$K = 10(4\pi/\lambda)^2 \log e = 349.023$ dB/inch² at X-band ($\nu = 8420$ MHz)

Equation (3) involves five parameters, G_m , G_1 , G_2 , G_3 , and γ , and it may be used to fit the gain data at each of the stations and so determine the parameters G_m , S_y , S_z , C , and γ appropriate to each antenna. These may in turn be compared with predictions for these parameters based on theoretical models of the 70-m antenna performance.

It has been shown that predictions of 70-m antenna performance based on Geometrical Theory of Diffraction (GTD) calculations agree very well with those based on traditional ray tracing methods using the above formulation, provided the subreflector position is optimized to maximize the predicted gain [4]. Hence, the comparison referred to above should

permit a good check on such theoretical calculations, within the limitations imposed by the quality of the gain measurements at each station.

In order to carry out such a comparison it was first necessary to remove any known systematic effects from the data, such as attenuation due to atmospheric absorption. Thus, the gain in the absence of an atmosphere, $G_0(\alpha)$, is related to the measured gain including atmospheric absorption, $G(\alpha)$, by the relation

$$G_0(\alpha) = G(\alpha) + \frac{A_{0z}}{\sin \alpha} \quad (4)$$

where $G(\alpha)$ is obtained from the measured efficiency data, $\epsilon(\alpha)$,

$$G(\alpha) = 10 \log \epsilon(\alpha) + 10 \log \left(\frac{\pi D}{\lambda} \right)^2 \quad (5)$$

and A_{0z} , the zenith attenuation, is calculated from an atmospheric model based on surface measurements of temperature, pressure, and relative humidity taken simultaneously with the gain measurements.

Table 1 summarizes the results of the fitting for all three stations, listing the values of γ , S_y , S_z , and C determined for each of the days indicated.

The variations in the parameters listed in Table 1 most likely arise from three different sources: random measurement errors, systematic measurement errors, and the sensitivity of the parameters themselves to small changes in the data. The latter effect is due to the fact that the fitting functions $X_j(\alpha_i)$ defined in Eq. (3), although linearly independent, are not orthogonal, i.e.,

$$\sum_{i=1}^N X_j(\alpha_i) X_k(\alpha_i) \neq 0 \quad \text{for } j \neq k \quad (6)$$

where $j, k = 1, 2, 3$, and N = number of data points used in the fit [5]. This is especially significant for the correlation coefficient, which can take on a wide range of values, even changing sign as seen in the case of DSS-14 and -63, without significantly changing the goodness of the fit.

For comparison purposes, the parameter values determined from structural model calculations² are also listed in Table 1. These assume a value of $\gamma = 45$ deg, which is slightly different

² Roy Levy, personal communication.

from the fitting values listed in Table 1, so one cannot expect perfect agreement between the Table 1 and model calculation values for S_y , S_x , and C . However, small changes in the value of γ will not result in a significant change in shape if the remaining parameters remain fixed. Thus, the substantial differences actually observed between the theoretical and fitted values must be due to causes other than these small differences in γ . These could be any of those listed above, or differences between the assumed and actual antenna structure.

To illustrate the magnitude of the difference implied by the data listed in Table 1, Fig. 8 shows a comparison of the average gain curve $G_0(\alpha)$ for each station with the predictions based on the theoretical parameter values listed in the table (see Section III.E for details).

Table 2 lists the angle at which the final panel setting was carried out for each of the antennas.³ The agreement between these values and the average of the values found in Table 1 is quite good for DSS-14 and -43, but there is about a 4-deg difference for DSS-63. The reason for this difference is not known, but it should be noted that the data for this station are more sparse than for the other stations, and show greater scatter.

It is also possible that the elevation angle used to carry out the final panel setting may not be the one for which the total rms deviation of the antenna surface from the desired figure is minimum, i.e., the setting angle may not be the value γ appearing in the Ruze formula. This is because the rms deviation includes both short-range and long-range errors, and the latter, corresponding to low-order departure from the desired shape, could, on a random basis, be of such a symmetry that the rms deviation would be reduced in magnitude at some other elevation angle as a result of gravitationally induced flexure of the structure. This new angle would then obviously be γ by definition.

The data used for DSS-63 in the above analysis were obtained prior to the rebolting of the structural brace which had previously been found to be loose enough to permit some slippage. Figure 9 shows more recent measurements compared with the average for DOY 124 and 201; this new data reflects the configuration after the rebolting of the brace. It is seen that the new data tend to fall somewhat below the previous results at low elevation angles, and that the DOY 274 data do not fit the previous data or the DOY 246 data between 20 deg and 56 deg. On the other hand, the DOY 246 data agree reasonably well with the pre-rebolting results for 25 deg $< \alpha < 65$ deg, but tend to be somewhat high for $\alpha > 65$ deg.

³ Boris Seidel, personal communication.

Taken all in all, the results obtained after rebolting do not appear to indicate any significant change from the earlier results, except possibly for a lower gain at low elevation angles. However, the amount of data available and the lack of agreement between the two sets of data make it appear unwise to alter the final curve fit on the basis of these data. It appears that a systematic error is involved in the post-rebolting measurements.

B. Systematic Effects in the $\epsilon(\alpha)$ Measurements

The efficiency measurements at DSS-14 and DSS-63 show variations with elevation which in certain cases indicate the presence of systematic errors. These take the form of both periodic fluctuations and offsets; an analysis of these effects is carried out in Appendix B where it is shown that at DSS-14, for example, it appears that a small pointing error ($\Delta\phi = 1.2 \times 10^{-3}$ deg) has resulted in a small average reduction in measured efficiency amounting to a 0.028-dB gain loss.

Owing to the lack of any consistent indication of such an effect at all stations for all measurements, the above loss is treated as a probable error and added to the overall error budget for the gain measurements (see Section IV.F).

IV. Calibration Analysis

A. Computation of Efficiency

The efficiency data obtained at the individual stations are derived from the measured source temperature values by means of the relation

$$\epsilon = \frac{2kTC_r}{AS} \quad (7)$$

where

k = Boltzmann's constant

T = measured source temperature

C_r = source-size correction factor

A = area of antenna = $\frac{\pi D^2}{4}$

S = source flux density

It is seen that the computed efficiency values, and hence also the gain values, depend directly on the two quantities C_r and S , which must be determined for each source used in the calibration measurements, and of course, at each fre-

quency if measurements are to be made at more than a single frequency.

Values of C_r and S used in these calculations have been taken from JPL D-3801, rev. B, and apply to the 70-m antennas at X-band. Thus, one may rewrite Eq. (7) with a more specific notation to emphasize the fact that 70-m gains are being discussed,

$$\epsilon_{70} = \frac{2kT_{70}C_{r70}}{A_{70}S} \quad (8)$$

The values of S which appear in JPL D-3801 and the above equation were obtained by means of a series of measurements made using the 64-m antenna at Goldstone [6]. These measurements used Eq. (7) solved for S , but with values for the other parameters appropriate to the 64-m Goldstone antenna, i.e.,

$$S = \frac{2kT_{64}C_{r64}}{A_{64}\epsilon_{64}} \quad (9)$$

where

T_{64} = measured source temperature on 64-m antenna at Goldstone

C_{r64} = Goldstone 64-m source-size correction factor based on $\Phi_B = 2.25 \text{ min} = 0.0375 \text{ deg}$ [6]⁴

A_{64} = 64-m antenna area

ϵ_{64} = efficiency of 64-m antenna at Goldstone

The efficiency, ϵ_{64} , was obtained by calibrating the 64-m antenna against a single, specific source, 3C274, assuming its X-band flux density to be known

$$\epsilon_{64} = \frac{2kT_0C_{r0}}{A_{64}S_0} \quad (10)$$

where

T_0 = measured 3C274 source temperature, 64-m Goldstone antenna

C_{r0} = computed Goldstone 64-m correction factor for 3C274 = 1.085 ([6], and see Footnote 4)

S_0 = assumed X-band flux density for 3C274 = 46.00 Jy⁵

S_0 was taken from [7] as the best available estimate for this quantity at the time.

Combining Eqs. (8–10) one may write

$$\epsilon_{70} = \frac{2kT_{70}T_0}{A_{70}T_{64}} \times \frac{C_{r70}C_{r0}}{C_{r64}S_0} \quad (11)$$

The various terms on the right-hand side of Eq. (11) are subject to errors, and the cause and influence of these are discussed in the following sections.

B. Errors in C_r

The source-size correction factor C_r corrects the measured efficiency for the loss resulting from the fact that the source has an angular extent that may not be small relative to the antenna beamwidth. Its value is determined from the relationship

$$C_r = \left(\frac{S}{\frac{S_{on}}{\Omega_0} \otimes P} \right)_{max} \quad (12a)$$

where

$$S_{on} = B \otimes P_{on} \quad (12b)$$

$$\tilde{P} = \frac{\Omega_0 \tilde{P}_n}{\tilde{P}_{on}} \quad (12c)$$

B = source brightness function

P_n = antenna relative power pattern

P_{on} = mapping antenna relative power pattern

Ω_0 = mapping antenna beam solid angle

and \otimes means convolution while \tilde{P} = Fourier transform of P , etc. [8].

⁴These are the values appearing in JPL D-3801, rev. A. Rev. B of this document included some corrections necessitated by beamwidth changes resulting from changes in antenna feed on the 64-m antennas.

⁵The spectral formula for 3C274 actually yields $S = 46.02 \text{ Jy}$ at $\nu = 8420 \text{ MHz}$.

The reference to a “mapping antenna” above means that the flux density map of the source, S_{on} , used to compute C_r , has been obtained with an antenna whose beam solid angle $\Omega_0 \ll \Omega$, where the latter is the beam solid angle of the antenna being calibrated (64-m or 70-m). This insures that \tilde{P} , and hence P , defined by Eq. (12c) exist. Note also that

$$S = \frac{1}{\Omega_0} \int S_{on} d\Omega \quad (13)$$

Until recently, determinations of C_r have been based on Gaussian approximations to both the flux density map S_{on} and the antenna beams, and the computation of P by means of Eq. (12b) has been approximate and subject to error. Removal of these deficiencies has resulted in more accurate estimates of C_r for the important source 3C274 which, as seen from the discussion in Section IV.A above, plays a central role in the overall calibration process [8].

Specifically, the values of C_{r0} and C_{r70} for 3C274 have been increased according to Table 3. The impact of these changes will be discussed in Section IV.D.

C. Errors in Flux Density, S

The value of $S_0 = 46.00$ Jy taken from [7] is based on the analysis of all of the known measurements of 3C274, as well as other important antenna calibration sources, up to the year 1974, and is computed directly from the spectral formula

$$\log S \text{ (Jy)} = a + b \log \nu \text{ (MHz)} \quad (14)$$

with $a = 5.023 \pm 0.034$ and $b = -0.856 \pm 0.010$.

The above coefficients were obtained by the authors of [7] by a least-squares fitting to data over the frequency range $400 \text{ MHz} \leq \nu \leq 22285 \text{ MHz}$, but neither the exact data used nor the exact fitting procedure employed can be determined from their paper.

More recent measurements of this source have extended the frequency range up to 90 GHz, and it becomes clear from these newer data that one cannot obtain a reasonable fit with only two coefficients. If a power law of the form

$$y = \sum_{n=0}^3 a_n x^n \quad (15)$$

where $y = \log S \text{ (Jy)}$ and $x = \log \nu \text{ (MHz)}$, is used to fit the data over the entire range $400 \text{ MHz} \leq \nu \leq 90 \text{ GHz}$, then an unweighted fit results in the coefficients

$$a_0 = 3.9964$$

$$a_1 = 0.1733$$

$$a_2 = -0.3341$$

$$a_3 = 0.0352$$

with the resulting X-band value ($\nu = 8420 \text{ MHz}$) of $S_0 = 45.2037 \text{ Jy}$.

The resulting spectrum for 3C274 is shown in Fig. 10, and a number of comments are in order regarding this and other similar results obtained by different authors.

First, the use of a power law expansion such as Eq. (15) cannot be justified on any theoretical basis. The source 3C274 for example, has a complex angular structure reflecting a complex spatial structure, and different regions of the source are known to have very different spectra [7]. Thus, total flux density measurements such as those presented by the data points shown in Fig. 10 correspond to averages over the entire source, and any simple result, as for example Eq. (14) or (15), can only mirror a fortuitous circumstance and/or inadequate resolution in frequency. This means that an accurate spectrum might require terms higher than $n = 3$, for example, but in the absence of accurate measurements at a large number of frequencies one has no way of knowing how large n must be for a best fit. Obviously, if $n = N$, the number of data points, the fit becomes perfect, but not necessarily meaningful.

A second point is illustrated by the two straight line segments shown in Fig. 10, which correspond to estimates made by Ivanov and Stankevich based on a new absolute flux scale for radio astronomy [9]. This scale uses the so-called “artificial moon” method of calibration which, according to the authors, is free of many of the problems associated with other techniques such as the use of a reference dipole or reference horn, and it is seen that it produces values that are consistently below those shown in the figure, giving $S_0 = 41.96 \text{ Jy}$ at X-band, for example.

The artificial moon method itself is open to criticism, however, and a systematic study is presently underway to resolve such discrepancies. Meanwhile, the above discussion points up some of the difficulties involved in determining S_0 for use as an absolute calibration standard. Individual flux density measurements typically have quoted errors of $\pm 4-5$ percent, to which must be added systematic errors resulting from the particular procedures used.

D. Implications of Errors in C_r and S to 70-m Antenna Calibration Results

Using primes to represent quantities for which improved estimates have recently been obtained, Eq. (11) leads to the result

$$\frac{\epsilon'_{70}}{\epsilon_{70}} = \left(\frac{C'_{r70}}{C_{r70}} \right) \left(\frac{C'_{r64}}{C_{r64}} \right) \left(\frac{C'_{r0}}{C_{r0}} \right) \left(\frac{S'_0}{S_0} \right) \quad (16)$$

or, in terms of the resulting change in gain,⁶

$$\begin{aligned} \Delta G = G' - G = & 10 \log \left(\frac{C'_{r70}}{C_{r70}} \right) + 10 \log \left(\frac{C'_{r64}}{C_{r64}} \right) \\ & + 10 \log \left(\frac{C'_{r0}}{C_{r0}} \right) + 10 \log \left(\frac{S'_0}{S_0} \right) \quad (17) \end{aligned}$$

The two main sources that were used in the 70-m antenna gain calibrations are 3C274 and 3C123, and using the above formula one can compute the correction which should be applied to the measurements obtained for each source to allow for the improved values of C_r and S .

Since the term which depends on S_0 is the same for all sources, one has for this constant contribution

$$\Delta G_{S_0} = 10 \log \left(\frac{46.00}{45.2037} \right) = 0.076 \text{ dB} \quad (18)$$

where it is assumed, in the absence of better estimates, that the curve fit to the 3C274 spectrum given by Eq. (15) is probably better than that given in [7], which was based on more limited data.

For the remaining contributions the value of ΔG is different for the two sources. For 3C274, $C_{r64} = C_{r0}$ by definition, so that

$$\begin{aligned} \Delta G_{C_r} &= 10 \log \left(\frac{C'_{r70}}{C_{r70}} \right) = 10 \log \left(\frac{1.18}{1.106} \right) \\ &= 0.281 \text{ dB} \quad (19) \end{aligned}$$

⁶These expressions consider changes resulting from improved estimates of C_r and S , and do not take into account either the probable errors of such estimates, or errors in the measured temperatures appearing in Eq. (11). These are discussed in Section IV.F.

and hence

$$\Delta G(3C274) = 0.357 \text{ dB} \quad (20)$$

where the values for C_{r70} have been taken from Table 3.

For 3C123 no new computations of C_{r64} or C_{r70} have yet been made, but since this source is well represented by a pair of closely spaced Gaussian distributions, and the value of C_r is not large, any corrections ought to be small. Thus, in the absence of information to the contrary one can assume no change in C_{r64} or C_{r70} so that

$$\begin{aligned} \Delta G_{C_r} &= 10 \log \left(\frac{C'_{r0}}{C_{r0}} \right) = 10 \log \left(\frac{1.15}{1.085} \right) \\ &= 0.253 \text{ dB} \quad (21) \end{aligned}$$

and hence

$$\Delta G(3C123) = 0.329 \text{ dB} \quad (22)$$

In addition to 3C274 and 3C123, a limited number of measurements were made using sources 3C161 and 3C218. The former is small enough to be considered a point source, so here also there should be no change in C_{r64} or C_{r70} ; thus ΔG for this source should be the same as that for 3C123,

$$\Delta G(3C161) = 0.329 \text{ dB} \quad (23)$$

Source 3C218, on the other hand, is an extended source, so that in the absence of newly determined values for C_{r64} and C_{r70} it is impossible to determine a ΔG value for this source. Thus, no attempt has been made to use the efficiency measurements obtained with it.

The source 0521-365 is variable so that data on $\epsilon(\alpha)$ obtained with this source can be used to determine the shape of the gain curve, but not its absolute level. Fortunately, data were also taken using 3C274 at DSS-43, where 0521-365 was used, and hence, an absolute calibration of this antenna is possible.

The procedure used was to average the two $G_0(\alpha)$ curves obtained with 0521-365, average the two curves obtained with 3C274, and then determine the average difference between these two over the range of elevation angles for which they overlap ($13^\circ < \alpha < 42^\circ$). This difference was then combined with the ΔG value for 3C274 to obtain a corresponding correction for 0521-365,

$$\Delta G(0521-365) = 0.305 \text{ dB} \quad (24)$$

When the above corrections are applied to the individual runs at each of the 70-m stations, the gain curves shown in Figs. 11–16 are obtained, and it is seen that the spread between curves has been reduced and the overall gains increased.

In the following sections final estimates for the gain curves at each station are obtained, and an assessment is made of the probable errors involved in terms of the analysis made above.

E. Estimates of Gain versus Elevation for Individual 70-m Stations

The average gain characteristic for each DSS has been obtained by applying the corrections of Eqs. (20), (22), (23) and (24) to the data for each run at a given station, and then determining the best fit of the combined data sets to Eq. (3), as was previously done for each individual run (see Appendix A for a discussion of the quality of the fits).

For DSS-14 all six data sets have been used, while for DSS-43 and DSS-63 only the two sets each obtained with sources 0521-365 and 3C123, respectively, have been used.

The results of this final curve fitting are shown in Figs. 7 and 8, and Table 4 lists the fitting parameters for the three stations, together with the theoretical values shown in Table 1, and the design-expected peak gain [1]. The error estimates listed in the table for the measured peak gains G_m are based on the analysis carried out in the following section.

F. Estimates of Errors in Aperture Efficiency and Gain

From Eq. (7) one may express the variance of the efficiency, σ_ϵ^2 , as

$$\left(\frac{\sigma_\epsilon}{\epsilon}\right)^2 = \left(\frac{\sigma_T}{T}\right)^2 + \left(\frac{\sigma_{C_r}}{C_r}\right)^2 + \left(\frac{\sigma_s}{S}\right)^2 \quad (25)$$

where

σ_T^2 = variance of measured source temperature

$\sigma_{C_r}^2$ = variance of source-size correction factor

σ_s^2 = variance of source flux density

The measured source temperature variance, σ_T^2 , itself depends on many factors, not all of which can be accurately estimated. However, if one considers the measurements made

at a given station and with a given source, then the last two terms in Eq. (25) vanish, so that

$$\left(\frac{\sigma_T}{T}\right)^2 = \left(\frac{\sigma_\epsilon}{\epsilon}\right)^2 \bigg|_{\substack{\text{station,} \\ \text{source}}} \quad (26)$$

Examination of the data taken at all three stations shows that σ_ϵ^2 is comparable for each if one considers individual runs (see Figs. A-1–A-11). When all runs at a given station are considered, however, the variation is larger at DSS-14 than at the other two, and using this larger value as a conservative estimate, one obtains

$$\frac{\sigma_T}{T} = \frac{\sigma_\epsilon}{\epsilon} \bigg|_{\substack{\text{DSS14} \\ \text{3C123}}} = 0.010 \quad (27)$$

The remaining terms in Eq. (25) must be considered from the point of view of ensemble averages, and are estimated by

$$\frac{\sigma_{C_r}}{C_r} = 0.020 \quad (28)$$

$$\frac{\sigma_s}{S} = 0.040$$

the former being based on source-map and beamwidth accuracies [8], and the latter on quoted errors in the literature on source flux density measurements [7].⁷

Combining the above

$$\frac{\sigma_\epsilon}{\epsilon} = 0.046 \quad (29)$$

resulting in a corresponding gain error of

$$\sigma_G = \begin{matrix} +0.19 \\ -0.20 \end{matrix} \text{ dB} \quad (30)$$

If the estimated pointing loss found in Appendix B (0.028 dB) is added to the upper bound above, then the error estimate becomes

$$\sigma_G = \pm 0.21 \text{ dB} \quad (31)$$

⁷As mentioned earlier in this article, such errors are typically 4–5 percent. The smaller value is chosen because of a small degree of confidence stemming from the relative insensitivity of S_0 to various curve fits to the 3C274 spectral data.

V. Summary of 70-m S-Band Gain versus Elevation Measurements for DSS-14, DSS-43, and DSS-63

Compared with the X-band measurements, only a limited amount of data were gathered at the three DSSs at S-band. At DSS-14 only a single run was made, at DSS-43 three were made, and at DSS-63 two were made. Fortunately, the data at DSS-14 cover the range of elevation angles from $\alpha = 7$ deg to $\alpha = 84$ deg with the calibration source 3C123, while at DSS-43 the full range measurements with the variable source 0521-365 ($10 \text{ deg} < \alpha < 85 \text{ deg}$) are complemented by limited range data obtained with the calibration sources 3C274 and 3C218, thus permitting an absolute gain calibration of both stations in a manner similar to that employed in the X-band analysis.

At DSS-63 neither of the runs is suitable for analysis owing to the large amount of scatter present in the measurements, and consequently no attempt has been made to determine the S-band gain characteristics for this station directly.

However, as described below (see Section VI), it has nonetheless been possible to obtain a calibrated gain curve for this station at S-band by making limited use of the S-band data and combining this with the X-band results for the same station.

The results of the analysis of DSS-14, DSS-43, and DSS-63 data are summarized in Figs. 17 and 18, which show $G(\alpha)$ and $G_0(\alpha)$ respectively for each of these stations. As in the case of the X-band results, these curves represent the result of fitting to the Ruze formula and applying overall gain corrections resulting from updated C_r and S values obtained for S-band. The details of this analysis are given in the following sections.

VI. Analysis of S-Band Gain Measurements

Figures 19 and 20 show the results of fitting Eq. (3) to the measured data for DSS-14 and -43, using Eqs. (4) and (5) to transform $\epsilon(\alpha)$ into $G(\alpha)$ and $G_0(\alpha)$ as before, where for S-band ($\nu = 2295 \text{ MHz}$), $K = 25.9296 \text{ dB/in.}^2$, and for all stations the single value $A_{0z} = 0.0297$ has been used.

It is seen that the gain curves are very flat, as expected, thus making the estimate of the angle γ obtained from such a fit ambiguous. For this reason γ has been fixed at the values determined from the X-band fitting procedure for each of the two stations, and the S-band fits are obtained using only the four remaining parameters G_m , S_y , S_z , and C .

The DSS-43 curve is also seen to be anomalously low owing to the choice of an abnormally high assumed flux density

value for the variable source 0521-365 in computing $\epsilon(\alpha)$ from $T(\alpha)$ via Eq. (7). The absolute calibration of the S-band gains is discussed in the following section.

Comparison of the parameter values S_y and S_z obtained at X-band and at S-band for DSS-14 and -43 shows that there is reasonably good agreement in general, although the S-band values for DSS-43 appear somewhat higher than the corresponding X-band values for this station. However, by virtue of the flatness of the curves, the same ambiguity referred to above for the angle γ also exists to a considerable extent for the parameters S_y , S_z , and C , i.e., different combinations of these parameters will provide essentially the same $G_0(\alpha)$ curve within the experimental accuracy of the measurements.

In view of this it is of interest to see how well the S-band data are fit by the X-band parameters γ , S_y , S_z , and C . In principle, these ought to be the same at both frequencies, as the latter three depend only on how the antenna structure distorts as its elevation is changed from the value γ , which is itself, of course, a fixed quantity.

Such a comparison is made in Figs. 21 and 22, which show curves generated with the X-band parameters superimposed on the $G(\alpha)$ data points measured at S-band. The fits were obtained by adjusting the single remaining parameter G_m , the maximum gain, and it is seen from these figures that the resulting fits are very good. The σ values for the best fits to the S-band data, σ_{ss} , and the X-band parameter fits to the S-band data, σ_{xs} , are compared in Table 5, and it is seen that the latter are only slightly larger than the former, both being very small.

Since there is little to choose between the two fitting procedures considered above, and since the four-parameter set γ , S_y , S_z , C should be frequency independent, the X-band parametric fits to the S-band data are chosen as the final representations for the shape of the S-band gain curves for DSS-14 and -43.

While the DSS-63 data are not suitable for direct determination of the gain characteristics for this station, as mentioned in Section V, that taken on DOY 124 yield a maximum gain G_m which is very close to that found for the other two stations. This value of G_m , adjusted for calibration errors as discussed in Section VII, has been combined with the remaining X-band parameters for this station to determine its absolute S-band gain curve, once again taking advantage of the frequency-independent nature of these parameters. The results of this determination are shown in Figs. 17 and 18, and the fit to the S-band data from which the value of G_m is estimated is shown in Fig. 23.

VII. S-Band Calibration Analysis

Determination of the absolute maximum gains, G_m , for each of the three DSSs at S-band follows the same procedure described in Section IV, where newly determined values for the source flux densities, S , and source-size correction factors, C_r , are used to correct the measured gain values discussed in the previous section.

The analysis in Section IV follows exactly the same way for S-band, except that the 26-m station at DSS-13 was used in determining the S-band D-3801 values for S and C_r , rather than the 64-m station. These determinations were made by Klein and Stelzried [10] by essentially the same procedure that was later used by Turegano and Klein [6] at X-band, using source 3C274 as a standard to calibrate secondary standards, including 3C123 and 3C218.

One difference occurs at S-band however, and this is that the flux density assumed for 3C274 during the 26-m calibration measurements was not the same as that appearing in D-3801, as was the case at X-band. The reason for this difference is that at the time the 26-m measurements were made, the best estimate of this quantity was that due to Baars and Hartsuijker [11], namely $S = 140.3$ Jy, whereas at the time of writing D-3801 rev. A (June 30, 1987), the best estimate was that determined by Baars, Genzel, Pauliny-Toth, and Witzel, $S = 140.00$ Jy [7]. This value remained the same in D-3801 rev. B, and hence is the one used in determining S-band gains using the source 3C274.

As a matter of interest, yet another value for this quantity was determined by direct, absolute measurements using a calibrated horn reference by Freiley, Batelaan, and Bathker [12]. These authors obtained the value $S = 136.5 \pm 2.6$ Jy, which is significantly lower than the above values.⁸

The power law fit of Eq. (15) yields an S-band value ($\nu = 2295$ MHz) of 138.48 Jy, which is between the Baars et al. [7] estimate and that of Freiley et al. [12]. Given the tolerances for these measurements it seems reasonable to use the above value of 138.48 Jy and so maintain consistency with the X-band analysis, and this is done below.

As a consequence of the above-mentioned difference between the 3C274 S value used in D-3801 rev. B and that used by Klein and Stelzried, the ΔG values computed for 3C274 on the one hand, and 3C123 and 3C218 on the other, are different, i.e.,

$$\Delta G_{s_0} (3C274) = 10 \log \left(\frac{140.00}{138.48} \right) = 0.047 \text{ dB} \quad (32)$$

$$\Delta G_{s_0} (3C123/3C218) = 10 \log \left(\frac{140.3}{138.48} \right) = 0.057 \text{ dB} \quad (33)$$

Table 6 summarizes the results of recomputing the 3C274 26-m C_r values, C_{r0} , and the 70-m C_r values, C_{r70} , at S-band [8]. From these values the following ΔG_{C_r} values are readily obtained:

$$\Delta G_{C_r} (3C274) = 10 \log \left(\frac{1.205}{1.14} \right) = 0.241 \text{ dB} \quad (34)$$

$$\Delta G_{C_r} (3C123/3C218) = 10 \log \left(\frac{1.045}{1.035} \right) = 0.042 \text{ dB} \quad (35)$$

Combining these

$$\Delta G (3C274) = 0.288 \text{ dB} \quad (36)$$

$$\Delta G (3C123/3C218) = 0.099 \text{ dB} \quad (37)$$

In the above it has been assumed that, owing to the very small values of C_r for the 26-m and 70-m antennas for both 3C123 and 3C218, no significant changes in these values would occur as a result of recomputation.

When average differences are determined from gain measurements made at DSS-43 using the three sources 0521-365, 3C274, and 3C218, it is found that

$$G (3C218) - G (3C274) = 0.192 \text{ dB} \quad (38)$$

This should be equal to

$$\Delta G (3C274) - \Delta G (3C218) = 0.190 \text{ dB} \quad (39)$$

and it is seen that the agreement is excellent.

Combining these gain corrections with the measured gain using 0521-365, the gain correction for this source is found to be

$$\Delta G (0521-365) = 2.395 \text{ dB} \quad (40)$$

As mentioned above, this large value is the result of the use of an abnormally high flux density value for the efficiency calculations made at the station.

When the above gain corrections are applied to the curve fits obtained for each station, the G_m values listed in Table 7 are found.

⁸The frequency used by these authors was 2278.5 MHz. If their flux density is translated to 2295 MHz using the Baars, et al. [7] spectral index of -0.856, the result is another 0.6 percent lower.

According to the design estimates of Bathker and Slobin [1], the 70-m S-band peak gains should lie in the range 63.27–63.35 dBi, so the agreement between these estimates and the measured values is excellent.⁹

The error estimates included in Table 7 are based on an analysis similar to that described in Section IV.F, where the individual error contributions are

$$\begin{aligned}\frac{\sigma_T}{T} &= 0.035 \\ \frac{\sigma_{C_r}}{C_r} &= 0.015 \\ \frac{\sigma_s}{S} &= 0.02\end{aligned}\quad (41)$$

so that

$$\begin{aligned}\frac{\sigma_\epsilon}{\epsilon} &= 0.025 \\ \sigma_G &= \pm 0.11 \text{ dB}\end{aligned}\quad (42)$$

The 2-percent error estimate for S-band flux density is based on the very careful work of Freiley et al. [12], plus the fact that the new value for S obtained by the curve fitting procedure described in Section IV.C is within 2 percent of both their estimate and that due to Baars et al. [7].

VIII. Summary and Conclusions

The final curve fits to the X-band data (Fig. 8) indicate that there are distinct differences between the gain characteristics

of the three DSS 70-m antennas. The highest peak gain is achieved by DSS-63 ($G_m = 74.29$ dBi at $\gamma = 47.7$ deg), while the flattest characteristic, and that most closely approximating the theoretical performance, occurs at DSS-14.

Comparison of the peak gains listed in Table 4 with the design-expected performance reported by Bathker and Slobin [1], $G_m = 74.32^{+0.05}_{-0.14}$ dBi, shows that the two are consistent when allowance is made for the probable errors in both cases, i.e., the upper bounds of the Table 4 values exceed the lower bound of 74.18 dBi for the design expectations.

The situation with respect to the actual shapes of the gain curves, however, is less satisfactory. The three antennas show distinctly different behavior, and only one, DSS-14, is in good agreement with predictions based on structural model calculations.¹⁰

If the measured curve shown in Fig. 8 for DSS-14 is displaced upward to coincide with the theoretical curve at the peak, the two virtually lie on top of one another for $10 \text{ deg} \leq \alpha \leq 60 \text{ deg}$, and the maximum difference between them is 0.26 dB at $\alpha = 90 \text{ deg}$. However, if the same thing is done for DSS-63, discrepancies amounting to 0.5 to 0.6 dB exist at low and high elevations respectively. For DSS-43 these differences amount to 0.5 dB at each end.

Based on estimates of the probable measurement errors inherent in the characteristics shown in Fig. 8, it seems unlikely that these discrepancies are measurement related, especially since the three antennas behave quite differently from one another.

The relatively good agreement found between calculated and measured peak gains, on the other hand, has been achieved as a consequence of improved estimates of source flux densities and source-size correction factors for the natural radio sources used to calibrate the antennas [8]. Here, corrections on the order of 0.3 dB have brought the measured gains to within 0.15 dB of the theoretical value, on the average.

⁹These authors' analysis was carried out assuming a frequency of 2285 MHz, so their gain results have been translated to 2295 MHz under the assumption that the aperture efficiency is sensibly constant over this small range.

¹⁰Roy Levy, personal communication.

Acknowledgments

The authors would like to thank Dan Bathker, Michael Klein, and Roy Levy for their continued interest in the analysis presented in this article, and their very helpful criticism regarding several important points discussed. Thanks are also due to Timothy Pham for his assistance in carrying out the curve fitting and producing the figures for the article, and last but not least, to Ted Peng for his encouragement and patience in seeing the work to its completion.

References

- [1] D. A. Bathker and S. D. Slobin, "DSN 70-M Antenna Microwave Optics Design and Performance Improvements Part I: Design Optimization," *TDA Progress Report 42-97*, Jet Propulsion Laboratory, Pasadena, California, this issue.
- [2] J. Ruze, "Antenna Tolerance Theory—A Review," *Proc. IEEE*, vol. 54, no. 4, pp. 640–663, April 1966.
- [3] R. Levy, "A Method for Selecting Antenna Rigging Angles to Improve Performance," *Space Programs Summary 37-65*, vol. II, Jet Propulsion Laboratory, Pasadena, California, pp. 72–76, September 30, 1970.
- [4] J. M. Schredder, "Seventy-Meter Antenna Performance Predictions: GTD Analysis Compared with Traditional Ray-Tracing Methods," *TDA Progress Report 42-92*, vol. October–December, Jet Propulsion Laboratory, Pasadena, California, pp. 166–174, February 15, 1988.
- [5] P. R. Bevington, *Data Reduction and Error Analysis for the Physical Sciences*, New York: McGraw-Hill, p. 144, 1969.
- [6] J. A. Turegano and M. J. Klein, "Calibration Radio Sources for Radio Astronomy: Precision Flux Density Measurements at 8420 MHz," *Astron. Astrophys.*, vol. 86, pp. 46–49, 1980.
- [7] J. M. W. Baars, R. Genzel, I. I. K. Pauliny-Toth, and A. Witzel, "The Absolute Spectrum of Cas A; An Accurate Flux Density Scale and a Set of Secondary Calibrators," *Astron. Astrophys.*, vol. 61, pp. 99–106, 1977.
- [8] M. J. Klein and P. H. Richter, "Accurate Radio Astronomy Correction Factors C_r for Extended Sources," to be submitted to the *TDA Progress Report*.
- [9] V. P. Ivanov and K. S. Stankevich, "Absolute Flux Scale for Radioastronomy (Review)," *Izvestiya Vysshikh Uchebnykh Zavedenni, Radiofizika*, vol. 29, no. 1, pp. 3–27, January 1986.
- [10] M. J. Klein and C. T. Stelzried, "Calibration Radio Sources for Radio Astronomy: Precision Flux-Density Measurements at 2295 MHz," *Astron. J.*, vol. 81, no. 12, pp. 1078–83, 1976.
- [11] J. M. W. Baars and A. P. Hartsuijker, "The Decrease of Flux Density of Cassiopeia A and the Absolute Spectra of Cassiopeia A, Cygnus A, and Taurus A," *Astron. Astrophys.*, vol. 17, pp. 172–181, 1972.
- [12] A. J. Freiley, P. D. Batelaan, and D. A. Bathker, "Absolute Flux Density Calibrations of Radio Sources: 2.3 GHz," JPL Technical Memorandum 33-806, Jet Propulsion Laboratory, Pasadena, California, p. 4-12, December 1, 1977.

Table 1. Ruze-Levy X-band fitting parameters obtained from individual runs at the three 70-m stations; theoretical values calculated by Levy are also shown for comparison

DSS	DOY	γ , deg	S_y , in.	S_z , in.	C
14	100	42.76	0.075	0.063	0.855
14	101	47.32	0.083	0.078	0.775
14	109	41.27	0.121	0.119	0.964
14	114	46.21	0.049	0.022	-0.997
14	115/116	46.74	0.092	0.075	0.650
14	143	48.31	0.074	0.040	0.152
43	192/193	47.73	0.074	0.087	0.389
43	193/194	44.68	0.053	0.079	0.096
63	124	46.96	0.132	0.133	0.820
63	201	48.20	0.059	0.048	-0.820
63	207	42.95	0.059	0.046	-0.970
Theoretical Values		45.00	0.032	0.041	0.030

Table 2. Holographic setting angles for the three 70-m antennas

DSS	Setting angle, deg
14	47.0
43	47.3
63	41.8

Table 3. Comparison of old and new source-size correction factors for source 3C274 with the 64-m antennas (C_{r0}) and the 70-m antennas (C_{r70}) at X-band

	Old value	New value
C_{r0}	1.085	1.15
C_{r70}	1.106	1.18

Table 4. Final Ruze-Levy X-band parameter fits for the three 70-m antennas based on overall averages of calibrated data

DSS	γ , deg	G_m , dB	S_y , in.	S_z , in.	C
14	45.930	74.172 ± 0.21	0.0462	0.0209	-0.9935
43	46.155	74.092 ± 0.21	0.0665	0.0857	0.3255
63	46.836	74.284 ± 0.21	0.0645	0.0702	-0.0300
Theoretical Values	45.000	$74.32^{+0.05}_{-0.14}$	0.032	0.041	0.030

Table 5. Comparison of the standard deviations for fitting S-band data with X-band and S-band Ruze-Levy parameters

DSS	σ_{xs} , dB	σ_{ss} , dB
14	0.015	0.012
43	0.017	0.015

Table 6. Comparison of old and new source-size correction factors for source 3C274 with the 26-m antenna (C_{r0}) and the 70-m antennas (C_{r70}) at S-band

	Old value	New value
C_{r0}	1.035	1.045
C_{r70}	1.14	1.205

Table 7. Final S-band peak gains (no atmosphere) for the three 70-m antennas

DSS	G_m , dB
14	63.301 ± 0.11
43	63.354 ± 0.11
63	63.361 ± 0.11

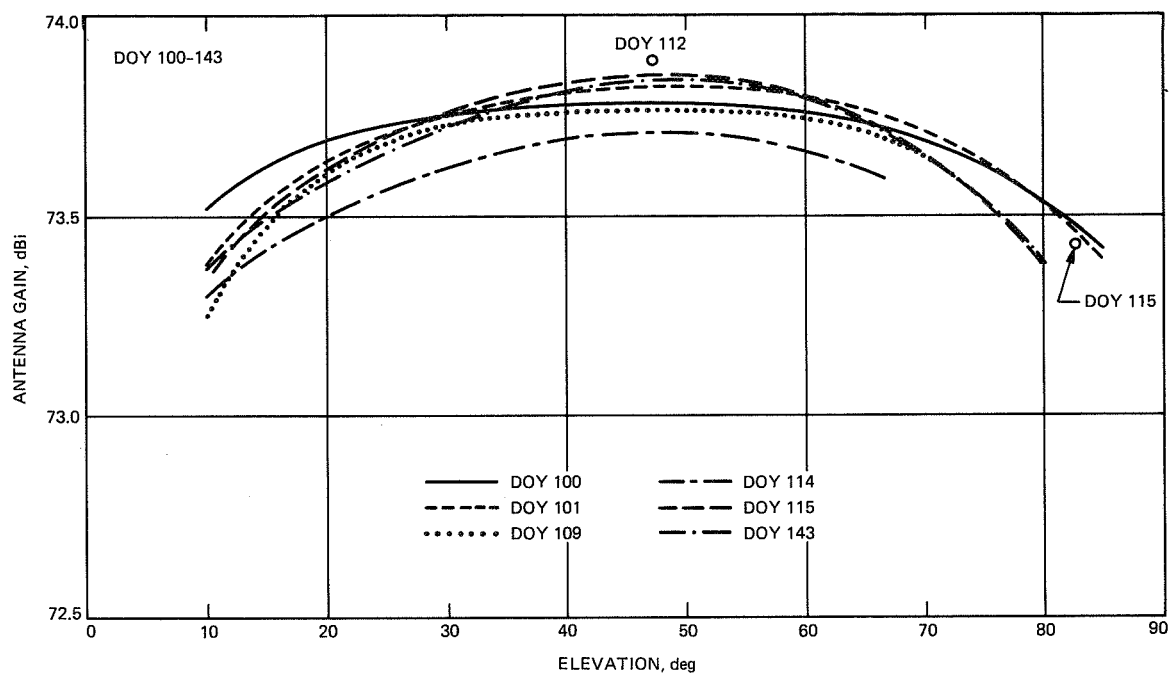


Fig. 1. X-band gain versus elevation for the 70-m antenna at DSS-14 based on uncalibrated data and including atmospheric absorption.

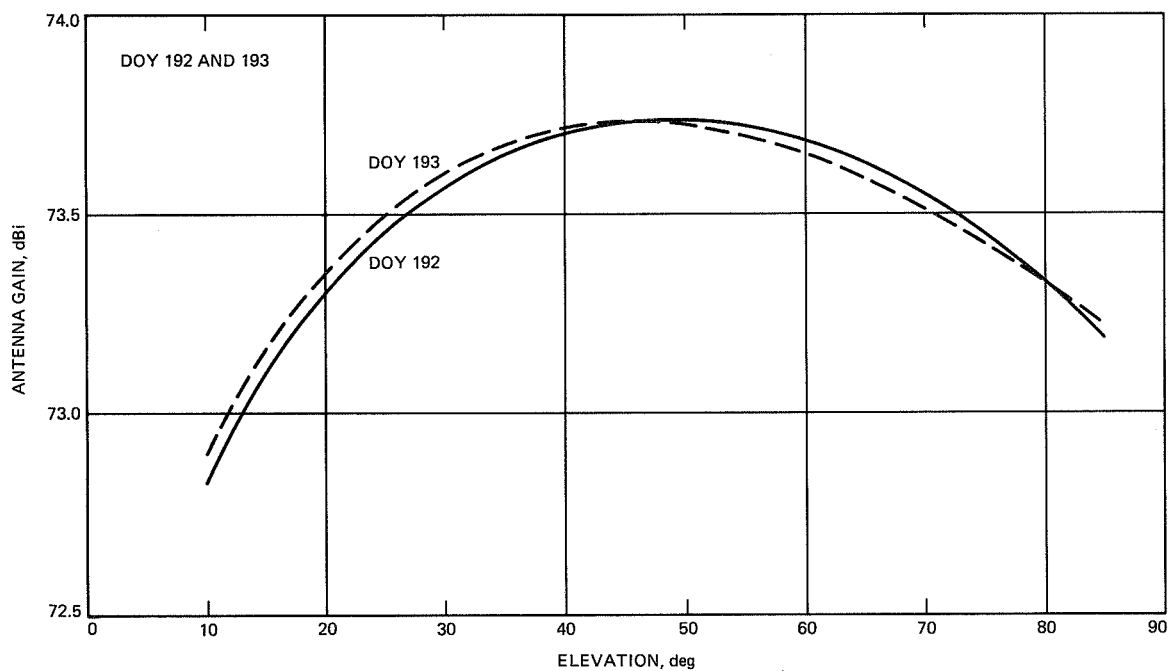


Fig. 2. X-band gain versus elevation for the 70-m antenna at DSS-43 based on uncalibrated data and including atmospheric absorption.

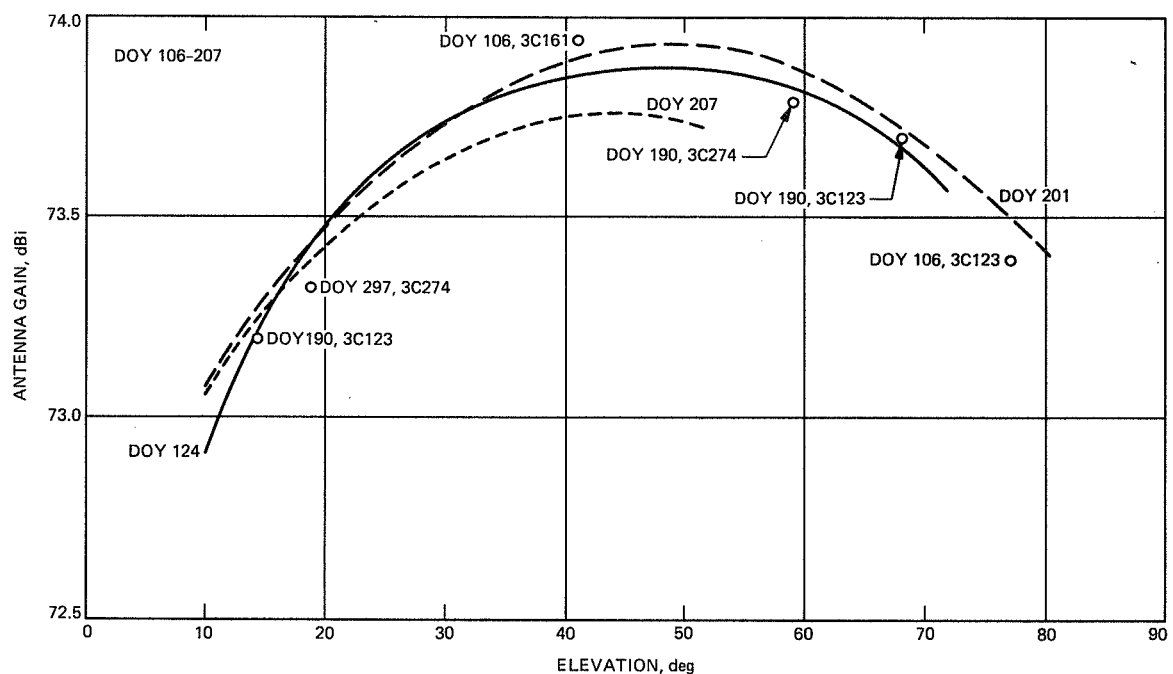


Fig. 3. X-band gain versus elevation for the 70-m antenna at DSS-63 based on uncalibrated data and including atmospheric absorption.

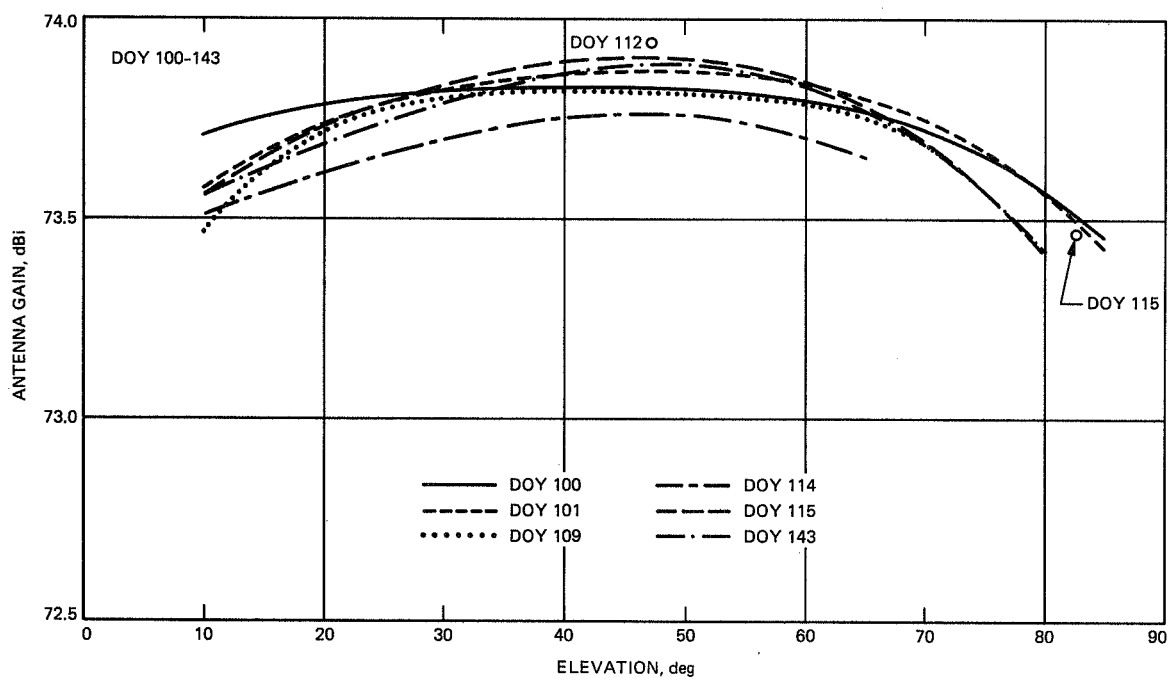


Fig. 4. X-band gain versus elevation for the 70-m antenna at DSS-14 based on uncalibrated data. Atmospheric absorption has been removed.

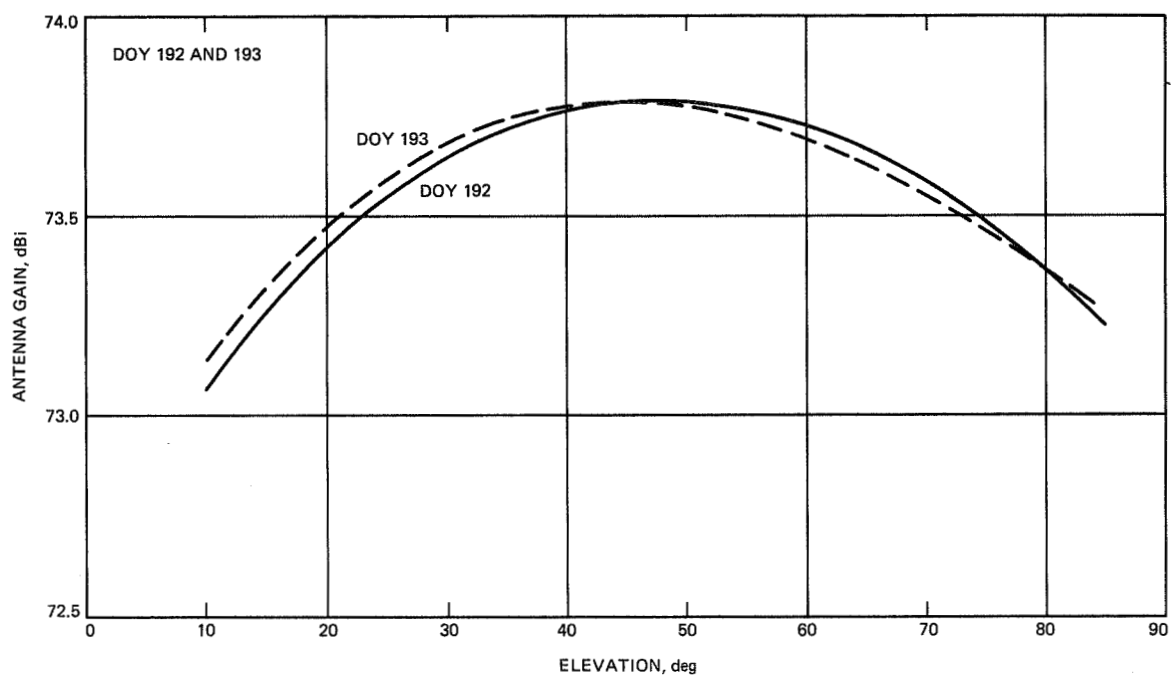


Fig. 5. X-band gain versus elevation for the 70-m antenna at DSS-43 based on uncalibrated data. Atmospheric absorption has been removed.

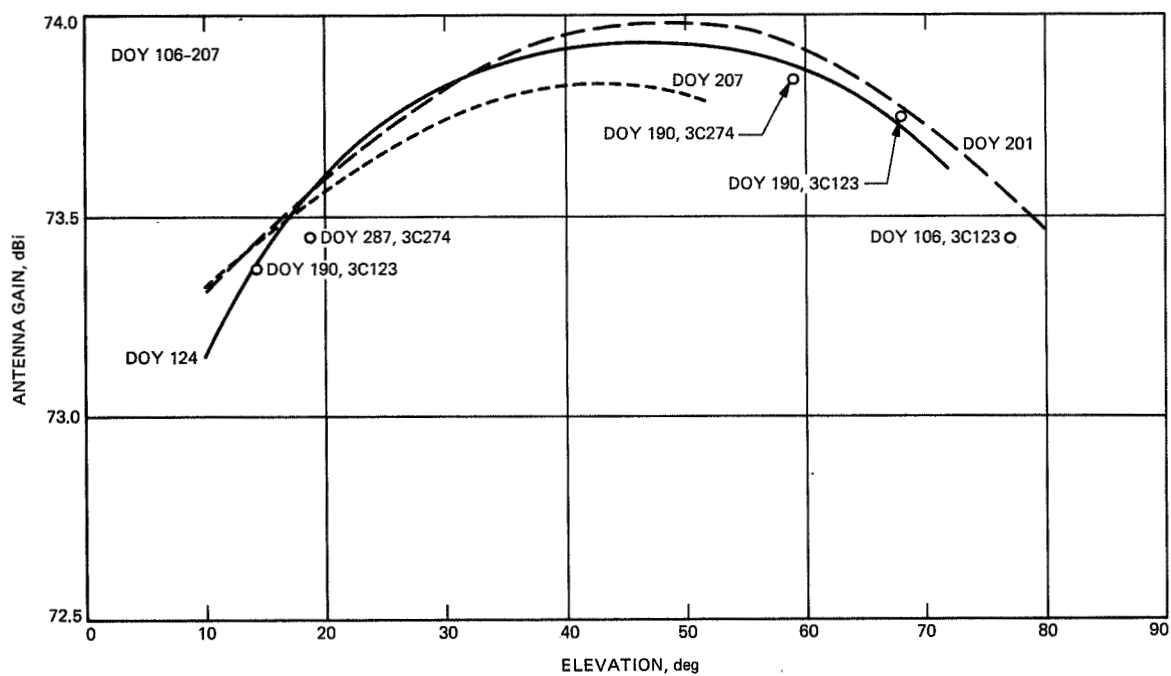


Fig. 6. X-band gain versus elevation for the 70-m antenna at DSS-63 based on uncalibrated data. Atmospheric absorption has been removed.

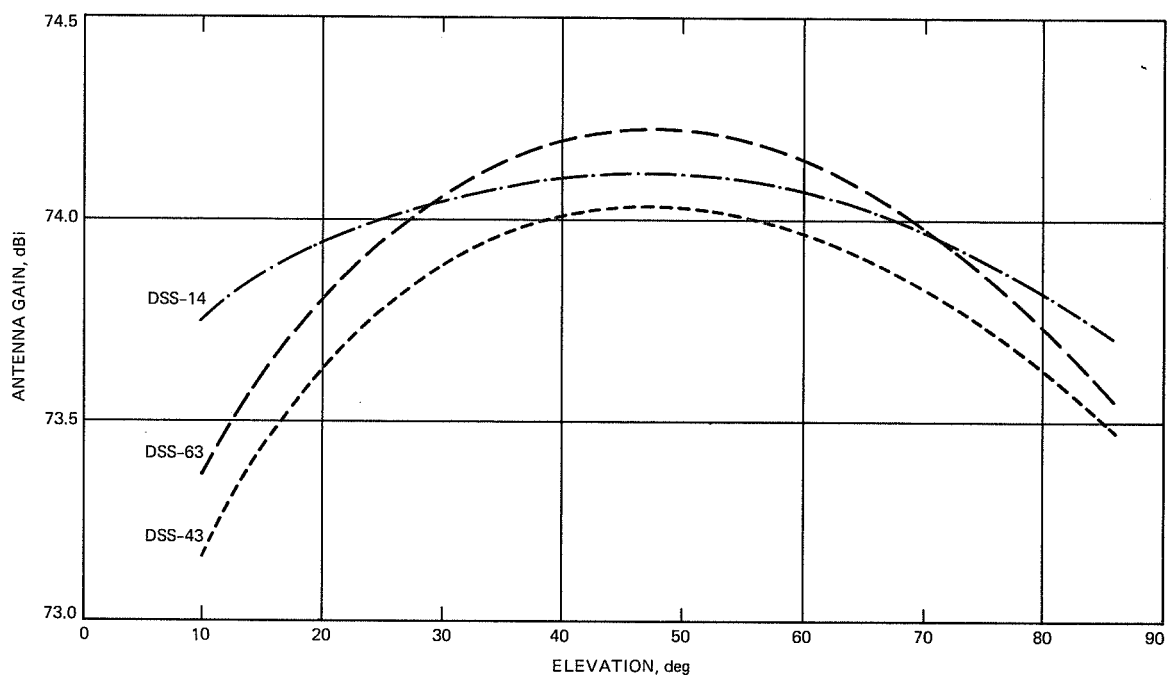


Fig. 7. Calibrated, average X-band gain characteristics for the 70-m antennas, including absorption due to a clear, dry atmosphere.

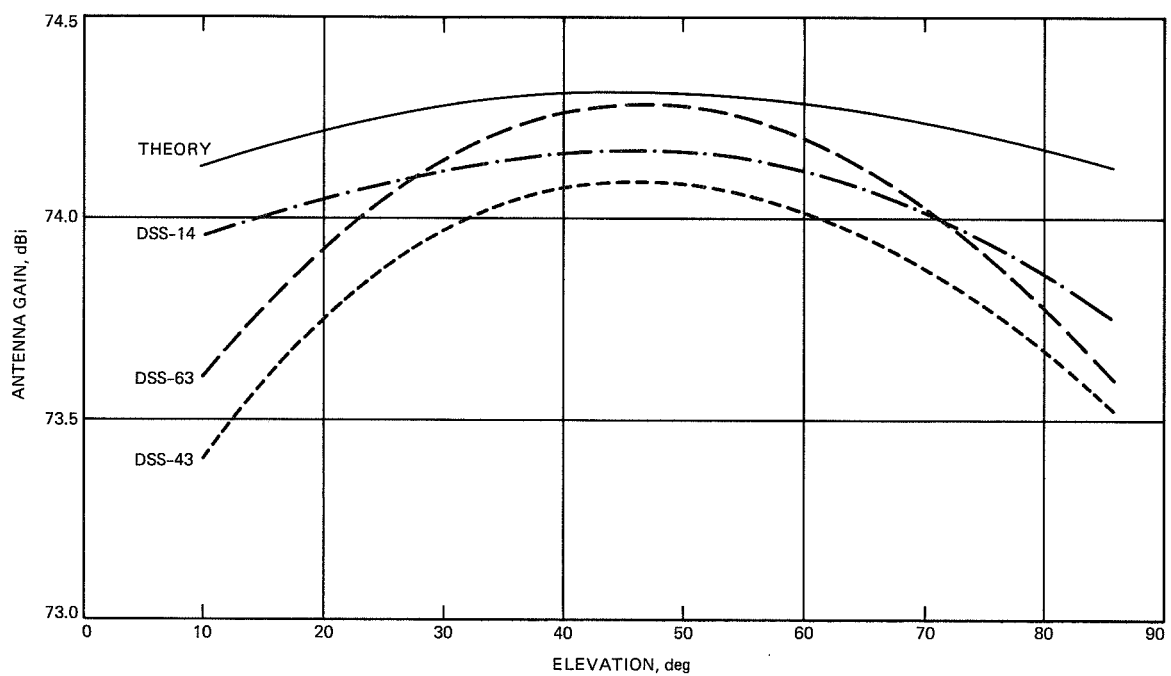


Fig. 8. Calibrated, average X-band gain characteristics for the 70-m antennas; no atmospheric absorption has been included.

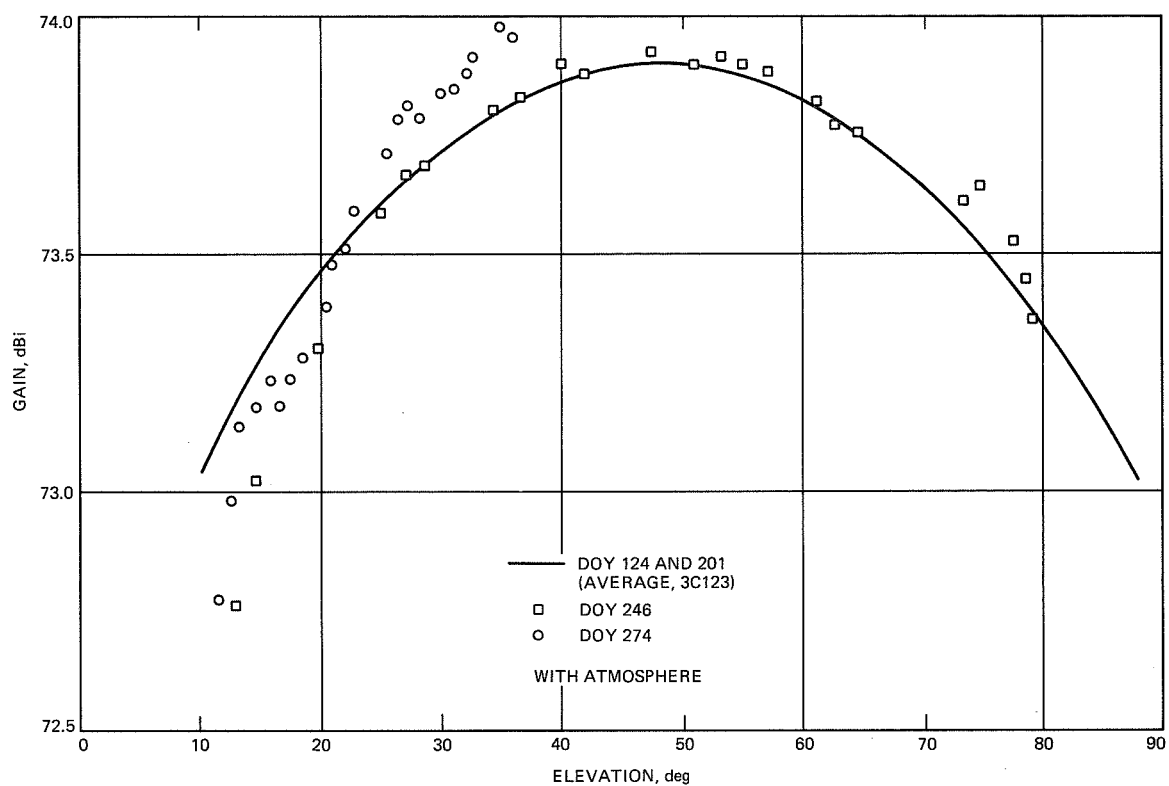


Fig. 9. Comparison of the X-band gain characteristics at DSS-63 before and after rebolting the structural brace.

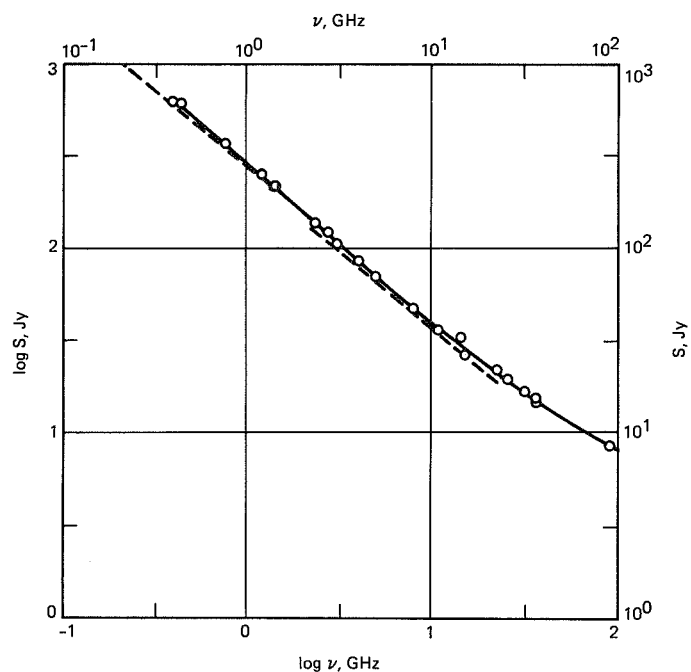


Fig. 10. Flux density spectrum for source 3C274. The points correspond to measured values obtained by various workers, and the solid curve is a cubic power law fit based on equal weighting. The dashed linear curves are estimates based on the artificial-moon calibration method.

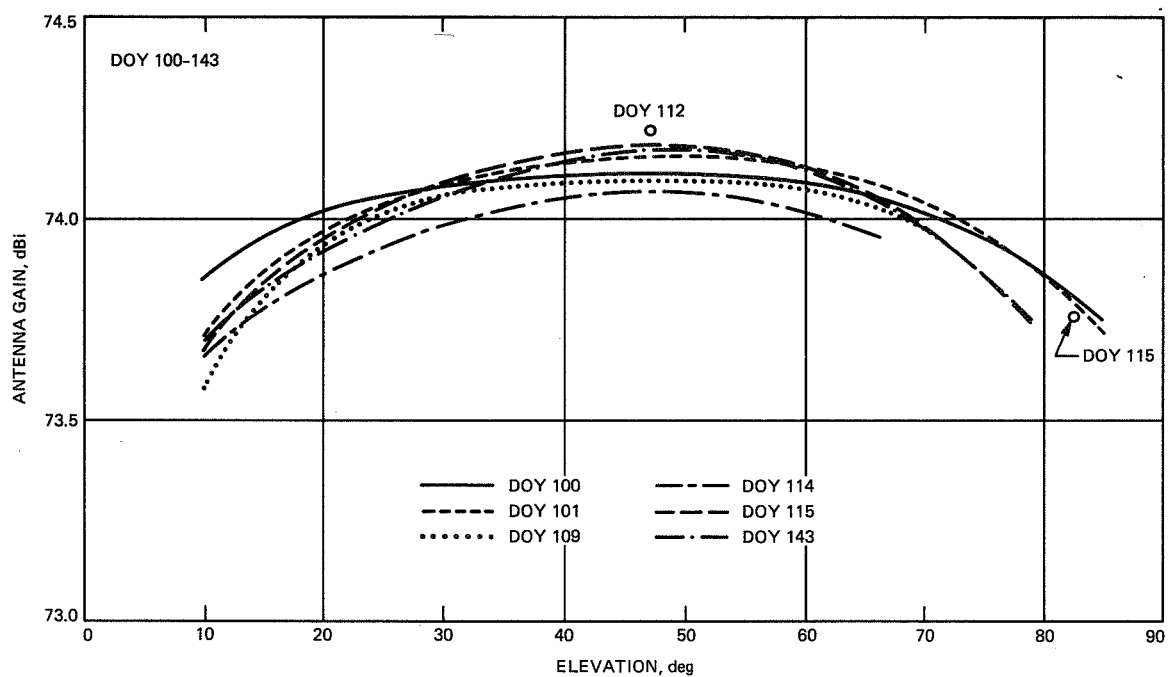


Fig. 11. X-band gain versus elevation for the 70-m antenna at DSS-14 including calibration adjustments and atmospheric absorption.

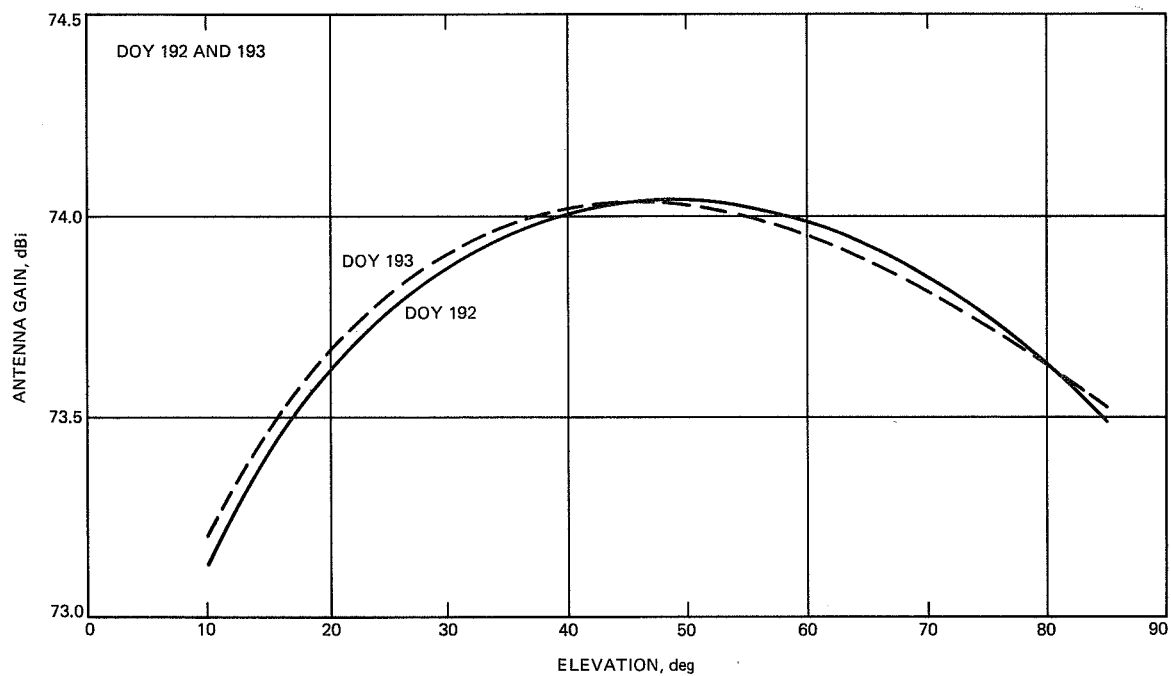


Fig. 12. X-band gain versus elevation for the 70-m antenna at DSS-43 including calibration adjustments and atmospheric absorption.

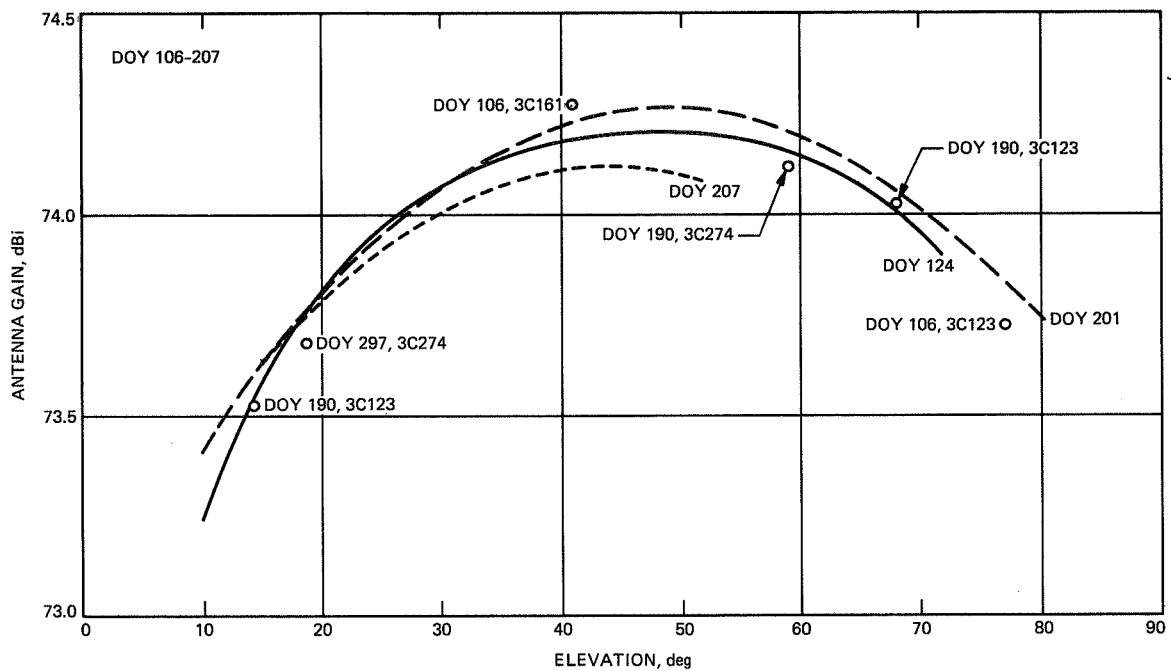


Fig. 13. X-band gain versus elevation for the 70-m antenna at DSS-63 including calibration adjustments and atmospheric absorption.

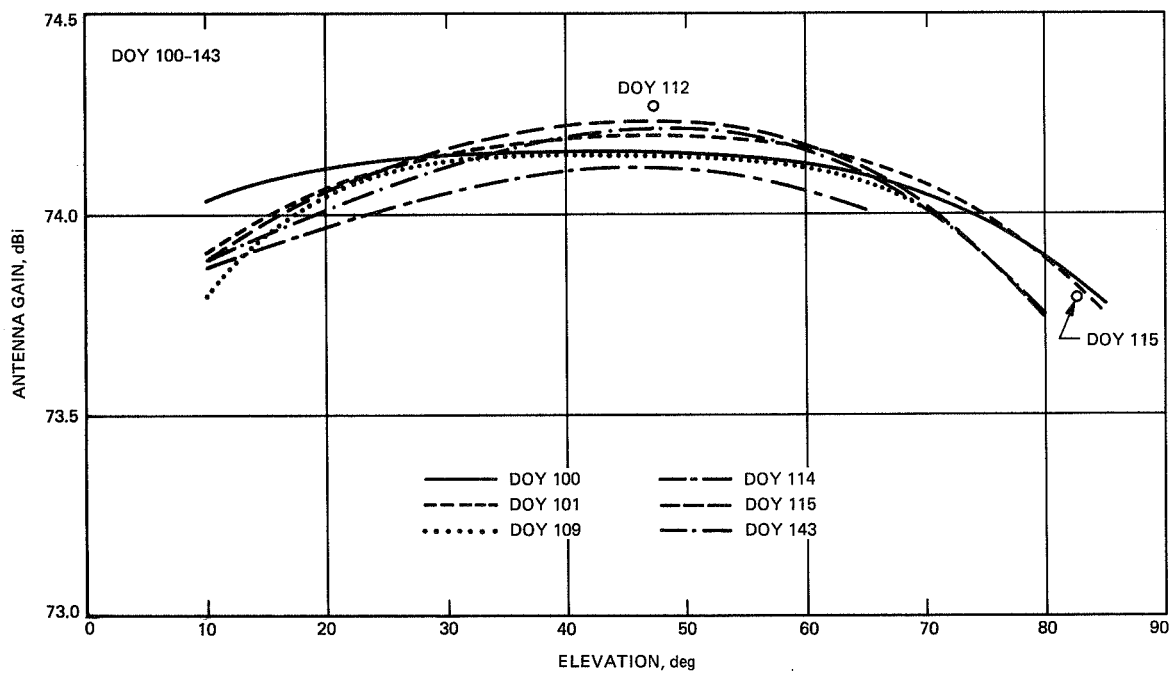


Fig. 14. X-band gain versus elevation for the 70-m antenna at DSS-14 including calibration adjustments; atmospheric absorption has been removed.

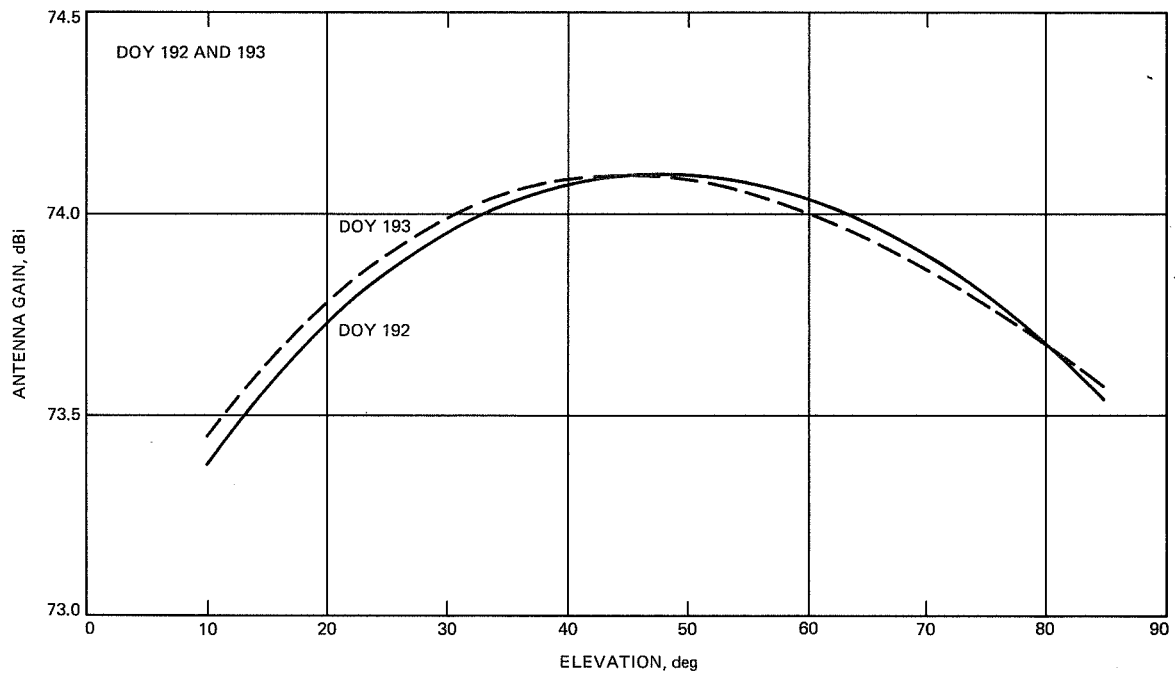


Fig. 15. X-band gain versus elevation for the 70-m antenna at DSS-43 including calibration adjustments; atmospheric absorption has been removed.

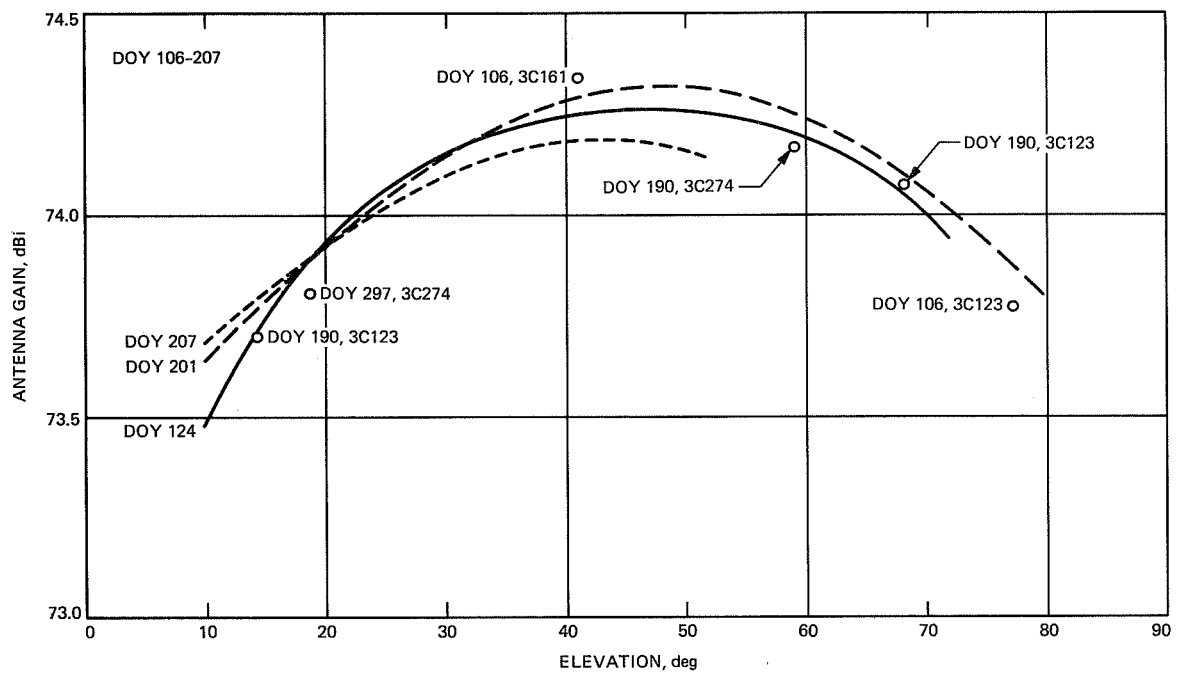


Fig. 16. X-band gain versus elevation for the 70-m antenna at DSS-63 including calibration adjustments; atmospheric absorption has been removed.

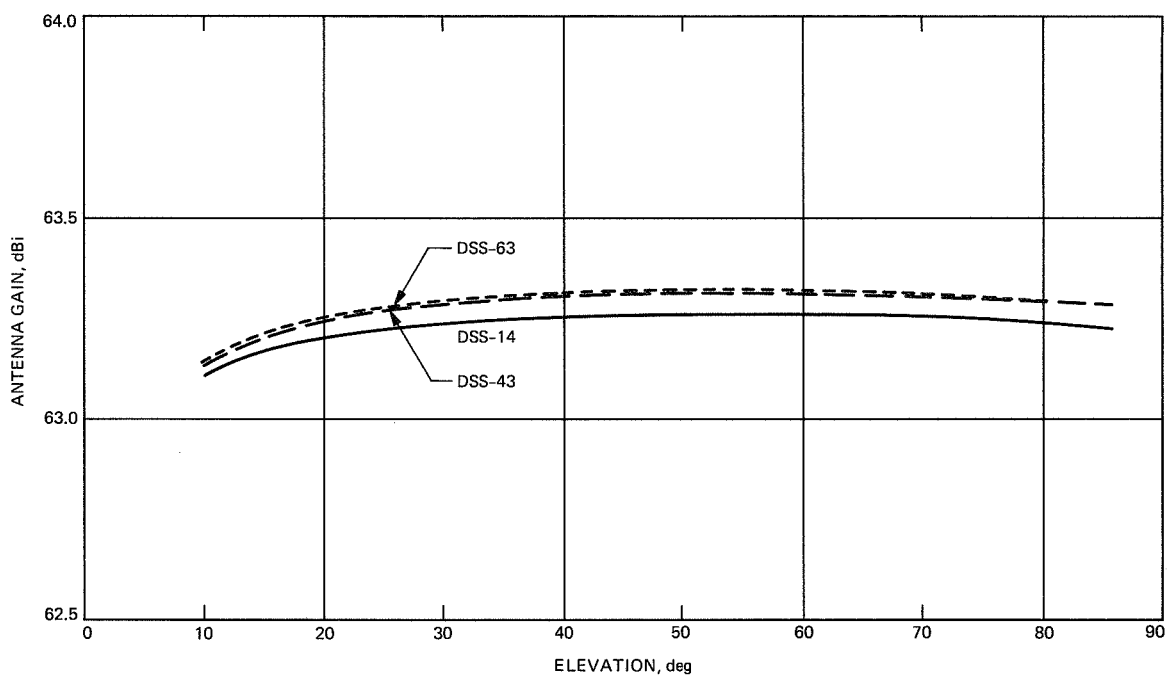


Fig. 17. Calibrated, average S-band gain characteristics for the 70-m antennas at DSS-14 and DSS-43 including absorption due to a clear, dry atmosphere.

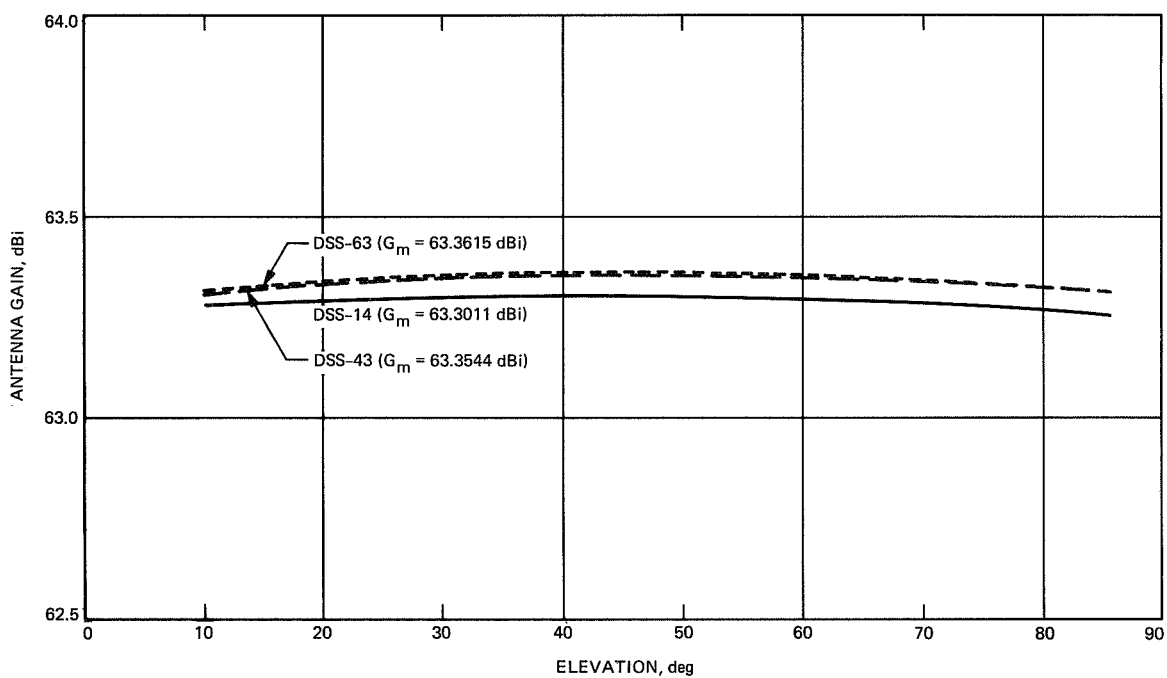


Fig. 18. Calibrated, average S-band gain characteristics for the 70-m antennas at DSS-14 and DSS-43; no atmospheric absorption has been included.

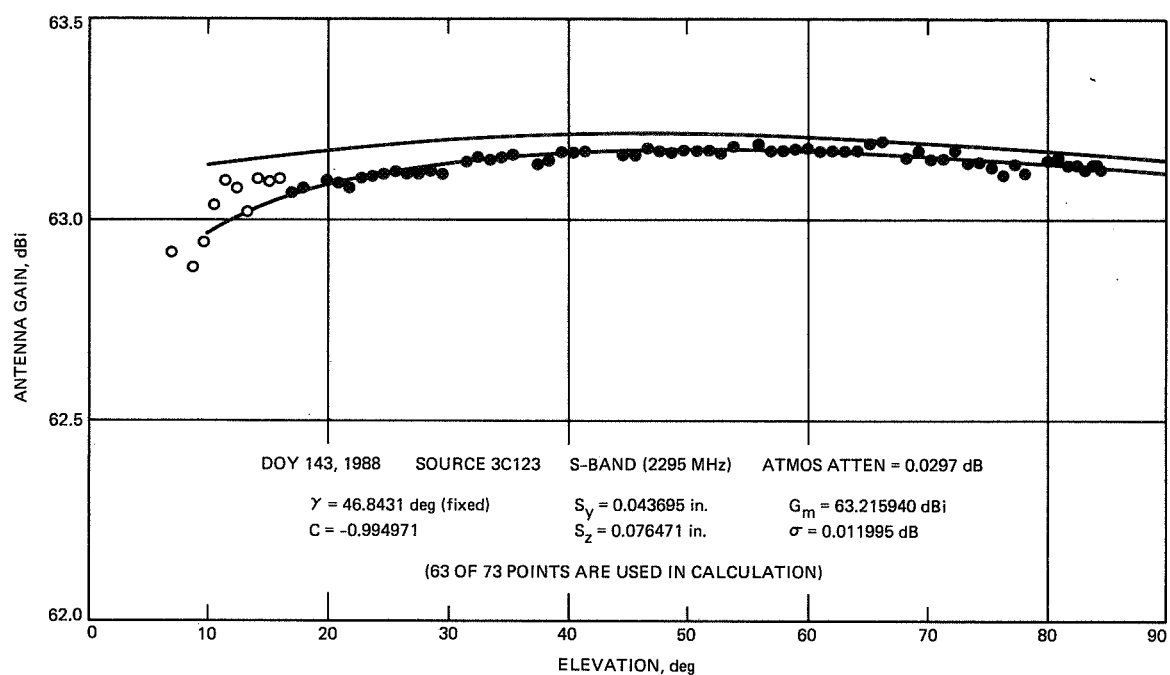


Fig. 19. S-band gain versus elevation for the 70-m antenna at DSS-14 based on uncalibrated data. The lower curve includes atmospheric absorption.

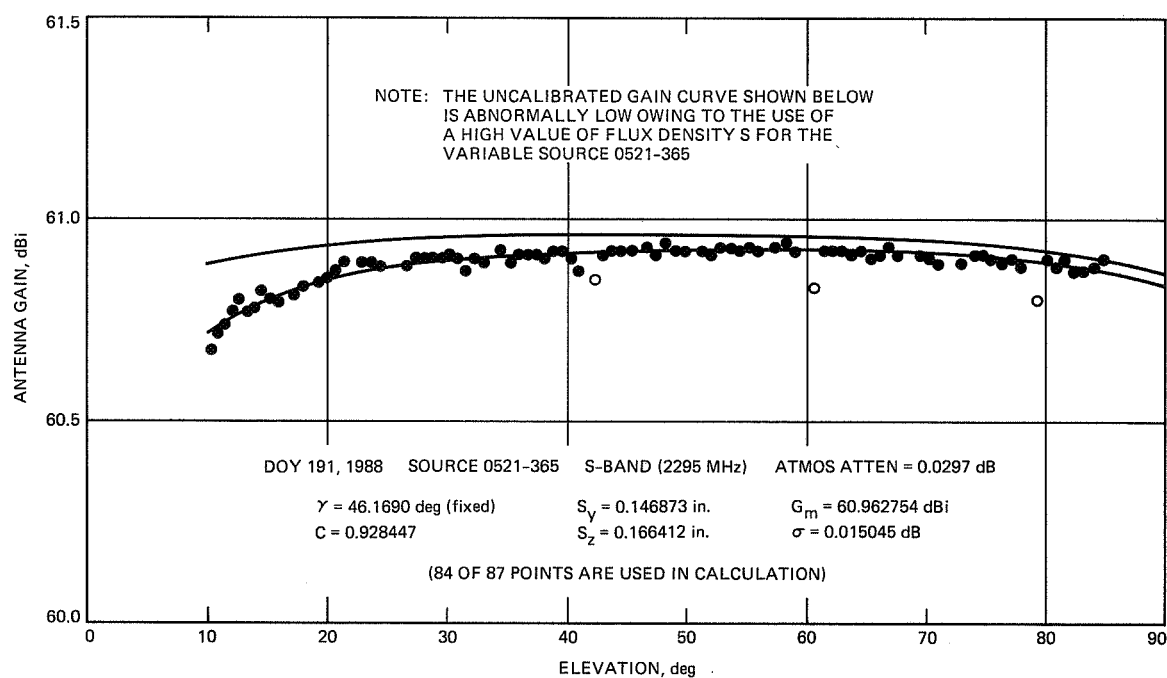


Fig. 20. S-band gain versus elevation for the 70-m antenna at DSS-43 based on uncalibrated data. The lower curve includes atmospheric absorption.

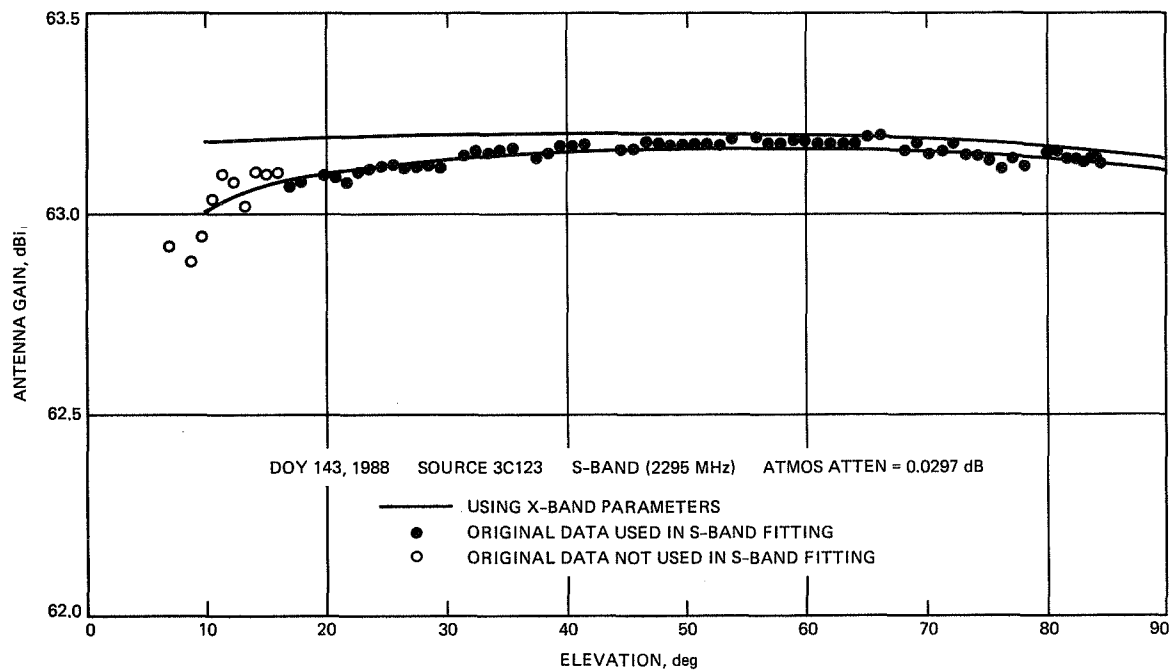


Fig. 21. The same data is presented as in Fig. 19, except that the curve fit is based on the Ruze-Levy parameters obtained at X-band.

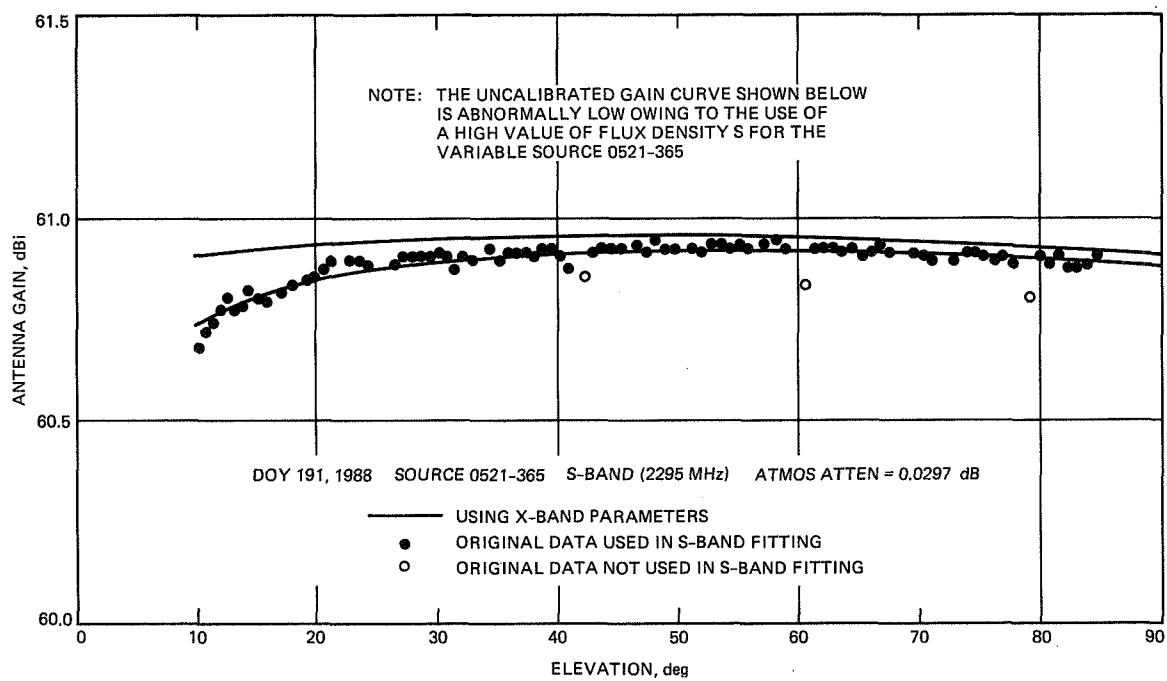


Fig. 22. The same data is presented as in Fig. 20, except that the curve fit is based on the Ruze-Levy parameters obtained at X-band.

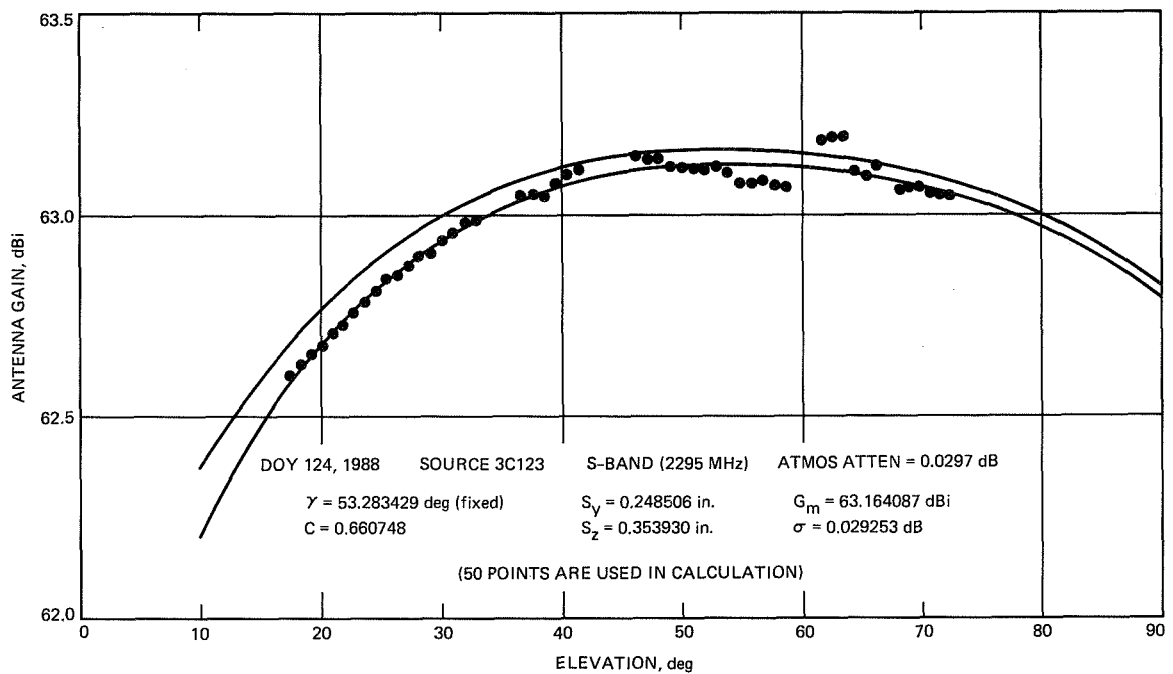


Fig. 23. S-band gain versus elevation for the 70-m antenna at DSS-63 based on uncalibrated data. The lower curve includes atmospheric absorption. A systematic error has caused excessive gain loss at low elevations, but the peak gain is in agreement with measurements at DSS-14 and DSS-43.

Appendix A

Curve Fits to Individual Runs and Stations

The results of curve fitting to the efficiency data from individual runs at DSS-14 (DOY 100–143), DSS-43 (DOY 192–194), and DSS-63 (DOY 124–207) are shown in Figs. A-1–A-3. The data points shown in these figures are the $G(\alpha)$ values computed directly from the $\epsilon(\alpha)$ values measured at each station by means of Eq. (5). The upper curve is the result of fitting to the corresponding $G_0(\alpha)$ values obtained from Eq. (4), and the lower curve is the corresponding $G(\alpha)$ curve obtained from Eq. (4) using the $G_0(\alpha)$ fit. Thus, the upper curve is the best fit to Eq. (3) and represents the antenna performance without atmospheric attenuation, while the lower curve corresponds to the actual performance at the station.

Since the $\epsilon(\alpha)$ values for each station are computed from the measured antenna temperatures $T(\alpha)$ by means of the relationship

$$\epsilon(\alpha) = \frac{T(\alpha)}{T_a} \quad (\text{A-1})$$

where

$$T_a = \frac{T_s}{C_r}$$

$$T_s = \frac{\pi D^2 S}{8k} = 100 \text{ percent efficient source temperature for antenna of diameter } D$$

C_r = source-size correction factor

S = source flux density

k = Boltzmann's constant

the gain $G_0(\alpha)$ may be expressed as

$$G_0(\alpha) = \frac{A_{0z}}{\sin \alpha} + 10 \log T(\alpha) + 10 \log \left(\frac{8\pi k}{\lambda^2} \right) + 10 \log \left(\frac{C_r}{S} \right) \quad (\text{A-2})$$

This explicitly shows that the elevation dependence enters through both the attenuation correction and the measured antenna temperatures $T(\alpha)$, so that the shape of the $G_0(\alpha)$ curve depends to some extent on the value of A_{0z} chosen. However, the variation in this parameter at a given station is generally less than 0.005 dB for good weather, so that at the lowest elevation for which the model should be used (10 deg) the corresponding error in $G_0(\alpha)$ amounts to less than 0.03 dB. Thus, one can assume that in the absence of systematic errors in the measurement of $T(\alpha)$, the values of γ , G_1 , G_2 , and G_3 in Eq. (3) should be reasonably accurate.

The maximum gain, G_m , on the other hand, obviously depends directly on the assumed values for the source flux density S and source-size correction factor C_r , and the accuracy of these parameters is discussed in Section IV.

Figures A-4–A-6 show the results of fitting to the combined calibrated data sets for the individual stations as discussed in Section IV.E. The curves shown are those appearing in Fig. 8 (no atmosphere), and it is seen that the rms error of the fits is ~ 0.03 – 0.05 dB for all three stations.

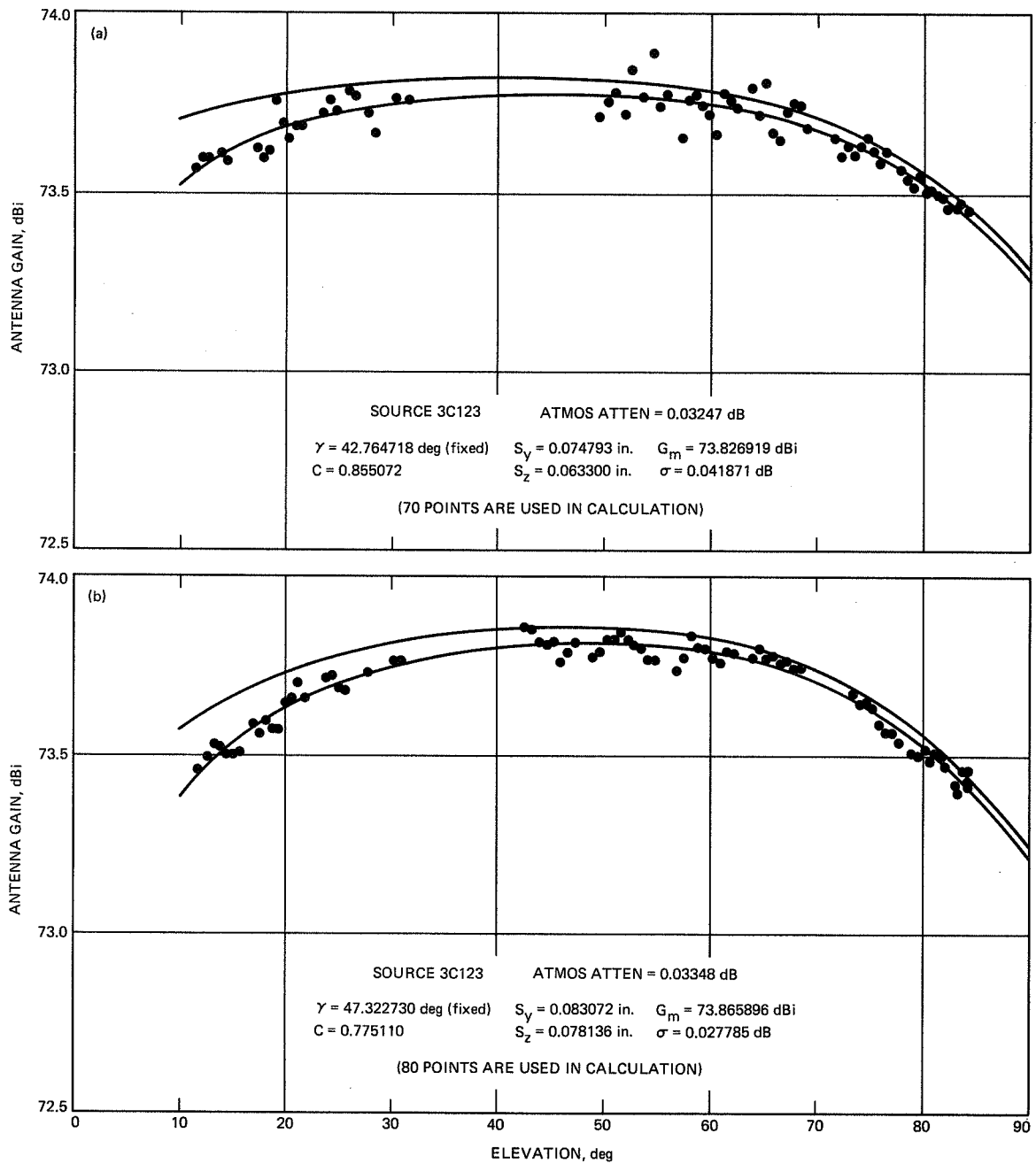


Fig. A-1. Uncalibrated X-band gain versus elevation data for DSS-14 showing Ruze-Levy curve fits for each individual run: (a) DOY 100, (b) DOY 101, (c) DOY 109, (d) DOY 114, (e) DOY 115, and (f) DOY 143. The lower curves include atmospheric absorption.

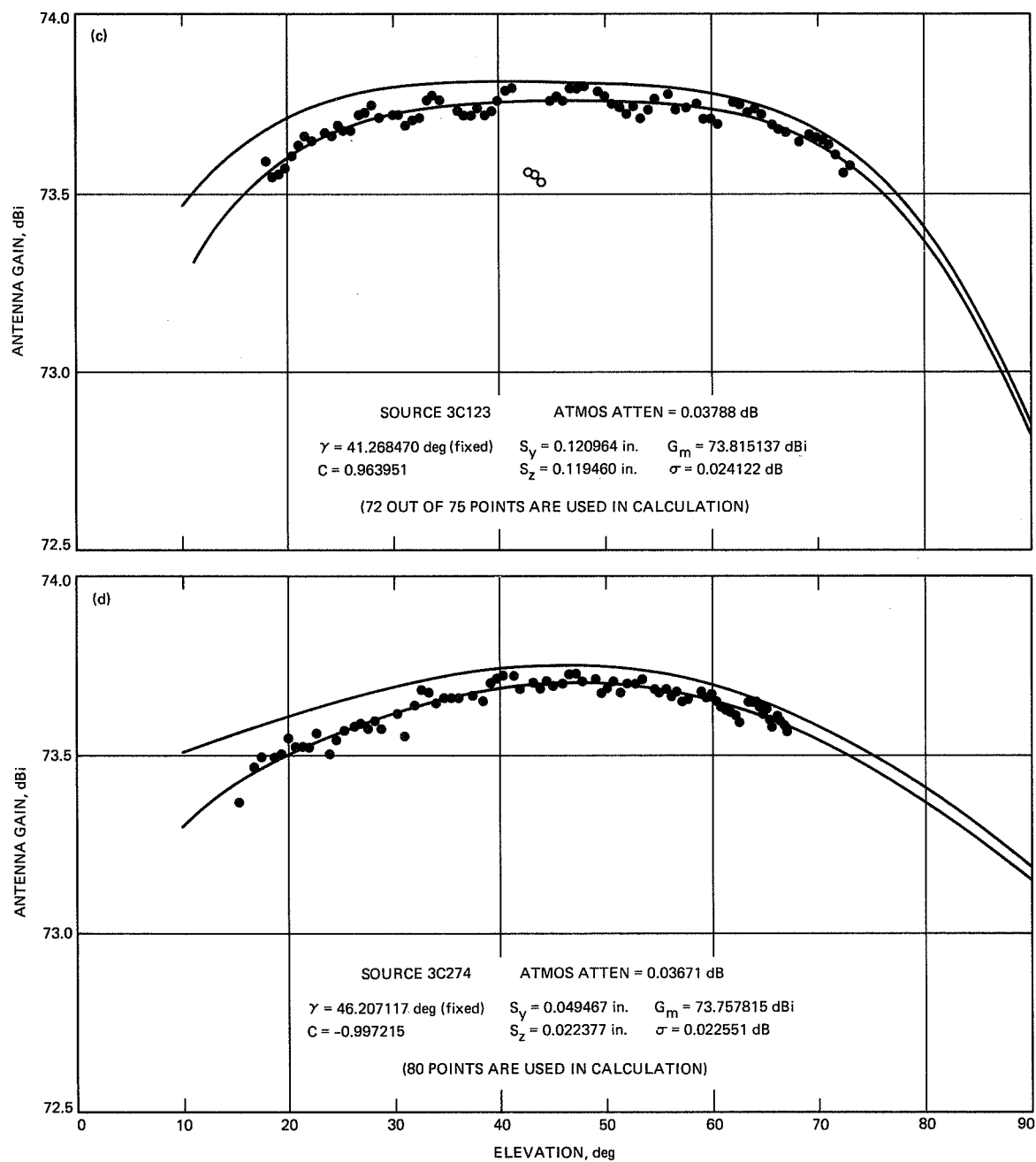


Fig. A-1 (contd)

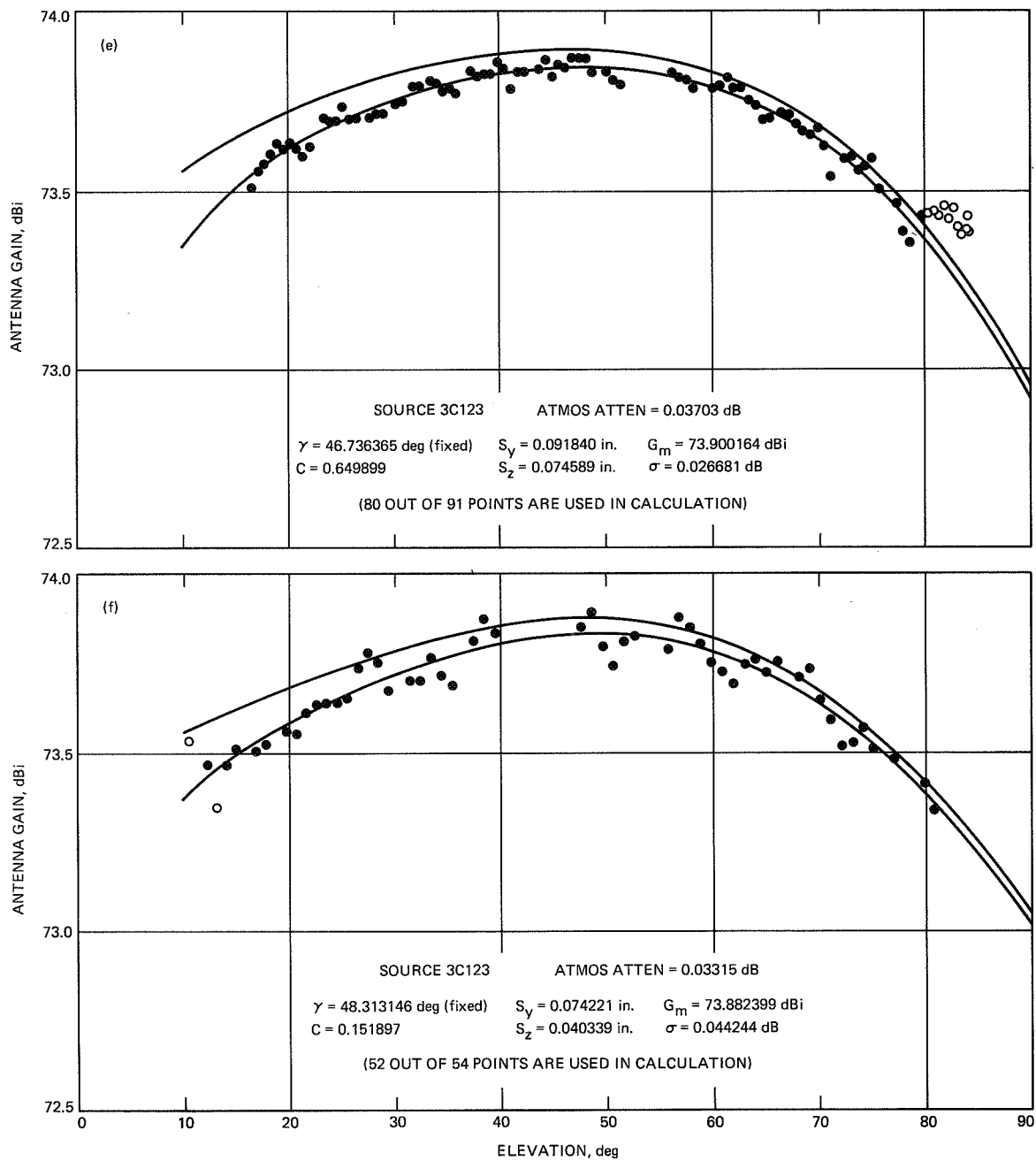


Fig A-1 (contd)

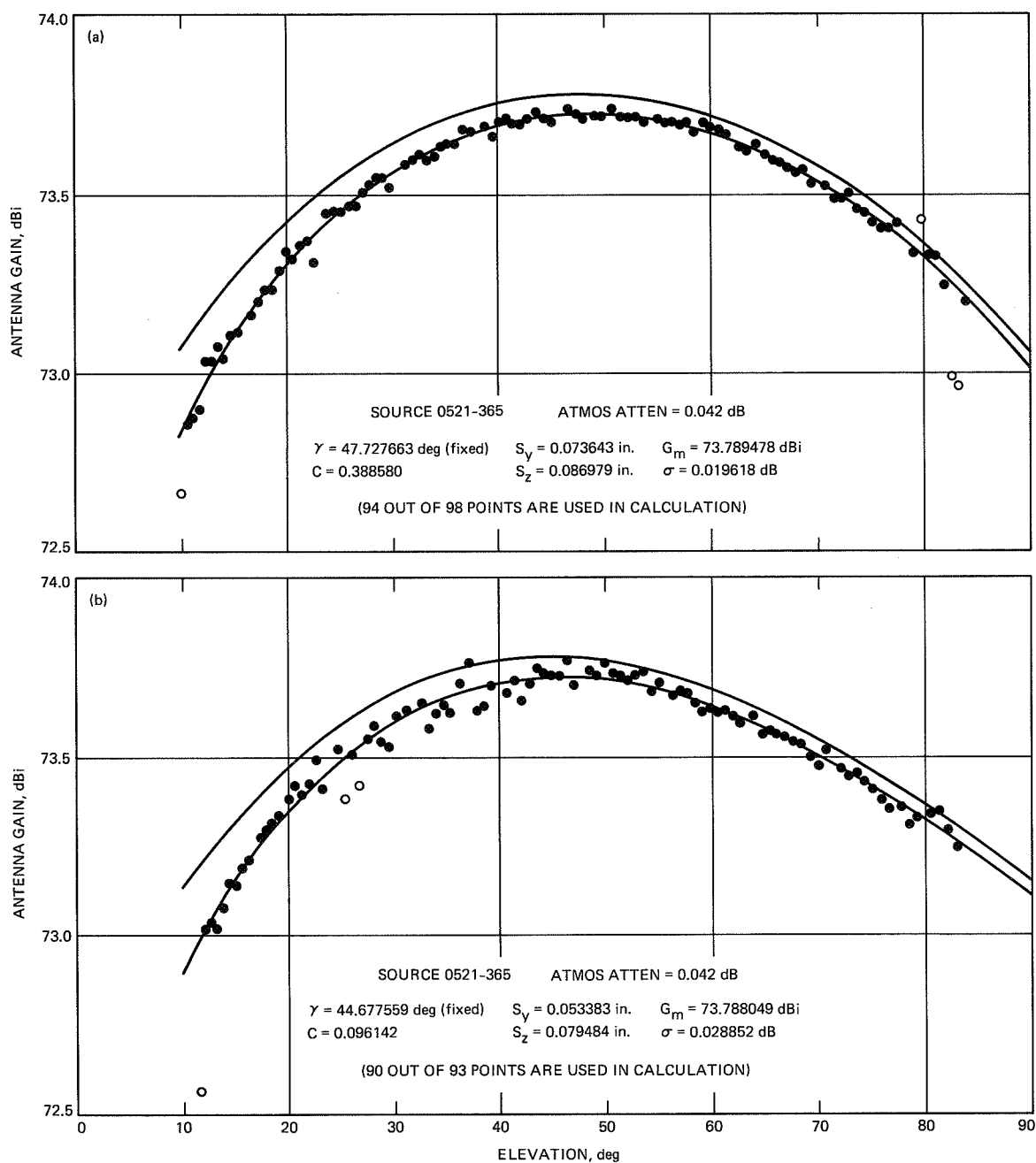


Fig. A-2. Uncalibrated X-band gain versus elevation data for DSS-43 showing Ruze-Levy curve fits for each individual run: (a) DOY 192; (b) DOY 193; (c) DOY 193; and (d) DOY 194. The lower curves (or data points) include atmospheric absorption.

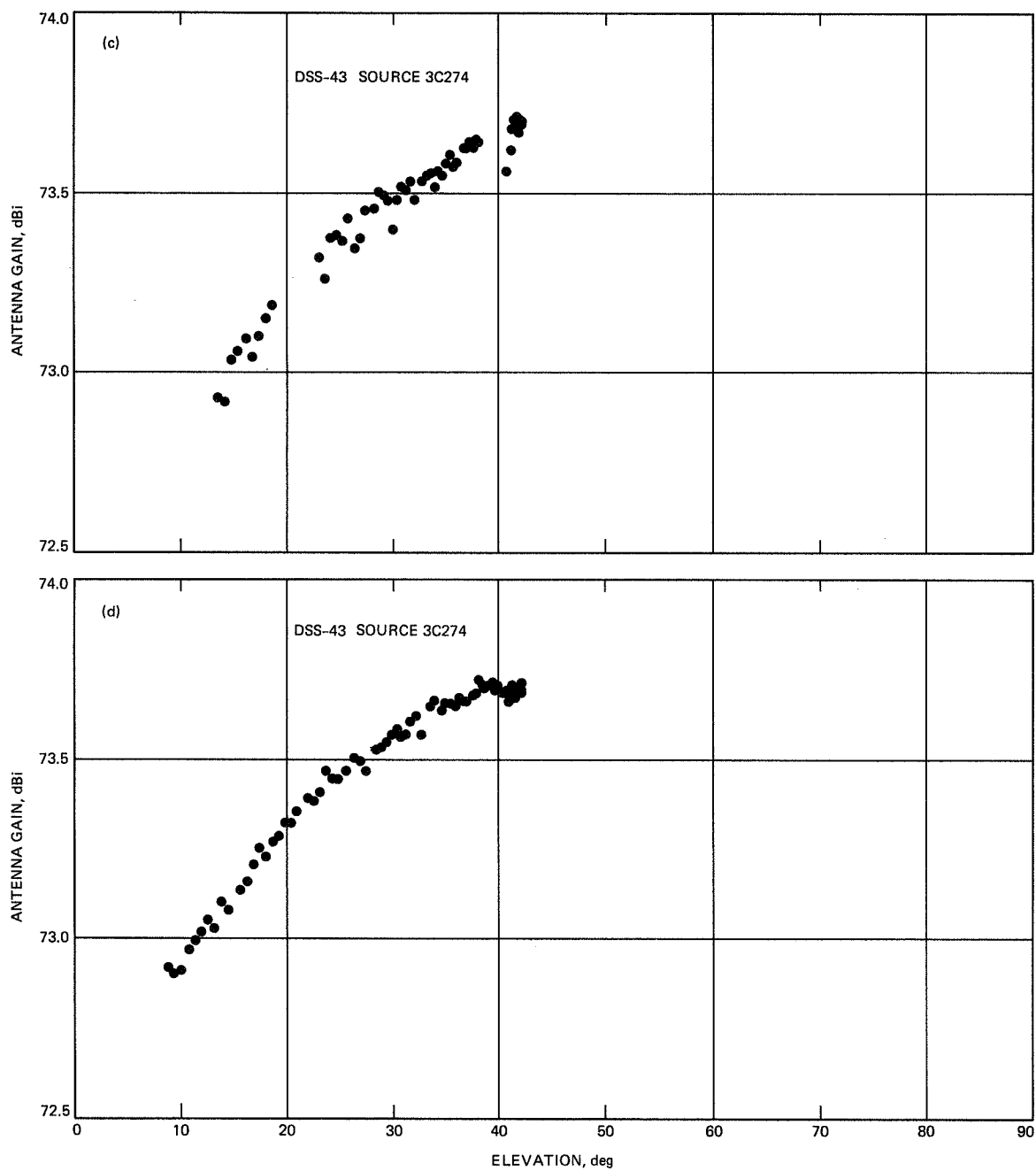


Fig. A-2 (contd)

C-5

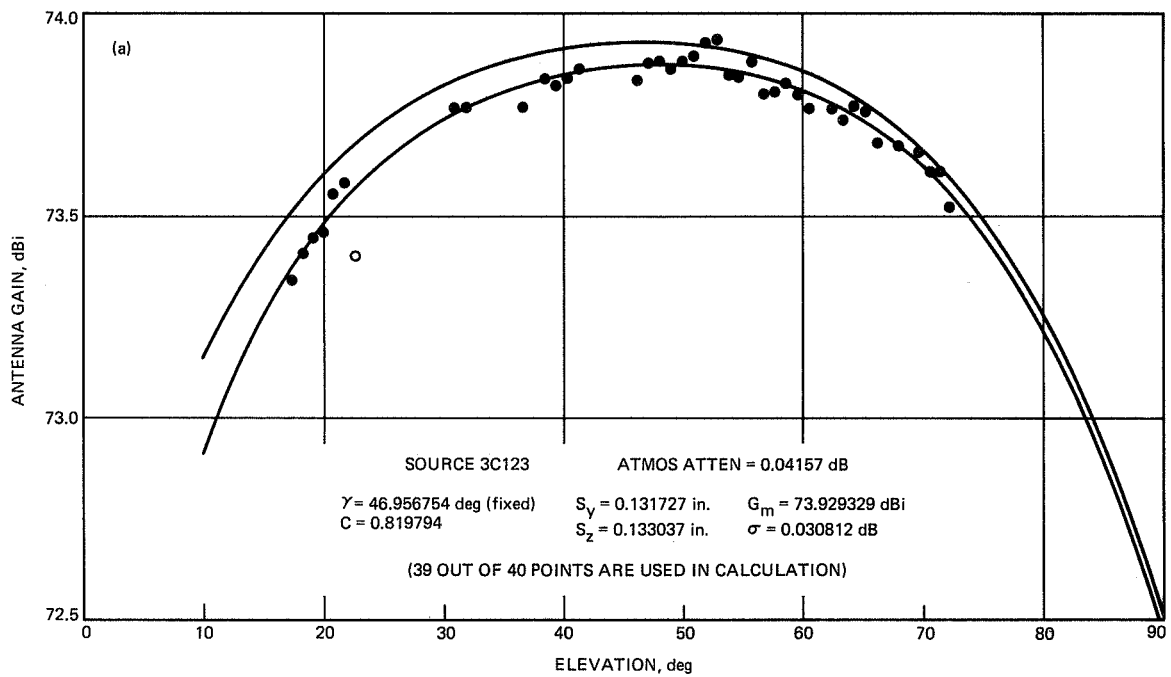


Fig. A-3. Uncalibrated X-band gain versus elevation data for DSS-63 showing Ruze-Levy curve fits for each individual run: (a) DOY 124, (b) DOY 201, and (c) DOY 207. The lower curves include atmospheric absorption.

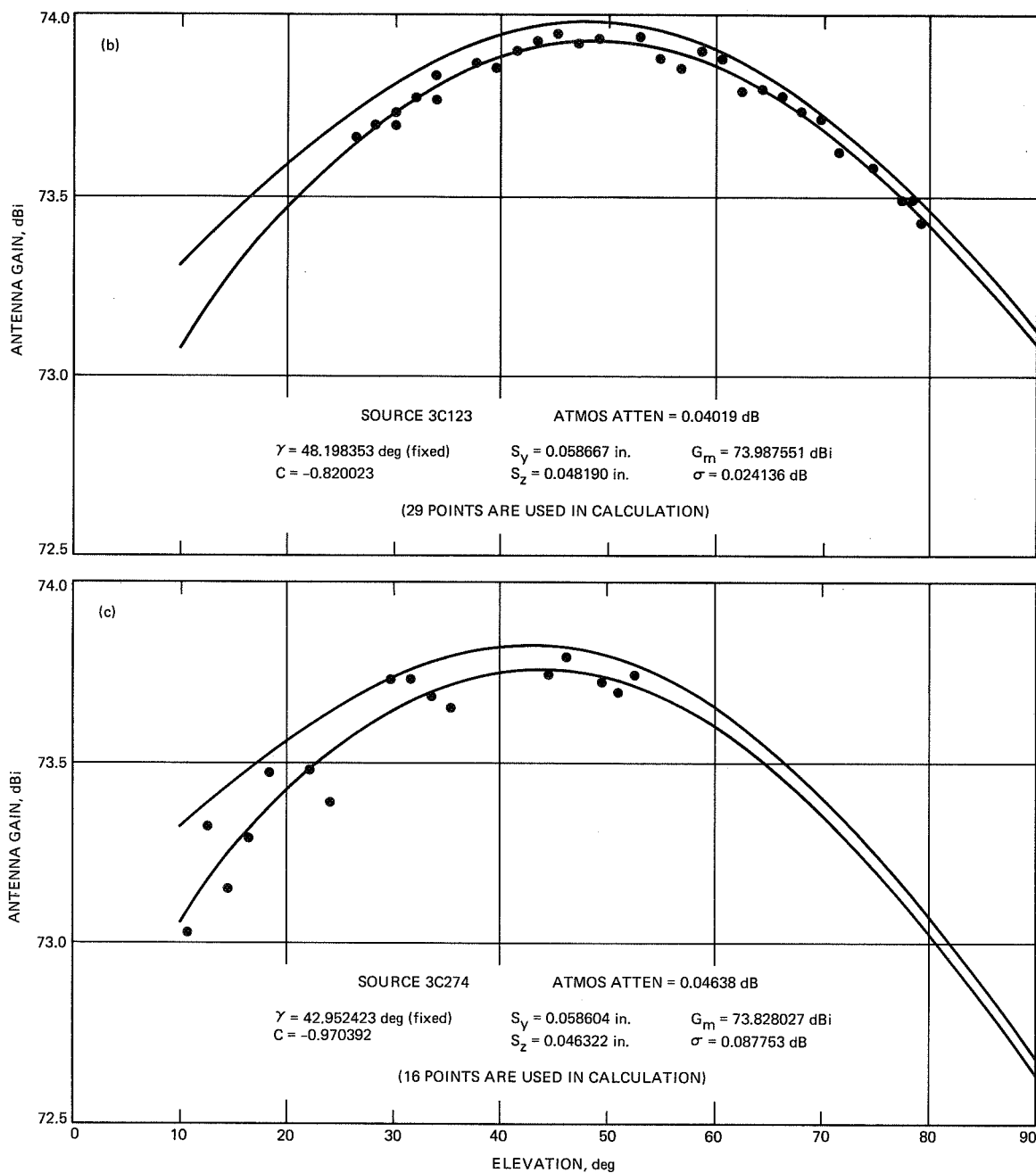


Fig. A-3 (contd)

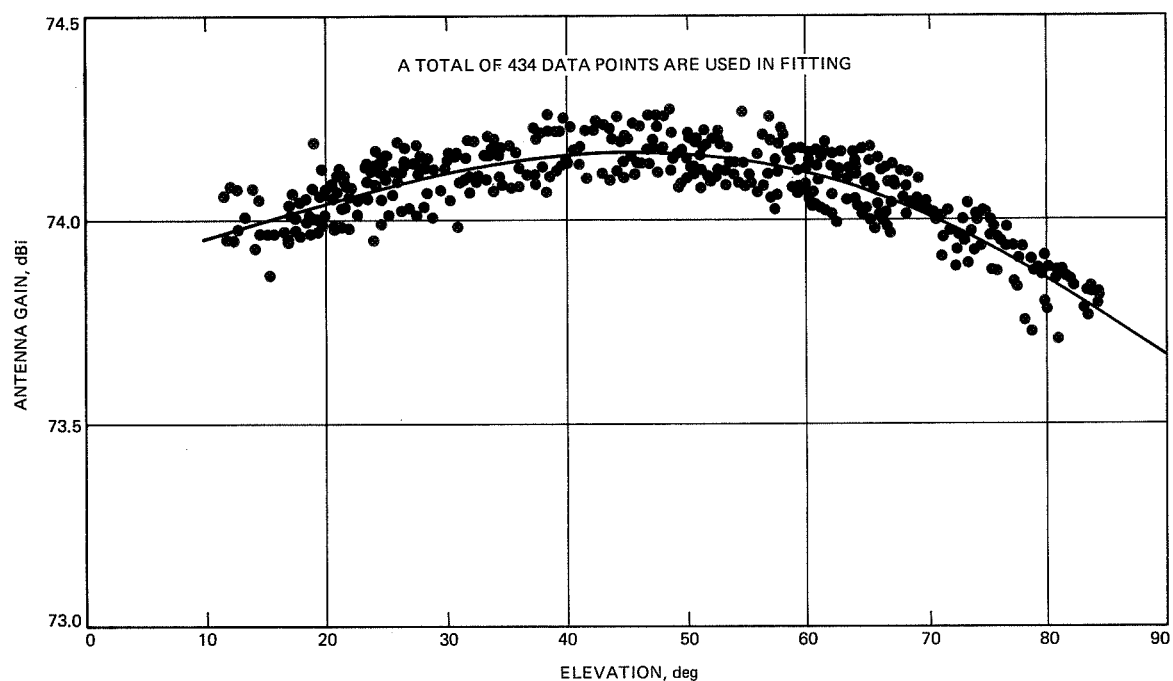


Fig. A-4. Ruze-Levy curve fits to the combined, calibrated data for DSS-14 (no atmospheric absorption).

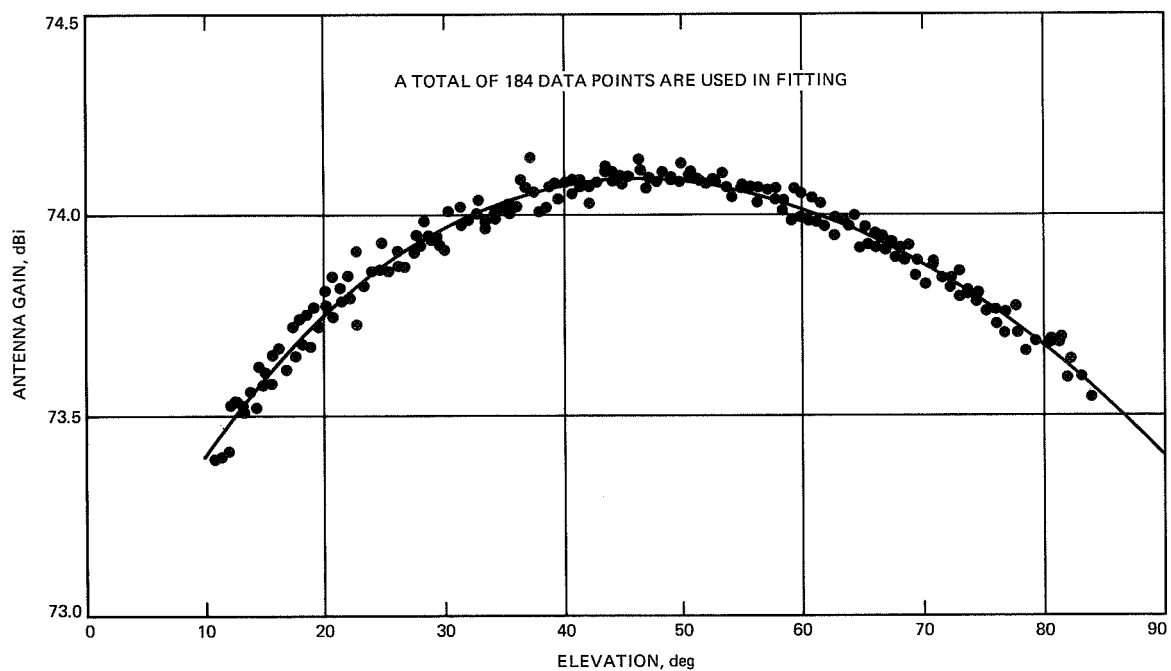


Fig. A-5. Ruze-Levy curve fits to the combined, calibrated data for DSS-43 (no atmospheric absorption).

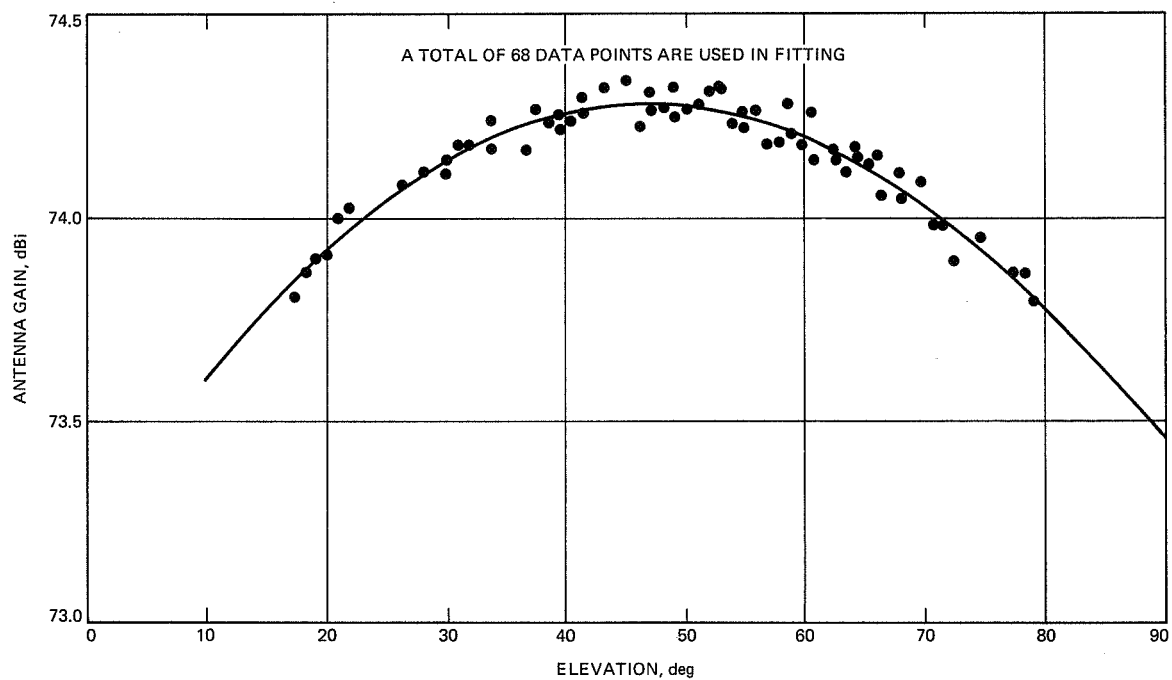


Fig. A-6. Ruze-Levy curve fits to the combined, calibrated data for DSS-63 (no atmospheric absorption).

Appendix B

Periodic Measurement Errors and Systematic Offsets

I. Periodic Errors

Measurements made at DSS-14 show distinctive systematic errors, the most pronounced example of which is found in the data for DOY 109, which show a periodic fluctuation superimposed on the $\epsilon(\alpha)$ curve (see Fig. A-1c). This is most clearly seen over the range $26 \text{ deg} < \alpha < 60 \text{ deg}$, but appears to persist to some degree over the entire range of elevation angles at which measurements were made. Also, there is an indication of the same behavior in the data obtained on other days at this station.

Analysis of the DOY 109 data also reveals a similar periodicity in the pointing coefficient C_p . The two effects are compared in Fig. B-1 where $C_p - 1$ and ϵ are each plotted as a function of elevation angle α for the range $26 \text{ deg} < \alpha < 42 \text{ deg}$. It can be seen that not only do each of these show a periodic behavior, but that the two show a strong correlation as well. If a linear trend $\bar{\epsilon}(\alpha)$ is subtracted from the $\epsilon(\alpha)$ data, then the correlation between $C_p - 1$ and $\epsilon - \bar{\epsilon}$ appears as shown in Fig. B-2. The correlation coefficient is found to be $r = -0.581$, which corresponds to a probability that the two quantities are uncorrelated of ~ 0.006 . The correlation is furthermore seen to be negative, as would be the case if there were a causal relationship between the pointing coefficient and measured efficiency, i.e., if the measured temperature $T(\alpha)$ were reduced as the result of a pointing error.

Since these data were obtained with the APCAL program operating in closed-loop mode, the pointing coefficient has not actually been used to correct the ϵ values.¹ However, one may determine the extent to which the periodic pointing offset shown in Fig. B-1 contributes to the observed periodic efficiency loss shown in the same figure by comparing the sinusoidal curve fit to the efficiency data with the correlation between efficiency and pointing coefficient.

The least squares sinusoidal fit has the form

$$\epsilon - \bar{\epsilon} = C \cos(k\alpha + \phi) \quad (\text{B-1})$$

with $C = 4.0149 \times 10^{-3}$, $k = 54.750$, and $\phi = 88.9 \text{ deg}$, while the linear correlation is of the form

$$\epsilon - \bar{\epsilon} = a - b(C_p - 1) \quad (\text{B-2})$$

with $a = 2.9305 \times 10^{-3}$ and $b = 0.5752$.

The efficiency and pointing coefficient are related to one another by the equation

$$\epsilon = \frac{\epsilon_m}{C_p} \quad (\text{B-3})$$

where ϵ_m is the value of ϵ for perfect pointing ($C_p = 1$). If a linear approximation is made to this hyperbolic relation for $C_p \geq 1$,

$$\epsilon - \bar{\epsilon} = (\epsilon_m - \bar{\epsilon}) - \epsilon_m(C_p - 1) \quad (\text{B-4})$$

From Eq. (B-1), $\epsilon_m - \bar{\epsilon} = C$, and taking $\epsilon_m = 0.626$ from the original data (average maximum gain for $26 \text{ deg} < \alpha < 42 \text{ deg}$), the results of the linear correlation, Eq. (B-2), may be compared with the theoretical relationship, Eq. (B-4). This is done in Fig. B-2, where it is seen that the two are very close, thus implying that the observed periodic variation in efficiency has been caused by a periodic pointing error.

The periodic pointing error is thus seen to be of the form

$$C_p - 1 = \frac{C}{\epsilon_m} [1 - \cos(k\alpha + \phi)] \quad (\text{B-5})$$

where $C/\epsilon_m = 4.414 \times 10^{-3}$, which gives a consistent fit to the data of Fig. B-2. In terms of the pointing offset angle $\Delta\Phi$,

$$C_p = \exp \left[4 \ln 2 \left(\frac{\Delta\Phi}{\Phi_B} \right)^2 \right] \quad (\text{B-6})$$

where $\Phi_B = \text{HPBW} = 0.030 \text{ deg}$ for the 70-m antennas. Thus, expanding the above

$$C_p - 1 \approx 4 \ln 2 \left(\frac{\Delta\Phi}{\Phi_B} \right)^2 \quad (\text{B-7})$$

from which the maximum offset corresponding to $C_p - 1 = 4.414 \times 10^{-3}$ is $\Delta\Phi = 1.2 \times 10^{-3} \text{ deg}$.

¹G. Milford and J. Horter, *APCAL Technical Manual (Preliminary)*, JPL internal document, Jet Propulsion Laboratory, Pasadena, California, p. 27, May 1988.

In considering the periodic behavior above, the elevation angle α has been treated as the variable. For the range of elevations considered there is a nearly linear relationship between the elevation angle and Greenwich Mean Time (GMT) so that a simple transformation can be made to time as a variable. This leads to the time equivalent of Eq. (B-1),

$$\epsilon - \bar{\epsilon} = C \cos(\omega t + \phi) \quad (\text{B-8})$$

where it is found that $\omega = 11.6871$ deg/hr, giving a period for the oscillation of $T = 0.5626$ hr = 33 min 45 sec.

If a different interval is chosen for the analysis, then similar results are found but with somewhat different values for the fitting parameters. For example, for $44 \text{ deg} < \alpha < 61 \text{ deg}$, $C = 3.6670 \times 10^{-3}$, $k = 43.8613$, $\phi = -38.2655$ deg, and transforming to a time variable here, $\omega = 12.2083$ deg/hr, giving a period $T = 0.6723$ hr = 40 min 20 sec. Also, for this interval there is no identifiable periodicity in the pointing coefficient, and the correlation between $\epsilon - \bar{\epsilon}$ and $C_p - 1$ is random, thus indicating that either a dominant random component has been added to the pointing coefficient data, or the periodicity in $\epsilon(\alpha)$ is of a different origin here, which seems less likely.

The above analysis leads to the conclusion that the efficiency data for this run have likely been systematically reduced due to pointing errors so that the true efficiency values are given by $\epsilon_m(\alpha) = \epsilon(\alpha) + C$, where $\epsilon(\alpha)$ is the value obtained from the curve fitting procedure discussed in Section III.A. Expressed in terms of gain, this corresponds to taking the curve fits obtained and increasing them by approximately 0.028 dB.

Although the periodic variation in $\epsilon(\alpha)$ is clearly discernible in all of the DSS-14 data, its correlation with the computed pointing coefficient is not, so that in spite of the implication of the above analysis based on the DOY 109 data, there does not appear to be enough evidence to support a general conclusion that pointing errors have contributed 0.028 dB of loss to all, or even most of the DSS-14 gain measurements. In view of this, it seems prudent to treat the above as a probable error and include it in the overall error budget as discussed in Section IV.F.

II. Systematic Offsets

Efficiency data obtained at DSS-63 on DOY 201 show an interesting kind of hysteresis effect. The source, 3C123, was tracked in elevation from 26.34 deg to a maximum value of 79.36 deg, and then back down again to $\alpha = 66.02$ deg, thus providing an overlap of measurements over the range $66 \text{ deg} < \alpha < 76 \text{ deg}$.

Figure B-3 shows the efficiency data plotted versus elevation for this limited range, and it can be seen from this that the data obtained while the source was setting are consistently below that obtained when it was rising, the difference corresponding to some 0.07 dB.

In this case it appears that at least a partial explanation for the change may be found in the environmental data accompanying the run, according to which the only significant change that occurred was in wind velocity. The sky was clear throughout the entire run, and temperature, pressure, and relative humidity all remained quite stable as well. However, the wind velocity was reported as zero throughout most of the run but picked up to 10 mph (SW) sometime between GMT = 0812 and 0927, i.e., exactly when the change in efficiency appears to have taken place.

The situation is summarized in Fig. B-4, in which the efficiency and elevation angle are both plotted in terms of GMT, and the last notation of zero wind velocity (GMT = 0812) and the first entry of 10 mph (SW) wind velocity (GMT = 0927) are shown. It can be seen from this that approximately 50 minutes elapsed between the reading taken at maximum elevation (GMT = 085455) and the first reading taken as the source was setting (GMT = 094505), and that the former was also probably depressed as a result of wind, i.e., the wind may have actually picked up shortly before GMT = 0900.

As a check on this, the gain loss versus wind velocity data from 810-5 rev. D² for the 70-m antennas have been considered. Extrapolation of these data down to 10 mph results in a predicted gain loss of 0.034 dB. Since the 810-5 data represent the worst case attitude condition for gain loss resulting from wind-induced distortion, it appears that wind alone cannot account for the 0.07 dB loss shown in Fig. B-3.³

Another example of a systematic offset is provided by the data from DSS-14 on DOY 115 and 116. This run was begun when the source was rising and very close to its maximum altitude. Data were collected as it rose to its maximum altitude and then proceeded to set, covering the range of elevations from 84.23 deg down to 16.56 deg. However, the entire set of measurements, including both rising and setting, for $\alpha \geq 80.30$ deg shows a systematic offset amounting to $\Delta G = 0.12$ dB (see Fig. A-1d). No explanation for this can be found in the data provided with the report.

²Deep Space Network/Flight Project Interface Design Handbook, Vol I: Existing DSN Capabilities, Vol. II: Proposed DSN Capabilities, JPL 810-5, rev. D (internal documents), TCI-10, rev. D, Table 3, July 15, 1988 (Vol. I), November 1, 1986 (Vol. II).

³Roy Levy, personal communication.

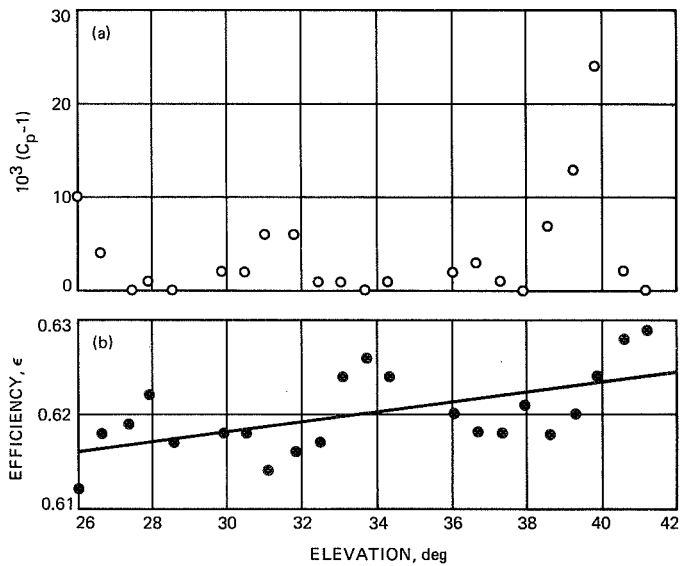


Fig. B-1. A comparison of X-band (a) pointing coefficient and (b) efficiency for DSS-14, DOY 109, showing correlation between the two quantities.

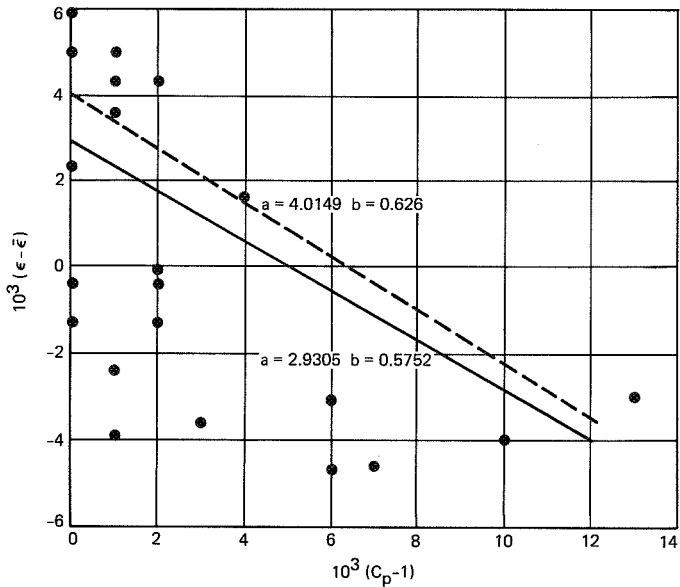


Fig. B-2. Correlation diagram for X-band efficiency versus pointing coefficient for DSS-14, DOY 109. The solid line is the linear regression curve for the data, and the dashed line corresponds to prediction based on a causal relationship between the two quantities.

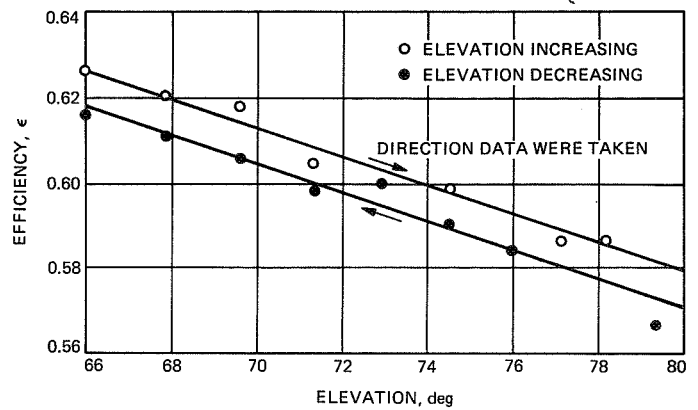


Fig. B-3. Comparison of the X-band efficiency curves obtained at DSS-63, DOY 201, for increasing and decreasing elevation. The approximately 0.07-dB difference is partially explained on the basis of a time-dependent wind-loading effect.

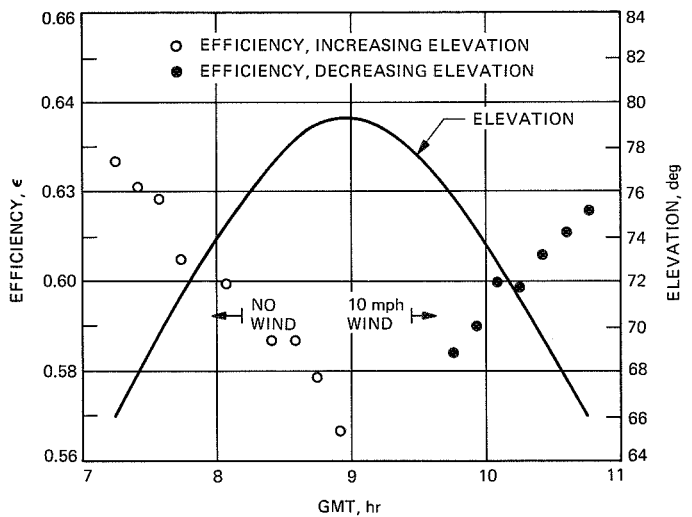


Fig. B-4. X-band efficiency and elevation angle versus GMT for DSS-63, DOY 201, showing the onset of a 10-mph (SW) wind between the rising and setting curves.

DSN 70-Meter Antenna X- and S-Band Calibration Part II: System Noise Temperature Measurements and Telecommunications Link Evaluation

S. D. Slobin and P. H. Richter
Telecommunications Systems Section

The X- and S-band system operating noise temperatures of the DSN 70-m antennas are presented. Models of atmosphere and ground noise temperature contributions, as they affect the antenna calibrations, are given for future use in telecommunications link modeling. The measured 70-m antenna network G/T performance is presented. Compared with the earlier 64-m antenna network, G/T improvements of from 1.8 dB to 2.5 dB, depending on elevation angle, were achieved. G/T comparisons are made with the DSN/Flight Project Design Handbook and the Voyager telecommunications design control table. Actual Voyager telecommunications link performance is compared with predictions made by TPAP (the Voyager telecommunications prediction and analysis program) and with measured performance of the individual 70-m antennas. A modification in the use of antenna gain, system noise temperature, and atmospheric attenuation in existing telecommunications design control tables is suggested.

I. Introduction

This article is the second part of a two-part article covering the final calibration of the DSN 70-meter antennas in their upgrade from the original 64-meter configuration. This update occurred over a two-year period from fall 1986 through fall 1988 and was planned to enhance DSN performance at the time of the Voyager Neptune encounter (August 1989). Part I [1] contains material on the X-band (8420 MHz) and S-band (2295 MHz) gains of the antennas in addition to a rather comprehensive analysis of calibration radio source fluxes and size corrections for both the 64-meter and 70-meter antennas. Part II (this article) reports on the S- and X-band system noise temperatures and models for atmosphere and ground

contributions to total system noise temperature. In addition, use of gain and noise temperature expressions in design control tables for telecommunications link analysis is also given. A comparison of measured 70-m antenna G/T (gain/system noise temperature) and the G/T model contained in the Voyager telecommunications prediction and analysis program (TPAP) is presented. Comparison of actual and TPAP-predicted Voyager telecommunications performance is presented as a test of the telecommunications link model used for that deep space mission.

The concept of "25-percent CD" weather is introduced here in order to clarify the description of weather-induced

atmospheric attenuation and system noise temperature effects. "CD" means "cumulative distribution" and in this particular case, refers to that noise temperature or attenuation value which is not exceeded 25 percent of the time. "Twenty-five-percent weather" will now be used to describe an average clear-sky condition with no visible liquid water (clouds or rain). Previously, the term "clear-dry" has been used for this condition and it has been confused with a lowest-loss atmosphere containing no water vapor or liquid water, which will now be referred to as "0-percent CD" weather.

The efficiency and noise temperature calibrations of the DSN 64-meter network, carried out in 1986 and 1987, are presented in [2-4]. The present 70-meter antenna gain and noise temperature calibrations will be compared to the earlier values.

II. Measured X- and S-Band System Noise Temperatures

Figure 1 shows the X-band system operating noise temperatures (T_{op} , for selected sets of data) at all three stations during the calibration period. The upper set is the raw input data (off-source noise temperatures) taken during the efficiency scans. It should be noted that the DSS-14 noise temperature data shown are taken without the dichroic reflector in place. It has been estimated previously¹ that this results in a 1.2-K lower T_{op} than when the antenna is in its normal configuration. This difference is readily seen in Fig. 1 when the DSS-14 near-zenith noise temperatures are compared with the mean noise temperature (20.9 K) of the other two stations. The 1.4-K difference is the sum of the dichroic contribution (1.2 K) and the atmosphere difference (0.2 K) between DSS-14 and the other two stations, as estimated from surface meteorological parameters that existed at the time of the efficiency measurements.

A without-atmosphere T_{op} model can be created from the measured values by subtracting out, on a point-by-point basis, the atmospheric contributions which existed at the time of the calibration tests. Based on actual surface meteorological values, the approximate values for the X-band zenith atmospheric noise temperature and attenuation contributions were

DSS-14: 2.28 K/airmass (0.037 dB/airmass)

DSS-43: 2.52 K/airmass (0.041 dB/airmass)

DSS-63: 2.48 K/airmass (0.040 dB/airmass)

The resulting without-atmosphere noise temperature values are shown as the bottom three data sets in Fig. 1. It was

decided to create a composite model of system noise temperature by averaging the DSS-43 and DSS-63 data. This decision is supported by the fact that the DSS-14 near-zenith data (adjusted upward by the 1.4-K difference from the other stations) lies very nearly between the other two curves. The final result is to have a zenith noise-temperature peak-to-peak spread of 0.5 K, which is 0.1 dB of the average value of 20.9 K. It is thus determined that the 70-m X-band antenna zenith T_{op} values with and without atmospheric contribution are

$$T_{op,zenith,x} = 20.9 \text{ K, with atmosphere}$$

$$T_{op,zenith,x} = 18.4 \text{ K, without atmosphere}$$

Similar data reduction techniques for a minimal amount of S-band calibration data yield

$$T_{op,zenith,s} = 18.3 \text{ K, with atmosphere}$$

$$T_{op,zenith,s} = 16.5 \text{ K, without atmosphere}$$

The S-band T_{op} model indicates an atmospheric noise temperature contribution of 1.80 K/airmass (0.029 dB/airmass) for the conditions which existed at the time of the calibration tests.

These zenith noise temperatures represent substantial improvements (lower noise temperature) over comparable values determined for the antennas in their 64-m configurations [2-4]. Typical without-atmosphere improvements were 1.5 K at S-band and 0.7 K at X-band. Complete descriptions of both 64-m and 70-m antenna design considerations are given in [5].

Figure 2 shows curves fitted to both X- and S-band values of T_{op} , with and without atmospheric contribution. The 1.2-K dichroic adjustment for DSS-14 is included in these curves.

At or above 10-deg elevation, the system noise temperature is given by

$$T_{op} = a_0 + a_1 \alpha + a_2 \alpha^2 + a_3 \alpha^3 \quad (1)$$

where

$$\alpha = \frac{1}{\theta}$$

and

$$\theta = \text{elevation angle, deg}$$

¹D. A. Bathker, personal communication.

Below 10-deg elevation, T_{op} is given by:

$$T_{op} = b_0 + b_1 \theta + b_2 \theta^2 \quad (2)$$

where

θ = elevation angle, deg

The coefficients for these expressions are given in Table 1.

Strictly speaking, T_{op} is the *total* system operating noise temperature and includes the atmosphere; however, in this article it is used to indicate noise temperatures with and without atmospheric effects included. It should be noted that there are no experimental data below 10-deg elevation angle; therefore, the latter noise temperature expression (Eq. 2) is totally an extrapolation and may have large errors (several K). On the basis of curve-fitting alone above 10-deg elevation, the error for X-band (with atmosphere) is ± 1.2 K ($3 - \sigma$); for S-band (with atmosphere) the error is ± 0.4 K ($3 - \sigma$). The data do not appear able to support an attempt to distinguish among the antennas at the 0.1- to 0.2-K level (zenith, with atmosphere), which is what one would see due to altitude differences of the stations.

Receiver and square-law detector non-linearities, VSWR of the ambient load, temperature readout errors, and numerous other contributions all conspire to reduce the calibration accuracy of the radiometer noise diodes used during the antenna measurements. Thus, the knowledge of the absolute X- or S-band T_{op} for the 70-m antennas is estimated² to be no better than ± 10 percent ($3 - \sigma$). This is a ± 2 -K error for a 20-K system.

III. Atmosphere and Ground Modeling for Telecommunications Link Analysis

It is seen in [1] that the X- and S-band antenna gain curves are presented without atmospheric effects included, i.e., as though the antenna existed in a vacuum. Indeed, gain and efficiency represent an inherent quality or condition of the antenna; outside influences should not be included in these characteristics. An antenna with poor efficiency may have large spillover and scattering noise temperature contributions, but for telecommunications link analysis the received signal power is only a function of antenna gain (without atmosphere) and atmospheric loss. Inherent in antenna gain are certain system losses such as those due to the waveguide and dichroic plate, but these are constant with time (unless the antenna is modified) and are not a function of elevation angle, as is the atmospheric loss.

²C. T. Stelzried, private communication.

The raw antenna noise temperature data are taken under a range of (usually) clear weather conditions. The data are corrected for the atmospheric conditions that existed at the time of the measurements, yielding a without-atmosphere determination of efficiency and gain. For telecommunications link analysis, a particular weather condition must be postulated. A description of X-band weather-related attenuation and noise temperature is given in the *DSN/Flight Project Interface Design Handbook*³ (herein referred to as "810-5"). A new revision of this document is being developed which will include updated S- and X-band performance, and the addition of Ka-band (32 GHz) performance estimates for use in the DSN.

A nominal clear-sky weather condition is postulated as one in which there are no clouds in the sky and the relative humidity is neither low (clear dry) nor high (clear humid). Based on the rule-of-thumb that clouds are not present 50 percent of the time, the "average" clear weather condition is defined as "25-percent weather" as discussed earlier. For comparison with previous "clear sky" (but otherwise uncharacterized) measurements, the concept of 25-percent weather is introduced.

The presentation of predicted antenna gains in 810-5 includes a clear-sky (but undefined) atmospheric loss. "Without-atmosphere" gains would not include this loss, and lacking information regarding test conditions during the gain measurements, one must assume that a nominal 25-percent weather condition existed. For a standard atmosphere [6] with a surface water vapor density of 7.5 g/m³ the surface parameters are:

Temperature = 15°C

Pressure = 1013 mb, at sea level

Relative Humidity = 58 percent

Using these surface values at the altitudes of the three DSN 70-m locations results in clear-sky, 25-percent weather zenith-effect models for the three locations as given in Table 2. Also shown for comparison is a DSS-14 condition with no water vapor (minimum-loss atmosphere, 0-percent weather) in acknowledgment of the fact that Goldstone may have a significantly lower average relative humidity than do the other two 70-m sites.

It is seen that the effects at the three sites are uniformly distributed with a mean close to the effects at DSS-63. (The mean height above sea level is 0.825 km.) The DSS-14 no-water-vapor case shows significantly lower atmospheric effects. Climatologically, Goldstone (DSS-14) is quite different from

³*Deep Space Network/Flight Project Interface Design Handbook*, Rev. D, JPL 810-5 (internal document), July 1988.

the other two locations. As an example, the mean rainfall there is 3.5 in./year. At DSS-43 it is 23.0 in./year, and at DSS-63 it is 19.6 in./year. Thus, the overseas sites receive about six times as much rain as does Goldstone. It is assumed that cloud effects are also proportionately larger.

For clear-sky (25-percent weather) modeling, it may be of little consequence whether one uses either the nominal or dry zenith models for DSS-14. The error in calculating the X-band received power level will be less than 0.1 dB at a 6-deg elevation angle. The noise temperature error calculated at the same elevation angle may be as much as 6 K out of a total T_{op} of about 50 K, resulting in a calculated SNR (signal-to-noise-ratio) error of about 0.5 dB. As given in Table 1 (cf. also Fig. 2) the without-atmosphere values of T_{op} reflect the effect of a changing spillover and scatter contribution as a function of elevation angle. All other contributions to noise temperature are constant with elevation angle, except for a slightly changing cosmic background contribution. (This contribution varies less than 1 K for all elevation angles over a wide range of weather conditions; although, for the sake of completeness, this variation should be accounted for in design control tables.) An estimate of 70-m antenna zenith ground (rear spillover plus quadripod scatter) contribution is 3.0 ± 0.5 K for X-band, and about 0.5 K more for S-band as a result of optimizing the X-band spillover design at the expense of S-band.⁴

The clear-sky (25-percent weather) total system noise temperatures at zenith are made up of the components shown in Table 3. Assuming nominal receiver values it can be seen from this table that the ground noise contribution may then be expressed as:

$$T_{ground,x} \text{ (K)} = T_{x,w/o atm} - 15.4 \quad (3)$$

$$T_{ground,s} \text{ (K)} = T_{s,w/o atm} - 13.0 \quad (4)$$

where $T_{w/o atm}$ is calculated from the values given in Table 1, and 15.4 K and 13.0 K are the receiver plus cosmic contributions to T_{op} at X- and S-bands, respectively.

Subtracting the 2.7-K cosmic background from the constants in the above two expressions, one then obtains the fixed receiver and waveguide contributions to system noise temperature, in this case 12.7 K (X-band) and 10.3 K (S-band). It should be noted that errors in the estimate of the "fixed" zenith ground contribution can be "traded-off" against noise

temperature contributions from receiver and waveguide to give the total zenith T_{op} values shown in Fig. 2.

It is seen then that at 30-deg elevation the total ground contributions at X- and S-bands are 5.0 K and 4.5 K, respectively. The changes from the X- and S-band zenith values are 2.0 K and 1.0 K, respectively.

The 1.80-K S-band atmosphere described earlier is that which existed during antenna calibration tests and is thus shown in Fig. 2. This is 0.1 K lower than shown in Table 3, but is not inconsistent with the agreement between the X-band model and experiment, as the X- and S-band data sets were not taken at the same time. In other words, the atmospheric attenuation and noise temperature during the S-band calibrations were slightly less than nominal.

By separating out the atmosphere and ground noise temperature contributions separately, these effects are more easily handled in design control tables when the effect of a particular weather condition is studied, when changes are made in antenna configuration, or when particular antenna components are modified in any manner.

IV. G/T Improvement with the 70-m Antenna Network

The gain/noise temperature (G/T) ratio is generally regarded as the key figure-of-merit for a telecommunications antenna and receiver system. For the 70-m upgrade project, the maximization of this ratio at X-band was a key design parameter.

Substantial X-band gain improvements over those of the 64-m antennas were made. For an accurate gain comparison, the peak 64-m antenna gains as reported in [2-4] must be adjusted upward as a result of studies made during the analysis in [1]. A redetermination of radio source 3C274 flux contributes a +0.076-dB change. A recalculation of the 3C274 source-size correction for the 64-m antennas results in two corrections, one for DSS-14 and one for DSS-43 and DSS-63. As given in the DSN radio source catalog,⁵ the source-size correction for 3C274 in use during the DSS-43 and DSS-63 calibrations was 1.085 (D-3801, rev. A). During the DSS-14 calibration the source-size correction was 1.089 (D-3801, rev. B). The latest calculated value [1] is 1.15, giving changes of +0.253 dB (DSS-43 and DSS-63) and +0.237 dB (DSS-14). Adding these to the 0.076-dB flux adjustment results in total gain changes of +0.313 dB (DSS-14) and +0.329 dB (DSS-43/63). Comparing the peak without-atmosphere gains of the

⁴D. A. Bathker, personal communication.

⁵DSN Radio Source List for Antenna Calibration, JPL D-3801, Rev. A and Rev. B, September 25, 1987, (internal document), hereafter referred to as D-3801.

64-m antennas (from [2-4], adjusted upward) and 70-m antennas [1], the gain improvements for each antenna are

DSS-14: +1.85 dB

DSS-43: +2.15 dB

DS-63: +2.37 dB

Of these totals, about 0.8 dB is due to area increase, and the remainder is due to efficiency improvement. The average X-band gain increase is about 2.1 dB, well above the project requirement of 1.9 dB. Repeating the results presented in [1], the final peak without-atmosphere gains and aperture efficiencies for the 70-m antennas are

DSS-14 (Goldstone): 74.172 dBi (68.50 percent)

DSS-43 (Canberra): 74.093 dBi (67.27 percent)

DSS-63 (Madrid): 74.287 dBi (70.34 percent)

The without-atmosphere noise temperature improvements (decreases) at zenith are discussed in Section II. The S-band improvement is about 0.4 dB, and the X-band improvement is about 0.2 dB.

Figure 3 shows the final 70-m X-band gain (as given in [1]) and system noise temperature performance compared with the model contained in the latest (1986 through 1988-era) 810-5 Design Handbook. This comparison is made to document the 1986 accuracy of predicting the G and T performance of the 1989 70-m antenna network. The initial predicted values were used in preliminary estimates of Voyager (and other) telecommunications link performances through the year 2000. The points plotted in the curves are measured values minus 810-5 modeled values (which include a clear-sky atmosphere). The measured 70-m gain values include a nominal 25-percent clear-sky weather attenuation (0.040 to 0.042 dB as given in Table 2) for comparison with the 810-5 values measured during what must now be assumed (years after the fact) to be also a 25-percent clear-sky condition. The zenith atmospheric attenuation value over the 0 to 50 percent CD (cumulative distribution) range is about 0.040 dB \pm 0.010 dB (cf. Table 2), which gives some idea of the maximum possible post facto error in the 25-percent CD assumption. The 70-m T_{op} values are those given in Table 1 and Fig. 2 (X-band with atmosphere).

It is seen that at low elevation angles, the measured (and extrapolated) T_{op} is much larger than the 810-5 model. This difference is 5.7 K at 5-deg elevation. Above 20-deg elevation, the difference is less than 1 K, with the measured values being larger than the 810-5 values. The measured 70-m antenna gain performance exceeded the model over most of the elevation

angle range, with a maximum difference for DSS-63 of about 0.3 dB at 35-50-deg elevation. Below 10-deg elevation, only DSS-14 exceeds the model; the other antennas are as much as 0.35 to 0.5 dB below the model at 5-deg elevation. The \pm 0.3 dB (\pm 7 percent) agreement range for all antennas extends from about 8-deg to 90-deg elevation.

The 810-5 modeled 70-m antenna performance was derived from a hybrid performance combination (increased by 1.9 dB) of the 64-m antennas as given in earlier versions of 810-5. The gain values used for DSS-14 and a combined DSS-43/63 differ uniformly by 0.12 dB and reflect the fact that the DSS-14 gain was somewhat higher than the gain of the overseas antennas. This difference underestimated the measured difference [2-4] of 0.40 dB, including adjustments. The shapes of the 810-5 gain curves reflect the flatter shapes of the DSS-14 and DSS-43 (64-m) curves, as compared to the DSS-63 (64-m) gain curve, which had a steep falloff at both low and high elevation angles [2-4]. This difference was due to a structural anomaly of the DSS-63 64-m antenna; the 70-m antennas are presently identical in construction. The 810-5 noise temperature values used were common to all antennas and give a zenith T_{op} value of 20.0 K. The tolerance of the 810-5 zenith noise temperature was \pm 3 K (σ not stated), which is comparable to the \pm 10-percent value given earlier in Section II.

Figure 4 shows the 810-5 G/T model and the measured G/T comparison for the 70-m antennas, in addition to a curve representing the 64-m network G/T performance. It is seen in the figure that the 810-5 models of 70-m performance (the pairs of data points, computed from G and T as described above) are quite accurate (\pm 0.2 dB) over the 15- to 90-deg elevation angle range. Below 15-deg elevation, the greater measured T_{op} results in performance not agreeing with the model. Note that DSS-14 almost perfectly matches the 810-5 model of G/T from 10-deg elevation to zenith.

The 64-m G/T curve shown in Fig. 4 is a hybrid curve and represents the best possible performance that might have been achieved by the 64-m network. The curve combines the highest gain (DSS-14) and lowest noise temperature (DSS-43), both with atmosphere, as given in [3, 4]. The 64-m gain value has been adjusted upward by 0.313 dB, as discussed above. Measured individual 64-m antenna performances were somewhat lower than shown in this figure, due to either lower gain or increased T_{op} . This hybrid model is used to show the *minimum* G/T improvement of the 70-m network over the 64-m network. Comparing the DSS-14 G/T performance, the improvement ranges from a minimum of 1.8 dB at zenith to a maximum of almost 2.5 dB at 10-deg elevation. From 20-deg to 80-deg the DSS-14 improvement is about 2.0 dB (\pm 0.2 dB).

It is seen that the 70-m antenna upgrade has resulted in a substantially more powerful DSN telecommunications operation than existed with the previous 64-m configuration.

V. Comparison of Measured DSN 70-m Antenna Performance, TPAP-Predicted Link Performance, and Actual Voyager Telecommunications Performance

An integral and absolutely vital part of the telecommunications link design control table (DCT) is an accurate description of the gain and system noise temperature characteristics of the antennas being used. Differences between measured performance and the DCT model (all other things being equal) will be reflected in either an excessive or inadequate link margin. The results, in short, will be unnecessary sacrifice of the quantity or the quality of pictures of Neptune (for example).

Clearly, two of the most important goals of the 70-m upgrade project were to obtain the maximum gain and the minimum noise temperature possible from the upgraded antennas. In telecommunications link operation, the maximum amount of data that can be received is directly proportional to the real G/T value of the receiving system at whatever elevation angle the spacecraft happens to be. It should be noted that in all discussions of G/T, one is talking about operational performance, and as such the effects of the atmosphere are included in both G and T. In order to maximize the data received, accurate predictions of link performance must be made in order to choose, among many other things, the transmitted data rate. Included in the link performance prediction are numerous other considerations among which are weather effects, spacecraft limit cycling (pointing), variations of transmitted power, and ground antenna pointing error (including conscan offset effect).

The Voyager design control table, TPAP (Telecommunications Prediction and Analysis Program), has within it models of antenna gain, system noise temperature, and certain adjustments for weather conditions more severe than the nominal 25-percent CD weather postulated for the 810-5 gain and noise temperature curves.

To verify the accuracy of TPAP, the following must be determined: (1) what antenna parameters are being used in the program, (2) whether they agree with an official project document or the 810-5 document, (3) whether they agree with the newly determined 70-m antenna performance characteristics [1], and (4) whether the Voyager telecommunications link actually operates as predicted.

It was found during the Voyager Uranus encounter (January 1986) using the DSN 64-m network, that there was an excess X-band link margin of approximately 1 to 2 dB, depending on the station, in benign weather conditions, as indicated by symbol signal-to-noise (SSNR) residuals.⁶ (The Voyager Uranus encounter, of course, was eminently successful.) Subsequent to that encounter, elements of the 64-m TPAP program were changed to reflect updated 810-5 Design Handbook values. Included in these changes were a ground antenna gain increase of +0.3 dB, and a T_{op} decrease of 2.1 K (+0.4-dB improvement). The total adjustment was +1.0 dB. With the 70-m upgrade, the changes to the telecommunications database to be used for Neptune encounter totaled 3.3 dB, including the 1.0 dB described above.

Because of inconsistencies between the TPAP computational methods and the presentation of the 810-5 link parameters, attempts were made within TPAP to approximate the 810-5 values for gain and noise temperature. The resulting gain and T_{op} values do not agree exactly with the 810-5 values. The TPAP T_{op} values are all 0.5 K lower than the 810-5 values, e.g., with a zenith value of 19.5 K. This discrepancy is caused by the fact that the atmospheric noise increase with elevation angle is generated within TPAP from an atmosphere attenuation model; in 810-5 the noise temperature increase (ground and atmosphere) is given as a separate input. The single gain curve in TPAP is a hybrid 64-m curve raised 1.9 dB, with downward adjustments of -0.2 dB made for an asymmetric statistical gain distribution, and -0.1 dB made for conscan pointing offset. The elements of the gain curve, before the 0.3-dB adjustment, are given in *Voyager Telecommunications Design Control Document*.⁷ Nevertheless, a single 70-m G/T curve can be generated from the TPAP parameters, and this can be compared with the three G/T curves shown for the 70-meter antennas (cf. Fig. 4).

Figure 5 shows the differences between the measured 70-m G/T and the model contained within TPAP. It is seen that the measured performance over the 20- to 90-deg elevation range tends to exceed the TPAP predictions for clear-sky conditions. A difference of as much as 0.3 dB exists (for DSS-14 at 20-deg elevation, and for DSS-63 at 35-deg elevation). At the lower elevation angles all antennas appear to drop off in performance compared to the TPAP model due to an incorrect 810-5/TPAP noise temperature model, and, in the cases of DSS-43 and DSS-63, there is a steep gain fall-off, more severe than in

⁶B. D. Madsen, personal communication.

⁷*Voyager Telecommunications Design Control Document*, JPL 618-257, rev. A (internal document), Jet Propulsion Laboratory, Pasadena, California, January 15, 1988.

the models. It should be noted that the excessive T_{op} values are compared with the TPAP model, not the slightly different 810-5 model. In actuality there was, in general, a decrease in real T_{op} contribution compared with the 64-meter network values. The present 810-5 and TPAP antenna performance models are somewhat unrealistic, but not so much as when they modeled the 64-m antenna performance.

Figure 6 shows the curves of Fig. 5 plotted with selected sets of Voyager symbol SNR (SSNR) residuals representing differences between actual Voyager telecommunications link performance and TPAP-predicted link performance. In the following discussion, "measured link" means measured 70-m antenna G/T, "modeled link" means the G/T model contained within the TPAP program, "actual performance" means actual Voyager SSNR, and "predicted performance" means TPAP-predicted Voyager SSNR. Comparisons among these four items require the use of the TPAP "transfer standards," in which accurate gain and noise temperature models (and numerous other factors) within TPAP imply an accurate prediction of received SSNR.

These data were recorded during the last quarter of 1988 and in early 1989. The straight line segments represent the Voyager 1 (Spacecraft 31) and Voyager 2 (Spacecraft 32) SSNR residuals during particular passes which appeared to represent the best actual performance of the link during the period mentioned (in other words, when everything was working well). These passes are annotated as STATION/SPACECRAFT/DOY. No appropriate data for DSS-43/Spacecraft-31 could be found. The data are restricted to the period after 1988 DOY 274, at which time there was a database change (an adjustment of system noise temperature) within TPAP. The comparison between measured link residuals (the curves) and actual performance residuals (the straight line segments) should be a valid test of the link model and telecommunications prediction methods used by the Voyager Project.

It is seen that for DSS-63 there is remarkable agreement between the actual Voyager excess performance (positive residuals) and the excess measured antenna G/T, compared with the TPAP models. Over the 20- to 50-deg elevation angle range, the agreement is within 0.1 dB, and shows as much as +0.3-dB link margin. For DSS-14 it appears that the Voyager link may be underperforming by as much as 0.2 dB over the elevation range 20- to 60-deg. The DSS-43 data appear to be 0.2 to 0.4 dB below what might be expected from the link. Again, these data were chosen from a very small number of passes, and given a larger database, higher performance may very well be seen. Long-term daily observations of the SSNR residuals by Voyager telecommunications analysts have not detected significantly inadequate performance of any sta-

tion.⁸ The uncertainty in both the G/T and SSNR residuals is about 0.2 dB (1- σ). No data were available at low elevation angles, thus it is not possible in this article to verify the large negative G/T residuals shown below 10-deg elevation.

VI. Use of Antenna Parameters in Telecommunications Design Control Tables

By the relationships given in [1] for S- and X-band antenna gain, and in this article for S- and X-band atmospheric contributions, ground noise temperatures, and microwave system constants, design control tables can be developed to predict G/T (gain/system noise temperature) for a given antenna, at a given elevation angle, for a given weather condition. The weather condition is referred to as "x-percent-weather," and is actually the cumulative distribution (CD) of the weather statistics at the point of interest. As an example, 90-percent weather (CD = 0.90) means that 90 percent of the time the weather effect (attenuation or noise temperature) is less than or equal to a particular value.

For example, consider the DSS-43 (Canberra) 70-m antenna, X-band, 90- through 10-deg elevation angle, 90-percent weather, worst month. Also included is a hot-body contribution at 0.5 K, as determined by methods presented in the 810-5 Design Handbook. Table 4 shows that portion of a design control table (DCT) concerned with antenna, atmosphere, and ground effects. The details of the calculation of each entry are given in the Appendix. It is seen in this example that in contrast to previous methods of calculating gain, attenuation, and noise temperature effects, atmospheric attenuation is not included in the antenna gain description, ground and atmosphere effects are separated, that there is not a single zenith T_{op} value which includes ground, atmosphere, receiver, waveguide, and cosmic contributions, and that the changes with elevation angle are simply calculated. The DCT portion presented here is formulated to lend itself to straightforward calculations by means of any spreadsheet program.

VII. Conclusion

The 70-meter antenna upgrade project has significantly improved the gain and noise temperature characteristics of the three large antennas in the NASA Deep Space Network.

⁸B. D. Madsen, personal communication.

Although the noise temperature improvements have been modest (0.2 to 0.4 dB at zenith), the peak gain increases have been substantial (1.85 to 2.37 dB over the comparable 64-m antennas). The combined effect of both contributions has been to increase the G/T (gain/noise temperature) performance of the DSN from a minimum of 1.8 dB to a maximum of 2.5 dB, compared to the best possible G/T of a 64-m antenna.

An analysis was made to determine the measured 70-m G/T performance compared with that presented in the 810-5 Design Handbook. It was found that compared to 810-5, the measured gains for all stations are within 0.3 dB from 8-deg elevation to zenith. The noise temperature agrees within 0.3 dB from 17-deg elevation to zenith. The G/T agreement is within 0.2 dB from 15-deg to zenith.

In anticipation of the Voyager Neptune encounter in August 1989, a comparison of measured 70-m antenna performance and actual Voyager telecommunications performance was made, both relative to the gain, noise temperature, and performance models contained within TPAP. Based on limited sets of link SSNR residuals for the period late-1988 through February 1989, it was found that the DSS-63 link at its best appears to perform in agreement with the measured 70-m antenna performance. In other words, they both appear to have the same amount of excess performance (up to 0.3 dB) compared to the models contained within TPAP. The DSS-14 link appears to be operating as much as 0.2 dB below its capability, although in agreement with the predictions of the TPAP model. The DSS-43 link appears to be operating as much as 0.3 to 0.4 dB below both its capability and its TPAP-predicted performance.

Acknowledgments

The authors wish to thank all of the engineers and technicians of the DSN for their efforts in gathering the enormous amount of data necessary to characterize the performance of the 70-meter antenna network.

Table 1. Coefficients of polynomial expressions for 70-m system noise temperatures, T_{op} , K

Coefficient	X-band $T_{x,w/atm}$	X-band $T_{x,w/o atm}$	S-band $T_{s,w/atm}$	S-band $T_{s,w/o atm}$
a_0	17.31485	16.79863	16.03823	15.73028
a_1	260.33790	133.73960	170.74070	61.51348
a_2	-444.55570	-738.87820	-329.81790	-284.86760
a_3	-146.17770	1376.48100	-65.32625	461.33590
b_0	70.64852	28.57571	47.82000	22.47123
b_1	-4.58767	-0.53753	-2.52123	-0.41137
b_2	0.13988	0.00960	0.07142	0.01142

Note: High-elevation limits for T_{op} expressions (Eq. 1):

$$\begin{aligned}
 &\text{if } T_{x,w/atm} < 20.9 \text{ then } T_{x,w/atm} = 20.9 \\
 &\text{if } T_{x,w/o atm} < 18.4 \text{ then } T_{x,w/o atm} = 18.4 \\
 &\text{if } T_{s,w/atm} < 18.3 \text{ then } T_{s,w/atm} = 18.3 \\
 &\text{if } T_{s,w/o atm} < 16.5 \text{ then } T_{s,w/o atm} = 16.5
 \end{aligned}$$

Table 2. Nominal clear-sky (25-percent weather) zenith atmospheric attenuation (A) and noise temperature (T) at DSN 70-m antenna locations

Station	X-band		S-band	
	A , dB	T , K	A , dB	T , K
DSS-14 0.993 km MSL	0.040	2.45	0.030	1.81
DSS-14 no water vapor (0-percent weather)	0.031	1.86	0.029	1.77
DSS-43 0.670 km MSL	0.042	2.60	0.032	1.93
DSS-63 0.812 km MSL	0.041	2.53	0.031	1.88

Table 3. Components of clear-sky (25-percent weather) total zenith system noise temperature, K

	Contribution to noise temperature, K	
	X-Band	S-Band
Receiver + waveguide	12.7 \pm 0.5	10.3 \pm 0.5
Atmosphere, nominal	2.5	1.9
Ground (spillover + scatter)	3.0 \pm 0.5	3.5 \pm 0.5
Cosmic background	2.7	2.7
Total	20.9	18.4

Table 4. Proposed Design Control Table (DCT); portion concerning antenna, atmosphere, and ground effects

1	Ground antenna diameter, m	Input	70.0000	70.0000	70.0000	70.0000	70.0000	70.0000
2	Frequency, GHz	Input	8.4200	8.4200	8.4200	8.4200	8.4200	8.4200
3	Wavelength, m		0.0356	0.0356	0.0356	0.0356	0.0356	0.0356
4	Elevation angle, deg	Input	90.0000	60.0000	45.0000	30.0000	20.0000	10.0000
5	Percent weather, CD	Input	0.9000	0.9000	0.9000	0.9000	0.9000	0.9000
6	Atmosphere attenuation total zenith, dB	Input	0.0700	0.0700	0.0700	0.0700	0.0700	0.0700
7	Atmosphere attenuation total at elevation, dB		0.0700	0.0808	0.0990	0.1400	0.2047	0.4031
8	Atmosphere loss factor L at elevation		1.0162	1.0188	1.0231	1.0328	1.0483	1.0973
9	Ground antenna gain without atmosphere, 100 percent, dBi		75.8148	75.8148	75.8148	75.8148	75.8148	75.8148
10	Ground antenna gain without atmosphere at elevation, dBi		73.3753	74.0412	74.0900	73.9494	73.7505	73.4673
11	Receiver noise, K	Input	3.5000	3.5000	3.5000	3.5000	3.5000	3.5000
12	Waveguide noise, K	Input	9.2000	9.2000	9.2000	9.2000	9.2000	9.2000
13	Atmosphere physical temperature, K		278.5000	278.5000	278.5000	278.5000	278.5000	278.5000
14	Atmosphere noise, total, K		4.4529	5.1354	6.2764	8.8346	12.8202	24.6871
15	Ground noise, K	Input	3.0000	3.2580	3.8880	5.0230	6.4360	8.9570
16	Hot-body noise without atmosphere, K	Input	0.5000	0.5000	0.5000	0.5000	0.5000	0.5000
17	Hot-body noise, K		0.4920	0.4908	0.4887	0.4841	0.4770	0.4557
18	Cosmic noise temperature, K		2.6568	2.6502	2.6392	2.6144	2.5757	2.4607
19	Total system noise temperature, T_{op} , K		23.3017	24.2344	25.9923	29.6561	35.0089	49.2604
20	Gain/ T_{op} , dB		59.6314	60.1160	59.8426	59.0883	58.1040	56.1392

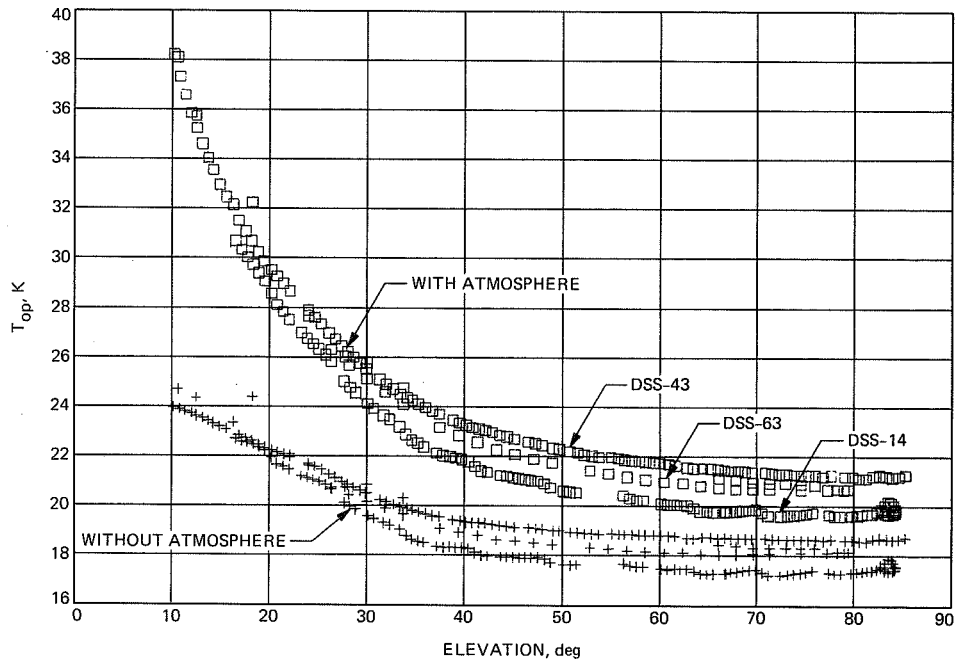


Fig. 1. The 70-m antenna X-band noise temperatures, with and without atmospheric contribution.

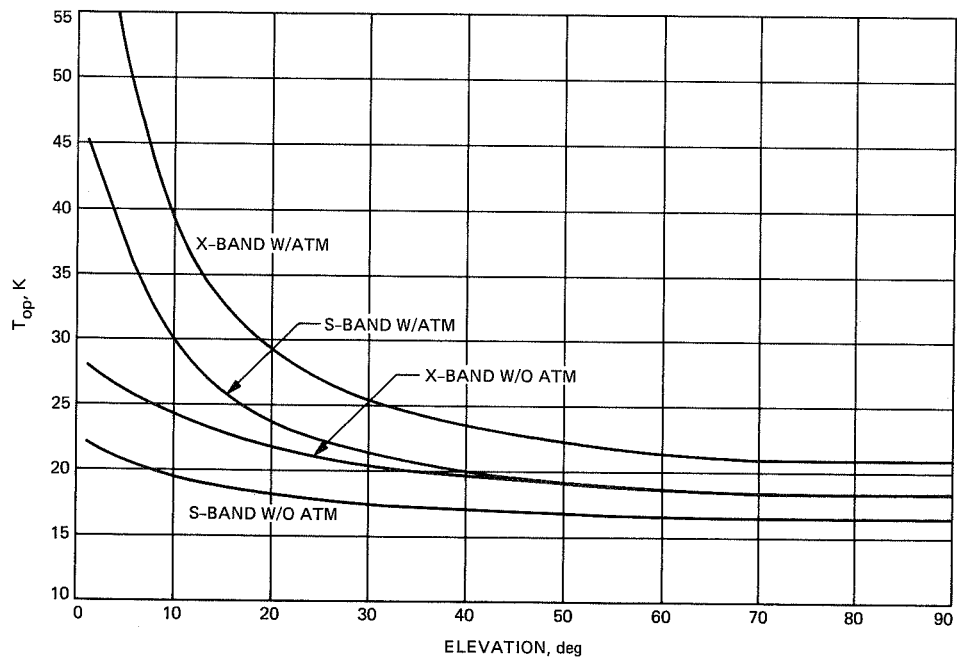


Fig. 2. S- and X-band noise temperature curve-fits, with and without atmospheric contribution.

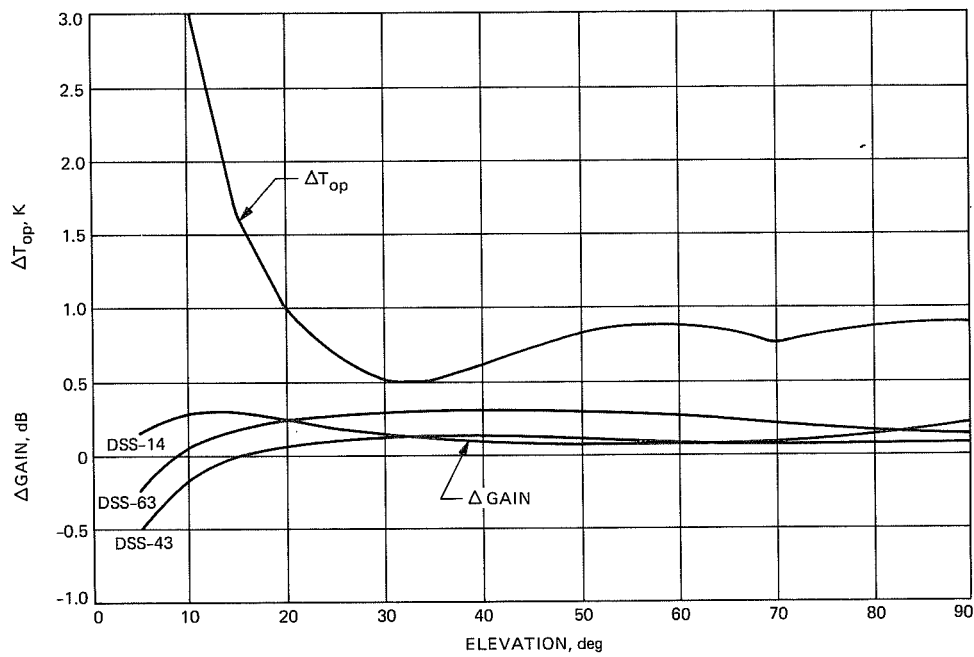


Fig. 3. The 70-m antenna measured minus 810-5 model of gain and system operating noise temperature.

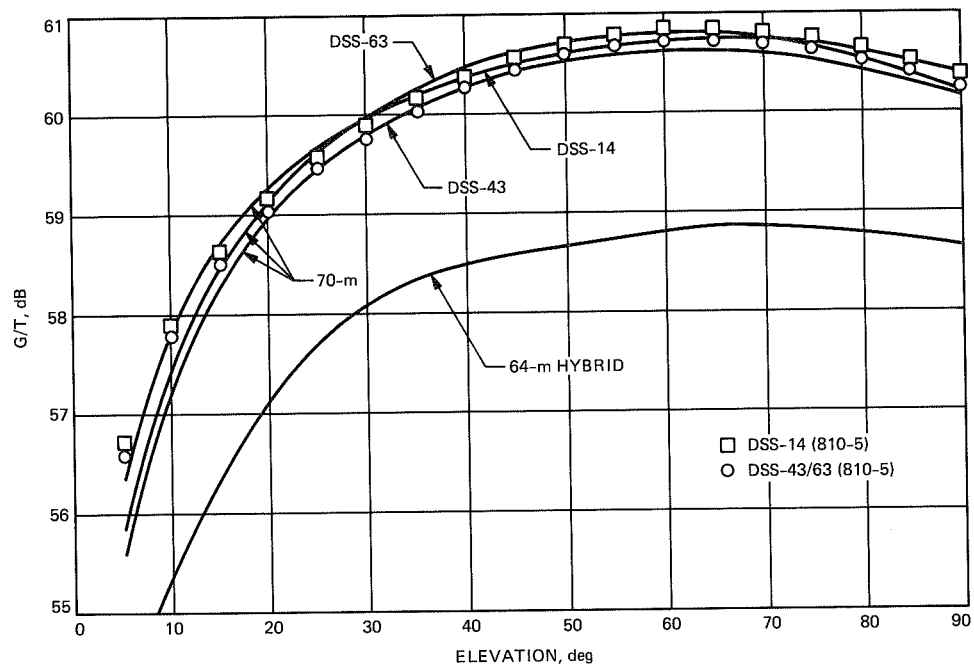


Fig. 4. Comparison of 70-m antenna measured and 810-5 G/T values, with best possible 64-m performance.

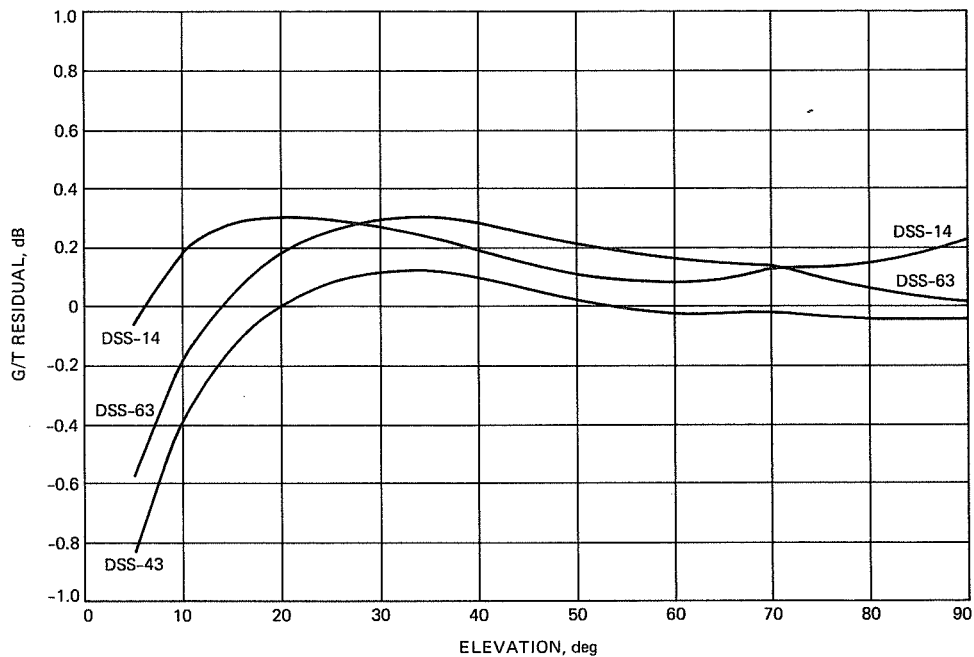


Fig. 5. The 70-m antenna measured G/T minus Voyager TPAP-predicted G/T.

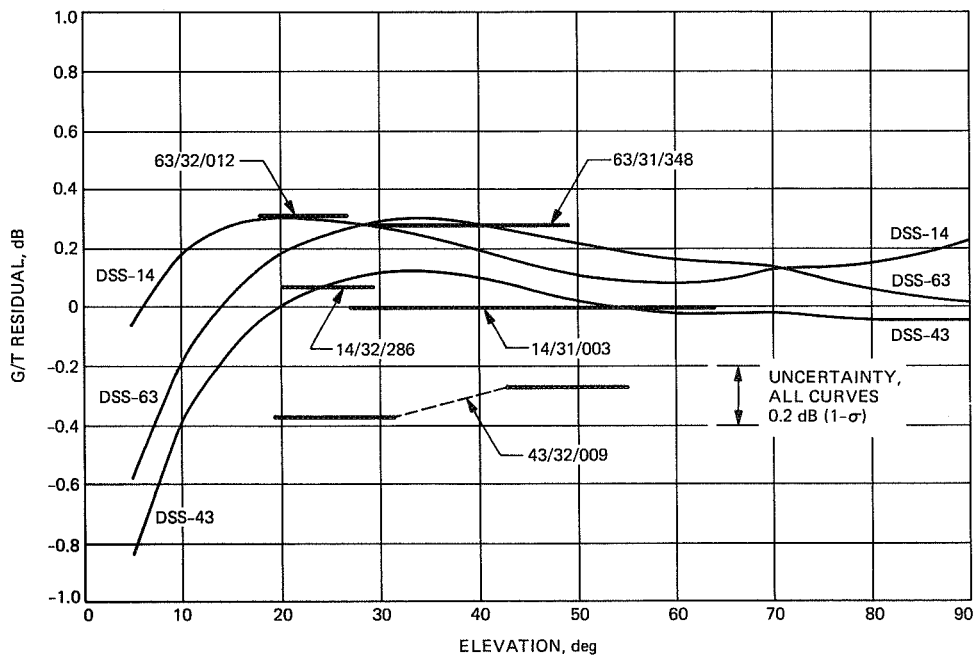


Fig. 6. The 70-m antenna measured G/T minus Voyager TPAP-predicted G/T, with Voyager SSNR residuals.

Appendix

Sample DCT for Antenna, Atmosphere, and Ground Effects

Following is a line-by-line listing of the entries in a design control table (cf. Table 4).

- Line 1: INPUT ground antenna diameter, DIAM, meters.
 Line 2: INPUT frequency, FREQ, GHz.
 Line 3: The wavelength, meters, is calculated from

$$WVLN = 0.29979/FREQ$$

- Line 4: INPUT elevation angle, ELEV, degrees.
 Line 5: INPUT percent weather, cumulative distribution, CD, (0-1).
 Line 6: INPUT total zenith atmospheric attenuation, AZEN, dB, for weather condition (CD) of interest. This will usually be found in an external source such as the 810-5 Design Handbook, or another source of measured or modeled weather effects. In the example presented here, the 0.070-dB value is calculated from values presented in the 810-5 Handbook, TCI-40: 0.033-dB baseline plus 0.037-dB increase.

- Line 7: The total atmospheric loss, dB, at the elevation angle of interest is calculated from

$$ADB = AZEN/\sin(ELEV)$$

This flat-earth model is accurate to within 4 percent down to an elevation angle of about 6 deg, in which case it overestimates the loss. The error at 12-deg elevation is an overestimate of about 1 percent.

- Line 8: The atmospheric loss factor (dimensionless) is calculated from

$$LATM = 10^{\frac{ADB}{10}}$$

- Line 9: The ground antenna gain, dBi, for 100-percent efficiency is calculated as a diagnostic only:

$$G100 = 10 \log_{10} \left(\frac{PI \cdot DIAM^2}{WVLN} \right)$$

where $PI = 3.14159265$.

- Line 10: Ground antenna gain, dBi, without atmosphere as a function of elevation angle is calculated from

$$GDB = 73.10 + (4.09421E-02)\theta - (4.20925E-04)\theta^2$$

where

θ = elevation angle, deg

This polynomial expression matches the DSS-43 without-atmosphere gain as presented in [1]. Expressions for gain will be found in the 810-5 design document, this article, or may be postulated for other frequencies. This calculated value should be compared with G100 for reasonableness.

- Line 11: INPUT ground receiver noise temperature, TRCVR, K.

- Line 12: INPUT ground antenna waveguide noise temperature, TWG, K.

Note: sum of lines 11 and 12 agrees with the value in Table 3.

- Line 13: Atmosphere mean physical temperature, K, calculated as a function of cumulative distribution CD to reflect the fact that weather effects which dominate at the higher CDs generally occur closer to the ground and thus have a higher physical temperature.

$$TPATM = 265 + 15 \times CD$$

- Line 14: Calculated atmospheric noise temperature, K:

$$TATM = TPATM \left(1 - \frac{1}{LATM} \right)$$

- Line 15: INPUT ground noise temperature TGRND, K, calculated, (external to the spreadsheet) from:

$$TGRND = T_{w/o atm} - 15.4$$

This is Eq. (3), this article. Expressions for the $T_{w/o atm}$ contribution will be found in the 810-5 Design Handbook, this article, or may be postulated for other configurations. For use in spreadsheet calculations, the polynomial expressions given in Table 1 may be too complex, hence external calculations for given elevation angles may be required. Simplifications to the Table 1 expressions may be used in some applications, with some loss of accuracy.

- Line 16: INPUT hot-body noise THOT, K, as given in 810-5, with the ground antenna pointing a fixed angular distance from the source. This may change during an encounter period.

Line 17: Hot-body noise, K, attenuated by the atmosphere is calculated from:

$$THOTP = \frac{THOT}{LATM}$$

Line 18: Cosmic noise temperature, K as attenuated by the atmosphere:

$$TCOS = \frac{2.7}{LATM}$$

Line 19: Total system noise temperature, T_{op} , K, as calculated from:

$$TOP = TRCVR + TWG + TATM \\ + TGRND + THOTP + TCOS$$

Line 20: G/T (gain/system noise temperature), dB, is calculated from:

$$GT = GDB - ADB - 10\log_{10}(TOP)$$

References

- [1] P. H. Richter and S. D. Slobin, "DSN 70-Meter Antenna X- and S-Band Calibration, Part I: Gain Measurements," *TDA Progress Report 42-97*, vol. January-March 1989, Jet Propulsion Laboratory, Pasadena, California, this issue.
- [2] S. D. Slobin, "DSS-63 64-Meter S- and X-Band Efficiency and System Noise Temperature Calibrations, July 1986," *TDA Progress Report 42-90*, vol. April-June 1987, Jet Propulsion Laboratory, Pasadena, California, pp. 103-115, August 15, 1987.
- [3] S. D. Slobin, "DSS-43 64-Meter S- and X-Band Efficiency and System Noise Temperature Calibrations, January 1987," *TDA Progress Report 42-90*, vol. April-June 1987, Jet Propulsion Laboratory, Pasadena, California, pp. 116-126, August 15, 1987.
- [4] S. D. Slobin, "DSS-14 64-Meter S- and X-Band Efficiency and System Noise Temperature Calibrations, September 1987," *TDA Progress Report 42-92*, vol. October-December 1987, Jet Propulsion Laboratory, Pasadena, California, pp. 138-146, February 15, 1988.
- [5] D. A. Bathker and S. D. Slobin, "DSN 70-M Antenna Microwave Optics Design and Performance Improvements: Part I," *TDA Progress Report 42-97*, vol. January-March 1989, Jet Propulsion Laboratory, Pasadena, California, this issue.
- [6] S. L. Valley, ed., *Handbook of Geophysics and Space Environments*, New York: McGraw-Hill, 1965.

Reanalysis, Compatibility, and Correlation in Analysis of Modified Antenna Structures

R. Levy

Ground Antenna and Facilities Engineering Section

A simple computational procedure is synthesized to process changes in the microwave-antenna pathlength-error measure when there are changes in the antenna structure model. The procedure employs structural modification reanalysis methods combined with new extensions of correlation analysis to provide the revised rms pathlength error. Mainframe finite-element-method processing of the structure model is required only for the initial unmodified structure, and elementary postprocessor computations develop and deal with the effects of the changes. Several illustrative computational examples are included. The procedure adapts readily to processing spectra of changes for parameter studies or sensitivity analyses.

I. Introduction

The capability to readily process changes or sequences of changes in antenna finite-element-method (F.E.M.) structure models is useful for design, parameter studies, or design sensitivity analyses. Otherwise these tasks entail major computational effort via ab initio processing. F.E.M. analysis of antenna structures is time-consuming and demanding of mainframe computer resources. It is necessary to solve simultaneous linear load-displacement equations of orders in the thousands. Processing the structural stiffness matrix and the vectors of external loading cases provides the displacements of the F.E.M. nodes. A change in any structural element property or boundary restraint changes the stiffness matrix and therefore normally requires repetition of the lengthy equation-solving operation. This article discusses short-cut approaches that can readily avoid reformulating and repeating the stiffness matrix equation solution for special cases of changing the initial struc-

ture. Following this it will be shown how to synthesize the antenna performance pathlength error measure with only a trivial amount of additional computation. The procedures used here are postprocessor applications that are independent of and require no coding or algorithm changes in the F.E.M. software used to process the initial model. The only interaction with the F.E.M. software is in the desirability of convenient access to the output results.

The approaches considered here that condense the analysis of modified structures depend upon linearity of the load-displacement formulation. Linearity implies that superposition of displacements is also valid when loadings are superimposed. The final response (displacements, member stresses, and forces) is obtained as the sum of the response of the initial system to the known external loadings and the response to particular unit "indicator" loading vectors [1] that are appropriately

scaled to ensure compatibility in the modified system. The scaling methods are derived from the method of "consistent deformations" [2] or extensions under the topic of "structural modification reanalysis" [3-6].

Although linearity permits superposition of linear response quantities from several loading cases, the antenna surface accuracy is more appropriately expressed in terms of the mean square least squares best-fitting pathlength error, or equivalently, the square root (rms) of this quantity. It will be shown here that it is not necessary to recompute the displacements at all the nodes of the antenna surface F.E.M. model by superposition and then to repeat the least-squares method computations to obtain the best-fitting surface for this new set of displacements. That procedure, which is too lengthy to perform for any reasonably sized model except by a computer of substantial capacity, can be replaced by simple postprocessor hand or desk-type calculator analysis. The simplified calculations use the already available mean square pathlength errors for the several loading cases and the correlation coefficients for these loadings to perform the necessary calculations in a few steps.

II. Analysis for Structure Modifications

A. Method of Consistent Deformations

This method will be used for the situation in which the reflector backup tipping structure is analyzed independently of the supporting alidade or pedestal. The tipping structure F.E.M. model has the reflector supported on the elevation axis bearings. However, as is customary, the boundary restraint that would be in the thrust direction of the bearings is omitted. That is, the support provides no restriction of the reflector motion in the direction of the axis (elevation axis) through the bearings. Consequently it is desirable to correct the reflector analysis for the actual restraint of the alidade in this direction. The consistent deformation condition is that the final reflector and alidade displacements along the axis of the bearings must agree.

The definitions below, in which all terms are derived from separate reflector and mount analyses, are used to solve this problem:

e_R = extension of the reflector from bearing to bearing due to the action of the external loading

e_M = extension of the mount from bearing to bearing due to the reactions from the loading on the reflector plus any other loading applied directly to the mount that is also associated with the same reflector loading case

f_R = extensional compliance of reflector for equal and opposite forces applied at each bearing point along the axis of bearings; that is, this compliance is the extension produced by an indicator loading across the bearings

f_M = compliance of the mount for an equilibrating indicator loading

These defined quantities are shown conceptually in Fig. 1. The bearing points are shown as "A" and "B," R_A and R_B are the corresponding reaction forces, and the indicator loading forces are denoted as " P_S ." Here the displacement quantities are arbitrarily shown as if point A is fixed and point B moves to B', but actually the quantities required are the differences in displacements (extensions) between the final positions of A and B. All quantities are assumed positive as shown and can be in any set of consistent dimensional units.

From superposition, the final extension of the reflector will be the original extension plus a scale factor R times the extension for the reflector model indicator load. The final extension of the mount will be the original plus the same scale factor times the effect for the mount model indicator load. These final extensions must be equal. That is,

$$e_R + Rf_R = e_M + Rf_M \quad (1)$$

or

$$R = \frac{(e_M - e_R)}{(f_R - f_M)} \quad (2)$$

The application is illustrated in the following examples:

Example 1. The following data are available from a 34-m antenna design:

Tipping-Structure-Only Model	Alidade-Only Model
$e_R = -0.71761$	$e_M = -0.09420$
$f_R = 0.54791$	$f_M = -0.76280$

Thus from Eq. (2)

$$R = \frac{(-0.09420 + 0.71761)}{(0.54791 + 0.76280)} = 0.47563$$

The final extensions are:

for the reflector $-0.71761 + (0.47563)(0.54791) = -0.4570$

for the alidade $-0.09420 - (0.47563)(0.76280) = -0.4570$

Analysis of the composite model of reflector combined with alidade found the final extension to be -0.4628 . The difference between this and the number computed above is attributed to roundoff and minor differences in the composite model and the stand-alone individual models.

Example 2. This is an example of satisfying more than one compatibility condition for reflector-mount analysis. Figure 2 shows the schematic of a half-structure subreflector model and its supporting mount in which all details not pertinent to this example have been omitted.

For the subreflector model, the external loading is in the positive z -coordinate direction (vertical), and the primary support in this direction is at node 10, but, similar to Example 1, there is no restraint at the node for motion in the x direction. Node 512 is in line vertically with node 10 and has no external restraints.

The mount attaches to the subreflector at nodes 10 and 512. It contains one bar between these nodes (parallel to the z axis). Node 10 is unrestrained and the restraints on node 512 allow motion in the z direction. The assumptions are (a) node 512 of the mount has no stiffness except in the z direction, and (b) displacements of the subreflector in the z direction do not produce other subreflector forces or reactions. With these assumptions there are two redundancies in the reflector and mount system and these provide the associated compatibility conditions. Similar to Example 1, one condition is that the displacements of subreflector and mount at node 10 in the x direction must be the same. The second condition is that the z -direction extensions between nodes 10 and 512 in both models must be the same.

The indicator loadings that are applied to each model are shown in the figure as P_x and P_z . They are applied in opposite senses for the two models since they are required to be consistent with internal equilibrium in the composite system. The following additional definitions are used:

U_R = vector containing the x displacement of subreflector node 10 as its first component and the extension between nodes 10 and 512 as the second

U_M = mount displacement vector with the same components as for the subreflector vector above

R = vector of scale factors to be found; these apply to the indicator loads

F_R = subreflector compliance matrix for the indicator loadings; row indices correspond with U_R and column indices correspond with the indicator loads

F_M = mount compliance matrix with indices as for F_R

The compliance matrix components are taken to be positive in the case of increasing the node 10 x -displacement component and lengthening the distance between nodes 10 and 512.

With these definitions the matrix compatibility equation becomes

$$U_R + F_R R = U_M + F_M R \quad (3)$$

Rearranging Eq. (3), the following equation is obtained:

$$(U_R - U_M) = (F_M - F_R)R \quad (4)$$

which can be solved for R .

Specific input data from the subreflector and mount analyses and the computed value of R are given in Table 1. Using either the left side or the right side of Eq. (3), the updated extensions can be computed from the value of R just found. The result is compared below with that obtained by a composite model analysis of subreflector and mount:

	Computed here	Composite model
x -displacement	0.07103	0.07118
z -extension	-0.02822	-0.02831

B. Parallel Element Method of Structural Modification Reanalysis

This method [6-8] uses superposition and compatibility to provide great simplicity in processing spectra of changes in properties for elemental members of the F.E.M. model. It is particularly simple in both concept and application when applied to the analysis [8] or design [9, 10] of predominately one-dimensional-type rod members used in antenna structures. The method invokes only elementary postprocessor computations that, except for the requirement that the F.E.M. analysis process additional self-equilibrating indicator loads [1] in the usual way, are independent of the F.E.M. software.

The method can be applied for rod, beam, plate, or other elements of the F.E.M. model, but here the application will be restricted to the rod-type elemental member. The concept is that for each particular "parent" member of the structure to

be changed, there is conceptually a "parallel" member attached to the structure in the same way as the parent. The area of the parallel member, positive for additions and negative for reductions, is the change in area of the parent. An independent indicator loading consisting of a pair of unit indicator loads (directed towards each other) is applied at the terminal nodes of each parent member in the original structure. The following is a summary of the algorithms in the notation of and abstracted from [8].

1. Notation.

U_I = the displacement matrix of the initial unmodified structure; the order is m (degrees of freedom) by k (number of external loading columns)

U_M = the displacement matrix to be found for the modified structure

U_D = the change in displacements, which is equal to the displacements for the forces of the parallel members acting as loads on the initial structure

U_S = the displacement matrix of the initial structure for the indicator loadings; the order is $m \times b$ (number of parent member changes)

R = a matrix of scale factors of magnitudes to be found for the indicator loadings; the order is $b \times k$

e_M = the matrix of final extensions of parent and parallel members in the modified structure; the order is $b \times k$

e_I = the matrix of initial extensions of the parent members; the order is $b \times k$

e_S = the matrix of extensions of the parent members for the indicator loadings; the order is $b \times b$

e_0 = a diagonal matrix of extensions of the parallel members when isolated from the structure and loaded by tensile indicator load pairs; the order is $b \times b$

2. Algorithms. It is evident that the displacement of the modified structure is equal to the displacements for the initial structure plus the changes. That is,

$$U_M = U_I + U_D \quad (5)$$

Since the change in displacements is equal to the displacements caused by the indicator loads multiplied by their scale factors, Eq. (5) is rewritten as

$$U_M = U_I + U_S R \quad (6)$$

Similarly for the extensions,

$$e_M = e_I + e_S R \quad (7)$$

Nevertheless, the extension for the isolated parallel members when subjected to the scaled values of the indicator loadings must be the same for compatibility of parent and parallel member extensions, that is,

$$e_M = e_0 R \quad (8)$$

Combining Eqs. (7) and (8) leads to the following expression that can be solved for R ,

$$(e_0 - e_S) R = e_I \quad (9)$$

Once R has been determined, Eqs. (6) and (7) will provide the displacements and extensions of the modified structure.

Computation of the terms needed to formulate Eq. (9) is particularly simple for rod members of the structure. From Hooke's Law the extension of a rod in terms of its internal stress resultant force P , length L , area A , and Young's Modulus E is

$$e = \frac{PL}{AE} \quad (10)$$

Therefore all that is needed from the finite-element program to compute the extension terms are the output vectors of initial and indicator loading internal forces for the various external and indicator loadings. This allows Eq. (10) to be used as a simpler alternative to computing the extensions directly from the displacements of the terminal nodes. The extension of a typical isolated parallel member for an indicator loading of magnitude M (if not of unit magnitude) is

$$e_0 = \frac{ML}{A_D} \quad (11)$$

in which A_D is the area of the parallel member (equal to the change in area of parent member).

It is simple to show that if Eqs. (10) and (11) are used in Eq. (9), and both sides of Eq. (9) are premultiplied by the inverse of a diagonal matrix containing the AE/L terms, the following equation provides an alternative way to solve for R :

$$(A^* - P_S) R = P_I \quad (12)$$

in which A^* is a diagonal matrix containing the MA/A_D term appropriate to each row and P_S and P_I are the matrices of

internal forces of the parent members for the indicator loadings and for the external loadings.

The internal forces P_M for the modified structure are computed analogously to Eq. (5) as

$$P_M = P_I + P_D \quad (13)$$

where P_D is the change in force equal to [10]

$$P_S = (P_S + I_S)R \quad (14)$$

in which I_S is a quasi-identity matrix with one unity element in each row corresponding to the rows of R and is null elsewhere.

3. Comments.

- (1) If there is no parent member in the initial structure at a particular row, in Eq. (12) that row can be replaced by the formulation in terms of the extension as given in Eq. (9). A_D becomes the area of the member added.
- (2) If it is desired to remove a member, A_D should be the negative of the parent member area.
- (3) P_S is the negative of an identity matrix if the set of parent members is statically determinate. If any row of the matrix is null except for a negative unity on the diagonal, the associated parent member is essential to stability and cannot be removed.
- (4) Examination of the P_S matrix can provide an indication of the redundancy of the parent members. The stronger the off-diagonal coupling, the more redundant.
- (5) It is simple to process spectra of parent member changes because the formulations of Eq. (9) or Eq. (12) remain almost intact. The only terms that change are those that depend upon changes of A_D . It may be appropriate to substitute an arbitrarily small number for A_D that is several orders of magnitude smaller than the area of the parent if there is to be no modification for a particular parent member in one of these variations.

Example 3. Figure 3 is a sketch of the half-model of a 70-m antenna subreflector. The reflecting surface is modeled by plate elements and is stiffened by additional plates in the radial and circumferential directions. Supplementary truss structure behind and above the plates provides a backup and the means for attachment to the external supporting structure. The support system has been modified for illustrative purposes in this example and the vertical (z-axis direction) support system has been replaced by the three spring supports shown at points A, B, and C of the figure. The springs are

represented by rods in the model and the area parameter of the rods is to be varied. The computations are to be performed according to the procedures just given for the effect on two particular external loadings. The loadings are 1.0-g loads in the z- and in the y-coordinate directions.

The data, solution, and a sample check of computed forces and deflections derived from an F.E.M. analysis of the modified model are shown in Table 2. The small differences between the check results are attributed to round-off error and limited numbers of significant figures in the data transferred from the initial F.E.M. analysis. In [8] may be found a discussion of how the change in the loading due to changes in the weights of the modified members could be accounted for if necessary.

III. Correlation Analysis for RF Pathlength Performance of Modified Structures

A. Pathlength Error Vector Computation

The microwave antenna pathlength error computations that employ the deflections provided by the F.E.M. analysis are summarized here for ready reference. The linear relationship between the components of the pathlength error vector of the reflector with the Cartesian coordinate deflection components at the surface nodes was derived in [11]. This provided both the matrix relating pathlength error to deflection and the formulation of the least-squares procedure used to best-fit the deflected surface to an alternative surface that minimized the mean-square pathlength error. This formulation was extended in [12] which provided a single linear transformation matrix to express directly the relationship between the best-fitting pathlength error vector and the deflections. This transformation implicitly incorporated the least-squares fitting parameters and provided a one-to-one transformation from the triad of deflections at each node to the best-fit pathlength error of that node. This relationship is in the form

$$\rho = GU \quad (15)$$

in which ρ is the pathlength error vector, G is an invariant matrix essentially containing functions of the direction cosines of the ideal reflecting surface, and U contains the three-component deflection vector at each node.

Since the deflection vector for a combined loading can be assembled as the superposition of a linear combination of the displacement vectors for a set of independent loadings, a pivotal consequence is that the pathlength error vector can be assembled from the independent pathlength errors in the identical way. To be specific, if C is a vector of constants, U_j a matrix containing vectors of deflections for a set of individual loadings, ρ_j a matrix containing the corresponding best-

fit pathlength error vectors, and \mathbf{U} and $\boldsymbol{\rho}$ are the corresponding composite deflection and best-fitting pathlength errors, then when the deflection can be superimposed as

$$\mathbf{U} = \mathbf{U}_j \mathbf{C} \quad (16)$$

it also follows that

$$\boldsymbol{\rho} = \boldsymbol{\rho}_j \mathbf{C} \quad (17)$$

An additional favorable consequence is that superposition relationships similar to Eq. (17) also apply to other linear performance measures such as the least-squares best-fitting parameters, the boresight pointing errors, and subreflector offsets.

B. Mean Square Pathlength Error via Correlation Analysis

It is customary to consider a weighted mean-square pathlength error where the weights for microwave antennas depend upon an illumination factor and also the local area tributary to each node. However, if the weights are appropriately normalized so that they sum to unity, the weighting factors can be omitted for brevity in the following discussions without loss of generality. Then the mean-square pathlength error SS is the inner product

$$SS = \boldsymbol{\rho}^t \boldsymbol{\rho} \quad (18)$$

and the root-mean-square error is

$$rms = (SS)^{1/2} \quad (19)$$

When the pathlength error vector is found by superposition according to Eq. (17) then elementary matrix algebra will show that the mean square can be expressed as

$$SS = \mathbf{C}^t \mathbf{C} \mathbf{V} \mathbf{C} \quad (20)$$

in which $\mathbf{C} \mathbf{V}$ is the covariance matrix with elements given by

$$CV(i, j) = \boldsymbol{\rho}_i^t \boldsymbol{\rho}_j \quad (21)$$

The covariance matrix can be computed from the triple product of a diagonal matrix $\mathbf{R} \mathbf{M}$ of rms values of the best-fit pathlength errors for the independent loadings and a correlation matrix $\mathbf{C} \mathbf{R}$ as

$$\mathbf{C} \mathbf{V} = \mathbf{R} \mathbf{M} \mathbf{C} \mathbf{R} \mathbf{M} \quad (22)$$

In Eq. (22) the diagonal elements of matrix $\mathbf{R} \mathbf{M}$ are $rms_1, rms_2, \dots, rms_n$, where n is the number of loads that are superim-

posed. The coefficient of the i th row and j th column of the correlation matrix is defined as

$$CR(i, j) = \frac{\boldsymbol{\rho}_i^t \boldsymbol{\rho}_j}{(rms_i rms_j)} \quad (23)$$

It can be observed that the correlation matrix is symmetrical and has unity on the diagonal. The correlation matrix can be produced most conveniently as a by-product in the initial F.E.M. analysis [13] or alternatively by an independent post-processor.

In summary, postprocessor pathlength error computations for a linear combination of loadings are accomplished by applying Eqs. (22), (20), and (19), in that order.

Example 4. The rms pathlength error for the external loading will be computed for the antenna of Example 1. The following data are available from the tipping-structure-only analysis:

	RMS	Correlation coefficient
External loading	0.01090	-0.4331
Indicator loading	0.005705	

Therefore,

$$\mathbf{R} \mathbf{M} = \begin{bmatrix} 0.01090 & 0.00000 \\ 0.00000 & 0.005705 \end{bmatrix}$$

$$\mathbf{C} \mathbf{R} = \begin{bmatrix} 1.0000 & -0.4331 \\ -0.4331 & 1.0000 \end{bmatrix}$$

and

$$\mathbf{C} = \begin{pmatrix} 1.00000 \\ 0.47563 \end{pmatrix} \quad (R \text{ found from Ex. 1})$$

Then, from Eq. (22)

$$\mathbf{C} \mathbf{V} = \begin{bmatrix} 0.0001188 & -0.0000269 \\ -0.0000269 & 0.0000325 \end{bmatrix}$$

from Eq. (20)

$$SS = 1.0056\text{E}-04$$

from Eq. (19)

$$rms = 0.0100 \text{ (c.f. 0.0099 from composite model analysis of reflector and mount)}$$

Example 5. This is a supplement to Example 2. The pathlength error for the external loading as modified by the interaction with the mount will be computed here. The data and solution are shown in Table 3. The rms value of 0.0066 shown as the solution in the table was also obtained from the F.E.M. analysis of the composite reflector and mount. Actually there is agreement to within unity in the next (not shown) decimal figure.

If correlation analysis had not been used here, the conventional approach to predicting the rms number would be to take the root sum square (rss) of each of the three independent values times the applicable constant (C vector). That result would have led to the value of 0.0123. This inaccuracy is because the rss method is based upon an identity correlation matrix, which is far from the case here.

C. Pathlength Error Syntheses for Multiple Modified External Loadings

Up to this point the computation of pathlength error via correlation analysis for a modified structure treated the effect of modification for only one external loading condition. Frequently, however, the external loading of interest is a combination of two [12] (in the case of gravity loading on an antenna) or more (with the addition of other environmental cases) loadings. Consequently the previous formulation will be extended to include the cases of multiple external loadings for a modified antenna structure.

From superposition, similar to Eq. (17), the pathlength error vector for the external loading on the modified structure can be expressed as

$$\rho_M = \rho_{GM} C \quad (24)$$

in which ρ_M is the pathlength error vector for the modified structure when subjected to the combined external loading, ρ_{GM} is a matrix of the pathlength error vectors for the individual external loading cases of the modified structure, and C is a vector of combining coefficient factors for the external loading vectors.

Premultiplication of Eq. (24) by its transpose provides the desired mean-square pathlength error SS_M for the modified structure. That is

$$SS_M = C^t CV_M C \quad (25)$$

in which CV_M is the covariance matrix for the modified structure given by

$$CV_M = \rho_{GM}^t \rho_{GM} \quad (26)$$

It can be observed that once the modified covariance matrix CV_M is obtained it is trivial to complete the solution by means of Eq. (25). Consequently, the remainder of this discussion will concentrate on deriving an expression for this matrix.

External loading pathlength vectors that have been modified by the parallel element method can be expressed in terms of a matrix of unmodified pathlength error vectors ρ_G , a matrix ρ_I of pathlength errors for the indicator loadings, and R , the matrix of scale factors for the indicator loadings. Therefore, similarly to Eqs. (6) and (8), and with superposition in the form of Eq. (17), the modified pathlength error is

$$\rho_{GM} = \rho_G + \rho_I R \quad (27)$$

In the equation above, all the pathlength vectors are the least-squares best-fitting vectors.

Using Eq. (27) in Eq. (26) it can be shown, with some multiplication and rearrangement, that the desired covariance matrix can be expressed as the sum of four matrices. To do this, the following matrices that are all determined from F.E.M. analysis of the unmodified structure are defined:

RM_G = the diagonal matrix of rms values for the external loading; CR_G is the associated matrix of correlation coefficients

RM_I = the diagonal matrix of rms values for the indicator loads; CR_I is the associated matrix of correlation coefficients

CR_{GI} = the matrix of correlation coefficients for the external loadings with respect to the indicator loading

The above definitions are used in the computation of the following covariance matrices

$$CV_G = RM_G CR_G RM_G \quad (28)$$

$$CV_I = RM_I CR_I RM_I \quad (29)$$

$$CV_{GI} = RM_G CR_{GI} RM_I \quad (30)$$

Finally, omitting the manipulations, the following expression as the sum of four matrices can be developed for CV_M :

$$CV_M = CV_G + CV_{GI} R + (CV_{GI} R)^t + R^t CV_I R \quad (31)$$

The modified covariance matrix is square and of order equal to the number of external loads. The diagonal elements are the mean-square pathlength errors for the external loads on the modified structure and the off-diagonals are the pairwise covariances for these loads.

Example 6. The covariance matrix of the modified structure of Example 3 will be computed in this final example. The data and solution are shown in Table 4. The modified covariance matrix CV_M shown as the solution in Table 4 can be used as described in the preceding paragraph to furnish the rms value for the external loadings and their correlation coefficient. These are compared below with those obtained by a full F.E.M. analysis of the modified structure.

	Computed here	F.E.M. analysis
External z-loading rms	0.03922	0.03917
External y-loading rms	0.00862	0.00861
Correlation coefficient	0.8755	0.8753

IV. Summary

The synthesis of a readily applied procedure to compute the performance parameters of modified antenna structures has been presented. All the necessary computations can conveniently be developed by desk calculator or personal computer postprocessing. The input data needed consist of conventional mainframe computer analysis output for the unmodified structure. The synthesized procedure uses short-cut structure modification reanalysis methods to avoid reprocessing the modified finite-element-method structure model. Then, changes in the antenna root-mean-square pathlength error performance measure are computed for the modified structure by extended methods of correlation analysis. The complete modification and correlation analysis synthesis readily accommodates the processing of spectra of changes in the antenna structure for purposes such as for parameter studies or for design sensitivity analyses.

References

- [1] R. J. Melosh and R. Luik, "Multiple Configuration Analysis of Structures, *Journal of the Structural Division, ASCE*, vol. 94, no. ST11, pp. 2581-2596, November 1968.
- [2] J. L. Parcel and R. B. B. Moorman, *The Analysis of Statically Indeterminate Structures*, New York, New York: John Wiley & Sons Inc., pp. 3-5, 1955.
- [3] R. L. Sack, W. C. Carpenter, and G. L. Hatch, "Modification of Elements in Displacement Method," *AIAA Journal*, vol. 5, no. 8, pp. 1708-1710, September 1967.
- [4] J. S. Arora, "Survey of Structural Reanalysis Techniques," *Journal of the Structural Division, ASCE*, vol. 102, no. ST4, pp. 783-800, 1972.
- [5] A. B. Palazzolo, B. P. Wang, and W. D. Pilkey, "Static Reanalysis Methods," in *Structural Mechanics Software Series, vol. IV*, Eds. N. Perrone and W. D. Pilkey, pp. 413-460, Charlottesville: University Press of Virginia.
- [6] J. Sobieszczanski, "Matrix Algorithm for Structural Modification Based Upon Parallel Element Concept," *AIAA Journal*, vol. 7, no. 11, pp. 2132-2139, November 1969.

- [7] G. C. Best, "The Stress Area Method of Designing Beams," *Journal of the Aeronautical Sciences*, vol. 12, no. 3, pp. 298-304, July 1945.
- [8] R. Levy, "A NASTRAN Postprocessor for Structural Modification Reanalysis," *NASA Technical Memorandum X-2378*, vol. II, pp. 737-747, September 1971.
- [9] R. Levy, "Optimality Criteria Design and Stress Constraint Processing," *Proceedings of the International Symposium on Optimal Structural Design*, University of Arizona, Tucson, pp. 31-39, October 19-22, 1981.
- [10] R. Levy, "Stress Constraints and Screening for Optimality Criteria Design," *AIAA Journal*, vol. 21., no. 7, pp. 1028-1034, July 1983.
- [11] S. Utku and S. Barondess, "Computation of Weighted Root-Mean-Square Path Length Changes Caused by the Deformations and Imperfections of Rotational Paraboloidal Antennas," *Technical Memorandum 33-118*, Jet Propulsion Laboratory, Pasadena, California, March 1963.
- [12] R. Levy, "A Method for Selecting Antenna Rigging Angles to Improve Performance," *The Deep Space Network, SPS 37-65*, vol. II, Jet Propulsion Laboratory, Pasadena, California, pp. 72-76, September 1970.
- [13] R. Levy and D. Strain, "JPL-IDEAS Iterative Design of Antenna Structures," Computer Program CP-7282, submitted to *COSMIC*, November 1988.

Table 1. Data and solution for Example 2

Data	Solution
$U_R = \begin{pmatrix} 0.87642 \\ -0.32976 \end{pmatrix}$	$F_M - F_R = \begin{bmatrix} -0.40864 & 0.129000 \\ 0.129000 & -0.060766 \end{bmatrix}$
$U_M = \begin{pmatrix} 0.05865 \\ 0.0 \end{pmatrix}$	$U_M - U_R = \begin{pmatrix} 0.81777 \\ -0.32976 \end{pmatrix}$
$F_R = \begin{bmatrix} 0.394478 & -0.129000 \\ -0.129000 & 0.052867 \end{bmatrix}$	$R = \begin{pmatrix} -0.873343 \\ 3.57202 \end{pmatrix}$
$F_M = \begin{bmatrix} -0.014172 & 0.0 \\ 0.0 & -0.007899 \end{bmatrix}$	

Table 2. Data and solution for Example 3

Data:

Spring	External loading, P_I		Self-equilibrating indicator loading, $P_S (M = 1000)$		
	Z, 1.0-g	Y, 1.0-g	Load at A	Load at B	Load at C
A	-2451.0	8.6	-474.5	-262.8	-262.8
B	-2318.0	-625.3	-262.8	-868.6	131.4
C	-2031.0	616.8	-262.8	131.4	-868.6

Spring	Relative property change, A_D/A
A	-0.98
B	-0.99
C	0.20

Solution:

Spring	A^* (diagonal elements only, Eq. 10)
A	-0.10220408M = -102.20408
B	-0.10101010M = -101.01010
C	0.50000000M = 5000.00000

$$A^* - P_S = \begin{bmatrix} -545.908 & 262.800 & 262.800 \\ 262.800 & -141.501 & -131.400 \\ 262.800 & -131.400 & 5868.600 \end{bmatrix}$$

$$P_I = \begin{bmatrix} -2451.0 & 8.6 \\ -2318.0 & -625.3 \\ -2031.0 & 616.8 \end{bmatrix}$$

$$R = \begin{bmatrix} 116.718 & 19.979 \\ 233.475 & 41.397 \\ -0.345 & 0.137 \end{bmatrix} \quad (\text{See Eq. 12})$$

Checks:

Internal force check

Spring	Computed here (Eq. 14) External loading		Finite-element analysis External Loading	
	Z, 1.0-g	Y, 1.0-g	Z, 1.0-g	Y, 1.0-g
A	-2382	-407.7	-2378	-407.1
B	-2358	-418.2	-2355	-417.5
C	-2071	823.9	-2068	824.6

Deflection check

Node index	Computed here (Eq. y) External loading		Finite-element analysis External loading	
	Z, 1.0-g	Y, 1.0-g	Z, 1.0-g	Y, 1.0-g
124-2	-0.11722	-0.01454	-0.11706	-0.01451
124-3	3.12309	0.54772	3.1185	0.54688

Table 3. Data and solution for Example 5

<i>Data:</i>			
Loading case			
	rms	Correlation coefficients	
		Indicator X	Indicator Z
External	0.006647	0.9725	-0.8632
Indicator X	0.002335		-0.8297
Indicator Z	0.002845		
Loading factors			
$C = \begin{pmatrix} 1.000000 & \\ -0.873342 & (R(1)) \\ 3.57202 & (R(2)) \end{pmatrix}$			
<i>Solution:</i>			
$RM = \begin{bmatrix} 0.0066471 & 0.0 & 0.0 \\ 0.0 & 0.002335 & 0.0 \\ 0.0 & 0.0 & 0.002845 \end{bmatrix}$			
$CR = \begin{bmatrix} 1.0 & 0.9725 & -0.8632 \\ 0.9725 & 1.0 & -0.8297 \\ -0.8632 & -0.8297 & 1.0 \end{bmatrix}$			
$CV = 10^{-4} \times \begin{bmatrix} 0.441839 & 0.15094 & -0.163240 \\ 0.15094 & 0.05452 & -0.055118 \\ -0.163240 & -0.055118 & 0.080940 \end{bmatrix}$			
rms = 0.0066			

Table 4. Data and solution for Example 6

Data:

	Loading case	rms
	External Z	0.3359E-02
	External Y	0.4049E-02
	Indicator A	0.3590E-03
	Indicator B	0.2391E-03
	Indicator C	0.2499E-03

	Loading	Correlation			
		Ext. Y	Ind. A	Ind. B	Ind. C
External Z		-0.1103	0.7464	-0.5104	-0.5839
External Y			-0.0494	0.1740	-0.0955
Indicator A				-0.7201	-0.7499
Indicator B					0.0776

Solution:

$RM_G = \begin{bmatrix} 0.3359E-02 & 0.0 \\ 0.0 & 0.4049E-02 \end{bmatrix}$	$R = \begin{bmatrix} 116.718 & 19.979 \\ 233.475 & 41.397 \\ -0.345 & 0.137 \end{bmatrix} \quad (\text{from Table 2})$
$RM_I = \begin{bmatrix} 0.3590E-03 & 0.0 & 0.0 \\ 0.0 & 0.2391E-03 & 0.0 \\ 0.0 & 0.0 & 0.2499E-03 \end{bmatrix}$	$CR_G = \begin{bmatrix} 1.0000 & -0.1103 \\ -0.1103 & 1.0000 \end{bmatrix}$
$CV_G = 10^{-4} \times \begin{bmatrix} 0.112829 & -0.015500 \\ -0.015002 & 0.163944 \end{bmatrix}$	$CR_I = \begin{bmatrix} 1.0000 & -0.7201 & -0.7477 \\ -0.7201 & 1.0000 & 0.0776 \\ -0.7477 & 0.0776 & 1.0000 \end{bmatrix}$
$CV_{GI} = 10^{-6} \times \begin{bmatrix} 0.900070 & -0.409921 & -0.490134 \\ -0.071807 & 0.168452 & -0.096631 \end{bmatrix}$	$CR_{GI} = \begin{bmatrix} 0.7464 & -0.5104 & -0.5839 \\ -0.0494 & 0.1740 & -0.0955 \end{bmatrix}$
$CV_M = 10^{-2} \times \begin{bmatrix} 0.153825 & 0.029600 \\ 0.029600 & 0.007430 \end{bmatrix}$	$CV_I = 10^{-6} \times \begin{bmatrix} 0.128880 & -0.061812 & -0.067072 \\ -0.061811 & 0.057169 & 0.004637 \\ -0.067079 & 0.004637 & 0.062450 \end{bmatrix}$

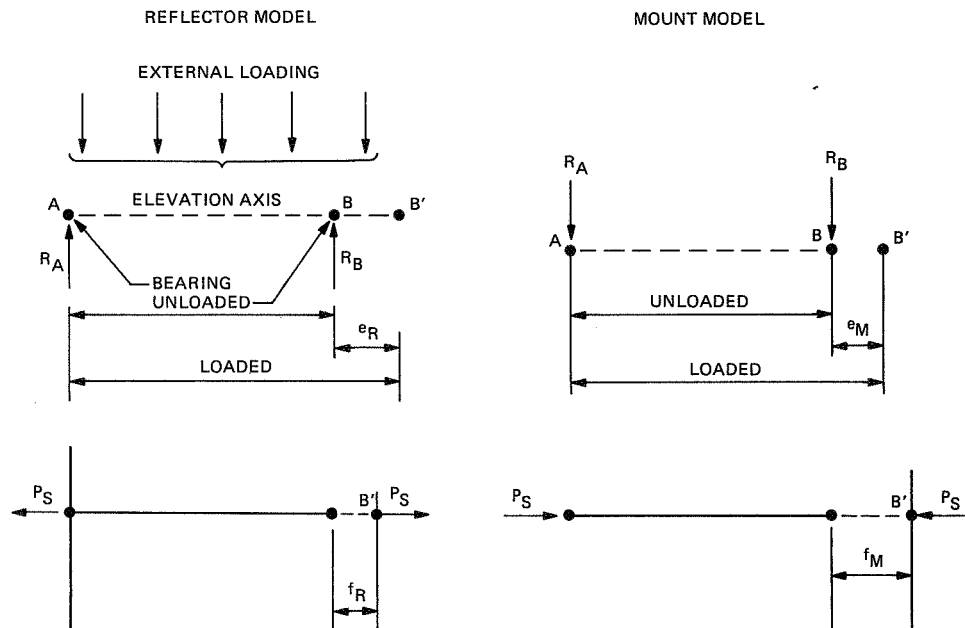


Fig. 1. Schematic for reflector-mount axis compatibility, Example 1.

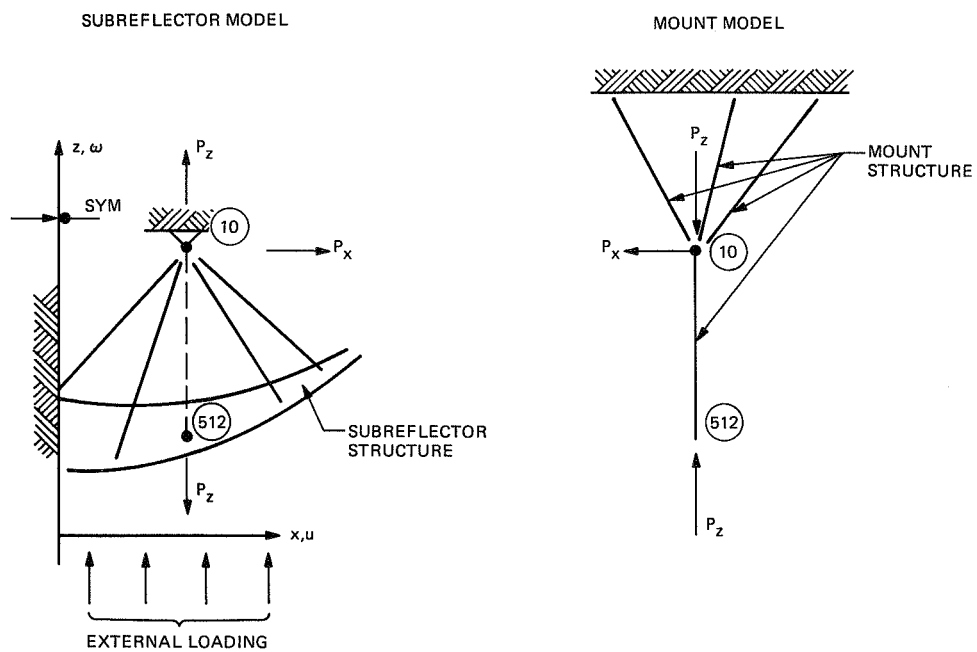


Fig. 2. Schematic for subreflector-mount model, Example 2.

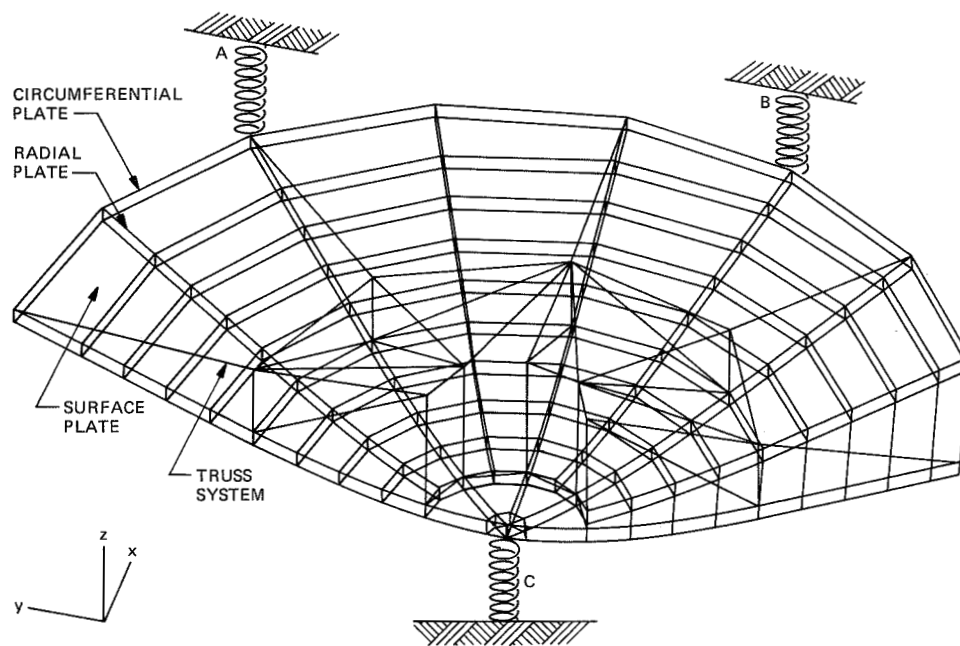


Fig. 3. Subreflector half-structure model, Example 3.